Ludwig-Maximilians-Universität München

Theory and application of the adjoint method in geodynamics and an extended review of analytical solution methods to the Stokes equation

Dissertation zur Erlangung des Doktorgrades
an der Fakultät für Geowissenschaften
der Ludwig-Maximilians-Universität München

vorgelegt von
André Horbach

München, 17. April 2020

Erstgutachter:
Prof. Dr. Hans-Peter Bunge
Sektion Geophysik
Department für Geo- und Umweltwissenschaften
Ludwig-Maximilians-Universität München
Theresienstraße 41
80333 München

Zweitgutachter:
Prof. Dr. Volker Michel
AG Geomathematik
Department Mathematik
Universität Siegen
Walter-Flex-Str. 3
57068 Siegen

Tag der mündlichen Prüfung:
17. Juli 2020

Contents

Summary

The initial condition problem with respect to the temperature distribution in the Earth's mantle is Pandora's box of geodynamics. The heat transport inside the Earth follows the principles of advection and conduction. But since conduction is an irreversible process, this mechanism leads to a huge amount of information getting lost over time. Due to this reason, a recovery of a detailed state of the Earth's mantle some million years ago is an intrinsically unsolvable problem. In this work we present a novel mathematical method, the adjoint method in geodynamics, that is not capable of solving but of circumventing the presented initial condition problem by reformulating this task in terms of an optimisation problem. We are aiming at a past state of the Earth's mantle that approaches the current and thus, observable state over time in an optimal way. To this end, huge computational resources are needed since the 'optimal' solution can only be found in an iterative process. In this work, we developed a new general operator formulation in order to determine the adjoint version of the governing equations of mantle flow and applied this method to the high-resolution numerical mantle circulation code TERRA. For our models, we used a global grid spacing of approx. 30 km and more than 80 million mesh elements. We found a reconstruction of the Earth's mantle at 40 Ma that is, with respect to our modelling parameters, consistent with today's observations, gathered from seismic tomography. With this published fundamental work, we are opening the door to a variety of future applications, e.g. a possible incorporation of geological and geodetic data sets as further constraints for the model trajectory over geological time scales.

Where high-resolution numerical models and even the implementation of inversion schemes have become feasible over the past decades due to increasing computational resources, in the community there is still a high demand for analytical solution methods. Restricting the physical parameter space in the governing equations, e.g. by only allowing for a radial varying viscosity, it can be shown that in some cases, the resulting simplified equations can even be solved in a (semi-)analytical way. In other words, in these simplified scenarios, no large scale computational resources or even high-performance clusters are needed but the solution for a global flow system can be determined in minutes even on a standard computer. Besides this apparent advantage, analytical and numerical solutions can even go hand-in-hand since numerical computer codes may be tested and benchmarked by means of these manufactured solutions. Here, we spend a large portion of this work with a detailed derivation of these analytical approaches. We basically start from scratch, having the intention to cover all possible traps and pitfalls on the way from the governing equations to their solutions and to provide a service to future scientists that are stuck somewhere in the middle of this road. Besides the derivation, we also present in detail how such an analytical approach can be used as a benchmark for a high-resolution mantle circulation code. We applied this theory to the prototype for a new high-performance mantle convection framework being developed in the Terra-Neo project and published the results along with a small portion of the derived theory.

In an additional chapter of this work, we focus on a detailed analysis of the current state of the Earth's gravitational field that is measured in an unimaginably accurate way by the recent satellite missions CHAMP, GRACE and GOCE. The origin of the link of our work to the gravitational field also lies in the analytical solution methods. It can be shown that due to the effect of flow induced dynamic topography, the Earth's gravity field is highly sensitive to the viscosity profile in the Earth's

mantle. We show that even without using any other external knowledge or data set, the gravitational field itself restricts the possible choices for the Earth's mantle viscosity to a well-defined parameter space. Furthermore, in the course of these examinations, we found that mantle processes are not capable of explaining the short wavelength signals in the observed gravity field at all, even with the best-fitting viscosity profile. To this end, we developed a simple crustal model that is only based on topographic data (ETOPO) and the principle of isostasy and showed that even with this very basic approach we can explain the majority of short length-scale features in the observed gravity signal. Finally, in combination with a (simple, static and analytic) mantle flow model based on a density field derived from seismic topography and mineralogy, we found a nearly perfect fit of modelled and observed gravitational data throughout all wavelengths under consideration (spherical harmonic degree and order up to $l = 100$).

Introduction

Over the past few decades, numerical codes that are designed to simulate dynamic processes in the Earth have become more and more sophisticated due to continuously increasing computational resources and the availability of modern supercomputers and high-performance clusters. Even the quest for exa-scale machines is not an unrealistic scenario any more. For geodynamicists this means that at the present time, it is possible to construct models of mantle flow with resolutions on the km-scale for the whole Earth's mantle (Burstedde et al., 2013; Rudi et al., 2015; Weismüller, 2016; Bauer, 2018). Where on the one hand, these models are permanently increasing in complexity and more and more additional physics are incorporated into the numerical codes, on the other hand the demand for analytical solution methods is still very high inside the geodynamics community. Analytical solution means that if we a-priori restrict the physical parameter space in the flow equations, e.g. by only allowing for a radial varying viscosity or assuming an incompressible flow, it can be shown that in some cases, the resulting simplified equations can even be solved in an analytical way. In other words, in these special scenarios, no large scale computational resources or even high-performance clusters are needed but the solution for a global flow system can be determined in minutes even on a standard computer. Besides this apparent advantage, analytical and numerical solutions can even go hand-in-hand since numerical computer codes may be tested and benchmarked by means of these manufactured solutions.

Due to increasing complexities in the numerical codes, it is a crucial task to develop efficient methods for the testing and verification of individual code components. Since analytical solutions can be designed to fulfil exactly these needs, they are of growing importance at the present time. To this end, the main part of our work is designed to give an extended review of these analytical approaches. We basically start from scratch, having the intention to cover all possible traps and pitfalls on the long road from the governing equations to their solutions. Our overall intention is to provide a service to all scientists that will deal with these analytic approaches in the future and to not miss out any crucial details in the derivation. Since in the course of this work, we will mainly focus on the mathematical details and perform a careful step-by-step derivation of the underlying equations of the Stokes matrix and propagator approach, here is the right place to give a brief historic overview how the analytic solutions methods have evolved over time.

The famous work by Hager and O'Connell (1978) was the first time appearance of a global flow model that was derived by analytical means. The authors used this concept to address the question if such a simple model can explain the dip angles of subduction zones when they enter the deep mantle. In the presented theory, the concept of a spherical harmonic analysis was applied to the governing equations in mantle dynamics. This is exactly the approach that we intend to rediscover in all details within the course of this thesis. The set of harmonic relations that were presented in their work still were of simple structure, they did not yet involve the coupling to the gravitational Poisson equation, i.e. self-gravity. Since there was no reference to the gravitational potential, also the concept of dynamic topography was not yet included in these equations. In order to achieve a scenario that can be compared to observations, in their work, a plate velocity data set was used for the velocity boundary condition at the Earth's surface. As we also will show in our work, it turns out that this is an inconsistent assumption due to the non-vanishing toroidal component of the plate velocity field, which the model is intrinsically not able to cope with. It should be mentioned that this work was

not the first time where a spherical harmonic approach was applied to the equations of motion. Also Hager and O'Connell (1978) states a reference to an earlier work by Takeuchi and Hasegawa (1965), where the main parts of the system of equations can already be found. At this point, we want to highlight the work by Takeuchi and Hasegawa (1965) also due to personal reasons. A tiny sub-clause in their publication yielded a real breakthrough in the derivations that we did for our work. As at one point we were completely stuck, the discovery of this sentence changed our overall perspective and led us to a path that in the end turned out to be a successful one.

This ground-breaking work by Hager and O'Connell (1978), in particular the demonstration of possible applications to real data of this new analytic approach, marks the starting point of a variety of proceeding publications. In Hager and O'Connell (1979) they provided an even more detailed extension of their original work on the subduction zone dip angles. The next essential step was then developed in Hager and O'Connell (1981) where the previous system of equations was coupled to the gravitational Poisson equation. In this certain work, the authors also revived the discussion about the application of plate velocities as a boundary condition at the Earth's surface and the most probable intrinsic inconsistency of this approach. A final step of extending the equations can be found in Panasyuk et al. (1996), where the effects of compressibility of the Earth's mantle are incorporated into the system of equations.

With the coupling of the Poisson equation to the Stokes system, it was possible to extend the examinations of the derived flow solutions in terms of the Earth's gravitational field. Soon, it became clear that the mechanism of dynamic topography, that is coupled to the radial stresses at both domain boundaries, needs to be incorporated into the equations. Here, the first publications that related surface topography and gravity anomalies, derived by analytical flow models, were Parsons and Daly (1983); Ricard et al. (1984); Hager (1984); Forte and Peltier (1987). The work by Richards and Hager (1984) provides an extended analysis of the explicit mathematical formalism that is needed for the new formulation of the boundary conditions due to dynamic topography. Moreover, this work also creates a link to the Love number formalism (see e.g., Love, 1911; Munk and MacDonald, 1960) since like the Love numbers, also the kernels that are derived by the analytical approach describe the response (velocity, stresses, gravity signal, topography) of the system to a certain stimulus (density anomaly). Even though a detailed analysis of the relation between gravity signal and dynamic topography became a popular research topic at these times, the observation that the gravitational signal is also indirectly dependent on the mantle flow properties has already been noticed in an early work by Pekeris (1935) where it is stated that the gravitational effect due to surface deformation is opposite in sign and comparable in magnitude to that of the driving density contrast. In particular, this observation yielded the definition of the *admittance* as the ratio between gravity signal and surface dynamic topography. A recent review of this ratio with respect to its meaning and interpretation can be found in Colli et al. (2016).

All of the previously mentioned publications show that the modelled gravitational field is strongly sensitive to the underlying viscosity profile that was assumed for the mantle flow. All models show that a general fit to the observed data can only be achieved by creating a viscosity difference between upper and lower mantle, where the upper mantle has a $2-3$ magnitudes lower viscosity than the lower mantle. Further studies (see e.g., Schaber et al., 2009) show that the quest for a unique best-fitting viscosity profile is an unsolvable task since there is an intrinsic trade-off between viscosity jump and thickness of the low-viscosity zone. This is an observation that also could be verified by models of post glacial rebound (see e.g., Paulson and Richards, 2009). In Chapter 4 of our work, we are uncovering exactly this process of using satellite derived gravity data to constrain the flow parameters in terms of the viscosity profile in a systematic way.

Nevertheless, it turns out that static flow models are intrinsically not capable of resolving this non-uniqueness. Thus, at this stage we are forced to leave the analytical approach behind and turn the head towards time-dependent solutions. The idea behind this approach is that by incorporating time

into the equations, we are not restricted any more to a single state of the Earth's mantle but are equipped with a whole time series (trajectory) that can be checked against suitable time-dependent data sets.

Time-dependency enters the system of the flow equations by including conservation of energy. The energy equation is a differential equation in terms of the temperature and thus, an initial condition is required. The heat transport inside the Earth follows the principles of advection and conduction. But since conduction is an irreversible process, this mechanism leads to a huge amount of information getting lost over time. Due to this reason, a recovery of a detailed state of the Earth's mantle some million years ago is an intrinsically unsolvable problem. Here we present a novel mathematical method, the adjoint method in geodynamics, that is not capable of solving but of circumventing the initial condition problem by reformulating this task in terms of an optimisation problem, i.e. we are aiming at a past state of the Earth's mantle that approaches the current and thus, observable state over time in an optimal way.

Our general aim is that with a consistent time-dependent model for the temperature evolution inside the Earth's mantle and thus, also for all derived data like e.g. the gravitational field or dynamic topography, we open the door to a potentially wide area of time-dependent data sets, especially from geology, which our model, i.e. our assumed model parameters, may be tested against in the future.

At the end of this introduction, we want to present the structure of this work in a more detailed way and give a short summary and an overview of the topics that are included in each chapter.

Outline of this work

Chapter 1: Mathematical preliminaries

The first chapter of this work builds up the mathematical foundation that is used within the whole thesis. Since the main part of this work deals with the detailed derivation of analytic solutions to the Stokes equation, our goal was to be as accurate as possible in setting up the mathematical basis. The analytic solution methods require a representation of the governing equations in terms of scalar, vector and tensor spherical harmonics. To this end, we give a detailed introduction to these special functions, including their basis, the Legendre polynomials and associated Legendre functions. At the end of this section we even briefly dive into spheres that are way beyond the scope of this work. Where in the course of this work, we will in general only consider harmonic degrees up to $l = 100$, the geodetic community has to operate in a completely different setting. Due to the high resolution of the measurements of current satellite missions, here, one has to cope with harmonic degrees beyond $l = 2500$, the *ultra-high* harmonics. Here, we give a brief overview of the main challenges that come to the fore when dealing with spherical harmonics in this ultra-high frequency band.

The end of this chapter forms one of the most crucial parts of this thesis. The representation of the various differential operators, i.e. divergence, gradient, curl, Laplace, in terms of spherical harmonics turns out to be the key for a successful transfer of the flow equations into the frequency domain that we will perform in Chapter 2.

Chapter 2: Continuum mechanics

Here, we give a brief introduction to the governing equations in mantle dynamics that are based on the physical principles of mass, momentum, angular momentum and energy conservation. In case of the Earth's mantle, due to the low Reynolds number, the momentum equation reduces to the time-independent Stokes equation. In the course of this chapter, we adapt the way of thinking in terms of harmonic coefficients that we have learned in the first chapter onto the derived conservation equations. We find explicit relations between the harmonic coefficients of the physical quantities under

consideration and in the end, we are able to transform these relations into a system of differential equations that can be solved by the famous propagator matrix method.

Chapter 3: A semi-analytic accuracy benchmark for 3-D Stokes flow

In this part of the work we investigate a special case of the equations that we derived in Chapter 2. Assuming the most simple scenario of an incompressible and isoviscous flow, the system of differential equations even reduces to a ordinary differential equation that can be solved in a straightforward way without applying the propagator matrix approach that was necessary in the previous chapter.

We demonstrate the importance of this special case by showing that in this way it is possible to set-up a straightforward and easy-to-implement test scenario, i.e. a benchmark, for numerical mantle circulation codes. Besides showing the theory, we also apply our derived test apparatus to the prototype for a new high-performance mantle convection framework being developed in the Terra-Neo project.

The results of this chapter are published together with some parts of the mathematical preliminaries (Chapter 1) and some foundations on continuum mechanics (Chapter 2) in the 'International Journal on Geomathematics' (GEM) (2020) as 'Horbach, A., Mohr, M., Bunge, H.-P.: A Semi-Analytic Accuracy Benchmark for Stokes Flow in 3-D Spherical Mantle Convection Codes', doi.org/10.1007/s13137-019-0137-3 (see Horbach et al., 2020).

Chapter 4: The Earth's gravitational field

In this chapter, we use satellite derived measurements of the Earth's gravity field in order to constrain the free parameter space of the analytic flow models that we derived in Chapter 2. Furthermore, we perform a harmonic analysis on the observed gravity field and try to relate different harmonic frequency bands to their different origin and the physical processes behind. Here we learn that mantle flow processes are in general not capable of explaining the high-frequency parts of the observed gravity field. To this end, we develop a simple crustal model, only based on topography data and isostasy. We find that already this basic model explains the main gravity signals in the higher harmonics.

Chapter 5: The adjoint method in geodynamics

Where all previous chapters have dealt with the static problem, in the final chapter of this work, we introduce time-dependency into the flow equations by means of the conservation of energy. Here we present a novel mathematical technique, the adjoint method, i.e. a strategy to overcome the intrinsic initial condition problem with respect to the temperature field. We present a detailed derivation of the adjoint equations in geodynamics using a general operator approach and apply the theory to the high-resolution numerical mantle circulation model TERRA. As a final result, we reconstructed a state of the Earth's mantle at 40 Ma that is, with respect to our modelling parameters, consistent with today's observations, gathered from seismic tomography.

The results of this chapter are published together with some parts of the mathematical preliminaries (Chapter 1) and some foundations on continuum mechanics (Chapter 2) in the 'International Journal on Geomathematics' (GEM) (2014) as 'Horbach, A., Bunge, H.-P., Oeser J.: The adjoint method in geodynamics: derivation from a general operator formulation and application to the initial condition problem in a high resolution mantle circulation model', doi.org/10.1007/s13137-014-0061-5 (see Horbach et al., 2014).

Chapter 1

Mathematical preliminaries

In this chapter we present fundamental mathematical techniques that are used throughout this whole work. We especially focus on properties of a spherical geometry, where the representation of differential operators in a spherical coordinate system plays an essential role. Furthermore, we investigate the role of scalar, vector and tensor spherical harmonics as appropriate basis systems for functions on the sphere.

1.1 General notation and basics

We denote the set of all positive integers as $\mathbb{N}$ and all non-negative integers as $\mathbb{N}_0$. The set of all integers is denoted by $\mathbb{Z}$, where $\mathbb{R}$ forms the set of all real numbers with $\mathbb{R}^+$ being all positive real numbers and $\mathbb{R}_0^+$ being all non-negative real numbers.

For two elements $x, y \in \mathbb{R}^n$, $n \in \mathbb{N}$, we define the Euclidean **scalar** (or **inner**) **product** (in the Euclidean case also denoted as **dot product**) as the mapping $\langle \cdot, \cdot \rangle : \mathbb{R}^n \times \mathbb{R}^n \to \mathbb{R}$ with

$$\langle x, y \rangle := x \cdot y := \sum_{i=1}^{n} x_i y_i \,, \tag{1.1}$$

and the Euclidean **norm** as the mapping $\| \cdot \| : \mathbb{R}^n \to \mathbb{R}$ with

$$\|x\| := |x| := \sqrt{\sum_{i=1}^{n} x_i^2} \,. \tag{1.2}$$

In general, every inner product $\langle \cdot, \cdot \rangle$ induces a norm $\| \cdot \|$ by $\| \cdot \| := \sqrt{\langle \cdot, \cdot \rangle}$, thus, we see that the Euclidean norm is the norm that is induced by the Euclidean scalar product. With respect to the Euclidean norm and scalar product, the vector triple $\epsilon^1 := (1,0,0)^T, \epsilon^2 := (0,1,0)^T, \epsilon^3 := (0,0,1)^T$ forms an orthonormal system in $\mathbb{R}^3$ and is called Euclidean basis system. Furthermore, in any Hilbert space H, the inner product can in general be used to define the angle $\alpha := \angle(x, y)$ between two elements $x, y \in H$. More precisely, we define

$$\alpha := \arccos \frac{\langle x, y \rangle}{\|x\| \|y\|} \,. \tag{1.3}$$

Due to the Cauchy-Schwarz(-Bunjakowski) inequality

$$\langle x, y \rangle \leq \|x\| \|y\| \,, \tag{1.4}$$

that is valid for all $x, y \in H$, we see that the argument of arccos in the previous equation is well-defined. For the Euclidean scalar product we find the well-known relation

$$x \cdot y = |x||y| \cos \alpha \,. \tag{1.5}$$

We see that in a geometrical sense, the dot product is a measure for the parallelism of two vectors. Its absolute value becomes maximal for $\alpha = 0$ and $\alpha = \pi$ (then $|x \cdot y| = |x||y|$) and minimal for $\alpha = \pi/2$ and $\alpha = 3\pi/2$ (then $|x \cdot y| = 0$).

The so-called **vector** (or **cross**) **product** is designed to reflect exactly the opposite. We define the mapping $\wedge : \mathbb{R}^3 \times \mathbb{R}^3 \to \mathbb{R}^3$ - sometimes also denoted by '$\times$' - as

$$x \wedge y := (|x||y| \sin \alpha)\, n \,, \tag{1.6}$$

where $n \in \mathbb{R}^3$ is a (normalised) vector that is orthogonal to either x and y. The natural ambiguity of the orthogonal vector is erased by the convention that (x, y, n) has to span a right-handed system. If x or y is the zero vector then $x \wedge y$ is defined to be zero. If x is parallel to y then there is also no unique orthogonal vector but due to $\sin \alpha = 0$, the vector product is zero anyway. In analogy to the dot product, the vector product is geometrically spoken a measure for the perpendicularity of two vectors. Its absolute value becomes maximal for $\alpha = \pi/2$ and $\alpha = 3\pi/2$ (then $|x \wedge y| = |x||y|$) and minimal for $\alpha = 0$ and $\alpha = \pi$ (then $|x \wedge y| = 0$). It can easily be verified that the absolute value of the vector product equals the area of the parallelogram that is spanned by x and y, since $|y| \sin \alpha$ equals its height. We will use this property later when we define surface integrals. Furthermore, it is also possible to define the vector product for n-dimensional spaces, i.e. find a vector that is orthogonal to $n-1$ given vectors, but here, we restrict ourselves to the $\mathbb{R}^3$.

It can be shown that the vector product satisfies the following conditions: First, it is anti-symmetric, i.e.

$$x \wedge y = -y \wedge x \tag{1.7}$$

for all $x, y \in \mathbb{R}^3$ - which implies that $x \wedge x = 0$ for all $x \in \mathbb{R}^3$ - and it is (bi-)linear, i.e.

$$(\lambda x + y) \wedge z = \lambda x \wedge z + y \wedge z \tag{1.8}$$

for all $x, y, z \in \mathbb{R}^3$ and $\lambda \in \mathbb{R}$. If we assume that there is a right-handed orthonormal system $\{\epsilon^i\}_{i=1,2,3}$ (not necessarily Cartesian) such that any $x \in \mathbb{R}^3$ can be represented as $\sum_i x_i \epsilon^i$ we find the well-known representation

$$\begin{aligned} x \wedge y &= \left(\sum_{i=1}^{3} x_i \epsilon^i \right) \wedge \left(\sum_{i=1}^{3} y_i \epsilon^i \right) = \sum_{i=1}^{3} \sum_{j=1}^{3} x_i y_j \epsilon^i \wedge \epsilon^j \\ &= x_1 y_1\, \epsilon^1 \wedge \epsilon^1 + x_1 y_2\, \epsilon^1 \wedge \epsilon^2 + x_1 y_3\, \epsilon^1 \wedge \epsilon^3 + \\ &\quad x_2 y_1\, \epsilon^2 \wedge \epsilon^1 + x_2 y_2\, \epsilon^2 \wedge \epsilon^2 + x_2 y_3\, \epsilon^2 \wedge \epsilon^3 + \\ &\quad x_3 y_1\, \epsilon^3 \wedge \epsilon^1 + x_3 y_2\, \epsilon^3 \wedge \epsilon^2 + x_3 y_3\, \epsilon^3 \wedge \epsilon^3 \\ &= x_1 y_2\, \epsilon^3 - x_1 y_3\, \epsilon^2 - x_2 y_1\, \epsilon^3 + x_2 y_3\, \epsilon^1 + x_3 y_1\, \epsilon^2 - x_3 y_2\, \epsilon^1 \\ &= \begin{pmatrix} x_2 y_3 - x_3 y_2 \\ x_3 y_1 - x_1 y_3 \\ x_1 y_2 - x_2 y_1 \end{pmatrix} . \end{aligned} \tag{1.9}$$

The combination of dot and vector product of the form

$$x \cdot (y \wedge z) \tag{1.10}$$

is called **triple product**. Since

$$|x \cdot (y \wedge z)| = |x||y \wedge z| \cos \alpha = A|x| \cos \alpha \,, \tag{1.11}$$

where A is the area of the parallelogram spanned by y and z and α the angle between x and the normal n of the area A, the absolute value of the triple product equals the volume of the parallelepiped spanned by x, y and z. This property will later be useful when we will define volume integrals. Using the representation (1.9) of the vector product, we find for the triple product that

$$\begin{aligned} x \cdot (y \wedge z) &= x \cdot \begin{pmatrix} y_2 z_3 - y_3 z_2 \\ y_3 z_1 - y_1 z_3 \\ y_1 z_2 - y_2 z_1 \end{pmatrix} \\ &= x_1(y_2 z_3 - y_3 z_2) - x_2(y_1 z_3 - y_3 z_1) + x_3(y_1 z_2 - y_2 z_1)\,. \end{aligned} \tag{1.12}$$

Due to Laplace' formula for determinants, we can identify the previous relation by means of a determinant, i.e. the determinant of the matrix that is built by the vectors x, y and z, i.e.

$$x \cdot (y \wedge z) = \det(x \mid y \mid z) = \det \begin{pmatrix} x_1 & y_1 & z_1 \\ x_2 & y_2 & z_2 \\ x_3 & y_3 & z_3 \end{pmatrix}. \tag{1.13}$$

Thus, the determinant of a matrix especially equals the volume of the parallelepiped that is spanned by its column (or row) vectors. This is not only true for the previously discussed case $\mathbb{R}^3$ but also for all dimensions $n \in \mathbb{N}$ (especially $n = 2$ where the parallelepiped is just a parallelogram).

If $A \in \mathbb{R}^{n\times l}, B \in \mathbb{R}^{l\times m}$, $n, m, l \in \mathbb{N}$ are two matrices, the matrix multiplication, which results in an $n \times m$ matrix, is defined by

$$AB := \left(\sum_{k=1}^{l} A_{ik} B_{kj} \right)_{i,j}. \tag{1.14}$$

A variation of the special case $l = 1$, where we have the multiplication of a column and a row vector, is called the **tensor** (or **dyadic**) **product** $\otimes : \mathbb{R}^n \times \mathbb{R}^m \to \mathbb{R}^{n\times m}$, $n, m \in \mathbb{N}$. More precisely, here we have for $x \in \mathbb{R}^n$ and $y \in \mathbb{R}^m$ that

$$x \otimes y := x\, y^T = (x_i y_j)_{i,j} = \begin{pmatrix} x_1 y_1 & \dots & x_1 y_m \\ \vdots & \ddots & \vdots \\ x_n y_1 & \dots & x_n y_m \end{pmatrix}. \tag{1.15}$$

For a vector $x \in \mathbb{R}^m$ and a matrix $A \in \mathbb{R}^{n\times m}$, $n, m \in \mathbb{N}$, we define the vector-matrix product $\cdot : \mathbb{R}^m \times \mathbb{R}^{n\times m} \to \mathbb{R}^n$ as the row-wise application of the dot product. More precisely, we have

$$x \cdot A := (x \cdot A_{i\cdot})_i = \sum_{i=1}^{n} x_i \left(A\epsilon^i \right), \tag{1.16}$$

where here, the ϵ^i, $i = 1, ..., n$, represent the Euclidean basis vectors in $\mathbb{R}^n$.

With $n, m \in \mathbb{N}$, $k \in \mathbb{N}_0$ and $D \subset \mathbb{R}^n$ and $W \subset \mathbb{R}^m$ we denote the space of all k-times continuously differentiable functions $F : D \to W$ as $\mathrm{C}^{(k)}(D, W)$. In case of $k = 0$, the space of all continuous functions, we use the abbreviation $\mathrm{C}(D, W) := \mathrm{C}^{(0)}(D, W)$ and we also allow $k = \infty$, the space of all arbitrarily often continuously differentiable functions (e.g. polynomials). Since in this work we will only consider scalar, vector and tensor valued functions, we define the convention to use upper case letters for scalar, lower case letters for vector and **bold** lower case letters for tensor valued functions and spaces. Especially, we define $\mathrm{C}^{(k)}(D) := \mathrm{C}^{(k)}(D, \mathbb{R})$ with elements $F, G, ...$, $\mathrm{c}^{(k)}(D) := \mathrm{C}^{(k)}(D, \mathbb{R}^3)$ with elements $f, g, ...$ and $\mathbf{c}(D) := \mathrm{C}^{(k)}(D, \mathbb{R}^3 \times \mathbb{R}^3)$ with elements $\mathbf{f}, \mathbf{g}, ...$ Furthermore, from now on - if not explicitly stated differently - $D \subset \mathbb{R}^3$ denotes a compact subset of $\mathbb{R}^3$ and Ω is defined as the unit sphere in $\mathbb{R}^3$, i.e. $\Omega := \{x \in \mathbb{R}^3 || x| = 1\}$. Note that using the Euclidean basis vectors, every vector field f may be represented by $f = \sum_i f_i \epsilon^i$ and every tensor field by $\mathbf{f} = \sum_{i,j} \mathbf{f}_{ij} \epsilon^i \otimes \epsilon^j$, where

f_i and $\mathbf{f}_{ij}$ are scalar functions.
The respective sets of all continuous scalar, vector and tensor valued functions $\mathrm{C}(D)$, $\mathrm{c}(D)$, $\mathbf{c}(D)$ can be equipped with a norm, the so-called maximum norm, i.e. for all $F \in \mathrm{C}(D)$, $f \in \mathrm{c}(D)$, $\mathbf{f} \in \mathbf{c}(D)$ we define

$$\begin{aligned} \|F\|_{\mathrm{C}(D)} &:= \|F\|_\infty := \max_{x \in D} |F(x)| \,, \\ \|f\|_{\mathrm{c}(D)} &:= \|f\|_\infty := \max_{x \in D} |f(x)| \,, \\ \|\mathbf{f}\|_{\mathbf{c}(D)} &:= \|\mathbf{f}\|_\infty := \max_{x \in D} |\mathbf{f}(x)| \,. \end{aligned} \tag{1.17}$$

The space of all scalar functions F on D that are p-integrable, i.e.

$$\left(\int_D |F(x)|^p \, \mathrm{d}x \right)^{\frac{1}{p}} < \infty \,, \tag{1.18}$$

is denoted by $\mathcal{L}^p(D)$, with $p > 1$. If we merge all functions that are equal except for null sets into equivalence classes, the set of all resulting equivalence classes can be equipped by a norm using the property above (this cannot be done without the equivalence classes because in that case, the norm would not be positive definite). More precisely, we define the set $\mathcal{N}^p(D) := \{F \in \mathcal{L}^p(D) | F = 0 \text{ almost everywhere}\}$ such that $\mathrm{L}^p(D) := \mathcal{L}^p(D)/\mathcal{N}^p(D)$ forms the set of all equivalence classes of almost everywhere identical functions $F \in \mathcal{L}^p(D)$. Now, for all $F \in \mathrm{L}^p(D)$ the p-norm is defined by

$$\|F\|_p := \left(\int_D |F(x)|^p \, \mathrm{d}x \right)^{\frac{1}{p}} . \tag{1.19}$$

In the special case of $p = 2$, we can even define a scalar product, the L^2 scalar product, where for $F, G \in \mathrm{L}^2(D)$, we set

$$\langle F, G \rangle_{\mathrm{L}^2(D)} := \int_D F(x) \, G(x) \, \mathrm{d}x \,. \tag{1.20}$$

We see that the L^2 norm is induced by the previously defined L^2 scalar product. Together with the L^2 scalar product, the space $\mathrm{L}^2(D)$ is a Hilbert space. Indeed, we can find a general relation of the p-norms and the previously defined maximum norm. For the special case of $D = \Omega$ we find for all $F \in \mathrm{C}(\Omega)$ that

$$\|F\|_{\mathrm{L}^p(\Omega)} \leq (4\pi)^{\frac{1}{p}} \, \|F\|_{\mathrm{C}(\Omega)} \,. \tag{1.21}$$

This relation also implies that $\mathrm{C}(\Omega) \subset \mathrm{L}^p(\Omega)$ for all $p > 1$. In 1D we find for the special case $D = [-1, 1]$ that

$$\|F\|_{\mathrm{L}^2([-1,1])} \leq 2^{\frac{1}{p}} \, \|F\|_{\mathrm{C}([-1,1])} \,, \tag{1.22}$$

and thus also $\mathrm{C}([-1, 1]) \subset \mathrm{L}^2([-1, 1])$. All of the previous definitions can be analogously transferred to vector and tensor fields. Here we denote the respective spaces as $\mathrm{l}^p(D)$ and $\mathbf{l}^p(D)$.

In spaces, where scalar products and norms are available, a variety of ways open up how to represent and even approximate elements within. Provided by an orthonormal system $\{u_n\}_{n \in \mathbb{N}}$ in the Hilbert space H, it can be shown that the following statements are equivalent:

a) The system $\{u_n\}_{n \in \mathbb{N}_0}$ is closed in X, i.e. for all $x \in X$ and for all $\epsilon > 0$ there exists an $N \in \mathbb{N}_0$ and coefficients $a_0, ..., a_N \in \mathbb{R}$ such that

$$\left\| x - \sum_{i=0}^{N} a_i u_i \right\|_X < \epsilon \,.$$

b) The **Fourier series** of an element $x \in X$ converges to x with respect to $\|\cdot\|_X$, i.e.

$$\lim_{N\to\infty} \left\| x - \sum_{i=0}^{N} \langle x, u_i\rangle_X \, u_i \right\|_X = 0 \,.$$

c) The **Parseval identities** hold, i.e. for all $x, y \in X$ we have:

$$\begin{aligned} \langle x, y\rangle_X &= \sum_{i=0}^{\infty} \langle x, u_i\rangle_X \, \langle y, u_i\rangle_X \,, \\ \|x\|_X^2 &= \sum_{i=0}^{\infty} |\langle x, u_i\rangle_X|^2 \,. \end{aligned} \tag{1.23}$$

d) The system $\{u_n\}_{n\in\mathbb{N}_0}$ is complete in X, i.e. let $x \in X$, then

$$\langle x, u_n\rangle_X = 0 \text{ for all } n \in \mathbb{N}_0 \;\Leftrightarrow\; x = 0 \,.$$

e) Each $x \in X$ is uniquely determined by its Fourier coefficients, i.e. let $x, y \in X$, then

$$\langle x, u_n\rangle_X = \langle y, u_n\rangle_X \text{ for all } n \in \mathbb{N}_0 \;\Leftrightarrow\; x = y \,.$$

The second Parseval identity can be regarded as a generalisation of Pythagoras' Theorem, i.e. the sum of the squares of each vector component - with respect to the orthonormal system - equals the square of the total vector length. Furthermore, this identity implies that due to the convergence of the series, for all $x \in X$ the inner product $\langle x, u_n\rangle_X$ converge to 0 for $n \to \infty$ or in other words, the elements u_n of the orthonormal system converge weakly to 0.

This is one of the most important fundamental theorems in the theory of Hilbert spaces. But note that this theorem just provides equivalences and no general statements for orthonormal systems. In general, one needs an *entrance* to this theorem via one of the conditions a)-e) to ensure that all other statements are also valid. Commonly, this is achieved via a), the closure property. A proof of this theorem can be found e.g. in Heuser (1986).

Regular surfaces

In the course of this work we will regularly come across functions that are defined on any kind of surfaces $\Sigma \subset \mathbb{R}^3$, like e.g. the Earth's surface or the core-mantle boundary. Since in most cases it will be necessary to analyse these functions with respect to their differential behaviour, we need to ensure that the application of the desired kind of differential operators is possible on the respective domain, i.e. the determination of a unique normal vector must be guaranteed for each $x \in \Sigma$, the surface needs to be kind of *smooth* and there may be no edges or double points. These requirements can formally be fulfilled if we assume that:

(i) For each $s \in \Sigma$ there exists an open set $V \subset \mathbb{R}^3$ with $s \in V$ such that there exists a parametrisation of $V \cap \Sigma$, i.e. there exists an open set $U \subset \mathbb{R}^2$ and a function $\phi : U \to V \cap \Sigma$ that is a homeomorphism (i.e. bijective and continuously invertible).

(ii) ϕ is differentiable and for each $u \in U$ the differential of ϕ, which is the linear mapping $D\phi(u) : \mathbb{R}^2 \to \mathbb{R}^3$ defined as $D\phi(u)(x) := J_\phi(u)x$, $x \in \mathbb{R}^2$, where $J_\phi(u)$ denotes the Jacobian of ϕ, evaluated at $u \in U$, is injective. This is equivalent to the condition that $\operatorname{rank}(J_\phi(u)) = 2$.

Property (i) ensures that the surface contains no edges or double points where property (ii) guarantees that we find a unique normal vector for each $s \in \Sigma$ and thus, it is also possible to define a unique tangential plane at each point in Σ. It can be shown that this tangential plane is spanned by the two

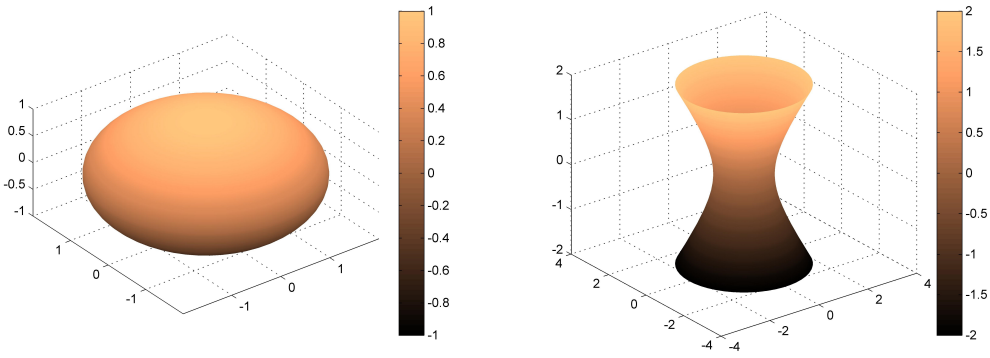

Figure 1.1: Left: rotational ellipsoid with the parametrisation $\phi(u,v) = (2\sqrt{1-t^2}\cos u, 2\sqrt{1-t^2}\sin u, t)^T$, $u \in [0, 2\pi[$, $t \in [-1,1]$. Right: hyperboloid with the parametrisation $\phi(u,v) = (\cos u - t\sin u, \sin u + t\cos u, t)^T$, $t \in [-2,2]$, $u \in [0, 2\pi[$.

column vectors of the Jacobian $J_\phi(s)$ at s. Since $J_\phi(s)$ has rank 2, the two column vectors always are linearly independent.

A surface Σ that satisfies the two previous conditions is called a **regular surface**. Common examples of a regular surface is the sphere, the ellipsoid or the hyperboloid which can be found in Figure 1.1. Contrarily, Figure 1.2 shows two examples of surfaces that are not regular. The surface on the left is defined by the parametrisation $\phi(u,v) = (u^3, v^3, uv)^T$, $u, v \in]-1,1[$. This surface satisfies property (i) but it can be easily shown that the Jacobian of ϕ does not have full rank for $(u,v) = (0,0)$, $\phi(u,v) = (0,0,0)^T$. Thus, it is not possible to define a unique normal vector at $(0,0,0)$ which can also be verified by just having an attentive view at the plot of the surface.

The surface on the right is defined by the parametrisation $\phi(u,v) = (\sin u, \sin 2u, v)^T$, $u \in]0, 2\pi[$, $v \in [0,1]$. We see that this is a parametrisation of a ribbon in shape of an 'eight'. Is can be shown that this is not a regular surface since the inverse of the parametrisation ϕ is not continuous for points of the form $(0,0,v)$, $v \in [0,1]$. Even - due to the definition of u (open interval) - the ribbon is open and not touching itself, at the endpoints, the distance to the other part of the ribbon is infinitely small such that the continuity of the inverse parametrisation is no longer satisfied. But if we e.g. refined the interval for u and changed it to $u \in]\frac{\pi}{2}, \frac{3\pi}{2}[$, the surface would be regular.

Just for the use in this work we define an additional third property that regular surfaces need to satisfy. This property does not belong to the definition of regular surfaces that can be commonly found in literature but is necessary for the applications in this work:

(iii) Σ divides $\mathbb{R}^3$ into a bounded inner region Σ_{int} and an unbounded outer region $\Sigma_{\text{ext}} = \mathbb{R}^3 \setminus \overline{\Sigma_{\text{int}}}$ with $\overline{\Sigma_{\text{int}}} = \Sigma_{\text{int}} \cup \Sigma$.

This means that Σ is *closed* in a geometrical sense which makes e.g. the hyperboloid not a regular surface any more. The definition of inner and outer regions allows us to define that from now on, all normal vectors point per definition into the outer region of the regular surface.

1.2 Differentiation in $\mathbb{R}^3$

Any $x \in \mathbb{R}^3 \setminus \{0\}$ can be uniquely represented by $x = r\xi$, where $r = |x|$ and $\xi \in \Omega$. A suitable way to represent an element on the unit sphere is the usage of the longitude and the polar distance (or the (co)latitude). These considerations lead to the following definition of spherical polar coordinates and

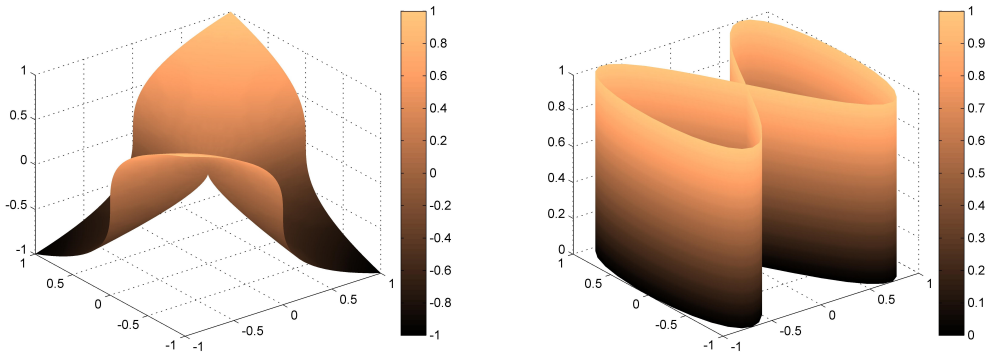

Figure 1.2: Left: A surface with parametrisation $\phi(u,v) = (u^3, v^3, uv)^T$, $u, v \in [-1,1]$. This surface does not satisfy the differentiability condition. At $(0,0,0)^T$ a normal vector to the surface cannot be defined. Right: A surface with the parametrisation $\phi(u,v) = (\sin u, \sin 2u, v)^T$, $u \in]0, 2\pi[$, $v \in [0,1]$. This is not a regular surface since the parametrisation is not continuously invertible.

their transformation into Cartesian coordinates. For any $x \in \mathbb{R}^3$ we find that:

$$x(r,\varphi,t) = r \begin{pmatrix} \sqrt{1-t^2}\cos\varphi \\ \sqrt{1-t^2}\sin\varphi \\ t \end{pmatrix} \quad \text{or} \quad x(r,\vartheta,\varphi) = r \begin{pmatrix} \sin\vartheta\cos\varphi \\ \sin\vartheta\sin\varphi \\ \cos\vartheta \end{pmatrix}, \tag{1.24}$$

where $r := |x| \in \mathbb{R}_0^+$ is the distance to the origin, $\varphi \in [0, 2\pi[$ the longitude, $t := \cos\vartheta \in [-1,1]$ the polar distance with the colatitude $\vartheta \in [0,\pi]$. This representation yields a (local) orthonormal basis of $\mathbb{R}^3$, the so-called moving orthonormal triad that can be obtained explicitly by calculating the (normalised) partial derivatives of the representation above. Here we find that

$$\frac{\partial x}{\partial r} = \begin{pmatrix} \sqrt{1-t^2}\cos\varphi \\ \sqrt{1-t^2}\sin\varphi \\ t \end{pmatrix}, \quad \frac{\partial x}{\partial \varphi} = \begin{pmatrix} -r\sqrt{1-t^2}\sin\varphi \\ r\sqrt{1-t^2}\cos\varphi \\ 0 \end{pmatrix}, \quad \frac{\partial x}{\partial t} = \begin{pmatrix} -\frac{rt}{\sqrt{1-t^2}}\cos\varphi \\ -\frac{rt}{\sqrt{1-t^2}}\sin\varphi \\ r \end{pmatrix}, \tag{1.25}$$

and we denote their respective absolute value by

$$b_r := \left|\frac{\partial x}{\partial r}\right| = 1\,, \quad b_\varphi := \left|\frac{\partial x}{\partial \varphi}\right| = r\sqrt{1-t^2}\,, \quad b_t := \left|\frac{\partial x}{\partial t}\right| = \frac{r}{\sqrt{1-t^2}}\,. \tag{1.26}$$

Thus, our local orthonormal basis can be determined as

$$\epsilon^r(\varphi,t) = \begin{pmatrix} \sqrt{1-t^2}\cos\varphi \\ \sqrt{1-t^2}\sin\varphi \\ t \end{pmatrix}, \; \epsilon^\varphi(\varphi) = \begin{pmatrix} -\sin\varphi \\ \cos\varphi \\ 0 \end{pmatrix}, \; \epsilon^t(\varphi,t) = \begin{pmatrix} -t\cos\varphi \\ -t\sin\varphi \\ \sqrt{1-t^2} \end{pmatrix} \tag{1.27}$$

where $\epsilon^r \wedge \epsilon^\varphi = \epsilon^t$, $\epsilon^\varphi \wedge \epsilon^t = \epsilon^r$ and $\epsilon^t \wedge \epsilon^r = \epsilon^\varphi$, or alternatively

$$\epsilon^r(\vartheta,\varphi) = \begin{pmatrix} \sin\vartheta\cos\varphi \\ \sin\vartheta\sin\varphi \\ \cos\vartheta \end{pmatrix}, \; \epsilon^\vartheta(\vartheta,\varphi) = \begin{pmatrix} \cos\vartheta\cos\varphi \\ \cos\vartheta\sin\varphi \\ -\sin\vartheta \end{pmatrix}, \; \epsilon^\varphi(\varphi) = \begin{pmatrix} -\sin\varphi \\ \cos\varphi \\ 0 \end{pmatrix}. \tag{1.28}$$

where $\epsilon^r \wedge \epsilon^\vartheta = \epsilon^\varphi$, $\epsilon^\vartheta \wedge \epsilon^\varphi = \epsilon^r$ and $\epsilon^\varphi \wedge \epsilon^r = \epsilon^\vartheta$. Note that $\epsilon^t = -\epsilon^\vartheta$.

In the geophysical and geodetic community it is common to use the colatitude ϑ what implies the

usage of ϵ^{ϑ}, where in the geomathematical community, people are quite familiar with the polar distance t and ϵ^t as the third basis vector. In this work we will consequently follow the geomathematical approach.

The inverse mapping, representing the Cartesian basis vectors in terms of the local basis can easily be determined as

$$\begin{aligned}
\epsilon^1 &= \sqrt{1-t^2}\,\cos\varphi\,\epsilon^r - \sin\varphi\,\epsilon^\varphi - t\cos\varphi\,\epsilon^t \\
\epsilon^2 &= \sqrt{1-t^2}\,\sin\varphi\,\epsilon^r + \cos\varphi\,\epsilon^\varphi - t\sin\varphi\,\epsilon^t \\
\epsilon^3 &= t\,\epsilon^r + \sqrt{1-t^2}\,\epsilon^t\,.
\end{aligned} \tag{1.29}$$

Applying this result to the dyadic products, we find the following conversion rules for the tensor basis vectors:

$$\begin{aligned}
\epsilon^{11} &= \left(1-t^2\right)\cos^2\varphi\,\epsilon^{rr} - \sqrt{1-t^2}\sin\varphi\cos\varphi\,\epsilon^{r\varphi} - t\sqrt{1-t^2}\cos^2\varphi\,\epsilon^{rt} \\
&\quad - \sqrt{1-t^2}\sin\varphi\cos\varphi\,\epsilon^{\varphi r} + \sin^2\varphi\,\epsilon^{\varphi\varphi} + t\sin\varphi\cos\varphi\,\epsilon^{\varphi t} \\
&\quad - t\sqrt{1-t^2}\cos^2\varphi\,\epsilon^{tr} + t\sin\varphi\cos\varphi\,\epsilon^{t\varphi} + t^2\cos^2\varphi\,\epsilon^{tt}\,, \\
\epsilon^{12} &= \left(1-t^2\right)\sin\varphi\cos\varphi\,\epsilon^{rr} + \sqrt{1-t^2}\cos^2\varphi\,\epsilon^{r\varphi} - t\sqrt{1-t^2}\sin\varphi\cos\varphi\,\epsilon^{rt} \\
&\quad - \sqrt{1-t^2}\sin^2\varphi\,\epsilon^{\varphi r} - \sin\varphi\cos\varphi\,\epsilon^{\varphi\varphi} + t\sin^2\varphi\,\epsilon^{\varphi t} \\
&\quad - t\sqrt{1-t^2}\sin\varphi\cos\varphi\,\epsilon^{tr} - t\cos^2\varphi\,\epsilon^{t\varphi} + t^2\sin\varphi\cos\varphi\,\epsilon^{tt}\,, \\
\epsilon^{21} &= \left(1-t^2\right)\sin\varphi\cos\varphi\,\epsilon^{rr} - \sqrt{1-t^2}\sin^2\varphi\,\epsilon^{r\varphi} - t\sqrt{1-t^2}\sin\varphi\cos\varphi\,\epsilon^{rt} \\
&\quad + \sqrt{1-t^2}\cos^2\varphi\,\epsilon^{\varphi r} - \sin\varphi\cos\varphi\,\epsilon^{\varphi\varphi} - t\cos^2\varphi\,\epsilon^{\varphi t} \\
&\quad - t\sqrt{1-t^2}\sin\varphi\cos\varphi\,\epsilon^{tr} + t\sin^2\varphi\,\epsilon^{t\varphi} + t^2\sin\varphi\cos\varphi\,\epsilon^{tt}\,, \\
\epsilon^{22} &= \left(1-t^2\right)\sin^2\varphi\,\epsilon^{rr} + \sqrt{1-t^2}\sin\varphi\cos\varphi\,\epsilon^{r\varphi} - t\sqrt{1-t^2}\sin^2\varphi\,\epsilon^{rt} \\
&\quad + \sqrt{1-t^2}\sin\varphi\cos\varphi\,\epsilon^{\varphi r} + \cos^2\varphi\,\epsilon^{\varphi\varphi} - t\sin\varphi\cos\varphi\,\epsilon^{\varphi t} \\
&\quad - t\sqrt{1-t^2}\sin^2\varphi\,\epsilon^{tr} - t\sin\varphi\cos\varphi\,\epsilon^{t\varphi} + t^2\sin^2\varphi\,\epsilon^{tt}\,, \\
\epsilon^{13} &= t\sqrt{1-t^2}\,\cos\varphi\,\epsilon^{rr} + \left(1-t^2\right)\,\cos\varphi\,\epsilon^{rt} \\
&\quad - t\,\sin\varphi\,\epsilon^{\varphi r} - \sqrt{1-t^2}\,\sin\varphi\,\epsilon^{\varphi t} - t^2\,\cos\varphi\,\epsilon^{tr} - t\sqrt{1-t^2}\,\cos\varphi\,\epsilon^{tt}\,, \\
\epsilon^{31} &= t\sqrt{1-t^2}\,\cos\varphi\,\epsilon^{rr} - t\,\sin\varphi\,\epsilon^{r\varphi} - t^2\,\cos\varphi\,\epsilon^{rt} \\
&\quad + \left(1-t^2\right)\,\cos\varphi\,\epsilon^{tr} - \sqrt{1-t^2}\,\sin\varphi\,\epsilon^{t\varphi} - t\sqrt{1-t^2}\,\cos\varphi\,\epsilon^{tt}\,, \\
\epsilon^{33} &= t^2\,\epsilon^{rr} + t\sqrt{1-t^2}\,\epsilon^{rt} + t\sqrt{1-t^2}\,\epsilon^{tr} - \left(1-t^2\right)\,\epsilon^{tt}\,, \\
\epsilon^{23} &= t\sqrt{1-t^2}\,\sin\varphi\,\epsilon^{rr} + \left(1-t^2\right)\,\sin\varphi\,\epsilon^{rt} \\
&\quad + t\,\cos\varphi\,\epsilon^{\varphi r} + \sqrt{1-t^2}\,\cos\varphi\,\epsilon^{\varphi t} - t^2\,\sin\varphi\,\epsilon^{tr} - t\sqrt{1-t^2}\,\sin\varphi\,\epsilon^{tt}\,, \\
\epsilon^{32} &= t\sqrt{1-t^2}\,\sin\varphi\,\epsilon^{rr} + t\,\cos\varphi\,\epsilon^{r\varphi} - t^2\,\sin\varphi\,\epsilon^{rt} \\
&\quad + \left(1-t^2\right)\,\sin\varphi\,\epsilon^{tr} + \sqrt{1-t^2}\,\cos\varphi\,\epsilon^{t\varphi} - t\sqrt{1-t^2}\,\sin\varphi\,\epsilon^{tt}\,,
\end{aligned} \tag{1.30}$$

where $\epsilon^{ij} := \epsilon^i \otimes \epsilon^j$ for all $i,j = 1,2,3$ and $i,j = r,\varphi,t$ respectively.

The Jacobian of the coordinate transformation from Cartesian to spherical polar coordinates can be derived as

$$J := \begin{pmatrix} \sqrt{1-t^2}\,\cos\varphi & -r\sqrt{1-t^2}\,\sin\varphi & -r\frac{t}{\sqrt{1-t^2}}\cos\varphi \\ \sqrt{1-t^2}\,\sin\varphi & r\sqrt{1-t^2}\,\cos\varphi & -r\frac{t}{\sqrt{1-t^2}}\sin\varphi \\ t & 0 & r \end{pmatrix}, \tag{1.31}$$

with its inverse

$$J^{-1} := \begin{pmatrix} \sqrt{1-t^2}\cos\varphi & \sqrt{1-t^2}\sin\varphi & t \\ -\frac{1}{r}\frac{1}{\sqrt{1-t^2}}\sin\varphi & \frac{1}{r}\frac{1}{\sqrt{1-t^2}}\cos\varphi & 0 \\ -\frac{t}{r}\sqrt{1-t^2}\cos\varphi & -\frac{t}{r}\sqrt{1-t^2}\sin\varphi & \frac{1}{r}\left(1-t^2\right) \end{pmatrix}. \tag{1.32}$$

Thus, the partial derivatives transform in the following way:

$$\begin{aligned} \partial_x &= \sqrt{1-t^2}\cos\varphi\,\partial_r - \frac{1}{r}\frac{1}{\sqrt{1-t^2}}\sin\varphi\,\partial_\varphi - \frac{t}{r}\sqrt{1-t^2}\cos\varphi\,\partial_t\,, \\ \partial_y &= \sqrt{1-t^2}\sin\varphi\,\partial_r + \frac{1}{r}\frac{1}{\sqrt{1-t^2}}\cos\varphi\,\partial_\varphi - \frac{t}{r}\sqrt{1-t^2}\sin\varphi\,\partial_t\,, \\ \partial_z &= t\,\partial_r + \frac{1}{r}\left(1-t^2\right)\partial_t\,. \end{aligned} \tag{1.33}$$

In the following we will introduce differential operators that will regularly be used in this work and state how they can be represented in terms of the previously introduced spherical polar coordinates. Since these representations build the foundation of most following chapters, all derivations (or at least sketches of the derivations) will be explicitly given here.

1.2.1 Gradient

Let $D \subset \mathbb{R}^3$. The **gradient** $\nabla : \mathrm{C}^{(1)}(D) \to \mathrm{c}(D)$ transfers a continuously differentiable scalar field F into a vector field ∇F by

$$\nabla F := \sum_{i=1}^{3} \left(\partial_i F\right) \epsilon^i\,, \tag{1.34}$$

i.e. the gradient is defined as the column vector of all partial derivatives of F. It can be shown that - geometrically speaking - the vector $\nabla F(x)$ always points into the direction of the steepest slope at $x \in D$ which makes it a very useful tool e.g. for solving minimisation problems (see e.g. the conjugate gradient method in Fletcher and Reeves, 1964).

In order to find a representation of the gradient in terms of the spherical polar coordinates, we may exploit the orthogonality of the underlying coordinate system. Hence it is possible to determine the respective components by projecting the gradient - as it was defined above - onto each of the three basis vectors ϵ^r, ϵ^φ and ϵ^t. For the r-component we then find:

$$\begin{aligned} \left(\nabla F\right)_r &= \epsilon^r \cdot \nabla F \\ &= \frac{1}{b_r}\frac{\partial x}{\partial r} \cdot \nabla F \\ &= \frac{1}{b_r}\left(\frac{\partial F}{\partial x_1}\frac{\partial x_1}{\partial r} + \frac{\partial F}{\partial x_2}\frac{\partial x_2}{\partial r} + \frac{\partial F}{\partial x_3}\frac{\partial x_3}{\partial r}\right). \end{aligned} \tag{1.35}$$

At this point, we can make use of the chain rule, inversely, to find:

$$\left(\nabla F\right)_r = \frac{1}{b_r}\,\partial_r F\,. \tag{1.36}$$

Since all transformations can analogously also be performed for the two other spherical components, we can immediately state the following result:

$$\nabla F = \left(\frac{1}{b_r}\,\partial_r F\right)\epsilon^r + \left(\frac{1}{b_\varphi}\,\partial_\varphi F\right)\epsilon^\varphi + \left(\frac{1}{b_t}\,\partial_t F\right)\epsilon^t\,. \tag{1.37}$$

Using (1.26), we eventually arrive at the spherical polar coordinate representation of the gradient:

$$\nabla F = \epsilon^r \partial_r F + \frac{1}{r}\left(\epsilon^\varphi \frac{1}{\sqrt{1-t^2}}\,\partial_\varphi F + \epsilon^t \sqrt{1-t^2}\,\partial_t F\right). \tag{1.38}$$

Based on this equality, for functions $F \in \mathrm{C}^{(1)}(\Omega)$ on Ω we call the operator ∇^* with

$$\nabla^* F := \epsilon^\varphi \frac{1}{\sqrt{1-t^2}}\,\partial_\varphi F + \epsilon^t \sqrt{1-t^2}\,\partial_t F\,, \tag{1.39}$$

which is r-times the tangential part of ∇, the **surface gradient** on Ω (see e.g., Backus, 1986; Fletcher and Reeves, 1964). Furthermore, we define a closely related operator, the **surface curl gradient** L^* as the cross product of the evaluation point $\xi \in \Omega$ and the surface gradient, i.e.

$$L^* F(\xi) := \xi \wedge \nabla^* F(\xi) = -\epsilon^\varphi \sqrt{1-t^2}\,\partial_t F(\xi) + \epsilon^t \frac{1}{\sqrt{1-t^2}}\,\partial_\varphi F(\xi)\,. \tag{1.40}$$

Both differential operators will play an important role in the next sections when we talk about basis functions of $\mathrm{l}^2(D)$, the vector spherical harmonics. Another motivation for the definition of both operator is the so-called **spherical Helmholtz decomposition** of vector fields. It can be shown that any $f \in \mathrm{c}^{(1)}(\Omega)$ can be represented as

$$f(\xi) = \xi\, F_1(\xi) + \nabla^* F_2(\xi) + L^* F_3(\xi)\,, \tag{1.41}$$

for any $\xi \in \Omega$, where $F_1, F_2, F_3 \in \mathrm{C}^{(1)}(\Omega)$ are three scalar functions that are uniquely determined for each f. Since both ∇^* and L^* are purely tangential operators, we immediately see that in general $F_1 = f_r$ must hold.

It is also possible to define the gradient of vector fields. The result then is a tensor field, where - interpreted as a matrix - the respective rows and columns contain the partial derivatives of each component of f. More precisely, $\nabla : \mathrm{c}^{(1)}(D) \to \mathbf{c}(D)$ is defined as the dyadic product of f and the nabla operator, i.e.

$$\nabla f := f \otimes \nabla := \sum_{i,j} \nabla_j \left(f_i\, \epsilon^i\right) \otimes \epsilon^j\,, \tag{1.42}$$

where the ϵ^i can represent any basis system - in our case especially the Cartesian or spherical polar system. Applying the product rule then yields

$$\begin{aligned} \nabla f &= \sum_{i,j} \left((\nabla_j f_i)\, \epsilon^i \otimes \epsilon^j + f_i \left(\nabla_j \epsilon^i\right) \otimes \epsilon^j \right) \\ &= \sum_{i,j} (\nabla_j f_i)\, \epsilon^i \otimes \epsilon^j + \sum_i f_i\, \nabla \epsilon^i\,. \end{aligned} \tag{1.43}$$

We find that for the calculation of the second sum we need to determine the vector gradient $\nabla \epsilon^i$ of the basis vectors ϵ^i for $i = 1, 2, 3$ or $i = r, \varphi, r$ respectively. In Cartesian coordinates, $\nabla \epsilon^i = 0$ for all $i = 1, 2, 3$ since the basis vectors are static. Furthermore, $\nabla_i = \partial_i$ in (1.43) for all $i = 1, 2, 3$ which then simply yields

$$\nabla f = \sum_{i,j=1}^{3} \partial_j f_i\, \epsilon^i \otimes \epsilon^j\,. \tag{1.44}$$

for the representation of the vector gradient in Cartesian coordinates. In spherical polar coordinates, the partial derivatives of the basis vectors do not vanish since they move with the location. For the respective derivatives we find, applying (1.38) to (1.26), that

$$\begin{aligned} &\nabla_r \epsilon^r = 0, && \nabla_\varphi \epsilon^r = \frac{1}{r}\,\epsilon^\varphi, && \nabla_t \epsilon^r = \frac{1}{r}\,\epsilon^t\,, \\ &\nabla_r \epsilon^\varphi = 0, && \nabla_\varphi \epsilon^\varphi = \frac{1}{r}\left(\frac{t}{\sqrt{1-t^2}}\,\epsilon^t - \epsilon^r\right), && \nabla_t \epsilon^\varphi = 0\,, \\ &\nabla_r \epsilon^t = 0, && \nabla_\varphi \epsilon^t = -\frac{1}{r}\frac{t}{\sqrt{1-t^2}}\,\epsilon^\varphi, && \nabla_t \epsilon^t = -\frac{1}{r}\,\epsilon^r\,. \end{aligned} \tag{1.45}$$

Note that these relations are very important and will also be necessary for the derivation of the spherical polar coordinate representation of all following differential operators. Now, using (1.45) we find for the vector gradient of the basis vectors:

$$\begin{aligned}
\nabla\epsilon^r &= \sum_j \left(\nabla_j \epsilon^r\right) \otimes \epsilon^j = \frac{1}{r}\left(\epsilon^\varphi \otimes \epsilon^\varphi + \epsilon^t \otimes \epsilon^t\right) , \\
\nabla\epsilon^\varphi &= \sum_j \left(\nabla_j \epsilon^\varphi\right) \otimes \epsilon^j = \frac{1}{r}\left(\frac{t}{\sqrt{1-t^2}}\,\epsilon^t \otimes \epsilon^\varphi - \epsilon^r \otimes \epsilon^\varphi\right) , \\
\nabla\epsilon^t &= \sum_j \left(\nabla_j \epsilon^t\right) \otimes \epsilon^j = -\frac{1}{r}\left(\frac{t}{\sqrt{1-t^2}}\,\epsilon^\varphi \otimes \epsilon^\varphi + \epsilon^r \otimes \epsilon^t\right) .
\end{aligned} \tag{1.46}$$

Together with (1.43) these relations finally determine the spherical polar coordinate representation of the vector gradient, here in matrix notation:

$$\nabla f = \begin{pmatrix} \partial_r f_r & \frac{1}{r}\frac{1}{\sqrt{1-t^2}}\,\partial_\varphi f_r - \frac{1}{r} f_\varphi & \frac{1}{r}\sqrt{1-t^2}\,\partial_t f_r - \frac{1}{r} f_t \\ \partial_r f_\varphi & \frac{1}{r}\frac{1}{\sqrt{1-t^2}}\,\partial_\varphi f_\varphi - \frac{1}{r}\frac{t}{\sqrt{1-t^2}}\,f_t + \frac{1}{r} f_r & \frac{1}{r}\sqrt{1-t^2}\,\partial_t f_\varphi \\ \partial_r f_t & \frac{1}{r}\frac{1}{\sqrt{1-t^2}}\,\partial_\varphi f_t + \frac{1}{r}\frac{t}{\sqrt{1-t^2}}\,f_\varphi & \frac{1}{r}\sqrt{1-t^2}\,\partial_t f_t + \frac{1}{r} f_r \end{pmatrix}_{r,\varphi,t} . \tag{1.47}$$

In the context of the stress tensor σ that will be introduced in the next chapter, the transposed vector gradient will also play an important role:

$$\left(\nabla f\right)^T = \nabla \otimes f = \sum_{i,j} \epsilon^i \otimes \nabla_i \left(f_j\, \epsilon^j\right) . \tag{1.48}$$

Since both Cartesian and spherical polar coordinates are orthonormal systems in $\mathbb{R}^3$ - i.e. the transformation matrix between the two systems is orthogonal ($A^{-1} = A^T$) - in order to find the respective representation of this operator in spherical polar coordinates it is sufficient to transpose the matrix representation of ∇f from above without further calculations, i.e.

$$\left(\nabla f\right)^T = \begin{pmatrix} \partial_r f_r & \partial_r f_\varphi & \partial_r f_t \\ \frac{1}{r}\frac{1}{\sqrt{1-t^2}}\,\partial_\varphi f_r - \frac{1}{r} f_\varphi & \frac{1}{r}\frac{1}{\sqrt{1-t^2}}\,\partial_\varphi f_\varphi - \frac{1}{r}\frac{t}{\sqrt{1-t^2}}\,f_t + \frac{1}{r} f_r & \frac{1}{r}\frac{1}{\sqrt{1-t^2}}\,\partial_\varphi f_t + \frac{1}{r}\frac{t}{\sqrt{1-t^2}}\,f_\varphi \\ \frac{1}{r}\sqrt{1-t^2}\,\partial_t f_r - \frac{1}{r} f_t & \frac{1}{r}\sqrt{1-t^2}\,\partial_t f_\varphi & \frac{1}{r}\sqrt{1-t^2}\,\partial_t f_t + \frac{1}{r} f_r \end{pmatrix} . \tag{1.49}$$

1.2.2 Vector surface gradient

Replacing the nabla operator in the definitions above with their surface equivalents, the surface gradient ∇^* and the surface curl gradient L^* we are able to define two additional operators, the **vector surface gradient** $\nabla^*\otimes : \mathrm{c}^{(1)}(\Omega) \to \mathbf{c}(\Omega)$ with

$$\nabla^* \otimes f = \sum_{i,j} \epsilon^i \otimes \nabla_i^* \left(f_j\, \epsilon^j\right) = \sum_{i,j} \left(\nabla_i^* f_j\right) \epsilon^i \otimes \epsilon^j + \sum_j f_j\, \nabla^* \otimes \epsilon^j , \tag{1.50}$$

and the **vector surface curl gradient** $L^*\otimes : \mathrm{c}^{(1)}(\Omega) \to \mathbf{c}(\Omega)$ with

$$\mathrm{L}^* \otimes f = \sum_{i,j} \epsilon^i \otimes \mathrm{L}_i^* \left(f_j\, \epsilon^j\right) = \sum_{i,j} \left(\mathrm{L}_i^* f_j\right) \epsilon^i \otimes \epsilon^j + \sum_j f_j\, \mathrm{L}^* \otimes \epsilon^j . \tag{1.51}$$

These operators will later be helpful to define basis functions for tensor fields, the tensor spherical harmonics.

The vector surface gradient of the basis vectors can immediately be deduced from (1.45). Here we find that

$$\begin{aligned}
\nabla^* \otimes \epsilon^r &= \sum_i \epsilon^i \otimes (\nabla_i^* \epsilon^r) = \epsilon^\varphi \otimes \epsilon^\varphi + \epsilon^t \otimes \epsilon^t \,, \\
\nabla^* \otimes \epsilon^\varphi &= \sum_i \epsilon^i \otimes (\nabla_i^* \epsilon^\varphi) = \frac{t}{\sqrt{1-t^2}}\, \epsilon^\varphi \otimes \epsilon^t - \epsilon^\varphi \otimes \epsilon^r \,, \\
\nabla^* \otimes \epsilon^t &= \sum_i \epsilon^i \otimes \left(\nabla_i^* \epsilon^t\right) = -\frac{t}{\sqrt{1-t^2}}\, \epsilon^\varphi \otimes \epsilon^\varphi - \epsilon^t \otimes \epsilon^r \,.
\end{aligned} \tag{1.52}$$

and together with the definition (1.39) of ∇^* we immediately find:

$$\nabla^* \otimes f = \begin{pmatrix} 0 & 0 & 0 \\ \frac{1}{\sqrt{1-t^2}}\, \partial_\varphi f_r - f_\varphi & \frac{1}{\sqrt{1-t^2}}\, \partial_\varphi f_\varphi - \frac{t}{\sqrt{1-t^2}}\, f_t + f_r & \frac{1}{\sqrt{1-t^2}}\, \partial_\varphi f_t + \frac{t}{\sqrt{1-t^2}}\, f_\varphi \\ \sqrt{1-t^2}\, \partial_t f_r - f_t & \sqrt{1-t^2}\, \partial_t f_\varphi & \sqrt{1-t^2}\, \partial_t f_t + f_r \end{pmatrix} . \tag{1.53}$$

Also for the spherical polar coordinate representation of the vector surface curl gradient we first need to determine the results of its application to the basis vectors. First, for the partial derivatives we find that

$$\begin{aligned}
&\mathrm{L}_r^* \epsilon^r = 0 \,, && \mathrm{L}_\varphi^* \epsilon^r = -\epsilon^t \,, && \mathrm{L}_t^* \epsilon^r = \epsilon^\varphi \,, \\
&\mathrm{L}_r^* \epsilon^\varphi = 0 \,, && \mathrm{L}_\varphi^* \epsilon^\varphi = 0 \,, && \mathrm{L}_t^* \epsilon^\varphi = \frac{t}{\sqrt{1-t^2}}\, \epsilon^t - \epsilon^r \,, \\
&\mathrm{L}_r^* \epsilon^t = 0 \,, && \mathrm{L}_\varphi^* \epsilon^t = \epsilon^r \,, && \mathrm{L}_t^* \epsilon^t = -\frac{t}{\sqrt{1-t^2}}\, \epsilon^\varphi \,.
\end{aligned} \tag{1.54}$$

Leading to

$$\begin{aligned}
\mathrm{L}^* \otimes \epsilon^r &= \sum_i \epsilon^i \otimes (\mathrm{L}_i^* \epsilon^r) = -\epsilon^\varphi \otimes \epsilon^t + \epsilon^t \otimes \epsilon^\varphi \,, \\
\mathrm{L}^* \otimes \epsilon^\varphi &= \sum_i \epsilon^i \otimes (\mathrm{L}_i^* \epsilon^\varphi) = \frac{t}{\sqrt{1-t^2}}\, \epsilon^t \otimes \epsilon^t - \epsilon^t \otimes \epsilon^r \,, \\
\mathrm{L}^* \otimes \epsilon^t &= \sum_i \epsilon^i \otimes \left(\mathrm{L}_i^* \epsilon^t\right) = \epsilon^\varphi \otimes \epsilon^r - \frac{t}{\sqrt{1-t^2}}\, \epsilon^t \otimes \epsilon^\varphi \,.
\end{aligned} \tag{1.55}$$

And together with the definition (1.40) of L^* we finally find that

$$L^* \otimes f = \begin{pmatrix} 0 & 0 & 0 \\ -\sqrt{1-t^2}\, \partial_t f_r + f_t & -\sqrt{1-t^2}\, \partial_t f_\varphi & -\sqrt{1-t^2}\, \partial_t f_t - f_r \\ \frac{1}{\sqrt{1-t^2}}\, \partial_\varphi f_r - f_\varphi & \frac{1}{\sqrt{1-t^2}}\, \partial_\varphi f_\varphi - \frac{t}{\sqrt{1-t^2}}\, f_t + f_r & \frac{1}{\sqrt{1-t^2}}\, \partial_\varphi f_t + \frac{t}{\sqrt{1-t^2}}\, f_\varphi \end{pmatrix} . \tag{1.56}$$

We notice that in contrast to the surface gradient and the surface curl gradient that generate purely tangential vector fields, the tensor gradients do <u>not</u> generate purely tangential tensor fields due to the non-vanishing first column even if the initial vector field is purely tangential.

The apparent application of both tensor gradients to the surface gradient and the surface curl gradient (of a scalar field F) itself will reveal some interesting relations. Moreover, in the next section we will learn that these operators will provide the foundation for constructing (some of the) basis functions we will need to describe tensor fields. Therefore, we will now explicitly state the result of these applications. Also using

$$\begin{aligned}
\sqrt{1-t^2}\, \partial_t \frac{1}{\sqrt{1-t^2}}\, \partial_\varphi &= \partial_t \partial_\varphi + \frac{t}{1-t^2}\, \partial_\varphi \,, \\
\sqrt{1-t^2}\, \partial_t \sqrt{1-t^2}\, \partial_t &= \partial_t \left(1-t^2\right) \partial_t + t\, \partial_t \,,
\end{aligned} \tag{1.57}$$

we find for $F \in \mathrm{C}^{(2)}(\Omega)$:

$$\nabla^* \otimes \nabla^* F = \begin{pmatrix} 0 & 0 & 0 \\ -\frac{1}{\sqrt{1-t^2}}\,\partial_\varphi F & \frac{1}{1-t^2}\,\partial_{\varphi^2}^2 F - t\,\partial_t F & \frac{t}{1-t^2}\,\partial_\varphi F + \partial_\varphi \partial_t F \\ -\sqrt{1-t^2}\,\partial_t F & \frac{t}{1-t^2}\,\partial_\varphi F + \partial_\varphi \partial_t F & \partial_t\left(1-t^2\right)\partial_t F + t\,\partial_t F \end{pmatrix}. \tag{1.58}$$

$$\nabla^* \otimes L^* F = \begin{pmatrix} 0 & 0 & 0 \\ \sqrt{1-t^2}\,\partial_t F & -\frac{t}{1-t^2}\,\partial_\varphi F - \partial_\varphi \partial_t F & \frac{1}{1-t^2}\,\partial_{\varphi^2}^2 F - t\,\partial_t F \\ -\frac{1}{\sqrt{1-t^2}}\,\partial_\varphi F & -\partial_t\left(1-t^2\right)\partial_t F - t\,\partial_t F & \frac{t}{1-t^2}\,\partial_\varphi F + \partial_\varphi \partial_t F \end{pmatrix}. \tag{1.59}$$

$$L^* \otimes \nabla^* F = \begin{pmatrix} 0 & 0 & 0 \\ \sqrt{1-t^2}\,\partial_t F & -\frac{t}{1-t^2}\,\partial_\varphi F - \partial_\varphi \partial_t F & -\partial_t\left(1-t^2\right)\partial_t F - t\,\partial_t F \\ -\frac{1}{\sqrt{1-t^2}}\,\partial_\varphi F & \frac{1}{1-t^2}\,\partial_{\varphi^2}^2 F - t\,\partial_t F & \frac{t}{1-t^2}\,\partial_\varphi F + \partial_\varphi \partial_t F \end{pmatrix}. \tag{1.60}$$

$$L^* \otimes L^* F = \begin{pmatrix} 0 & 0 & 0 \\ \frac{1}{\sqrt{1-t^2}}\,\partial_\varphi F & \partial_t\left(1-t^2\right)\partial_t F + t\,\partial_t F & -\frac{t}{1-t^2}\,\partial_\varphi F - \partial_\varphi \partial_t F \\ \sqrt{1-t^2}\,\partial_t F & -\frac{t}{1-t^2}\,\partial_\varphi F - \partial_\varphi \partial_t F & \frac{1}{1-t^2}\,\partial_{\varphi^2}^2 F - t\,\partial_t F \end{pmatrix}. \tag{1.61}$$

When we have a closer look at these representations, we notice that we can make a majority of the components vanish if we combine the tensors in a smart way. More precisely, we find

$$\begin{aligned} &\left(\nabla^* \otimes \nabla^* + L^* \otimes L^*\right) F \\ &= \begin{pmatrix} 0 & 0 & 0 \\ 0 & \frac{1}{1-t^2}\,\partial_{\varphi^2}^2 F + \partial_t\left(1-t^2\right)\partial_t F & 0 \\ 0 & 0 & \frac{1}{1-t^2}\,\partial_{\varphi^2}^2 F + \partial_t\left(1-t^2\right)\partial_t F \end{pmatrix} \\ &= \left(\epsilon^\varphi \otimes \epsilon^\varphi + \epsilon^t \otimes \epsilon^t\right) \Delta^* F\,, \end{aligned} \tag{1.62}$$

where $\Delta^* := \frac{1}{1-t^2}\,\partial_{\varphi^2}^2 + \partial_t\left(1-t^2\right)\partial_t$ is the **Laplace-Beltrami operator** (sometimes in literature just **Beltrami operator**) of the unit sphere. In analogy, we also find

$$\left(\nabla^* \otimes L^* - L^* \otimes \nabla^*\right) F = \left(\epsilon^\varphi \otimes \epsilon^t - \epsilon^t \otimes \epsilon^\varphi\right) \Delta^* F\,. \tag{1.63}$$

Later, we will learn that the Beltrami operator may also be identified with the tangential part of the Laplace operator Δ, which then also justifies the notation Δ^*.

1.2.3 Divergence

The **divergence** $\mathrm{div} : \mathrm{c}^{(1)}(D) \to \mathrm{C}(D)$ transfers a continuously differentiable vector field f into a scalar field $\mathrm{div}\, f$ and is defined as the dot product of the nabla operator and f - and therefore commonly also denoted by $\nabla \cdot f$. More precisely, we have:

$$\begin{aligned} \mathrm{div}\, f := \nabla \cdot f &:= \sum_i \epsilon^i \cdot \nabla_i f = \sum_{i,j} \epsilon^i \cdot \nabla_i \left(f_j\, \epsilon^j\right) \\ &= \sum_{i,j} \left(\left(\nabla_i f_j\right) \epsilon^i \cdot \epsilon^j + f_j\, \epsilon^i \cdot \nabla_i \epsilon^j\right) \\ &= \sum_i \nabla_i f_i + \sum_i f_i\, \nabla \cdot \epsilon^i\,. \end{aligned} \tag{1.64}$$

In analogy to the vector gradient (1.43), for Cartesian coordinates it holds that $\nabla \cdot \epsilon^i = 0$ for all $i = 1, 2, 3$ since the basis vectors are static. The above definition then simplifies to

$$\nabla \cdot f = \sum_{i=1}^{3} \partial_i f_i\,. \tag{1.65}$$

In order to yield the respective representation of the divergence in spherical polar coordinates we need to determine the divergence of the three basis vectors. Applying again (1.45) we find that

$$\begin{aligned} \nabla \cdot \epsilon^r &= \sum_i \epsilon^i \cdot (\nabla_i \epsilon^r) = \frac{2}{r}\,, \\ \nabla \cdot \epsilon^\varphi &= \sum_i \epsilon^i \cdot (\nabla_i \epsilon^\varphi) = 0\,, \\ \nabla \cdot \epsilon^t &= \sum_i \epsilon^i \cdot \left(\nabla_i \epsilon^t\right) = -\frac{1}{r}\frac{t}{\sqrt{1-t^2}}\ . \end{aligned} \tag{1.66}$$

Inserting these results into (1.64) immediately yields the spherical polar coordinate representation of the divergence:

$$\begin{aligned} \nabla \cdot f &= \partial_r f_r + \frac{1}{r}\left(\frac{1}{\sqrt{1-t^2}}\,\partial_\varphi f_\varphi + \sqrt{1-t^2}\,\partial_t f_t\right) + \frac{2}{r}\,f_r - \frac{1}{r}\frac{t}{\sqrt{1-t^2}}\,f_t \\ &= \left(\partial_r + \frac{2}{r}\right) f_r + \frac{1}{r}\left(\frac{1}{\sqrt{1-t^2}}\,\partial_\varphi f_\varphi + \partial_t\left(\sqrt{1-t^2}\,f_t\right)\right)\,. \end{aligned} \tag{1.67}$$

It is also possible to develop a corresponding consistent definition to the divergence for the previously introduced surface operators ∇^* and L^*. More precisely we define:

$$\begin{aligned} \nabla^* \cdot f &:= \sum_{i,j} \epsilon^i \cdot \nabla_i^* \left(f_j\, \epsilon^j\right) = \sum_i \nabla_i^* f_i + \sum_i f_i\, \nabla^* \cdot \epsilon^i\,, \\ \mathrm{L}^* \cdot f &:= \sum_{i,j} \epsilon^i \cdot \mathrm{L}_i^* \left(f_j\, \epsilon^j\right) = \sum_i \mathrm{L}_i^* f_i + \sum_i f_i\, \mathrm{L}^* \cdot \epsilon^i\ , \end{aligned} \tag{1.68}$$

for a vector function $f \in \mathrm{c}^{(1)}(\Omega)$. We call $\nabla^* \cdot f$ the **surface divergence** of f and $\mathrm{L}^* \cdot f$ the **surface curl divergence** of f. The application to the spherical polar coordinate basis vectors yields

$$\begin{aligned} \nabla^* \cdot \epsilon^r &= \sum_i \epsilon^i \cdot (\nabla_i^* \epsilon^r) = 2\,, \\ \nabla^* \cdot \epsilon^\varphi &= \sum_i \epsilon^i \cdot (\nabla_i^* \epsilon^\varphi) = 0\,, \\ \nabla^* \cdot \epsilon^t &= \sum_i \epsilon^i \cdot \left(\nabla_i^* \epsilon^t\right) = -\frac{t}{\sqrt{1-t^2}}\ . \end{aligned} \tag{1.69}$$

and

$$\begin{aligned} \mathrm{L}^* \cdot \epsilon^r &= \sum_i \epsilon^i \cdot (\mathrm{L}_i^* \epsilon^r) = 0\,, \\ \mathrm{L}^* \cdot \epsilon^\varphi &= \sum_i \epsilon^i \cdot (\mathrm{L}_i^* \epsilon^\varphi) = \frac{t}{\sqrt{1-t^2}}\ , \\ \mathrm{L}^* \cdot \epsilon^t &= \sum_i \epsilon^i \cdot \left(\mathrm{L}_i^* \epsilon^t\right) = 0\,. \end{aligned} \tag{1.70}$$

Inserting these results into (1.68) then immediately yields the explicit spherical polar coordinate representation of $\nabla^* \cdot f$ and $\mathrm{L}^* \cdot f$:

$$\begin{aligned} \nabla^* \cdot f &= \frac{1}{\sqrt{1-t^2}}\,\partial_\varphi f_\varphi + \partial_t\left(\sqrt{1-t^2}\,f_t\right) + 2 f_r\,, \\ \mathrm{L}^* \cdot f &= \frac{1}{\sqrt{1-t^2}}\,\partial_\varphi f_t - \partial_t\left(\sqrt{1-t^2}\,f_\varphi\right)\ . \end{aligned} \tag{1.71}$$

From these representations it can easily be verified that

$$\begin{aligned} \nabla^* \cdot L^* &= L^* \cdot \nabla^* = 0\,, \\ \nabla^* \cdot \nabla^* &= L^* \cdot L^* = \Delta^*\,. \end{aligned} \tag{1.72}$$

The divergence operator is also defined for tensor fields, formally as the vector-matrix product of the nabla operator and a tensor field $\mathbf{f}$. More precisely we define the tensor divergence $\nabla\cdot : \mathbf{c}^{(1)}(D) \to \mathrm{c}(D)$ as

$$\begin{aligned} \operatorname{div}\mathbf{f} := \nabla\cdot\mathbf{f} &:= \sum_i \left(\nabla_i \mathbf{f}\right)\epsilon^i = \sum_{i,j,k} \left(\nabla_i \left(\mathbf{f}_{jk}\,\epsilon^j \otimes \epsilon^k\right)\right)\epsilon^i \\ &= \sum_{i,j,k} \left(\nabla_i \mathbf{f}_{jk}\left(\epsilon^j \otimes \epsilon^k\right)\epsilon^i + \mathbf{f}_{jk}\left(\nabla_i\epsilon^j \otimes \epsilon^k + \epsilon^j \otimes \nabla_i\epsilon^k\right)\epsilon^i\right) \\ &= \sum_{i,j} \nabla_i \mathbf{f}_{ji}\,\epsilon^j + \sum_{i,j,k} \mathbf{f}_{jk}\left(\nabla_i\epsilon^j \otimes \epsilon^k + \epsilon^j \otimes \nabla_i\epsilon^k\right)\epsilon^i \\ &= \sum_{i,j} \nabla_i \mathbf{f}_{ji}\,\epsilon^j + \sum_{i,j} \mathbf{f}_{ij}\,\nabla\cdot\epsilon^{ij}\,. \end{aligned} \tag{1.73}$$

Again, in Cartesian coordinates the second sum vanishes due to the static basis vectors and we find

$$\nabla\cdot\mathbf{f} = \sum_{i,j=1}^{3} \partial_i \mathbf{f}_{ji}\,\epsilon^j\,. \tag{1.74}$$

When $\mathbf{f}$ is identified as a matrix, this can be interpreted as an application of the (scalar) divergence to each row of $\mathbf{f}$. For the representation in spherical polar coordinates we again need the results of the application of this operator to the respective basis vectors. Using

$$\sum_i \left(\nabla_i\epsilon^j \otimes \epsilon^k\right)\epsilon^i = \nabla_k\epsilon^j\,, \tag{1.75}$$

for all $j,k = r,\varphi,t$, we find:

$$\begin{aligned} \nabla\cdot\epsilon^{rr} &= \nabla_r\epsilon^r + \sum_i \left(\epsilon^r \otimes \nabla_i\epsilon^r\right)\epsilon^i = \frac{2}{r}\,\epsilon^r\,, \\ \nabla\cdot\epsilon^{\varphi r} &= \nabla_r\epsilon^\varphi + \sum_i \left(\epsilon^\varphi \otimes \nabla_i\epsilon^r\right)\epsilon^i = \frac{2}{r}\,\epsilon^\varphi\,, \\ \nabla\cdot\epsilon^{tr} &= \nabla_r\epsilon^t + \sum_i \left(\epsilon^t \otimes \nabla_i\epsilon^r\right)\epsilon^i = \frac{2}{r}\,\epsilon^t\,, \\ \nabla\cdot\epsilon^{r\varphi} &= \nabla_\varphi\epsilon^r + \sum_i \left(\epsilon^r \otimes \nabla_i\epsilon^\varphi\right)\epsilon^i = \frac{1}{r}\,\epsilon^\varphi\,, \\ \nabla\cdot\epsilon^{\varphi\varphi} &= \nabla_\varphi\epsilon^\varphi + \sum_i \left(\epsilon^\varphi \otimes \nabla_i\epsilon^\varphi\right)\epsilon^i = \frac{1}{r}\left(\frac{t}{\sqrt{1-t^2}}\,\epsilon^t - \epsilon^r\right)\,, \\ \nabla\cdot\epsilon^{t\varphi} &= \nabla_\varphi\epsilon^t + \sum_i \left(\epsilon^t \otimes \nabla_i\epsilon^\varphi\right)\epsilon^i = -\frac{1}{r}\frac{t}{\sqrt{1-t^2}}\,\epsilon^\varphi\,, \\ \nabla\cdot\epsilon^{rt} &= \nabla_t\epsilon^r + \sum_i \left(\epsilon^r \otimes \nabla_i\epsilon^t\right)\epsilon^i = \frac{1}{r}\left(\epsilon^t - \frac{t}{\sqrt{1-t^2}}\,\epsilon^r\right)\,, \\ \nabla\cdot\epsilon^{\varphi t} &= \nabla_t\epsilon^\varphi + \sum_i \left(\epsilon^\varphi \otimes \nabla_i\epsilon^t\right)\epsilon^i = -\frac{1}{r}\frac{t}{\sqrt{1-t^2}}\,\epsilon^\varphi\,, \\ \nabla\cdot\epsilon^{tt} &= \nabla_t\epsilon^t + \sum_i \left(\epsilon^t \otimes \nabla_i\epsilon^t\right)\epsilon^i = -\frac{1}{r}\left(\epsilon^r + \frac{t}{\sqrt{1-t^2}}\,\epsilon^t\right)\,. \end{aligned} \tag{1.76}$$

Inserting these results into (1.73) then immediately yields the spherical polar coordinate representation of the tensor divergence:

$$\begin{aligned}
\nabla\cdot\mathbf{f} = \quad & \epsilon^r\left(\left(\partial_r+\frac{2}{r}\right)\mathbf{f}_{rr}+\frac{1}{r}\left(\frac{1}{\sqrt{1-t^2}}\,\partial_\varphi\mathbf{f}_{r\varphi}+\partial_t\left(\sqrt{1-t^2}\,\mathbf{f}_{rt}\right)-\mathbf{f}_{\varphi\varphi}-\mathbf{f}_{tt}\right)\right)\\
& +\epsilon^\varphi\left(\left(\partial_r+\frac{2}{r}\right)\mathbf{f}_{\varphi r}+\frac{1}{r}\left(\frac{1}{\sqrt{1-t^2}}\,\partial_\varphi\mathbf{f}_{\varphi\varphi}+\partial_t\left(\sqrt{1-t^2}\,\mathbf{f}_{\varphi t}\right)+\mathbf{f}_{r\varphi}-\frac{t}{\sqrt{1-t^2}}\,\mathbf{f}_{t\varphi}\right)\right)\\
& +\epsilon^t\left(\left(\partial_r+\frac{2}{r}\right)\mathbf{f}_{tr}+\frac{1}{r}\left(\frac{1}{\sqrt{1-t^2}}\,\partial_\varphi\mathbf{f}_{t\varphi}+\partial_t\left(\sqrt{1-t^2}\,\mathbf{f}_{tt}\right)+\mathbf{f}_{rt}+\frac{t}{\sqrt{1-t^2}}\,\mathbf{f}_{\varphi\varphi}\right)\right)\\
= \quad & \epsilon^r\left(\nabla\cdot\mathbf{f}_{r\cdot}-\frac{1}{r}\left(\mathbf{f}_{\varphi\varphi}+\mathbf{f}_{tt}\right)\right)\\
& +\epsilon^\varphi\left(\nabla\cdot\mathbf{f}_{\varphi\cdot}+\frac{1}{r}\left(\mathbf{f}_{r\varphi}-\frac{t}{\sqrt{1-t^2}}\,\mathbf{f}_{t\varphi}\right)\right)\\
& +\epsilon^t\left(\nabla\cdot\mathbf{f}_{t\cdot}+\frac{1}{r}\left(\mathbf{f}_{rt}+\frac{t}{\sqrt{1-t^2}}\,\mathbf{f}_{\varphi\varphi}\right)\right).
\end{aligned}\tag{1.77}$$

Furthermore, it can easily be shown that for a scalar field G and a tensor field $\mathbf{f}$ it holds that

$$\nabla\cdot(G\mathbf{f}) = \nabla G\cdot\mathbf{f}+G\,\nabla\cdot\mathbf{f}\,. \tag{1.78}$$

In the context of continuum mechanics, we will later find that for a velocity field v it is only possible to have a non-zero divergence without violating conservation of mass, if we allow for spatial and/or temporal density variations. Therefore, a velocity field with non-zero divergence is called **compressible**, a velocity field with zero divergence **incompressible**.

1.2.4 Curl

Another very important differential operator - especially in fluid dynamics - is the **curl** (or sometimes **rotation**) of a vector field f. The mapping $\operatorname{curl}:\mathrm{c}^{(1)}(D)\to\mathrm{c}(D)$ transfers a continuously differentiable vector field f into another vector field $\operatorname{curl} f$ and is formally defined as the vector product of the nabla operator and f - and therefore commonly also denoted by $\nabla\wedge f$. More precisely, we have:

$$\begin{aligned}
\operatorname{curl} f := \nabla\wedge f &:= \sum_i \epsilon^i\wedge\nabla_i f = \sum_{i,j}\epsilon^i\wedge\nabla_i\left(f_j\,\epsilon^j\right)\\
&= \sum_{i,j}\left(\left(\nabla_i f_j\right)\epsilon^i\wedge\epsilon^j+f_j\,\epsilon^i\wedge\nabla_i\epsilon^j\right)\\
&= \sum_{i,j}\left(\nabla_i f_j\right)\epsilon^i\wedge\epsilon^j+\sum_i f_i\,\nabla\wedge\epsilon^i\,.
\end{aligned}\tag{1.79}$$

In Cartesian coordinates the second sum vanishes again and we find

$$\nabla\wedge f=\sum_{i,j=1}^{3}\left(\partial_i f_j\right)\epsilon^i\wedge\epsilon^j=\begin{pmatrix}\partial_2 f_3-\partial_3 f_2\\ \partial_3 f_1-\partial_1 f_3\\ \partial_1 f_2-\partial_2 f_1\end{pmatrix}. \tag{1.80}$$

In order to yield the respective representation of the curl in spherical polar coordinates we need to determine the curl of the three basis vectors. Applying again (1.45) we find that

$$\begin{aligned}
\nabla\wedge\epsilon^r &= \sum_i\epsilon^i\wedge\left(\nabla_i\epsilon^r\right)=0\,,\\
\nabla\wedge\epsilon^\varphi &= \sum_i\epsilon^i\wedge\left(\nabla_i\epsilon^\varphi\right)=\frac{1}{r}\left(\frac{t}{\sqrt{1-t^2}}\,\epsilon^r+\epsilon^t\right),\\
\nabla\wedge\epsilon^t &= \sum_i\epsilon^i\wedge\left(\nabla_i\epsilon^t\right)=-\frac{1}{r}\,\epsilon^\varphi\,.
\end{aligned}\tag{1.81}$$

Inserting these results into (1.79) immediately yields the spherical polar coordinate representation of the curl:

$$\begin{aligned}\nabla \wedge f = \quad & \frac{1}{r}\,\epsilon^r \left(\frac{1}{\sqrt{1-t^2}}\,\partial_\varphi f_t - \partial_t \left(\sqrt{1-t^2}\, f_\varphi \right) \right) \\ & + \frac{1}{r}\,\epsilon^\varphi \left(\sqrt{1-t^2}\,\partial_t f_r - \partial_r \left(r f_t \right) \right) \\ & + \frac{1}{r}\,\epsilon^t \left(\partial_r \left(r f_\varphi \right) - \frac{1}{\sqrt{1-t^2}}\,\partial_\varphi f_r \right) .\end{aligned} \tag{1.82}$$

From these representations we can - in combination with (1.67) - easily find that the curl of a vector field f is always divergence-free. Furthermore, in combination with (1.38) the curl of a gradient field ($f = \nabla F$) also always vanishes, i.e.

$$\begin{aligned}\nabla \cdot (\nabla \wedge f) &= 0\,, \\ \nabla \wedge \nabla F &= 0\,.\end{aligned} \tag{1.83}$$

In addition, vector fields with a zero curl are called **irrotational**.

1.2.5 Laplacian

At last, we want to introduce the **Laplacian** Δ that is defined as the application of the divergence to the gradient of a scalar field F or a vector field f. Since the combination of two differential operators of first order generates second derivatives, here we require functions that are two times continuously differentiable. Hence, for a scalar field F, we define the Laplacian $\Delta : \mathrm{C}^{(2)}(D) \to \mathrm{C}(D)$ as

$$\Delta F := \nabla \cdot \nabla F\,. \tag{1.84}$$

Applying the explicit representation of the divergence and the gradient in Cartesian coordinates we find that the Laplacian reveals itself as the sum of the second (partial) derivatives of F:

$$\Delta F = \sum_{i=1}^{3} \partial_i \left(\partial_i F \right) = \sum_{i=1}^{3} \partial_{x_i^2}^2 F\,. \tag{1.85}$$

For spherical polar coordinates we find the following representation of the Laplacian, also just exploiting the results of the previous subsections:

$$\begin{aligned}\Delta F &= \left(\partial_r + \frac{2}{r} \right) (\nabla F)_r + \frac{1}{r} \left(\frac{1}{\sqrt{1-t^2}}\,\partial_\varphi \left(\nabla F \right)_\varphi + \partial_t \left(\sqrt{1-t^2}\, \left(\nabla F \right)_t \right) \right) \\ &= \left(\partial_r + \frac{2}{r} \right) \partial_r F + \frac{1}{r^2} \left(\frac{1}{\sqrt{1-t^2}}\,\partial_\varphi \left(\frac{1}{\sqrt{1-t^2}}\,\partial_\varphi F \right) + \partial_t \left(\sqrt{1-t^2}\,\sqrt{1-t^2}\,\partial_t F \right) \right) \\ &= \left(\partial_{r^2}^2 + \frac{2}{r}\,\partial_r + \frac{1}{r^2} \left(\frac{1}{1-t^2}\,\partial_{\varphi^2}^2 + \partial_t \left(1-t^2 \right) \partial_t \right) \right) F \\ &= \left(\Delta^r + \frac{1}{r^2}\,\Delta^* \right) F\,,\end{aligned} \tag{1.86}$$

where Δ^* denotes the already introduced Laplace-Beltrami operator and Δ^r the radial Laplacian

$$\Delta^r := \partial_{r^2}^2 + \frac{2}{r}\,\partial_r \left(= \frac{1}{r^2}\,\partial_r \left(r^2 \partial_r \right) \right) . \tag{1.87}$$

In analogy to the scalar case, the Laplacian of a vector field f is also defined as the application of the (tensor) divergence to the (vector) gradient of f, i.e. we define $\Delta : \mathrm{c}^{(2)}(D) \to \mathrm{c}(D)$ as

$$\Delta f := \nabla \cdot \nabla f\,. \tag{1.88}$$

In Cartesian coordinates this reduces to

$$\Delta f = \sum_{i,j=1}^{3} \partial_i \left(\nabla f\right)_{ji} \epsilon^j = \sum_{i,j=1}^{3} \partial_i \left(\partial_i f_j\right) \epsilon^j = \sum_{i,j=1}^{3} \partial_{x_i^2}^2 f_j \, \epsilon^j = \sum_{j=1}^{3} \Delta f_j \, \epsilon^j \,. \tag{1.89}$$

which can also be interpreted as a (row-wise) application of the scalar Laplacian to the vector components of f.

In spherical polar coordinates we find that

$$\begin{aligned} \Delta f = \quad & \epsilon^r \left(\nabla \cdot \left(\nabla f\right)_{r\cdot} - \frac{1}{r} \left(\left(\nabla f\right)_{\varphi\varphi} + \left(\nabla f\right)_{tt} \right) \right) \\ & + \epsilon^\varphi \left(\nabla \cdot \left(\nabla f\right)_{\varphi\cdot} + \frac{1}{r} \left(\left(\nabla f\right)_{r\varphi} - \frac{t}{\sqrt{1-t^2}} \left(\nabla f\right)_{t\varphi} \right) \right) \\ & + \epsilon^t \left(\nabla \cdot \left(\nabla f\right)_{t\cdot} + \frac{1}{r} \left(\left(\nabla f\right)_{rt} + \frac{t}{\sqrt{1-t^2}} \left(\nabla f\right)_{\varphi\varphi} \right) \right) . \end{aligned} \tag{1.90}$$

With

$$\begin{aligned} \nabla \cdot \left(\nabla f\right)_{r\cdot} &= \Delta f_r - \frac{1}{r^2} \left(\frac{1}{\sqrt{1-t^2}} \, \partial_\varphi f_\varphi + \partial_t \left(\sqrt{1-t^2} \, f_t \right) \right) , \\ \nabla \cdot \left(\nabla f\right)_{\varphi\cdot} &= \Delta f_\varphi + \frac{1}{r^2} \left(\frac{1}{\sqrt{1-t^2}} \, \partial_\varphi f_r - \frac{t}{1-t^2} \, \partial_\varphi f_t \right) , \\ \nabla \cdot \left(\nabla f\right)_{t\cdot} &= \Delta f_t + \frac{1}{r^2} \left(\frac{t}{1-t^2} \, \partial_\varphi f_\varphi + \partial_t \left(\sqrt{1-t^2} \, f_r \right) \right) , \end{aligned} \tag{1.91}$$

we finally find that

$$\begin{aligned} \Delta f = \quad & \epsilon^r \left(\Delta f_r - \frac{2}{r^2} \frac{1}{\sqrt{1-t^2}} \, \partial_\varphi f_\varphi - \frac{2}{r^2} \, \partial_t \left(\sqrt{1-t^2} \, f_t \right) - \frac{2}{r^2} \, f_r \right) \\ & + \epsilon^\varphi \left(\Delta f_\varphi + \frac{2}{r^2} \frac{1}{\sqrt{1-t^2}} \, \partial_\varphi f_r - \frac{2}{r^2} \frac{t}{1-t^2} \, \partial_\varphi f_t - \frac{1}{r^2} \frac{1}{1-t^2} \, f_\varphi \right) \\ & + \epsilon^t \left(\Delta f_t + \frac{2}{r^2} \frac{t}{1-t^2} \, \partial_\varphi f_\varphi + \frac{2}{r^2} \sqrt{1-t^2} \, \partial_t f_r - \frac{1}{r^2} \frac{1}{1-t^2} \, f_t \right) . \end{aligned} \tag{1.92}$$

Moreover, it can easily be verified that the application of the divergence to the transposed gradient $\left(\nabla f\right)^T$ yields:

$$\nabla \cdot \left(\nabla f\right)^T = \nabla \left(\nabla \cdot f \right) . \tag{1.93}$$

The following special relations involving the Beltrami operator and the radial Laplacian will also be used in the course of this work. These equalities only require product and chain rule to be proven but nevertheless should be stated here. For $F \in \mathrm{C}^{(3)}(\Omega)$ we find:

$$\begin{aligned} \Delta^* \left(\frac{1}{\sqrt{1-t^2}} \, \partial_\varphi \right) F &= \left(\frac{1}{\sqrt{1-t^2}} \, \partial_\varphi \right) \Delta^* F + \frac{1}{1-t^2} \left(\frac{1}{\sqrt{1-t^2}} \, \partial_\varphi \right) F \\ &\quad + \frac{2t}{1-t^2} \, \partial_\varphi \left(\sqrt{1-t^2} \, \partial_t \right) F \,, \\ \Delta^* \left(\sqrt{1-t^2} \, \partial_t \right) F &= \left(\sqrt{1-t^2} \, \partial_t \right) \Delta^* F + \frac{1}{1-t^2} \left(\sqrt{1-t^2} \, \partial_t \right) F \\ &\quad - \frac{2t}{1-t^2} \, \partial_\varphi \left(\frac{1}{\sqrt{1-t^2}} \, \partial_\varphi \right) F \,. \end{aligned} \tag{1.94}$$

Functions that satisfy the **Laplace equation**

$$\Delta F = 0 \,, \tag{1.95}$$

are called **harmonic**. The study of such harmonic functions is called **potential theory**. In the next section we will find that such harmonic functions will play an important role when developing basis functions on the unit sphere, the so-called spherical harmonics. In case of a non-vanishing right-hand side this differential equation is called **Poisson equation**. We will revisit this kind of equation especially in Chapter 4 when we discuss the Earth's gravity field and the gravitational potential.

A special case, i.e. solutions of the Laplace equation that are *radially symmetric*, can be derived quite straightforwardly even for the general case of $N \in \mathbb{N}$ dimensions. These solutions play an important role in the concept of deriving **fundamental solutions** (sometimes also denoted as **Green's functions**, where strictly speaking, the expression 'Green's function' implies the incorporation of respective boundary conditions). In general, a fundamental solution of a (linear partial) differential equation $L_x F = H$ is defined as a **distribution** $G(x, y)$ that satisfies $L_x G = \delta_x$ in the distributional sense. Here, L_x is the respective differential operator (with respect to x) and δ_x denotes the (x-)delta distribution. Equality in the distributional sense means that for any $\Psi \in D$, where D is an appropriate set of (test) functions (in many cases continuously differentiable functions with a compact support), it holds that

$$\int L_x G(x, y)\, \Psi(y)\, \mathrm{d}y = \int \delta_x(y)\, \Psi(y)\, \mathrm{d}y\,, \tag{1.96}$$

where the expression on the right-hand side is not a Riemann integral but a common notation for the defining property of the delta distribution, i.e.

$$\int \delta_x(y)\, \Psi(y)\, \mathrm{d}y := \int \delta(x - y)\, \Psi(y)\, \mathrm{d}y := \Psi(x)\,. \tag{1.97}$$

In this way, we can understand (1.96) as

$$\int L_x G(x, y)\, \Psi(y)\, \mathrm{d}y = \Psi(x)\,, \tag{1.98}$$

The power of this strategy reveals by showing that due to the linearity of the differential operator, a solution of the original differential equation $L_x F = H$ can be found by combining various fundamental solutions. More precisely, it can be shown (see e.g., Wermer, 1974) that if the right-hand side H of the differential equation is also contained in the space of test functions D, the following integral exists and it holds that

$$F(x) = \int G(x, y)\, H(y)\, \mathrm{d}y\,. \tag{1.99}$$

Note that the fundamental solution G does not depend on the heterogeneity H. This has the practical advantage that for a varying H, one does not need to determine new fundamental solutions. The only required step in order to find a solution to the respective differential equation is the evaluation of the previous integral. This property will be of big advantage when we will discuss fundamental solutions to the Stokes equation in Chapter 2, where the right-hand side of the differential equation essentially reflects the density anomalies in the Earth's mantle.
If the differential operator L_x even has constant coefficients (like e.g. the Laplace operator), it can be shown that the fundamental solutions are invariant with respect to translation. This implies that the two parameter dependency of $G(x, y)$ simplifies to a dependency on the distance between x and y, i.e. $G(x, y) = G(x-y)$, where we define the one-parameter fundamental solution $G(x-y) := G(0, x-y)$ as the distributional solution to $L_x G = \delta_0$. The representation (1.99) of the solution F then turns into the convolution

$$F(x) = \int G(x - y)\, H(y)\, \mathrm{d}y = (G * H)(x)\,. \tag{1.100}$$

Now, returning to the Laplace equation, we assume - as already annouced - the solution F to be radially symmetric, i.e. $F(x) = F(|x|) = F(r)$ for all x with $r = |x|$. Then, we find for any component of the

Laplace operator, i.e. the second partial derivative with respect to any component x_i, $i = 1, ..., N$, $N \in \mathbb{N}$, using the chain and product rule that

$$\begin{aligned} \partial^2_{x_i^2} F(x) &= \partial_i \left(\partial_i F(r)\right) = \partial_i \left(F^{'}(r)\,\frac{x_i}{r}\right) \\ &= F^{''}(r)\,\frac{x_i^2}{r^2} + F^{'}(r)\left(\frac{1}{r} - \frac{x_i^2}{r^3}\right). \end{aligned} \tag{1.101}$$

For the Laplace operator we then find

$$\begin{aligned} \Delta F(x) &= \sum_{i=1}^{N} \partial^2_{x_i^2} F(r) = \sum_{i=1}^{N} F^{''}(r)\,\frac{x_i^2}{r^2} + F^{'}(r)\left(\frac{1}{r} - \frac{x_i^2}{r^3}\right) \\ &= F^{''}(r) + F^{'}(r)\,\frac{N-1}{r}\,. \end{aligned} \tag{1.102}$$

Since we require F to satisfy $\Delta F = 0$ we find by substituting $G := F^{'}$ and separation of variables that

$$\begin{aligned} & G^{'}(r) + G(r)\,\frac{N-1}{r} = 0 \\ \Rightarrow & \int \frac{1}{G}\,\mathrm{d}G = (1-N)\int \frac{1}{r}\,\mathrm{d}r \\ \Rightarrow & \ln(|G(r)|) = (1-N)\ln(r) + \tilde{C} \\ \Rightarrow & G(r) = C\,r^{1-N} \end{aligned} \tag{1.103}$$

with an integration constant $C \in \mathbb{R}$. Re-substituting and integrating yields for the solution F of the Laplace equation

$$F(r) = \int C\,r^{1-N} = \begin{cases} \frac{C}{2-N}\,r^{2-N}\,, & N \neq 2 \\ C\,\ln(r)\,, & N = 2\,. \end{cases} \tag{1.104}$$

Thus, especially for the 3-D case, we find that

$$F(r) = -C\,\frac{1}{r} \quad \left(\text{i.e. } F(x) = -C\,\frac{1}{|x|}\right) \tag{1.105}$$

is a (radially symmetric) solution to the Laplace equation (not defined for $x = 0$). The similarity of the Laplace equation to the defining distributional equation of a fundamental solution $LG = \delta$ reveals that the previously found expression may also play an important role in the concept of determining fundamental solutions of the Laplace operator. And indeed, it can be shown (see e.g., Wermer, 1974) that (1.105) with the constant $C = 1/4\pi$ satisfies $\Delta F(x) = \delta(x)$ for all $x \in \mathbb{R}^3$ in the distributional sense. Furthermore, since the Laplacian has constant coefficients, we can immediately solve $\Delta F = H$ for any arbitrary right-hand side H - the Poisson equation - using the convolution ansatz of (1.100), i.e.

$$F(x) = -\left(\frac{1}{4\pi|\,\cdot\,|} * H\right)(x) = -\int \frac{H(y)}{4\pi|x-y|}\,\mathrm{d}y\,. \tag{1.106}$$

As an example, if we choose $H(x) := 4\pi G\rho(x)$, where G is the gravitational constant and ρ a density field, we obtain

$$F(x) = -G\int \frac{\rho(y)}{|x-y|}\,\mathrm{d}y\,, \tag{1.107}$$

which is the well-known integral representation of Newton's gravitational potential. Due to these relations, we can already deduce from here that the gravitational potential U satisfies the Poisson equation

$$\Delta U(x) = 4\pi G\rho(x)\,, \tag{1.108}$$

for all x in the considered domain. In particular, this yields

$$\Delta U(x) = 0\,, \tag{1.109}$$

for all x with $\rho(x) = 0$, i.e. the gravitational potential is harmonic outside the masses. Please note that all previous considerations are based on the knowledge of the fundamental solution, which we just stated and did not prove here (see e.g., Wermer, 1974). Nevertheless, at least we will prove the last relation (1.109) explicitly in Chapter 4.

Where we intentionally remained imprecise in the notation of the integrals in the previous equations, in the next section, we will investigate a variety of possible integration methods in $\mathbb{R}^3$ - line, surface and volume integrals - in a detailed way.

1.3 Integration in $\mathbb{R}^3$

In this section we present different types of integrals that will be used in this work and state afterwards some essential relations that build the bridge between these integrals on the one hand and the previously introduced differential operators on the other hand.

First, we define a **path** γ as a continuously differentiable function $\gamma : [a, b] \to \mathbb{R}^3$ with $a, b \in \mathbb{R}$ and $a < b$. Its image $\gamma([a, b])$ is called a **curve**. Now, let $F \in \mathrm{C}^{(1)}(D)$ be a scalar function where $\gamma([a, b]) \subset D$. In analogy to the Riemann integral, in order to approximate the contribution of each part of the curve to the total integral, we subdivide the domain $[a, b]$ of the path into $N \in \mathbb{N}$ equally spaced - by $\Delta t := (b - a)/N$ - intervals with boundary points t_i, $i = 1, ..., N + 1$. Now, we can approximate each contribution by multiplying the value of F at one arbitrary point inside the interval, e.g. at the left boundary, with the length of the curve corresponding to that interval, i.e. $|\gamma(t_{i+1}) - \gamma(t_i)| = |\gamma(t_i + \Delta t) - \gamma(t_i)|$ for the i-th interval. We then find as an approximation R_N for the total integral:

$$R_N = \sum_{i=1}^{N} F(\gamma(t_i)) \, |\gamma(t_i + \Delta t) - \gamma(t_i)| \; . \tag{1.110}$$

The mean value theorem now states that in each interval, there exists an s_i with

$$\gamma(t_i + \Delta t) - \gamma(t_i) = \gamma'(s_i)\Delta t\,. \tag{1.111}$$

Inserting this result into the previous equation we find that

$$R_N = \sum_{i=1}^{N} F(\gamma(t_i)) \, |\gamma'(s_i)| \, \Delta t\,. \tag{1.112}$$

In the limit $N \to \infty$, t_i and s_i fall into the same point and the sum turns into an integral where $\Delta t \to \mathrm{d}t$. Thus, we define the **line integral** of F along γ as

$$\int\limits_{\gamma} F(x) \, \mathrm{d}s(x) := \int\limits_{a}^{b} F(\gamma(t)) \, |\gamma'(t)| \, \mathrm{d}t\,. \tag{1.113}$$

This definition can be regarded as an extension of the *ordinary* Riemann integral. Instead of integrating a function along the real axis, here, we even allow for a curved *base line*.

This definition of a line integral can also be extended to vector fields $f \in \mathrm{c}^{(1)}(D)$ in a straightforward manner. The only difference to the scalar case is that at each line segment, we first have to

determine the part of the vector field that follows the direction of the line segment - represented by the tangential vectors to the curve - and thus contributes to the integral. This immediately yields the following definition for a line integral of a vector field f:

$$\int_\gamma f(x) \cdot \mathrm{d}s(x) := \int_\gamma f(x) \cdot \tau(x)\, \mathrm{d}s(x) = \int_a^b \left(f(\gamma(t)) \cdot \tau(\gamma(t))\right) |\gamma'(t)|\, \mathrm{d}t\,, \tag{1.114}$$

where $\tau(x)$ is the unit tangential to the curve at $x \in \gamma([a,b])$. But as we have already seen in the derivation of the scalar line integral, the tangential is nothing else than the derivative of the path, we find

$$\int_\gamma f(x) \cdot \mathrm{d}s(x) = \int_a^b \left(f(\gamma(t)) \cdot \frac{\gamma'(t)}{|\gamma'(t)|}\right) |\gamma'(t)|\, \mathrm{d}t = \int_a^b f(\gamma(t)) \cdot \gamma'(t)\, \mathrm{d}t\,. \tag{1.115}$$

In contrast to the line integral of a scalar field, we notice that the line integral of a vector field is not independent of the parametrisation of the curve since its tangential is not unique, i.e. it depends on the direction we go along the curve. More precisely, the magnitude of the integral is unique but its sign depends on the direction of the curve.

Gradient fields, i.e. vector fields f that can be represented by a scalar function G through $f = \nabla G$ have the important (and nice) property that their line integrals are in general independent of the path and only depend on the value of G at the two end points of the curve. Since, due to the chain rule,

$$\frac{\mathrm{d}}{\mathrm{d}t}\, G(\gamma(t)) = \nabla G(\gamma(t)) \cdot \gamma'(t)\,, \tag{1.116}$$

we find that

$$\begin{aligned} \int_\gamma f(x) \cdot \mathrm{d}s(x) = \int_\gamma \nabla G(x) \cdot \mathrm{d}s(x) &= \int_a^b \nabla G(\gamma(t)) \cdot \gamma'(t)\, \mathrm{d}t = \int_a^b \frac{\mathrm{d}}{\mathrm{d}t}\, G(\gamma(t))\, \mathrm{d}t \\ &= G(\gamma(b)) - G(\gamma(a))\,. \end{aligned} \tag{1.117}$$

If we integrate along a closed path, i.e. $a = b$, the line integral of a gradient field always vanishes.

In analogy to a line integral it is also possible to define the integral of a scalar field across a surface Σ. To ensure that the surface has a unique normal vector at each point, we require the surface to be a regular surface as defined above, i.e. there is a parametrisation $\Phi : U \to \mathbb{R}^3$, where $U = [a,b] \times [c,d]$, $a, b, c, d \in \mathbb{R}$ with $\Phi(U) = \Sigma$. Now, we divide both domains $[a,b]$ and $[c,d]$ of the surface parametrisation into $N \in \mathbb{N}$ equally spaced - by $\Delta s := (b-a)/N$ and $\Delta t := (d-c)/N$ - intervals with boundary points s_i, t_i, $i = 1, ..., N+1$. Again, each contribution can now be approximated by multiplying the value of F at one arbitrary point of the surface, e.g. at the point, corresponding to the left boundary of the parametrisation, with the area $A_{i,j}$ of the part of the surface corresponding the current intervals that we estimate by calculating the area of the parallelogram, spanned by the two connecting lines in each direction, which we can express in terms of the vector product. Thus, we find as an approximation R_N of the total integral:

$$\begin{aligned} R_N &= \sum_{i,j=1}^{N} F(\Phi(s_i,t_j)) A_{i,j} \\ &= \sum_{i,j=1}^{N} F(\Phi(s_i,t_j)) |\Phi(s_i+\Delta s, t_j) - \Phi(s_i,t_j)||\Phi(s_i,t_j+\Delta t) - \Phi(s_i,t_j)| \sin(\alpha_{i,j}) \\ &= \sum_{i,j=1}^{N} F(\Phi(s_i,t_j)) |(\Phi(s_i+\Delta s, t_j) - \Phi(s_i,t_j)) \wedge (\Phi(s_i,t_j+\Delta t) - \Phi(s_i,t_j))|\,, \end{aligned} \tag{1.118}$$

where $\alpha_{i,j}$ is the angle between the spanning vectors of the area $A_{i,j}$. Again, applying the mean value theorem yields

$$R_N = \sum_{i,j=1}^{N} F(\Phi(s_i,t_j)) \left|\partial_s\Phi(u_{i,j},t_j) \wedge \partial_t\Phi(s_i,v_{i,j})\right| \Delta t\, \Delta s\,, \tag{1.119}$$

with $s_i \le u_{i,j} \le s_{i+1}$ and $t_j \le v_{i,j} \le t_{j+1}$ for all $i,j = 1,...,N$. Again, in the limit $N \to \infty$, all points fall together and the sum turns into an integral. Thus, we are able to define the **surface integral** of F across a (regular) surface Σ as

$$\int_\Sigma F(x)\,\mathrm{d}\omega(x) := \int_a^b \int_c^d F(\Phi(s,t)) \left|\partial_s\Phi(s,t) \wedge \partial_t\Phi(s,t)\right| \,\mathrm{d}t\,\mathrm{d}s\,. \tag{1.120}$$

As an example, as we have already learned, we can represent any point x on the surface of a ball B_R with radius $R \in \mathbb{R}$ by the parametrisation $\Phi : [0,2\pi] \times [-1,1]$ with

$$\Phi(\varphi,t) = R \begin{pmatrix} \sqrt{1-t^2}\,\cos\varphi \\ \sqrt{1-t^2}\,\sin\varphi \\ t \end{pmatrix}. \tag{1.121}$$

We then find that

$$\begin{aligned} \left|\partial_\varphi\Phi(\varphi,t) \wedge \partial_t\Phi(\varphi,t)\right| &= R^2 \left| \begin{pmatrix} -\sqrt{1-t^2}\,\sin\varphi \\ \sqrt{1-t^2}\,\cos\varphi \\ 0 \end{pmatrix} \wedge \begin{pmatrix} -\frac{t}{\sqrt{1-t^2}}\,\cos\varphi \\ -\frac{t}{\sqrt{1-t^2}}\,\sin\varphi \\ 1 \end{pmatrix} \right| \\ &= R^2 \left| \begin{pmatrix} \sqrt{1-t^2}\,\cos\varphi \\ \sqrt{1-t^2}\,\sin\varphi \\ t \end{pmatrix} \right| = R^2\,, \end{aligned} \tag{1.122}$$

and thus e.g.

$$\int_{\partial B_R} 1\,\mathrm{d}\omega(x) = \int_{-1}^{1} \int_0^{2\pi} R^2\,\mathrm{d}\varphi\,\mathrm{d}t = 4\pi R^2\,, \tag{1.123}$$

which is the surface area ∂B_R of B_R.

At this point we should also mention a special kind of functions that will play an important role especially in the context of spherical harmonics, the **zonal functions**. A zonal function $G_\xi \in \mathrm{L}^2(\Omega)$ with respect to $\xi \in \Omega$ (also called ξ-zonal function) is a function on the unit sphere, that for any $\eta \in \Omega$ only depends on the distance of η and ξ. More precisely, if $G \in \mathrm{L}^2([-1,1])$ and $\xi \in \Omega$, the function G_ξ, defined by

$$G_\xi(\eta) := G(\xi \cdot \eta)\,, \tag{1.124}$$

for all $\eta \in \Omega$, is called a ξ-zonal function. If we especially choose $\xi = \epsilon^3$, due to construction, we have $\epsilon^3 \cdot \eta = t$ (see (1.121)), the polar distance of η, and the surface integral of G_{ϵ^3} across the unit sphere turns into

$$\int_\Omega G_{\epsilon^3}(\eta)\,\mathrm{d}\omega(\eta) = \int_\Omega G\left(\epsilon^3 \cdot \eta\right)\,\mathrm{d}\omega(\eta) = \int_{-1}^{1} \int_0^{2\pi} G(t)\,\mathrm{d}\varphi\,\mathrm{d}t = 2\pi \int_{-1}^{1} G(t)\,\mathrm{d}t\,. \tag{1.125}$$

The previous relation is even not restricted to ϵ^3-zonal functions but applicable to any ξ-zonal function with $\xi \in \Omega$ since it is possible to transfer any $\xi \in \Omega$ to the north pole ϵ^3 by a rotation A (with

$\det(A) = 1$). It can be shown that under such a rotation, the integral on the right-hand side does not change. Thus, we have for any zonal function $G_\xi \in \mathrm{L}^2(\Omega)$, $\xi \in \Omega$, that

$$\int_\Omega G_\xi(\eta)\,\mathrm{d}\omega(\eta) = 2\pi \int_{-1}^{1} G(t)\,\mathrm{d}t\,. \tag{1.126}$$

This means that it is possible to transfer the surface integral of a zonal function into an ordinary one-dimensional integral and vice versa, the integral of a scalar function on the interval $[-1, 1]$ can be transferred into a surface integral in the presented way.

In analogy to the line integrals, also the concept of surface integral can be extended to vector fields. One possible way is just to interpret the integral component-wise, i.e. the result of the integral is again a vector. We define

$$\int_\Sigma f(x)\,\mathrm{d}\omega(x) := \sum_{i=1}^{3} \left(\int_\Sigma f_i(x)\,\mathrm{d}\omega(x) \right) \epsilon^i\,. \tag{1.127}$$

Another physically concept that becomes interesting when investigating surfaces, is the so-called **flux**. In a very general way, flux is just defined as a quantity that passes through a surface. If we interpret this quantity as the vector field $f \in \mathrm{c}^{(1)}(D)$, we immediately find that the part of the vector field that is tangential to the surface, does not cross it, and therefore has no contribution to the flux. We only have to take into account the part of f that is normal to the surface. This immediately leads to the following definition of the flux of f across a surface Σ:

$$\int_\Sigma f(x) \cdot \mathrm{d}\omega(x) := \int_\Sigma \left(f(x) \cdot n(x)\right)\,\mathrm{d}\omega(x) = \int_a^b \int_c^d \left(f(\Phi(s,t)) \cdot n(\Phi(s,t))\right)\,\mathrm{d}t\,\mathrm{d}s\,, \tag{1.128}$$

where $n(x)$ is the (outer) unit normal vector to Σ at x. Since we can identify n with the cross product of the partial derivatives of the parametrisation Φ, we find - in analogy to the line integrals - that

$$\begin{aligned}
&\int_\Sigma f(x) \cdot \mathrm{d}\omega(x) \\
&= \int_a^b \int_c^d \left(f(\Phi(s,t)) \cdot \frac{\partial_s\Phi(s,t) \wedge \partial_t\Phi(s,t)}{|\partial_s\Phi(s,t) \wedge \partial_t\Phi(s,t)|} \right) |\partial_s\Phi(s,t) \wedge \partial_t\Phi(s,t)|\,\mathrm{d}t\,\mathrm{d}s \\
&= \int_a^b \int_c^d f(\Phi(s,t)) \cdot \left(\partial_s\Phi(s,t) \wedge \partial_t\Phi(s,t)\right)\,\mathrm{d}t\,\mathrm{d}s\,.
\end{aligned} \tag{1.129}$$

Since we can identify the last expression as a triple product, we also find the following representation for the flux:

$$\begin{aligned}
\int_\Sigma f(x) \cdot \mathrm{d}\omega(x) &= \int_a^b \int_c^d \det(f \mid \partial_s\Phi \mid \partial_t\Phi)\,\mathrm{d}t\,\mathrm{d}s \\
&= \int_a^b \int_c^d \det \begin{pmatrix} f_1 & \partial_s\Phi_1 & \partial_t\Phi_1 \\ f_2 & \partial_s\Phi_2 & \partial_t\Phi_2 \\ f_3 & \partial_s\Phi_3 & \partial_t\Phi_3 \end{pmatrix} \mathrm{d}t\,\mathrm{d}s\,.
\end{aligned} \tag{1.130}$$

The last integral type we want to discuss, is the volume integral of a scalar field $F \in \mathrm{C}^{(1)}(D)$. It is a natural extension of the line and surface integral to three dimensions. Instead of a line part or an area

of a surface, here we consider a part of a volume as the basis of the integral, which is multiplied by the value of the scalar field corresponding to this volume. In analogy to lines and surfaces, we also need a parametrisation for the volume V, which then naturally consists of three free parameters, i.e. we have a parametrisation $\Phi : U \to \mathbb{R}^3$, with $U = [a,b] \times [c,d] \times [e,f]$, $a,b,c,d,e,f \in \mathbb{R}$ and $\Phi(U) = V \subset D$. Without further derivation, it can easily be deduced from all previous considerations that the volume of one volume element can be represented by the triple product of the three partial derivatives of Φ. This immediately leads to the following definition of the volume integral of F:

$$\begin{aligned}
\int_V F(x)\,\mathrm{d}V(x) &:= \int_U F(\Phi(s,t,u))\,|\partial_s\Phi(s,t,u)\cdot(\partial_t\Phi(s,t,u)\wedge\partial_u\Phi(s,t,u))|\;\mathrm{d}u\,\mathrm{d}t\,\mathrm{d}s \\
&= \int_a^b\int_c^d\int_e^f F(\Phi(s,t,u))\,|\det\left(\partial_s\Phi \mid \partial_t\Phi \mid \partial_u\Phi\right)|\;\mathrm{d}u\,\mathrm{d}t\,\mathrm{d}s \\
&= \int_a^b\int_c^d\int_e^f F(\Phi(s,t,u))\left|\det\begin{pmatrix}\partial_s\Phi_1 & \partial_t\Phi_1 & \partial_u\Phi_1\\ \partial_s\Phi_2 & \partial_t\Phi_2 & \partial_u\Phi_2\\ \partial_s\Phi_3 & \partial_t\Phi_3 & \partial_u\Phi_3\end{pmatrix}\right|\mathrm{d}u\,\mathrm{d}t\,\mathrm{d}s \\
&= \int_a^b\int_c^d\int_e^f F(\Phi(s,t,u))\,|\det(J(\Phi(s,t,u)))|\;\mathrm{d}u\,\mathrm{d}t\,\mathrm{d}s \\
&= \int_a^b\int_c^d\int_e^f F(\Phi(s,t,u))\,|\det(\nabla\Phi(s,t,u))|\;\mathrm{d}u\,\mathrm{d}t\,\mathrm{d}s\,,
\end{aligned} \tag{1.131}$$

where J is the Jacobian, i.e. the vector gradient, of the volume parametrisation Φ. Except for a component-wise application, there is no additional reasonable definition of a volume integral for vector fields.

As an example, we again consider a solid ball B_R with radius $R \in \mathbb{R}$ and use the already known parametrisation (1.121) but additionally let r vary to have $\Phi(r,\varphi,t)$. We already know the Jacobian of Φ from (1.31) and therefore find applying Laplace' rule for the determinant:

$$\det(J(\Phi(r,\varphi,t)) = t^2r^2 + r^2(1-t^2) = r^2\,. \tag{1.132}$$

Thus, the (unweighted) volume integral over the solid ball B_R becomes

$$\int_{B_R} 1\,\mathrm{d}V(x) = \int_0^R\int_0^{2\pi}\int_{-1}^1 r^2\,\mathrm{d}t\,\mathrm{d}\varphi\,\mathrm{d}r = 4\pi\int_0^R r^2\,\mathrm{d}r = \frac{4}{3}\pi R^3\,, \tag{1.133}$$

which is the volume of the solid ball B_R.

One of the most important features of the previously discussed integral types is that, under certain conditions, it is possible to transfer one integral into another. There are a couple of useful identities that build the bridge between line, surface and volume integrals on the one hand and the previously introduced differential operators on the other hand. These transfer mechanisms will especially be crucial for the derivations of the integral and differential representations of the governing equations in continuum mechanics. We start with a relation between volume and surface integrals, more precisely the flux, the so-called **Gauss' theorem** (also **divergence theorem**). It can be shown that for an arbitrary volume $V \subset \mathbb{R}^3$ which is bounded by a regular surface ∂V, we find for a vector field $f \in \mathrm{c}^{(1)}(V)$ that

$$\int_V \nabla\cdot f(x)\,\mathrm{d}V(x) = \int_{\partial V} f(x)\cdot\,\mathrm{d}\omega(x)\,, \tag{1.134}$$

i.e. the flux of f through the boundary of V equals its divergence inside the volume. Since the volume V can be of arbitrary shape, especially also arbitrarily small, the divergence can be interpreted as a representation of the flux in the infinitesimal limit. In other words, the divergence at a point x measures the presence of sources and sinks of f at this point.

To prove this relation we approximate the volume V by $N \in \mathbb{N}$ rectangular shaped blocks V_i, $i = 1, ..., N$ that fall into the coordinate axes x_1, x_2 and x_3 and such that we have $\bigcup_{i=1}^{N} V_i \xrightarrow{N\to\infty} V$. Due to construction, the fluxes through the surfaces of any inner cube equals the negative flux through the respective surface of its adjacent block, thus, all fluxes in the interior cancel each other and only the contributions of the surfaces at the boundary that have no adjacent blocks remain. Therefore, we can easily deduce that in the limit $N \to \infty$, the sum of the fluxes through the surfaces of all cubes equals the flux just through the outer boundary of the volume, i.e.

$$\lim_{N\to\infty} \sum_{i=1}^{N} \int\limits_{\partial V_i} f(x) \cdot \mathrm{d}\omega(x) = \int\limits_{\partial V} f(x) \cdot \mathrm{d}\omega(x)\,. \tag{1.135}$$

The flux through one specific block V_i, $i = 1, ..., N$, can be divided into the contribution of the six sides, where two of them are always pairwise parallel and their normal vectors are the canonical unit vectors ϵ^1, ϵ^2 and ϵ^3. Defining $I_{i,1} \times I_{i,2} \times I_{i,3} := [a_{i,1}, a_{i,2}] \times [b_{i,1}, b_{i,2}] \times [c_{i,1}, c_{i,2}] = V_i$ with $a_{i,1} \le x_1 \le a_{i,2}$, $b_{i,1} \le x_2 \le b_{i,2}$ and $c_{i,1} \le x_3 \le c_{i,2}$ and furthermore, writing $f(x) = f(x_1, x_2, x_3)$ to emphasize the explicit dependence of f on the three components of x, we find using the mean value theorem of differentiation that

$$\begin{aligned}
\int\limits_{\partial V_i} f(x) \cdot \mathrm{d}\omega(x) &= \int\limits_{I_{i,2}} \int\limits_{I_{i,3}} \left(f_1(a_{i,2}, x_2, x_3) - f_1(a_{i,1}, x_2, x_3)\right) \mathrm{d}x_2\, \mathrm{d}x_3 \\
&\quad + \int\limits_{I_{i,1}} \int\limits_{I_{i,3}} \left(f_2(x_1, b_{i,2}, x_3) - f_2(x_1, b_{i,1}, x_3)\right) \mathrm{d}x_1\, \mathrm{d}x_3 \\
&\quad + \int\limits_{I_{i,1}} \int\limits_{I_{i,2}} \left(f_3(x_1, x_2, c_{i,2}) - f_3(x_1, x_2, c_{i,1})\right) \mathrm{d}x_1\, \mathrm{d}x_2 \\
&= |I_{i,1}| \int\limits_{I_{i,2}} \int\limits_{I_{i,3}} \partial_1 f_1(\bar{a_i}, x_2, x_3)\, \mathrm{d}x_2\, \mathrm{d}x_3 \\
&\quad + |I_{i,2}| \int\limits_{I_{i,1}} \int\limits_{I_{i,3}} \partial_2 f_2(x_1, \bar{b_i}, x_3)\, \mathrm{d}x_1\, \mathrm{d}x_3 \\
&\quad + |I_{i,3}| \int\limits_{I_{i,1}} \int\limits_{I_{i,2}} \partial_3 f_3(x_1, x_2, \bar{c_i})\, \mathrm{d}x_1\, \mathrm{d}x_2\,,
\end{aligned} \tag{1.136}$$

for some values $a_{i,1} \le \bar{a_i} \le a_{i,2}$, $b_{i,1} \le \bar{b_i} \le b_{i,2}$ and $c_{i,1} \le \bar{c_i} \le c_{i,2}$. Applying the mean value theorem of integration, the previous relation turns into

$$\begin{aligned}
\int\limits_{\partial V_i} f(x) \cdot \mathrm{d}\omega(x) &= \left(\partial_1 f_1(\bar{a_i}, \tilde{b_i}, \tilde{c_i} + \partial_2 f_2(\tilde{a_i}, \bar{b_i}, \hat{c_i}) + \partial_3 f_3(\hat{a_i}, \hat{b_i}, \bar{c_i})\right) |I_{i,1}||I_{i,2}||I_{i,3}| \\
&= \left(\partial_1 f_1(\bar{a_i}, \tilde{b_i}, \tilde{c_i}) + \partial_2 f_2(\tilde{a_i}, \bar{b_i}, \hat{c_i}) + \partial_3 f_3(\hat{a_i}, \hat{b_i}, \bar{c_i})\right) |V_i|\,,
\end{aligned} \tag{1.137}$$

for some $a_{i,1} \le \tilde{a_i}/\hat{a_i} \le a_{i,2}$, $b_{i,1} \le \tilde{b_i}/\hat{b_i} \le b_{i,2}$, $c_{i,1} \le \tilde{c_i}/\hat{c_i} \le c_{i,2}$. For the limit $N \to \infty$, all cubes become infinitesimal small and all points on the right-hand side of the equation fall into one point.

Thus, we finally find

$$\begin{aligned}\lim_{N\to\infty}\sum_{i=1}^{N}\int\limits_{\partial V_i} f(x)\cdot \mathrm{d}\omega(x) &= \lim_{N\to\infty}\sum_{i=1}^{N}\left(\partial_1 f_1(\bar{a_i},\tilde{b_i},\tilde{c_i})+\partial_2 f_2(\tilde{a_i},\bar{b_i},\hat{c_i})+\partial_3 f_3(\hat{a_i},\hat{b_i},\bar{c_i})\right)|V_i| \\ &= \int\limits_V \left(\partial_1 f_1(x)+\partial_2 f_2(x)+\partial_3 f_3(x)\right)\mathrm{d}V(x) \\ &= \int\limits_V \nabla\cdot f(x)\,\mathrm{d}V(x)\,.\end{aligned} \tag{1.138}$$

A similar conversion rule can be found for surface and line integral. Here, we find the following relation involving the curl instead of the divergence in Gauss' Theorem. The so-called **Stokes' Law** states that for any regular surface Σ that is bounded by $\partial\Sigma$ we find that

$$\int\limits_\Sigma (\nabla\wedge f(x))\cdot \mathrm{d}\omega(x) = \int\limits_{\partial\Sigma} f(x)\cdot \mathrm{d}s(x)\,. \tag{1.139}$$

We see that in the infinitesimal limit, the curl is equivalent to the (closed) line integral around a point x, which can be physically interpreted as the circulation around or at this point. In analogy to the divergence, we prove this relation by approximating the surface Σ by $N\in\mathbb{N}$ rectangles Σ_i, $i=1,...,N$ of three types that fall into the coordinate planes x_2/x_3, x_3/x_1 and x_1/x_2 respectively, and such that we have $\bigcup_{i=1}^N \Sigma_i \xrightarrow{N\to\infty} \Sigma$. Due to construction, the line integral contribution at one side of one rectangle equals the exact negative contribution of the respective side of its adjacent rectangle. Thus, in analogy to the divergence, all contributions in the interior of the surface cancel each other and only the lines at the boundary of the surface without an adjacent rectangle remain. Therefore, we can easily deduce that in the limit $N\to\infty$, the sum of the line integrals around all surfaces Σ_i in the interior equals the line integral just around the outer boundary of the surface, i.e.

$$\lim_{N\to\infty}\sum_{i=1}^{N}\int\limits_{\partial\Sigma_i} f(x)\cdot \mathrm{d}s(x) = \int\limits_{\partial\Sigma} f(x)\cdot \mathrm{d}s(x)\,. \tag{1.140}$$

The line integral around one specific rectangle Σ_i, $i=1,...,N$, can be divided into the contribution of the four sides, where two of them are always pairwise parallel and their tangential vectors are the canonical unit vectors ϵ^1,ϵ^2 or ϵ^3, depending on the specific type of the rectangle. We now say that the contribution of one rectangle can be expressed by three terms, each representing a rectangle $\Sigma_{i,j}$, $j=1,2,3$ of one type, where only one term is not equal to zero. We - hypothetically - arrange these three areas as the front, left and lower side of a rectangle that is defined by $I_{i,1}\times I_{i,2}\times I_{i,3} := [a_{i,1},a_{i,2}]\times[b_{i,1},b_{i,2}]\times[c_{i,1},c_{i,2}]$ with $a_{i,1}\le x_1\le a_{i,2}$, $b_{i,1}\le x_2\le b_{i,2}$ and $c_{i,1}\le x_3\le c_{i,2}$. Furthermore, we write $f(x)=f(x_1,x_2,x_3)$ to emphasize the explicit dependence of f on the three components of x. Again, we also apply the mean value theorem of differentiation and obtain - always respecting the correct orientation of the line integrals with respect to the right-hand rule - that

$$\begin{aligned}&\int\limits_{\partial\Sigma_i} f(x)\cdot \mathrm{d}s(x) = \sum_{j=1}^{3}\int\limits_{\partial\Sigma_{i,j}} f(x)\cdot \mathrm{d}s(x) \\ &= \int\limits_{I_{i,2}} \left(f_2(a_{i,2},x_2,c_{i,1})-f_2(a_{i,1},x_2,c_{i,1})\right)\mathrm{d}x_2 + \int\limits_{I_{i,1}} \left(f_1(x_1,b_{i,1},c_{i,1})-f_1(x_1,b_{i,2},c_{i,1})\right)\mathrm{d}x_1 \\ &\quad + \int\limits_{I_{i,3}} \left(f_3(a_{i,1},b_{i,2},x_3)-f_3(a_{i,1},b_{i,1},x_3)\right)\mathrm{d}x_3 + \int\limits_{I_{i,2}} \left(f_2(a_{i,1},x_2,c_{i,1})-f_2(a_{i,1},x_2,c_{i,2})\right)\mathrm{d}x_2 \\ &\quad + \int\limits_{I_{i,3}} \left(f_3(a_{i,1},b_{i,1},x_3)-f_3(a_{i,2},b_{i,1},x_3)\right)\mathrm{d}x_3 + \int\limits_{I_{i,1}} \left(f_1(x_1,b_{i,1},c_{i,2})-f_1(x_1,b_{i,1},c_{i,1})\right)\mathrm{d}x_1\end{aligned}$$

$$
\begin{aligned}
= \; & |I_{i,1}| \int\limits_{I_{i,2}} \partial_1 f_2(\bar{a_i}, x_2, c_{i,2}) \, \mathrm{d}x_2 - |I_{i,2}| \int\limits_{I_{i,1}} \partial_2 f_1(x_1, \bar{b_i}, c_{i,2}) \, \mathrm{d}x_1 \\
& + |I_{i,2}| \int\limits_{I_{i,3}} \partial_2 f_3(a_{i,2}, \tilde{b_i}, x_3) \, \mathrm{d}x_3 - |I_{i,3}| \int\limits_{I_{i,2}} \partial_3 f_2(a_{i,2}, x_2, \bar{c_i}) \, \mathrm{d}x_2 \\
& + |I_{i,3}| \int\limits_{I_{i,1}} \partial_3 f_1(x_1, b_{i,1}, \tilde{c_i}) \, \mathrm{d}x_1 - |I_{i,1}| \int\limits_{I_{i,3}} \partial_1 f_3(\tilde{a_i}, b_{i,1}, x_3) \, \mathrm{d}x_3 \, .
\end{aligned} \tag{1.141}
$$

for some values $a_{i,1} \leq \bar{a_i}/\tilde{a_i} \leq a_{i,2}$, $b_{i,1} \leq \bar{b_i}/\tilde{b_i} \leq b_{i,2}$ and $c_{i,1} \leq \bar{c_i}/\tilde{c_i} \leq c_{i,2}$. Applying the mean value theorem of integration, the previous relation then turns into

$$
\begin{aligned}
\int\limits_{\partial\Sigma_i} f(x) \cdot \mathrm{d}s(x) = & \left(\partial_1 f_2(\bar{a_i}, \hat{b_i}, c_{i,2}) - \partial_2 f_1(\hat{a_i}, \bar{b_i}, c_{i,2}) \right) |I_{i,1}||I_{i,2}| \\
& + \left(\partial_2 f_3(a_{i,2}, \tilde{b_i}, \hat{c_i}) - \partial_3 f_2(a_{i,2}, \dot{b_i}, \bar{c_i}) \right) |I_{i,2}||I_{i,3}| \\
& + \left(\partial_3 f_1(\dot{a_i}, b_{i,1}, \tilde{c_i}) - \partial_1 f_3(\tilde{a_i}, b_{i,1}, \dot{c_i}) \right) |I_{i,3}||I_{i,1}| \\
= & \left(\partial_2 f_3(a_{i,2}, \tilde{b_i}, \hat{c_i}) - \partial_3 f_2(a_{i,2}, \dot{b_i}, \bar{c_i}) \right) |\Sigma_{i,1}| \\
& + \left(\partial_3 f_1(\dot{a_i}, b_{i,1}, \tilde{c_i}) - \partial_1 f_3(\tilde{a_i}, b_{i,1}, \dot{c_i}) \right) |\Sigma_{i,2}| \\
& + \left(\partial_1 f_2(\bar{a_i}, \hat{b_i}, c_{i,2}) - \partial_2 f_1(\hat{a_i}, \bar{b_i}, c_{i,2}) \right) |\Sigma_{i,3}| \, .
\end{aligned} \tag{1.142}
$$

for some $a_{i,1} \leq \hat{a_i}/\dot{a_i} \leq a_{i,2}$, $b_{i,1} \leq \hat{b_i}/\dot{b_i} \leq b_{i,2}$, $c_{i,1} \leq \hat{c_i}/\dot{c_i} \leq c_{i,2}$. For the limit $N \to \infty$, again all areas become infinitesimal small and all points on the right-hand side of the equation fall into one point. Thus, we finally find

$$
\begin{aligned}
\lim_{N\to\infty} \sum_{i=1}^{N} \int\limits_{\partial\Sigma_i} f(x) \cdot \mathrm{d}s(x) = & \lim_{N\to\infty} \sum_{i=1}^{N} \left(\partial_2 f_3(a_{i,2}, \tilde{b_i}, \hat{c_i}) - \partial_3 f_2(a_{i,2}, \dot{b_i}, \bar{c_i}) \right) |\Sigma_{i,1}| \\
& + \left(\partial_3 f_1(\dot{a_i}, b_{i,1}, \tilde{c_i}) - \partial_1 f_3(\tilde{a_i}, b_{i,1}, \dot{c_i}) \right) |\Sigma_{i,2}| \\
& + \left(\partial_1 f_2(\bar{a_i}, \hat{b_i}, c_{i,2}) - \partial_2 f_1(\hat{a_i}, \bar{b_i}, c_{i,2}) \right) |\Sigma_{i,3}| \\
= & \int\limits_{\Sigma} (\nabla \wedge f(x)) \cdot n(x) \, \mathrm{d}\omega(x) = \int\limits_{\Sigma} (\nabla \wedge f(x)) \cdot \mathrm{d}\omega(x) \, .
\end{aligned} \tag{1.143}
$$

since for all $j = 1, 2, 3$, ϵ^j is the unit normal vector to the plane $\Sigma_{i,j}$.

A direct consequence of Gauss' theorem are the first and second Green's identities. Defining $f := F \, \nabla G$ for two scalar fields $F \in \mathrm{C}^{(1)}(D)$ and $G \in \mathrm{C}^{(2)}(D)$ and inserting it into (1.134) we find

$$
\begin{aligned}
\int\limits_{V} \left(F(x) \, \Delta G(x) + \nabla F(x) \cdot \nabla G(x) \right) \mathrm{d}V(x) = & \int\limits_{\partial V} \left(F(x) \, \nabla G(x) \right) \cdot \mathrm{d}\omega(x) \\
= & \int\limits_{\partial V} \left(F(x) \, \nabla_n G(x) \right) \mathrm{d}\omega(x) \, ,
\end{aligned} \tag{1.144}
$$

which is Green's first identity. Here, $\nabla_n F := \nabla F \cdot n$ denotes the so-called normal derivative of F. Interchanging the position of F and G (also assuming $F \in \mathrm{C}^{(2)}(D)$ now), subtracting the result from the previous equation, we arrive at Green's second identity:

$$
\int\limits_{V} \left(F(x) \, \Delta G(x) - G(x) \, \Delta F(x) \right) \mathrm{d}V(x) = \int\limits_{\partial V} \left(F(x) \, \nabla_n G(x) - G(x) \, \nabla_n F(x) \right) \mathrm{d}\omega(x) \, . \tag{1.145}
$$

Since Green's identities involve the Laplacian it turns out that these relations are quite useful in potential theory, where harmonic functions, i.e. functions F that satisfy $\Delta F = 0$, are investigated properly. Indeed, in the next section we will have a closer look at such harmonic functions on the unit sphere.

1.4 Spherical harmonics

1.4.1 Scalar spherical harmonics I

In this chapter we will present the so-called (scalar) **spherical harmonics**. These special functions form a basis system for squared integrable scalar functions that are defined on the unit sphere Ω. Since these functions play an essential role in spherical analysis and provide the basis for most of the topics in this work, we will have a detailed look at these functions and their origin, mainly following Freeden et al. (1998) and Michel (2013), two reference books for this topic. Furthermore, we took additional input from non-published notes for a lecture in Geomathematics (Mayer, 2007), which provides a great summary of this topic.

Spherical harmonics are defined as restrictions of homogeneous, harmonic polynomials to the unit sphere Ω. A polynomial H_l, defined on $\mathbb{R}^3$, is called homogeneous of degree $l \in \mathbb{N}$ if for any scalar $\lambda \in \mathbb{R}$ it holds that $H_l(\lambda x) = \lambda^l H_l(x)$ for all $x \in \mathbb{R}^3$. The space of all homogeneous polynomials of degree l is denoted by $\mathrm{Hom}_l(\mathbb{R}^3)$. It can be shown that the set of all monomials $\{x \mapsto \prod_i x_i^{\alpha_i} \mid \sum_i \alpha_i = l\}$ form a basis of $\mathrm{Hom}_l(\mathbb{R}^3)$. The number of these monomials is equal to the number of possible ways to select $D-1$ (number of vector components, where the first component is fixed) from a total of $D-1+l$ (free vector components + degree) items, where D is the dimension of the domain, i.e.

$$\dim\left(\mathrm{Hom}_l\left(\mathbb{R}^D\right)\right) = \begin{pmatrix} D-1+l \\ D-1 \end{pmatrix}. \tag{1.146}$$

Thus, for $D = 3$ we find

$$\dim\left(\mathrm{Hom}_l\left(\mathbb{R}^3\right)\right) = \begin{pmatrix} l+2 \\ 2 \end{pmatrix} = \frac{(l+2)(l+1)}{2}. \tag{1.147}$$

The space of all homogeneous polynomials of degree l on $\mathbb{R}^3$ that are additionally harmonic, i.e. $\Delta H_l = 0$, is denoted by $\mathrm{Harm}_l(\mathbb{R}^3)$. It can be shown that any $H_l \in \mathrm{Harm}_l(\mathbb{R}^3)$ can be represented using homogeneous polynomials of degree 0 to l, where all polynomials with degree $< l-1$ are determined by a recurrence formula from the polynomials of degree l and $l-1$. Thus, the dimension of $\mathrm{Harm}_l(\mathbb{R}^3)$ is equal to the number of free parameters of these two polynomials, i.e. $l+1$ and l, thus

$$\dim\left(\mathrm{Harm}_l\left(\mathbb{R}^3\right)\right) = 2l+1. \tag{1.148}$$

We define a spherical harmonic Y_l of degree l as the restriction of a homogeneous harmonic polynomial of degree l to the unit sphere Ω, i.e. $Y_l = H_l \mid \Omega$, where $H_l \in \mathrm{Harm}_l(\mathbb{R}^3)$. Furthermore, we denote the space of all spherical harmonics of degree l by $\mathrm{Harm}_l(\Omega) := \mathrm{Harm}_l(\mathbb{R}^3) \mid \Omega$.

It can be shown that spherical harmonics of different degrees are orthogonal in the sense of $\mathrm{L}^2(\Omega)$, i.e.

$$\int_\Omega Y_n(\xi)\, Y_m(\xi)\, \mathrm{d}\omega(\xi) = 0 \tag{1.149}$$

for $m \neq n$. Now, let $H_l \in \mathrm{Harm}_l(\mathbb{R}^3)$ and $Y_l \in \mathrm{Harm}_l(\Omega)$ be its restriction to the unit sphere. Since H_l is harmonic and homogeneous, we find for any $x = r\xi$, $r = |x|, \xi \in \Omega$:

$$0 = \Delta H_l(x) = \Delta H_l(r\xi) = \Delta\left(r^l\, Y_l(\xi)\right). \tag{1.150}$$

Applying the spherical polar representation (1.86) of the Laplace operator we find

$$0 = Y_l(\xi)\,\Delta^r r^l + r^{l-2}\Delta^* Y_l(\xi) = l(l+1)\,r^{l-2}\,Y_l(\xi) + r^{l-2}\Delta^* Y_l(\xi) \tag{1.151}$$

and thus

$$\Delta^* Y_l(\xi) = -l(l+1)\,Y_l(\xi), \tag{1.152}$$

i.e. any spherical harmonic Y_l of degree l is an eigenfunction of the Beltrami operator Δ^* to the eigenvalue $-l(l+1)$. This is one of the most essential properties of spherical harmonics and will be used repeatedly throughout this whole work.

To reveal the dimension of $\mathrm{Harm}_l(\Omega)$, we let $\{H_{l,m}\}_{m=1,\dots,2l+1}$ be a linearly independent system in $\mathrm{Harm}_l(\mathbb{R}^3)$ with their respective restrictions $\{Y_{l,m}\}_{m=1,\dots,2l+1}$ and state the (natural) assumption that by the restriction of the space to Ω, also the dimension is reduced, i.e. $\dim\left(\mathrm{Harm}_l(\Omega)\right) < 2l+1$. Then, if we construct a function $F \in \mathrm{Harm}_l(\Omega)$ that satisfies

$$F(\xi) := \sum_{m=1}^{2l+1} a_m Y_{l,m}(\xi) = 0 \tag{1.153}$$

for all $\xi \in \Omega$, there must be at least one set of non-trivial coefficients $a_m \in \mathbb{R}$, $m = 1, \dots, 2l+1$, such that the previous equation holds, since the $Y_{l,m}$ cannot be linearly independent. Now we consider the so-called **Interior Dirichlet Problem (IDP)**, where we seek a function $G \in \mathrm{C}^{(2)}(\Omega_{\mathrm{int}}) \cap \mathrm{C}^{(1)}(\Omega)$ that is harmonic in the interior and equals a given function $F \in \mathrm{C}(\Omega)$ on Ω, i.e.

$$\Delta G(x) = 0 \quad \text{for all } x \in \Omega_{\mathrm{int}}\,, \quad G(\xi) = F(\xi) \quad \text{for all } \xi \in \Omega\,. \tag{1.154}$$

Assuming that F has the representation as assumed above, it can easily be verified (in analogy to (1.151)) that a solution to the IDP is given by

$$G(x) = \sum_{m=1}^{2l+1} a_m r^l\, Y_{l,m}(\xi)\,. \tag{1.155}$$

On the other hand, also $G \equiv 0$ is a (trivial) solution to the IDP. In general, it can be shown - with the help of Green's identities - that the IDP is uniquely solvable. Thus, both found solutions must be equal, i.e., also using that the $Y_{l,m}$ are restrictions of the $H_{l,m}$:

$$G(x) = \sum_{m=1}^{2l+1} a_m r^l\, Y_{l,m}(\xi) = \sum_{m=1}^{2l+1} a_m H_{l,m}(x) = 0 \tag{1.156}$$

for all $x \in \Omega_{\mathrm{int}}$. Since the $H_{l,m}$ are polynomials, the previous equation can only be satisfied if G is the zero polynomial, i.e. $G(x) = 0$ for all $x \in \mathbb{R}^3$. Since the $H_{l,m}$ are linearly independent, the previous equation implies that $a_i = 0$ for all $i = 1, \dots, 2l+1$, which is a contradiction to our original assumption. Thus, we showed that indeed

$$\dim\left(\mathrm{Harm}_l(\Omega)\right) = \dim\left(\mathrm{Harm}_l(\mathbb{R}^3)\right) = 2l+1\,. \tag{1.157}$$

In accordance to the geophysical and geodetic community, from now on, we denote an ($\mathrm{L}^2(\Omega)$-) orthonormal system of $\mathrm{Harm}_l(\Omega)$ by $\{Y_{l,m}\}_{m=-l,\dots,l}$ and call the second index **order** of the spherical harmonic, in contrast to the geomathematical literature, where the order m is regularly denoted by $m = 1, \dots, 2l+1$. For such an ONS, the following very important relation, the so-called **addition theorem** of scalar spherical harmonics, can be shown. For any $\xi, \eta \in \Omega$, it holds that

$$\sum_{m=-l}^{l} Y_{l,m}(\xi)\, Y_{l,m}(\eta) = \frac{2l+1}{4\pi}\, P_l(\xi \cdot \eta)\,, \tag{1.158}$$

where P_l is the so-called **Legendre polynomial** of degree l. In literature, this relation is sometimes regarded as the extension of the trigonometrical relation

$$\cos(\alpha)\cos(\beta) + \sin(\alpha)\sin(\beta) = \cos(\alpha - \beta) \tag{1.159}$$

to the sphere, since $P_l(\xi \cdot \eta)$ only depends on the (cosine of the) angle between ξ and η and the spherical harmonics consist of linear combinations of sine and cosine functions as we will see later in this section. In the special case of $\xi = \eta$ we trivially find

$$\sum_{m=-l}^{l} \left(Y_{l,m}(\xi)\right)^2 = \frac{2l+1}{4\pi}\,, \tag{1.160}$$

since $P_l(1) = 1$ for all $l \in \mathbb{N}$ (see below). This relation then can be regarded as the extension of

$$\cos^2(\alpha) + \sin^2(\alpha) = 1 \tag{1.161}$$

to the sphere. The proof of the addition theorem is not trivial and requires a lot of additional theory (see e.g., Freeden et al., 1998). Here, we only state an interesting general equality that is used to build the bridge to the Legendre polynomials. It can be shown (see e.g., Hobson, 1955) that for any $x \in \mathbb{R}^3 \setminus \{0\}$

$$(\partial_i)^l \frac{1}{|x|} = (-1)^l \frac{(2l)!}{l!\,2^l} \frac{1}{|x|^{2l+1}} \left(\sum_{s=0}^{[l/2]} (-1)^s \frac{l!\,(2l-2s)!}{(2l)!\,(l-s)!\,s!} |x|^{2s}\, \Delta^s \right) x_i^l\,, \tag{1.162}$$

where

$$\left[\frac{l}{2}\right] = \frac{1}{2}\left(l - \frac{1}{2}\left(1 - (-1)^l\right)\right) \tag{1.163}$$

is the Gauss bracket and Δ^s denotes a s-times application of the Laplace operator. Later we will state an explicit representation of the Legendre polynomials that is similar to the right-hand side of the previous equation.

1.4.2 Legendre polynomials

Now, we have a more detailed look at the Legendre polynomials $\{P_l\}_{l\in\mathbb{N}}$ themselves since the addition theorem suggests a close relationship between them and the spherical harmonics. In this section, we will provide a lot of details and include a variety of own calculations and derivations where it seemed appropriate, since this can basically not be found in any textbook. We consider this to be quite helpful or even necessary to gain a deeper insight into this topic.

In general, there are various - equivalent - ways to introduce the Legendre polynomials. From a historical point of view, for the first time they were discovered in Legendre (1785) when investigating the multipole expansion of the electric potential of a point source at $x \in \mathbb{R}^3$ with $x = r\xi$, $r \in \mathbb{R}, \xi \in \Omega$. The potential at a point $y \in \mathbb{R}^3$ with $y = R\eta$, $R \in \mathbb{R}, \eta \in \Omega$ is proportional to the inverse distance $1/|x-y|$ between both points. Assuming - without loss of generality - that $R > r$, this expression can be reformulated as

$$\frac{1}{|x-y|} = \frac{1}{\sqrt{\langle x-y, x-y\rangle}} = \frac{1}{\sqrt{R^2 - 2\,x\cdot y + r^2}} = \frac{1}{R\sqrt{1 - 2\left(\frac{r}{R}\right)\xi\cdot\eta + \left(\frac{r}{R}\right)^2}}\,, \tag{1.164}$$

where the square-root term on the right-hand side can be interpreted as a more general function

$$f_t(h) := \frac{1}{\sqrt{1-2ht+h^2}}\,. \tag{1.165}$$

In the case of the inverse distance, the scalar product $\xi \cdot \eta$ plays the role of t and the ratio of both vector norms, i.e. r/R, plays the role of h, such that we have

$$\frac{1}{|x-y|} = \frac{1}{R} f_{(\xi\cdot\eta)}\left(\frac{r}{R}\right) . \tag{1.166}$$

Expanding f_t in a power series in h, i.e. a Taylor series centred at 0, we can (formally - the series does not necessarily converge) represent f_t as

$$f_t(h) = \sum_{l=0}^{\infty} \frac{f_t^{(l)}(0)}{l!} h^l . \tag{1.167}$$

But indeed, it can be shown that for a fixed $t \in [-1,1]$ this Taylor series has a convergence radius of 1, more precisely, it converges for any $h \in]-1,1[$. We see that due to the assumption of $R > r$ and $t = \xi \cdot \eta$, both conditions are especially satisfied for the case of the inverse distance. The coefficients of this power series - that are dependent on the choice of t - turn out to be polynomials in t. They are called **Legendre polynomials** (of the first kind) and are denoted by $P_l(t)$, i.e. we define

$$P_l(t) := \frac{f_t^{(l)}(0)}{l!} , \tag{1.168}$$

$t \in]-1,1[$, such that we have per definition

$$f_t(h) = \frac{1}{\sqrt{1-2ht+h^2}} = \sum_{l=0}^{\infty} P_l(t)\, h^l . \tag{1.169}$$

For the inverse distance, this yields the well-known representation

$$\frac{1}{|x-y|} = \sum_{l=0}^{\infty} \frac{r^l}{R^{l+1}} P_l(\xi \cdot \eta) , \tag{1.170}$$

which, in combination with the addition theorem (1.158), immediately yields a representation of the inverse distance in terms of spherical harmonics, i.e.

$$\frac{1}{|x-y|} = \sum_{l=0}^{\infty} \sum_{m=-l}^{l} \frac{4\pi}{2l+1} \frac{r^l}{R^{l+1}} Y_{l,m}(\xi)\, Y_{l,m}(\eta) . \tag{1.171}$$

The index l of a Legendre polynomial is called **degree** and it turns out that this degree coincides with the polynomial degree of P_l. The definition (1.168) already provides us with an explicit instruction to calculate the Legendre polynomials, e.g. for the first three degrees, we find that

$$\begin{aligned}
P_0(t) &= \frac{f_t^{(0)}(0)}{0!} = \left.\frac{1}{\sqrt{1-2ht+h^2}}\right|_{h=0} = 1 , \\
P_1(t) &= \frac{f_t^{(1)}(0)}{1!} = \left.\frac{t-h}{(1-2ht+h^2)^{\frac{3}{2}}}\right|_{h=0} = t , \\
P_2(t) &= \frac{f_t^{(2)}(0)}{2!} = \frac{1}{2}\left.\left(\frac{3t^2-4ht+2h^2-1}{(1-2ht+h^2)^{\frac{5}{2}}}\right)\right|_{h=0} = \frac{1}{2}\left(3t^2-1\right) .
\end{aligned} \tag{1.172}$$

From here, we can already guess that the l-th Legendre polynomial seems to be a polynomial of degree l. But we notice that this calculation becomes very tedious for higher degrees. Nevertheless, taking the first derivative with respect to h on both sides of (1.169), which yields

$$\frac{t-h}{(1-2ht+h^2)^{\frac{3}{2}}} = \sum_{l=1}^{\infty} l\, P_l(t)\, h^{l-1} = \sum_{l=0}^{\infty} (l+1)\, P_{l+1}(t)\, h^l , \tag{1.173}$$

and inserting again the expression from (1.169) gives us

$$\begin{aligned}(t-h)\sum_{l=0}^{\infty} P_l(t)\,h^l &= (1-2ht+h^2)\sum_{l=0}^{\infty}(l+1)\,P_{l+1}(t)\,h^l \\ \Leftrightarrow \quad \sum_{l=0}^{\infty}\left(t\,P_l(t)\,h^l - P_l(t)\,h^{l+1}\right) & \\ = \sum_{l=0}^{\infty}\left((l+1)\,P_{l+1}(t)\,h^l - 2t(l+1)\,P_{l+1}(t)\,h^{l+1} + (l+1)\,P_{l+1}(t)\,h^{l+2}\right)&\,.\end{aligned} \tag{1.174}$$

Expressing all parts in terms of the same exponent in h yields

$$\begin{aligned}&\sum_{l=0}^{\infty} t\,P_l(t)\,h^l - \sum_{l=1}^{\infty} P_{l-1}(t)\,h^l \\ =&\sum_{l=0}^{\infty}(l+1)\,P_{l+1}(t)\,h^l - \sum_{l=1}^{\infty} 2tl\,P_l(t)\,h^l + \sum_{l=2}^{\infty}(l-1)\,P_{l-1}(t)\,h^l.\end{aligned} \tag{1.175}$$

By comparison of the coefficients we find the following (recurrence) relation between the Legendre polynomials of different degrees for $l \geq 1$:

$$(l+1)\,P_{l+1}(t) = (2l+1)\,t\,P_l(t) - l\,P_{l-1}(t)\,, \tag{1.176}$$

or equivalently

$$l\,P_l(t) = (2l-1)\,t\,P_{l-1}(t) - (l-1)\,P_{l-2}(t)\,, \tag{1.177}$$

for $l \geq 2$. In combination with the *initial values* $P_0(t) = 1$ and $P_1(t) = t$ from (1.172) - figuratively also called **seed values** or **seeds** - this provides an efficient way to evaluate Legendre polynomials of higher degrees. Basically, since for $l = 1$ the second term on the right-hand side cancels due to the factor $(l-1)$, we can just ignore the (non-existing) P_{-1} (or define $P_{-1} \equiv 0$), which makes the previous relation even valid for $l = 1$. Thus, technically speaking, P_0 remains the only seed in the recurrence scheme.

From this recurrence relation, we can deduce that with ascending degree, also the polynomial degree rises by 1 due to the factor of t, such that indeed, $\deg(P_l) = l$ for all $l \in \mathbb{N}$. Furthermore, it can be shown that the Legendre polynomials are orthogonal in the sense of L^2, i.e.

$$\langle P_m, P_n\rangle_{\mathrm{L}^2([-1,1])} = \int_{-1}^{1} P_m(t)\,P_n(t)\,\mathrm{d}t = 0 \tag{1.178}$$

for $m \neq n$. By these two properties, along with the normalisation condition that $P_l(1) = 1$ for all $l \in \mathbb{N}$, the Legendre polynomials are also uniquely determined. Thus, they are also introduced by many authors as the one and only system of polynomials on the interval $[-1, 1]$ that satisfy the three conditions stated above.

Moreover, simply combining (1.169) and (1.173), we find that

$$\frac{1-h^2}{(1-2ht+h^2)^{\frac{3}{2}}} = \frac{1}{\sqrt{1-2ht+h^2}} + \frac{2h(t-h)}{(1-2ht+h^2)^{\frac{3}{2}}} = \sum_{l=0}^{\infty}(2l+1)\,P_l(t)\,h^l\,. \tag{1.179}$$

Now exploiting the orthogonality of the Legendre polynomials and the fact that $P_0(t) = 1$ for all $t \in [-1, 1]$, the previous relation yields the following impressive result:

$$\frac{1}{2}\int_{-1}^{1}\frac{1-h^2}{(1-2ht+h^2)^{\frac{3}{2}}}\,\mathrm{d}t = \frac{1}{2}\sum_{l=0}^{\infty}(2l+1)\,h^l\int_{-1}^{1} P_l(t)\,P_0(t)\,\mathrm{d}t = 1\,, \tag{1.180}$$

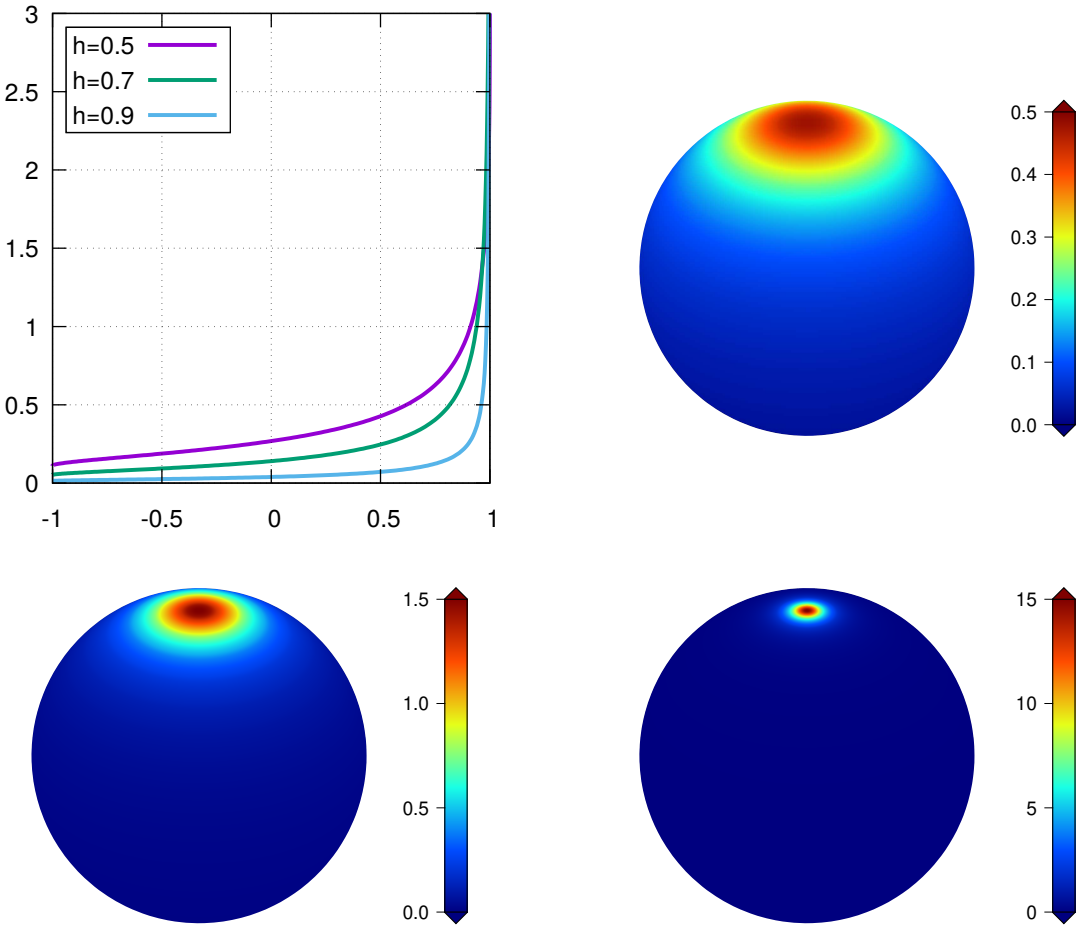

Figure 1.3: Top left: Abel-Poisson kernels on the interval [-1,1] for the values $h = 0.5$, $h = 0.7$ and $h = 0.9$. Top right: Abel-Poisson kernel on the sphere for the value $h = 0.5$. Bottom left: Abel-Poisson kernel on the sphere for the value $h = 0.7$. Bottom right: Abel-Poisson kernel on the sphere for the value $h = 0.9$. For all spherical plots, the reference point $\xi \in \Omega$ was chosen to be the North pole.

or equivalently, using the zonal function conversion rule (1.126),

$$\frac{1}{4\pi} \int_{\Omega} \frac{1-h^2}{(1-2h(\xi\cdot\eta)+h^2)^{\frac{3}{2}}} \, \mathrm{d}\omega(\eta) = 1 \,, \tag{1.181}$$

for any $\xi \in \Omega$. In Figure 1.3 we show a plot of both functions, the function on the left-hand side in (1.180) on the interval $[-1,1]$ and the corresponding zonal function from (1.181) on the sphere, both for different values of h. We see that for increasing values of h, on the interval $[-1,1]$ the function shows more and more similarity to a delta distribution with a peak at $t = 1$. Furthermore, since the integral over the whole interval remains finite - and especially equals 1 - for all $h \in]-1,1[$, we can actually interpret the function as a kind of delta sequence that approaches the delta distribution as $h \to 1$ (from below). On the sphere, we see exactly the same behaviour with the peak at $\eta = \xi$. Thus,

we potentially could expect that for any $F \in \mathrm{L}^2([-1,1])$ there is a behaviour like

$$\lim_{h\to 1-} \frac{1}{2} \int_{-1}^{1} \frac{1-h^2}{(1-2ht+h^2)^{\frac{3}{2}}} F(t)\,\mathrm{d}t = F(1)\,, \tag{1.182}$$

and equivalently in the context of the zonal function, for any $F \in \mathrm{L}^2(\Omega)$ that

$$\lim_{h\to 1-} \frac{1}{4\pi} \int_{\Omega} \frac{1-h^2}{(1-2h(\xi\cdot\eta)+h^2)^{\frac{3}{2}}} F(\eta)\,\mathrm{d}\omega(\eta) = F(\xi)\,, \tag{1.183}$$

for all $\xi \in \Omega$. And indeed, the previous relation can be formally proven for any $F \in \mathrm{C}(\Omega)$ (see e.g., Freeden et al., 1998; Michel, 2013) and is called **Poisson integral formula**. The function

$$K_h(\xi,\eta) := \frac{1}{4\pi} \frac{1-h^2}{(1-2h(\xi\cdot\eta)+h^2)^{\frac{3}{2}}} \tag{1.184}$$

is called **Abel-Poisson kernel** and also plays a crucial role in the context of Sobolev spaces, spherical splines and wavelets (see e.g., Horbach, 2008). The systematics that is described by the Poisson integral formula is called **approximate identity**. For a fixed h that we choose for the Abel-Poisson kernel, we can find an approximation to F, using (1.183), where in the limit $h \to 1-$, this approximation converges to the actual function F.

Now we return to the Legendre polynomials. The orthogonality is a very important property, since the system $\{P_l\}_{l=0,\dots,N}$ for any $N \in \mathbb{N}$ can now be regarded as a basis system for all polynomials of degree $l \leq N$. Since also the monomials $\{x^l\}_{l=0,\dots,N}$ form a basis system, due to uniqueness, the Legendre polynomials are the result of the application of the Gram-Schmidt orthogonalisation scheme to this set of monomials. But this condition is also of special interest since Rodrigues (1816) showed that orthogonal polynomials can - under some additional conditions that are satisfied here - be represented by an explicit reconstruction formula. In case of the Legendre polynomials, this **Rodrigues' formula** (also known as **Ivory-Jacobi formula**) (see Ivory, 1824; Jacobi, 1827, for a historical context) states as:

$$P_l(t) = \frac{1}{2^l\, l!} \left(\frac{\mathrm{d}}{\mathrm{d}t}\right)^l (t^2-1)^l \tag{1.185}$$

for all $l \in \mathbb{N}$. There are similar Rodrigues' formulae for other systems of orthogonal polynomials like e.g. the Laguerre polynomials and the Hermite polynomials. This explicit representation of the Legendre polynomials now opens the door to a variety of further applications and representations. Amongst others, this formula e.g. leads to the representation

$$P_l(t) = \sum_{s=0}^{[l/2]} (-1)^s \frac{(2l-2s)!}{2^l\,(l-2s)!\,(l-s)!\,s!}\, t^{l-2s} \tag{1.186}$$

that now reminds of the right-hand side of (1.162). Furthermore, we can use (1.185) to show the following recurrence formula, including derivatives of the Legendre polynomials (using the abbreviation $\mathrm{d}_t := \frac{\mathrm{d}}{\mathrm{d}t}$):

$$\begin{aligned}
\mathrm{d}_t P_{l+1}(t) &= \frac{1}{2^{l+1}(l+1)!}\, \mathrm{d}_t^{l+2} \left(t^2-1\right)^{l+1} \\
&= \frac{2(l+1)}{2^{l+1}(l+1)!}\, \mathrm{d}_t^{l+1} t \left(t^2-1\right)^{l} \\
&= \frac{1}{2^l\, l!}\, \mathrm{d}_t^{l} \left(\left(t^2-1\right)^{l} + 2lt^2 \left(t^2-1\right)^{l-1}\right) \\
&= \frac{1}{2^l\, l!}\, \mathrm{d}_t^{l} \left(\left(t^2-1\right)^{l} + 2l \left(\left(t^2-1\right)^{l-1} + \left(t^2-1\right)^{l}\right)\right) \\
&= (2l+1)\, P_l(t) + \mathrm{d}_t P_{l-1}\,,
\end{aligned} \tag{1.187}$$

or in an equivalent representation

$$(2l+1)\,P_l(t) = \frac{\mathrm{d}}{\mathrm{d}t}\left(P_{l+1}(t) - P_{l-1}(t)\right)\,. \tag{1.188}$$

In literature, using the Rodrigues representation is also the most common way to prove the orthogonality of the Legendre polynomials (by iterative partial integration). But since the orthogonality originally even was a condition for the validity of the Rodrigues formula, this is - historically speaking - not a consistent way.

Furthermore, the Rodrigues representation can be used to show that the Legendre polynomial of degree l is a solution to the so-called **Legendre differential equation**

$$\left(\frac{\mathrm{d}}{\mathrm{d}t}\left(1-t^2\right)\frac{\mathrm{d}}{\mathrm{d}t}\right)P(t) + \left(l(l+1) - \frac{m^2}{1-t^2}\right)P(t) = 0 \tag{1.189}$$

in case of $m = 0$. In other words, the Legendre polynomials are eigenfunctions of the **Legendre operator**

$$\mathrm{L}_t := \frac{\mathrm{d}}{\mathrm{d}t}\left(1-t^2\right)\frac{\mathrm{d}}{\mathrm{d}t} \tag{1.190}$$

to the corresponding eigenvalue $\lambda_l = -l(l+1)$. Note that these eigenvalues coincide with the eigenvalues of the spherical harmonics with respect to the Beltrami operator. In literature, this is also a popular way to introduce and define the Legendre polynomials, i.e. as the polynomial eigenfunctions of the Legendre operator L_t. Since we introduced the Legendre polynomials in a different way - with the help of the Taylor series of the inverse distance - we are now able to prove this important property via already shown identities. Here, also the product rule for arbitrary orders of differentiation plays a key role, i.e. for two n-times differentiable functions f and g, we have

$$(fg)^{(n)} = \sum_{k=0}^{n}\binom{n}{k} f^{(k)}\,g^{(n-k)}\,. \tag{1.191}$$

Respecting this differentiation rule, we find that

$$\begin{aligned}&\mathrm{d}_t^{l+2}\left(1-t^2\right)\left(t^2-1\right)^l\\ =&\left(1-t^2\right)\mathrm{d}_t^{l+2}\left(t^2-1\right)^l - 2t(l+2)\,\mathrm{d}_t^{l+1}\left(t^2-1\right)^l - (l+1)(l+2)\,\mathrm{d}_t^{l}\left(t^2-1\right)^l\,.\end{aligned} \tag{1.192}$$

For the Legendre polynomial P_l of degree $l \in \mathbb{N}$, we can then show, using (1.185) and (1.192), that

$$\begin{aligned}\mathrm{L}_t P_l(t) &= \mathrm{d}_t\left(1-t^2\right)\mathrm{d}_t P_l(t)\\ &= \frac{1}{2^l\,l!}\,\mathrm{d}_t\left(1-t^2\right)\mathrm{d}_t^{l+1}\left(t^2-1\right)^l\\ &= \frac{1}{2^l\,l!}\left(\left(1-t^2\right)\mathrm{d}_t^{l+2}\left(t^2-1\right)^l - 2t\,\mathrm{d}_t^{l+1}\left(t^2-1\right)^l\right)\\ &= \frac{1}{2^l\,l!}\left(-\mathrm{d}_t^{l+2}\left(t^2-1\right)^{l+1} + 2t(l+1)\,\mathrm{d}_t^{l+1}\left(t^2-1\right)^l\right) + (l+1)(l+2)\,P_l(t)\\ &= \frac{1}{2^l\,l!}\left(-2(l+1)\,\mathrm{d}_t^{l+1}\,t\left(t^2-1\right)^l + 2t(l+1)\,\mathrm{d}_t^{l+1}\left(t^2-1\right)^l\right) + (l+1)(l+2)\,P_l(t)\\ &= \frac{1}{2^l\,l!}\left(-2(l+1)^2\,\mathrm{d}_t^{l}\left(t^2-1\right)^l\right) + (l+1)(l+2)\,P_l(t)\\ &= -\,l(l+1)\,P_l(t)\,.\end{aligned} \tag{1.193}$$

This property will be essential for the derivation of an explicit representation of the spherical harmonics. Since (1.189) is a linear differential equation of second order, there are two sets of (linearly independent) functions that satisfy this relation. The solutions that are not the Legendre polynomials,

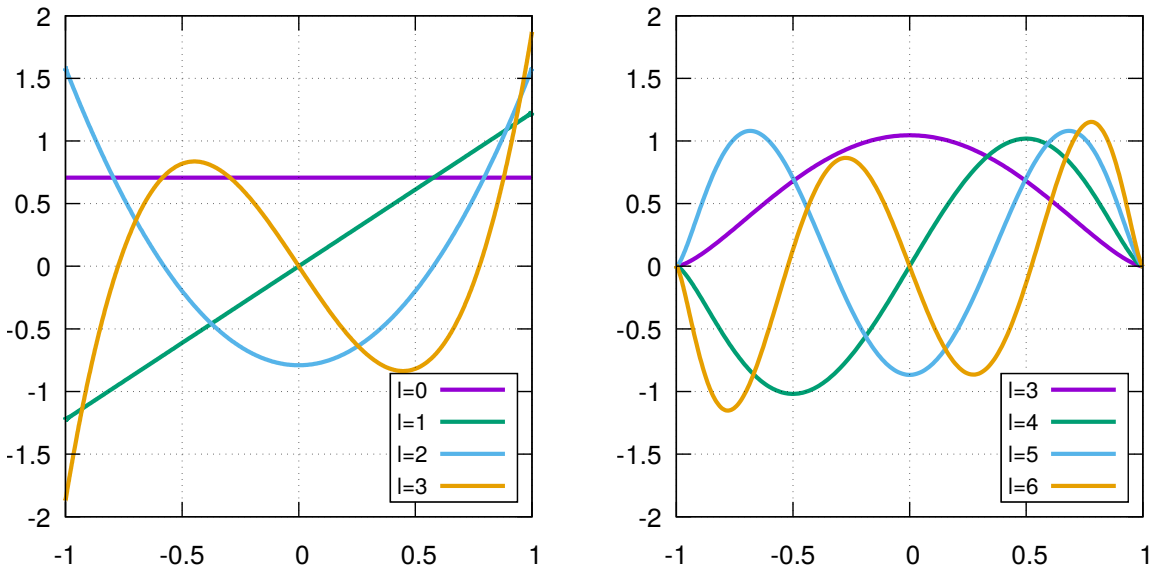

order $m = 0$

order $m = 3$

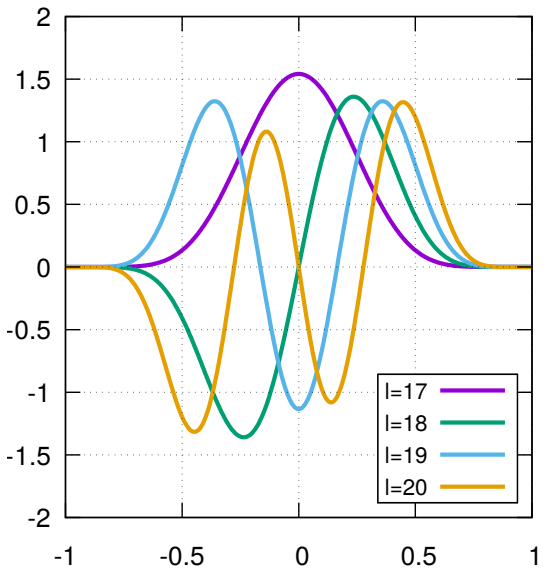

order $m = 17$

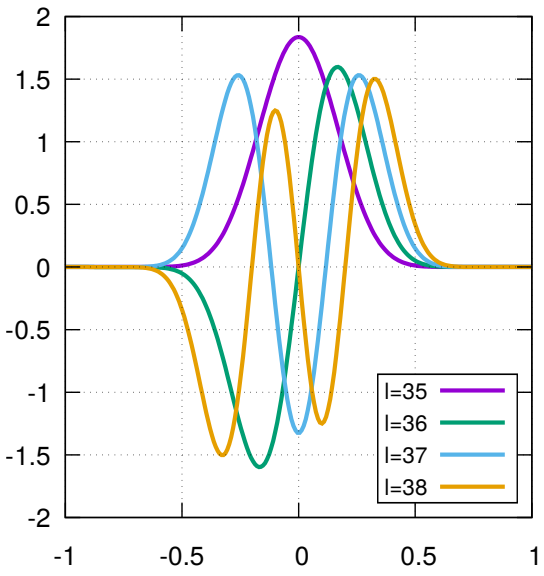

order $m = 35$

Figure 1.4: Normalised associated Legendre polynomials of different degrees and orders. In each plot, we fixed the order m and varied the degree l. In the plot on the top left, the order is set to $m = 0$, thus, here we find the ordinary (normalised) Legendre polynomials.

are called **Legendre functions of the second kind** and are often denoted by $Q_l(t)$ in literature. They are no polynomials and have singularities at $t = \pm 1$.

In the general case that the second parameter m in (1.189) is a positive integer not equal to 0, the Legendre equation also has two sets of non-trivial solutions. The first set of solutions that are connected to the Legendre polynomials are denoted by $P_{l,m}(t)$ and are called **associated Legendre polynomials** or also **associated Legendre functions** of degree l and order m. Here, the expression 'function' is more appropriate than 'polynomial' since the $P_{l,m}$ are only polynomials if m is even (see below). The second set of solutions is closely connected to the Legendre functions of the second kind and are thus denoted by $Q_{l,m}(t)$ and called **associated Legendre functions of the second kind**. In the case of $m = l$, the associated Legendre polynomials are called sectoral. In Figure 1.4 we show the plots of a selection of associated Legendre functions of different degrees and orders.

It can be shown that the associated Legendre functions (of the first and second kind) can be calculated explicitly by differentiating the ordinary Legendre functions in the following way:

$$\begin{aligned} P_{l,m}(t) &= (1-t^2)^{\frac{m}{2}} \left(\frac{\mathrm{d}}{\mathrm{d}t}\right)^m P_l(t)\,, \\ Q_{l,m}(t) &= (1-t^2)^{\frac{m}{2}} \left(\frac{\mathrm{d}}{\mathrm{d}t}\right)^m Q_l(t)\,. \end{aligned} \tag{1.194}$$

Thus, we find e.g.

$$\begin{aligned} P_{1,1}(t) &= \sqrt{1-t^2}\,, \\ P_{2,1}(t) &= 3t\sqrt{1-t^2}\,, \\ P_{2,2}(t) &= 3\left(1-t^2\right)\,. \end{aligned} \tag{1.195}$$

In the previous relations, some authors introduce an additional factor of $(-1)^m$ which is called the **Cordon-Shortley phase**. This factor is commonly used in quantum mechanics (introduced in Condon and Shortley, 1935) whereas it is omitted in most mathematical, geophysical and geodetic literature. Thus, we also neglect it here in this work. Furthermore, we see the expected identities $P_{l,0} \equiv P_l$ and $Q_{l,0} \equiv Q_l$ and due to the factor of $(1-t^2)^{m/2}$ we also see that the resulting function is a polynomial (of degree l) only in the case that m is an even integer. If m is odd, the associated Legendre functions are polynomials (of degree $l-1$) that are multiplied by the factor of $\sqrt{1-t^2}$. Due to this factor, we can also immediately deduce that - except for $m = 0$ - all associated Legendre polynomials equal zero for $|t| = 1$, i.e. $P_{l,m}(-1) = P_{l,m}(1) = 0$ for all $m > 0$. In the following, we restrict ourselves again to the Legendre polynomials of the first kind. Combined with Rodrigues' formula the previous equation can be reformulated as

$$P_{l,m}(t) = \frac{(1-t^2)^{\frac{m}{2}}}{2^l\, l!} \left(\frac{\mathrm{d}}{\mathrm{d}t}\right)^{l+m} (t^2-1)^l\,. \tag{1.196}$$

This representation yields a natural extension of the associated Legendre polynomials to negative values of m. Furthermore, from here, we can deduce that $P_{l,m} \equiv 0$ for $m > l$. We will not need the extension to negative m in the process of constructing an explicit representation of spherical harmonics and thus, we will only consider positive values of m in the following. Moreover, using $\mathrm{d}_t^n t^n = n!$, the previous representation yields for the sectoral polynomials that

$$\begin{aligned} P_{l,l}(t) &= \frac{(1-t^2)^{\frac{l}{2}}}{2^l\, l!} \left(\frac{\mathrm{d}}{\mathrm{d}t}\right)^{2l} (t^2-1)^l = \left(1-t^2\right)^{\frac{l}{2}} \frac{(2l)!}{2^l\, l!} = \left(1-t^2\right)^{\frac{l}{2}} \prod_{i=1}^{l} (2i-1) \\ &= \left(1-t^2\right)^{\frac{l}{2}} (2l-1)!!\,, \end{aligned} \tag{1.197}$$

where $n!! := \prod_{i=0}^{\frac{n}{2}-1}(n-2i)$ is the double factorial.

We now prove that (1.194) is valid by showing that the previously defined functions indeed satisfy the Legendre differential equation. First, we show - again using (1.191) - that

$$\begin{aligned} \mathrm{d}_t^m \mathrm{L}_t &= \mathrm{d}_t^m \left(\left(1-t^2\right) \mathrm{d}_t^2 - 2t\, \mathrm{d}_t \right) \\ &= \left(1-t^2\right) \mathrm{d}_t^{m+2} - 2tm\, \mathrm{d}_t^{m+1} - m(m-1)\, \mathrm{d}_t^m - 2t\, \mathrm{d}_t^{m+1} - 2m\, \mathrm{d}_t^m \\ &= \left(1-t^2\right) \mathrm{d}_t^{m+2} - 2t(m+1)\, \mathrm{d}_t^{m+1} - m(m+1)\, \mathrm{d}_t^m \,. \end{aligned} \tag{1.198}$$

Furthermore, the application of the Legendre operator to an associated Legendre polynomial yields

$$\begin{aligned} &\mathrm{L}_t P_{l,m}(t) \\ &= \mathrm{d}_t \left(1-t^2\right) \mathrm{d}_t P_{l,m}(t) \\ &= \mathrm{d}_t \left(1-t^2\right) \mathrm{d}_t \left(1-t^2\right)^{\frac{m}{2}} \mathrm{d}_t^m P_l(t) \\ &= \mathrm{d}_t \left(1-t^2\right) \left(\left(1-t^2\right)^{\frac{m}{2}} \mathrm{d}_t^{m+1} - tm \left(1-t^2\right)^{\frac{m-2}{2}} \mathrm{d}_t^m \right) P_l(t) \\ &= (1-t^2)^{\frac{m}{2}} \left(\left(1-t^2\right) \mathrm{d}_t^{m+2} - t(m+2)\, \mathrm{d}_t^{m+1} - m\, \mathrm{d}_t^m - tm\, \mathrm{d}_t^{m+1} + \frac{t^2\, m^2}{1-t^2}\, \mathrm{d}_t^m \right) P_l(t) \\ &= (1-t^2)^{\frac{m}{2}} \left(\left(1-t^2\right) \mathrm{d}_t^{m+2} - 2t(m+1)\, \mathrm{d}_t^{m+1} - m(m+1)\, \mathrm{d}_t^m + \frac{m^2}{1-t^2}\, \mathrm{d}_t^m \right) P_l(t) \,. \end{aligned} \tag{1.199}$$

Now, inserting (1.198) into (1.199) and using the already proven eigenfunction property (1.193) of the Legendre polynomials, we indeed find that

$$\begin{aligned} \mathrm{L}_t P_{l,m}(t) &= (1-t^2)^{\frac{m}{2}} \left(\mathrm{d}_t^m \mathrm{L}_t + \frac{m^2}{1-t^2}\, \mathrm{d}_t^m \right) P_l(t) \\ &= (1-t^2)^{\frac{m}{2}} \left(-l(l+1) + \frac{m^2}{1-t^2} \right) \mathrm{d}_t^m P_l(t) \\ &= \left(-l(l+1) + \frac{m^2}{1-t^2} \right) P_{l,m}(t) \,. \end{aligned} \tag{1.200}$$

In analogy to Rodrigues' formula for the Legendre polynomials, the representation (1.196) is also not suitable for determining explicit representations of the associated Legendre polynomials in an efficient way. To overcome this problem, we developed the recurrence formula (1.177) for the (ordinary) Legendre polynomials. In order to prepare the derivation of a similar scheme, we first transfer the relation (1.188) to the associated Legendre polynomials. Here, we find

$$\begin{aligned} (2l+1)\, P_{l,m}(t) &= \left(1-t^2\right)^{\frac{m}{2}} \mathrm{d}_t^m (2l+1)\, P_l(t) \\ &= \left(1-t^2\right)^{\frac{m}{2}} \mathrm{d}_t^{m+1} \left(P_{l+1}(t) - P_{l-1}(t) \right) \\ &= \frac{1}{\sqrt{1-t^2}} \left(P_{l+1,m+1}(t) - P_{l-1,m+1}(t) \right) \,, \end{aligned} \tag{1.201}$$

or equivalently

$$(2l-1)\sqrt{1-t^2}\, P_{l-1,m-1}(t) = P_{l,m}(t) - P_{l-2,m}(t) \,. \tag{1.202}$$

Now, by exploiting the recurrence relation (1.177) and inserting it into (1.194) we find that

$$\begin{aligned} l\, P_{l,m}(t) &= l\, (1-t^2)^{\frac{m}{2}} \mathrm{d}_t^m P_l(t) \\ &= (1-t^2)^{\frac{m}{2}} \mathrm{d}_t^m \left((2l-1) t\, P_{l-1}(t) - (l-1)\, P_{l-2}(t) \right) \\ &= (1-t^2)^{\frac{m}{2}} \left((2l-1) \left(t\, \mathrm{d}_t^m P_{l-1}(t) + m\, \mathrm{d}_t^{m-1} P_{l-1}(t) \right) - (l-1)\, \mathrm{d}_t^m P_{l-2}(t) \right) \\ &= (2l-1) t\, P_{l-1,m}(t) + (2l-1) m \sqrt{1-t^2}\, P_{l-1,m-1}(t) - (l-1)\, P_{l-2,m}(t) \,. \end{aligned} \tag{1.203}$$

In combination with (1.202) we can represent the previous recurrence scheme in an even more compact way and notice a structure that is very similar to the recurrence scheme of the ordinary Legendre polynomials:

$$(l-m)\,P_{l,m}(t) = (2l-1)t\,P_{l-1,m}(t) - (l+m-1)\,P_{l-2,m}(t)\,. \tag{1.204}$$

As we should expect, for the case $m = 0$, the previous relations transfers into (1.177). In principle, for each degree $l \geq 1$, this scheme is valid for all orders $m = 0, ..., l$ (in the case $m = l-1$ the second term on the right-hand side vanishes) but in the case of $m = l$, we do not gain any information but only the trivial relation $0 = 0$. Thus, for the sectoral polynomials, we need to apply the original relation (1.203) and find:

$$P_{l,l}(t) = (2l-1)\sqrt{1-t^2}\,P_{l-1,l-1}(t)\,. \tag{1.205}$$

Note that for each order m, the sectoral polynomial $P_{m,m}$, that can be reconstructed by (1.205) from the respective sectoral polynomial of one degree less, serves as a seed for the recurrence relation (1.204).
We already learned in (1.178) that Legendre polynomials of different degrees are orthogonal to each other. Also the associated Legendre polynomials satisfy orthogonality relations. First, for a fixed order m, the polynomials of different degrees are orthogonal to each other, i.e. for a fixed $m \in \mathbb{N}$

$$\langle P_{l,m}, P_{j,m}\rangle_{\mathrm{L}^2([-1,1])} = \int_{-1}^{1} P_{l,m}(t)\,P_{j,m}(t)\,\mathrm{d}t = 0 \tag{1.206}$$

for $l \neq j$. In contrast, for a fixed degree $l \in \mathbb{N}$, the associated polynomials of different orders are not orthogonal to each other in the L^2-sense but orthogonal with respect to the weight function $(1-t^2)^{-1}$. More precisely, for a fixed $l \in \mathbb{N}$ we have

$$\int_{-1}^{1} P_{l,m}(t)\,P_{l,n}(t)\left(1-t^2\right)^{-1}\,\mathrm{d}t = 0 \tag{1.207}$$

for $m \neq n$. In the case of $l = j$ in (1.206), it can be shown - commonly also using Rodrigues' formula - that the integral, which then can be identified with the L^2 norm, can be determined as

$$\|P_{l,m}\|_2 = \left(\int_{-1}^{1}\left(P_{l,m}(t)\right)^2\,\mathrm{d}t\right)^{\frac{1}{2}} = \sqrt{\frac{2}{2l+1}\frac{(l+m)!}{(l-m)!}}\,. \tag{1.208}$$

Thus, for the case of $m = 0$ - the ordinary Legendre polynomials - we gain

$$\|P_l\|_2 = \sqrt{\frac{2}{2l+1}}\,. \tag{1.209}$$

We notice that, where the norm of the Legendre polynomials decreases with increasing degree l, the norm of the associated Legendre polynomials dramatically increases for increasing degree and order, e.g. for the sectoral polynomial - with has the largest norm among all orders for a fixed degree - of degree $l = 10$ we already have $\|P_{10,10}\| \approx 10^8$. Since for double precision, the *Institute of Electrical and Electronic Engineers* (IEEE) standard 754 for binary floating-point arithmetic (Coonen, 1980) allows the allocation of numbers of an absolute value between $\approx 2^{-1024}$ and 2^{1024} - which equals the range of $\approx 10^{-308}$ and 10^{308} - the norm of the sectoral associated Legendre functions provides a natural border for the implementation of the Legendre polynomials. This double precision limit is reached for $l = 150$, where we have $\|P_{150,150}\| \approx 1.42 \cdot 10^{306}$. For $l = 151$, the sectoral norm already generates an *overflow*.

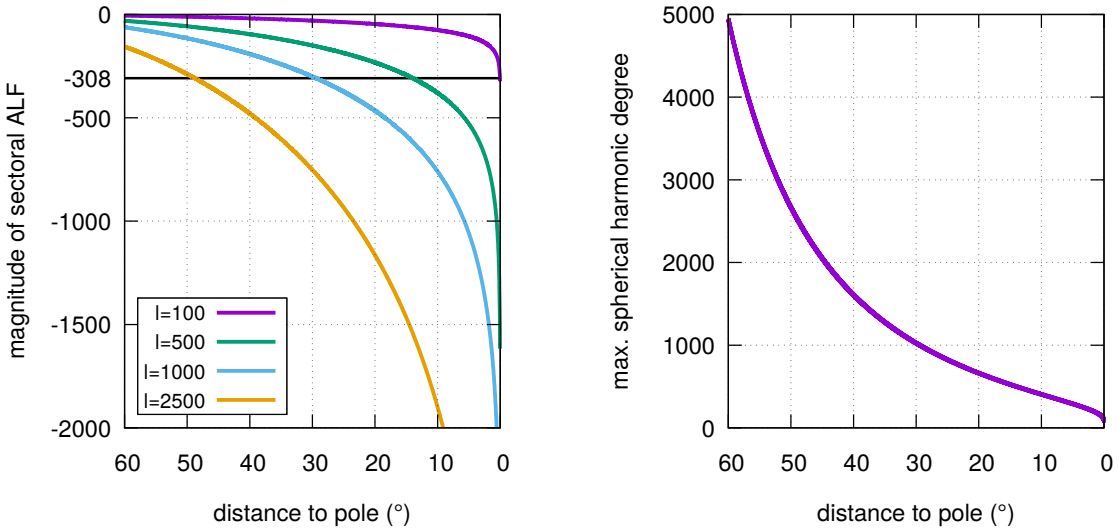

Figure 1.5: Left: magnitude of the sectoral associated Legendre function (ALF) of different degrees, evaluated at various latitudes, measured in angular distance to the pole(s). Right: plot of the crossing points of the curves on the left plot with the underflow barrier at the magnitude -308 for all harmonic degrees. These crossing points are a measure of the maximum harmonic degree still available at each latitude.

Thus in practice, the previously presented recurrence formulae turn out to be numerically very unstable and it is in general very convenient to use the normalised polynomials and also to include the normalisation factors already in the recurrence schemes. More precisely, if we define the normalised polynomials as

$$\bar{P}_{l,m} := \frac{P_{l,m}}{\|P_{l,m}\|} \tag{1.210}$$

and insert $P_{l,m} = \|P_{l,m}\|\bar{P}_{l,m}$ into the recurrence schemes (1.204) and (1.205), we gain the following relations for the normalised associated Legendre polynomials:

$$\begin{aligned} \bar{P}_{l,m}(t) &= \sqrt{\frac{2l+1}{(l+m)(l-m)}}\left(\sqrt{2l-1}\,t\,\bar{P}_{l-1,m}(t) - \sqrt{\frac{(l+m-1)(l-m-1)}{2l-3}}\,\bar{P}_{l-2,m}(t)\right), \\ \bar{P}_{l,l}(t) &= \sqrt{\frac{2l+1}{2l}}\,\sqrt{1-t^2}\,\bar{P}_{l-1,l-1}(t) \end{aligned} \tag{1.211}$$

with the (only) seed $\bar{P}_{0,0}(t) = 1/\sqrt{2}$. This (normalised) scheme is much more stable than the original recurrence relation from a numerical point of view and is recommended to be implemented for an explicit calculation of the Legendre polynomials. Indeed, we also used the previous scheme to calculate the associated Legendre polynomials wherever it was necessary within this work. From here - or alternatively just by including the normalisation into the product representation (1.197) - we see that the normalised sectoral polynomials can also be rewritten as

$$\bar{P}_{l,l}(t) = \left(1-t^2\right)^{\frac{l}{2}}\sqrt{\frac{(2l+1)!!}{2(2l)!!}} = \frac{\left(1-t^2\right)^{\frac{l}{2}}}{\sqrt{2}}\prod_{i=1}^{l}\sqrt{\frac{2i+1}{2i}}\,. \tag{1.212}$$

From all previous representations we see that the norm of the associated Legendre functions is not the only trouble zone where problems can arise from during the evaluation of the polynomials. Since

the factor $(1-t^2)^{l/2}$ equals 0 for $|t| = 1$ and the polynomials are continuous, there is a neighbourhood around the points $t = -1$ and $t = 1$ - which equal the poles if we identify t with the polar distance - where the value of the Legendre polynomials becomes very small and is almost approaching 0. Due to the degree l in the exponent, this problem becomes more and more evident with increasing degree. As we have learned before, if the value descends below the barrier of 10^{-308}, we create an *underflow* and the evaluation of the Legendre function is not possible any more. In Figure 1.5 we plot the magnitude of the value of the sectoral polynomial of degrees $l = 100, 500, 1000, 2500$ at different latitudes (using the polar distance $t = \cos\varphi$) together with the underflow barrier at magnitude -308. We see that for $l = 100$, basically for all latitudes, we are still above the barrier, but already for $l = 500$ we cannot even more reach all points that are 10 degrees or closer to the pole. For $l = 1000$ we already cross the barrier at 30 degrees and for $l = 2500$ we cannot even reach half of the upper/lower sphere any more. On the right plot in Figure 1.5 we plot exactly these crossing points with the underflow barrier at -308 for all harmonic degrees. In this way we get for each latitude a maximum harmonic degree which is still evaluable there. In the subsection about *spherical harmonic synthesis* we will learn strategies how to evaluate a spherical harmonic series in spite of the presented underflow problems.

As a final remark in this section it should be mentioned that there are also recurrence formulae for integrals of the associated Legendre polynomials. These are especially useful for the calculation of the gravitational potential of a spherical cube and we will discuss them later in a more detailed way in Chapter 4.

1.4.3 Scalar spherical harmonics II

We now return to the spherical harmonics and focus on deriving an explicit representation. We already learned that a spherical harmonic of degree l is an eigenfunction of the Beltrami operator with respect to the eigenvalue $-l(l+1)$. Thus, applying the spherical polar representation of Δ^*, where we now recognise the Legendre operator L_t, we find

$$\left(\frac{1}{1-t^2}\,\partial_{\varphi^2}^2 + \partial_t\left(1-t^2\right)\partial_t\right) Y_{l,m} = \left(\frac{1}{1-t^2}\,\partial_{\varphi^2}^2 + \mathrm{L}_t\right) Y_{l,m} = -l(l+1)\,Y_{l,m}\,. \tag{1.213}$$

Now, we do a separation ansatz and assume that a spherical harmonic, that depends on the spherical coordinates φ and t, can be represented as a product of two functions that each depend on only one of the two variables, i.e. we assume $Y_{l,m}(\varphi, t) = A(\varphi)B(t)$ for some functions A and B. Inserting this ansatz into the previous equation yields

$$\begin{aligned} 0 &= \left(\frac{1}{1-t^2}\,\partial_{\varphi^2}^2 + \mathrm{L}_t + l(l+1)\right) A(\varphi)\,B(t) \\ &= A(\varphi)\left(\mathrm{L}_t + l(l+1)\right) B(t) + B(t)\left(\frac{1}{1-t^2}\,\partial_{\varphi^2}^2\right) A(\varphi)\,. \end{aligned} \tag{1.214}$$

Due to (1.189) we notice that the associated polynomials would be an appropriate choice for the function $B(t)$. By choosing $B(t) = P_{l,m}(t)$ for some degree l and order m and inserting (1.189) into the previous equation, we can eliminate the Legendre operator and find

$$\begin{aligned} 0 &= A(\varphi)\,\frac{m^2}{1-t^2}\,P_{l,m}(t) + P_{l,m}(t)\left(\frac{1}{1-t^2}\,\partial_{\varphi^2}^2\right) A(\varphi) \\ &= \frac{1}{1-t^2}\;P_{l,m}(t)\left(\partial_{\varphi^2}^2 + m^2\right) A(\varphi)\,. \end{aligned} \tag{1.215}$$

At last, we now require the function A to satisfy

$$\left(\partial_{\varphi^2}^2 + m^2\right) A(\varphi) = 0 \tag{1.216}$$

for all $\varphi \in [0, 2\pi]$. This property is fulfilled by both trigonometric functions $\sin(m\varphi)$ and $\cos(m\varphi)$. Thus, we now know that a spherical harmonic of degree $l \in \mathbb{N}$ is the product of an associated Legendre

polynomial of degree l and a sine or cosine function, where the order m of the Legendre polynomial corresponds to the frequency parameter of sine and cosine. Since for each degree l there are $l+1$ eligible orders and for each order, the respective associated Legendre polynomial can be combined with one of both sin or cos, we have $2(l+1)$ possible combinations. But since $\sin(0 \cdot \varphi)$ is the zero function and thus, per definition, does not contribute to a system of basis functions, $(2l+1)$ eligible combinations remain. This corresponds well to the dimension of $\mathrm{Harm}_l(\Omega)$ that is already known from (1.157). Indeed, due to the orthogonality of sin and cos it can easily be shown that the presented system of functions forms an orthonormal system with respect to the L^2 norm. Thus, including the normalisation of the trigonometrical functions, i.e.

$$\int_0^{2\pi} \sin^2(m\varphi)\,\mathrm{d}\varphi = \int_0^{2\pi} \cos^2(m\varphi)\,\mathrm{d}\varphi = \pi \quad \text{and} \quad \int_0^{2\pi} \mathrm{d}\varphi = 2\pi \tag{1.217}$$

we can denote an orthonormal system of spherical harmonics of degree l by

$$Y_{l,m}(\varphi,t) := \sqrt{\frac{1}{(1+\delta_{m,0})\pi}}\,\bar{P}_{l,|m|}(t) \begin{cases} \cos(|m|\varphi)\,, & m = 0,...,l \\ \sin(|m|\varphi)\,, & m = -l,...,-1\,. \end{cases} \tag{1.218}$$

In the following, we want to explicitly state all spherical harmonics up to degree and order 2. Especially, the degree 2 representations will be of use in Chapter 4, where we find a link between the harmonic coefficients of the Earth's gravitational potential and the inertia tensor. It holds that

$$\begin{aligned}
Y_{0,0}(\varphi,t) &= \sqrt{\frac{1}{4\pi}}\,, & Y_{1,0}(\varphi,t) &= \sqrt{\frac{3}{4\pi}}\,t\,, \\
Y_{1,1}(\varphi,t) &= \sqrt{\frac{3}{4\pi}}\sqrt{1-t^2}\,\cos\varphi\,, & Y_{1,-1}(\varphi,t) &= \sqrt{\frac{3}{4\pi}}\sqrt{1-t^2}\,\sin\varphi\,, \\
Y_{2,0}(\varphi,t) &= \sqrt{\frac{5}{16\pi}}\left(3t^2-1\right)\,, & Y_{2,1}(\varphi,t) &= \sqrt{\frac{15}{4\pi}}\,t\,\sqrt{1-t^2}\,\cos\varphi\,, \\
Y_{2,-1}(\varphi,t) &= \sqrt{\frac{15}{4\pi}}\,t\,\sqrt{1-t^2}\,\sin\varphi\,, & Y_{2,2}(\varphi,t) &= \sqrt{\frac{15}{16\pi}}\left(1-t^2\right)\cos(2\varphi)\,, \\
Y_{2,-2}(\varphi,t) &= \sqrt{\frac{15}{16\pi}}\left(1-t^2\right)\sin(2\varphi)\,.
\end{aligned} \tag{1.219}$$

Figure 1.6 shows the illustration of spherical harmonics of different degrees and orders. We see that the spherical harmonic representation can be compared with a Fourier analysis in 1-D and the degree l can be interpreted as the frequency where the order m characterises the structure of the function. Spherical harmonics with order $m = 0$ are called **zonal** spherical harmonics since they are only dependent on the polar distance and constant with respect to the longitude (compare to the zonal functions in (1.126)). In accordance to the associated Legendre polynomials, spherical harmonics with order $|m| = l$ are called **sectoral** and all other combinations are declared as **tesseral** spherical harmonics.

But in spite of this explicit representation, at this point, it is still an open question how the spherical harmonics can help us to represent and also approximate functions on the unit sphere, which is our primary goal. Since we know from the Weierstrass theorem that a continuous function on an interval can be approximated arbitrarily well by polynomials, we hope to have a similar behaviour for continuous functions on the sphere and the spherical harmonics that also basically consist of polynomials of different degrees. Indeed, the bulk part of the answer to this question is already contained in the Poisson integral formula (1.183). Using the abbreviation

$$F_{l,m} := \langle F, Y_{l,m} \rangle_{\mathrm{L}^2} = \int_\Omega F(\eta)\,Y_{l,m}\,,(\eta)\,\mathrm{d}\omega(\eta) \tag{1.220}$$

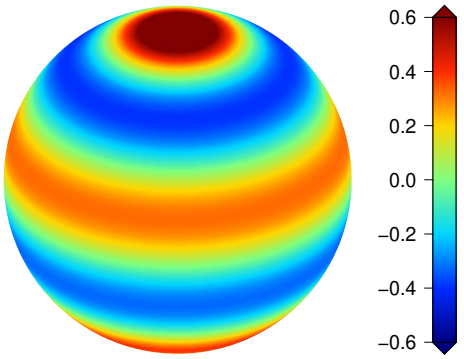

zonal spherical harmonic of degree 5 and order 0

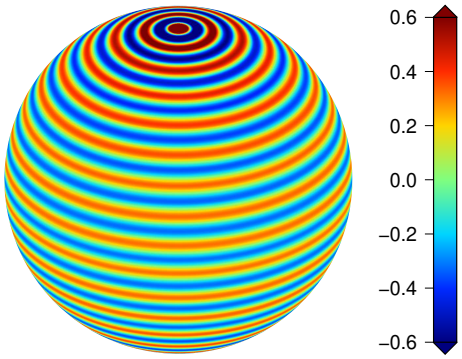

zonal spherical harmonic of degree 35 and order 0

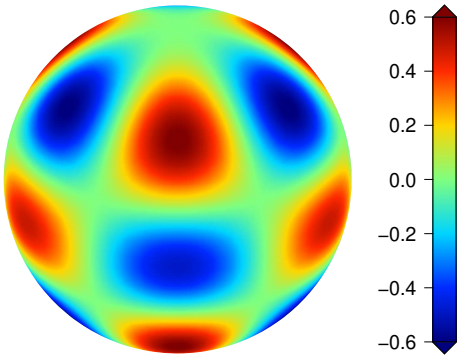

tesseral spherical harmonic of degree 5 and order 3

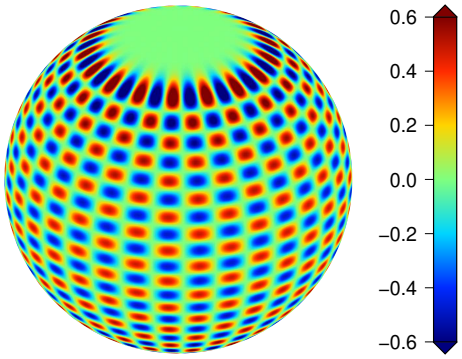

tesseral spherical harmonic of degree 35 and order 17

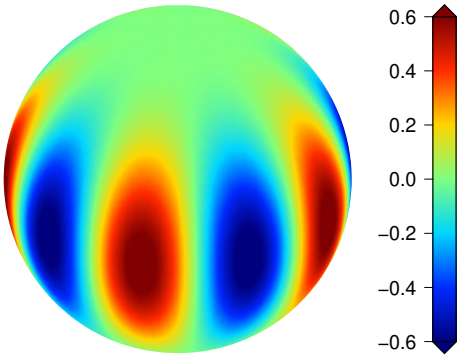

sectoral spherical harmonic of degree 5 and order 5

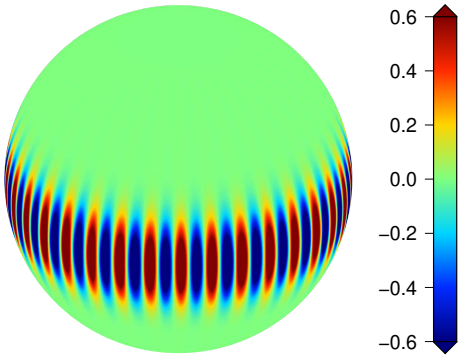

sectoral spherical harmonic of degree 35 and order -35

Figure 1.6: Normalised scalar spherical harmonics of different degrees and orders.

for the L^2 Fourier coefficients, the application of the addition theorem (1.158) and the relation (1.179) yields for a fixed $h \in]-1,1[$, $F \in \mathrm{C}(\Omega)$ and $\xi \in \Omega$ that

$$\begin{aligned}\sum_{l=0}^{\infty}\sum_{m=-l}^{l} h^l\, F_{l,m} Y_{l,m}(\xi) &= \sum_{l=0}^{\infty}\sum_{m=-l}^{l} h^l \int_{\Omega} F(\eta)\, Y_{l,m}(\eta)\, Y_{l,m}(\xi)\,\mathrm{d}\omega(\eta) \\ &= \frac{1}{4\pi}\sum_{l=0}^{\infty}\int_{\Omega}(2l+1)\, h^l\, P_l(\xi\cdot\eta)\, F(\eta)\,\mathrm{d}\omega(\eta) \\ &= \frac{1}{4\pi}\int_{\Omega}\frac{1-h^2}{(1-2h(\xi\cdot\eta)+h^2)^{\frac{3}{2}}}\, F(\eta)\,\mathrm{d}\omega(\eta)\,.\end{aligned} \tag{1.221}$$

It is allowed to interchange summation and integration in the previous steps due to Lebesgue's dominated convergence theorem (see e.g., Heuser, 1981). And from the Poisson integral formula, we know that in the limit $h \to 1-$, the previous integral converges pointwise to $F(\xi)$, i.e. we have

$$\lim_{h\to 1-}\sum_{l=0}^{\infty} h^l \sum_{m=-l}^{l} F_{l,m}\, Y_{l,m}(\xi) = F(\xi)\,. \tag{1.222}$$

Furthermore, it can be shown that for a fixed $h \in]0,1[$, the series converges *uniformly* with respect to ξ. The immediate consequence of the previous results is that the system of spherical harmonics $\{Y_{l,m}\}_{l\in\mathbb{N}_0, m=-l,\dots,l}$ is closed in $\mathrm{C}(\Omega)$ with respect to $\|\cdot\|_{\mathrm{C}(\Omega)}$. But since $\mathrm{C}(\Omega)$ is not a Hilbert space (only a Pre-Hilbert space, equipped with the L^2-norm), we have not yet found an entrance to the fundamental theorem (1.23), which would provide us with desired approximation properties in terms of a Fourier series.

But from here, we can quite easily build a bridge to the space $\mathrm{L}^2(\Omega)$ since on the one hand, there is an explicit connection between both norms, i.e. we know from (1.21) that $\|F\|_{\mathrm{L}^2(\Omega)} \le \sqrt{4\pi}\,\|F\|_{\mathrm{C}(\Omega)}$ for all $F \in \mathrm{C}(\Omega)$, and on the other hand, we know that the space $\mathrm{C}(\Omega)$ is dense in $\mathrm{L}^2(\Omega)$ with respect to $\|\cdot\|_{\mathrm{L}^2(\Omega)}$. In combination, these two properties yield that actually, the system $\{Y_{l,m}\}_{l\in\mathbb{N}_0, m=-l,\dots,l}$ is also closed in $\mathrm{L}^2(\Omega)$ with respect to $\|\cdot\|_{\mathrm{L}^2(\Omega)}$, which finally provides an entrance to the fundamental theorem.

From (1.23) b) we now immediately gain the desired property of the convergence of the Fourier series, i.e. for any $F \in \mathrm{L}^2(\Omega)$ we find that

$$\lim_{N\to\infty}\left\| F - \sum_{l=0}^{N}\sum_{m=-l}^{l} F_{l,m}\, Y_{l,m}\right\|_{\mathrm{L}^2(\Omega)} = 0\,, \tag{1.223}$$

where $F_{l,m}$ are the Fourier coefficients of F as already defined in (1.220). The Fourier series with respect to the spherical harmonics is sometimes also referred to as **Laplace series**. In the special case of a ϵ^3-zonal function, i.e. if F does not vary with φ but only with the polar distance t, only the zonal coefficients in the Laplace series remain - this can easily be verified using (1.218). Furthermore, we can identify F with a corresponding function $G \in \mathrm{L}^2([-1,1])$ (see also (1.126)) and we end up with the **Legendre series**, fulfilling

$$\lim_{N\to\infty}\left\| G - \sum_{l=0}^{N} G_l\, \bar{P}_l\right\|_{\mathrm{L}^2([-1,1])} = 0\,, \tag{1.224}$$

where

$$G_l := \int_{-1}^{1} G(t)\, \bar{P}_l(t)\,\mathrm{d}t\,, \tag{1.225}$$

$l \in \mathbb{N}_0$, denote the Legendre coefficients.

An essential implication of (1.223) and (1.224) is that these equalities only state convergence in the sense of L^2 (!) which does not imply pointwise convergence. This means that in general, for $F \in \mathrm{L}^2(\Omega)$ and $\xi \in \Omega$ we have

$$F(\xi) \neq \sum_{l=0}^{\infty} \sum_{m=-l}^{l} F_{l,m}\, Y_{l,m}(\xi)\,. \tag{1.226}$$

But if we want to use the spherical harmonic series as an approximation and representation method for functions on the sphere in practice, pointwise convergence would be an inevitably necessary condition. Luckily, Jackson (1912) proved for the Legendre series that indeed the Lipschitz continuity of F serves as a sufficient condition for a pointwise convergence. Based on this work, Gronwall (1914) was able to prove the same behaviour for the Laplace series. Thus, from now on, if not stated differently, we assume every function that we discuss in the context of spherical harmonics to be at least Lipschitz continuous - or even continuously differentiable, what implies Lipschitz continuity - such that we ensure to have

$$F(\xi) = \sum_{l=0}^{\infty} \sum_{m=-l}^{l} F_{l,m}\, Y_{l,m}(\xi)\,. \tag{1.227}$$

If there exists an $L \in \mathbb{N}_0$ such that the series turns into a finite summation, i.e. F even satisfies

$$F(\xi) = \sum_{l=0}^{L} \sum_{m=-l}^{l} F_{l,m}\, Y_{l,m}(\xi) \tag{1.228}$$

for all $\xi \in \Omega$, i.e. $F_{l,m} = 0$ for all $l > L$ or in other words, all Fourier coefficients above a certain degree L vanish, F is called **(L-)bandlimited**. Note that in literature, a function is sometimes called L-bandlimited if all Fourier coefficients of degree $l \geq L$ are equal to zero (see e.g., Driscoll and Healy, 1994; McEwen and Wiaux, 2011). These different conventions may cause confusion.

Expansion to a spherical shell

Though it is nice to have basis functions in $\mathrm{L}^2(\Omega)$, almost all physical quantities that will be discussed within this work are not defined on the unit sphere Ω but on a sphere Ω_R with radius $R \neq 1$. If we focus on problems related to e.g. circulation within the Earth's mantle, we will investigate quantities like velocity, pressure or temperature which are defined in a thick spherical shell Ω_E which is bounded by the Earth's surface and the core-mantle boundary.

It can quite easily be shown that the concept of spherical harmonics can be extended to general spheres with radius $R > 0$ (see e.g., Freeden and Michel, 2004; Luther, 2007) but for our purposes this is not even necessary. Due to the fact that the space $\mathrm{L}^2(\Omega)$ is isomorphic to $\mathrm{L}^2(\Omega_R)$ for any $R > 0$, any function $F \in \mathrm{L}^2(\Omega_R)$ can uniquely be identified with a function $G \in \mathrm{L}^2(\Omega)$ on the unit sphere. We can define the isomorphism $T : \mathrm{L}^2(\Omega_R) \to \mathrm{L}^2(\Omega)$ by $TF = G$ with $G(\xi) := F(R\xi)$ for all $\xi \in \Omega$. Reversely the inverse T^{-1} can be determined as $T^{-1}G = F$ with $F(x) := G(\frac{x}{R})$ for all $x \in \Omega_R$.

Thus, for a scalar field $F \in \mathrm{L}^2(\Omega_R)$ (Lipschitz continuous to guarantee the pointwise convergence) and the corresponding scalar field $G \in \mathrm{L}^2(\Omega)$ on the unit sphere as defined above we find that

$$\begin{aligned} F(x) = F(R\xi) = G(\xi) &= \sum_{l,m} \int_{\Omega} G(\eta)\, Y_{l,m}(\eta)\, \mathrm{d}\omega(\eta)\, Y_{l,m}(\xi) \\ &= \sum_{l,m} \int_{\Omega} F(R\eta)\, Y_{l,m}(\eta)\, \mathrm{d}\omega(\eta)\, Y_{l,m}(\xi) \\ &= \sum_{l,m} F^{(R)}_{l,m}\, Y_{l,m}(\xi)\,, \end{aligned} \tag{1.229}$$

where the spherical harmonic coefficients of F are defined as

$$F_{l,m}^{(R)} := \int_{\Omega} F(R\eta)\, Y_{l,m}(\eta)\, \mathrm{d}\omega(\eta)\,. \tag{1.230}$$

If we extend these properties even to a spherical shell we find for $F \in \mathrm{L}^2(\Omega_E)$ with $\alpha, \beta > 0$ that

$$\begin{aligned} F(x) &= \sum_{l,m} \int_{\Omega} F(r\eta)\, Y_{l,m}(\eta)\, \mathrm{d}\omega(\eta)\, Y_{l,m}(\xi) \\ &= \sum_{l,m} F_{l,m}(r)\, Y_{l,m}(\xi)\,, \end{aligned} \tag{1.231}$$

where the spherical harmonic coefficients now are dependent on r ($x = r\xi$):

$$F_{l,m}(r) := \int_{\Omega} F(r\eta)\, Y_{l,m}(\eta)\, \mathrm{d}\omega(\eta) \tag{1.232}$$

for all $r \in [\alpha, \beta]$.

Spherical Harmonic Analysis

Equipped with a pointwise converging Fourier series from a theoretical point of view, we want to briefly discuss computational / numerical aspects and challenges that occur when applying the spherical harmonic series in practice. Basically, on the one hand, the Fourier series now allows one to approximate a given Lipschitz continuous function F on the unit sphere, or in practice a function that is sampled on a certain spherical grid, by a truncated series up to a certain harmonic degree. In literature, this is referred to as **global spherical harmonic analysis**. In other words, here it is possible to separate contributions from different degrees, i.e. *frequencies*, of the total function. For this task, it is necessary to compute the respective spherical harmonic coefficients $F_{l,m}$ according to (1.220). Here, the task is to determine a variety of spherical integrals, where especially the evaluation of the spherical harmonic $Y_{l,m}$ at a specified set of points on the sphere is needed.
On the other hand - since a function is uniquely determined by its Fourier coefficients - in the case that the coefficients $F_{l,m}$ are given, one can reconstruct the original function - or in practice an approximation of the function up to a certain degree - by applying (1.227). In literature, this task is referred to as **global spherical harmonic synthesis**.

We start with the explicit Fourier series (1.227) and see that with a simple rearrangement, i.e. an interchange of degree and order, we gain further insight into the structure of this representation. This turns out to be very helpful in the context of implementation aspects. Also applying the explicit representation (1.218) we find that

$$\begin{aligned} F(\xi) &= \sum_{l=0}^{\infty} \sum_{m=-l}^{l} F_{l,m}\, Y_{l,m}(\xi) \\ &= \sum_{m=0}^{\infty} \sum_{l=m}^{\infty} \left(F_{l,m}\, Y_{l,m}(\xi) + F_{l,-m}\, Y_{l,-m}(\xi) \right) \\ &= \sum_{m=0}^{\infty} \sqrt{\frac{1}{(1+\delta_{m,0})\pi}} \left(\cos(m\varphi) \sum_{l=m}^{\infty} F_{l,m}\, \bar{P}_{l,m}(t) + \sin(m\varphi) \sum_{l=m}^{\infty} F_{l,-m}\, \bar{P}_{l,m}(t) \right)\,. \end{aligned} \tag{1.233}$$

Furthermore, using the abbreviations

$$\begin{aligned} A_m(t) &:= \sum_{l=m}^{\infty} F_{l,m}\, \bar{P}_{l,m}(t)\,, \\ B_m(t) &:= \sum_{l=m}^{\infty} F_{l,-m}\, \bar{P}_{l,m}(t)\,, \\ \lambda_m &:= \sqrt{\frac{1}{(1+\delta_{m,0})\pi}}\,, \end{aligned} \tag{1.234}$$

we arrive at

$$F(\xi(\varphi,t)) = \sum_{m=0}^{\infty} \lambda_m \left(A_m(t)\cos(m\varphi) + B_m(t)\sin(m\varphi)\right)\,. \tag{1.235}$$

This representation reveals that the spherical harmonic expansion can be regarded as a one-dimensional Fourier expansion in each latitude (or polar distance), where the $\lambda_m A_m$ and $\lambda_m B_m$ are the latitude dependent Fourier coefficients with respect to the (non-normalised) sine and cosine functions. We also notice that the coefficients A_m and B_m are defined as a series - or a sum in the finite case - of associated Legendre polynomials of a fixed order m.

A similar observation can be made for the determination of the Fourier coefficients if we apply (1.218) to (1.220). Here we find

$$\begin{aligned} F_{l,m} &= \int_{\Omega} F(\eta)\, Y_{l,m}(\eta)\, \mathrm{d}\omega(\eta) \\ &= \int_{-1}^{1} \bar{P}_{l,|m|}(t) \left(\int_0^{2\pi} \lambda_m \left\{ \begin{array}{c} \cos(|m|\varphi) \\ \sin(|m|\varphi) \end{array} \right\} F(\varphi,t)\, \mathrm{d}\varphi \right) \mathrm{d}t \\ &= \int_{-1}^{1} \bar{P}_{l,|m|}(t) \left\{ \begin{array}{c} A_m(t) \\ B_m(t) \end{array} \right\} \mathrm{d}t\,. \end{aligned} \tag{1.236}$$

We notice that also the determination of the Fourier coefficients $F_{l,m}$ can be divided into a two-step analysis. First, one can calculate the one-dimensional Fourier coefficients of F with respect to the trigonometrical basis system, built from sine and cosine functions. The result equals the coefficients $A_m(t)$ and $B_m(t)$ which serve as input for the integral in combination with an associated Legendre function.

Especially in the geodetic community, the task of determining the Fourier coefficients of a spherical function from a given set of samples is of fundamental importance. Due to novel satellite missions, the Earth's gravity field can be sampled in a more and more detailed resolution. Thus, there is an intrinsic need of finding efficient algorithms to derive spherical harmonic coefficients even of very high degree and order from the given data set.
First investigations were already done by Gauss and Neumann in the early 19th century since at this time global magnetic data became available (Gauss, 1839) what triggered research in the context of an appropriate global representation of the data. In his early work, Gauss approached this task in a very natural and straightforward way. He reformulated the problem in terms of a minimisation problem, i.e. given a data set y_i, $i = 1, ..., N$, $N \in \mathbb{N}$, for a representation up to a specified degree $L \in \mathbb{N}_0$ find Fourier coefficients c_j, $j = 1, ..., M$ - where $M = (L+1)^2$ equals the total number of Fourier coefficients up to degree L - such that the total approximation error of the Fourier series with respect

to the data becomes minimal. More precisely, we are looking for a coefficient vector $c_{\text{opt}} \in \mathbb{R}^M$ with

$$c_{\text{opt}} = \underset{c \in \mathbb{R}^M}{\arg\min} \, \|Ac - y\|_{\mathbb{R}^N} \,, \tag{1.237}$$

where the i-th row of $A \in \mathbb{R}^{N \times M}$ consists of the values of the respective basis function - the spherical harmonics - at the evaluation point corresponding to y_i. This is nothing else than the well-known least-squares approach. A solution to the previous equation can e.g. be found by applying a QR decomposition. Alternatively, one can show that the previous relation is equivalent to the normal equation

$$\left(A^T A\right) c_{\text{opt}} = A^T y \,. \tag{1.238}$$

This can e.g. be solved by determining the inverse $(A^T A)^{-1}$ directly or - since the matrix $A^T A$ is positive definite - using the Cholesky decomposition, a conjugate gradient method and/or some additional regularisation techniques. The main advantage of this Gaussian least-squares formulation is that it is applicable to any given data vector y. There is no explicit requirement at which points of the domain the data has to be given. This is in contrast to the methods we will present in the following paragraphs. We will see that there are various methods that even guarantee an exact and not only approximate determination of the Fourier coefficients but each of them has strict requirements on the distribution of the data points. This is one of the main reasons why even today the least-squares method is very popular in the context of a spherical harmonic analysis.

Almost at the same time as Gauss, Neumann (1838) dealt with the same subject but used a different approach. He mainly followed the two-step analysis that we presented in (1.236) and showed that under certain circumstances it is even possible to calculate the desired integrals exactly and not just approximatively. A sufficient condition for an exact representation of these integrals is the so-called **discrete orthogonality** of the involved basis functions. Discrete orthogonality means that the basis functions fulfil the orthogonality condition - up to a certain index / degree $L \in \mathbb{N}_0$ - even if only an evaluation at a finite point set (that has to be determined) is considered, i.e. for an orthogonal system $\{B_l\}_{l \in \mathbb{N}_0}$ it holds that

$$\sum_{i=0}^{N} w_i \, B_j(x_i) \, B_k(x_i) = \delta_{j,k} \,, \tag{1.239}$$

for all $j, k \leq L$ and some x_i, $i = 0, ..., N$ and where w_i are some weights, dependent on the evaluation points. This discrete orthogonality then guarantees the exact reproduction of an L-bandlimited function F. Expressing F in terms of the basis functions as $F(x) = \sum_{m=0}^{L} a_m B_m(x)$, we find

$$\begin{aligned} \sum_{m=0}^{L} \left(\sum_{i=0}^{N} w_i \, B_m(x_i) \, F(x_i) \right) B_m(x) &= \sum_{m=0}^{L} \sum_{i=0}^{N} w_i \, B_m(x_i) \sum_{j=0}^{L} a_j \, B_j(x_i) \, B_m(x) \\ &= \sum_{j=0}^{L} \sum_{m=0}^{L} a_j \sum_{i=0}^{N} w_i \, B_j(x_i) \, B_m(x_i) \, B_m(x) \\ &= \sum_{m=0}^{L} a_m \, B_m(x) \,. \end{aligned} \tag{1.240}$$

Due to the uniqueness of the coefficients, this implies

$$a_m = \sum_{i=0}^{N} w_i \, B_m(x_i) \, F(x_i) \,, \tag{1.241}$$

for all $m = 0, ..., L$. In other words, given the discrete orthogonality, the Fourier coefficients a_m are indeed determined only by the values of the function F and the basis functions B_m at a finite number of grid points x_i, $i = 0, ..., N$. The remaining task is the determination of the required distribution of

these points and the weights w_i such that (1.239) is fulfilled.

Indeed, for the trigonometrical basis system it can be shown that - on the domain $[0, 2\pi]$ - for a given degree $L \in \mathbb{N}_0$ it holds that

$$\begin{aligned} \frac{1}{L} \sum_{i=0}^{2L-1} \sin(j\varphi_i) \sin(k\varphi_i) &= (1 - \delta_{j,0} - \delta_{j,L})\, \delta_{j,k}\,, \\ \frac{1}{L} \sum_{i=0}^{2L-1} \cos(j\varphi_i) \cos(k\varphi_i) &= (1 + \delta_{j,0} + \delta_{j,L})\, \delta_{j,k}\,, \\ \sum_{i=0}^{2L-1} \sin(j\varphi_i) \cos(k\varphi_i) &= 0\,, \end{aligned} \tag{1.242}$$

for all $0 \leq j, k \leq L$, in the case that $\varphi_i := i\pi/(2L)$, $i = 0, ..., 2L-1$, i.e. for an equiangular grid across the domain $[0, 2\pi]$. At first sight, the number of required grid points equals exactly twice the value of the degree L. But we notice that the orthogonality condition for the sine terms does not hold for $j = 0$ and $j = L$. Where the $j = 0$ case is just not defined due to construction, the behaviour for $j = L$ means that the coefficients for the L-degree sine cannot be reconstructed using this ansatz. Fortunately, this scenario can simply be avoided by increasing the bandlimit degree by 1 such that a reconstruction of the L-degree sine coefficient is just not necessary. Thus, applying (1.241) we can state that for an L-bandlimited function, the Fourier coefficients a_m (cosine) and b_m (sine), $m = 0, ..., L$ with respect to the trigonometrical functions can be determined by

$$\begin{aligned} \left\{ \begin{array}{c} a_m \\ b_m \end{array} \right\} &= \frac{1}{L+1} \sum_{i=0}^{2L+1} \frac{1}{(1+\delta_{m,0})} \left\{ \begin{array}{c} \cos(m\varphi_i) \\ \sin(m\varphi_i) \end{array} \right\} F(\varphi_i) \\ &= \frac{\pi}{L+1} \sum_{i=0}^{2L+1} \lambda_m^2 \left\{ \begin{array}{c} \cos(m\varphi_i) \\ \sin(m\varphi_i) \end{array} \right\} F(\varphi_i)\,, \end{aligned} \tag{1.243}$$

using an equiangular grid with $\varphi_i := i\pi/(L+1)$, $i = 0, ..., 2L+1$. The previously presented method is well-known as the **Discrete Fourier Transform (DFT)**.

Now returning to the spherical harmonic representation and applying this result to (1.235) we immediately see that

$$\left\{ \begin{array}{c} A_m(t) \\ B_m(t) \end{array} \right\} = \frac{\pi}{L+1} \sum_{i=0}^{2L+1} \lambda_m \left\{ \begin{array}{c} \cos(m\varphi_i) \\ \sin(m\varphi_i) \end{array} \right\} F(\xi(\varphi_i, t))\,, \tag{1.244}$$

Furthermore, also taking (1.236) into account, we can conclude that in general, for every L-bandlimited function F (with respect to the trigonometrical functions), it holds that

$$\int_0^{2\pi} \left\{ \begin{array}{c} \cos(m\varphi) \\ \sin(m\varphi) \end{array} \right\} F(\varphi)\, \mathrm{d}\varphi = \frac{\pi}{L+1} \sum_{i=0}^{2L+1} \left\{ \begin{array}{c} \cos(m\varphi_i) \\ \sin(m\varphi_i) \end{array} \right\} F(\varphi_i)\,, \tag{1.245}$$

and especially for $m = 0$ this yields

$$\int_0^{2\pi} F(\varphi)\, \mathrm{d}\varphi = \frac{\pi}{L+1} \sum_{i=0}^{2L+1} F(\varphi_i)\,. \tag{1.246}$$

We now insert (1.244) into (1.236) to find that the determination of the spherical harmonic coefficients of an L-bandlimited function simplifies after the first discretisation step to

$$F_{l,m} = \frac{\pi}{L+1} \sum_{i=0}^{2L+1} \lambda_m \left\{ \begin{array}{c} \cos(|m|\varphi_i) \\ \sin(|m|\varphi_i) \end{array} \right\} \int_{-1}^{1} \bar{P}_{l,|m|}(t)\, F(\xi(\varphi_i, t))\, \mathrm{d}t\,. \tag{1.247}$$

Now, the second step is to find a similar discretisation method for the Legendre functions and then to apply this method to the remaining Legendre integral. Neumann (1838) showed that here, the task of finding weights and grid points to fulfil the discrete orthogonality condition (1.239) can be reformulated as the task to find coefficients w_i and grid points t_i, $i = 1, ..., 2L+1$, that satisfy

$$\int_{-1}^{1} t^n \,\mathrm{d}t = \sum_{i=1}^{2L+1} w_i \, t_i^n \,, \tag{1.248}$$

for all $n = 0, ..., 2L$. In contrast to the longitudinal case, here we start with the index 1 in the notation of weights and grid points. Since the product of two Legendre functions $\bar{P}_{j,m}$ and $\bar{P}_{k,m}$ of the same order is a polynomial of degree $j + k$ - since the order of the product equals $2m$ which is in any case an even number - we can represent this product using monomials by

$$\bar{P}_{j,m}(t) \, \bar{P}_{k,m}(t) = \sum_{n=0}^{j+k} a_n \, t^n \,, \tag{1.249}$$

for some coefficients a_n, $n = 0, ..., j + k$. In our case, we can restrict ourselves to Legendre functions of degree $\leq L$ such that $j + k \leq 2L$ since the underlying function was assumed to be L-bandlimited. This representation in combination with the condition (1.248) then yields

$$\begin{aligned} \int_{-1}^{1} \bar{P}_{j,m}(t) \, \bar{P}_{k,m}(t) \,\mathrm{d}t &= \sum_{n=0}^{2L} a_n \int_{-1}^{1} t^n \,\mathrm{d}t \\ &= \sum_{i=1}^{2L+1} w_i \sum_{n=0}^{2L} a_n \, t_i^n \\ &= \sum_{i=1}^{2L+1} w_i \, \bar{P}_{j,m}(t_i) \, \bar{P}_{k,m}(t_i) \,, \end{aligned} \tag{1.250}$$

which indeed proves the orthogonality condition (1.239) for the weights and points generated by (1.248). Since we can express the integral on the left-hand side of (1.248) analytically, this relation can be reformulated as a system of linear equations:

$$\begin{pmatrix} 1 & \dots & 1 \\ t_1 & \dots & t_{2L+1} \\ \vdots & & \vdots \\ t_1^{2L} & \dots & t_{2L+1}^{2L} \end{pmatrix} \begin{pmatrix} w_1 \\ w_2 \\ \vdots \\ w_{2L+1} \end{pmatrix} = \begin{pmatrix} 2 \\ 0 \\ \vdots \\ \frac{2}{2L+1} \end{pmatrix} . \tag{1.251}$$

The n-th entry (starting from 0) of the vector on the right-hand side represents the value of $\int_{-1}^{1} t^n \,\mathrm{d}t$ which is zero if n is odd and equals $2/(n+1)$ in case that n is even. The matrix on the left-hand side is a square **Vandermonde matrix** which is invertible if and only if the $t_1, ..., t_{2L+1}$ are pairwise distinct. This means that in order to guarantee a discrete orthogonality of the Legendre functions up to degree L, if suffices to choose $2L + 1$ arbitrary pairwise distinct points that are distributed along the interval $[-1, 1]$. The respective weights are then uniquely determined by (1.251). This procedure can be found in literature as **Neumann's first method**.

Since the previous system of linear equations turns out to be numerically unstable, a slight variation of this procedure is recommended. It can be noticed that the choice of the monomials as basis functions in (1.249) is not unique. If here an orthogonal basis system is chosen, all but the 0-th entry of the vector on the right-hand side of (1.251) vanish. If we use the normalised Legendre polynomials

Table 1.1: This table shows the weights w_j, $j = 1, ..., 2L+1$ (approximate up to 3 digits) and the corresponding evaluation points (colatitude) to be used within the Driscoll-Healy quadrature for the cases $L = 0, 1, 2, 3$. We see that the weights are symmetric with respect to the equator and they sum up to 2.

	$\frac{1}{8}\pi$	$\frac{1}{6}\pi$	$\frac{1}{4}\pi$	$\frac{1}{3}\pi$	$\frac{3}{8}\pi$	$\frac{1}{2}\pi$	$\frac{5}{8}\pi$	$\frac{2}{3}\pi$	$\frac{3}{4}\pi$	$\frac{5}{6}\pi$	$\frac{7}{8}\pi$	$\sum w_j$
$L=0$	-	-	-	-	-	2	-	-	-	-	-	2
$L=1$	-	-	$\frac{2}{3}$	-	-	$\frac{2}{3}$	-	-	$\frac{2}{3}$	-	-	2
$L=2$	-	$\frac{14}{45}$	-	$\frac{18}{45}$	-	$\frac{26}{45}$	-	$\frac{18}{45}$	-	$\frac{14}{45}$	-	2
$L=3$	0.178	-	0.248	-	0.393	0.362	0.393	-	0.248	-	0.178	2

instead of the monomial basis, the system of linear equations turns into

$$\begin{pmatrix} \bar{P}_0(t_1) & \dots & \bar{P}_0(t_{2L+1}) \\ \bar{P}_1(t_1) & \dots & \bar{P}_1(t_{2L+1}) \\ \vdots & & \vdots \\ \bar{P}_{2L}(t_1) & \dots & \bar{P}_{2L}(t_{2L+1}) \end{pmatrix} \begin{pmatrix} w_1 \\ w_2 \\ \vdots \\ w_{2L+1} \end{pmatrix} = \begin{pmatrix} \sqrt{2} \\ 0 \\ \vdots \\ 0 \end{pmatrix}. \tag{1.252}$$

This system of equations can also be thought of as the result of the application of various Gauss elimination steps to (1.251). Now applying this result to the functions $A(t)$, $B(t)$ and their defining equations from (1.234), we find that

$$F_{l,m} = \sum_{j=1}^{2L+1} w_j \, \bar{P}_{l,|m|}(t_j) \left\{ \begin{array}{c} A_m(t_j) \\ B_m(t_j) \end{array} \right\}, \tag{1.253}$$

and in combination with (1.244) this yields the following (exact) representation of the spherical harmonic coefficients only using finite sums:

$$\begin{aligned} F_{l,m} &= \frac{\pi}{L+1} \lambda_m \sum_{j=1}^{2L+1} w_j \, \bar{P}_{l,|m|}(t_j) \sum_{i=0}^{2L+1} \left\{ \begin{array}{c} \cos(m\varphi_i) \\ \sin(m\varphi_i) \end{array} \right\} F(\xi(\varphi_i, t_j)) \\ &= \frac{\pi}{L+1} \sum_{i=0}^{2L+1} \sum_{j=1}^{2L+1} w_j \, Y_{l,m}(\xi(\varphi_i, t_j)) \, F(\xi(\varphi_i, t_j)) \,. \end{aligned} \tag{1.254}$$

If we compare this relation to the original definition of the Fourier coefficients $F_{l,m}$ we find that

$$\int_\Omega F(\eta) \, Y_{l,m}(\eta) \, \mathrm{d}\omega(\eta) = \frac{\pi}{L+1} \sum_{i=0}^{2L+1} \sum_{j=1}^{2L+1} w_j \, Y_{l,m}(\xi(\varphi_i, t_j)) \, F(\xi(\varphi_i, t_j)) \,, \tag{1.255}$$

and especially for the case $m = 0$ that

$$\int_\Omega F(\eta) \, \mathrm{d}\omega(\eta) = \frac{\pi}{L+1} \sum_{i=0}^{2L+1} \sum_{j=1}^{2L+1} w_j \, F(\xi(\varphi_i, t_j)) \,, \tag{1.256}$$

for any L-bandlimited function $F \in \mathrm{L}^2(\Omega)$ on the sphere. As an example, for the simple case of $F \equiv 1$ we indeed find that

$$\int_\Omega 1 \, \mathrm{d}\omega(\eta) = \frac{\pi}{L+1} \sum_{i=0}^{2L+1} \sum_{j=1}^{2L+1} w_j = 2\pi \sum_{j=1}^{2L+1} w_j = 4\pi \,. \tag{1.257}$$

Table 1.2: This table shows the weights w_j, $j = 1, ..., L+1$ (approximate up to 3 digits) and the corresponding evaluation points (colatitude) to be used within the Gauss-Legendre quadrature for the cases $L = 0, 1, 2, 3$. We see that the requirement that the sum of the weights have to equal 2 is not fulfilled for lower degrees (except $L = 0$). This reflects the approximation behaviour of the used formula for the zeros of the Legendre polynomials.

	$\frac{3}{18}\pi$	$\frac{3}{14}\pi$	$\frac{3}{10}\pi$	$\frac{7}{18}\pi$	$\frac{1}{2}\pi$	$\frac{11}{18}\pi$	$\frac{7}{10}\pi$	$\frac{11}{14}\pi$	$\frac{15}{18}\pi$	$\sum w_j$
$L = 0$	-	-	-	-	2	-	-	-	-	2
$L = 1$	-	-	0.947	-	-	-	0.947	-	-	1.894
$L = 2$	-	0.497	-	-	0.889	-	-	0.497	-	1.883
$L = 3$	0.296	-	-	0.647	-	0.647	-	-	0.296	1.886

In analogy to the longitude, an appropriate choice for the latitudinal grid is an equiangular distribution of the evaluation points, i.e. we define $\vartheta_i := i\pi/(2L+2)$ - with the respective polar distances $t_i = \cos\vartheta_i$, $i = 1, ..., 2L+1$. There are two main reasons why this case is of special interest. First, in many applications, the available data is given on an equiangular grid (e.g. the topographic data set ETOPO that we will also use within this work) and second, Driscoll and Healy (1994) showed that in the equiangular case, it is possible to find the following closed expression for the weights w_j:

$$w_j = \frac{2}{L+1} \sin\vartheta_j \sum_{k=0}^{L} \frac{\sin((2k+1)\,\vartheta_j)}{2k+1}\,. \tag{1.258}$$

This is a very useful property since in this case, we avoid the task of solving the system of linear equations (1.251) or (1.252), including all respective numerical inaccuracies and challenges. In Table 1.1 we show the Driscoll-Healy grid points and their respective weights for the cases $L = 0, 1, 2$. Here, it can also be verified that the sum of the weights equals 2 as prescribed in (1.251) and (1.252). For the spherical harmonic coefficients we then find the following explicit representation using the Driscoll-Healy grid:

$$F_{l,m} = \frac{2\pi}{(L+1)^2}\,\lambda_m \sum_{j=1}^{2L+1} \bar{P}_{l,|m|}(t_j) \sin\vartheta_j \sum_{k=0}^{L} \frac{\sin((2k+1)\,\vartheta_j)}{2k+1} \sum_{i=0}^{2L+1} \left\{ \begin{array}{c} \cos(m\varphi_i) \\ \sin(m\varphi_i) \end{array} \right\} F(\xi(\varphi_i, t_j))\,. \tag{1.259}$$

Since in the previous cases, the required number of grid points in latitudinal direction $(2L+1)$ is almost of identical size as in the longitudinal direction $(2L+2)$, one could have the intuition that there should be a possibility to optimise - i.e. to reduce - the amount of required data since the latitudinal domain is only half the size of the longitude. And indeed, also Neumann (1838) showed that it is possible to reduce the amount of latitudinal grid points to $L+1$ if their location is chosen in a particular way. This number also turns out to be the theoretical minimum for the amount of required latitudinal grid points such that no further optimisation can be achieved.

To this concern, Neumann (1838) adopted the quadrature integration rule that was earlier found by Gauss (1814), where he showed that by choosing the evaluation points in a special way, a one-dimensional integral can be determined exactly by a finite sum in case the investigated function is a polynomial. Based on the work of Gauss, Jacobi (1826) showed that the required evaluation points coincide with the zeros of orthogonal polynomials. Using e.g. the Legendre polynomials then leads to the Gauss-Legendre quadrature. Neumann (1838) applied this rule to the remaining integral of the

Legendre functions in (1.247) and showed that the following representation is valid:

$$\int_{-1}^{1} \bar{P}_{l,m}(t)\, F(\xi(\varphi,t))\, \mathrm{d}t = \sum_{j=1}^{L+1} w_j\, \bar{P}_{l,m}(t_j)\, F(\xi(\varphi,t_j))\,, \tag{1.260}$$

where t_j, $j = 1, ..., L+1$ are the zeros of $\bar{P}_{L+1}$, the Legendre polynomial of degree $L+1$. In literature, this method is referred to as **Neumann's second method**. Here, the weights are given by

$$w_j = \frac{(2L+1)\left(1-t_j^2\right)}{(L+1)^2\, \bar{P}_L(t_j)^2}\,. \tag{1.261}$$

Using the Gauss-Legendre grid, the spherical harmonic coefficients then can be explicitly determined by

$$F_{l,m} = \frac{(2L+1)\pi}{(L+1)^3}\, \lambda_m \sum_{j=1}^{L+1} \left(1-t_j^2\right) \frac{\bar{P}_{l,|m|}(t_j)}{\bar{P}_L(t_j)^2} \sum_{i=0}^{2L+1} \left\{ \begin{array}{c} \cos(m\varphi_i) \\ \sin(m\varphi_i) \end{array} \right\} F(\xi(\varphi_i,t_j))\,. \tag{1.262}$$

Besides the obvious advantage of reducing the number of required grid points by a factor of 2, the grid is simultaneously also the drawback of this quadrature rule. There is no elementary representation of the roots of the Legendre polynomials such that they cannot be determined straightforwardly. Furthermore, in most applications the values of the function that needs to be evaluated are available on a regular, mainly on an equiangular, grid and not coincidently at the roots of Legendre polynomials. This means that the data would need to be preprocessed first and interpolated to the required grid before the quadrature procedure could be applied. Due to these reasons, in practice, the Driscoll-Healy grid is the preferred choice in most cases in spite of the larger amount of required data. At least there are quite accurate approximative representations for the zeros of the Legendre polynomials like e.g.

$$x_k \approx \cos\left(\frac{4k-1}{4n+2}\,\pi\right)\,, \tag{1.263}$$

for the k-th zero, $k = 1, ..., n$, of the Legendre polynomial of degree $n \in \mathbb{N}$ (see e.g., Abramowitz and Stegun, 1965). In Table 1.2 we show the Gauss-Legendre grid points - using the previous approximation for the zeros - and their respective weights for the cases $L = 0, 1, 2, 3$. From previous results, we know that the sum of the weights should always equal 2. Here we see a significant mismatch for low orders which is due to the approximation quality of the previous formula for the zeros of the Legendre polynomials which is quite bad for low degrees and becomes better with increasing degree (see also Abramowitz and Stegun, 1965). But since for the lower degrees, the zeros of the Legendre polynomials can still be determined analytically, here, it is recommended to use these representations instead of the approximative formula (1.263).

In Figure 1.7 we show the distribution of the required grid points for the Driscoll-Healy (green stars) and the Gauss-Legendre (blue triangles) grid in case of a bandlimit of $L = 5$, with and without including their respective weights. We see that due to construction, the general grid point density is much higher in polar regions than at the equator. But actually, this might not only be considered as a shortcoming of this method but can also be an advantageous feature since e.g. magnetic data also shows a higher density data distribution at the poles (see e.g., Mayer, 2003).

We deeply acknowledge the work by Sneeuw (1994), where a very detailed and inspiring summary and an outline of the historical context of all the previously presented methods can be found.

Further optimisation techniques can be found e.g. in Healy et al. (2003), where efficient algorithmic techniques are presented for calculating all spherical harmonic coefficients up to a certain degree and order. Here, the concept of Fast Fourier Transforms (FFT) and recurrence formulae for the Legendre functions are applied, using *shifted* Legendre polynomials. Furthermore, McEwen and Wiaux

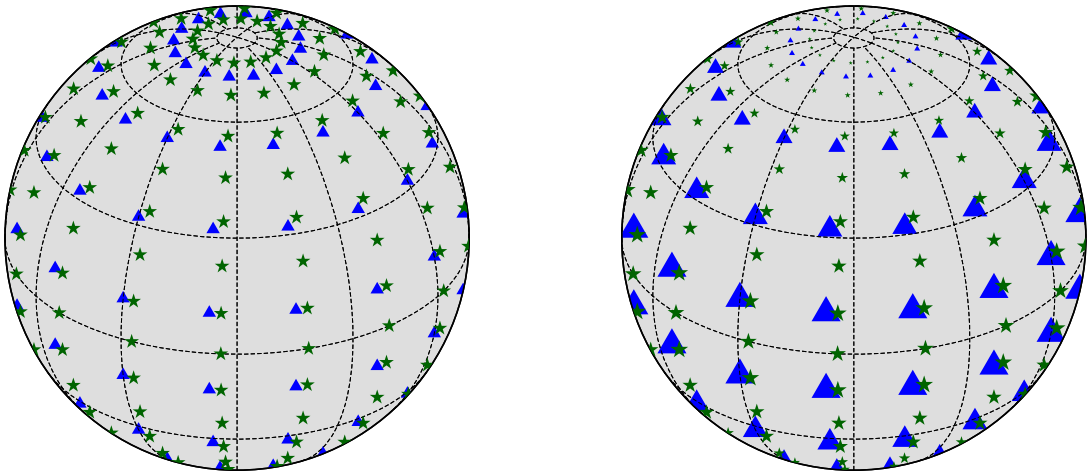

Figure 1.7: Grid point distribution for the Driscoll-Healy (green stars) and the Gauss-Legendre quadrature (blue triangles) in case of a bandlimit of $L = 5$. The point density along a fixed longitude is approximately half for the Gauss-Legendre quadrature compared to the Driscoll-Healy grid. In the left plot, all points are plotted with the same size to illustrate the high point density in the polar regions. In the right plot, the size of each point equals its weight within the respective quadrature rule. In order to minimise overlapping of symbols, we shifted all longitudes of the Driscoll-Healy points by 3 degrees to the East.

(2011) found a novel sampling theorem that features the advantages from both Driscoll-Healy and Gauss-Legendre grid. They found the possibility of using an equiangular grid, consisting of only $L+1$ latitudinal parallels. This method, that uses spin spherical harmonics and a topological connection of the sphere to the torus, even shows an improved numerical stability compared to the Driscoll-Healy and Gauss-Legendre reconstruction method. Also here, a review of the historical evolution of the presented methods of a spherical harmonic analysis can be found.

Spherical Harmonic Synthesis

As we already learned, *spherical harmonic synthesis* denotes the task of reconstructing a function $F \in \mathrm{C}^{(1)}(\Omega)$ on the sphere by means of its spherical harmonic coefficients. Applying the fundamental theorem and the rearrangement of the summation of degree and order that we presented in (1.233)-(1.235) we found that for a maximum reconstruction degree $L \in \mathbb{N}_0$ we have

$$F(\xi(\varphi,t)) = \sum_{m=0}^{L} \lambda_m \left(A_m(t)\cos(m\varphi) + B_m(t)\sin(m\varphi) \right) , \tag{1.264}$$

$\xi \in \Omega$, where $A(t)$ and $B(t)$ are weighted sums of associated Legendre functions of a fixed order m:

$$\begin{aligned} A_m(t) &= \sum_{l=m}^{L} F_{l,m}\, \bar{P}_{l,m}(t) , \\ B_m(t) &= \sum_{l=m}^{L} F_{l,-m}\, \bar{P}_{l,m}(t) . \end{aligned} \tag{1.265}$$

In the spherical harmonic synthesis, the previous representation is especially useful and the supposedly trivial interchange of degree and order reveals again its real strength. The so-called **Clenshaw**

algorithm provides an efficient and numerically stable method to calculate exactly these kind of weighted sums that are required in the synthesis. In a more general form, here we consider a truncated series of the form

$$S_N(x) := \sum_{k=0}^{N} a_k(x)\, F_k(x)\,, \tag{1.266}$$

where $a_k(x) \in \mathbb{R}$, $k = 0, ..., N$, $N \in \mathbb{N}$, are given coefficients and F_k is a sequence of functions - defined on some domain D - that can be represented by a two-level recurrence scheme, i.e. for $k \geq 2$ the k-nth member of the sequence can be found by

$$F_k(x) = A_k(x)\, F_{k-1}(x) + B_k(x)\, F_{k-2}(x)\,, \tag{1.267}$$

for all $x \in D$, where $A_k(x)$ and $B_k(x)$, $k = 2, ..., N$, are pre-determined coefficients. Clenshaw (1955) says that under this condition, the sum $S_N(x)$ can be calculated without determining the values of the functions $F_k(x)$ explicitly. This is a very powerful method especially for the case that the explicit calculation of the values $F_k(x)$ is rather complicated (or just impossible). To determine S_N explicitly, we first define auxiliary coefficients $U_k(x)$, $k = N, ..., 1$, by the inverse recurrence scheme

$$U_k(x) := a_k + A_{k+1}(x)\, U_{k+1}(x) + B_{k+2}(x)\, U_{k+2}(x) \tag{1.268}$$

with the initial values $U_{N+1}(x) = U_{N+2}(x) = 0$. Then, it can be shown that $S_N(x)$ is determined by

$$S_N(x) = (a_0 + B_2(x)\, U_2(x))\, F_0(x) + U_1(x)\, F_1(x)\,. \tag{1.269}$$

If (1.267) is also valid for $k = 1$, i.e. A_1 is given and $B_1 \equiv 0$ such that $F_1(x) = A_1(x)F_0(x)$, it is possible to calculate an additional step in the Clenshaw algorithm and gain $U_0(x) = a_0 + A_1(x)U_1(x) + B_2(x)U_2(x)$. Under this condition (1.269) simplifies to

$$S_N(x) = U_0(x)\, F_0(x)\,. \tag{1.270}$$

Here, we see that the first function of the sequence F_0 serves as a seed. It should be noted that the well-known **Horner scheme** for evaluating polynomials is a special case of the Clenshaw algorithm, i.e. for the monomials it trivially holds that $A_k(x) = x$ and $B_k(x) = 0$ for all $k = 1, ..., N$ and all $x \in D$ in the recurrence scheme (1.267).

For the case of the (normalised associated) Legendre polynomials of a fixed order $m \in \mathbb{N}$, (1.211) determines the recurrence coefficients A_k and B_k as

$$A_k(t) = \sqrt{\frac{(2k+1)(2k-1)}{(k+m)(k-m)}}\,, \quad B_k(t) = -\sqrt{\frac{(2k+1)(k+m-1)(k-m-1)}{(k+m)(k-m)(2k-3)}}\,, \tag{1.271}$$

for $k = m+1, ..., N$. Since in the recurrence procedure of the associated Legendre polynomials, the coefficients are only defined for $k > m$, the Clenshaw algorithm terminates here and we find for any coefficients $a_l \in \mathbb{R}$, $l = m, ..., N$, that

$$\sum_{l=m}^{N} a_l(t)\, \bar{P}_{l,m}(t) = U_m(t)\, \bar{P}_{m,m}(t)\,, \tag{1.272}$$

where the coefficients U_k, $k = m, ..., N+2$ are defined by (1.268). We notice that in the previous representation the sectoral polynomials $\bar{P}_{m,m}$ serve as a seed and need to be calculated a-priori, e.g. by the product representation (1.212).

In spite of the Clenshaw algorithm being capable of avoiding an explicit calculation of the associated Legendre functions, especially since the sectoral functions still serve as a seed, the method as presented also does not solve the underflow problem, illustrated in Figure 1.5. But here, Holmes and Featherstone (2002) provide a very elegant way to circumvent this scenario by substituting the Legendre functions everywhere inside the summation by $\tilde{P}_{l,m}(t)/(1-t^2)^{l/2}$ to avoid the conflict at the poles. Then, in a concluding step, the Horner scheme is used to include the factor of $(1-t^2)^{l/2}$ again iteratively. In this way, the underflow problems can be perfectly avoided. Actually, in this process, an additional scaling by 10^{-280} is needed to prevent overflow. But with this scaling, all calculation steps turn out to be in a numerically secure range.

We deeply acknowledge the work by Holmes and Featherstone (2002) since, in addition to the previously mentioned strategy to take account of the numerical problems, they also give a helpful and interesting overview of the historical development in this field of research.

1.4.4 Vector spherical harmonics

In the final sections of this chapter, we will (briefly) show that (and how) the concept of scalar spherical harmonics as basis functions can also be extended to vector fields and tensor fields. This will become of essential significance in the following chapters where we will investigate the basic conservation laws - including various vector and tensor fields (e.g. stress tensor) - in terms of a spherical harmonic representation.

In analogy to the scalar case it can be shown that it is possible to represent a function $f \in \mathrm{l}^2(\Omega)$ as follows:

$$f(\xi) = \sum_{i=1}^{3} \sum_{l=0_i}^{\infty} \sum_{m=-l}^{l} f_{l,m}^{(i)}\, \mathcal{Y}_{l,m}^{(i)}(\xi)\,, \tag{1.273}$$

for all $\xi \in \Omega$, where we define the individual starting index 0_i for the harmonic degree as

$$0_i := \begin{cases} 0\,, & i = 1\,, \\ 1\,, & i = 2,3\,. \end{cases} \tag{1.274}$$

Furthermore, we find the Fourier coefficients

$$f_{l,m}^{(i)} := \int_{\Omega} f(\eta) \cdot \mathcal{Y}_{l,m}^{(i)}(\eta)\, \mathrm{d}\omega(\eta)\,, \quad i = 1,2,3\,. \tag{1.275}$$

The so-called vector spherical harmonics are given by

$$\begin{aligned} \mathcal{Y}_{l,m}^{(1)}(\xi) &:= Y_{l,m}(\xi)\, \xi \\ \mathcal{Y}_{l,m}^{(2)}(\xi) &:= \frac{1}{\mu_l}\, \nabla^* Y_{l,m}(\xi) \\ \mathcal{Y}_{l,m}^{(3)}(\xi) &:= \frac{1}{\mu_l}\, \mathrm{L}^* Y_{l,m}(\xi) = \frac{1}{\mu_l}\, \xi \wedge \nabla^* Y_{l,m}(\xi)\,, \end{aligned} \tag{1.276}$$

where $\mu_l := \sqrt{l(l+1)}$ is a degree dependent normalisation factor. These functions form an orthonormal basis system in $\mathrm{l}^2(\Omega)$. Note that the vector spherical harmonics with upper index 2 and 3 are not defined for $l = 0$. Inserting the already known spherical polar coordinate representation of the respective differential operators we find the following explicit representation of a vector field f:

$$\begin{aligned} f = \sum_{l,m} \epsilon^r\, f_{l,m}^{(1)}\, Y_{l,m} &+ \epsilon^{\varphi}\, \frac{1}{\mu_l} \left(f_{l,m}^{(2)}\, \frac{1}{\sqrt{1-t^2}}\, \partial_{\varphi} - f_{l,m}^{(3)}\, \sqrt{1-t^2}\, \partial_t \right) Y_{l,m} \\ &+ \epsilon^{t}\, \frac{1}{\mu_l} \left(f_{l,m}^{(2)}\, \sqrt{1-t^2}\, \partial_t + f_{l,m}^{(3)}\, \frac{1}{\sqrt{1-t^2}}\, \partial_{\varphi} \right) Y_{l,m}\,. \end{aligned} \tag{1.277}$$

Note that the extension of the previous definition to a thick spherical shell - that we already derived for the scalar spherical harmonics - also holds for the vectorial case, i.e. for a vector field $f \in \mathrm{l}^2(\Omega_E)$ (Lipschitz continuous) we find that:

$$f(x) = \sum_{i=1}^{3} \sum_{l=0_i}^{\infty} \sum_{m=-l}^{l} f_{l,m}^{(i)}(r)\, \mathcal{Y}_{l,m}^{(i)}(\xi) \tag{1.278}$$

for all $x \in \Omega_{\alpha,\beta}$, $x = r\xi$, $\xi \in \Omega$ with

$$f_{l,m}^{(i)}(r) := \int_{\Omega} f(r\eta) \cdot \mathcal{Y}_{l,m}^{(i)}(\eta)\, \mathrm{d}\omega(\eta)\,, \tag{1.279}$$

for $i = 1, 2, 3$. From now on, in our notation, we assume all vector fields to be Lipschitz continuous to guarantee the pointwise convergence as stated above.

The part of the vector field that is associated with the $\mathcal{Y}_{l,m}^{(3)}$ vector spherical harmonic is called **toroidal** part, the part related to the $\mathcal{Y}_{l,m}^{(1)}$ and $\mathcal{Y}_{l,m}^{(2)}$ vector spherical harmonic is called **poloidal** part. We will have a more detailed look at this separation and the physical interpretation behind this in the final section of this chapter. There, we will find that under certain conditions it is possible to represent both poloidal and toroidal part of a vector field only with the help of one scalar function respectively. In this case it is possible to describe the total vector field just by two scalar functions or in other words, the intrinsic three free variables of a vector field can be reduced to two.

1.4.5 Tensor spherical harmonics

In this subsection, we will expand our knowledge about scalar and vector spherical harmonics even to tensor fields. Instead of 1 (scalar) or 3 (vector) types of basis functions, in the tensorial case we will need to introduce 9 types of different (and orthogonal) basis functions. In analogy to the scalar and vector spherical harmonics it can be shown that it is possible to represent a function $\mathbf{f} \in \mathbf{l}^2(\Omega)$ as follows:

$$\mathbf{f}(\xi) = \sum_{i,j=1}^{3} \sum_{l=0_{i,j}}^{\infty} \sum_{m=-l}^{l} \mathbf{f}_{l,m}^{(i,j)}\, \boldsymbol{\mathcal{Y}}_{l,m}^{(i,j)}(\xi)\,, \tag{1.280}$$

for all $\xi \in \Omega$, where we define the individual starting index $0_{i,j}$ for the harmonic degree as

$$0_{i,j} := \begin{cases} 0\,, & (i,j) \in \{(1,1),(2,2),(3,3)\}\,, \\ 1\,, & (i,j) \in \{(1,2),(1,3),(2,1),(3,1)\}\,, \\ 2\,, & (i,j) \in \{(2,3),(3,2)\}\,. \end{cases} \tag{1.281}$$

Furthermore, we find the Fourier coefficients

$$\mathbf{f}_{l,m}^{(i,j)} := \int_{\Omega} \mathbf{f}(\eta) \cdot \boldsymbol{\mathcal{Y}}_{l,m}^{(i,j)}(\eta)\, \mathrm{d}\omega(\eta)\,, \quad i,j = 1,2,3\,. \tag{1.282}$$

The so-called tensor spherical harmonics are given by:

$$\begin{aligned}
\boldsymbol{\mathcal{Y}}_{l,m}^{(1,1)}(\xi) &:= \xi \otimes Y_{l,m}(\xi)\,\xi = (\epsilon^r \otimes \epsilon^r)\, Y_{l,m}(\xi)\,, \\
\boldsymbol{\mathcal{Y}}_{l,m}^{(1,2)}(\xi) &:= \xi \otimes \frac{1}{\mu_l} \nabla^* Y_{l,m}(\xi) \\
&= \frac{1}{\mu_l} (\epsilon^r \otimes \epsilon^\varphi) \frac{1}{\sqrt{1-t^2}} \partial_\varphi Y_{l,m}(\xi) + \frac{1}{\mu_l} \left(\epsilon^r \otimes \epsilon^t\right) \sqrt{1-t^2}\, \partial_t Y_{l,m}(\xi)\,, \\
\boldsymbol{\mathcal{Y}}_{l,m}^{(1,3)}(\xi) &:= \xi \otimes \frac{1}{\mu_l} \mathrm{L}^* Y_{l,m}(\xi) \\
&= -\frac{1}{\mu_l} (\epsilon^r \otimes \epsilon^\varphi) \sqrt{1-t^2}\, \partial_t Y_{l,m}(\xi) + \frac{1}{\mu_l} \left(\epsilon^r \otimes \epsilon^t\right) \frac{1}{\sqrt{1-t^2}} \partial_\varphi Y_{l,m}(\xi)\,,
\end{aligned}$$

$$
\begin{aligned}
\boldsymbol{\mathcal{Y}}^{(2,1)}_{l,m}(\xi) &:= \frac{1}{\mu_l}\,\nabla^* Y_{l,m}(\xi)\otimes\xi \\
&= \frac{1}{\mu_l}\,(\epsilon^\varphi\otimes\epsilon^r)\,\frac{1}{\sqrt{1-t^2}}\,\partial_\varphi Y_{l,m}(\xi) + \frac{1}{\mu_l}\left(\epsilon^t\otimes\epsilon^r\right)\sqrt{1-t^2}\,\partial_t Y_{l,m}(\xi)\,, \\
\boldsymbol{\mathcal{Y}}^{(3,1)}_{l,m}(\xi) &:= \frac{1}{\mu_l}\,\mathrm{L}^* Y_{l,m}(\xi)\otimes\xi \\
&= -\frac{1}{\mu_l}\,(\epsilon^\varphi\otimes\epsilon^r)\,\sqrt{1-t^2}\,\partial_t Y_{l,m}(\xi) + \frac{1}{\mu_l}\left(\epsilon^t\otimes\epsilon^r\right)\frac{1}{\sqrt{1-t^2}}\,\partial_\varphi Y_{l,m}(\xi)\,, \\
\boldsymbol{\mathcal{Y}}^{(2,3)}_{l,m}(\xi) &:= \frac{1}{\bar{\mu}_l}\left(\nabla^*\otimes\nabla^* - \mathrm{L}^*\otimes\mathrm{L}^*\right)\,Y_{l,m}(\xi) + \frac{2}{\bar{\mu}_l}\,\nabla^* Y_{l,m}(\xi)\otimes\xi \\
&= \frac{2}{\bar{\mu}_l}\left(t\,\partial_t + \partial_t\left(1-t^2\right)\partial_t - \frac{\Delta^*}{2}\right)\left(\epsilon^t\otimes\epsilon^t - \epsilon^\varphi\otimes\epsilon^\varphi\right)Y_{l,m}(\xi) \\
&\quad + \frac{2}{\bar{\mu}_l}\left(\partial_\varphi\partial_t + \frac{t}{1-t^2}\,\partial_\varphi\right)\left(\epsilon^\varphi\otimes\epsilon^t + \epsilon^t\otimes\epsilon^\varphi\right)Y_{l,m}(\xi)\,, \\
\boldsymbol{\mathcal{Y}}^{(3,2)}_{l,m}(\xi) &:= \frac{1}{\bar{\mu}_l}\left(\nabla^*\otimes\mathrm{L}^* + \mathrm{L}^*\otimes\nabla^*\right)\,Y_{l,m}(\xi) + \frac{2}{\bar{\mu}_l}\,\mathrm{L}^* Y_{l,m}(\xi)\otimes\xi \\
&= \frac{2}{\bar{\mu}_l}\left(\partial_\varphi\partial_t + \frac{t}{1-t^2}\,\partial_\varphi\right)\left(\epsilon^t\otimes\epsilon^t - \epsilon^\varphi\otimes\epsilon^\varphi\right)Y_{l,m}(\xi) \\
&\quad - \frac{2}{\bar{\mu}_l}\left(t\,\partial_t + \partial_t\left(1-t^2\right)\partial_t - \frac{\Delta^*}{2}\right)\left(\epsilon^\varphi\otimes\epsilon^t + \epsilon^t\otimes\epsilon^\varphi\right)Y_{l,m}(\xi) \\
\boldsymbol{\mathcal{Y}}^{(2,2)}_{l,m}(\xi) &:= \frac{1}{\sqrt{2}}\left(\epsilon^\varphi\otimes\epsilon^\varphi + \epsilon^t\otimes\epsilon^t\right)Y_{l,m}(\xi)\,, \\
\boldsymbol{\mathcal{Y}}^{(3,3)}_{l,m}(\xi) &:= \frac{1}{\sqrt{2}}\left(\epsilon^t\otimes\epsilon^\varphi - \epsilon^\varphi\otimes\epsilon^t\right)Y_{l,m}(\xi)\,,
\end{aligned}
\tag{1.283}
$$

where $\mu_l := \sqrt{l(l+1)}$, $\bar{\mu}_l := \sqrt{2l(l+1)(l(l+1)-2)}$. These functions form an orthonormal basis system in $\mathbf{l}^2(\Omega)$.

Here, we already made explicit use of the spherical coordinate representation of the surface tensor gradient and the surface tensor curl gradient. In particular, we used (1.58) - (1.63) where we determined a variety of useful connections between these operators. If we have a closer look at the transformations, we see that the additional terms $2\,\mathrm{L}^* Y_{l,m}(\xi)\otimes\xi$ and $2\,\nabla^* Y_{l,m}(\xi)\otimes\xi$ in the $(2,3)$ and $(3,2)$ harmonic serve as a 'correction' in order to erase all radial dependencies and form purely tangential harmonics. Furthermore, note that the radial harmonics are constructed in analogy to the vector harmonics such that especially we find here:

$$
\begin{aligned}
\epsilon^r\cdot\mathbf{f} = \mathbf{f}\epsilon^r &= \sum_{i,j=1}^{3}\sum_{l=0_{i,j}}^{\infty}\sum_{m=-l}^{l}\mathbf{f}^{(i,j)}_{l,m}\,\boldsymbol{\mathcal{Y}}^{(i,j)}_{l,m}\epsilon^r \\
&= \sum_{l=0_{i,j}}^{\infty}\sum_{m=-l}^{l}\left(\epsilon^r\mathbf{f}^{(1,1)}\,Y_{l,m} + \frac{1}{\mu_l}\left(\mathbf{f}^{(2,1)}\,\nabla^* Y_{l,m} + \mathbf{f}^{(3,1)}\,\mathrm{L}^* Y_{l,m}\right)\right)\,.
\end{aligned}
\tag{1.284}
$$

Comparing the previous equation with the vector harmonic representation (1.273) we can immediately conclude that in this special case the vector and tensor harmonic coefficients transfer in the following way:

$$
\begin{aligned}
(\epsilon^r\cdot\mathbf{f})^{(1)}_{l,m} &= (\mathbf{f}\epsilon^r)^{(1)}_{l,m} = \mathbf{f}^{(1,1)}_{l,m}\,, \\
(\epsilon^r\cdot\mathbf{f})^{(2)}_{l,m} &= (\mathbf{f}\epsilon^r)^{(2)}_{l,m} = \mathbf{f}^{(2,1)}_{l,m}\,, \\
(\epsilon^r\cdot\mathbf{f})^{(3)}_{l,m} &= (\mathbf{f}\epsilon^r)^{(3)}_{l,m} = \mathbf{f}^{(3,1)}_{l,m}\,.
\end{aligned}
\tag{1.285}
$$

This relation will especially be useful in the next chapter in the context of the Stokes equation and the stress tensor.

In analogy to the vectorial case, the normalisation factors can be calculated by determining the respective adjoint operators and transforming the normalisation integral in terms of scalar spherical harmonics by using the theorems of Gauss and Stokes. Furthermore, note that only the diagonal tensor harmonics, i.e. $(1,1)$, $(2,2)$ and $(3,3)$ are defined for degree $l = 0$, the summation for all other harmonics starts with $l = 1$, except for the harmonics $(2,3)$ and $(3,2)$ that are only defined from degree $l = 2$ on.

The extension of the previous definition to a thick spherical shell - that we already derived for the scalar and vector spherical harmonics - also holds for the tensorial case, i.e. for a tensor field $f \in \mathbf{l}^2(\Omega_E)$ (Lipschitz continuous) we find that:

$$\mathbf{f}(x) = \sum_{i,j=1}^{3} \sum_{l=0_{i,j}}^{\infty} \sum_{m=-l}^{l} \mathbf{f}_{l,m}^{(i,j)}(r)\, \boldsymbol{\mathcal{Y}}_{l,m}^{(i,j)}(\xi) \tag{1.286}$$

for all $x \in \Omega_{\alpha,\beta}$, $x = r\xi$, $\xi \in \Omega$ with

$$\mathbf{f}_{l,m}^{(i,j)}(r) := \int_{\Omega} \mathbf{f}(r\eta) \cdot \boldsymbol{\mathcal{Y}}_{l,m}^{(i,j)}(\eta)\, \mathrm{d}\omega(\eta)\,, \tag{1.287}$$

for $i,j = 1,2,3$. From now on, in our notation, we assume all tensor fields to be Lipschitz continuous to guarantee the point-wise convergence as stated above.

1.5 Spectral representation of differential operators

In the course of this work it will in particular be very useful to represent the result of an application of the various differential operators that we introduced in this chapter, i.e. divergence, gradient, curl and Laplacian, to a scalar, vector and resp. tensor field in terms of the previously defined spherical harmonics. In the following we will use the spherical polar coordinate representation of the various differential operators in order to build the bridge to the spherical harmonic representation.

Divergence

We start with the divergence of a vector field $f \in \mathrm{c}^{(1)}(D)$, $D \subset \mathbb{R}^3$. Since the application of the divergence to a vector field yields a scalar field, it should be possible to represent this resulting scalar field in terms of scalar spherical harmonics. Indeed, using the vector spherical harmonic representation of f and inserting the explicit definition from (1.277) into the spherical polar coordinate representation of the divergence, we find that:

$$\begin{aligned}
(\nabla \cdot f)(x) &= \left(\partial_r + \frac{2}{r}\right) f_r + \frac{1}{r}\left(\frac{1}{\sqrt{1-t^2}}\,\partial_\varphi f_\varphi + \partial_t\left(\sqrt{1-t^2}\, f_t\right)\right) \\
&= \sum_{l,m}\Bigg[\left(\partial_r + \frac{2}{r}\right)\left(f_{l,m}^{(1)}(r)\, Y_{l,m}(\xi)\right) \\
&\qquad + \frac{1}{r\mu_l}\frac{1}{\sqrt{1-t^2}}\,\partial_\varphi\left(f_{l,m}^{(2)}(r)\,\frac{1}{\sqrt{1-t^2}}\,\partial_\varphi - f_{l,m}^{(3)}(r)\,\sqrt{1-t^2}\,\partial_t\right) Y_{l,m}(\xi) \\
&\qquad + \frac{1}{r\mu_l}\,\partial_t\left(\sqrt{1-t^2}\,\left(f_{l,m}^{(2)}(r)\,\sqrt{1-t^2}\,\partial_t + f_{l,m}^{(3)}(r)\,\frac{1}{\sqrt{1-t^2}}\,\partial_\varphi\right) Y_{l,m}(\xi)\right)\Bigg] \\
&= \sum_{l,m}\left[\left(\partial_r + \frac{2}{r}\right)\left(f_{l,m}^{(1)}(r)\, Y_{l,m}(\xi)\right) + \frac{1}{r\mu_l}\, f_{l,m}^{(2)}(r)\left(\frac{1}{1-t^2}\,\partial_{\varphi^2}^2 + \partial_t\left(1-t^2\right)\partial_t\right) Y_{l,m}(\xi)\right].
\end{aligned} \tag{1.288}$$

Here we notice that all $f^{(3)}_{l,m}$ terms cancel each other. This should not be a surprising result since the coefficients $f^{(3)}_{l,m}$ belong to the $\mathcal{Y}^{(3)}_{l,m}$ vector spherical harmonic - which represents the toroidal part of f - that is defined as the surface curl gradient of a scalar spherical harmonic $Y_{l,m}$. Thus, since in general $\nabla \cdot (\nabla \wedge \cdot) = 0$, the divergence per definition always cancels out the toroidal part of the vector field which it is applied to.

Furthermore, we recognise the Beltrami operator in the $f^{(2)}_{l,m}$ term and use the eigenvector property of the spherical harmonics, i.e. $\Delta^* Y_{l,m} = -l(l+1)\, Y_{l,m}$. Additionally, from now on we will neglect the explicit dependences on r and ξ in our notation and e.g. just write $Y_{l,m}$ instead of $Y_{l,m}(\xi)$. Nevertheless, for the following calculations one should always remind that a partial derivative with respect to r only acts on the spherical harmonic coefficients and not on the spherical harmonics itself. On the other hand, partial derivatives with respect to φ or t only act on the spherical harmonics and not on the coefficients. Note that this separation is a very valuable advantage of the spherical harmonic representation. The previous equation can now be written as:

$$\nabla \cdot f = \sum_{l,m} \left(\left(\partial_r + \frac{2}{r} \right) f^{(1)}_{l,m} - \frac{l(l+1)}{r\mu_l}\, f^{(2)}_{l,m} \right) Y_{l,m} \,. \tag{1.289}$$

In other words, the scalar spherical harmonic coefficients of the divergence of a vector field f can be determined as:

$$\boxed{(\nabla \cdot f)_{l,m} = \left(\partial_r + \frac{2}{r} \right) f^{(1)}_{l,m} - \frac{l(l+1)}{r\mu_l}\, f^{(2)}_{l,m} \,.} \tag{1.290}$$

Curl

We continue by applying the same procedure to the curl of a vector field $f \in \mathrm{c}^{(2)}(D)$, $D \subset \mathbb{R}^3$. Since the application of the curl to a vector field yields again a vector field, it should be possible to represent the result of such an application in terms of vector spherical harmonics. In analogy to the previous analysis of the divergence, here we also use the vector spherical harmonic representation of f and insert the explicit definition from (1.277) into the spherical polar coordinate representation of the curl. First we look at each component individually and consolidate the results afterwards. We find that:

$$\begin{aligned}
(\nabla \wedge f)_r &= \frac{1}{r} \left(\frac{1}{\sqrt{1-t^2}}\, \partial_\varphi f_t - \partial_t \left(\sqrt{1-t^2}\, f_\varphi \right) \right) \\
&= \sum_{l,m} \left[\frac{1}{r\mu_l} \frac{1}{\sqrt{1-t^2}}\, \partial_\varphi \left(\left(f^{(2)}_{l,m} \sqrt{1-t^2}\, \partial_t + f^{(3)}_{l,m} \frac{1}{\sqrt{1-t^2}}\, \partial_\varphi \right) Y_{l,m} \right) \right. \\
&\qquad \left. - \frac{1}{r\mu_l}\, \partial_t \left(\sqrt{1-t^2} \left(\left(f^{(2)}_{l,m} \frac{1}{\sqrt{1-t^2}}\, \partial_\varphi - f^{(3)}_{l,m} \sqrt{1-t^2}\, \partial_t \right) Y_{l,m} \right) \right) \right] \\
&= \sum_{l,m} \frac{1}{r\mu_l} \left(\frac{1}{1-t^2}\, \partial^2_{\varphi^2} + \partial_t \left(1-t^2\right) \partial_t \right) \left(f^{(3)}_{l,m}\, Y_{l,m} \right) \,.
\end{aligned} \tag{1.291}$$

Applying again the eigenvector property of the spherical harmonics we can write the previous equation as:

$$(\nabla \wedge f)_r = -\sum_{l,m} \frac{l(l+1)}{r\mu_l}\, f^{(3)}_{l,m}\, Y_{l,m} \,. \tag{1.292}$$

We go on with the lateral components.

$$\begin{aligned}(\nabla \wedge f)_\varphi &= \frac{1}{r}\left(\sqrt{1-t^2}\,\partial_t f_r - \partial_r\left(r f_t\right)\right)\\ &= \sum_{l,m}\frac{1}{r}\left(\sqrt{1-t^2}\,\partial_t\left(f^{(1)}_{l,m}\,Y_{l,m}\right) - \frac{1}{\mu_l}\left(\partial_r r\left(f^{(2)}_{l,m}\sqrt{1-t^2}\,\partial_t + f^{(3)}_{l,m}\frac{1}{\sqrt{1-t^2}}\,\partial_\varphi\right)\right)Y_{l,m}\right)\\ &= -\sum_{l,m}\frac{1}{r}\left(\frac{1}{\mu_l}\,\partial_r\left(r f^{(3)}_{l,m}\right)\frac{1}{\sqrt{1-t^2}}\,\partial_\varphi - \left(f^{(1)}_{l,m} - \frac{1}{\mu_l}\,\partial_r\left(r f^{(2)}_{l,m}\right)\right)\sqrt{1-t^2}\,\partial_t\right)Y_{l,m}\,.\end{aligned} \tag{1.293}$$

For the t-component we find that:

$$\begin{aligned}(\nabla \wedge f)_t &= \frac{1}{r}\left(\partial_r\left(r f_\varphi\right) - \frac{1}{\sqrt{1-t^2}}\,\partial_\varphi f_r\right)\\ &= \sum_{l,m}\frac{1}{r}\left(-\frac{1}{\sqrt{1-t^2}}\,\partial_\varphi\left(f^{(1)}_{l,m}\,Y_{l,m}\right) + \frac{1}{\mu_l}\left(\partial_r r\left(f^{(2)}_{l,m}\frac{1}{\sqrt{1-t^2}}\,\partial_\varphi - f^{(3)}_{l,m}\sqrt{1-t^2}\,\partial_t\right)\right)Y_{l,m}\right)\\ &= -\sum_{l,m}\frac{1}{r}\left(\frac{1}{\mu_l}\,\partial_r\left(r f^{(3)}_{l,m}\right)\sqrt{1-t^2}\,\partial_t + \left(f^{(1)}_{l,m} - \frac{1}{\mu_l}\,\partial_r\left(r f^{(2)}_{l,m}\right)\right)\frac{1}{\sqrt{1-t^2}}\,\partial_\varphi\right)Y_{l,m}\,.\end{aligned} \tag{1.294}$$

Now we compare $(\nabla\wedge f)_r$, $(\nabla\wedge f)_\varphi$ and $(\nabla\wedge f)_t$ to the explicit vector spherical harmonic representation of (1.273) and (1.277) to reformulate the previously derived three equations as

$$\nabla \wedge f = -\sum_{l,m}\left(\frac{l(l+1)}{r\mu_l}\,f^{(3)}_{l,m}\,\mathcal{Y}^{(1)}_{l,m} + \frac{1}{r}\,\partial_r\left(r f^{(3)}_{l,m}\right)\mathcal{Y}^{(2)}_{l,m} + \frac{1}{r}\left(\mu_l f^{(1)}_{l,m} - \partial_r\left(r f^{(2)}_{l,m}\right)\right)\mathcal{Y}^{(3)}_{l,m}\right)\,. \tag{1.295}$$

In other words, this means that the vector spherical harmonic coefficients of $\nabla \wedge f$ can be written as:

$$\boxed{\begin{aligned}(\nabla \wedge f)^{(1)}_{l,m} &= -\frac{l(l+1)}{r\mu_l}\,f^{(3)}_{l,m}\,,\\ (\nabla \wedge f)^{(2)}_{l,m} &= -\frac{1}{r}\,\partial_r\left(r f^{(3)}_{l,m}\right)\,,\\ (\nabla \wedge f)^{(3)}_{l,m} &= -\frac{1}{r}\left(\mu_l f^{(1)}_{l,m} - \partial_r\left(r f^{(2)}_{l,m}\right)\right)\,.\end{aligned}} \tag{1.296}$$

We can cross-check this result by inserting the derived coefficients into (1.290) and indeed, we find that the divergence of the curl vanishes, as expected.

Furthermore, we notice that the poloidal part of $\nabla \wedge f$ is only influenced by the toroidal part of f and vice versa. In other words, the curl transforms a purely poloidal into a purely toroidal vector field and a purely toroidal field into a purely poloidal one. Theoretically, in that way it is possible to create an infinite series of purely poloidal and toroidal fields by iteratively applying the curl to a purely poloidal or toroidal field.

As we will need this result in the course of this work, we also explicitly determine the next 'iteration', the curl of the curl of f. Since we already know the coefficients of $\nabla \wedge f$ it is possible to immediately deduce the desired coefficients from (1.296) without extensive calculations:

$$\boxed{\begin{aligned}(\nabla \wedge \nabla \wedge f)^{(1)}_{l,m} &= \frac{l(l+1)}{r^2\mu_l}\left(\mu_l f^{(1)}_{l,m} - \partial_r\left(r f^{(2)}_{l,m}\right)\right)\,,\\ (\nabla \wedge \nabla \wedge f)^{(2)}_{l,m} &= \frac{1}{r}\,\partial_r\left(\mu_l f^{(1)}_{l,m} - \partial_r\left(r f^{(2)}_{l,m}\right)\right)\,,\\ (\nabla \wedge \nabla \wedge f)^{(3)}_{l,m} &= \frac{1}{r}\left(\frac{l(l+1)}{r}\,f^{(3)}_{l,m} - \partial^2_{r^2}\left(r f^{(3)}_{l,m}\right)\right)\,.\end{aligned}} \tag{1.297}$$

Gradient

We go on and analyse the gradient of a scalar function in terms of the vector spherical harmonics. We start by restating the spherical polar coordinate representation of the gradient of a scalar field $F \in \mathrm{C}^{(1)}(D)$, $D \subset \mathbb{R}^3$:

$$\nabla F = \left(\epsilon^r \, \partial_r + \frac{1}{r} \left(\epsilon^\varphi \, \frac{1}{\sqrt{1-t^2}} \, \partial_\varphi + \epsilon^t \, \sqrt{1-t^2} \, \partial_t \right) \right) F \, . \tag{1.298}$$

Inserting the scalar spherical harmonic representation of F yields:

$$\nabla F = \sum_{l,m} \left(\epsilon^r \, \partial_r + \frac{1}{r} \left(\epsilon^\varphi \, \frac{1}{\sqrt{1-t^2}} \, \partial_\varphi + \epsilon^t \, \sqrt{1-t^2} \, \partial_t \right) \right) F_{l,m} \, Y_{l,m} \, . \tag{1.299}$$

As before, we compare the term on the right-hand side to the explicit vector spherical harmonic representation of (1.273) and (1.277) to reformulate the previous equation as

$$\nabla F = \sum_{l,m} \left((\partial_r F_{l,m}) \, \mathcal{Y}^{(1)}_{l,m} + \frac{\mu_l}{r} \, F_{l,m} \, \mathcal{Y}^{(2)}_{l,m} \right) \, . \tag{1.300}$$

Thus, the vector spherical harmonic coefficients of ∇F can be written as:

$$\boxed{\begin{aligned} (\nabla F)^{(1)}_{l,m} &= \partial_r F_{l,m} \, , \\ (\nabla F)^{(2)}_{l,m} &= \frac{\mu_l}{r} \, F_{l,m} \, , \\ (\nabla F)^{(3)}_{l,m} &= 0 \, . \end{aligned}} \tag{1.301}$$

Again, we can cross-check this result by inserting these coefficients into (1.296) and (1.297) and find that - as expected - both terms vanish.

In analogy to the vectorial case it should also be possible to represent the gradient of a vector field f in terms of the previously defined tensor spherical harmonics. As before, we use the explicit vector spherical harmonic representation (1.277) of f and insert it into the spherical polar coordinate representation (1.47) of ∇f. We find that:

$$\begin{aligned} \nabla f = & \sum_{l,m} (\epsilon^r \otimes \epsilon^r) \, \partial_r f^{(1)}_{l,m} \, Y_{l,m} \\ & + \sum_{l,m} (\epsilon^\varphi \otimes \epsilon^r) \, \frac{1}{\mu_l} \left(\partial_r f^{(2)}_{l,m} \, \frac{1}{\sqrt{1-t^2}} \, \partial_\varphi - \partial_r f^{(3)}_{l,m} \, \sqrt{1-t^2} \, \partial_t \right) Y_{l,m} \\ & + \sum_{l,m} \left(\epsilon^t \otimes \epsilon^r \right) \frac{1}{\mu_l} \left(\partial_r f^{(2)}_{l,m} \, \sqrt{1-t^2} \, \partial_t + \partial_r f^{(3)}_{l,m} \, \frac{1}{\sqrt{1-t^2}} \, \partial_\varphi \right) Y_{l,m} \\ & + \sum_{l,m} (\epsilon^r \otimes \epsilon^\varphi) \, \frac{1}{r\mu_l} \left(\left(\mu_l f^{(1)}_{l,m} - f^{(2)}_{l,m} \right) \frac{1}{\sqrt{1-t^2}} \, \partial_\varphi + f^{(3)}_{l,m} \, \sqrt{1-t^2} \, \partial_t \right) Y_{l,m} \\ & + \sum_{l,m} \left(\epsilon^r \otimes \epsilon^t \right) \frac{1}{r\mu_l} \left(\left(\mu_l f^{(1)}_{l,m} - f^{(2)}_{l,m} \right) \sqrt{1-t^2} \, \partial_t - f^{(3)}_{l,m} \, \frac{1}{\sqrt{1-t^2}} \, \partial_\varphi \right) Y_{l,m} \end{aligned} \tag{1.302}$$

$$
\begin{aligned}
&+\sum_{l,m}\left(\epsilon^{\varphi}\otimes\epsilon^{\varphi}\right)\frac{1}{r\mu_l}\left(\mu_l f_{l,m}^{(1)}+f_{l,m}^{(2)}\left(\frac{1}{1-t^2}\,\partial_{\varphi^2}^2-t\,\partial_t\right)-f_{l,m}^{(3)}\left(\partial_\varphi\partial_t+\frac{t}{1-t^2}\,\partial_\varphi\right)\right)Y_{l,m}\\
&+\sum_{l,m}\left(\epsilon^{t}\otimes\epsilon^{t}\right)\frac{1}{r\mu_l}\left(\mu_l f_{l,m}^{(1)}+f_{l,m}^{(2)}\left(t\,\partial_t+\partial_t\left(1-t^2\right)\partial_t\right)+f_{l,m}^{(3)}\left(\partial_\varphi\partial_t+\frac{t}{1-t^2}\,\partial_\varphi\right)\right)Y_{l,m}\\
&+\sum_{l,m}\left(\epsilon^{\varphi}\otimes\epsilon^{t}\right)\frac{1}{r\mu_l}\left(f_{l,m}^{(2)}\left(\partial_\varphi\partial_t+\frac{t}{1-t^2}\,\partial_\varphi\right)-f_{l,m}^{(3)}\left(t\,\partial_t+\partial_t\left(1-t^2\right)\partial_t\right)\right)Y_{l,m}\\
&+\sum_{l,m}\left(\epsilon^{t}\otimes\epsilon^{\varphi}\right)\frac{1}{r\mu_l}\left(f_{l,m}^{(2)}\left(\partial_\varphi\partial_t+\frac{t}{1-t^2}\,\partial_\varphi\right)+f_{l,m}^{(3)}\left(\frac{1}{1-t^2}\,\partial_{\varphi^2}^2-t\,\partial_t\right)\right)Y_{l,m}\,.
\end{aligned}
$$

If we compare this representation to the definition of the tensor spherical harmonics we see that first, we need to introduce the Beltrami operator into the purely tangential parts of ∇f before being able to determine the desired tensor harmonic coefficients. We can reformulate these parts of ∇f as

$$
\begin{aligned}
(\nabla f)_{\varphi,\varphi}&=\sum_{l,m}\frac{1}{r\mu_l}\left(\mu_l f_{l,m}^{(1)}-f_{l,m}^{(2)}\left(t\,\partial_t+\partial_t\left(1-t^2\right)\partial_t-\frac{\Delta^*}{2}\right)+f_{l,m}^{(2)}\,\frac{\Delta^*}{2}\right.\\
&\qquad\left.-f_{l,m}^{(3)}\left(\partial_\varphi\partial_t+\frac{t}{1-t^2}\,\partial_\varphi\right)\right)Y_{l,m}\,,\\
(\nabla f)_{t,t}&=\sum_{l,m}\frac{1}{r\mu_l}\left(\mu_l f_{l,m}^{(1)}+f_{l,m}^{(2)}\left(t\,\partial_t+\partial_t\left(1-t^2\right)\partial_t-\frac{\Delta^*}{2}\right)+f_{l,m}^{(2)}\,\frac{\Delta^*}{2}\right.\\
&\qquad\left.+f_{l,m}^{(3)}\left(\partial_\varphi\partial_t+\frac{t}{1-t^2}\,\partial_\varphi\right)\right)Y_{l,m}\,,\\
(\nabla f)_{\varphi,t}&=\sum_{l,m}\frac{1}{r\mu_l}\left(f_{l,m}^{(2)}\left(\partial_\varphi\partial_t+\frac{t}{1-t^2}\,\partial_\varphi\right)\right.\\
&\qquad\left.-f_{l,m}^{(3)}\left(t\,\partial_t+\partial_t\left(1-t^2\right)\partial_t-\frac{\Delta^*}{2}\right)-\frac{\Delta^*}{2}\,f_{l,m}^{(3)}\right)Y_{l,m}\,,\\
(\nabla f)_{t,\varphi}&=\sum_{l,m}\frac{1}{r\mu_l}\left(f_{l,m}^{(2)}\left(\partial_\varphi\partial_t+\frac{t}{1-t^2}\,\partial_\varphi\right)\right.\\
&\qquad\left.-f_{l,m}^{(3)}\left(t\,\partial_t+\partial_t\left(1-t^2\right)\partial_t-\frac{\Delta^*}{2}\right)+\frac{\Delta^*}{2}\,f_{l,m}^{(3)}\right)Y_{l,m}\,.
\end{aligned}
\tag{1.303}
$$

Now, comparing (1.302) and (1.303) with the definition of the tensor harmonics (1.283) and using the eigenvalue property of the Beltrami operator we find the following representation of ∇f in terms of the tensor spherical harmonics:

$$
\begin{aligned}
\nabla f=\sum_{l,m}&\left(\partial_r f_{l,m}^{(1)}\,\boldsymbol{\mathcal{Y}}_{l,m}^{(1,1)}+\partial_r f_{l,m}^{(2)}\,\boldsymbol{\mathcal{Y}}_{l,m}^{(2,1)}+\partial_r f_{l,m}^{(3)}\,\boldsymbol{\mathcal{Y}}_{l,m}^{(3,1)}+\frac{1}{r}\left(\mu_l f_{l,m}^{(1)}-f_{l,m}^{(2)}\right)\boldsymbol{\mathcal{Y}}_{l,m}^{(1,2)}\right.\\
&+\frac{1}{r}\left(\sqrt{2}f_{l,m}^{(1)}-\frac{l(l+1)}{\sqrt{2}\mu_l}\,f_{l,m}^{(2)}\right)\boldsymbol{\mathcal{Y}}_{l,m}^{(2,2)}+\frac{\bar{\mu}_l}{2r\mu_l}\,f_{l,m}^{(3)}\,\boldsymbol{\mathcal{Y}}_{l,m}^{(3,2)}\\
&\left.-\frac{1}{r}f_{l,m}^{(3)}\,\boldsymbol{\mathcal{Y}}_{l,m}^{(1,3)}+\frac{\bar{\mu}_l}{2r\mu_l}\,f_{l,m}^{(2)}\,\boldsymbol{\mathcal{Y}}_{l,m}^{(2,3)}-\frac{l(l+1)}{\sqrt{2}r\mu_l}\,f_{l,m}^{(3)}\,\boldsymbol{\mathcal{Y}}_{l,m}^{(3,3)}\right)\,.
\end{aligned}
\tag{1.304}
$$

Thus, we finally find the following tensor spherical harmonic coefficients of the vector gradient ∇f:

$$\begin{array}{lll}
(\nabla f)^{(1,1)}_{l,m} = \partial_r f^{(1)}_{l,m}\,, & (\nabla f)^{(1,2)}_{l,m} = \dfrac{1}{r}\left(\mu_l f^{(1)}_{l,m} - f^{(2)}_{l,m}\right), & (\nabla f)^{(1,3)}_{l,m} = -\dfrac{1}{r}\, f^{(3)}_{l,m}\,, \\
(\nabla f)^{(2,1)}_{l,m} = \partial_r f^{(2)}_{l,m}\,, & (\nabla f)^{(2,2)}_{l,m} = \dfrac{1}{r}\left(\sqrt{2} f^{(1)}_{l,m} - \dfrac{l(l+1)}{\sqrt{2}\mu_l}\, f^{(2)}_{l,m}\right), & (\nabla f)^{(2,3)}_{l,m} = \dfrac{\bar{\mu}_l}{2r\mu_l}\, f^{(2)}_{l,m}\,, \\
(\nabla f)^{(3,1)}_{l,m} = \partial_r f^{(3)}_{l,m}\,, & (\nabla f)^{(3,2)}_{l,m} = \dfrac{\bar{\mu}_l}{2r\mu_l}\, f^{(3)}_{l,m}\,, & (\nabla f)^{(3,3)}_{l,m} = -\dfrac{l(l+1)}{\sqrt{2}r\mu_l}\, f^{(3)}_{l,m}\,.
\end{array} \tag{1.305}$$

In analogy, we can determine the following tensor harmonic coefficients for the transposed gradient $(\nabla f)^T$. Due to construction of the tensor harmonics, we find that all coefficients remain the same as in ∇f except for the $(1,2)/(2,1)$ and $(1,3)/(3,1)$ coefficients that are interchanged:

$$\begin{array}{lll}
(\nabla f)^{T(1,1)}_{l,m} = \partial_r f^{(1)}_{l,m}\,, & (\nabla f)^{T(1,2)}_{l,m} = \partial_r f^{(2)}_{l,m}\,, & (\nabla f)^{T(1,3)}_{l,m} = \partial_r f^{(3)}_{l,m}\,, \\
(\nabla f)^{T(2,1)}_{l,m} = \dfrac{1}{r}\left(\mu_l f^{(1)}_{l,m} - f^{(2)}_{l,m}\right), & (\nabla f)^{T(2,2)}_{l,m} = (\nabla f)^{(2,2)}_{l,m}\,, & (\nabla f)^{T(2,3)}_{l,m} = \dfrac{\bar{\mu}_l}{2r\mu_l}\, f^{(2)}_{l,m}\,, \\
(\nabla f)^{T(3,1)}_{l,m} = -\dfrac{1}{r}\, f^{(3)}_{l,m}\,, & (\nabla f)^{T(3,2)}_{l,m} = \dfrac{\bar{\mu}_l}{2r\mu_l}\, f^{(3)}_{l,m}\,, & (\nabla f)^{T(3,3)}_{l,m} = -\dfrac{l(l+1)}{\sqrt{2}r\mu_l}\, f^{(3)}_{l,m}\,.
\end{array} \tag{1.306}$$

As a preparation for the upcoming sections, applying the relation (1.285), in particular we find that

$$\begin{aligned}
(\epsilon^r \cdot (\nabla f))^{(1)}_{l,m} &= \partial_r f^{(1)}_{l,m}, \\
(\epsilon^r \cdot (\nabla f))^{(2)}_{l,m} &= \partial_r f^{(2)}_{l,m}, \\
(\epsilon^r \cdot (\nabla f))^{(3)}_{l,m} &= \partial_r f^{(3)}_{l,m}\,,
\end{aligned} \tag{1.307}$$

and

$$\begin{aligned}
\left(\epsilon^r \cdot (\nabla f)^T\right)^{(1)}_{l,m} &= \partial_r f^{(1)}_{l,m}\,, \\
\left(\epsilon^r \cdot (\nabla f)^T\right)^{(2)}_{l,m} &= \frac{1}{r}\left(\mu_l f^{(1)}_{l,m} - f^{(2)}_{l,m}\right), \\
\left(\epsilon^r \cdot (\nabla f)^T\right)^{(3)}_{l,m} &= -\frac{1}{r}\, f^{(3)}_{l,m}\,.
\end{aligned} \tag{1.308}$$

Laplacian

At last, we focus on the Laplacian, first, applied to a scalar field F. We start by using the spherical harmonic representation of the (scalar) Laplacian, i.e.

$$\Delta F = \left(\partial^2_{r^2} + \frac{2}{r}\,\partial_r + \frac{1}{r^2}\,\Delta^*\right) F\,. \tag{1.309}$$

We do not express the Beltrami operator by its individual components since as before, in the next step we will exploit the eigenvector property of the spherical harmonic. More precisely, inserting the scalar spherical harmonic representation of F then yields:

$$\begin{aligned}\Delta F &= \sum_{l,m} \left(\partial_{r^2}^2 + \frac{2}{r}\,\partial_r + \frac{1}{r^2}\,\Delta^*\right) F_{l,m}\, Y_{l,m} \\ &= \sum_{l,m} \left(\partial_{r^2}^2 + \frac{2}{r}\,\partial_r - \frac{l(l+1)}{r^2}\right) F_{l,m}\, Y_{l,m}\,.\end{aligned} \tag{1.310}$$

Thus, the spherical harmonic coefficients of ΔF are given by

$$\boxed{(\Delta F)_{l,m} = \left(\partial_{r^2}^2 + \frac{2}{r}\,\partial_r - \frac{l(l+1)}{r^2}\right) F_{l,m}\,.} \tag{1.311}$$

Since the Laplacian is also defined for a vector field f we can present this application in terms of the vector spherical harmonics. First, in analogy to the curl, we look at each component individually and consolidate the results afterwards.

$$\begin{aligned}(\Delta f)_r &= \Delta f_r - \frac{2}{r^2}\,f_r - \frac{2}{r^2}\frac{1}{\sqrt{1-t^2}}\,\partial_\varphi f_\varphi - \frac{2}{r^2}\,\partial_t\left(\sqrt{1-t^2}\,f_t\right) \\ &= \sum_{l,m}\Bigg[\left(\Delta^r + \frac{1}{r^2}\,\Delta^* - \frac{2}{r^2}\right) f_{l,m}^{(1)}\, Y_{l,m} \\ &\qquad - \frac{2}{r^2\mu_l}\,\partial_t\left(\sqrt{1-t^2}\,\left(f_{l,m}^{(2)}\,\sqrt{1-t^2}\,\partial_t + f_{l,m}^{(3)}\,\frac{1}{\sqrt{1-t^2}}\,\partial_\varphi\right)\right) Y_{l,m} \\ &\qquad - \frac{2}{r^2\mu_l}\frac{1}{\sqrt{1-t^2}}\,\partial_\varphi\left(f_{l,m}^{(2)}\,\frac{1}{\sqrt{1-t^2}}\,\partial_\varphi - f_{l,m}^{(3)}\,\sqrt{1-t^2}\,\partial_t\right) Y_{l,m}\Bigg] \\ &= \sum_{l,m}\left[\left(\Delta^r - \frac{l(l+1)+2}{r^2}\right) f_{l,m}^{(1)} - \frac{2}{r^2\mu_l}\,f_{l,m}^{(2)}\left(\partial_t\left(1-t^2\right)\partial_t + \frac{1}{1-t^2}\,\partial_{\varphi^2}^2\right)\right] Y_{l,m}\,.\end{aligned} \tag{1.312}$$

We recognise the Beltrami operator in the $f_{l,m}^{(2)}$ part and furthermore we see that the $f_{l,m}^{(3)}$ part vanishes. Thus, we can simplify the previous equation to:

$$(\Delta f)_r = \sum_{l,m}\left(\left(\Delta^r - \frac{l(l+1)+2}{r^2}\right) f_{l,m}^{(1)} + \frac{2l(l+1)}{r^2\mu_l}\,f_{l,m}^{(2)}\right) Y_{l,m}\,. \tag{1.313}$$

We go on with the lateral components.

$$\begin{aligned}(\Delta f)_\varphi &= \Delta(f_\varphi) + \frac{2}{r^2}\frac{1}{\sqrt{1-t^2}}\,\partial_\varphi f_r - \frac{2}{r^2}\frac{t}{1-t^2}\,\partial_\varphi f_t - \frac{1}{r^2}\frac{1}{1-t^2}\,f_\varphi \\ &= \sum_{l,m}\Bigg[\frac{2}{r^2}\,f_{l,m}^{(1)}\,\frac{1}{\sqrt{1-t^2}}\,\partial_\varphi Y_{l,m} \\ &\qquad - \frac{2}{r^2\mu_l}\frac{t}{1-t^2}\,\partial_\varphi\left(f_{l,m}^{(2)}\,\sqrt{1-t^2}\,\partial_t + f_{l,m}^{(3)}\,\frac{1}{\sqrt{1-t^2}}\,\partial_\varphi\right) Y_{l,m} \\ &\qquad + \frac{1}{\mu_l}\left(\Delta^r + \frac{1}{r^2}\,\Delta^* - \frac{1}{r^2}\frac{1}{1-t^2}\right)\left(f_{l,m}^{(2)}\,\frac{1}{\sqrt{1-t^2}}\,\partial_\varphi - f_{l,m}^{(3)}\,\sqrt{1-t^2}\,\partial_t\right) Y_{l,m}\Bigg]\,.\end{aligned} \tag{1.314}$$

Note that here, the Beltrami operator does not directly act on $Y_{l,m}$ because of the $\frac{1}{\sqrt{1-t^2}}$ and $\sqrt{1-t^2}$ terms in front of the spherical harmonics. We need to introduce the correction terms from (1.94) which then yield a substantial reduction of complexity:

$$(\Delta f)_\varphi = \sum_{l,m} \left[\frac{2}{r^2} f^{(1)}_{l,m} \frac{1}{\sqrt{1-t^2}} \partial_\varphi + \frac{1}{\mu_l} \left(\Delta^r - \frac{l(l+1)}{r^2} \right) \left(f^{(2)}_{l,m} \frac{1}{\sqrt{1-t^2}} \partial_\varphi - f^{(3)}_{l,m} \sqrt{1-t^2}\, \partial_t \right) \right] Y_{l,m} \,. \tag{1.315}$$

In analogy, we find for the t-component that

$$\begin{aligned} (\Delta f)_t &= \Delta(f_t) + \frac{2}{r^2} \frac{t}{1-t^2} \partial_\varphi f_\varphi + \frac{2}{r^2} \sqrt{1-t^2}\, \partial_t f_r - \frac{1}{r^2} \frac{1}{1-t^2} f_t \\ &= \sum_{l,m} \left[\frac{2}{r^2} f^{(1)}_{l,m} \sqrt{1-t^2}\, \partial_t Y_{l,m} \right. \\ &\quad + \frac{2}{r^2 \mu_l} \frac{t}{1-t^2} \partial_\varphi \left(f^{(2)}_{l,m} \frac{1}{\sqrt{1-t^2}} \partial_\varphi - f^{(3)}_{l,m} \sqrt{1-t^2}\, \partial_t \right) Y_{l,m} \\ &\quad \left. + \frac{1}{\mu_l} \left(\Delta^r + \frac{1}{r^2} \Delta^* - \frac{1}{r^2} \frac{1}{1-t^2} \right) \left(f^{(2)}_{l,m} \sqrt{1-t^2}\, \partial_t + f^{(3)}_{l,m} \frac{1}{\sqrt{1-t^2}} \partial_\varphi \right) Y_{l,m} \right] . \end{aligned} \tag{1.316}$$

Using (1.94) also yields the desired simplifications:

$$(\Delta f)_t = \sum_{l,m} \left[\frac{2}{r^2} f^{(1)}_{l,m} \sqrt{1-t^2}\, \partial_t + \frac{1}{\mu_l} \left(\Delta^r - \frac{l(l+1)}{r^2} \right) \left(f^{(2)}_{l,m} \sqrt{1-t^2}\, \partial_t + f^{(3)}_{l,m} \frac{1}{\sqrt{1-t^2}} \partial_\varphi \right) \right] Y_{l,m} \,. \tag{1.317}$$

Again, we compare $(\Delta f)_r$, $(\Delta f)_\varphi$ and $(\Delta f)_t$ to the explicit vector spherical harmonic representation of (1.273) and (1.277) to reformulate the previously derived three equations as

$$\begin{aligned} \Delta f = \sum_{l,m} \left[\left(\left(\Delta^r - \frac{l(l+1)+2}{r^2} \right) f^{(1)}_{l,m} + \frac{2l(l+1)}{r^2 \mu_l} f^{(2)}_{l,m} \right) \mathcal{Y}^{(1)}_{l,m} \right. \\ \left. + \left(\frac{2\mu_l}{r^2} f^{(1)}_{l,m} + \left(\Delta^r - \frac{l(l+1)}{r^2} \right) f^{(2)}_{l,m} \right) \mathcal{Y}^{(2)}_{l,m} + \left(\Delta^r - \frac{l(l+1)}{r^2} \right) f^{(3)}_{l,m} \mathcal{Y}^{(3)}_{l,m} \right] . \end{aligned} \tag{1.318}$$

Thus, to state the final result, the vector spherical harmonic coefficients of Δf can be written as:

$$\boxed{\begin{aligned} (\Delta f)^{(1)}_{l,m} &= \left(\Delta^r - \frac{l(l+1)+2}{r^2} \right) f^{(1)}_{l,m} + \frac{2l(l+1)}{r^2 \mu_l} f^{(2)}_{l,m} \,, \\ (\Delta f)^{(2)}_{l,m} &= \left(\Delta^r - \frac{l(l+1)}{r^2} \right) f^{(2)}_{l,m} + \frac{2\mu_l}{r^2} f^{(1)}_{l,m} \,, \\ (\Delta f)^{(3)}_{l,m} &= \left(\Delta^r - \frac{l(l+1)}{r^2} \right) f^{(3)}_{l,m} \,. \end{aligned}} \tag{1.319}$$

As a side remark, we are aware that - since $\mu_l = \sqrt{l(l+1)}$ - the factor in front of the $f^{(2)}_{l,m}$ term in the first harmonic could also be written as $2\mu_l/r^2$ to illustrate the symmetry to the second harmonic. But in general, we do not cancel the normalisation factor μ_l with the Beltrami eigenvalue $-l(l+1)$ in order to keep track of the origin of the respective factors.

With the derivation of the scalar, vector and tensor spherical harmonic coefficients of all differential operators that will be used within the next chapters, we have gained a very powerful tool to

examine all types of governing equations that we will come across within this work in terms of a spectral analysis. In the next two chapters we will find that this spectral approach will lead to a variety of simplifications of the underlying equations and - under certain conditions - even the determination of analytic solutions, that will open the door to a variety of different applications. But first, to finish this chapter, we will have a look at a special kind of vector fields.

1.6 Mie representation

We start this subsection by introducing a special type of functions, so-called **solenoidal** (Greek: *pipe-shaped*) functions. We will find that this property is strongly related to the physical property of incompressibility of a fluid, which can - to first order - be assumed for the circulation in the Earth's mantle. Due to this direct application it is worth looking at these functions in a more detailed way.

To be able to introduce the principle of solenoidality we need to remember the concept of regular surfaces that we introduced in the first section of the preliminaries. We recall that a regular surface Σ divides the space $\mathbb{R}^3$ into a bounded inner Σ_{int} and an unbounded outer part Σ_{ext}. Moreover, it is possible to determine for each $x \in \Sigma$ a unique normal vector that points into the outer region Σ_{ext}.

Now, let $\Omega_{\alpha,\beta} \subset \mathbb{R}^3$ be a spherical shell with $0 \leq \alpha < \beta \leq \infty$. Then, a vector field $f \in \mathrm{c}^{(1)}(\Omega_{\alpha,\beta})$ is called solenoidal if for every regular surface $\Sigma \subset \Omega_{\alpha,\beta}$ we have

$$\int_{\Sigma} f(x) \cdot n(x) \, \mathrm{d}\omega(x) = 0 \,, \tag{1.320}$$

where n is the outer normal field on Σ, i.e. the total flux of f across the surface Σ vanishes. Because this holds for every arbitrary regular surface inside $\Omega_{\alpha,\beta}$ we may conclude that there are no (positive or negative) sources of f inside Σ which would relate the statement above to the divergence of f. Indeed, with the help of Gauss' Theorem (1.134) it can easily be shown that:

$$f \text{ solenoidal in } \Omega_{\alpha,\beta} \quad \Rightarrow \quad \nabla \cdot f = 0 \text{ in } \Omega_{\alpha,\beta} \,.$$

Probably, one would expect that due to Gauss' Theorem both properties are equivalent but this is only true for sufficiently *nice* domains, e.g. for $\mathbb{R}^3$ or star-shaped domains in general. Even if we just remove the origin from $\mathbb{R}^3$ a divergence-free field does not need to be solenoidal any more. If we e.g. consider the function $f : \Omega_{\alpha,\beta} \to \mathbb{R}^3$ with $\alpha > 0$ and $\beta > \alpha$ arbitrary with $f(x) = x/|x|^3$, $x \in \Omega_{\alpha,\beta}$, we find that

$$\begin{aligned} \nabla \cdot f &= \sum_{i=1}^{3} \partial_i \frac{x_i}{|x|^3} = \sum_{i=1}^{3} \frac{1}{|x|^3} - 3\frac{x_i^2}{|x|^5} \\ &= \frac{1}{|x|^5} \left(3|x|^2 - 3 \sum_{i=1}^{3} x_i^2 \right) = 0 \,, \end{aligned} \tag{1.321}$$

but for any sphere Ω_r with $\alpha < r < \beta$ we find that

$$\begin{aligned} \int_{\Omega_r} f \cdot n(x) \, \mathrm{d}\omega(x) &= \int_{\Omega_r} \frac{x}{|x|^3} \cdot \frac{x}{|x|} \, \mathrm{d}\omega(x) \\ &= \int_{\Omega_r} \frac{1}{|x|^2} \, \mathrm{d}\omega(x) = \frac{1}{r^2} \int_{\Omega_r} 1 \, \mathrm{d}\omega(x) \\ &= \frac{1}{r^2} \left(4\pi r^2 \right) = 4\pi \,. \end{aligned} \tag{1.322}$$

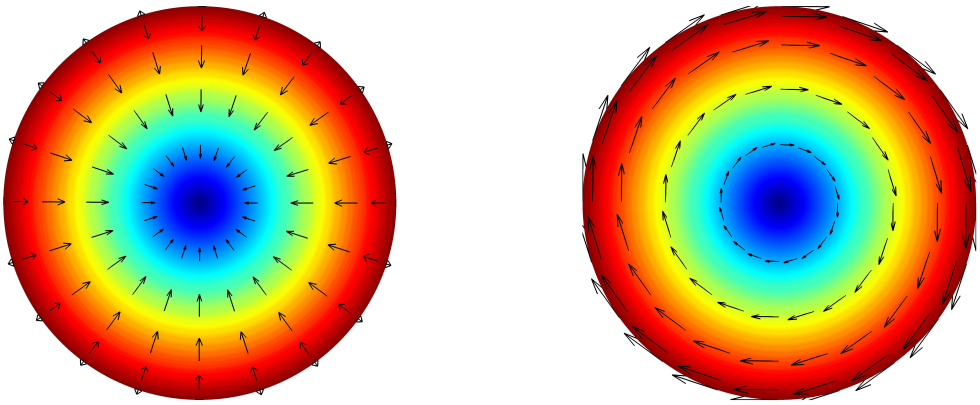

Figure 1.8: An illustration of a purely poloidal (left) and toroidal (right) vector field. The colours indicate the amplitude of the vectors, descending from red (large) to blue (small).

But nevertheless it can be shown - also quite easily by using Gauss' Theorem - that if the domain is a thick spherical shell, both properties are equivalent if and only if we enforce a zero flux through one of the shell boundaries in addition to the zero divergence of f, i.e.

$$\int_{\Omega_\alpha} f \cdot n(x) \, \mathrm{d}\omega(x) = 0 \quad \text{or} \quad \int_{\Omega_\beta} f \cdot n(x) \, \mathrm{d}\omega(x) = 0 \,. \tag{1.323}$$

In case of Earth's mantle flow, this property will hold since we will assume that there is neither flow out of the Earth's surface nor from the core-mantle boundary into the outer core. We will refer to this assumption later as the **no-outflow condition**.

Particularly, from the above relations it can be deduced that if f is divergence-free and satisfies one of the conditions in (1.323), the other condition must also be satisfied. For the Earth's mantle this implies that if we have a divergence-free velocity field and enforce a no-outflow condition at the Earth's surface, the no-outflow condition is also automatically fulfilled for the core-mantle boundary.

One of the most relevant properties of solenoidal fields is the so-called **Mie representation**. Using the general Helmholtz decomposition of vector fields (see e.g., Freeden et al., 1998) it can be shown that it is possible to describe a solenoidal vector field entirely by only two (unique) scalar fields S and Q. In other words, the intrinsic three free parameters of a vector field can be reduced to two. More precisely, for $f \in \mathrm{c}^{(1)}(\Omega_{\alpha,\beta})$ solenoidal there are two unique scalar field $S, Q \in \mathrm{C}^{(2)}(\Omega_{\alpha,\beta})$ with

$$\int_{\Omega_r} S(x) \, \mathrm{d}\omega(x) = \int_{\Omega_r} Q(x) \, \mathrm{d}\omega(x) = 0 \,, \tag{1.324}$$

for any sphere Ω_r with $\alpha \leq r \leq \beta$, which satisfy that

$$f = -\nabla \wedge L^* S - L^* Q = \nabla \wedge \nabla \wedge S\xi + \nabla \wedge Q\xi \,, \tag{1.325}$$

where $x = r\xi$, $\xi \in \Omega$. The first part, including the scalar field S, represents the poloidal part of f where the second part, including the scalar field Q, represents the toroidal part of f. In literature, it is also common to use the more apparent notation of P for the poloidal and T for the toroidal scalar. We deliberately go a different way here because otherwise, P and T could be confused with pressure and temperature, respectively, in particular in Chapter 3. A few paragraphs below, we will explicitly find

the connection to the poloidal-toroidal decomposition that we already know from the vector spherical harmonic representation. Containing plots of purely poloidal and toroidal fields, Figure 1.8 illustrates the nomenclature since the poloidal field lines are directed towards (or away from) the poles, where the toroidal field lines form a circle (i.e. torus) around the poles.

The minus sign originates from the definition of the surface curl gradient L^* and is just convention. In literature one can also find the previous equality without the minus sign which is an equivalent statement. Both can easily be transformed into each other by choosing $\tilde{S} := -S$ and $\tilde{Q} := -Q$ to arrive at $f = -\nabla \wedge \nabla \wedge \tilde{S}\xi - \nabla \wedge \tilde{Q}\xi = \nabla \wedge L^*S + L^*Q$. Additionally, one can find definitions where ξ is replaced by x but also this is just a (normalising) convention.

If f satisfies the conditions above we can now analyse the previous representation in terms of the vector spherical harmonics. With the results of the previous section that provides us with the vector spherical harmonic coefficients of the curl (1.296) and the double curl (1.297), we can immediately find the following relations for the vector spherical harmonic coefficients of f:

$$\begin{aligned}
f^{(1)}_{l,m} &= \frac{l(l+1)}{r^2\mu_l}\left(\mu_l\,(S\xi)^{(1)}_{l,m} - \partial_r\left(r\,(S\xi)^{(2)}_{l,m}\right)\right) - \frac{l(l+1)}{r\mu_l}\,(Q\xi)^{(3)}_{l,m}\,, \\
f^{(2)}_{l,m} &= \frac{1}{r}\,\partial_r\left(\mu_l\,(S\xi)^{(1)}_{l,m} - \partial_r\left(r\,(S\xi)^{(2)}_{l,m}\right)\right) - \frac{1}{r}\,\partial_r\left(r\,(Q\xi)^{(3)}_{l,m}\right)\,, \\
f^{(3)}_{l,m} &= \frac{1}{r}\left(\frac{l(l+1)}{r}\,(S\xi)^{(3)}_{l,m} - \partial^2_{r^2}\left(r\,(S\xi)^{(3)}_{l,m}\right)\right) - \frac{1}{r}\left(\mu_l\,(Q\xi)^{(1)}_{l,m} - \partial_r\left(r\,(Q\xi)^{(2)}_{l,m}\right)\right)\,.
\end{aligned} \tag{1.326}$$

Here, the only things missing are the vector spherical harmonic coefficients of $S\xi$ and $Q\xi$ but this determination is trivial since ξ only induces a radial component in the simplest possible way and both tangential coefficients vanish. More precisely we have

$$\begin{aligned}
(S\xi)^{(1)}_{l,m} &= S_{l,m}\,, \\
(S\xi)^{(2)}_{l,m} &= 0\,, \\
(S\xi)^{(3)}_{l,m} &= 0\,,
\end{aligned} \tag{1.327}$$

and an analogous statement for Q. Inserting this result into (1.326) then yields the final representation for the harmonic coefficients of a solenoidal vector field:

$$\boxed{\begin{aligned}
f^{(1)}_{l,m} &= \frac{l(l+1)}{r^2}\,S_{l,m}\,, \\
f^{(2)}_{l,m} &= \frac{\mu_l}{r}\,\partial_r S_{l,m}\,, \\
f^{(3)}_{l,m} &= -\frac{\mu_l}{r}\,Q_{l,m}\,.
\end{aligned}} \tag{1.328}$$

Again, here we explicitly see that the three determining coefficients for the vector field f only depend on the two scalar functions S and Q, where S can be found in both poloidal components and Q only in the toroidal component of f.

In Chapter 3 of this work, we will learn that exactly this property will help us to develop an analytic benchmark for the special case of an incompressible flow - which yields a divergence-free velocity field and therefore the previously derived representation of the harmonic coefficients of the velocity field.

Chapter 2

Continuum mechanics

"You can compare mass conservation with your wallet. If you take money out of it, the amount inside becomes equally less. Well, it's a little bit different with governments. They eventually just print money and then suddenly, there is more, though actually, there is still none ... erm ... we better do not consider this case here."

Prof. Paul Wagner, University of Vienna

2.1 Conservation laws

In this section, we briefly introduce conservation laws that build the foundation for a mathematical formulation of flow inside the Earth's mantle. There is an uncountable number of literature for classic continuum mechanics, here, we just want to point to the standard work by Landau and Lifshitz (1959) and in addition to Bunge and Kennett (2008) that build the bridge to modern geodynamic applications. Wherever one finds the theory in our work not to be detailed enough, both previously mentioned books will provide the desired supplementary material.

2.1.1 Conservation of mass

Conservation of mass builds on the basic assumption that within a closed system, mass cannot be created or be destroyed out of nothing. Looking at an arbitrary volume V inside the system, this means that if ever the total mass in the interior of V changes over time due to mass transportation (induced by an existing flow field with velocity v), exactly this amount of mass must have passed through its boundary in the same time. In Chapter 1 we learned that the *flux* of a vector field f across a surface Σ - see (1.128) - can be regarded as a measure of the amount of f passing through this surface. In case that we identify f with a velocity field v, we gain the volume flux (unit: m^3/s)

$$\int_{\Sigma} v(x) \cdot \mathrm{d}\omega(x)\,, \tag{2.1}$$

a measure of how much volume passes through Σ per time. By additionally weighting this amount by the respective density at each point, we gain the mass flux across the surface

$$\int_{\Sigma} (\rho(x)\, v(x)) \cdot \mathrm{d}\omega(x)\,. \tag{2.2}$$

Equipped with these quantities, we can formulate the above stated principle of mass conservation as

$$\partial_t \int_V \rho(x)\,\mathrm{d}V(x) + \int_{\partial V} (\rho(x)\,v(x)) \cdot \mathrm{d}\omega(x) = 0\,, \tag{2.3}$$

where the first term describes the change of the total mass of the volume V per time, which is balanced by the respective mass flux across the boundary ∂V of V. Interchanging integration and differentiation and applying Gauss' divergence theorem (1.134) to convert the surface into a volume integral we gain:

$$\int_V \left(\partial_t \rho(x) + \nabla \cdot (\rho(x)\,v(x))\right)\,\mathrm{d}V(x) = 0\,. \tag{2.4}$$

Since the previous relation must hold for each volume V inside the domain of interest, we can conclude that the integral itself has to vanish, i.e.

$$\partial_t \rho + \nabla \cdot (\rho v) = 0\,, \tag{2.5}$$

which is the so-called **continuity equation** (compare to the continuity equation in electrodynamics which describes the conservation of charges).

For applications in the Earth's mantle it is appropriate to neglect time variations of the density - i.e. acoustic waves - since the acoustic wave speed is many magnitudes higher than the velocity of Earth's mantle flow and thus, does not play any role when looking at the Earth's mantle circulation over geological time scales. This is called the **anelastic limit**. With $\partial_t \rho = 0$ the continuity equation then turns into

$$\nabla \cdot (\rho v) = \rho\,\nabla \cdot v + v \cdot \nabla \rho = 0\,. \tag{2.6}$$

From the Preliminary Earth Model *PREM* (Dziewonski and Anderson, 1981) we learned that the density inside the Earth's mantle has a clear radial dependence mainly due to the increasing pressure with depth. The difference in magnitude is of approximately a factor of 2 from the Moho to the core-mantle boundary (CMB). Since the lateral density variations - a few percent of the respective radial mean density - that drive the Earth's mantle flow are significantly smaller than these radial variations we may neglect the lateral dependence of ρ and only consider a radial dependent background density $\rho_0(r)$ in the continuity equation above.

In the next subsection we will see that also in the momentum equation, the lateral density variations will only enter the system in the buoyancy term combined with the gravitational acceleration where in all other terms it is sufficient to refer only to the background density $\rho_0(r)$. This approximation is called the **Boussinesq approximation** (Boussinesq, 1903), an approximation that is thus appropriate and also regularly used for simulations of the Earth's mantle circulation.

Due to these considerations the continuity equation simplifies to

$$\nabla \cdot (\rho_0 v) = \rho_0\,\nabla \cdot v + v \cdot \nabla \rho_0 = \rho_0\,\nabla \cdot v + v_r\,\partial_r \rho_0 = 0\,. \tag{2.7}$$

In this chapter we will from now on denote radial derivatives with dotted variables since they will appear regularly especially in the section about the spectral representation of the governing equations, i.e. here we define $\dot{\rho}_0 := \partial_r \rho_0$. Furthermore, we introduce a new variable

$$\chi(r) := r\frac{\dot{\rho}_0(r)}{\rho_0(r)} = r\frac{\partial \ln \rho_0}{\partial r} = \frac{\partial \ln \rho_0}{\partial \ln r}\,, \tag{2.8}$$

which is called the **compressible factor** that includes all parts of the continuity equation that are related to density variations. The scaling factor r is just a convention to transfer χ to the order of unity. Indeed, in a realistic Earth model, e.g. when we consider the radial density profile of *PREM*,

compressible factors in the range of $-1.0 < \chi < 1.0$ can be found for almost all parts in the mantle except for regions of phase changes in the upper mantle, where density jumps are significantly larger. Also except for some of these special regions, $\chi(r)$ is negative throughout the whole mantle since the density increases with depth. Using this convention, we then end up with

$$\nabla \cdot v = -\frac{\chi}{r}\, v_r \,. \tag{2.9}$$

If we even assume a constant density and neglect the factor of 2 in the radial profile, i.e. we assume *incompressibility* of the Earth's mantle, we obviously find $\chi(r) = 0$ that transfers the continuity equation into its simplest form

$$\nabla \cdot v = 0 \,, \tag{2.10}$$

i.e. we find that in case of an incompressible flow, the corresponding velocity field is divergence-free.

2.1.2 Conservation of momentum

Applying conservation of mass and momentum to a viscous fluid, we find the Cauchy-Euler equation of motion. It states a relation between the inertia forces on the left-hand side of the equation that are balanced by surface forces acting on the volume, entering the equation via the **Cauchy stress tensor** σ and external body forces b, that commonly represent forces like e.g. the gravitational or the Coriolis force. In differential notation it holds that

$$\rho \, \mathrm{D}_t v = \nabla \cdot \sigma + b \,, \tag{2.11}$$

where $\mathrm{D}_t := \partial_t \cdot + (v \cdot \nabla) \cdot$ denotes the material time derivative where $\partial_t v$ represents the temporal and $v \cdot \nabla v$ the advective acceleration.

Now, in order to connect the stress tensor σ explicitly to the velocity field v, a constitutive law has to be applied that describes the general response of the material - change in volume and/or shape - to an external force. The Earth's mantle may be regarded as a highly viscous **Newtonian fluid**. The fundamental property of such a fluid is the linear relation between stress and the applied strain rate $\dot{e}$. The representation of the strain rate tensor can be derived as

$$\dot{e} = \frac{1}{2} \left(\nabla v + (\nabla v)^T \right) \,. \tag{2.12}$$

Where the strain rate may represent both changes in volume and shape, there are two additional principles that contribute to a possible change in volume, the hydrostatic pressure P_h - which even applies when the fluid is at rest - and the expansion rate of the volume, expressed by the divergence of v. Summarising all described effects we end up with the following (general) constitutive relation for Newtonian fluids:

$$\begin{aligned} \sigma &= -P_h \, \mathbb{1}_3 + \lambda \, (\nabla \cdot v) \, \mathbb{1}_3 + 2\eta \dot{e} \\ &= (-P_h + \lambda \, \nabla \cdot v) \, \mathbb{1}_3 + \eta \left(\nabla v + (\nabla v)^T \right) \,, \end{aligned} \tag{2.13}$$

where the proportionality constants λ and η reflect specific material properties. Here, λ denotes the **first Lamé parameter** - compare to *Young's modulus* in the context of elasticity - and η represents the **(dynamic) viscosity** of the fluid (also **second Lamé parameter**) - compare to the *shear modulus* in the context of elasticity).

In particular, please note in the previous representation that σ is symmetric, i.e. $\sigma = \sigma^T$. This is a very important property since it can be shown that in general, **conservation of angular momentum** is equivalent to the stress tensor being symmetric. Thus, under the assumption of a Newtonian rheology, as in our approach, conservation of angular momentum is intrinsically fulfilled.

In order to also distinguish formally between the different contributions, it is appropriate to divide the total stress tensor into two parts: one part that is only responsible for changes in volume and a second part that is only responsible for changes in shape, i.e. pure shear stress. It can be shown that in general only the trace of σ is responsible for changes in volume. This means that dividing σ into a traceless and a non-traceless part - which is called the **deviatoric** stress tensor - would acknowledge for these two types of stress. We find that

$$\operatorname{tr}(\sigma) = -3P_h + 3\lambda\,\nabla\cdot v + 2\eta\,\nabla\cdot v = -3P_h + (3\lambda + 2\eta)\,\nabla\cdot v\,, \tag{2.14}$$

and thus, $\mathbf{d}$, the deviatoric part of σ, can be defined as:

$$\begin{aligned}\mathbf{d} &:= \sigma - \frac{1}{3}\operatorname{tr}(\sigma)\,\mathbb{1}_3 = \sigma - \left(-P_h + \left(\lambda + \frac{2}{3}\,\eta\right)\nabla\cdot v\right)\mathbb{1}_3 \\ &= \eta\left(\nabla v + (\nabla v)^T - \frac{2}{3}\,(\nabla\cdot v)\,\mathbb{1}_3\right).\end{aligned} \tag{2.15}$$

Obviously, $\operatorname{tr}(\mathbf{d}) = 0$. The total stress tensor σ then states as

$$\begin{aligned}\sigma &= \left(-P_h + \left(\lambda + \frac{2}{3}\,\eta\right)\nabla\cdot v\right)\mathbb{1}_3 + \mathbf{d} \\ &= (-P_h + \zeta\,\nabla\cdot v)\,\mathbb{1}_3 + \eta\left(\nabla v + (\nabla v)^T - \frac{2}{3}\,(\nabla\cdot v)\,\mathbb{1}_3\right),\end{aligned} \tag{2.16}$$

where $\zeta := \lambda + \frac{2}{3}\eta$ is the **volume** (also **bulk** or **second**) **viscosity** - compare to the *bulk modulus* in elasticity. The volume viscosity is a material dependent property that measures its resistance against imposed changes in volume. Landau and Lifshitz (1959) describes it as a measure of the relaxation time that is required for the fluid to restore thermodynamic equilibrium. Thus, together with $\nabla\cdot v$ - which represents the expansion rate of the material - it forms a part of the stress tensor that counteracts the compression effect due to the hydrostatic pressure. Therefore, it is convenient to unite both effects under the roof of a total pressure variable, i.e. from now on, we define $P := P_h - \zeta\,\nabla\cdot v$ and end up with

$$\sigma = -P\,\mathbb{1}_3 + \eta\left(\nabla v + (\nabla v)^T - \frac{2}{3}\,(\nabla\cdot v)\,\mathbb{1}_3\right). \tag{2.17}$$

In the Earth's mantle, due to the small expansion rates, relaxation times are considerably small and thus, the hydrostatic pressure P_h dominates $\zeta\,\nabla\cdot v$ by far such that in our case we can safely assume $P = P_h$. For the special case of an incompressible flow ($\nabla\cdot v = 0$), $\zeta\,\nabla\cdot v$ vanishes anyway and the total stress tensor even reduces to

$$\sigma = -P\,\mathbb{1}_3 + \eta\left(\nabla v + (\nabla v)^T\right). \tag{2.18}$$

But for now, we continue with the more general - compressible - formulation (2.17) and insert it into (2.11) to find the **Cauchy-Euler equation** for Newtonian fluids:

$$\begin{aligned}\rho\,\mathrm{D}_t v &= \nabla\cdot(-P\,\mathbb{1}_3 + \mathbf{d}) + b \\ &= \nabla\cdot\left(-P\,\mathbb{1}_3 + \eta\left(\nabla v + (\nabla v)^T - \frac{2}{3}\,(\nabla\cdot v)\,\mathbb{1}_3\right)\right) + b \\ &= -\nabla P + \nabla\cdot\left(\eta\left(\nabla v + (\nabla v)^T - \frac{2}{3}\,(\nabla\cdot v)\,\mathbb{1}_3\right)\right) + b\,.\end{aligned} \tag{2.19}$$

At this point, it is possible - and crucial - to compare the magnitude and thus, the importance of both sides of the previous balance equation. Here we find the inertia forces on the left-hand side and the viscous forces on the right-hand side. The non-dimensional **Reynolds number**

$$\mathrm{Re} := \frac{\rho v d}{\eta}\,, \tag{2.20}$$

where d is a characteristic length scale and v a characteristic velocity, exactly describes the relation of both balanced forces. With $\rho \approx 3 \cdot 10^3\,\mathrm{kg/m^3}$, $v \approx 1\,\mathrm{cm/yr} = 3 \cdot 10^{-10}\,\mathrm{m/s}$, $d \approx 1000\,\mathrm{km} = 10^6\,\mathrm{m}$ and $\eta \approx 10^{21}\,\mathrm{Pas}\,(\mathrm{kg}/(\mathrm{m}\cdot\mathrm{s}))$ we find a Reynolds number of $\mathrm{Re} \approx 10^{-21}$. This small Reynolds number means that in the Earth's mantle the inertia force is significantly ($\approx 10^{21}$ times) smaller than the viscous force and thus, may be dropped in the previous equation, i.e. $\rho\,\mathrm{D}_t v \approx 0$. The remaining balance equation is often referred to as the **Stokes equation**:

$$-\nabla P + \nabla \cdot \left(\eta \left(\nabla v + (\nabla v)^T - \frac{2}{3} (\nabla \cdot v)\, \mathbb{1}_3 \right) \right) = -b\,. \tag{2.21}$$

We notice that this equation does no longer contain any time derivatives. This implies that the balance between surface (left-hand side) and body (right-hand side) forces is reached instantaneously. Later we will see that thus, in mantle circulation codes, time dependency is introduced to the system only by the energy equation.

If we have a closer look at the Stokes equation, we see that further simplification can be achieved in case of a spatially constant viscosity $\eta(x) = \hat{\eta}_0$. We use the 'hat'-notation to distinguish this constant value from a radially varying background viscosity profile η_0 that we will introduce a few paragraphs below. In that special case, it is possible to drag $\hat{\eta}_0$ out of the divergence operator and together with $\nabla \cdot (\nabla v)^T = \nabla (\nabla \cdot v)$ we arrive at

$$-\nabla P + \hat{\eta}_0 \left(\Delta v + \frac{1}{3} \nabla (\nabla \cdot v) \right) = -b\,. \tag{2.22}$$

If we additionally assume incompressibility, the Stokes equation then even turns into a *Poisson equation*:

$$\hat{\eta}_0\, \Delta v = \nabla P - b\,. \tag{2.23}$$

The assumption of a spatially non-varying viscosity is certainly not true for the Earth's mantle, where a narrow layer of low viscosity in the upper mantle, the asthenosphere, is at least 100 times less viscous than the lower mantle (see e.g., Hager and O'Connell, 1979; Hager, 1984, or the following sections here in this work).
Nevertheless, it can be shown (in particular see Chapter 3) that it is possible to derive analytic solutions to the Poisson equation (2.23) by exploiting the spectral representation of the underlying operators and functions. Since the existence of analytic solutions is crucial for constructing objective test scenarios for numerical codes, this simplified version of the Stokes equation is of large interest - not only in the geophysics community.

Finally, in order to complete our investigations with respect to the momentum equation, we still have to determine the body force(s) b. The predominant mechanism driving mass transport inside the Earth's mantle is thermal buoyancy, i.e. in a more general term: gravity. Denoting the gravitational potential by U, the gravitational force generated by the density field ρ is given by:

$$b = -\rho\, \nabla U\,, \tag{2.24}$$

where U is determined by the Poisson equation (see (1.108) and Chapter 4):

$$\Delta U = 4\pi G \rho\,, \tag{2.25}$$

with the gravitational constant G. When we investigated the conservation of mass in the previous section, we introduced a radially dependent background density $\rho_0(r)$ which allows us now to separate lateral density variations from the total density field. For this purpose, we define $\tilde{\rho}(x) := \rho(x) - \rho_0(r)$, where $x = r\xi$ with $\xi \in \Omega$. In analogy, we can divide $U = U_0 + \tilde{U}$ with $\Delta U_0 = 4\pi G \rho_0$ and $\Delta \tilde{U} = 4\pi G \tilde{\rho}$

into contributions from the radial density profile and the lateral variations. This transforms (2.24) then into

$$\begin{aligned} b &= -\left(\rho_0 + \tilde{\rho}\right) \nabla \left(U_0 + \tilde{U}\right) \\ &= -\left(\rho_0 \nabla U_0 + \rho_0 \nabla \tilde{U} + \tilde{\rho}\, \nabla U_0 + \tilde{\rho}\, \nabla \tilde{U}\right) . \end{aligned} \tag{2.26}$$

We define $g_0 := |\nabla U_0|$ which is the reference gravitational acceleration, generated only by the radial density profile. Note that since $U_0 = U_0(r)$, also $g_0 = g_0(r)$ is a radially dependent quantity. Since per definition, there are no lateral density variations in the background profile, $(\nabla U_0)(x)$ points in the (positive) ϵ^r direction (since the force $-\nabla U_0$ is directed towards the centre of the Earth) for each $x \in \Omega_E$, i.e. $\nabla U_0 = g_0 \epsilon^r$. Furthermore, we will drop from now on the second order term $\tilde{\rho}\, \nabla \tilde{U}$ that is reasonably small compared to the remaining terms in the previous equation and end up with a sufficiently accurate first order approximation:

$$b = -\left(g_0 \rho_0 \epsilon^r + \rho_0 \nabla \tilde{U} + g_0 \tilde{\rho} \epsilon^r\right) . \tag{2.27}$$

Here, $g_0 \tilde{\rho} \epsilon^r$ is the buoyancy force, generated by lateral density variations, the main driving mechanism behind mantle circulation. $\rho_0 \nabla \tilde{U}$ is called **self-gravity**, a minor effect that takes into account the change of the gravitational potential due to the lateral mass anomalies. This term is sometimes neglected, also because of the reason that under this assumption, the Poisson equation of the disturbed gravitational potential $\Delta \tilde{U} = 4\pi G \tilde{\rho}$ can be removed from the total set of equations. Nevertheless, e.g. Panasyuk et al. (1996) showed that self-gravity has a considerable effect (up to $\approx 50\%$ on the low harmonic degrees) on the calculation of synthetic geoids and gravity fields from mantle circulation models and thus, may not be neglected in general. Furthermore, if we incorporate self-gravity in the governing equations, we also have to consider that the disturbed potential $\tilde{U}$ changes the hydrostatic pressure state outside the spherical shell, i.e. in the Earth's core and the exterior, which results in a difference in the normal stress levels at the boundaries - $\rho_c \tilde{U}$ and $\rho_a \tilde{U}$, where ρ_c is the mean density of the core and $\rho_a (= 0)$ is the density outside the Earth - with respect to the undisturbed reference state. We will need to include these conditions when we explicitly formulate the boundary conditions for the total system of equations in Chapter 4.

The term $g_0 \rho_0 \epsilon^r$ expresses the gravitational force that is only generated by the radial density model, which determines a hydrostatic state of equilibrium. Thus, this force exactly cancels out the corresponding hydrostatic pressure gradient which is directed in the opposite direction. More precisely we find $\nabla P_0 = -g_0 \rho_0 \epsilon^r$, where P_0 denotes the hydrostatic pressure generated by the background model. These considerations then yield

$$b = \nabla P_0 - \rho_0 \nabla \tilde{U} - g_0 \tilde{\rho} \epsilon^r . \tag{2.28}$$

Inserting this result into the Stokes equation (2.21), we find that we may subtract the hydrostatic pressure from the total pressure gradient, defining $\tilde{P} := P - P_0$, what yields the following final representation of the complete Stokes equation including an explicit formulation of the body forces b:

$$-\nabla \tilde{P} + \nabla \cdot \left(\eta \left(\nabla v + (\nabla v)^T - \frac{2}{3} (\nabla \cdot v)\, \mathbb{1}_3\right)\right) = \rho_0 \nabla \tilde{U} + g_0 \tilde{\rho} \epsilon^r . \tag{2.29}$$

As we already stated before, the assumption of a constant viscosity in order to further simplify the previous equation would not be justified. Nevertheless, to first order, it is appropriate and convenient to assume that - in analogy to the radial background density profile - the viscosity does not vary laterally but only radially, i.e. $\eta(x) = \eta_0(r)$, where $\eta_0(r)$ is a radially varying background viscosity. At the end of this chapter, we will find that with this assumption it is even still possible to derive (semi-)analytic solutions to the Stokes equation. For a purely radially dependent viscosity, we find

$\nabla\eta_0 = \partial_r\eta_0\epsilon^r = \dot{\eta}_0\epsilon^r$ and with $\nabla\cdot(\eta_0\sigma) = \eta_0\nabla\cdot\sigma + \nabla\eta_0\cdot\sigma$, (2.29) becomes

$$-\nabla\tilde{P} + \eta_0\left(\Delta v + \frac{1}{3}\nabla(\nabla\cdot v)\right) + \dot{\eta}_0\left(\epsilon^r\cdot\nabla v + \epsilon^r\cdot(\nabla v)^T - \frac{2}{3}(\nabla\cdot v)\,\epsilon^r\right) = \rho_0\nabla\tilde{U} + g_0\tilde{\rho}\epsilon^r\,. \quad (2.30)$$

Due to the appearance of projections of ∇v onto the r-component, from here, we may deduce that a representation of the whole previous equation in spherical polar coordinates, especially of the included differential operators (see Chapter 1), will be helpful to gain even more insights into the nature of the equation and the relation between the different physical quantities. Indeed, we will revisit this equation in Section 2.2 and analyse it in terms of spherical polar coordinates.

2.1.3 Conservation of energy

As we have learned before, in the low-Reynolds-number limit of the Navier-Stokes equation, i.e. the Stokes equation, we no longer find any time-dependency, the balance of forces is reached instantaneously. But in addition, there are time-dependent processes that transport the energy that is fed into to system by bottom heating from the Earth's core through the Earth's mantle. There are mainly two ways to achieve this, advection and conduction, and it depends on the flow regime and the domain geometry, which of them are dominating. For the Earth's interior, we find that advection is the dominant mechanism of heat transport, where at the thermal boundary layers - the Earth's surface and the CMB - conduction is dominating. In case of the Earth, we are faced with an additional non-negligible heat source, which is internal heating, generated by the decay of radiogenic isotopes. Taking all the previously presented mechanisms into account, we end up with the following energy balance, formulated in terms of the temperature T:

$$\partial_t T + v\cdot\nabla T - \kappa\,\Delta T + H = 0\,, \quad (2.31)$$

where $v\cdot\nabla T$ is the advective, $\kappa\,\Delta T$ the conductive part, with the thermal diffusivity κ and H represents the additional radiogenic heat source.

Where the velocity field v couples to the momentum equation in a direct way, we do not find the temperature T in the equation of motion since here, density anomalies are the driving forces. In order to make the total system of equations remain solvable, we thus need a connection between temperature and density. Such a relation that connects different material parameters is called **equation of state**. In a historical perspective, Boyle's law, that states that for an ideal gas, the product of pressure and volume remains constant (assuming a constant temperature), i.e. $PV = \text{const.}$, can be regarded as the first discovered equation of state. Later, the anti-proportionality constant could be determined as $PV = nRT$, where n is the amount of substance [mol] of the gas, R the universal gas constant and T the temperature. This relation is called the **ideal gas law**. It can be imagined that by translating all these theoretical and experimental considerations to fluids and solids, one opens the door to a large area of research and complexity. Early and still commonly used results for fluids and solids are the Murnaghan (Murnaghan, 1944) and the Birch-Murnaghan (Birch, 1947) equations of state, where pressure, volume and the compressibility factor of a material are related to each other.

When returning to density and temperature, in order to keep things simple, we may use a natural first-order approach where an increase in temperature is connected to the respective volume expansion just by a multiplicative factor. This factor is called the **thermal expansion coefficient** α [1/K] and gives the percentage increase of a volume per Kelvin. We now introduce $T_0 := T_0(r)$ as a radially dependent reference temperature that identifies with the respective reference density $\rho_0(r)$ from above. If we now increase (decrease) the temperature by an absolute value of $\tilde{T}$ (starting from T_0), due to the expanding (contracting) volume, the density decreases (increases) to

$$\rho = \frac{1}{1+\alpha\tilde{T}}\,\rho_0\,. \quad (2.32)$$

Restating the previous equation in terms of the absolute density variation $\tilde{\rho} = \rho - \rho_0$, we find that

$$\tilde{\rho} = \left(\frac{1}{1 + \alpha \tilde{T}} - 1 \right) \rho_0 = - \frac{\alpha \tilde{T} \rho_0}{1 + \alpha \tilde{T}} \, . \tag{2.33}$$

For small values of $\alpha \tilde{T}$ it is possible to neglect this term in the denominator of the term on the right-hand side since the percentage error ϵ_{err} that would be caused by this simplification exactly equals

$$\epsilon_{\text{err}} = \frac{\frac{\alpha \tilde{T} \rho_0}{1}}{\frac{\alpha \tilde{T} \rho_0}{1 + \alpha \tilde{T}}} - 1 = 1 + \alpha \tilde{T} - 1 = \alpha \tilde{T} \, . \tag{2.34}$$

In an Earth-like scenario, α is approximately of magnitude 10^{-5} and lateral temperature variations are at most of the order of 10^3, such that one ends up with values in the range of a few percent for $\alpha \tilde{T}$. Thus, also the maximum error lies in the range of a few percent and it is safe to approximate the previous relation between density and temperature variations to first order as

$$\tilde{\rho} = - \alpha \tilde{T} \rho_0 \, . \tag{2.35}$$

Equipped with this equation of state, the coupling between momentum and energy equation is complete. In order to illustrate the connection between density and temperature even further, we may substitute the previously found relation directly into the momentum equation. The complete Stokes equation (2.29) then turns into

$$- \nabla \tilde{P} + \nabla \cdot \left(\eta \left(\nabla v + (\nabla v)^T - \frac{2}{3} (\nabla \cdot v) \, \mathbb{1}_3 \right) \right) = \rho_0 \nabla \tilde{U} - g_0 \alpha \tilde{T} \rho_0 \epsilon^r \, , \tag{2.36}$$

which reduces under the assumption of incompressibility to

$$- \nabla \tilde{P} + \nabla \cdot \left(\eta \left(\nabla v + (\nabla v)^T \right) \right) = \hat{\rho}_0 \nabla \tilde{U} - g_0 \alpha \tilde{T} \hat{\rho}_0 \epsilon^r \, . \tag{2.37}$$

Note that here, due to the incompressibility, we use a globally constant reference density $\hat{\rho}_0$ instead of the radially varying ρ_0. In the isoviscous case, i.e. $\eta(x) = \hat{\eta}_0$ (compare to (2.22)), (2.36) turns into:

$$- \nabla \tilde{P} + \hat{\eta}_0 \left(\Delta v + \frac{1}{3} \nabla (\nabla \cdot v) \right) = \rho_0 \nabla \tilde{U} - g_0 \alpha \tilde{T} \rho_0 \epsilon^r \, . \tag{2.38}$$

In the following sections, our focus remains on the static problem such that we will again neglect the energy equation for now and proceed with the Stokes equation in the 'density format' (2.29), resp. (2.30). But we will use the Stokes equation in the 'temperature format' again in the next chapter where we build the bridge from the static solutions to time-dependent mantle circulation models and show that analytic solutions to the Stokes equation may be well-suited to test numerical models and to construct benchmark scenarios.

The energy equation in its full pride will cross again our path in the final chapter of this thesis where we will open Pandora's box and discuss if there is a possibility to cope with its inherent initial condition problem. Since (2.31) is a differential equation with respect to temperature, initial and boundary conditions are needed such that this equation may be solved. While the boundary conditions (temperature at the surface and the CMB) do not provide large problems (to first order), the initial condition (temperature distribution at some point in the past, usually in the range of millions of years) is apparently indeterminable. In Chapter 5 we will discuss a very elegant solution strategy for navigating out of this trouble.

2.2 Spectral representation and analytic solutions

For now, we return to the static problem. In this section, we will apply the mathematical strategies presented in Chapter 1 to the previously derived Stokes equation. This is one of the most important

parts of this work since the results of this section will provide the basis for the following chapters. With the help of a spherical harmonic representation of the physical quantities and the representation of all differential operators in spherical polar coordinates, we will be able to convert the second order non-linear partial differential equation into a set of first order ordinary differential equations.

This technical simplification directly leads to the possibility of deriving analytic solutions to (special cases of) the Stokes equation. We will use the results of this section e.g. in Chapter 3 (for the case of incompressibility and constant viscosity) to derive a method of creating objective benchmark test scenarios for mantle circulation codes. Furthermore, in Chapter 4 we will use the following results to analytically determine the velocity and stress field induced by a certain buoyancy field (e.g. derived from seismic tomography) even under the Earth-like condition of a radially varying viscosity profile. We will find that these procedures naturally yield further applications like e.g. the determination of flow-induced dynamic topography and gravitational signals (geoid, gravitational acceleration).

In order to perform these transformations, the only restriction we have to face is that the viscosity η may only vary radially, as we already discussed in Section 2.1.2. Thus, from now on, we set $\eta(x) = \eta_0(r)$ (compare to (2.30)). This is a legitimate assumption if we focus on investigating the properties of Earth's mantle flow to first order. In the real world, viscosity may strongly be dependent on temperature, such that especially in regions with subducting slabs or rising plumes there are significant lateral temperature gradients which induce non-negligible lateral viscosity variations. But a simulation of these more realistic scenarios would require a more complex equation of state in the governing equations. Numerical codes may be adapted to this but it should not be very surprising that these complexities are beyond analytical approaches.

2.2.1 Continuity equation

We start the transformation by restating the already derived continuity equation (2.9), an equivalent formulation of the conservation of mass in the anelastic limit:

$$\nabla \cdot v = -\frac{\chi}{r}\, v_r \,. \tag{2.39}$$

We now represent the velocity field v in terms of vector spherical harmonics, using the notation introduced in Chapter 1. Since the (background) density (and later also the viscosity η in the Stokes equation) may only vary radially, a harmonic representation is not useful for these quantities, so they remain as $\rho_0 := \rho_0(r)$ (and therefore also $\chi := \chi(r)$ and later $\eta_0 := \eta_0(r)$ respectively). The vector spherical harmonic representation of the divergence (1.290) then directly yields

$$\left(\partial_r + \frac{2}{r}\right) v^{(1)}_{l,m} - \frac{l(l+1)}{r\mu_l}\, v^{(2)}_{l,m} = -\frac{\chi}{r}\, v^{(1)}_{l,m} \,, \tag{2.40}$$

for all $l \in \mathbb{N}$ and $m = -l, ..., l$. From now on we will focus on one individual l and m and drop the harmonic degrees of the coefficients in our notation. Furthermore, we change the upper vector index to a lower index. To avoid confusion we will in the following also extend the coefficients of scalar fields (e.g. pressure P) by a (lower) vector index '1'. Otherwise, one could not distinguish between the harmonic coefficient and the function itself. In the new notation - and using the already introduced dot notation for the radial derivative - the previous equation reformulates as

$$\boxed{\dot{v}_1 = -\frac{2+\chi}{r}\, v_1 + \frac{l(l+1)}{r\mu_l}\, v_2 \,.} \tag{A1}$$

Furthermore, we separated the coefficient that contains a radial derivative ($\dot{v}_1$) from all other quantities. In the following subsections our goal will be to find similar relations for the radial derivative of all other harmonic coefficients of the involved physical quantities in order to build a system of ordinary differential equations. In our further notation, we will from now on denote equations that contain

information about the poloidal coefficients (harmonic coefficients '1' and '2') of the different physical quantities with (A) and equations relating toroidal coefficients (harmonic coefficient '3') with (B). Equations that are not directly relevant but that will be helpful in course of the further derivation are denoted by (H).

2.2.2 Stress tensor

Before we continue by applying the procedure above in exactly the same way to the previously derived Stokes equation, we first have a look at the original representation of the stress tensor of a Newtonian fluid itself and restate (2.17) - replacing $\eta(x)$ by $\eta_0(r)$ - where we learned that:

$$\sigma = -P\mathbb{1}_3 + \eta_0 \left(\nabla v + (\nabla v)^T - \frac{2}{3} (\nabla \cdot v) \mathbb{1}_3 \right) . \tag{2.41}$$

When we discussed the momentum equation we learned that the hydrostatic pressure that is part of the total stress tensor cancels with the hydrostatic pressure that is introduced into the equation by the gravitational (body) force (compare to (2.29)). Thus, also here it suffices to consider the 'disturbed' (non-hydrostatic) part of the stress tensor, i.e. $\tilde{\sigma} := \sigma - P_0 \mathbb{1}_3$. Combining the previous representation of the stress tensor with the continuity equation (2.9) we find that

$$\tilde{\sigma} = -\tilde{P}\mathbb{1}_3 + \eta_0 \left(\nabla v + (\nabla v)^T + \frac{2}{3} \left(\frac{\chi}{r} v_r \right) \mathbb{1}_3 \right) . \tag{2.42}$$

Now, applying the spherical polar coordinate representation of the vector gradient (1.47), we find the following relations for each of the different components of the (disturbed) stress tensor. We will not explicitly need these relations in the further course of this work but we state them here for the sake of completeness. Note that due to the symmetry (conservation of angular momentum) there are only 6 independent components of $\tilde{\sigma}$. If we look for the representation of σ instead of $\tilde{\sigma}$, the only difference is that $\tilde{P}$ has to be substituted by P. We find that:

$$\begin{aligned}
\tilde{\sigma}_{rr} &= -\tilde{P} + \frac{2\eta_0}{r} \left(r\, \partial_r v_r + \frac{\chi}{3} v_r \right) , \\
\tilde{\sigma}_{\varphi\varphi} &= -\tilde{P} + \frac{2\eta_0}{r} \left(v_r + \frac{1}{\sqrt{1-t^2}} \partial_\varphi v_\varphi - \frac{t}{\sqrt{1-t^2}} v_t + \frac{\chi}{3} v_r \right) , \\
\tilde{\sigma}_{tt} &= -\tilde{P} + \frac{2\eta_0}{r} \left(v_r + \sqrt{1-t^2}\, \partial_t v_t + \frac{\chi}{3} v_r \right) , \\
\tilde{\sigma}_{r\varphi} &= \frac{\eta_0}{r} \left(r\, \partial_r v_\varphi + \frac{1}{\sqrt{1-t^2}} \partial_\varphi v_r - v_\varphi \right) (= \tilde{\sigma}_{\varphi r}) , \\
\tilde{\sigma}_{rt} &= \frac{\eta_0}{r} \left(r\, \partial_r v_t + \sqrt{1-t^2}\, \partial_t v_r - v_t \right) (= \tilde{\sigma}_{tr}) , \\
\tilde{\sigma}_{\varphi t} &= \frac{\eta_0}{r} \left(\frac{1}{\sqrt{1-t^2}} \partial_\varphi v_t + \frac{t}{\sqrt{1-t^2}} v_\varphi + \sqrt{1-t^2}\, \partial_t v_\varphi \right) (= \tilde{\sigma}_{t\varphi}) .
\end{aligned} \tag{2.43}$$

But what we really need is to keep thinking in terms of spherical harmonic coefficients and not of the six individual components above. Thus, based on (1.305), the tensor harmonic representation of ∇v, and (1.306), the tensor harmonic representation of $(\nabla v)^T$ that we derived in the previous chapter, we can extract information about the harmonic coefficients of the stress tensor from (2.42). The remaining parts - the pressure and divergence term - are only present on the diagonal of $\tilde{\sigma}$. Here, we can directly infer from (1.283) that all tensor harmonic coefficients vanish except for

$$\begin{aligned}
\left(\left(-\tilde{P} + \frac{2}{3}\eta_0 \frac{\chi}{r} v_r \right) \mathbb{1}_3 \right)^{(1,1)}_{l,m} &= -\tilde{P}_1 + \frac{2}{3}\eta_0 \frac{\chi}{r} v_1 , \\
\left(\left(-\tilde{P} + \frac{2}{3}\eta_0 \frac{\chi}{r} v_r \right) \mathbb{1}_3 \right)^{(2,2)}_{l,m} &= \sqrt{2} \left(-\tilde{P}_1 + \frac{2}{3}\eta_0 \frac{\chi}{r} v_1 \right) ,
\end{aligned} \tag{2.44}$$

where we already used the notation with the lower index for the spherical harmonic coefficients of $\tilde{P}$ and V. Now also including the ∇v and $(\nabla v)^T$ parts, we find that

$$\begin{aligned}
\tilde{\sigma}_{1,1} &= -\tilde{P}_1 + \frac{2}{3}\eta_0 \frac{\chi}{r}\, v_1 + 2\eta_0 \dot{v}_1 \,, & \tilde{\sigma}_{1,2} &= \eta_0 \left(\dot{v}_2 - \frac{v_2}{r} + \frac{\mu_l}{r}\, v_1 \right) \,, \\
\tilde{\sigma}_{1,3} &= \eta_0 \left(\dot{v}_3 - \frac{v_3}{r} \right) \,, & \tilde{\sigma}_{2,1} &= \eta_0 \left(\dot{v}_2 - \frac{v_2}{r} + \frac{\mu_l}{r}\, v_1 \right) \,, \\
\tilde{\sigma}_{3,1} &= \eta_0 \left(\dot{v}_3 - \frac{v_3}{r} \right) \,, & \tilde{\sigma}_{2,3} &= \eta_0 \frac{\bar{\mu_l}}{r\mu_l}\, v_2 \,, \\
\tilde{\sigma}_{2,2} &= \sqrt{2} \left(-\tilde{P}_1 + \frac{2\eta_0}{r} \left(\frac{\chi}{3} + 1 \right) v_1 - \eta_0 \frac{l(l+1)}{r\mu_l}\, v_2 \right) \,, & \tilde{\sigma}_{3,2} &= \eta_0 \frac{\bar{\mu_l}}{r\mu_l}\, v_3 \,, \\
\tilde{\sigma}_{3,3} &= -\sqrt{2}\, \eta_0 \frac{l(l+1)}{r\mu_l}\, v_3 \,.
\end{aligned} \tag{2.45}$$

Note that the tensor harmonic coefficients are not 'symmetric' since $\tilde{\sigma}_{2,3} \neq \tilde{\sigma}_{3,2}$ but this is not related to the symmetry of the stress tensor itself, this just arises naturally from the construction of the tensor harmonics.

Stress is a surface force and thus, in general, the stress at a point $x \in \mathbb{R}^3$ depends on the surface under consideration which the stress has to be applied to. The stress tensor is constructed in a way that the stress vector $s(x)$ (in literature also denoted as traction vector or surface traction) with respect to the surface Σ - where $x \in \Sigma$ - can be determined by

$$s(x) = \sigma(x)\, n(x) \,, \tag{2.46}$$

where n is the unit normal vector to Σ at $x \in \Sigma$. It is common to split the resulting stress into two components, the **normal stress** $s_n := (s(x) \cdot n(x))\, n(x)$ that operates orthogonal to the plane and the remaining part, the **shear** (or **tangential**) **stress** $s_t(x) := s(x) - s_n(x)$ that acts parallel to the plane. In this work, where we are only considering scenarios inside a spherical shell, the plane of consideration will always be a sphere with a certain radius around the origin, especially both domain boundaries. The stresses exerted onto these planes will play an essential role e.g. when we will define appropriate boundary conditions for flow inside the mantle or when we will discuss the phenomena of dynamic topography. Due to the spherical symmetry and the transformation into spherical polar coordinates, we immediately see that the normal vector of all planes is equal to the ϵ^r basis vector. The previous equation then transforms into

$$s(x) = \sigma(x)\, \epsilon^r(x) \,. \tag{2.47}$$

Now, using (1.285) and - again - considering just the disturbed quantities, we can immediately determine the vector harmonic coefficients of the (disturbed) stress vector $\tilde{s}$ as

$$\begin{aligned}
\tilde{s}_1 &= \tilde{\sigma}_{1,1} = -\tilde{P}_1 + \frac{2}{3}\eta_0 \frac{\chi}{r}\, v_1 + 2\eta_0 \dot{v}_1 \,, \\
\tilde{s}_2 &= \tilde{\sigma}_{2,1} = \eta_0 \left(\dot{v}_2 - \frac{v_2}{r} + \frac{\mu_l}{r}\, v_1 \right) \,, \\
\tilde{s}_3 &= \tilde{\sigma}_{3,1} = \eta_0 \left(\dot{v}_3 - \frac{v_3}{r} \right) \,.
\end{aligned} \tag{2.48}$$

In order to simplify the notation in the course of the further derivation of the harmonic relations, from now on, we will neglect the special 'tilde' labelling for the disturbed quantities and write e.g. σ instead of $\tilde{\sigma}$. Nevertheless, we have to keep in mind that σ, P, U and ρ in fact denote disturbed quantities. We also change the notation for the harmonic coefficients of the stress vector and define $\sigma_1 := s_1$, $\sigma_2 := s_2$ and $\sigma_3 := s_3$ to emphasise the direct connection to the harmonic coefficients of the stress tensor itself.

In analogy to the continuity equation in the previous chapter, separating the derived quantities from the others yields the following relations that help to extend our system of differential equations. We do not execute this separation for the first equation since in the previous subsection, the continuity equation already provided us with information about $\dot{v}_1$. Nevertheless, this equation will be very useful in the next subsection in order to substitute the (harmonic coefficient of the) pressure field inside the relations that we will gain from analysing the Stokes equation. Therefore, here, we separate the harmonic coefficient of the pressure field and denote the relation by (H1):

$$\boxed{P_1 = -\sigma_1 + 2\eta_0 \dot{v}_1 + \frac{2}{3}\eta_0 \frac{\chi}{r}\, v_1 \,.} \tag{H1}$$

$$\boxed{\dot{v}_2 = -\frac{\mu_l}{r}\, v_1 + \frac{v_2}{r} + \frac{\sigma_2}{\eta_0} \,.} \tag{A2}$$

$$\boxed{\dot{v}_3 = \frac{v_3}{r} + \frac{\sigma_3}{\eta_0} \,.} \tag{B1}$$

We notice that at this point, we already gained differential equations for all harmonic coefficients of the velocity field v. In the next subsection we will learn that the Stokes equation will provide us with respective differential equations for the harmonic coefficients of the stress vector, resp. tensor.

2.2.3 Stokes equation

Now, we refocus on the Stokes equation (2.30) and analyse the first (vector) harmonic coefficient by exploiting the derivation of the harmonic coefficients of the respective differential operators of the previous chapter. After also inserting the final representation (2.9) of the continuity equation - neglecting the tilde notation for the disturbed quantities - the Stokes equation becomes

$$-\nabla P + \eta_0 \left(\Delta v - \frac{1}{3} \nabla \left(\frac{\chi}{r}\, v_r \right) \right) + \dot{\eta}_0 \left((\nabla v)_{r\cdot} + (\nabla v)_{\cdot r} + \frac{2}{3} \left(\frac{\chi}{r}\, v_r \right) \epsilon^r \right) = \rho_0 \nabla U + g_0 \rho \epsilon^r \,. \tag{2.49}$$

Using the harmonic coefficient representations (1.301), (1.319), (1.305), (1.307) and (1.308) we immediately find for the first vector harmonic coefficient that:

$$\begin{aligned} 0 = &-\dot{P}_1 + \eta_0 \left(\ddot{v}_1 + \frac{2}{r}\, \dot{v}_1 - \frac{l(l+1)+2}{r^2}\, v_1 + \frac{2l(l+1)}{r^2 \mu_l}\, v_2 - \frac{1}{3} \partial_r \left(\frac{\chi}{r}\, v_1 \right) \right) \\ &+ 2\dot{\eta}_0 \left(\dot{v}_1 + \frac{1}{3} \left(\frac{\chi}{r}\, v_1 \right) \right) - \rho_0 \dot{U}_1 - g_0 \rho_1 \,. \end{aligned} \tag{2.50}$$

Now, the first goal has to be to remove the pressure field P from the previous equation since - as already discussed in the previous subsection - we try to find relations that only involve the stress tensor, the velocity field and the body forces. Obviously, we can use the first radial derivative of (H1), i.e.

$$\boxed{\dot{P}_1 = -\dot{\sigma}_1 + 2\dot{\eta}_0 \dot{v}_1 + 2\eta_0 \ddot{v}_1 + \frac{2}{3} \dot{\eta}_0 \frac{\chi}{r}\, v_1 + \frac{2}{3} \eta_0 \partial_r \left(\frac{\chi}{r}\, v_1 \right) \,.} \tag{$\dot{\text{H}}$1}$$

and replace $\dot{P}_1$ in (2.50) to find

$$\begin{aligned} 0 = &\dot{\sigma}_1 - 2\dot{\eta}_0 \dot{v}_1 - 2\eta_0 \ddot{v}_1 - \frac{2}{3} \dot{\eta}_0 \frac{\chi}{r}\, v_1 - \frac{2}{3} \eta_0 \partial_r \left(\frac{\chi}{r}\, v_1 \right) + 2\dot{\eta}_0 \left(\dot{v}_1 + \frac{1}{3} \left(\frac{\chi}{r}\, v_1 \right) \right) - \rho_0 \dot{U}_1 - g_0 \rho_1 \\ &+ \eta_0 \left(\ddot{v}_1 + \frac{2}{r}\, \dot{v}_1 - \frac{l(l+1)+2}{r^2}\, v_1 + \frac{2l(l+1)}{r^2 \mu_l}\, v_2 - \frac{1}{3} \partial_r \left(\frac{\chi}{r}\, v_1 \right) \right) \\ = &\dot{\sigma}_1 + \eta_0 \left(-\ddot{v}_1 + \frac{2}{r}\, \dot{v}_1 - \frac{l(l+1)+2}{r^2}\, v_1 + \frac{2l(l+1)}{r^2 \mu_l}\, v_2 - \partial_r \left(\frac{\chi}{r}\, v_1 \right) \right) - \rho_0 \dot{U}_1 - g_0 \rho_1 \,. \end{aligned} \tag{2.51}$$

We can already guess that at the end, this relation will provide us a differential equation with respect to $\dot{\sigma}_1$. But we notice that now, we even have to deal with a second order derivative, i.e. $\ddot{v}_1$. An appropriate way to replace this term is to use the first radial derivative of (A1), i.e.

$$\boxed{\ddot{v}_1 = -\frac{2}{r}\,\dot{v}_1 + \frac{2}{r^2}\,v_1 - \partial_r\left(\frac{\chi}{r}\,v_1\right) + \frac{l(l+1)}{r\mu_l}\,\dot{v}_2 - \frac{l(l+1)}{r^2\mu_l}\,v_2\,.} \tag{$\dot{\text{A1}}$}$$

Now, we replace $\ddot{v}_1$ in (2.51) and separate the harmonic coefficient of σ to find:

$$\dot{\sigma}_1 = \eta_0\left(-\frac{4}{r}\,\dot{v}_1 + \frac{l(l+1)+4}{r^2}\,v_1 + \frac{l(l+1)}{r\mu_l}\,\dot{v}_2 - \frac{3l(l+1)}{r^2\mu_l}\,v_2\right) + \rho_0\dot{U}_1 + g_0\rho_1\,. \tag{2.52}$$

In order to eliminate the first order derivative $\dot{v}_2$, we substitute (A2) into the previous equation to find:

$$\dot{\sigma}_1 = \frac{l(l+1)}{r\mu_l}\,\sigma_2 + \eta_0\left(-\frac{4}{r}\,\dot{v}_1 + \frac{4}{r^2}\,v_1 - \frac{2l(l+1)}{r^2\mu_l}\,v_2\right) + \rho_0\dot{U}_1 + g_0\rho_1\,. \tag{2.53}$$

We notice the radial derivative of the harmonic coefficient of the (disturbed) gravitational potential $\dot{U}_1$ in the previous relation. In contrast to the other derived variables, i.e. $\dot{P}_1$, $\dot{v}_1$ and $\dot{v}_2$, there is no additional information, resp. equation, with respect to $\dot{U}_1$ that we can use here to replace this derivative. We know that U is related to ρ by the gravitational Poisson equation but this equation even contains second derivatives what makes this equation not suitable for a simplification of the previous one. Thus, there is no other possibility than to keep $\dot{U}_1$ in the equation as it is. Therefore, from now on, we have to basically treat $\dot{U}_1$ like a non-derived variable and in order to take this into account, we will introduce an auxiliary variable and use the notation $W_1 := \dot{U}_1$.

Furthermore, we remove the first order derivative $\dot{v}_1$ by inserting (A1), the relation derived from the continuity equation, to arrive at

$$\boxed{\dot{\sigma}_1 = 4\,(3+\chi)\,\frac{\eta_0}{r^2}\,v_1 - 6l(l+1)\frac{\eta_0}{r^2\mu_l}\,v_2 + \frac{l(l+1)}{r\mu_l}\,\sigma_2 + \rho_0 W_1 + g_0\rho_1\,.} \tag{A3}$$

We continue by applying exactly the same procedure to the second vector harmonic coefficient of both sides of the Stokes equation. Applying again the respective harmonic coefficients of the differential operators from the previous chapter yields:

$$\begin{aligned} 0 = &-\frac{\mu_l}{r}\,P_1 + \eta_0\left(\ddot{v}_2 + \frac{2}{r}\,\dot{v}_2 - \frac{l(l+1)}{r^2}\,v_2 + \frac{2\mu_l}{r^2}\,v_1 - \frac{1}{3}\frac{\mu_l\chi}{r^2}\,v_1\right) \\ &+ \dot{\eta}_0\left(\dot{v}_2 + \frac{\mu_l}{r}\,v_1 - \frac{v_2}{r}\right) - \frac{\mu_l}{r}\rho_0 U_1\,. \end{aligned} \tag{2.54}$$

We substitute the pressure field P_1 again by applying (H1):

$$\begin{aligned} 0 = &\frac{\mu_l}{r}\,\sigma_1 + \eta_0\left(\ddot{v}_2 + \frac{2}{r}\,\dot{v}_2 - \frac{2\mu_l}{r}\,\dot{v}_1 - \frac{l(l+1)}{r^2}\,v_2 + \frac{\mu_l\,(2-\chi)}{r^2}\,v_1\right) \\ &+ \dot{\eta}_0\left(\dot{v}_2 + \frac{\mu_l}{r}\,v_1 - \frac{v_2}{r}\right) - \frac{\mu_l}{r}\rho_0 U_1\,. \end{aligned} \tag{2.55}$$

As before, we have to deal with a second derivative, $\ddot{v}_2$. Obviously, we can replace this quantity by using the radial derivative of (A2), i.e.

$$\boxed{\ddot{v}_2 = \frac{\dot{\sigma}_2}{\eta_0} - \frac{\dot{\eta}_0}{{\eta_0}^2}\,\sigma_2 - \frac{\mu_l}{r}\,\dot{v}_1 + \frac{\mu_l}{r^2}\,v_1 + \frac{\dot{v}_2}{r} - \frac{v_2}{r^2}\,.} \tag{$\dot{\text{A2}}$}$$

We insert this result into (2.55) and separate $\dot{\sigma}_2$ since here, this seems to be the crucial quantity for the differential equation. We find

$$\begin{aligned}\dot{\sigma}_2 = \frac{\dot{\eta}_0}{\eta_0}\,\sigma_2 - \frac{\mu_l}{r}\,\sigma_1 + \eta_0\left(-\frac{3}{r}\,\dot{v}_2 + \frac{3\mu_l}{r}\,\dot{v}_1 + \frac{l(l+1)+1}{r^2}\,v_2 - \frac{\mu_l\,(3-\chi)}{r^2}\,v_1\right)\\ + \dot{\eta}_0\left(-\dot{v}_2 - \frac{\mu_l}{r}\,v_1 + \frac{v_2}{r}\right) + \frac{\mu_l}{r}\rho_0 U_1\,.\end{aligned} \tag{2.56}$$

In order to remove $\dot{v}_2$ we apply (A2) to find

$$\dot{\sigma}_2 = -\frac{3}{r}\,\sigma_2 - \frac{\mu_l}{r}\,\sigma_1 + \eta_0\left(\frac{3\mu_l}{r}\,\dot{v}_1 + \frac{l(l+1)-2}{r^2}\,v_2 + \frac{\mu_l\chi}{r^2}\,v_1\right) + \frac{\mu_l}{r}\rho_0 U_1\,. \tag{2.57}$$

Finally, after also replacing $\dot{v}_1$ by using (A1) we gain the final result

$$\boxed{\dot{\sigma}_2 = -2\,(3+\chi)\,\frac{\eta_0\mu_l}{r^2}\,v_1 + (4l(l+1)-2)\,\frac{\eta_0}{r^2}\,v_2 - \frac{\mu_l}{r}\,\sigma_1 - \frac{3}{r}\,\sigma_2 + \frac{\mu_l}{r}\rho_0 U_1\,.} \tag{A4}$$

We end this subsection by applying the already familiar procedure to the third vector harmonic coefficient of both sides of the Stokes equation. Here, we find:

$$0 = \eta_0\left(\ddot{v}_3 + \frac{2}{r}\,\dot{v}_3 - \frac{l(l+1)}{r^2}\,v_3\right) + \dot{\eta}_0\left(\dot{v}_3 - \frac{v_3}{r}\right)\,. \tag{2.58}$$

In order to replace the second order derivative $\ddot{v}_3$ we use the radial derivative of (B1), i.e.

$$\boxed{\ddot{v}_3 = \frac{\dot{v}_3}{r} - \frac{v_3}{r^2} + \frac{\dot{\sigma}_3}{\eta_0} - \frac{\dot{\eta}_0}{{\eta_0}^2}\,\sigma_3\,.} \tag{$\dot{\text{B}}$1}$$

We insert this result into (2.58) and separate $\dot{\sigma}_3$ to find

$$\dot{\sigma}_3 = \frac{\dot{\eta}_0}{\eta_0}\,\sigma_3 + \eta_0\left(-\frac{3}{r}\,\dot{v}_3 + \frac{l(l+1)+1}{r^2}\,v_3\right) + \dot{\eta}_0\left(-\dot{v}_3 + \frac{v_3}{r}\right)\,. \tag{2.59}$$

Inserting (B1) then yields the final result

$$\boxed{\dot{\sigma}_3 = (l(l+1)-2)\,\frac{\eta_0}{r^2}\,v_3 - \frac{3}{r}\,\sigma_3\,.} \tag{B2}$$

As already announced in the previous subsection, we notice that the Stokes equation now has provided us with an ordinary differential equation for all three harmonic coefficients of the stress vector. Furthermore, note the astonishing result that all derivatives $\dot{\eta}_0$ of the viscosity cancel each other in each of the previously derived relations, even if $\dot{\eta}_0$ is present in the original Stokes equation. Thus, in spite of the assumption that the viscosity may vary radially, we do not have to take derivatives into account and the equations remain easier to handle.

2.2.4 Poisson equation

Summarising the two previous subsection, we have already found four differential equations (A1) - (A4) for the poloidal coefficients and two equations (B1) and (B2) for the toroidal coefficients. Since with v_3 and σ_3 the governing equations only contain two toroidal coefficients, the system of equations created by these two equations is already (potentially) solvable. With σ_1, σ_2, v_1, v_2, U_1 and W_1 there are 6 poloidal variables involved in the governing equations. Note that ρ does not play any role here since the overall task is to determine the stress and velocity field, i.e. the flow, given a certain density distribution, i.e. these coefficients are externally provided and serve as a constant in the derived equations.

Thus, there are still two poloidal equations needed to complete the system. Since until this point we have not considered the relation between the gravitational potential U and the density field ρ yet, we will have now a detailed look at the Poisson equation (2.25):

$$\Delta U = 4\pi G\rho\,. \tag{2.60}$$

We apply the same procedure as in the previous subsections and find, using (1.311) the following relation for the (scalar) harmonic coefficient of both sides of the equation:

$$\ddot{U}_1 + \frac{2}{r}\,\dot{U}_1 - \frac{l(l+1)}{r^2}\,U_1 = 4\pi G\rho_1\,. \tag{2.61}$$

Since we do not want to handle second derivatives, it seems appropriate to reformulate the previous relation in terms of W_1. We then immediate find

$$\boxed{\dot{W}_1 = -\frac{2}{r}\,W_1 + \frac{l(l+1)}{r^2}\,U_1 + 4\pi G\rho_1\,.} \tag{A6}$$

Now, the only thing missing to complete the system of differential equations is a relation between $\dot{U}_1$ and any non-derived variables but this is trivial since per definition it holds that

$$\boxed{\dot{U}_1 = W_1\,.} \tag{A5}$$

The previous two relations (A5) and (A6) now complete the poloidal part of the equation system. Note that in the special case when self-gravity is not taken into account in the Stokes equations, U_1 and W_1 are not present in the relations (A1) - (A4) and there would be no need to include the gravitational Poisson equation. The system (A1) - (A4) would already be complete and entirely decoupled from (A5) and (A6), which then just serve as a representation of the Poisson equation without any connection to the quantities representing the flow.

2.2.5 Summary: system of first order ODEs

We summarise all relations that were derived in the course of the previous subsections and briefly state their origin to get a decent overview. For the poloidal coefficients we have found the following relations:

(A1) - continuity equation:

$$\dot{v}_1 = -\frac{2+\chi}{r}\,v_1 + \frac{l(l+1)}{r\mu_l}\,v_2\,.$$

(A2) - stress-strain relation, 2nd vector harmonic:

$$\dot{v}_2 = -\frac{\mu_l}{r}\,v_1 + \frac{v_2}{r} + \frac{\sigma_2}{\eta_0}\,.$$

(A3) - Stokes equation, 1st vector harmonic:

$$\dot{\sigma}_1 = 4\,(3+\chi)\,\frac{\eta_0}{r^2}\,v_1 - 6l(l+1)\frac{\eta_0}{r^2\mu_l}\,v_2 + \frac{l(l+1)}{r\mu_l}\,\sigma_2 + \rho_0 W_1 + g_0\rho_1\,.$$

(A4) - Stokes equation, 2nd vector harmonic:

$$\dot{\sigma}_2 = -2\,(3+\chi)\,\frac{\eta_0\mu_l}{r^2}\,v_1 + (4l(l+1)-2)\,\frac{\eta_0}{r^2}\,v_2 - \frac{\mu_l}{r}\,\sigma_1 - \frac{3}{r}\,\sigma_2 + \frac{\mu_l}{r}\rho_0 U_1\,.$$

(A5) - definition of auxiliary quantity W_1:

$$\dot{U}_1 = W_1\,.$$

(A6) - gravitational Poisson equation:

$$\dot{W}_1 = -\frac{2}{r} W_1 + \frac{l(l+1)}{r^2} U_1 + 4\pi G \rho_1 \,.$$

For the toroidal coefficients we have found the following relations:

(B1) - stress-strain relation, 3rd vector harmonic:

$$\dot{v}_3 = \frac{v_3}{r} + \frac{\sigma_3}{\eta_0} \,.$$

(B2) - Stokes equation, 3rd vector harmonic:

$$\dot{\sigma}_3 = (l(l+1) - 2)\, \frac{\eta_0}{r^2}\, v_3 - \frac{3}{r}\, \sigma_3 \,.$$

Furthermore, due to construction it is possible to represent these equations also in a compact matrix form. For the poloidal part, we find that (A1)-(A6) can be represented by the system of differential equations

$$\dot{U}_A = A u_A + \alpha \,, \tag{2.62}$$

with

$$\begin{aligned} u_A &:= (v_1, v_2, \sigma_1, \sigma_2, U_1, W_1)^T \,, \\ A &:= \begin{pmatrix} -(2+\chi)/r & l(l+1)/(r\mu_l) & 0 & 0 & 0 & 0 \\ -\mu_l/r & 1/r & 0 & 1/\eta_0 & 0 & 0 \\ 4(3+\chi)\eta_0/r^2 & -6l(l+1)\eta_0/(r^2\mu_l) & 0 & l(l+1)/(r\mu_l) & 0 & \rho_0 \\ -2(3+\chi)\eta_0\mu_l/r^2 & (4l(l+1)-2)\eta_0/r^2 & -\mu_l/r & -3/r & \mu_l\rho_0/r & 0 \\ 0 & 0 & 0 & 0 & 0 & 1 \\ 0 & 0 & 0 & 0 & l(l+1)/r^2 & -2/r \end{pmatrix} , \\ \alpha &:= (0, 0, g_0\rho_1, 0, 0, 4\pi G\rho_1)^T \,. \end{aligned} \tag{2.63}$$

α is called the **driving vector** of the system since this vector contains the lateral density variations that are responsible for the existence of the flow. Without the driving vector - and neglecting the influence of boundary conditions for this moment - the system of differential equations would only have the trivial solution $u_A \equiv 0$, which means that there was no flow and the system was in equilibrium.

If we use the same notation for the toroidal part of the equation system, i.e.

$$\dot{u_B} = B u_B + \beta \,, \tag{2.64}$$

with

$$\begin{aligned} u_B &:= (v_3, \sigma_3)^T \,, \\ B &:= \begin{pmatrix} 1/r & 1/\eta_0 \\ (l(l+1)-2)\eta_0/r^2 & -3/r \end{pmatrix} , \\ \beta &:= (0, 0)^T \,, \end{aligned} \tag{2.65}$$

we see that there is indeed no driving vector for the toroidal part. This means that without imposing boundary conditions that generate a toroidal field, we find that $u_B \equiv 0$. This is a direct consequence of the assumption of a purely radially varying viscosity since with a full laterally dependent viscosity, there would be additional terms also in the toroidal parts of the equation.

Nevertheless, in numerical geodynamics it is common to impose a velocity field on the surface that has

been derived by plate motion history. In time-dependent simulations this is even necessary in order to generate realistic flow scenarios since it is mainly the boundary conditions that determine the detailed flow behaviour inside the mantle. If we do a harmonic analysis of a current plate motion velocity field model, we find that it (naturally) contains an essential toroidal component (see e.g., Hager and O'Connell, 1981). Since we just learned that our model does not intrinsically support toroidal flow, unfortunately such a data derived boundary condition would result in inconsistencies.

If we have a closer look at the matrices A and B we notice that the magnitude of the different components vary significantly from each other. This has an essential negative impact on the condition number of the matrix, which makes the numerical determination of the solution of a potential system of linear equations that contains A or B infeasible if not impossible. To approach this problem, we redefine some of the involved coefficients by multiplying the respective variables with appropriate scaling factors, including the normalisation factor μ_l of the tangential harmonics. Furthermore, since the factor $1/r$ is present in almost all components, it seems appropriate to extract this factor from the matrices. More precisely, we define the new system of coefficients as:

$$\begin{aligned}
\bar{v}_1 &:= v_1\,, & \bar{\sigma}_1 &:= \frac{r}{\hat{\eta}_0}\,\sigma_1\,, & \bar{U}_1 &:= r\frac{\hat{\rho}_0}{\hat{\eta}_0}\,U_1\,,\\
\bar{v}_2 &:= \frac{1}{\mu_l}\,v_2\,, & \bar{\sigma}_2 &:= \frac{r}{\mu_l\hat{\eta}_0}\,\sigma_2\,, & \bar{W}_1 &:= r^2\frac{\hat{\rho}_0}{\hat{\eta}_0}\,W_1\,,\\
\bar{v}_3 &:= \frac{1}{\mu_l}\,v_3\,, & \bar{\sigma}_3 &:= \frac{r}{\mu_l\hat{\eta}_0}\,\sigma_3\,,
\end{aligned} \tag{2.66}$$

where $\hat{\eta}_0$ is a constant reference viscosity (compare to (2.23)) and $\hat{\rho}_0$ a constant reference density. Additionally, we define $\eta_0^* := \eta_0/\hat{\eta}_0$ as the viscosity variation factor and $\rho_0^* := \rho_0/\hat{\rho}_0$ as the density variation factor. Due to the necessary radial scaling of some of the variables and the presence of radial derivatives in the system of equations, we have to reformulate all relations in terms of the new variables. In terms of the scaled quantities, the equations then state as:

(A1)

$$r\dot{\bar{v}}_1 = -\,(2+\chi)\,\bar{v}_1 + l(l+1)\,\bar{v}_2\,.$$

(A2)

$$r\dot{\bar{v}}_2 = -\bar{v}_1 + \bar{v}_2 + \frac{\bar{\sigma}_2}{\eta_0^*}\,.$$

(A3)

$$\begin{aligned}
& r\partial_r\left(\frac{\hat{\eta}_0}{r}\,\bar{\sigma}_1\right) = 4\,(3+\chi)\,\frac{\eta_0}{r}\,\bar{v}_1 - 6l(l+1)\frac{\eta_0}{r}\,\bar{v}_2 + \hat{\eta}_0\frac{l(l+1)}{r}\,\bar{\sigma}_2 + \frac{\rho_0^*\hat{\eta}_0}{r}\,\bar{W}_1 + r g_0\rho_1\\
\Leftrightarrow\quad & \hat{\eta}_0\left(\dot{\bar{\sigma}}_1 - \frac{\bar{\sigma}_1}{r}\right) = 4\,(3+\chi)\,\frac{\eta_0}{r}\,\bar{v}_1 - 6l(l+1)\frac{\eta_0}{r}\,\bar{v}_2 + \hat{\eta}_0\frac{l(l+1)}{r}\,\bar{\sigma}_2 + \frac{\rho_0^*\hat{\eta}_0}{r}\,\bar{W}_1 + r g_0\rho_1\\
\Leftrightarrow\quad & r\dot{\bar{\sigma}}_1 = 4\,(3+\chi)\,\eta_0^*\,\bar{v}_1 - 6l(l+1)\eta_0^*\,\bar{v}_2 + \bar{\sigma}_1 + l(l+1)\,\bar{\sigma}_2 + \rho_0^*\,\bar{W}_1 + \frac{g_0 r^2}{\hat{\eta}_0}\,\rho_1\,.
\end{aligned}$$

(A4)

$$\begin{aligned}
& r\partial_r\left(\frac{\mu_l\hat{\eta}_0}{r}\,\bar{\sigma}_2\right) = -2\,(3+\chi)\,\frac{\eta_0\mu_l}{r}\,\bar{v}_1 + (4l(l+1)-2)\,\frac{\mu_l\,\eta_0}{r}\,\bar{v}_2 - \hat{\eta}_0\frac{\mu_l}{r}\,\bar{\sigma}_1 - \mu_l\,\hat{\eta}_0\frac{3}{r}\,\bar{\sigma}_2 + \hat{\eta}_0\frac{\mu_l}{r}\rho_0^*\,\bar{U}_1\\
\Leftrightarrow\quad & \hat{\eta}_0\left(\dot{\bar{\sigma}}_2 - \frac{\bar{\sigma}_2}{r}\right) = -2\,(3+\chi)\,\frac{\eta_0}{r}\,\bar{v}_1 + (4l(l+1)-2)\,\frac{\eta_0}{r}\,\bar{v}_2 - \frac{\hat{\eta}_0}{r}\,\bar{\sigma}_1 - \frac{3\hat{\eta}_0}{r}\,\bar{\sigma}_2 + \frac{\hat{\eta}_0}{r}\rho_0^*\,\bar{U}_1\\
\Leftrightarrow\quad & r\dot{\bar{\sigma}}_2 = -2\,(3+\chi)\,\eta_0^*\,\bar{v}_1 + (4l(l+1)-2)\,\eta_0^*\,\bar{v}_2 - \bar{\sigma}_1 - 2\bar{\sigma}_2 + \rho_0^*\,\bar{U}_1\,.
\end{aligned}$$

(A5)

$$r\partial_r\left(\frac{\bar{U}_1}{r}\right) = \dot{\bar{U}}_1 - \frac{1}{r}\bar{U}_1 = \frac{\bar{W}_1}{r}$$
$$\Leftrightarrow \qquad r\dot{\bar{U}}_1 = \bar{W}_1 + \bar{U}_1\,.$$

(A6)

$$r^2\partial_r\left(\frac{\bar{W}_1}{r^2}\right) = -\frac{2}{r}\bar{W}_1 + \frac{l(l+1)}{r}\bar{U}_1 + \frac{4\pi G\hat{\rho}_0 r^2}{\hat{\eta}_0}\rho_1$$
$$\Leftrightarrow \quad \dot{\bar{W}}_1 - \frac{2}{r}\bar{W}_1 = -\frac{2}{r}\bar{W}_1 + \frac{l(l+1)}{r}\bar{U}_1 + \frac{4\pi G\hat{\rho}_0 r^2}{\hat{\eta}_0}\rho_1$$
$$\Leftrightarrow \qquad r\dot{\bar{W}}_1 = l(l+1)\bar{U}_1 + \frac{4\pi G\hat{\rho}_0 r^3}{\hat{\eta}_0}\rho_1\,.$$

(B1)

$$r\dot{\bar{v}}_3 = \bar{v}_3 + \frac{\bar{\sigma}_3}{\eta_0^*}\,.$$

(B2)

$$r\partial_r\left(\frac{\hat{\eta}_0}{r}\bar{\sigma}_3\right) = (l(l+1)-2)\frac{\eta_0}{r}\bar{v}_3 - \hat{\eta}_0\frac{3}{r}\bar{\sigma}_3$$
$$\Leftrightarrow \quad \hat{\eta}_0\left(\dot{\bar{\sigma}}_3 - \frac{\bar{\sigma}_3}{r}\right) = (l(l+1)-2)\frac{\eta_0}{r}\bar{v}_3 - \hat{\eta}_0\frac{3}{r}\bar{\sigma}_3$$
$$\Leftrightarrow \qquad r\dot{\bar{\sigma}}_3 = (l(l+1)-2)\,\eta_0^*\,\bar{v}_3 - 2\bar{\sigma}_3\,.$$

Summarised, we finally end up with the following linear systems of differential equations. The poloidal part transfers into:

$$r\dot{\bar{u}}_A = \bar{A}\bar{u}_A + \bar{\alpha}\,, \tag{2.67}$$

with

$$\bar{u}_A := \left(\bar{v}_1, \bar{v}_2, \bar{\sigma}_1, \bar{\sigma}_2, \bar{U}_1, \bar{W}_1\right)^T\,,$$
$$\bar{A} := \begin{pmatrix} -(2+\chi) & l(l+1) & 0 & 0 & 0 & 0 \\ -1 & 1 & 0 & 1/\eta_0^* & 0 & 0 \\ 4(3+\chi)\eta_0^* & -6l(l+1)\eta_0^* & 1 & l(l+1) & 0 & \rho_0^* \\ -2(3+\chi)\eta_0^* & (4l(l+1)-2)\eta_0^* & -1 & -2 & \rho_0^* & 0 \\ 0 & 0 & 0 & 0 & 1 & 1 \\ 0 & 0 & 0 & 0 & l(l+1) & 0 \end{pmatrix}, \tag{2.68}$$
$$\bar{\alpha} := \left(0, 0, \frac{g_0 r^2}{\hat{\eta}_0}\rho_1, 0, 0, \frac{4\pi G\hat{\rho}_0 r^3}{\hat{\eta}_0}\rho_1\right)^T = \bar{\alpha}_0\rho_1\,,$$

where we defined

$$\bar{\alpha}_0 := \left(0, 0, \frac{g_0 r^2}{\hat{\eta}_0}, 0, 0, \frac{4\pi G\hat{\rho}_0 r^3}{\hat{\eta}_0}\right)^T\,. \tag{2.69}$$

And for the toroidal equations we find that:

$$r\dot{\bar{u}}_B = \bar{B}\bar{u}_B + \bar{\beta}\,, \tag{2.70}$$

with

$$\begin{aligned} \bar{u}_B &:= (\bar{v}_3, \bar{\sigma}_3)^T \,, \\ \bar{B} &:= \begin{pmatrix} 1 & 1/\eta_0^* \\ (l(l+1)-2)\eta_0^* & -2 \end{pmatrix} , \\ \bar{\beta} &:= (0,0)^T \,. \end{aligned} \tag{2.71}$$

In literature, it is common to split the matrix $\bar{A}$ into three parts $\bar{A} = \bar{A}_\alpha + \bar{A}_\beta + \bar{A}_\gamma$ that illustrate the contributions from the different physical effects. We define

$$\bar{A}_\alpha := \begin{pmatrix} -2 & l(l+1) & 0 & 0 & 0 & 0 \\ -1 & 1 & 0 & 1/\eta_0^* & 0 & 0 \\ 12\eta_0^* & -6l(l+1)\eta_0^* & 1 & l(l+1) & 0 & 0 \\ -6\eta_0^* & (4l(l+1)-2)\eta_0^* & -1 & -2 & 0 & 0 \\ 0 & 0 & 0 & 0 & 1 & 1 \\ 0 & 0 & 0 & 0 & l(l+1) & 0 \end{pmatrix} , \tag{2.72}$$

and

$$\bar{A}_\beta := \begin{pmatrix} -\chi & 0 & 0 & 0 & 0 & 0 \\ 0 & 0 & 0 & 0 & 0 & 0 \\ 4\chi\eta_0^* & 0 & 0 & 0 & 0 & 0 \\ -2\chi\eta_0^* & 0 & 0 & 0 & 0 & 0 \\ 0 & 0 & 0 & 0 & 0 & 0 \\ 0 & 0 & 0 & 0 & 0 & 0 \end{pmatrix} , \quad \bar{A}_\gamma := \begin{pmatrix} 0 & 0 & 0 & 0 & 0 & 0 \\ 0 & 0 & 0 & 0 & 0 & 0 \\ 0 & 0 & 0 & 0 & 0 & \rho_0^* \\ 0 & 0 & 0 & 0 & \rho_0^* & 0 \\ 0 & 0 & 0 & 0 & 0 & 0 \\ 0 & 0 & 0 & 0 & 0 & 0 \end{pmatrix} . \tag{2.73}$$

where $\bar{A}_\alpha$ denotes the basis matrix, $\bar{A}_\beta$ the contribution due to compressibility and $\bar{A}_\gamma$ accounts for the effects from self-gravitation. As already mentioned before, note that in the basis matrix, the 5th and 6th row/column that correspond to the gravitational potential are decoupled from the other entries. The coupling is only (optionally) introduced by $\bar{A}_\gamma$. Thus, without taking self-gravity into account, a 4×4 matrix would be sufficient to determine all necessary flow parameters.

All presented matrices and vectors are still dependent on the radius r since the viscosity $\eta_0^*(r)$, the background density variation $\rho_0^*(r)$ and thus, also the background gravitational acceleration $g_0(r)$ and the compressible factor $\chi(r)$ may vary with depth. In practise, the domain, i.e. the Earth's mantle, will be divided into n layers, where in each layer, the above mentioned quantities are assumed to be constant. In the limit $n \to \infty$ we then find the continuous dependence on r. The number of layers is commonly determined by the origin of the data corresponding to the lateral density variations. An image of the Earth's mantle at the present time can e.g. be deduced by seismic tomographic data, where the number of layers is given by the used model and/or by the spatial data distribution that was used in order to derive the tomographic image.

In the next section we will present a standard method to solve the presented linear system of differential equations in a spherical shell. Here, the assumption of a layer-wise constant matrix will be essential for providing an appropriate and suitable solution method.

2.3 The propagator matrix technique

2.3.1 The 1-D approach

A spectral analysis of the Stokes and continuity equation has lead to a linear system of differential equations of the form

$$\dot{u}(r) = A(r)\, u(r) + \alpha(r) \,, \tag{2.74}$$

where $A \in \mathbb{R}^{n\times n}$, $n \in \mathbb{N}$ is a real matrix. For the special case $n = 1$, A is just a multiplicative factor $a(r) \in \mathbb{R}$ and the solution to this 1-D problem can be found by a standard exponential ansatz, first determining the solution for the homogeneous problem, i.e. $\alpha(r) \equiv 0$, then determining a particular solution for the inhomogeneous problem by variation of the constant. By separation of the variables we find for the homogeneous equation that

$$\ln(u(r)) = \int_{r_0}^{r} a(\tau)\,\mathrm{d}\tau + \tilde{c} \;\Rightarrow\; u(r) = e^{\left(\int_{r_0}^{r} a(\tau)\,\mathrm{d}\tau\right)} c\,, \tag{2.75}$$

with an integration constant $c \in \mathbb{R}$. The lower limit r_0 of the integration evolves from one boundary of the domain. Please keep in mind that one explicit boundary condition, i.e. $u(r_0) = u_0$ is required to find a specific solution to the differential equation. Based on the previous result, a solution for the inhomogeneous problem can be found by the assumption that also the constant c depends on r (variation of the constant), i.e. we assume

$$u(r) = e^{\left(\int_{r_0}^{r} a(\tau)\,\mathrm{d}\tau\right)} c(r) \;\Rightarrow\; \dot{u}(r) = e^{\left(\int_{r_0}^{r} a(\tau)\,\mathrm{d}\tau\right)} \dot{c}(r) + a(r)\,u(r)\,. \tag{2.76}$$

Comparing this to the 1-D version of (2.74) we see that this relation is true for

$$\alpha(r) = e^{\left(\int_{r_0}^{r} a(\tau)\,\mathrm{d}\tau\right)} \dot{c}(r)\,. \tag{2.77}$$

Thus, for $c(r)$ we find

$$\dot{c}(r) = e^{-\left(\int_{r_0}^{r} a(\tau)\,\mathrm{d}\tau\right)} \alpha(r) \;\Rightarrow\; c(r) = \int_{r_0}^{r} e^{-\left(\int_{r_0}^{s} a(\tau)\,\mathrm{d}\tau\right)} \alpha(s)\,\mathrm{d}s + C\,, \tag{2.78}$$

with an integration constant $C \in \mathbb{R}$. Inserting this result into the ansatz (2.76) we get

$$\begin{aligned} u(r) &= e^{\left(\int_{r_0}^{r} a(\tau)\,\mathrm{d}\tau\right)} \left(\int_{r_0}^{r} e^{-\left(\int_{r_0}^{s} a(\tau)\,\mathrm{d}\tau\right)} \alpha(s)\,\mathrm{d}s + C \right) \\ &= e^{\left(\int_{r_0}^{r} a(\tau)\,\mathrm{d}\tau\right)} C + \int_{r_0}^{r} e^{\left(\int_{s}^{r} a(\tau)\,\mathrm{d}\tau\right)} \alpha(s)\,\mathrm{d}s\,. \end{aligned} \tag{2.79}$$

Please verify that this specific $u(r)$ indeed satisfies the differential equation (2.74). The explicit value for C can be determined by choosing $r = r_0$ in the previous equation, since in that case, all integrals vanish and the equation reduces to $u(r_0) = C$. Thus, the integration constant C can be identified with the value of u at the inner boundary, which we will denote from now on by u_0. Note that u_0 does not necessarily need to be prescribed a-priori since it is also possible that $u_1 := u(r_1)$ is given, the value of u at the outer boundary. But in that case, the equation just needs to be rearranged. We will discuss this scenario explicitly a few paragraphs below.

For the special case that the multiplicative factor $a(r)$ is just a constant that does not depend on r, i.e. $a(r) = a$, the representation of u simplifies to:

$$u(r) = e^{a(r-r_0)}\,u_0 + \int_{r_0}^{r} e^{a(r-s)}\,\alpha(s)\,\mathrm{d}s\,. \tag{2.80}$$

In most applications, we are facing a mixed scenario where the domain is equally divided into n layers with thickness $\Delta r := (r_1 - r_0)/n$ where $a(r)$ is constant in each layer. We denote the different layer boundaries by b_i, $i = 1, ..., n+1$, where $b_1 = r_0$ and $b_{n+1} = r_1$ and we formally assume w.l.o.g. that the respective properties of each layer are defined at its lower boundary, i.e. the value of a for layer 1 is defined by $a(b_1)$, the value of a for layer n is defined by $a(b_n)$ and $a(b_{n+1})$ is not defined. In this case the solution transfers into:

$$u(b_k) = e^{\left(\sum_{i=2}^{k} a(b_{i-1})(b_i - b_{i-1})\right)} u_0 + \int_{b_1}^{b_k} e^{\left(\sum_{i=i_s}^{k} a(b_{i-1})(b_i - b_{i-1})\right)} \alpha(s)\,\mathrm{d}s\,, \tag{2.81}$$

for all $k = 1, ..., n+1$, where i_s is the layer number corresponding to the current value of the integration variable s. To dissolve the situation of a mixed continuous and discrete form in the second term, we also include the (natural) assumption that $\alpha(r)$, the driving vector (which is technically not yet a vector since we are still discussing the 1-D case), is also constant in each of the layers defined above, which yields

$$\begin{aligned} u(b_k) &= e^{\left(\sum_{i=2}^{k} a(b_{i-1})(b_i - b_{i-1})\right)} u_0 + \sum_{j=2}^{k} e^{\left(\sum_{i=j}^{k} a(b_{i-1})(b_i - b_{i-1})\right)} \alpha(b_{j-1})(b_j - b_{j-1}) \\ &= \left(\prod_{i=2}^{k} e^{a(b_{i-1})(b_i - b_{i-1})}\right) u_0 + \sum_{j=2}^{k} \left(\prod_{i=j}^{k} e^{a(b_{i-1})(b_i - b_{i-1})}\right) \alpha(b_{j-1})(b_j - b_{j-1})\,. \end{aligned} \tag{2.82}$$

In principle, the solution $u(r)$ is defined continuously for all $r \in [r_0, r_1]$, we just determine its value at the layer boundaries to simplify the calculation of the right-hand side of the equation. Note that in contrast to the 'material property' variables a and α that are defined for the n layers, the solution u is defined at the $n+1$ layer boundaries, where especially $u(b_1) = u(r_0) = u_0$ and $u(b_{n+1}) = u(r_1) = u_1$ are the boundary values at the inner and outer boundary.

As a side remark: In order to make the transfer from (2.81) to (2.82), in literature, the lateral density contrasts are sometimes expressed as a sum over delta impulses of *sheet density contrasts* $\sigma(r)$, i.e. $\tilde{\rho}(r) = \sum_i \sigma(b_i)\,\delta(r - b_i)$, where $\sigma(b_i) := \tilde{\rho}(b_i)(b_{i+1} - b_i)$ (see e.g., Richards and Hager, 1984; Panasyuk et al., 1996). Inserting this representation into (2.81) also exactly yields (2.82) but since there is no further advantage using these (artificial) sheet density contrasts, this detour is unnecessary. Even more, there are two shortfalls using this density representation, i.e. first, in most papers there is no proper definition of $\sigma(r)$ which is at least irritating or even misleading, e.g. in Richards and Hager (1984), $\sigma(r)$ is just introduced as 'sheet density' without any definition, thus, the reader is especially not aware of the important factor $(b_{i+1} - b_i)$, the layer thickness. Second, since the representation contains the delta distribution, this immediately leads the reader to the concept of fundamental solutions (Green's functions, kernels) but here, we need a completely different approach as we will learn in one of the following paragraphs. Therefore, there is no further need to follow the ansatz of (synthetic) sheet density contrasts.

Returning to (2.82), the expression

$$\mathrm{Pg}(b_i) := e^{a(b_i)(b_{i+1} - b_i)}\,, \tag{2.83}$$

is called **propagator** since it symbolises the transition from one layer to another (with ascending radius). We also define the **backward propagator** in the opposite direction as

$$\mathrm{Pgb}(b_i) := e^{a(b_i)(b_i - b_{i+1})}\,. \tag{2.84}$$

We immediately find that $\mathrm{Pg}(b_i)^{-1} = \mathrm{Pgb}(b_i)$ for all $i = 1, ..., n$. For the propagation between more than one layer, we introduce for $j \geq i$

$$\mathrm{Pg}(b_i, b_j) := \prod_{k=i}^{j-1} \mathrm{Pg}(b_k)\,, \tag{2.85}$$

as the propagator from layer i to j and accordingly,

$$\mathrm{Pgb}(b_j, b_i) := \prod_{k=i}^{j-1} \mathrm{Pgb}(b_k)\,, \tag{2.86}$$

as the backward propagator from j to i. Also here, for $j > i$ we immediately find that $\mathrm{Pg}(b_i, b_j)^{-1} = \mathrm{Pgb}(b_j, b_i)$. Furthermore, for the theoretical case of $i = j$, we get from the definition of the propagators that

$$\mathrm{Pg}(b_i, b_i) = \mathrm{Pgb}(b_i, b_i) = 1\,, \tag{2.87}$$

and for $i > j$ we define

$$\mathrm{Pg}(b_i, b_j) := \mathrm{Pgb}(b_j, b_i) := 0\,. \tag{2.88}$$

Furthermore, it holds that

$$\begin{aligned} \mathrm{Pg}(b_i, b_j)\,\mathrm{Pg}(b_j, b_k) &= \mathrm{Pg}(b_i, b_k)\,, \\ \mathrm{Pgb}(b_k, b_j)\,\mathrm{Pgb}(b_j, b_i) &= \mathrm{Pgb}(b_k, b_i)\,, \end{aligned} \tag{2.89}$$

for all $i \leq j \leq k$. Using this notation (2.82) then turns into its final form

$$u(b_k) = \mathrm{Pg}(b_1, b_k)\,u_0 + \sum_{j=1}^{k-1} \mathrm{Pg}(b_j, b_k)\,\alpha(b_j)(b_{j+1} - b_j)\,. \tag{2.90}$$

Now, with given u_0 and α, the solution u can be determined at each layer boundary b_i, $i = 1, ..., n+1$, using the previous equation. Basically, this is the final form of the solution u but at this point, it turns out that it is quite insightful to recall again the principle of *fundamental solutions* that we already discussed briefly in Chapter 1 in the context of the Laplace operator and harmonic functions.

2.3.2 Fundamental solutions

In Chapter 1 we learned that a *distribution* G that satisfies $(L_x G)(x) = \delta(x - y)$ in the distributional sense, for the respective differential operator L_x and various y, is called fundamental solution or Green's function to the operator L_x. As we have seen before, the term 'fundamental solution' evolves from the fact that by determining this special solution, the solution of the original differential equation $L_x F = H$ can be found for any inhomogeneity H without solving the original differential equation. More precisely, having found such a G, the solution F states as

$$F(x) = \int G(x, y)\,H(y)\,\mathrm{d}y\,. \tag{2.91}$$

This is a very popular strategy since first, in many cases, determining a distributional solution G turns out to be an easier task than solving the original differential equation. In particular, if the original equation is formulated as - or can be transformed - into an integral formulation, there may be a straightforward way to execute the transition into distributional space. Second, also from a physical perspective, fundamental solutions reveal much insight into the underlying differential equation. They represent the response of the system to a 'stimulus' just at a certain point y. Thus, by determining

a variety of fundamental solutions for different points y, one can gain much understanding about the different contributions to any solution to the general problem $LF = H$.

Fortunately, in our case, now returning to the original representation of the continuity (2.9) and of the momentum equation (2.30), we see that all underlying field equations are linear and the principle of fundamental solutions may be applied. In general, we could reformulate all equations - albeit vectorial - in the way $LF = H$, where L is a combination of linear differential operators. In (2.30), we notice that in our case the right-hand side, i.e. H in the previous formulation, only consists of the lateral density variations $\tilde{\rho}(r)$ - including some proportionality factors. Thus, a fundamental solution to the system would be the response to a (unit) density anomaly at a certain depth, i.e. in a certain layer b_j. This would be a very precious information since then, we could directly see how anomalies at different depth levels contribute to the total solution, i.e. the velocity field, the stress field and especially the gravitational signal.

Therefore, in order to construct fundamental solutions, we now choose the density anomaly to be $\tilde{\rho}(r) = \delta(r - b_j)$ for one fixed $j \in \{1, ..., n\}$, and with (2.68), the driving vector then becomes $\alpha(r) = \alpha_0(r)\,\delta(r - b_j)$. Note that at the moment, we are still considering the 1-D case where $\alpha_0(r)$ is just a multiplicative factor. Later, in the multidimensional case, α_0 then exactly takes the form (2.69). As a side remark, in the ansatz of the fundamental solution, a delta peak at $b_1 = r_0$, i.e. at a domain boundary, is theoretically and physically not meaningful and has to be ignored in the following considerations. At the end, when we will investigate the integral representation of the total solution, this will become meaningful again due to our layer convention that the properties of each layer are formally prescribed at their lower boundary.

Now, inserting this ansatz into (2.81) yields for all $k = 1, ..., n+1$, (compare to (2.90)) that

$$\begin{aligned} u^{(j)}(b_k) &= e^{\left(\sum_{i=2}^{k} a(b_{i-1})(b_i - b_{i-1})\right)} u_0^{(j)} + e^{\left(\sum_{i=j}^{k-1} a(b_i)(b_{i+1} - b_i)\right)} \alpha_0(b_j) \\ &= \left(\prod_{i=2}^{k} e^{a(b_{i-1})(b_i - b_{i-1})}\right) u_0^{(j)} + \left(\prod_{i=j}^{k-1} e^{a(b_i)(b_{i+1} - b_i)}\right) \alpha_0(b_j) \\ &= \mathrm{Pg}(b_1, b_k)\, u_0^{(j)} + \mathrm{Pg}(b_j, b_k)\, \alpha_0(b_j)\,. \end{aligned} \tag{2.92}$$

Here we introduced the upper index (j) to the solution u (and to the boundary value u_0) to denote that this certain u is a fundamental solution with respect to b_j. Note that for $k = j = 1$ the previous equation turns into

$$\begin{aligned} u_0^{(1)} &= \mathrm{Pg}(b_1, b_1)\, u_0^{(1)} + \mathrm{Pg}(b_1, b_1)\, \alpha_0(b_1) \\ &= u_0^{(1)} + \alpha_0(b_1)\,, \end{aligned} \tag{2.93}$$

leading to $\alpha_0(b_1) = 0$, which underlines the previously made statement that formally, a delta peak at the domain boundary is not meaningful. Furthermore, note that due to $\mathrm{Pg}(b_j, b_k) = 0$ for $j > k$, the driving vector only influences layers above the density anomaly and not below. This is due to the assumed a-priori known boundary condition u_0 at the inner boundary and only true if u_0 is indeed given. But in practice, in the multidimensional case, we will see that the boundary conditions for each individual component of u may not only be imposed at one of the domain boundaries but on different ones, i.e. for some components of u the value at r_1 and for some components, the value at r_0 could and will be prescribed. We see that if we evaluate the previous equation at the outer boundary of the domain, i.e. at $b_{n+1} = r_1$, we find the following relation between u_0 and u_1:

$$u_1^{(j)} = \mathrm{Pg}(r_0, r_1)\, u_0^{(j)} + \mathrm{Pg}(b_j, r_1)\, \alpha_0(b_j)\,. \tag{2.94}$$

Equivalently, rearranging the previous equation yields

$$\begin{aligned} u_0^{(j)} &= \mathrm{Pg}^{-1}(r_0, r_1) \left(u_1^{(j)} - \mathrm{Pg}(b_j, r_1)\, \alpha_0(b_j) \right) \\ &= \mathrm{Pgb}(r_1, r_0)\, u_1^{(j)} - \mathrm{Pgb}(r_1, b_j)\, \mathrm{Pgb}(b_j, r_0)\, \mathrm{Pg}(b_j, r_1)\, \alpha_0(b_j) \\ &= \mathrm{Pgb}(r_1, r_0)\, u_1^{(j)} - \mathrm{Pgb}(b_j, r_0)\, \alpha_0(b_j)\,. \end{aligned} \tag{2.95}$$

Both of these relations can equivalently be used to construct a system of linear equations to determine all remaining boundary values, the complete vector $u_0^{(j)}$, resp. $u_1^{(j)}$. Then, by applying again (2.92) or the following relation that can be gained by inserting (2.95) into (2.92):

$$\begin{aligned} u^{(j)}(b_k) &= \mathrm{Pg}(b_1, b_k)\, u_0^{(j)} + \mathrm{Pg}(b_j, b_k)\, \alpha_0(b_j) \\ &= \mathrm{Pg}(b_1, b_k) \left(\mathrm{Pgb}(r_1, r_0)\, u_1^{(j)} - \mathrm{Pgb}(b_j, r_0)\, \alpha_0(b_j) \right) + \mathrm{Pg}(b_j, b_k)\, \alpha_0(b_j) \\ &= \mathrm{Pgb}(r_1, b_k)\, u_1^{(j)} - \mathrm{Pgb}(b_j, b_k)\, \alpha_0(b_j)\, (1 - \delta_{j,k})\ . \end{aligned} \tag{2.96}$$

(to derive the third line one needs to evaluate three cases: $j > k$, $j = k$ and $j < k$) we are able to evaluate the solution vector $u^{(j)}$ at all desired layer boundaries by propagating the solution from r_0 (CMB) 'upwards' (2.92) or from r_1 (surface) 'downwards' (2.96). In the final section of this chapter, we will briefly discuss the range of appropriate boundary conditions and we will set up the respective resulting system of linear equations explicitly.

But first, we return to the original differential equation that we derived in the previous section and have a look at (2.67). We notice that there is an essential difference between this equation and the one we have discussed in this section so far: the additional factor of r on the left-hand side of the equation:

$$r\dot{u}(r) = a(r)\, u(r) + \alpha(r)\,. \tag{2.97}$$

But by a change of variables, defining $s := \ln(r)$ and the layer boundaries $s_i := \ln(b_i)$, $i = 1, ..., n+1$, respectively, it is possible to transfer both types of equations into each other. With

$$\frac{\mathrm{d}u}{\mathrm{d}r} = \frac{\mathrm{d}u}{\mathrm{d}s}\, \frac{\mathrm{d}s}{\mathrm{d}r} = \frac{1}{r}\, \frac{\mathrm{d}u}{\mathrm{d}s}\,, \tag{2.98}$$

we see that instead of (2.97), by substitution, we can equivalently solve the differential equation

$$\dot{w}(s) = a\left(e^s\right)\, w(s) + \alpha\left(e^s\right)\,, \tag{2.99}$$

where the 'dot' now symbolises the derivative with respect to s. Afterwards, we can determine the solution to our original system (2.97) by back substitution, i.e. $u(r) = w(\ln(r))$. In order to find a solution to the new system, we just follow all steps that we have discussed in this section so far. We directly step into (2.81) that now takes the form

$$w(s_k) = e^{\left(\sum_{i=2}^{k} a(b_{i-1})(s_i - s_{i-1}) \right)} w_0 + \int_{s_1}^{s_k} e^{\left(\sum_{i=i_s}^{k} a(b_{i-1})(s_i - s_{i-1}) \right)} \alpha\left(e^s\right)\, \mathrm{d}s\,, \tag{2.100}$$

for all $k = 1, ..., n+1$. We already re-substituted the discrete layers $e^{s_i} = b_i$, $i = 1, ..., n+1$, in the argument of the factor a. Also here, we see that the integration constant $w_0 := w(s_1) = u(r_0) = u_0$ turns out to be the inner boundary condition. Now, heading towards a distributional formulation, we again use the ansatz

$$\alpha\left(e^s\right) = \alpha_0\left(e^{s_j}\right)\, \delta\left(e^s - e^{s_j}\right) = \alpha_0(b_j)\, \delta(r - b_j)\,, \tag{2.101}$$

for one specific $j \in \{1, ..., n\}$ to arrive at

$$w^{(j)}(s_k) = e^{\left(\sum_{i=2}^{k} a(b_{i-1})(s_i - s_{i-1}) \right)} w_0 + \int_{s_1}^{s_k} e^{\left(\sum_{i=i_s}^{k} a(b_{i-1})(s_i - s_{i-1}) \right)} \alpha_0(b_j)\, \delta\left(r - b_j\right)\, \mathrm{d}s\,. \tag{2.102}$$

Where in standard conversion rules for integrals the Jacobian of the variable transformation comes into play, the situation is slightly different when the delta distribution is involved. Here, in general, it holds that

$$\delta(g(r)) = \sum_i \frac{\delta(r - x_i)}{|g'(x_i)|}\,, \tag{2.103}$$

where g is a continuously differentiable function with simple roots x_i, $i \in \mathbb{N}$. In our case, $g(r) = \ln(r) - \ln(b_j)$ with the only root $g(b_j) = 0$ and $g'(b_j) = 1/b_j$ and thus, here we find

$$\delta(s - s_j) = b_j\,\delta(r - b_j)\,, \tag{2.104}$$

for all $j = 1, ..., n$. Inserting this result into (2.102) and replacing w_0 by u_0 yields

$$\begin{aligned} w^{(j)}(s_k) &= e^{\left(\sum\limits_{i=2}^{k} a(b_{i-1})(s_i - s_{i-1})\right)} u_0 + \int\limits_{s_1}^{s_k} e^{\left(\sum\limits_{i=i_s}^{k} a(b_{i-1})(s_i - s_{i-1})\right)} \frac{\alpha_0(b_j)}{b_j}\,\delta\left(s - s_j\right)\,\mathrm{d}s \\ &= \left(\prod_{i=2}^{k} e^{a(b_{i-1})(s_i - s_{i-1})}\right) u_0 + \left(\prod_{i=j}^{k-1} e^{a(b_{i-1})(s_{i+1} - s_i)}\right) \frac{\alpha_0(b_j)}{b_j}\,. \end{aligned} \tag{2.105}$$

In analogy to (2.83), it now makes perfect sense to define the **logarithmic propagator** as:

$$\begin{aligned} \mathrm{lnPg}(b_i) &:= e^{a(b_i)(s_{i+1} - s_i)} = e^{a(b_i)(\ln(b_{i+1}) - \ln(b_i))} = e^{a(b_i)\ln\left(\frac{b_{i+1}}{b_i}\right)} \\ &= e^{\ln\left(\left(\frac{b_{i+1}}{b_i}\right)^{a(b_i)}\right)} = \left(\frac{b_{i+1}}{b_i}\right)^{a(b_i)}\,, \end{aligned} \tag{2.106}$$

and also the respective logarithmic backward propagator as

$$\mathrm{lnPgb}(b_i) := \left(\frac{b_i}{b_{i+1}}\right)^{a(b_i)}\,, \tag{2.107}$$

for all $i = 1, ..., n$. As a side remark: we are aware that it would be more consistent to define the logarithmic layers s_i as the argument of the logarithmic propagators but due to the back substitution later, the choice of the 'original' layer b_i turns out to be more convenient.

With these definitions, all essential relations (2.92) - (2.96) simply transfer to the logarithmic version of the differential equation by using the logarithmic propagators and the radial scaling of the driving vector. Explicitly, in analogy to the non-logarithmic case, the 'j-th' fundamental solution can now be written for all $k = 1, ..., n + 1$, as:

$$u^{(j)}(b_k) = w^{(j)}(s_k) = \mathrm{lnPg}(b_1, b_k)\,u_0^{(j)} + \mathrm{lnPg}(b_j, b_k)\,\frac{\alpha_0(b_j)}{b_j}\,, \tag{2.108}$$

or

$$u^{(j)}(b_k) = w^{(j)}(s_k) = \mathrm{lnPgb}(r_1, b_k)\,u_1^{(j)} - \mathrm{lnPgb}(b_j, b_k)\,\frac{\alpha_0(b_j)}{b_j}\,(1 - \delta_{j,k})\,, \tag{2.109}$$

with the logarithmic layer propagators

$$\begin{aligned} \mathrm{lnPg}(b_i, b_j) &:= \prod_{k=i}^{j-1} \mathrm{lnPg}(b_k) = \prod_{k=i}^{j-1} \left(\frac{b_{k+1}}{b_k}\right)^{a(b_k)}\,, \\ \mathrm{lnPgb}(b_j, b_i) &:= \prod_{k=i}^{j-1} \mathrm{lnPgb}(b_k)\,, \end{aligned} \tag{2.110}$$

for all $i, j = 1, ..., n+1$. Moreover, in analogy to (2.94), the relation between both boundary values u_0 and u_1 then becomes

$$u_1^{(j)} = \mathrm{lnPg}(r_0, r_1)\, u_0^{(j)} + \mathrm{lnPg}(b_j, r_1)\, \frac{\alpha_0(b_j)}{b_j}\,, \tag{2.111}$$

and in terms of the backward propagators

$$u_0^{(j)} = \mathrm{lnPgb}(r_1, r_0)\, u_1^{(j)} - \mathrm{lnPgb}(b_j, r_0)\, \frac{\alpha_0(b_j)}{b_j}\,. \tag{2.112}$$

Now that we have determined an explicit representation of a fundamental solution, we are finally able to solve our original differential equation using (2.91):

$$F(x) = \int G(x,y)\, H(y)\, \mathrm{d}y\,, \tag{2.113}$$

where in our case - as we have seen before - the role of H is taken by the density anomaly distribution $\tilde{\rho}(r)$, or more precisely, by their harmonic coefficients $\tilde{\rho}_{l,m}(r)$. The y-dependent G reflects the (discrete) j-dependent fundamental solutions $u_l^{(j)}$, $j = 1, ..., n$, that we derived above - now also including a lower index l to emphasise again the dependence on the harmonic degree. The integration domain reflects the radial dependence of j and $\tilde{\rho}$ and is bounded by the inner and outer domain boundaries r_0 and r_1.

Summarised, we find for the solution u of (2.97):

$$u_{l,m}(r) = \int_{r_0}^{r_1} u_l^{(j(r))}(b_k)\, \tilde{\rho}_{l,m}(r)\, \mathrm{d}r\,, \tag{2.114}$$

for all harmonic degrees $l \in \mathbb{N}$ and orders $m = -l, ..., l$, and where $j(r)$ indicates the respective discrete layer at radius r. Here, we still have a mixed discrete and continuous representation but in practise, this is immediately resolved because also $\tilde{\rho}$ is only provided at the discrete layers b_i and thus, we are also only interested in the solution u at the respective layers. The previous representation then turns into

$$\begin{aligned} u_{l,m}(b_k) &= \int_{r_0}^{r_1} u_l^{(j(r))}(b_k)\, \tilde{\rho}_{l,m}(b_k)\, \mathrm{d}r \\ &= \sum_{j=1}^{n} u_l^{(j)}(b_k)\, \tilde{\rho}_{l,m}(b_j)\, (b_{j+1} - b_j) \\ &= \sum_{j=1}^{n} u_l^{(j)}(b_k)\, \tilde{\rho}_{l,m}(b_j)\, \Delta r\,. \end{aligned} \tag{2.115}$$

In literature, the fundamental solutions $u_l^{(j)}$ are regularly also called **kernels** and denoted by $K_l^{(j)}$. Note that the kernels only depend on the harmonic degree l but not on the order m. The harmonic order only enters the system by the coefficients of the density anomalies $\tilde{\rho}_{l,m}$. Especially, for both domain boundaries, the Earth's surface and the CMB, we then find

$$\begin{aligned} u_{l,m}(r_0) &= \sum_{j=1}^{n} u_{0,l}^{(j)}\, \tilde{\rho}_{l,m}(b_j)\, \Delta r\,, \\ u_{l,m}(r_1) &= \sum_{j=1}^{n} u_{1,l}^{(j)}\, \tilde{\rho}_{l,m}(b_j)\, \Delta r\,, \end{aligned} \tag{2.116}$$

also introducing the harmonic degree l as one lower index to the boundary values. These relations are important since in practise we are often interested in the solution at both boundaries, like e.g. the gravitational response or the radial stresses at the Earth's surface and the CMB. At last, also inserting the explicit representation (2.108) of the fundamental solutions into (2.115) yields

$$u_{l,m}(b_k) = \sum_{j=1}^{n} \left(\mathrm{lnPg}_l(r_0, b_k)\, u_{0,l}^{(j)} + \mathrm{lnPg}_l(b_j, b_k)\, \frac{\alpha_0(b_j)}{b_j} \right) \tilde{\rho}_{l,m}(b_j)\, \Delta r\,, \tag{2.117}$$

for all $k = 2, ..., n$. Not that this representation is only valid for the layers inside the spherical shell, for the boundary values, (2.116) needs to be considered. One could also equivalently insert the representation of the fundamental solution (2.109) that is based on the outer boundary condition u_1. In this case, we arrive at:

$$u_{l,m}(b_k) = \sum_{j=1}^{n} \left(\mathrm{lnPgb}(r_1, b_k)\, u_{1,l}^{(j)} - \mathrm{lnPgb}(b_j, b_k)\, \frac{\alpha_0(b_j)}{b_j}\, (1 - \delta_{j,k}) \right) \tilde{\rho}_{l,m}(b_j)\, \Delta r\,. \tag{2.118}$$

2.3.3 The multidimensional case

The remaining (and essential) task remains to formulate all presented theory for the multidimensional case where the multiplicative factor $a(r)$ in the differential equation is an $n \times n$ matrix $A(r)$ with $n > 1$ and the driving vector $\alpha(r)$ turns into an n-dimensional vector. Luckily, all equations can be transferred in quite a straightforward way with the help of the matrix exponential function that is defined by

$$e^{tA} := \sum_{k=0}^{\infty} \frac{t^k}{k!}\, A^k\,, \tag{2.119}$$

$A \in \mathbb{R}^{n \times n}$, $t \in \mathbb{R}$. The matrix exponential basically satisfies all known properties of the one-dimensional exponential transferred into the multidimensional case, especially the differentiation property

$$\frac{\mathrm{d}}{\mathrm{d}t}\, e^{tA} = A e^{tA}\,. \tag{2.120}$$

The application of the matrix exponential and its properties to our system of linear equations also leads to propagators (see (2.83)) that now turn into **propagator matrices**

$$\mathrm{Pg}(b_i) = e^{A(b_i)(b_{i+1} - b_i)}\,. \tag{2.121}$$

Furthermore, also the logarithmic propagators (2.106) turn into corresponding propagator matrices

$$\mathrm{lnPg}(b_i) = \left(\frac{b_{i+1}}{b_i} \right)^{A(b_i)}\,. \tag{2.122}$$

Here, we find the general matrix exponential function x^A, $x \in \mathbb{R}$, where there is no fundamental representation like the series of the matrix exponential e^A, but Gantmacher (1960) showed that in general, for any matrix function $f(A)$ it is sufficient to know the value of the function at the eigenvalues λ_i, $i = 1, ..., n$, of A to calculate the explicit value of $f(A)$. More precisely, in case of a minimal polynomial of A that has no multiple roots - which can be shown to be valid in our case - $f(A)$ is determined by the distinct eigenvalues of A, i.e. the roots of the minimal polynomial, λ_i, $i = 1, ..., m$, $m \leq n$, by

$$f(A) = \sum_{i=1}^{m} \frac{(A - \lambda_1 \mathbb{1}_n) \cdots (A - \lambda_{i-1} \mathbb{1}_n)\, (A - \lambda_{i+1} \mathbb{1}_n) \cdots (A - \lambda_m \mathbb{1}_n)}{(\lambda_i - \lambda_1) \cdots (\lambda_i - \lambda_{i-1})\, (\lambda_i - \lambda_{i+1}) \cdots (\lambda_i - \lambda_m)}\, f(\lambda_i)\,. \tag{2.123}$$

Thus, in order to explicitly calculate the propagator matrices corresponding to the linear system of differential equations that we derived in the previous section, it is essential to determine the eigenvalues of the Stokes matrices $\bar{A}$ (2.68) and $\bar{B}$ (2.71), i.e. the roots of their respective characteristic polynomials. We will perform these calculations in a detailed way in the next subsection.

In the multidimensional case, there is one essential error source that one should be well aware of. The important additivity property

$$e^{A+B} = e^A\, e^B \tag{2.124}$$

for exponential functions is only valid for the matrix exponential if A and B commute, i.e. $AB = BA$, which is in general not true. Recalling the derivation of the propagators, we see that we applied this relation in (2.82) in order to formulate transitions from one layer to another in terms of recurring (matrix) multiplications. This was basically the source of the definition of the propagators. But for non-commutative matrices, this essential step is not valid. In general, an additional correction term appears when the previous relation is applied to general matrices. Here, we find that

$$e^{A+B} = e^A\, e^B\, e^{C_1}\,, \tag{2.125}$$

where C_1 can be determined explicitly by just applying the series representation (2.119) to e^{A+B}. To first order, one finds that $C_1 \approx -[A,B]/2$, where $[A,B] := AB - BA$ is the so-called **commutator** of A and B. This can be interpreted as a measure of how far the matrices are away from being commutative. Via the **Baker-Campbell formula** (see e.g., Achilles and Bonfiglioli, 2012, for a historical overview) a complete representation of C_1 only in terms of commutators can be found. But not only the additivity property is a potential error source, also when we change the order of matrix multiplications, additional correction terms are introduced into the system. More precisely, it holds that

$$e^A\, e^B = e^B\, e^A\, e^{C_2}\,, \tag{2.126}$$

where $C_2 \approx [A,B]$ to first order. We have used such rearrangements e.g. to show the transitivity property (2.89) of the propagators.

Summarised, this means that essential steps in the previous derivation provide potential error sources if the Stokes matrices $\bar{A}(r)$ (see (2.68)) of adjacent layers are not commutative. Since most entries of the matrices are constant or dependent on the harmonic degree l that also does not change from layer to layer, the problem reduces to the behaviour of the radially dependent properties density and viscosity. In the simplest case of incompressibility and a constant viscosity, the Stokes matrices are perfectly commutative and all previous steps are exact. Furthermore, since we only observe density contrasts of approximately a factor of 2 from the surface to the CMB, where the viscosity can easily vary between 3 or 4 magnitudes, the viscosity stratification has by far the main impact on the potential error. Thus, when explicitly choosing a viscosity profile, one should keep in mind to reduce the jumps between two adjacent layers as far as possible. Obviously, also increasing the number of layers and thus, reducing the discontinuities, helps to minimise these problems. Panasyuk et al. (1996) states that dividing the Earth's mantle into ≈ 30 layers suffices to guarantee 'almost' commutative matrices but nevertheless, it mainly depends on the choice of the underlying viscosity profile.

We did some basic numerical tests to investigate this error source in a slightly more detailed way. Using an equidistant radial profile of 128 layers between the Earth's surface at a radius of 6370 km and the CMB at 3480 km we see that the radius ratios that are needed for the logarithmic propagators (and inverse ratios for the backward propagators) are very close to 1. More precisely the ratio is varying from 1.0036 (surface) to 1.0065 (CMB) and the inverse ratio from 0.9965 (surface) to 0.9935 (CMB). Thus, all logarithmic propagators are close to the unit matrix. Moreover, we found that the matrix multiplication of two propagators provides less error (compared to the exact solution) if the

propagator with the smaller exponential base is multiplied from the left instead of from the right. This is just an empirical observation but this is something one should be aware of. Using the 'wrong' multiplication direction would provide additional and non-negligible errors. In practise, this means that using the standard logarithmic propagators and the propagation direction from the CMB to the surface, $\mathrm{lnPg}(b_i, b_j)$, $i < j$ should be calculated as

$$\mathrm{lnPg}(b_i, b_j) = \prod_{k=i}^{j-1} \mathrm{lnPg}(b_k) = \mathrm{lnPg}(b_{j-1})\,\mathrm{lnPg}(b_{j-2}) \cdots \mathrm{lnPg}(b_i)\,, \tag{2.127}$$

where the multiplication of the backward propagators should be executed in the opposite direction, i.e.

$$\mathrm{lnPgb}(b_j, b_i) = \prod_{k=i}^{j-1} \mathrm{lnPgb}(b_k) = \mathrm{lnPg}(b_i)\,\mathrm{lnPg}(b_{i+1}) \cdots \mathrm{lnPg}(b_{j-1})\,. \tag{2.128}$$

As already mentioned before, in the incompressible and isoviscous case, the propagator matrices are commutative and the multiplication direction does not affect the result.

2.3.4 Eigenvalues of the Stokes matrix

As we learned before, the determination of the eigenvalues of the Stokes matrices $\bar{A}$ and $\bar{B}$ is crucial for an explicit calculation of the (logarithmic) propagators (see (2.123)). We state the two matrices here again for convenience:

$$\bar{A} = \begin{pmatrix} -(2+\chi) & l(l+1) & 0 & 0 & 0 & 0 \\ -1 & 1 & 0 & 1/\eta_0^* & 0 & 0 \\ 4(3+\chi)\eta_0^* & -6l(l+1)\eta_0^* & 1 & l(l+1) & 0 & \rho_0^* \\ -2(3+\chi)\eta_0^* & (4l(l+1)-2)\eta_0^* & -1 & -2 & \rho_0^* & 0 \\ 0 & 0 & 0 & 0 & 1 & 1 \\ 0 & 0 & 0 & 0 & l(l+1) & 0 \end{pmatrix}, \tag{2.129}$$

and

$$\bar{B} := \begin{pmatrix} 1 & 1/\eta_0^* \\ (l(l+1)-2)\eta_0^* & -2 \end{pmatrix}. \tag{2.130}$$

For the 2×2 matrix $\bar{B}$, we immediately find that

$$\begin{aligned} \left|\bar{B} - \lambda \mathbb{1}_2\right| &= (1-\lambda)(-2-\lambda) - l(l+1) + 2 = \lambda^2 + \lambda - l(l+1) \\ &= \left(\lambda + \frac{1}{2}\right)^2 - \frac{1}{4} - l(l+1) = \left(\lambda + \frac{1}{2}\right)^2 - \left(l + \frac{1}{2}\right)^2 . \end{aligned} \tag{2.131}$$

Thus, we see that $\lambda_1^{(\bar{B})} = l$ and $\lambda_2^{(\bar{B})} = -l - 1$. We continue with the matrix $\bar{A}$. Here, we can exploit its block structure with the zero block in the lower left corner and calculate the required determinants by

$$\left|\bar{A} - \lambda \mathbb{1}_6\right| = |A_1|\,|A_2|\,, \tag{2.132}$$

with

$$\begin{aligned} A_1 &:= \begin{vmatrix} 1-\lambda & 1 \\ l(l+1) & -\lambda \end{vmatrix}, \\ A_2 &:= \begin{vmatrix} -(2+\chi+\lambda) & l(l+1) & 0 & 0 \\ -1 & 1-\lambda & 0 & 1/\eta_0^* \\ 4(3+\chi)\eta_0^* & -6l(l+1)\eta_0^* & 1-\lambda & l(l+1) \\ -2(3+\chi)\eta_0^* & (4l(l+1)-2)\eta_0^* & -1 & -(2+\lambda) \end{vmatrix}. \end{aligned} \tag{2.133}$$

For the 2×2 matrix A_1 we find

$$\begin{aligned} |A_1| &= -\lambda(1-\lambda) - l(l+1) = \lambda^2 - \lambda - l(l+1) \\ &= \left(\lambda - \frac{1}{2}\right)^2 - \frac{1}{4} - l(l+1) = \left(\lambda - \frac{1}{2}\right)^2 - \left(l + \frac{1}{2}\right)^2 . \end{aligned} \tag{2.134}$$

and thus, $\lambda_1^{(\bar{A})} = -l$ and $\lambda_2^{(\bar{A})} = l+1$ for the first two eigenvalues of $\bar{A}$. Now, we use Laplace's rule and expand the 4×4 matrix A_2 along the first row to find:

$$\begin{aligned} |A_2| = &-(2+\chi+\lambda) \begin{vmatrix} 1-\lambda & 0 & 1/\eta_0^* \\ -6l(l+1)\eta_0^* & 1-\lambda & l(l+1) \\ (4l(l+1)-2)\eta_0^* & -1 & -(2+\lambda) \end{vmatrix} \\ &- l(l+1) \begin{vmatrix} -1 & 0 & 1/\eta_0^* \\ 4(3+\chi)\eta_0^* & 1-\lambda & l(l+1) \\ -2(3+\chi)\eta_0^* & -1 & -(2+\lambda) \end{vmatrix} . \end{aligned} \tag{2.135}$$

Again using Laplace's rule and expanding each of the 3×3 matrices along the first row, we find

$$\begin{aligned} |A_2| = &-(2+\chi+\lambda)\left[(1-\lambda)\left[-(1-\lambda)(2+\lambda) + l(l+1)\right]\right. \\ &\qquad \left. + 6l(l+1) - (1-\lambda)\left(4l(l+1)-2\right)\right] \\ &- l(l+1)\left[(1-\lambda)(2+\lambda) - l(l+1) - 4\left(3+\chi\right) + (1-\lambda)\left(2\left(3+\chi\right)\right)\right] \\ = &\lambda^4 + (2+\chi)\lambda^3 - (2l(l+1)+1)\lambda^2 - (2+\chi)\left(l(l+1)+1\right)\lambda \\ &+ l(l+1)\left(l(l+1) - (2+\chi)\right) . \end{aligned} \tag{2.136}$$

We try to guess one of the roots of this polynomial in λ by inserting one of the already known eigenvalues, e.g. $\lambda_1^{(\bar{A})} = -l$. This procedure is successful if $\bar{A}$ has eigenvalues with an algebraic multiplicity of more than 1. And indeed, by polynomial division we can verify that $-l$ is a root of $|A_2|$ and we find:

$$|A_2| = (\lambda + l)\left[\lambda^3 + \left((2+\chi) - l\right)\lambda^2 - \left(l^2 + (4+\chi)\,l + 1\right)\lambda + (l+1)\left(l(l+1) - (2+\chi)\right)\right] . \tag{2.137}$$

We also insert the other already known root $\lambda_2^{(\bar{A})} = l+1$ and indeed we find that:

$$|A_2| = (\lambda + l)\left(\lambda - (l+1)\right)\left[\lambda^2 + (3+\chi)\lambda - \left(l(l+1) - (2+\chi)\right)\right] . \tag{2.138}$$

Thus, the remaining two eigenvalues are determined as

$$\lambda_{5/6}^{(\bar{A})} = -\frac{3+\chi}{2} \pm \frac{1}{2}\sqrt{4\left(l + \frac{1}{2}\right)^2 + \chi\left(\chi+2\right)} . \tag{2.139}$$

In the special case of an incompressible flow ($\chi = 0$), we find that $\lambda_5^{(\bar{A})} = l-1$ and $\lambda_6^{(\bar{A})} = -l-2$.

Summarising the previous results, the eigenvalues of $\bar{A}$ and $\bar{B}$ - in a rearranged order - read as:

$$\begin{aligned} \lambda_{1/5}^{(\bar{A})} &= -l , & \lambda_1^{(\bar{B})} &= l , \\ \lambda_{2/6}^{(\bar{A})} &= l+1 , & \lambda_2^{(\bar{B})} &= -l-1 , \\ \lambda_3^{(\bar{A})} &= -\frac{3+\chi}{2} + \frac{1}{2}\sqrt{4\left(l+\frac{1}{2}\right)^2 + \chi\left(\chi+2\right)} \\ &= l-1 \text{ for } \chi = 0 , \\ \lambda_4^{(\bar{A})} &= -\frac{3+\chi}{2} - \frac{1}{2}\sqrt{4\left(l+\frac{1}{2}\right)^2 + \chi\left(\chi+2\right)} \\ &= -l-2 \text{ for } \chi = 0 . \end{aligned} \tag{2.140}$$

Note that neither the viscosity η_0^* nor the density variation factor ρ_0^* that both play a crucial role in the Stokes matrices appear in the eigenvalue but next to the harmonic degree l, also the compressibility factor χ can be found.

With the previously derived (distinct) eigenvalues we are finally able to explicitly calculate the respective logarithmic propagators for every layer boundary b_i, $i = 1, ..., n+1$, by

$$\mathrm{lnPg}(b_i) = \sum_{k=1}^{4} \frac{\left(\bar{A} - \lambda_1^{(\bar{A})}\mathbb{1}_n\right)\cdots\left(A - \lambda_{k-1}^{(\bar{A})}\mathbb{1}_n\right)\left(A - \lambda_{k+1}^{(\bar{A})}\mathbb{1}_n\right)\cdots\left(A - \lambda_4^{(\bar{A})}\mathbb{1}_n\right)}{\left(\lambda_k^{(\bar{A})} - \lambda_1^{(\bar{A})}\right)\cdots\left(\lambda_k^{(\bar{A})} - \lambda_{k-1}^{(\bar{A})}\right)\left(\lambda_k^{(\bar{A})} - \lambda_{k+1}^{(\bar{A})}\right)\cdots\left(\lambda_k^{(\bar{A})} - \lambda_4^{(\bar{A})}\right)} \left(\frac{b_{i+1}}{b_i}\right)^{\lambda_k^{(\bar{A})}} . \tag{2.141}$$

The only missing part now is how to choose valid and meaningful boundary conditions such that our derived system of equations can be solved in practice. We will discuss this topic in the following section of this chapter.

2.4 Boundary conditions

In general, for a differential equation there are two main and common types of boundary conditions. First, the **Dirichlet condition** where you set the discussed quantity to an explicit value at the boundary. Second, the **Neumann condition** where you make some assumption on the (normal) derivative of the quantity instead of the quantity itself along the boundaries.

Here, the solution vector $\bar{u}_A$ of the poloidal part of the Stokes system consists of six unknowns, the radial velocity $\bar{v}_1$, the poloidal velocity $\bar{v}_2$, the radial stress $\bar{\sigma}_1$, the poloidal stress $\bar{\sigma}_2$, the gravitational potential $\bar{U}_1$ and the radial derivative of the gravitational potential $\bar{W}_1$. Thus, in total, we need to formulate six boundary conditions in order to gain a (uniquely) solvable system of equations.

We start with the gravitational potential. There is no subjective decision on how to formulate the boundary conditions since its values at the boundaries are explicitly determined by Newton's gravitational law. By providing both values at the surface and at the CMB, we already find two of the required six conditions. To this end, we need a result from a subsequent chapter of this work where we investigate Newton's law in a more detailed way, especially in terms of a spherical harmonic representation. In the previous section, we formulated the system of the governing differential equations in terms of fundamental solutions, i.e. also for the boundary conditions we need to consider the case of a unit density anomaly - that is formally described with the help of the delta distribution - at a certain layer boundary b_j, $j \in \{1, ..., n+1\}$. In this case, for $R > b_j$ Newton's law turns into (4.28):

$$U_{l,m}(R) = -\frac{4\pi G}{2l+1}\, b_j \left(\frac{b_j}{R}\right)^{l+1} , \tag{2.142}$$

and in the case of $R < b_j$ into (4.29):

$$U_{l,m}(R) = -\frac{4\pi G}{2l+1}\, b_j \left(\frac{R}{b_j}\right)^{l} , \tag{2.143}$$

for all respective harmonic degrees l and orders m. Inserting the domain boundaries r_0 and r_1 and using again our previous notation, these results immediately lead to the conditions

$$U_1(r_0) = -\frac{4\pi G}{2l+1}\, b_j \left(\frac{r_0}{b_j}\right)^{l} , \quad U_1(r_1) = -\frac{4\pi G}{2l+1}\, b_j \left(\frac{b_j}{r_1}\right)^{l+1} , \tag{2.144}$$

and in analogy for the scaled quantity:

$$\bar{U}_1(r_0) = -\frac{4\pi G}{2l+1}\, \frac{\hat{\rho}_0}{\hat{\eta}_0}\, r_0^2 \left(\frac{r_0}{b_j}\right)^{l-1} , \quad \bar{U}_1(r_1) = -\frac{4\pi G}{2l+1}\, \frac{\hat{\rho}_0}{\hat{\eta}_0}\, b_j^2 \left(\frac{b_j}{r_1}\right)^{l} , \tag{2.145}$$

Since we are interested in flow solutions inside a closed system, for the velocity field, a natural assumption should be that we do not want the flow to exceed the boundaries of our domain. This means that we do not allow for any outflow out and inflow into the domain. This **no-outflow condition** translates into a vanishing radial velocity at both boundaries. More precisely, we require the radial velocity (and scaled quantities) to satisfy

$$v_1(r_0) = \bar{v}_1(r_0) = 0\,, \quad v_1(r_1) = \bar{v}_1(r_1) = 0\,. \tag{2.146}$$

For the tangential part of the velocity, there are mainly two possible ways - that are related to the Dirichlet and Neumann condition - to model an appropriate physical behaviour. First, we can decide to just externally prescribe the velocity field at the boundaries, this is called the **no-slip condition**. The easiest way would be the special case of zero velocity, the simulation of a fixed wall. Further, we could also think about prescribing actual data that arise from plate tectonic observations - converted into a spherical harmonic representation. Probably the main drawback of this possibility is the inconsistency between data and model. Where the observed plate velocities have a large contribution from the toroidal component (e.g., Hager and O'Connell, 1978), the presented model intrinsically is not able to generate toroidal motion, especially since no lateral viscosity variations are supported.

Second, we can also imagine not to prescribe any velocity externally but let the boundary move with the motion of the fluid. This is called the **free-slip condition**. In this case, there is no direct restriction on the tangential velocity component itself, it behaves in the way whatever the fluid dictates. Here, we only have to make sure to avoid any (frictional) force between boundary and motion and set the shear (i.e. tangential) stress to zero. Technically, due to the direct relation between velocity field and stress tensor, this translates into a (weighted) Neumann condition for the velocity field. More details on this relation and a comparison between spherical and Cartesian case can be found in the subsequent Chapter 3. Since the objectively best proxy to reality, i.e. imposing actual plate velocity data at the surface, leads to inconsistencies, in this work we will use the free-slip condition as our preferred assumption at the boundaries, both the surface and the CMB. But nevertheless, in general, one may think about four different cases that we will investigate in the following.

The no-slip/no-slip case

In this case, we prescribe the (poloidal) velocity field v_2 explicitly both at the inner and at the outer boundary of the domain. For consistency reasons, we still assume the velocity field to only possess a poloidal component and neglect a possible forced toroidal field at any boundary. For the surface, we introduce the fixed velocity v_S and for the CMB, the (fixed) velocity v_C. Both v_S and v_C implicitly are dependent on the harmonic degree. We then find that

$$v_2(r_0) = v_C\,, \quad v_2(r_1) = v_S\,, \tag{2.147}$$

and in analogy for the scaled quantity:

$$\bar{v}_2(r_0) = \frac{1}{\mu_l}\, v_C\,, \quad \bar{v}_2(r_1) = \frac{1}{\mu_l}\, v_S\,. \tag{2.148}$$

Together with the no-outflow condition (2.146) and the expressions for the gravitational potential (2.145) we are equipped with the required six boundary conditions for our system of linear differential equations. Now we explicitly make use of equation (2.111), applied to the scaled Stokes system, i.e.

$$\bar{u}_1^{(j)} = \mathrm{lnPg}(r_0, r_1)\, \bar{u}_0^{(j)} + \mathrm{lnPg}(b_j, r_1)\, \frac{\bar{\alpha}_0(b_j)}{b_j}\,, \tag{2.149}$$

to relate the conditions on both boundaries to one another. Introducing the abbreviations

$$\begin{aligned}\gamma^{(l)} &:= \frac{4\pi G}{2l+1}\, b_j^2 \left(\frac{b_j}{r_1}\right)^l ,\\ \psi^{(l-1)} &:= \frac{4\pi G}{2l+1}\, r_0^2 \left(\frac{r_0}{b_j}\right)^{l-1} ,\\ P^{(0)} &:= \mathrm{lnPg}(r_0, r_1)\,,\\ P^{(j)} &:= \mathrm{lnPg}(b_j, r_1)\,,\end{aligned} \tag{2.150}$$

we arrive at

$$\begin{pmatrix} 0 \\ -v_S/\mu_l \\ -\bar{\sigma}_1(r_1) \\ -\bar{\sigma}_2(r_1) \\ \gamma^{(l)}\hat{\rho}_0/\hat{\eta}_0 \\ -\bar{W}_1(r_1) \end{pmatrix} = P^{(0)} \begin{pmatrix} 0 \\ -v_C/\mu_l \\ -\bar{\sigma}_1(r_0) \\ -\bar{\sigma}_2(r_0) \\ \psi^{(l-1)}\hat{\rho}_0/\hat{\eta}_0 \\ -\bar{W}_1(r_0) \end{pmatrix} - P^{(j)} \begin{pmatrix} 0 \\ 0 \\ g_0 b_j/\hat{\eta}_0 \\ 0 \\ 0 \\ 4\pi G\hat{\rho}_0 b_j^2/\hat{\eta}_0 \end{pmatrix} . \tag{2.151}$$

Rearranging the previous relations in terms of the six unknown variables then yields a system of linear equations $Cx = b$ with

$$C = \begin{pmatrix} -P^{(0)}_{1,3} & -P^{(0)}_{1,4} & -P^{(0)}_{1,6} & 0 & 0 & 0 \\ -P^{(0)}_{2,3} & -P^{(0)}_{2,4} & -P^{(0)}_{2,6} & 0 & 0 & 0 \\ -P^{(0)}_{3,3} & -P^{(0)}_{3,4} & -P^{(0)}_{3,6} & 1 & 0 & 0 \\ -P^{(0)}_{4,3} & -P^{(0)}_{4,4} & -P^{(0)}_{4,6} & 0 & 1 & 0 \\ -P^{(0)}_{5,3} & -P^{(0)}_{5,4} & -P^{(0)}_{5,6} & 0 & 0 & 0 \\ -P^{(0)}_{6,3} & -P^{(0)}_{6,4} & -P^{(0)}_{6,6} & 0 & 0 & 1 \end{pmatrix}, \quad x = \begin{pmatrix} \bar{\sigma}_1(r_0) \\ \bar{\sigma}_2(r_0) \\ \bar{W}_1(r_0) \\ \bar{\sigma}_1(r_1) \\ \bar{\sigma}_2(r_1) \\ \bar{W}_1(r_1) \end{pmatrix},$$

$$\begin{aligned} b &= \begin{pmatrix} P^{(0)}_{1,2} v_C/\mu_l - P^{(0)}_{1,5}\psi^{(l-1)}\hat{\rho}_0/\hat{\eta}_0 + (P^{(j)}_{1,\cdot}\cdot\bar{\alpha}_0)/b_j & \\ P^{(0)}_{2,2} v_C/\mu_l - P^{(0)}_{2,5}\psi^{(l-1)}\hat{\rho}_0/\hat{\eta}_0 + (P^{(j)}_{2,\cdot}\cdot\bar{\alpha}_0)/b_j & -v_S/\mu_l \\ P^{(0)}_{3,2} v_C/\mu_l - P^{(0)}_{3,5}\psi^{(l-1)}\hat{\rho}_0/\hat{\eta}_0 + (P^{(j)}_{3,\cdot}\cdot\bar{\alpha}_0)/b_j & \\ P^{(0)}_{4,2} v_C/\mu_l - P^{(0)}_{4,5}\psi^{(l-1)}\hat{\rho}_0/\hat{\eta}_0 + (P^{(j)}_{4,\cdot}\cdot\bar{\alpha}_0)/b_j & \\ P^{(0)}_{5,2} v_C/\mu_l - P^{(0)}_{5,5}\psi^{(l-1)}\hat{\rho}_0/\hat{\eta}_0 + (P^{(j)}_{5,\cdot}\cdot\bar{\alpha}_0)/b_j & +\gamma^{(l)}\hat{\rho}_0/\hat{\eta}_0 \\ P^{(0)}_{6,2} v_C/\mu_l - P^{(0)}_{6,5}\psi^{(l-1)}\hat{\rho}_0/\hat{\eta}_0 + (P^{(j)}_{6,\cdot}\cdot\bar{\alpha}_0)/b_j & \end{pmatrix} \\ &= \begin{pmatrix} P^{(0)}_{1,2} v_C/\mu_l - P^{(0)}_{1,5}\psi^{(l-1)}\hat{\rho}_0/\hat{\eta}_0 + (P^{(j)}_{1,3} g_0 b_j + P^{(j)}_{1,6} 4\pi G\hat{\rho}_0 b_j^2)/\hat{\eta}_0 & \\ P^{(0)}_{2,2} v_C/\mu_l - P^{(0)}_{2,5}\psi^{(l-1)}\hat{\rho}_0/\hat{\eta}_0 + (P^{(j)}_{2,3} g_0 b_j + P^{(j)}_{2,6} 4\pi G\hat{\rho}_0 b_j^2)/\hat{\eta}_0 & -v_S/\mu_l \\ P^{(0)}_{3,2} v_C/\mu_l - P^{(0)}_{3,5}\psi^{(l-1)}\hat{\rho}_0/\hat{\eta}_0 + (P^{(j)}_{3,3} g_0 b_j + P^{(j)}_{3,6} 4\pi G\hat{\rho}_0 b_j^2)/\hat{\eta}_0 & \\ P^{(0)}_{4,2} v_C/\mu_l - P^{(0)}_{4,5}\psi^{(l-1)}\hat{\rho}_0/\hat{\eta}_0 + (P^{(j)}_{4,3} g_0 b_j + P^{(j)}_{4,6} 4\pi G\hat{\rho}_0 b_j^2)/\hat{\eta}_0 & \\ P^{(0)}_{5,2} v_C/\mu_l - P^{(0)}_{5,5}\psi^{(l-1)}\hat{\rho}_0/\hat{\eta}_0 + (P^{(j)}_{5,3} g_0 b_j + P^{(j)}_{5,6} 4\pi G\hat{\rho}_0 b_j^2)/\hat{\eta}_0 & +\gamma^{(l)}\hat{\rho}_0/\hat{\eta}_0 \\ P^{(0)}_{6,2} v_C/\mu_l - P^{(0)}_{6,5}\psi^{(l-1)}\hat{\rho}_0/\hat{\eta}_0 + (P^{(j)}_{6,3} g_0 b_j + P^{(j)}_{6,6} 4\pi G\hat{\rho}_0 b_j^2)/\hat{\eta}_0 & \end{pmatrix}, \end{aligned} \tag{2.152}$$

that can now be solved by any standard routine. In the special (and common) case of $v_C = v_S = 0$ the vector b reduces to

$$b = \begin{pmatrix} -P^{(0)}_{1,5}\psi^{(l-1)}\hat{\rho}_0/\hat{\eta}_0 + (P^{(j)}_{1,\cdot}\cdot\bar{\alpha}_0)/b_j & \\ -P^{(0)}_{2,5}\psi^{(l-1)}\hat{\rho}_0/\hat{\eta}_0 + (P^{(j)}_{2,\cdot}\cdot\bar{\alpha}_0)/b_j & \\ -P^{(0)}_{3,5}\psi^{(l-1)}\hat{\rho}_0/\hat{\eta}_0 + (P^{(j)}_{3,\cdot}\cdot\bar{\alpha}_0)/b_j & \\ -P^{(0)}_{4,5}\psi^{(l-1)}\hat{\rho}_0/\hat{\eta}_0 + (P^{(j)}_{4,\cdot}\cdot\bar{\alpha}_0)/b_j & \\ -P^{(0)}_{5,5}\psi^{(l-1)}\hat{\rho}_0/\hat{\eta}_0 + (P^{(j)}_{5,\cdot}\cdot\bar{\alpha}_0)/b_j & +\gamma^{(l)}\hat{\rho}_0/\hat{\eta}_0 \\ -P^{(0)}_{6,5}\psi^{(l-1)}\hat{\rho}_0/\hat{\eta}_0 + (P^{(j)}_{6,\cdot}\cdot\bar{\alpha}_0)/b_j & \end{pmatrix}. \tag{2.153}$$

At this point, it should also be mentioned that instead of (2.111), also the equivalent rearrangement (2.112) in terms of the backward propagators may be used. Here we found that

$$\bar{u}_0^{(j)} = \mathrm{lnPgb}(r_1, r_0)\, \bar{u}_1^{(j)} - \mathrm{lnPgb}(b_j, r_0)\, \frac{\bar{\alpha}_0(b_j)}{b_j}\,. \tag{2.154}$$

Using this representation and keeping the vector x of the unknown quantities the same as above, furthermore introducing the abbreviations $B^{(0)} := \mathrm{lnPgb}(r_1, r_0)$ and $B^{(j)} := \mathrm{lnPgb}(b_j, r_0)$, we arrive at the system of linear equations $C^{(B)}x = b^{(B)}$ with

$$C^{(B)} = \begin{pmatrix} 0 & 0 & 0 & -B_{1,3}^{(0)} & -B_{1,4}^{(0)} & -B_{1,6}^{(0)} \\ 0 & 0 & 0 & -B_{2,3}^{(0)} & -B_{2,4}^{(0)} & -B_{2,6}^{(0)} \\ 1 & 0 & 0 & -B_{3,3}^{(0)} & -B_{3,4}^{(0)} & -B_{3,6}^{(0)} \\ 0 & 1 & 0 & -B_{4,3}^{(0)} & -B_{4,4}^{(0)} & -B_{4,6}^{(0)} \\ 0 & 0 & 0 & -B_{5,3}^{(0)} & -B_{5,4}^{(0)} & -B_{5,6}^{(0)} \\ 0 & 0 & 1 & -B_{6,3}^{(0)} & -B_{6,4}^{(0)} & -B_{6,6}^{(0)} \end{pmatrix},$$

$$b^{(B)} = \begin{pmatrix} B_{1,2}^{(0)} v_S/\mu_l - B_{1,5}^{(0)} \gamma^{(l)} \hat{\rho}_0/\hat{\eta}_0 - (B_{1,\cdot}^{(j)} \cdot \bar{\alpha}_0)/b_j & \\ B_{2,2}^{(0)} v_S/\mu_l - B_{2,5}^{(0)} \gamma^{(l)} \hat{\rho}_0/\hat{\eta}_0 - (B_{2,\cdot}^{(j)} \cdot \bar{\alpha}_0)/b_j & -v_C/\mu_l \\ B_{3,2}^{(0)} v_S/\mu_l - B_{3,5}^{(0)} \gamma^{(l)} \hat{\rho}_0/\hat{\eta}_0 - (B_{3,\cdot}^{(j)} \cdot \bar{\alpha}_0)/b_j & \\ B_{4,2}^{(0)} v_S/\mu_l - B_{4,5}^{(0)} \gamma^{(l)} \hat{\rho}_0/\hat{\eta}_0 - (B_{4,\cdot}^{(j)} \cdot \bar{\alpha}_0)/b_j & \\ B_{5,2}^{(0)} v_S/\mu_l - B_{5,5}^{(0)} \gamma^{(l)} \hat{\rho}_0/\hat{\eta}_0 - (B_{5,\cdot}^{(j)} \cdot \bar{\alpha}_0)/b_j & +\psi^{(l-1)} \hat{\rho}_0/\hat{\eta}_0 \\ B_{6,2}^{(0)} v_S/\mu_l - B_{6,5}^{(0)} \gamma^{(l)} \hat{\rho}_0/\hat{\eta}_0 - (B_{6,\cdot}^{(j)} \cdot \bar{\alpha}_0)/b_j & \end{pmatrix}, \tag{2.155}$$

which is equivalent to the forward propagator system $Cx = b$. Not only do we state this result for the sake of completeness, the presence of two equivalent equation systems also is of immediate practical use. Solving both systems simultaneously and comparing the results provides a first, simple indicator of the integrity of the solution. Possible differences can give an insight into numerical / scaling problems first, in the formulation of the system of equations and second, in the numerical solver itself. And indeed, it turns out that with increasing harmonic degree l, it becomes more and more likely that the difference between both solutions exceeds negligible ranges. This is due to the increasing condition number of the Stokes matrix with larger harmonic degrees.

The free-slip/free-slip case

As we have discussed before, in the free-slip case, we impose the condition that the tangential (poloidal) part of the stress vanishes, where on the other side, there are no restrictions on the poloidal velocity field as in the no-slip case. More precisely, now we have

$$\sigma_2(r_0) = \bar{\sigma}_2(r_0) = 0\,, \quad \sigma_2(r_1) = \bar{\sigma}_2(r_1) = 0\,, \tag{2.156}$$

and $\bar{v}_2(r_0)$ and $\bar{v}_2(r_1)$ become unknown quantities again. Under these considerations, our basis equation becomes

$$\begin{pmatrix} 0 \\ -\bar{v}_2(r_1) \\ -\bar{\sigma}_1(r_1) \\ 0 \\ \gamma^{(l)}\hat{\rho}_0/\hat{\eta}_0 \\ -\bar{W}_1(r_1) \end{pmatrix} = P^{(0)} \begin{pmatrix} 0 \\ -\bar{v}_2(r_0) \\ -\bar{\sigma}_1(r_0) \\ 0 \\ \psi^{(l-1)}\hat{\rho}_0/\hat{\eta}_0 \\ -\bar{W}_1(r_0) \end{pmatrix} - P^{(j)} \begin{pmatrix} 0 \\ 0 \\ g_0 b_j/\hat{\eta}_0 \\ 0 \\ 4\pi G\hat{\rho}_0 b_j^2/\hat{\eta}_0 \\ 0 \end{pmatrix}. \tag{2.157}$$

The resulting (forward propagator) system of linear equations then turns into $Cx = b$ with

$$C = \begin{pmatrix} -P^{(0)}_{1,3} & -P^{(0)}_{1,2} & -P^{(0)}_{1,6} & 0 & 0 & 0 \\ -P^{(0)}_{2,3} & -P^{(0)}_{2,2} & -P^{(0)}_{2,6} & 0 & 1 & 0 \\ -P^{(0)}_{3,3} & -P^{(0)}_{3,2} & -P^{(0)}_{3,6} & 1 & 0 & 0 \\ -P^{(0)}_{4,3} & -P^{(0)}_{4,2} & -P^{(0)}_{4,6} & 0 & 0 & 0 \\ -P^{(0)}_{5,3} & -P^{(0)}_{5,2} & -P^{(0)}_{5,6} & 0 & 0 & 0 \\ -P^{(0)}_{6,3} & -P^{(0)}_{6,2} & -P^{(0)}_{6,6} & 0 & 0 & 1 \end{pmatrix}, \quad x = \begin{pmatrix} \bar{\sigma}_1(r_0) \\ \bar{v}_2(r_0) \\ \bar{W}_1(r_0) \\ \bar{\sigma}_1(r_1) \\ \bar{v}_2(r_1) \\ \bar{W}_1(r_1) \end{pmatrix},$$

$$b = \begin{pmatrix} -P^{(0)}_{1,5}\psi^{(l-1)}\hat{\rho}_0/\hat{\eta}_0 + (P^{(j)}_{1,\cdot} \cdot \bar{\alpha}_0)/b_j & \\ -P^{(0)}_{2,5}\psi^{(l-1)}\hat{\rho}_0/\hat{\eta}_0 + (P^{(j)}_{2,\cdot} \cdot \bar{\alpha}_0)/b_j & \\ -P^{(0)}_{3,5}\psi^{(l-1)}\hat{\rho}_0/\hat{\eta}_0 + (P^{(j)}_{3,\cdot} \cdot \bar{\alpha}_0)/b_j & \\ -P^{(0)}_{4,5}\psi^{(l-1)}\hat{\rho}_0/\hat{\eta}_0 + (P^{(j)}_{4,\cdot} \cdot \bar{\alpha}_0)/b_j & \\ -P^{(0)}_{5,5}\psi^{(l-1)}\hat{\rho}_0/\hat{\eta}_0 + (P^{(j)}_{5,\cdot} \cdot \bar{\alpha}_0)/b_j & +\gamma^{(l)}\hat{\rho}_0/\hat{\eta}_0 \\ -P^{(0)}_{6,5}\psi^{(l-1)}\hat{\rho}_0/\hat{\eta}_0 + (P^{(j)}_{6,\cdot} \cdot \bar{\alpha}_0)/b_j & \end{pmatrix}. \tag{2.158}$$

where now, in comparison to the no-slip/no-slip case, $\bar{v}_2$ takes the place of $\bar{\sigma}_2$ in the vector of unknown quantities x. Here, we only state the system of equations for the forward propagators. The equivalent system for the backward propagators can be derived in analogy to the no-slip/no-slip case.

The no-slip/free-slip case

In theory, there are also two possible mixed cases, no-slip at the surface/CMB and free-slip at the CMB/surface. Here, we find a combination of the two already considered cases before. First, when we force a no-slip condition at the surface and a free-slip condition at the inner domain boundary, the CMB, the propagator equation turns into

$$\begin{pmatrix} 0 \\ -v_S/\mu_l \\ -\bar{\sigma}_1(r_1) \\ -\bar{\sigma}_2(r_1) \\ \gamma^{(l)}\hat{\rho}_0/\hat{\eta}_0 \\ -\bar{W}_1(r_1) \end{pmatrix} = P^{(0)} \begin{pmatrix} 0 \\ -\bar{v}_2(r_0) \\ -\bar{\sigma}_1(r_0) \\ 0 \\ \psi^{(l-1)}\hat{\rho}_0/\hat{\eta}_0 \\ -\bar{W}_1(r_0) \end{pmatrix} - P^{(j)} \begin{pmatrix} 0 \\ 0 \\ g_0 b_j/\hat{\eta}_0 \\ 0 \\ 4\pi G\hat{\rho}_0 b_j^2/\hat{\eta}_0 \\ 0 \end{pmatrix}. \tag{2.159}$$

and the system of linear equations to solve states as $Cx = b$ with

$$C = \begin{pmatrix} -P^{(0)}_{1,3} & -P^{(0)}_{1,2} & -P^{(0)}_{1,6} & 0 & 0 & 0 \\ -P^{(0)}_{2,3} & -P^{(0)}_{2,2} & -P^{(0)}_{2,6} & 0 & 0 & 0 \\ -P^{(0)}_{3,3} & -P^{(0)}_{3,2} & -P^{(0)}_{3,6} & 1 & 0 & 0 \\ -P^{(0)}_{4,3} & -P^{(0)}_{4,2} & -P^{(0)}_{4,6} & 0 & 1 & 0 \\ -P^{(0)}_{5,3} & -P^{(0)}_{5,2} & -P^{(0)}_{5,6} & 0 & 0 & 0 \\ -P^{(0)}_{6,3} & -P^{(0)}_{6,2} & -P^{(0)}_{6,6} & 0 & 0 & 1 \end{pmatrix}, \quad x = \begin{pmatrix} \bar{\sigma}_1(r_0) \\ \bar{v}_2(r_0) \\ \bar{W}_1(r_0) \\ \bar{\sigma}_1(r_1) \\ \bar{\sigma}_2(r_1) \\ \bar{W}_1(r_1) \end{pmatrix},$$

$$b = \begin{pmatrix} -P^{(0)}_{1,5}\psi^{(l-1)}\hat{\rho}_0/\hat{\eta}_0 + (P^{(j)}_{1,\cdot} \cdot \bar{\alpha}_0)/b_j & \\ -P^{(0)}_{2,5}\psi^{(l-1)}\hat{\rho}_0/\hat{\eta}_0 + (P^{(j)}_{2,\cdot} \cdot \bar{\alpha}_0)/b_j & -v_S/\mu_l \\ -P^{(0)}_{3,5}\psi^{(l-1)}\hat{\rho}_0/\hat{\eta}_0 + (P^{(j)}_{3,\cdot} \cdot \bar{\alpha}_0)/b_j & \\ -P^{(0)}_{4,5}\psi^{(l-1)}\hat{\rho}_0/\hat{\eta}_0 + (P^{(j)}_{4,\cdot} \cdot \bar{\alpha}_0)/b_j & \\ -P^{(0)}_{5,5}\psi^{(l-1)}\hat{\rho}_0/\hat{\eta}_0 + (P^{(j)}_{5,\cdot} \cdot \bar{\alpha}_0)/b_j & +\gamma^{(l)}\hat{\rho}_0/\hat{\eta}_0 \\ -P^{(0)}_{6,5}\psi^{(l-1)}\hat{\rho}_0/\hat{\eta}_0 + (P^{(j)}_{6,\cdot} \cdot \bar{\alpha}_0)/b_j & \end{pmatrix}. \tag{2.160}$$

The free-slip/no-slip case

Now, as the last case, forcing a free-slip condition at the surface and a no-slip condition at the CMB, we gain the following propagator equation:

$$\begin{pmatrix} 0 \\ -\bar{v}_2(r_1) \\ -\bar{\sigma}_1(r_1) \\ 0 \\ \gamma^{(l)}\hat{\rho}_0/\hat{\eta}_0 \\ -\bar{W}_1(r_1) \end{pmatrix} = P^{(0)} \begin{pmatrix} 0 \\ -v_C/\mu_l \\ -\bar{\sigma}_1(r_0) \\ -\bar{\sigma}_2(r_0) \\ \psi^{(l-1)}\hat{\rho}_0/\hat{\eta}_0 \\ -\bar{W}_1(r_0) \end{pmatrix} - P^{(j)} \begin{pmatrix} 0 \\ 0 \\ g_0 b_j/\hat{\eta}_0 \\ 0 \\ 4\pi G\hat{\rho}_0 b_j^2/\hat{\eta}_0 \\ 0 \end{pmatrix}. \tag{2.161}$$

Then, the system of linear equations turns into $Cx = b$ with

$$C = \begin{pmatrix} -P^{(0)}_{1,3} & -P^{(0)}_{1,4} & -P^{(0)}_{1,6} & 0 & 0 & 0 \\ -P^{(0)}_{2,3} & -P^{(0)}_{2,4} & -P^{(0)}_{2,6} & 0 & 1 & 0 \\ -P^{(0)}_{3,3} & -P^{(0)}_{3,4} & -P^{(0)}_{3,6} & 1 & 0 & 0 \\ -P^{(0)}_{4,3} & -P^{(0)}_{4,4} & -P^{(0)}_{4,6} & 0 & 0 & 0 \\ -P^{(0)}_{5,3} & -P^{(0)}_{5,4} & -P^{(0)}_{5,6} & 0 & 0 & 0 \\ -P^{(0)}_{6,3} & -P^{(0)}_{6,4} & -P^{(0)}_{6,6} & 0 & 0 & 1 \end{pmatrix}, \quad x = \begin{pmatrix} \bar{\sigma}_1(r_0) \\ \bar{\sigma}_2(r_0) \\ \bar{W}_1(r_0) \\ \bar{\sigma}_1(r_1) \\ \bar{v}_2(r_1) \\ \bar{W}_1(r_1) \end{pmatrix},$$

$$b = \begin{pmatrix} P^{(0)}_{1,2} v_C/\mu_l - P^{(0)}_{1,5}\psi^{(l-1)}\hat{\rho}_0/\hat{\eta}_0 + (P^{(j)}_{1,\cdot}\cdot\bar{\alpha}_0)/b_j \\ P^{(0)}_{2,2} v_C/\mu_l - P^{(0)}_{2,5}\psi^{(l-1)}\hat{\rho}_0/\hat{\eta}_0 + (P^{(j)}_{2,\cdot}\cdot\bar{\alpha}_0)/b_j \\ P^{(0)}_{3,2} v_C/\mu_l - P^{(0)}_{3,5}\psi^{(l-1)}\hat{\rho}_0/\hat{\eta}_0 + (P^{(j)}_{3,\cdot}\cdot\bar{\alpha}_0)/b_j \\ P^{(0)}_{4,2} v_C/\mu_l - P^{(0)}_{4,5}\psi^{(l-1)}\hat{\rho}_0/\hat{\eta}_0 + (P^{(j)}_{4,\cdot}\cdot\bar{\alpha}_0)/b_j \\ P^{(0)}_{5,2} v_C/\mu_l - P^{(0)}_{5,5}\psi^{(l-1)}\hat{\rho}_0/\hat{\eta}_0 + (P^{(j)}_{5,\cdot}\cdot\bar{\alpha}_0)/b_j + \gamma^{(l)}\hat{\rho}_0/\hat{\eta}_0 \\ P^{(0)}_{6,2} v_C/\mu_l - P^{(0)}_{6,5}\psi^{(l-1)}\hat{\rho}_0/\hat{\eta}_0 + (P^{(j)}_{6,\cdot}\cdot\bar{\alpha}_0)/b_j \end{pmatrix}. \tag{2.162}$$

Summary

We notice that the final system of linear equations is similar throughout all combinations of assumed boundary conditions. Thus, introducing some auxiliary variables, we can merge all these systems into one. This description is especially useful for implementing the equations on a computer. Defining

$$f_C := \begin{cases} 1\,, & \text{free-slip at the CMB} \\ 0\,, & \text{no-slip at the CMB} \end{cases}, \quad f_S := \begin{cases} 1\,, & \text{free-slip at the surface} \\ 0\,, & \text{no-slip at the surface} \end{cases}, \tag{2.163}$$

all four versions of the propagator equation fall into:

$$\begin{pmatrix} 0 \\ -\bar{v}_2(r_1)f_S - v_S/\mu_l(1-f_S) \\ -\bar{\sigma}_1(r_1) \\ -\bar{\sigma}_2(r_1)(1-f_S) \\ \gamma^{(l)}\hat{\rho}_0/\hat{\eta}_0 \\ -\bar{W}_1(r_1) \end{pmatrix} = P^{(0)} \begin{pmatrix} 0 \\ -\bar{v}_2(r_0)f_C - v_C\mu_l(1-f_C) \\ -\bar{\sigma}_1(r_0) \\ -\bar{\sigma}_2(r_0)(1-f_C) \\ \psi^{(l-1)}\hat{\rho}_0/\hat{\eta}_0 \\ -\bar{W}_1(r_0) \end{pmatrix} - P^{(j)} \begin{pmatrix} 0 \\ 0 \\ g_0 b_j/\hat{\eta}_0 \\ 0 \\ 4\pi G\hat{\rho}_0 b_j^2/\hat{\eta}_0 \\ 0 \end{pmatrix}. \tag{2.164}$$

For the resulting system of linear equations, we gain $Cx = b$ with

$$C = \begin{pmatrix} -P^{(0)}_{1,3} & -P^{(0)}_{1,2(2-f_C)} & -P^{(0)}_{1,6} & 0 & 0 & 0 \\ -P^{(0)}_{2,3} & -P^{(0)}_{2,2(2-f_C)} & -P^{(0)}_{2,6} & 0 & f_S & 0 \\ -P^{(0)}_{3,3} & -P^{(0)}_{3,2(2-f_C)} & -P^{(0)}_{3,6} & 1 & 0 & 0 \\ -P^{(0)}_{4,3} & -P^{(0)}_{4,2(2-f_C)} & -P^{(0)}_{4,6} & 0 & 1-f_S & 0 \\ -P^{(0)}_{5,3} & -P^{(0)}_{5,2(2-f_C)} & -P^{(0)}_{5,6} & 0 & 0 & 0 \\ -P^{(0)}_{6,3} & -P^{(0)}_{6,2(2-f_C)} & -P^{(0)}_{6,6} & 0 & 0 & 1 \end{pmatrix}, \quad x = \begin{pmatrix} \bar{\sigma}_1(r_0) \\ \bar{v}_2(r_0) f_C + \bar{\sigma}_2(r_0)(1-f_C) \\ \bar{W}_1(r_0) \\ \bar{\sigma}_1(r_1) \\ \bar{v}_2(r_1) f_S + \bar{\sigma}_2(r_1)(1-f_S) \\ \bar{W}_1(r_1) \end{pmatrix},$$

$$b = \begin{pmatrix} P^{(0)}_{1,2} v_C/\mu_l(1-f_C) - P^{(0)}_{1,5}\psi^{(l-1)}\hat{\rho}_0/\hat{\eta}_0 + (P^{(j)}_{1,\cdot}\cdot\bar{\alpha}_0)/b_j & \\ P^{(0)}_{2,2} v_C/\mu_l(1-f_C) - P^{(0)}_{2,5}\psi^{(l-1)}\hat{\rho}_0/\hat{\eta}_0 + (P^{(j)}_{2,\cdot}\cdot\bar{\alpha}_0)/b_j & -v_S/\mu_l(1-f_S) \\ P^{(0)}_{3,2} v_C/\mu_l(1-f_C) - P^{(0)}_{3,5}\psi^{(l-1)}\hat{\rho}_0/\hat{\eta}_0 + (P^{(j)}_{3,\cdot}\cdot\bar{\alpha}_0)/b_j & \\ P^{(0)}_{4,2} v_C/\mu_l(1-f_C) - P^{(0)}_{4,5}\psi^{(l-1)}\hat{\rho}_0/\hat{\eta}_0 + (P^{(j)}_{4,\cdot}\cdot\bar{\alpha}_0)/b_j & \\ P^{(0)}_{5,2} v_C/\mu_l(1-f_C) - P^{(0)}_{5,5}\psi^{(l-1)}\hat{\rho}_0/\hat{\eta}_0 + (P^{(j)}_{5,\cdot}\cdot\bar{\alpha}_0)/b_j & +\gamma^{(l)}\hat{\rho}_0/\hat{\eta}_0 \\ P^{(0)}_{6,2} v_C/\mu_l(1-f_C) - P^{(0)}_{6,5}\psi^{(l-1)}\hat{\rho}_0/\hat{\eta}_0 + (P^{(j)}_{6,\cdot}\cdot\bar{\alpha}_0)/b_j & \end{pmatrix}. \tag{2.165}$$

For the sake of completeness, here we also state the merged system using the backward propagators. For the same vector of unknowns x as above we find the system $C^{(B)}x = b^{(B)}$ with

$$C^{(B)} = \begin{pmatrix} 0 & 0 & 0 & -B^{(0)}_{1,3} & -B^{(0)}_{1,2(2-f_S)} & -B^{(0)}_{1,6} \\ 0 & f_C & 0 & -B^{(0)}_{2,3} & -B^{(0)}_{2,2(2-f_S)} & -B^{(0)}_{2,6} \\ 1 & 0 & 0 & -B^{(0)}_{3,3} & -B^{(0)}_{3,2(2-f_S)} & -B^{(0)}_{3,6} \\ 0 & 1-f_C & 0 & -B^{(0)}_{4,3} & -B^{(0)}_{4,2(2-f_S)} & -B^{(0)}_{4,6} \\ 0 & 0 & 0 & -B^{(0)}_{5,3} & -B^{(0)}_{5,2(2-f_S)} & -B^{(0)}_{5,6} \\ 0 & 0 & 1 & -B^{(0)}_{6,3} & -B^{(0)}_{6,2(2-f_S)} & -B^{(0)}_{6,6} \end{pmatrix},$$

$$b^{(B)} = \begin{pmatrix} B^{(0)}_{1,2} v_S/\mu_l(1-f_S) - B^{(0)}_{1,5}\gamma^{(l)}\hat{\rho}_0/\hat{\eta}_0 - (B^{(j)}_{1,\cdot}\cdot\bar{\alpha}_0)/b_j & \\ B^{(0)}_{2,2} v_S/\mu_l(1-f_S) - B^{(0)}_{2,5}\gamma^{(l)}\hat{\rho}_0/\hat{\eta}_0 - (B^{(j)}_{2,\cdot}\cdot\bar{\alpha}_0)/b_j & -v_C/\mu_l(1-f_C) \\ B^{(0)}_{3,2} v_S/\mu_l(1-f_S) - B^{(0)}_{3,5}\gamma^{(l)}\hat{\rho}_0/\hat{\eta}_0 - (B^{(j)}_{3,\cdot}\cdot\bar{\alpha}_0)/b_j & \\ B^{(0)}_{4,2} v_S/\mu_l(1-f_S) - B^{(0)}_{4,5}\gamma^{(l)}\hat{\rho}_0/\hat{\eta}_0 - (B^{(j)}_{4,\cdot}\cdot\bar{\alpha}_0)/b_j & \\ B^{(0)}_{5,2} v_S/\mu_l(1-f_S) - B^{(0)}_{5,5}\gamma^{(l)}\hat{\rho}_0/\hat{\eta}_0 - (B^{(j)}_{5,\cdot}\cdot\bar{\alpha}_0)/b_j & +\psi^{(l-1)}\hat{\rho}_0/\hat{\eta}_0 \\ B^{(0)}_{6,2} v_S/\mu_l(1-f_S) - B^{(0)}_{6,5}\gamma^{(l)}\hat{\rho}_0/\hat{\eta}_0 - (B^{(j)}_{6,\cdot}\cdot\bar{\alpha}_0)/b_j & \end{pmatrix}. \tag{2.166}$$

Numerical calculations show that the condition number of the matrix C attains only half the value of the condition number of the matrix $C^{(B)}$ for any harmonic degree l. This is probably one of the reasons why in practice, it turns out that solving the forward propagator equation $Cx = b$ is much more stable than solving the backward propagator equation $C^{(B)}x = b^{(B)}$. But in theory, both systems of equations are mathematically equivalent.

2.5 Kernel gallery I

In the final section of this chapter, we present some graphical illustrations of solutions of the Stokes system in terms of fundamental solutions for different harmonic degrees. Defining a radial viscosity and density stratification, we are now able to solve the governing flow equations in an explicit manner. Solving the system of linear equations that we introduced above provides us with fundamental solutions for the velocity field, stress field and gravitational potential (and radial derivative of the latter)

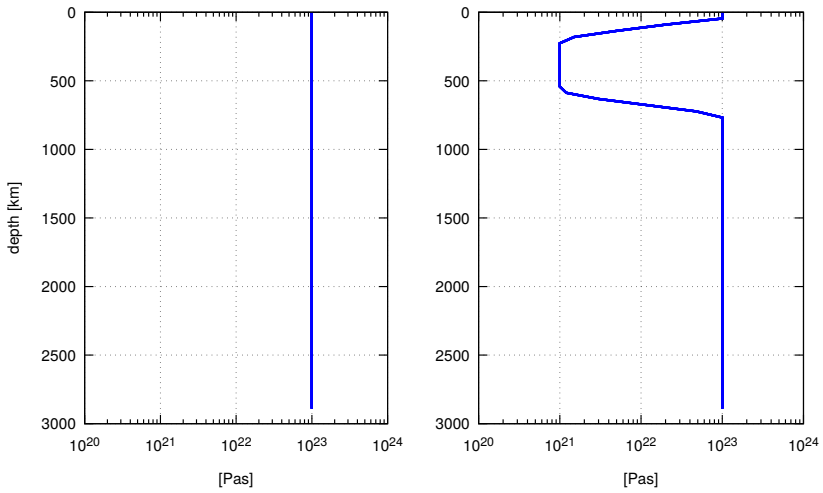

Figure 2.1: The two different radial viscosity profiles that were chosen for the examples in this section. First, a uniform viscosity of 10^{23} Pas and second, a profile that contains a viscosity reduction of a factor 100 in the upper mantle.

at each respective radial layer, assuming a density anomaly at an a-priori defined location inside the domain.

Here we follow two main ways of setting up an example. First, we keep the radial layer fixed where we want to observe the respective quantity and vary the location of the density anomaly. These are classic plots of the fundamental solutions, i.e. kernels, that illustrate which influence a density anomaly at a certain depth has on the total signal. Here, we choose the location of observation to be the Earth's surface. Furthermore, we calculate the solutions for two choices of boundary conditions, i.e. first, no-slip at both boundaries and second, free-slip at both boundaries. In addition, we perform all calculations for the two different viscosity profiles that are shown in Figure 2.1. First, we assume the simplest case of a uniform viscosity (of 10^{23} Pas), second, we choose a profile with a low viscosity zone in the upper mantle. The reason why we choose explicitly this profile will be explained in further detail in Chapter 4.

The solutions for all six quantities under consideration are shown in Figure 2.2, 2.3, 2.4 and 2.5. In particular, we see that the radial velocity is zero in all four examples, which is due to the no-outflow condition. In the no-slip cases, also the tangential velocity vanishes, where in the free-slip cases, the tangential stresses are zero. In the models with the low-viscosity zone, we see that the radial and tangential stresses induced by density anomalies below this zone are nearly cancelled out or in other words, blocked by the low viscosity channel. In the gravitational potential, we basically see the expected result that masses near the surface have a larger impact on the gravity field than masses that are located deeper in the mantle. In addition, we see that the gravitational potential does not vary with the changing flow properties.

In the second set of our examples, we fix the location of the density anomaly at 1600 km depth and vary the layer where we observe the quantity of interest, i.e. the velocity field, the stress field and the gravitational potential. In these plots we see how the values of the respective quantities explicitly change inside the mantle. Basically, this is a 1-D spherical harmonic illustration of the 3-D mantle structure. The flow properties are varied in the same way as in the first set of our examples. The results are presented in Figure 2.6, 2.7, 2.8 and 2.9. Again, we nicely see the effect of the different boundary conditions. The radial velocity always vanishes at both boundaries, where in the no-slip case, also the tangential velocities vanish. In the free-slip case, we notice a zero tangential stress at

both boundaries. In general, we see a jump in radial stress and a jump in the radial gravitational acceleration at the location of the mass. In the equations, the origin of this jump can be found in the non-vanishing components 3 and 6 of the driving vector. In the plots, the jump in the gravitational acceleration can immediately be explained by looking at the gravitational potential which takes its maximal absolute value at the mass itself.

Before applying the mathematical foundation to real data, in the next chapter, we first investigate a special case of the governing equations, which is the scenario of an incompressible flow. In that case, we are able to apply the Mie representation (1.328) for the velocity field which will lead to further simplifications of the spectral representation of the governing equations. In case of a uniform viscosity, a direct analytic relation between velocity field and driving forces can be found. Here, the propagator approach is no longer necessary and the remaining system of equations becomes very simple. This will allow us to construct a 'first level' benchmark for mantle circulation solvers, a benchmark that can be implemented straightforwardly in order to check the integrity of an underlying numerical code.

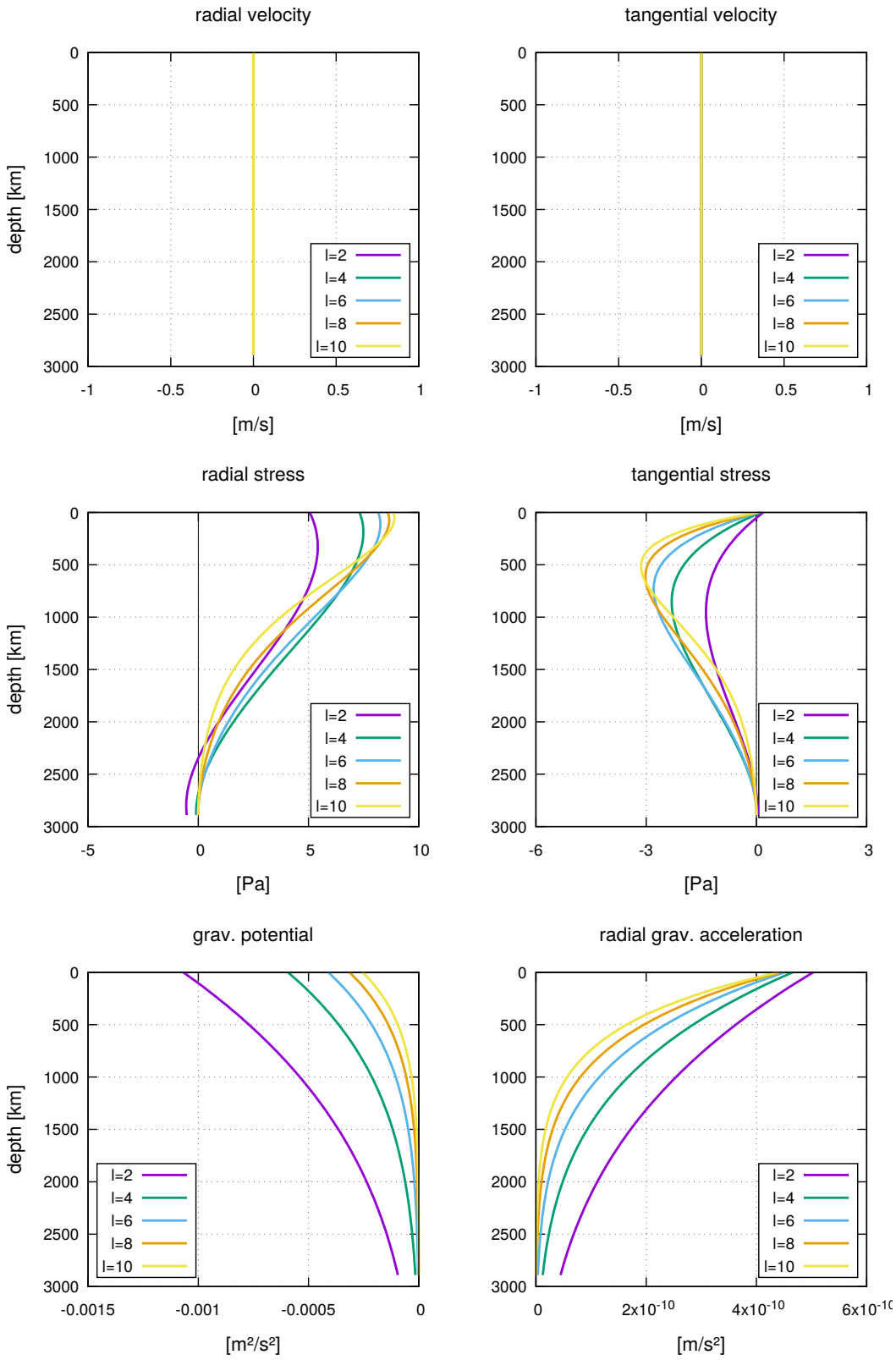

Figure 2.2: Solution of the Stokes equation system at the surface for a unit density anomaly of unit radial extension, placed at various depth levels. The flow parameters are no-slip at both boundaries and a uniform viscosity profile.

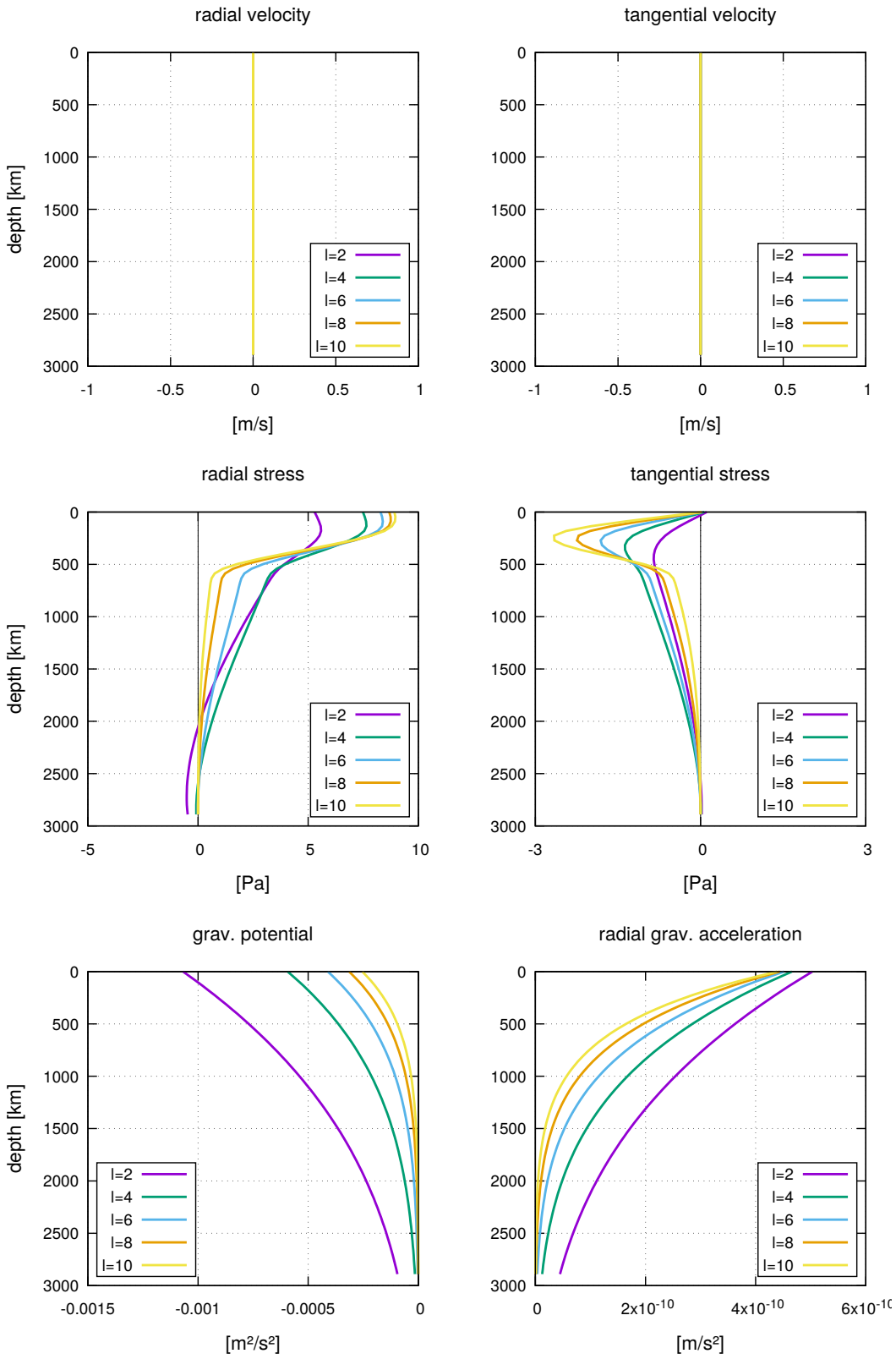

Figure 2.3: Solution of the Stokes equation system at the surface for a unit density anomaly of unit radial extension, placed at various depth levels. The flow parameters are no-slip at both boundaries and a viscosity profile with a low viscosity zone in the upper mantle.

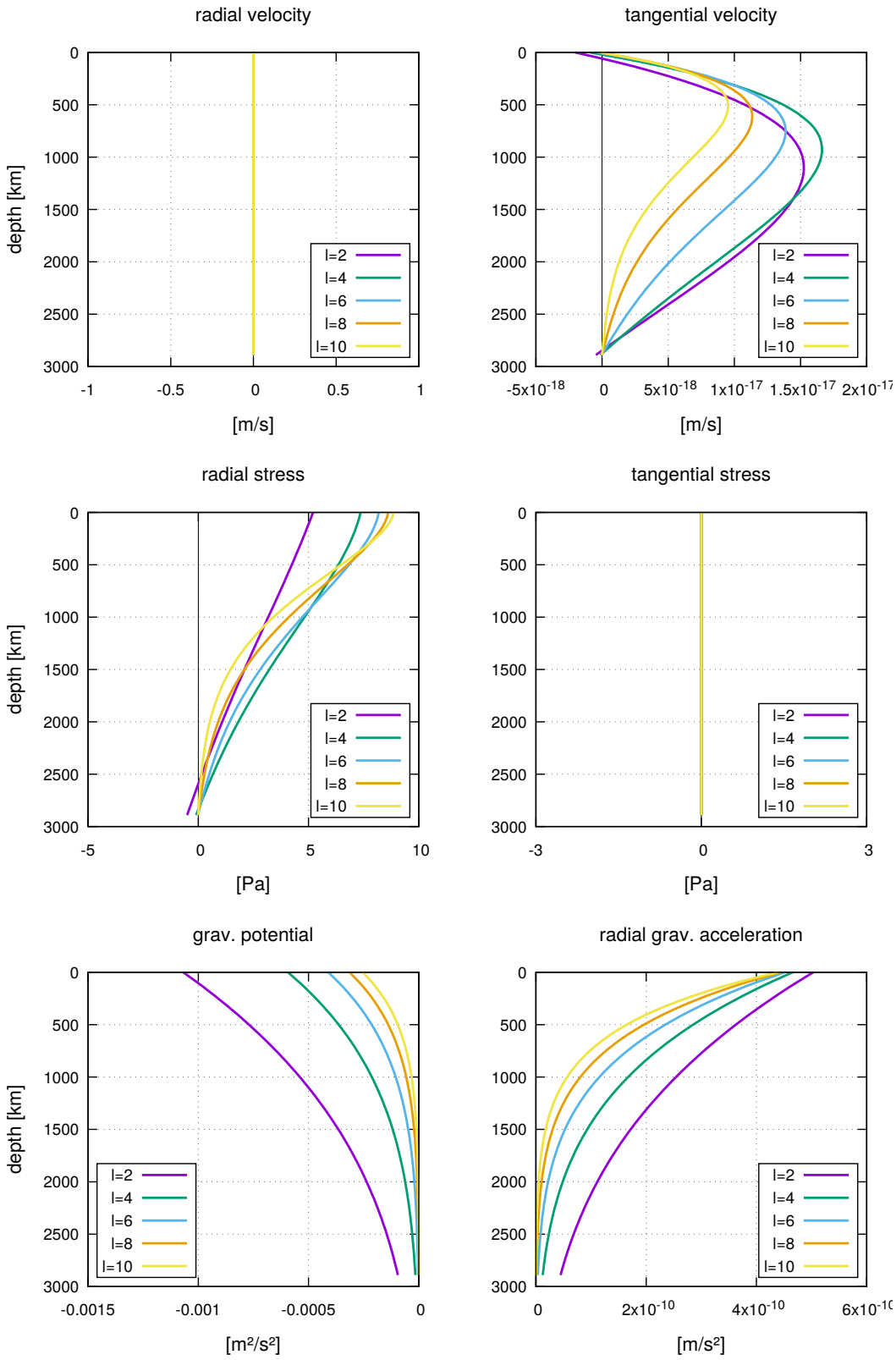

Figure 2.4: Solution of the Stokes equation system at the surface for a unit density anomaly of unit radial extension, placed at various depth levels. The flow parameters are free-slip at both boundaries and a uniform viscosity profile.

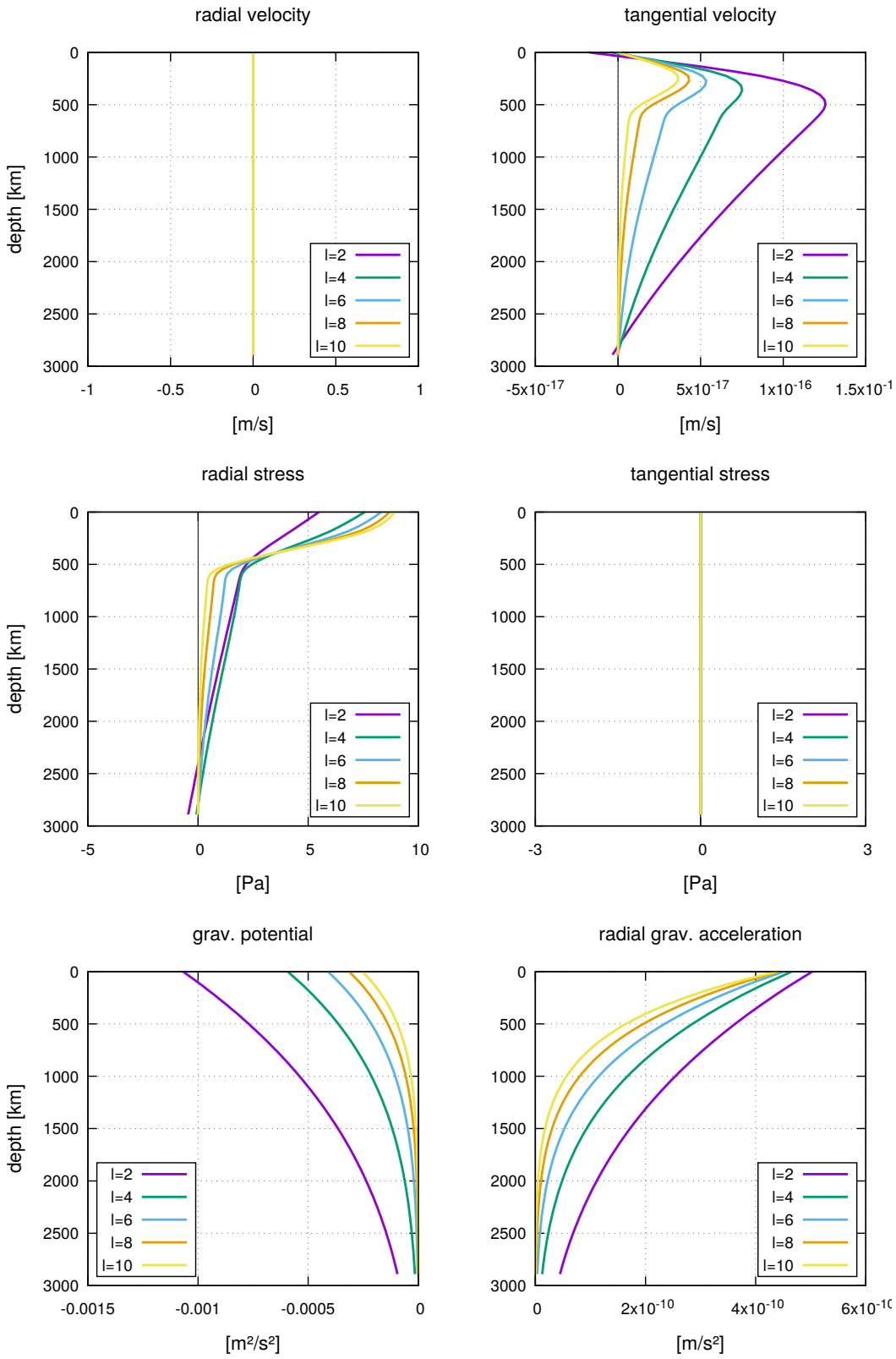

Figure 2.5: Solution of the Stokes equation system at the surface for a unit density anomaly of unit radial extension, placed at various depth levels. The flow parameters are free-slip at both boundaries and a viscosity profile with a low viscosity zone in the upper mantle.

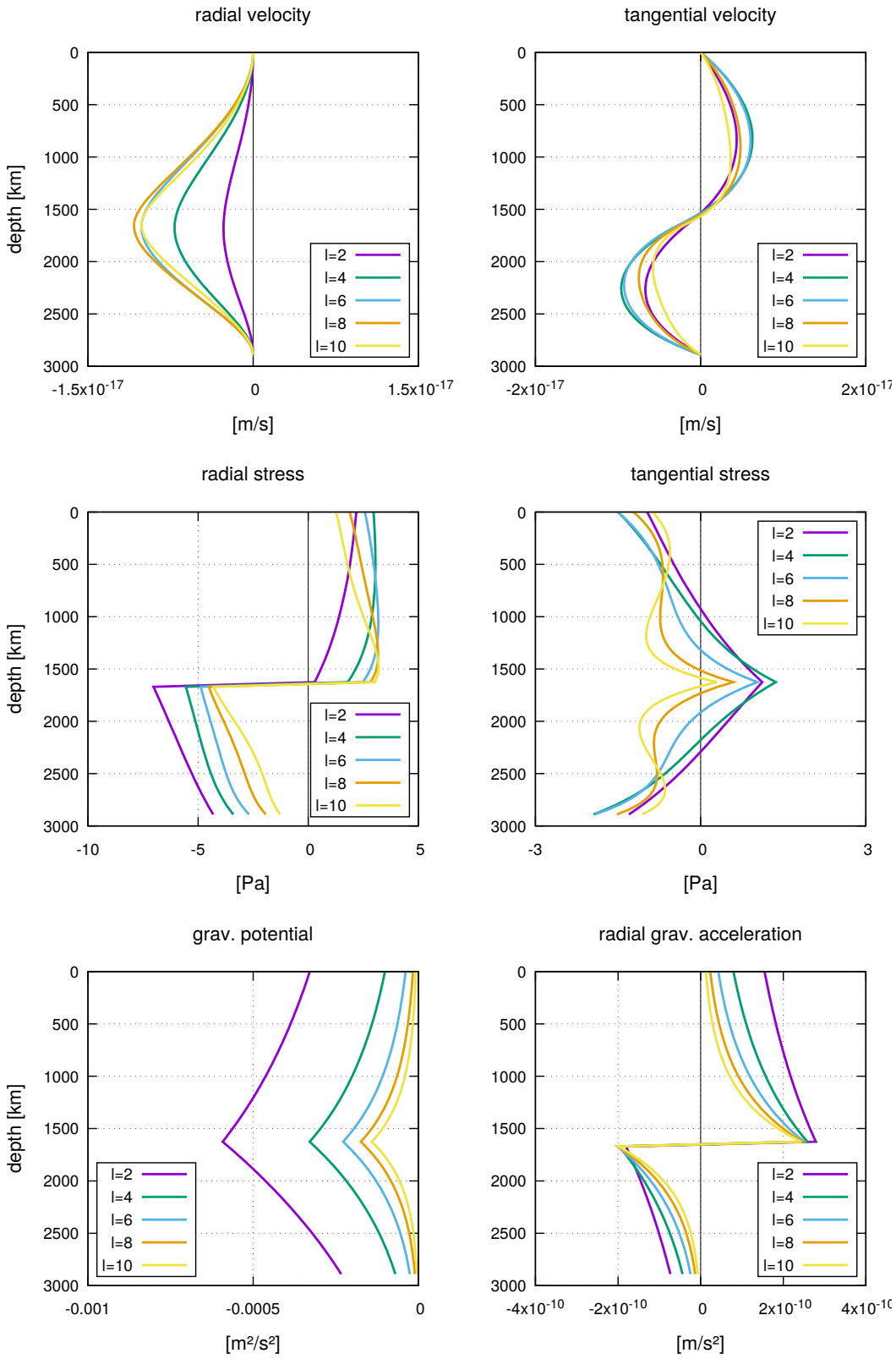

Figure 2.6: Solution of the Stokes equation system at various depth levels for a unit density anomaly of unit radial extension, placed at a depth of 1600 km. The flow parameters are no-slip at both boundaries and a uniform viscosity profile.

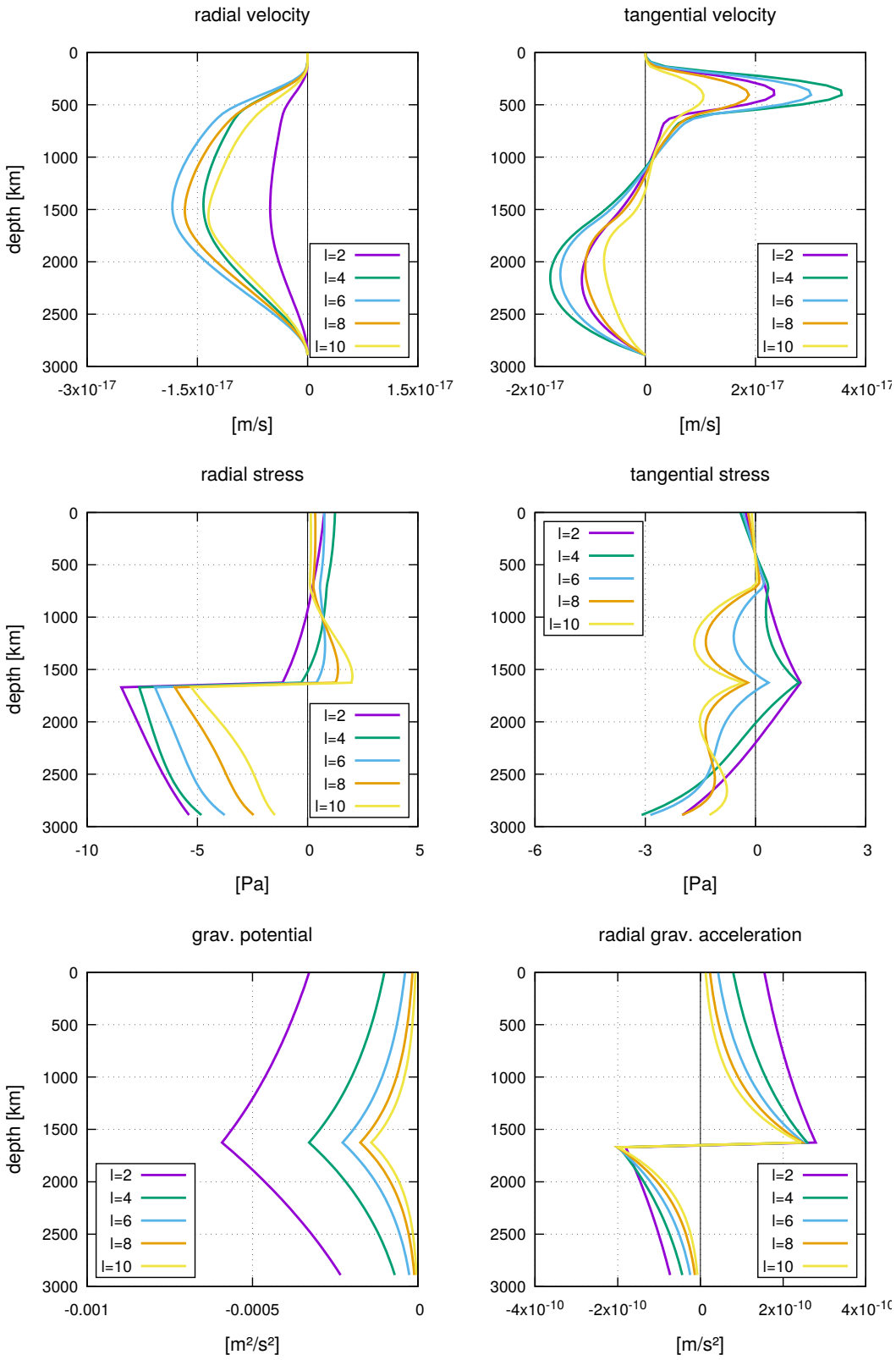

Figure 2.7: Solution of the Stokes equation system at various depth levels for a unit density anomaly of unit radial extension, placed at a depth of 1600 km. The flow parameters are no-slip at both boundaries and a viscosity profile with a low viscosity zone in the upper mantle.

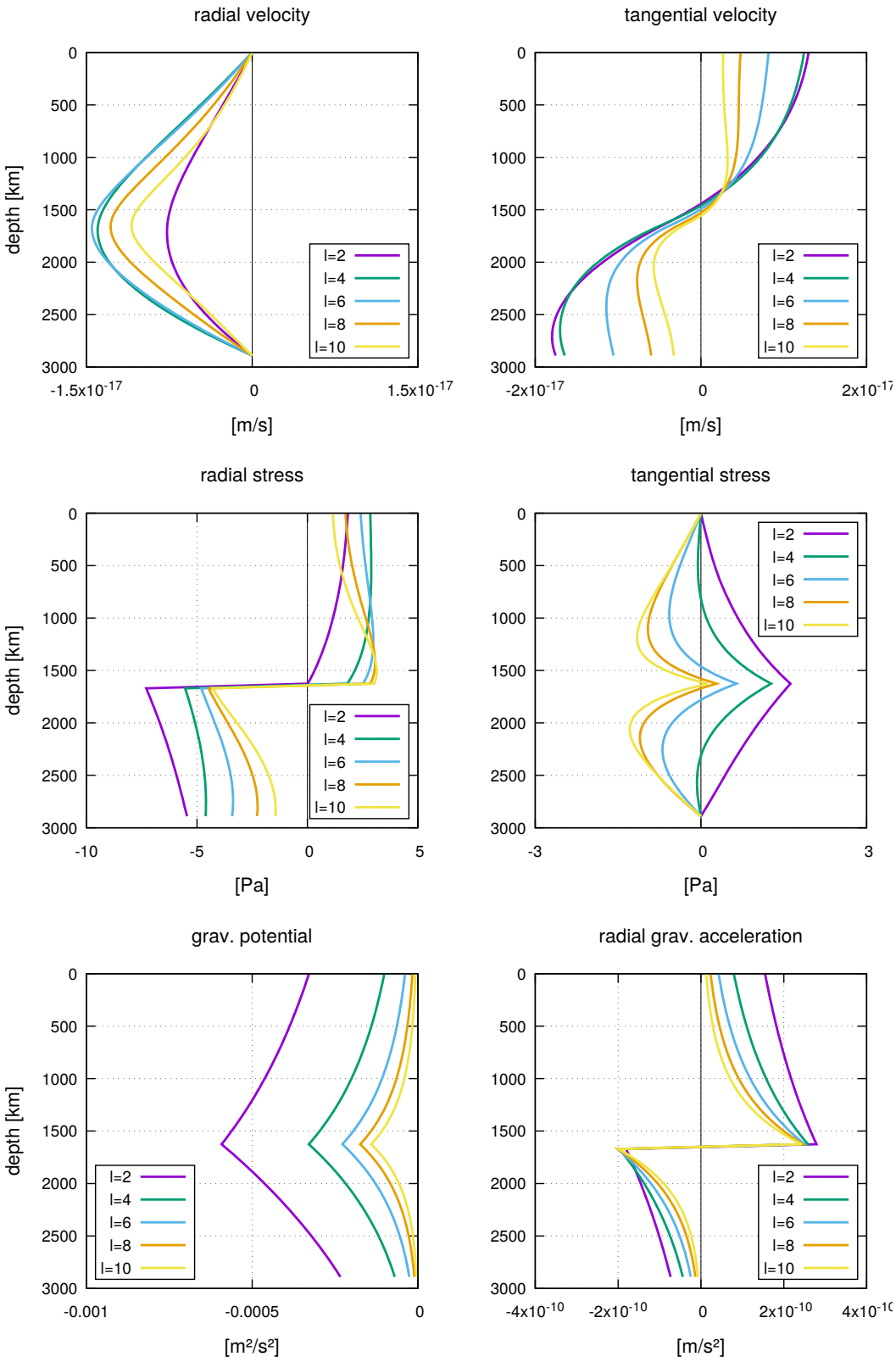

Figure 2.8: Solution of the Stokes equation system at various depth levels for a unit density anomaly of unit radial extension, placed at a depth of 1600 km. The flow parameters are free-slip at both boundaries and a uniform viscosity profile.

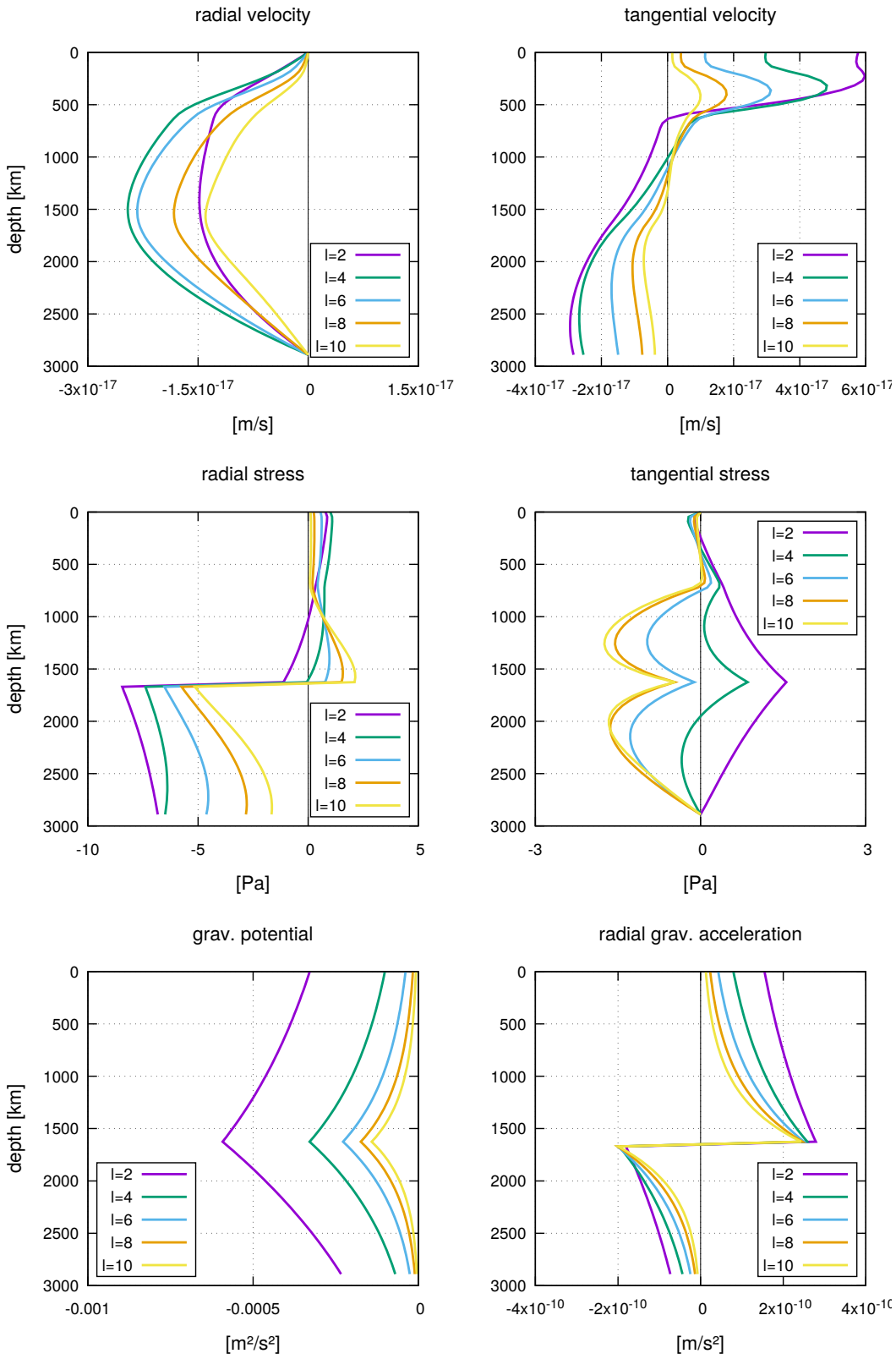

Figure 2.9: Solution of the Stokes equation system at various depth levels for a unit density anomaly of unit radial extension, placed at a depth of 1600 km. The flow parameters are free-slip at both boundaries and a viscosity profile with a low viscosity zone in the upper mantle.

Chapter 3

A semi-analytic accuracy benchmark for 3-D Stokes flow

This chapter is published together with some parts of the mathematical preliminaries (Chapter 1) and some foundations on continuum mechanics (Chapter 2) in the 'International Journal on Geomathematics' (GEM) (2020) as 'Horbach, A., Mohr, M., Bunge, H.-P.: A Semi-Analytic Accuracy Benchmark for Stokes Flow in 3-D Spherical Mantle Convection Codes', doi.org/10.1007/s13137-019-0137-3 (see Horbach et al., 2020). Here we use the spherical harmonic representation of the governing flow equations, that we derived in the previous chapter, in the special case of an incompressible and isoviscous flow regime. In this simplified scenario, it is possible to construct an objective, easy-to-implement semi-analytic benchmark for numerical mantle convection codes, where even the previously presented propagator matrix approach can be avoided.

The following sections are taken one-to-one from the publication except for Section 3.2, which we adjusted in order to follow the *flow* of this work and to build a connection to the derivations that we have performed in the previous chapters.

3.1 Introduction

Mantle convection is a primary driving force for large scale tectonic activity of our planet. Processes from plate tectonics at the Earth's surface to the thermal structure at the core mantle boundary are influenced by it, making mantle convection studies essential for our understanding of how our planet works. Mantle convection is governed by hydrodynamic field equations, expressing fundamental laws of mass, momentum and energy conservation (see Jarvis and Mckenzie, 1980, for an extended derivation of the mantle convection equations). Their non-linear nature and the geometric and time scales involved necessitate computational solution approaches.

Much progress in our understanding of mantle convection has been achieved through numerical simulations exploring the influence of key parameters on the mantle flow regime (see recent reviews by Tackley, 2012; Zhong and Liu, 2016). The current forward studies of convection are bound to grow further in importance as they will take advantage of next-generation computational architectures. New computational platforms will allow geodynamicists to discretise Earth's mantle at the km-scale (Burstedde et al., 2013; Rudi et al., 2015; Weismüller, 2016; Bauer, 2018), providing unprecedented opportunities to explore the convection process from local to global scales.

In addition to the forward modelling approach, new optimisation techniques based on the adjoint method (e.g., Bunge et al., 2003; Ismail-Zadeh et al., 2004; Horbach et al., 2014; Ghelichkhan and Bunge, 2016, 2018) are coming to the fore as a powerful approach to the recovery of past deep Earth

structure. The inverse approach to mantle convection links current to past mantle flow states, potentially allowing one to resolve uncertain modelling parameters by testing mantle convection models against observations gleaned from the geologic record (e.g., Colli et al., 2018).

The above makes it clear that numerical simulation is a crucial tool for geodynamicists to advance our understanding of mantle dynamics. Thus, it is not surprising that numerous benchmark studies have been performed to verify the accuracy of the solution methods deployed. Commonly, for one or a few well-defined problem(s), one computes key output variables, such as the Nusselt number or the peak flow velocity, with different computer codes at high numerical resolution, and reports the convergence behaviour as a function of resolution. For instance, for 2-D convection problems important benchmark studies were conducted by Blankenbach et al. (1989); van Keken et al. (1997); Gerya and Yuen (2003). For 3-D spherical convection codes an early benchmark problem includes the *European Benchmark* reported in Bunge (1997) and Richards et al. (2001). This benchmark, also reported in Zhong et al. (2008), involves two cases of low Rayleigh number (Ra=14,000), isoviscous and incompressible convection at steady-state, having either a tetrahedral or a cubic flow symmetry. More recently Kameyama et al. (2013) described a linear stability analysis on the onset of thermal convection of a fluid in a spherical shell, where a spectral representation of the flow equations included a temperature-dependent viscosity that varied in radial direction.

Comparing convection-related key output variables from different modelling codes is one strategy to approach the benchmark problem. A drawback comes from the fact that it is difficult to identify potential error sources should one obtain different results for different modelling codes, as they involve coupled solutions for mass, momentum and energy conservation. This makes it attractive to explore benchmark solutions targeted specifically to the respective conservation equations. To this end Popov et al. (2014) presented analytical solutions for benchmarking 2-D and 3-D Cartesian geodynamic Stokes problems. For 3-D spherical geometry Takeuchi and Hasegawa (1965); Richards and Hager (1984); Ricard et al. (1984) developed semi-analytical solutions for Stokes flow with radially varying viscosity, using a spectral analysis of the governing equations and the propagator matrix technique (Gantmacher, 1960). In this approach, one ends up with a linear system of differential equations that connects the harmonic coefficients of the flow velocity field, stress tensor and gravitational potential - in case of non-neglected self-gravity.

Here we address the benchmark problem for the momentum balance in 3-D spherical geometry from a similar perspective using scalar and vector spherical harmonics as basis functions for the underlying physical quantities. Our primary goal is to present a benchmark that is intended to play the role of an initial *first level* test within a hierarchy of benchmark set-ups of ascending complexity. In our opinion, this is a crucial step to systematically investigate any shortcomings in the numerical code implementation. Per definition, such a *first level benchmark* should be based on an analytic solution, so it can easily be implemented by everyone with minimal scope for error sources. It should also reflect as little physical complexities as possible, which arguably are primarily of rheological nature.

Indeed, we prove that under the assumption of incompressibility and a uniform viscosity it is possible to gain a direct relation between velocity field and driving forces. The latter can be evaluated without solving a whole linear system of differential equations. This is the essential difference of our method to the propagator matrix approach, where algebraic functions of matrices need to be calculated, matrix multiplications must be performed and a more complex (and potentially numerically more unstable) system of linear equations has to be solved. All of the above provide additional error sources, also regarding numerical aspects, compared to our method. We regard the propagator approach as a *second level* benchmark, where more complex physics can be addressed, such as a radially varying viscosity and density profile and self-gravitational effects.

Here, the simplicity of the resulting equations allows us to develop a set-up of analytical benchmarks that is easily implemented and applied to any numerical convection code in 3-D spherical geometry.

As proof of concept we present results for our analytical benchmark obtained with the prototype for a new high-performance mantle convection framework being developed in the Terra-Neo project (see e.g., Weismüller et al., 2015; Bauer et al., 2016, 2019).

3.2 Analytic solutions to the incompressible Stokes equation

As we already mentioned at the begin of this chapter, in this part of the work we want to consider a special case of the equations that we have derived in the course of the previous chapter. We will see that assuming incompressibility and an isoviscous flow regime, the governing equations of mantle flow simplify in such a significant way that the propagator approach will no longer be necessary and we find a direct connection in form of an ordinary differential equation between the harmonic coefficients of velocity and temperature.

In the following, the procedure is to investigate the governing equations of mantle flow in terms of harmonic coefficients. We restate the results of the previous chapter and look how the relations simplify using the assumptions from above. First, we restate the continuity equation that reduces in case of an incompressible flow ($\chi = 0$) to (2.10):

$$\nabla \cdot v = 0\,. \tag{3.1}$$

The key here - and what is different to the basis equations in the propagator approach - is that with the above statement we are able to enforce the Mie representation for the velocity field v and represent it solely in terms of two scalar functions S and Q, where S represents the poloidal part and Q the toroidal part of v. More precisely, according to (1.328) we can deduce from now on for the respective harmonic coefficients that

$$\begin{aligned} v_1 &= \frac{l(l+1)}{r^2}\, S_1\,, \\ v_2 &= \frac{\mu_l}{r}\, \dot{S}_1\,, \\ v_3 &= -\frac{\mu_l}{r}\, Q_1\,, \end{aligned} \tag{3.2}$$

where we stick to the already familiar notation of the lower index '1' for the harmonic coefficients of a scalar field and the 'dot' symbol that indicates the radial derivative. We proceed with the momentum equation and use the *temperature version* (2.38) in order to emphasise the immediate connection to a numerical mantle circulation code - where temperature is the key quantity - that we want to build here:

$$-\nabla \tilde{P} + \hat{\eta}_0 \left(\Delta v + \frac{1}{3} \nabla \left(\nabla \cdot v \right) \right) = \rho_0 \nabla \tilde{U} - g_0 \alpha \tilde{T} \rho_0 \epsilon^r\,. \tag{3.3}$$

Applying incompressibility (3.1) and assuming a constant density $\rho_0(r) = \hat{\rho}_0$ (see (2.66) for the first appearance of this notation) and a constant gravitational acceleration $g_0(r) = \hat{g}_0$ throughout the whole domain, and further, also neglecting the second-order effect of self-gravity $\rho_0 \nabla \tilde{U}$ within the body forces, we arrive at

$$-\nabla \tilde{P} + \hat{\eta}_0 \Delta v = -g_0 \alpha \tilde{T} \hat{\rho}_0 \epsilon^r\,. \tag{3.4}$$

As in the previous chapter, the key to a deeper insight into the equations is the thinking in terms of harmonic coefficients. We start again with the first harmonic coefficient and here, we can go back to (2.50) and find, using $\eta_0 = \hat{\eta}_0$ (isoviscous) ($\Rightarrow \dot{\eta}_0 = 0$), $\chi = 0$ (incompressible) and $U_1 = 0$ (no self-gravity), that

$$-\dot{P}_1 + \hat{\eta}_0 \left(\ddot{v}_1 + \frac{2}{r} \dot{v}_1 - \frac{l(l+1)+2}{r^2}\, v_1 + \frac{2l(l+1)}{r^2 \mu_l}\, v_2 \right) = -\hat{g}_0 \alpha T_1 \hat{\rho}_0\,, \tag{3.5}$$

where we also - in analogy to the previous chapter - neglect the 'tilde' notation for the disturbed quantities. For the second harmonic coefficient, we go back to (2.54) and find - using the same assumptions as above - that

$$-\frac{\mu_l}{r}\,P_1+\eta_0\left(\ddot{v}_2+\frac{2}{r}\,\dot{v}_2-\frac{l(l+1)}{r^2}\,v_2+\frac{2\mu_l}{r^2}\,v_1\right)=0\,. \tag{3.6}$$

We notice that we can eliminate the pressure coefficients P_1 by taking the first radial derivative of the second equation and substitute the result into the first one. Multiplying by r/μ_l and taking the derivative of the second relation yields

$$-\dot{P}_1+\hat{\eta}_0\left(\frac{r}{\mu_l}\,\dddot{v}_2+\frac{3}{\mu_l}\,\ddot{v}_2-\frac{l(l+1)}{r\mu_l}\,\dot{v}_2+\frac{l(l+1)}{r^2\mu_l}\,v_2+\frac{2}{r}\,\dot{v}_1-\frac{2}{r^2}\,v_1\right)=0\,. \tag{3.7}$$

By inserting (3.7) into (3.5) we find

$$\ddot{v}_1-\frac{l(l+1)}{r^2}\,v_1-\frac{r}{\mu_l}\,\dddot{v}_2-\frac{3}{\mu_l}\,\ddot{v}_2+\frac{l(l+1)}{r\mu_l}\,\dot{v}_2+\frac{l(l+1)}{r^2\mu_l}\,v_2=-\frac{\hat{g}_0\hat{\rho}_0\alpha}{\hat{\eta}_0}\,T_1\,, \tag{3.8}$$

which is a direct relation between poloidal velocity coefficients and the temperature (without the detour of involving the stress tensor). Note that the harmonic coefficient representation (1.296) of the curl and (1.297) of the double curl reveals that the previously executed operation, i.e. $f_1-\partial_r(rf_2)$ for a vector field f, can also be interpreted as determining the third harmonic coefficient of the curl of f or - which is identical - the first (or radial) coefficient of the double curl of f.

Since we assumed v to be incompressible we can now apply the Mie representation (3.2) and express v_1 and v_2 in terms of the scalar field coefficients S_1. Using

$$\begin{aligned}
\dot{v}_1&=\partial_r\left(\frac{l(l+1)}{r^2}\,S_1\right)=\frac{l(l+1)}{r^2}\left(\dot{S}_1-\frac{2}{r}\,S_1\right),\\
\ddot{v}_1&=\frac{l(l+1)}{r^2}\left(\ddot{S}_1-\frac{4}{r}\,\dot{S}_1+\frac{6}{r^2}\,S_1\right),\\
\dot{v}_2&=\mu_l\partial_r\left(\frac{1}{r}\,\dot{S}_1\right)=\mu_l\left(\frac{1}{r}\,\ddot{S}_1-\frac{1}{r^2}\,\dot{S}_1\right),\\
\ddot{v}_2&=\mu_l\left(\frac{1}{r}\,\dddot{S}_1-\frac{2}{r^2}\,\ddot{S}_1+\frac{2}{r^3}\,\dot{S}_1\right),\\
\dddot{v}_2&=\mu_l\left(\frac{1}{r}\,\ddddot{S}_1-\frac{3}{r^2}\,\dddot{S}_1+\frac{6}{r^3}\,\ddot{S}_1-\frac{6}{r^4}\,\dot{S}_1\right),
\end{aligned} \tag{3.9}$$

we then find

$$\ddddot{S}_1-\frac{l(l+1)}{r^4}\left(2r^2\ddot{S}_1-4r\dot{S}_1+(6-l(l+1))\,S_1\right)=\frac{\hat{g}_0\hat{\rho}_0\alpha}{\hat{\eta}_0}\,T_1\,. \tag{3.10}$$

The left-hand side of the previous equation can be reformulated into a more compact way such that finally, we find that the scalar harmonic coefficients S_1 of the poloidal part of v must satisfy the following fourth-order ordinary differential equation:

$$\boxed{\left(\partial_{r^2}^2-\frac{l(l+1)}{r^2}\right)^2 S_1(r)=\frac{\hat{g}_0\hat{\rho}_0\alpha}{\hat{\eta}_0}\,T_1(r)\,,} \tag{3.11}$$

for all $r\in[r_0,r_1]$.

We go on by inspecting the toroidal part, i.e. the third harmonic coefficient, of the Stokes equation. Due to the results of the previous chapter, the expected result should be obvious. Even without

the assumptions of a 'simple' flow scenario as stated above, we have learned that the toroidal part in our model generally vanishes. We should find exactly this result also here. For the third harmonic coefficient we go back to (2.58) and find

$$\hat{\eta}_0 \left(\ddot{v}_3 + \frac{2}{r} \dot{v}_3 - \frac{l(l+1)}{r^2} v_3 \right) = 0 \,. \tag{3.12}$$

As a side remark, in analogy to the poloidal part, also here we find an interpretation of the previous step in context of the curl, i.e. the harmonic coefficients (1.296) reveal that the toroidal part f_3 of a vector field f is equivalent to the radial harmonic coefficient of the curl.

We again use the Mie representation of v and express v_3 in terms of the scalar field Q. For the radial derivatives we then find

$$\begin{aligned} \dot{v}_3 &= -\mu_l \partial_r \left(\frac{1}{r} Q_1 \right) = -\mu_l \left(\frac{1}{r} \dot{Q}_1 - \frac{1}{r^2} Q_1 \right) , \\ \ddot{v}_3 &= -\mu_l \left(\frac{1}{r} \ddot{Q}_1 - \frac{2}{r^2} \dot{Q}_1 + \frac{2}{r^3} Q_1 \right) . \end{aligned} \tag{3.13}$$

By inserting these relations into (3.12) we immediately find the following second-order ordinary differential equation for the toroidal part of v:

$$\boxed{\left(\partial_{r^2}^2 - \frac{l(l+1)}{r^2} \right) Q_1(r) = 0 \,,} \tag{3.14}$$

for all $r \in [r_0, r_1]$.

For any $l \in \mathbb{N}_0$ this second-order ODE is a Cauchy-Euler differential equation. It can be shown that its general solution is given by

$$Q(r) = c_1 r^{(l+1)} + c_2 r^{-l} \,, \quad r \in [r_0, r_1] \,, \tag{3.15}$$

with constants c_1, $c_2 \in \mathbb{R}$. The latter are fixed by the velocity boundary conditions. Let us now impose the constraint that the velocity at the domain boundaries Ω_{r_0} and Ω_{r_1} does not contain any toroidal part, i.e. we enforce $Q(r_0) = Q(r_1) = 0$. Then (3.15) yields $c_1 = c_2 = 0$ and consequently $Q \equiv 0$ must hold in Ω_{r_0,r_1}.

Here, we demonstrated again that in a simple, incompressible convection model, with spatially constant viscosity, the velocity field v will not contain any toroidal components, if these are not explicitly imposed at the boundaries. In other words, this means that in such a simple model, the buoyancy forces alone are unable to produce motion of tectonic plates on the Earth's surface, which are naturally containing toroidal components.

3.3 Boundary conditions

3.3.1 The no-outflow condition

Since (3.11) is a fourth-order differential equation, four boundary conditions, in practice two at each boundary, the surface and the CMB, need to be imposed on the harmonic coefficients Q_1 in order to solve this equation. When discussing the Mie representaion, we learned that here, it is required to fulfill the no-outflow condition

$$v_r(x) = 0 \,, \tag{3.16}$$

for all $x \in \Omega_{r_0} \cup \Omega_{r_1}$, which already states a Dirichlet boundary condition for the radial component of v. Using the Mie representation (3.2) we immediately find that the no-outflow condition directly transfers into the following condition for the harmonic coefficients of S:

$$S_1(r_0) = S_1(r_1) = 0\,. \tag{3.17}$$

These are the first two boundary conditions we need the coefficients S_1 to satisfy. For the other two conditions that are required, we have to think about additional physical properties we want the model to satisfy. In other words, which restrictions do we want to impose on the tangential parts of v, i.e. v_φ and v_t at the boundaries of our domain. Basically, there are two physically appropriate options we may choose for each of the two boundaries:

3.3.2 The no-slip boundary condition

In case of a no-slip boundary condition, we assume a rigid boundary, fixed in time and space, which means that - in addition to the zero radial component that is forced by the no-outflow condition, we also assume that the tangential components of the velocity vanish at the respective boundary, i.e.

$$v_\varphi(x) = v_t(x) = 0\,, \tag{3.18}$$

for all $x \in \Omega_{r_0} \cup \Omega_{r_1}$. This is again a Dirichlet boundary condition, here, for both of the tangential components of v. Again, using the Mie representation (3.2) and the fact that the harmonic coefficients Q_1 of the toroidal part of v vanish, we see that these assumptions directly transfer into the following condition for the harmonic coefficients of S:

$$\dot{S}_1\left(r_0\right) = \dot{S}_1\left(r_1\right) = 0\,. \tag{3.19}$$

We see that assuming the no-slip case at both boundaries together with the no-outflow condition gives us the required four additional constraints for the scalar function S in order to be able to solve the fourth-order differential equation (3.11).

3.3.3 The free-slip boundary condition

Going back to Section 2.2.2, we learned that the shear stress is represented by the σ_2 and σ_3 coefficients of the stress vector s. In (2.48) we found the relations

$$\begin{aligned} \sigma_2 &= \hat{\eta}_0 \left(\dot{v}_2 - \frac{v_2}{r} + \frac{\mu_l}{r}\, v_1 \right)\,, \\ \sigma_3 &= \hat{\eta}_0 \left(\dot{v}_3 - \frac{v_3}{r} \right)\,. \end{aligned} \tag{3.20}$$

Since there is no toroidal velocity v_3 the toroidal shear stress coefficient σ_3 just vanishes. Considering the poloidal part, we may set $v_1 = 0$ due to the no-outflow condition at the boundaries and apply the Mie representation (3.2) and (3.9) to substitute v_2 and $\dot{v}_2$. This immediately yields the condition

$$0 = \dot{v}_2 - \frac{v_2}{r} = r\partial_r \left(\frac{1}{r}\, v_2 \right) = r\mu_l \partial_r \left(\frac{1}{r^2}\, \dot{S}_1 \right)\,, \tag{3.21}$$

such that summarised, we find the following two conditions for both domain boundaries:

$$\partial_r \left(\frac{1}{r^2}\, \dot{S}_1 \right)(r_0) = \partial_r \left(\frac{1}{r^2}\, \dot{S}_1 \right)(r_1) = 0\,. \tag{3.22}$$

In analogy to the no-slip case, we see that assuming a free-slip behaviour at both boundaries together with the no-outflow condition provides the four constraints to the scalar function S that are required to solve the fourth-order differential equation (3.11). Obviously, it is also possible to use a combination of no- and free-slip conditions for both boundaries.

3.3.4 A side remark: The Cartesian perspective

Having a look at the relations in (3.20) and (3.21) that are formulated in terms of the velocity coefficients, we see that the free-slip condition, i.e.

$$\partial_r \left(\frac{1}{r} v_2 \right) = 0 \,, \quad \partial_r \left(\frac{1}{r} v_3 \right) = 0 \,, \tag{3.23}$$

shows up as a kind of Neumann condition for the tangential coefficients, but with an additional weighting factor of $1/r$. This weighting factor arises from the spherical geometry of the domain. To illustrate this point, we want to have a short review on the Cartesian case and show how the respective relations evolve in this case. We consider a 3-D Cartesian box and assume the bottom (Σ_0) and the top (Σ_1) faces of the box to be parallel to the x_1x_2-plane.

In analogy to the previous section, in the free-slip case we need the shear stress at the boundaries to vanish. Applying the gradient in Cartesian coordinates to the stress tensor representation (2.18) the stress tensor becomes

$$\sigma = \begin{pmatrix} -P + 2\eta\partial_1 v_1 & \eta\left(\partial_1 v_2 + \partial_2 v_1\right) & \eta\left(\partial_1 v_3 + \partial_3 v_1\right) \\ \eta\left(\partial_1 v_2 + \partial_2 v_1\right) & -P + 2\eta\partial_2 v_2 & \eta\left(\partial_2 v_3 + \partial_3 v_2\right) \\ \eta\left(\partial_1 v_3 + \partial_3 v_1\right) & \eta\left(\partial_2 v_3 + \partial_3 v_2\right) & -P + 2\eta\partial_3 v_3 \end{pmatrix} . \tag{3.24}$$

In the case of the described Cartesian box, the outer normal of the boundary surfaces Σ_0 and Σ_1 points into the x_3-direction, so we find for the traction at a point $x \in \Sigma_0 \cup \Sigma_1$ that

$$s(x) = \sigma(x)n(x) = \pm\sigma(x) \begin{pmatrix} 0 \\ 0 \\ 1 \end{pmatrix} = \pm \begin{pmatrix} \eta\left(\partial_1 v_3 + \partial_3 v_1\right) \\ \eta\left(\partial_2 v_3 + \partial_3 v_2\right) \\ -P + 2\eta\partial_3 v_3 \end{pmatrix} . \tag{3.25}$$

If here we also assume a no-outflow condition, which states in this scenario as

$$v_3(x) = 0 \,, \tag{3.26}$$

for all $x \in \Sigma_0 \cup \Sigma_1$, the derivatives in x_1- and x_2-direction of the x_3-component of the velocity vanish at the boundaries. Inserting this result into (3.25) yields

$$s(x) = \pm \begin{pmatrix} \eta\partial_3 v_1 \\ \eta\partial_3 v_2 \\ -P + 2\eta\partial_3 v_3 \end{pmatrix} . \tag{3.27}$$

In this geometry, the shear stress is the stress in x_1- and x_2-direction, so if we want to assure the shear stress to vanish, (3.27) implies that we have to impose the constraints

$$\partial_3 v_1 = \partial_3 v_2 = 0 \,, \tag{3.28}$$

at the boundaries. In other words, the normal derivative of the tangential components must vanish. This result looks remarkably similar to the constraints in the scenario of a spherical geometry but in contrast, it can be noticed that in the Cartesian case no additional weighting factor $1/r$ is found.

3.4 The benchmark

3.4.1 General setting

In the previous section we discussed two different boundary conditions for the fourth-order ordinary differential equation (3.11), which we restate here for convenience:

$$\left(\partial_{r^2}^2 - \frac{l(l+1)}{r^2} \right)^2 S_1(r) = \frac{\hat{g}_0 \hat{\rho}_0 \alpha}{\hat{\eta}_0} T_1(r) \,. \tag{3.29}$$

Given these boundary conditions and a right-hand side, i.e. a temperature distribution inside the domain or more precisely the spherical harmonic coefficients T_1, (3.29) provides a way to reconstruct S - in case (3.29) possesses a solution to the prescribed right-hand side. This would be the normal condition encountered in a numerical model, where we seek a velocity field for a given buoyancy field. It represents an inverse approach to the equation. However, our idea to derive an accuracy benchmark for evaluating existing numerical codes evolves from a forward consideration of equation (3.29). The general scheme is presented in Figure 3.1. At first we prescribe a velocity field with the desired boundary conditions, no-slip or free-slip. Next we compute the resulting temperature distribution applying the differential operator of (3.29). This temperature field is fed into the numerical code, which we use to compute a numerical approximation of the velocity field. This result can then directly be compared to the a-priori defined velocity structure to quantify the quality of the numerical approximation.

Thus, in order to execute the benchmark, first, we need to construct a radially dependent scalar function $H(r)$ that satisfies the no-slip, free-slip or mixed boundary conditions as described in the previous section. $H(r)$ then plays the role of the radially dependent harmonic coefficients of the poloidal velocity potential $S_1(r)$ in (3.29). While there are infinitely many ways to accomplish this, the only constraints arise from the pre-described four boundary conditions. The latter imply that the chosen basis function needs to have at least 4 free parameters. From the desire of constructing an as-simple-as-possible test scenario, one would select an ansatz function that is as smooth as possible to avoid artificial complexities. This naturally leads to a polynomial approach and the Hermite interpolation problem, corresponding to the chosen set of boundary conditions. Upon choosing a third-order polynomial, we find for the no-slip case that the interpolation problem leads to the trivial solution $H \equiv 0$, such that it is required to include an additional free parameter. More precisely, we need to determine coefficients $a, b, c, d \in \mathbb{R}$ such that

$$H(r) = H_0 + ar + br^2 + cr^3 + dr^4 \,. \tag{3.30}$$

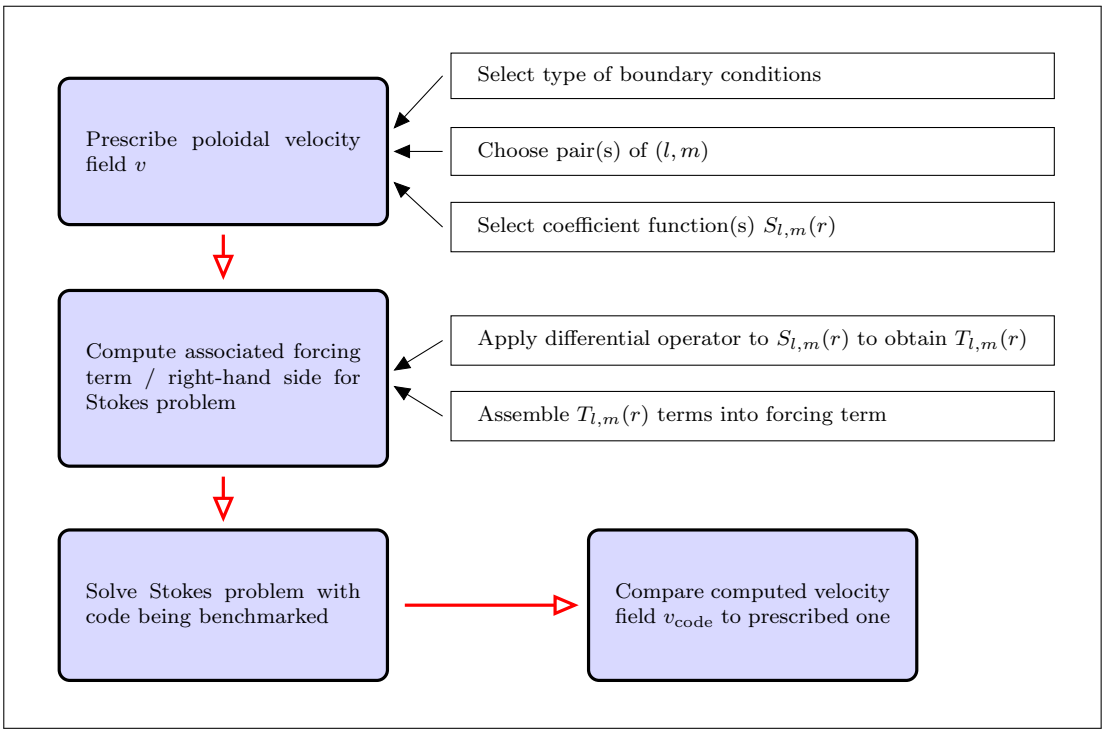

Figure 3.1: Schematics of the individual steps of the benchmark.

where H_0 is an additional free parameter that must be chosen a-priori and that allows one to adjust the amplitude of the desired velocity field / temperature variations. We point out that it is not necessary to assume that H is a polynomial. More general, we can reformulate the previous equation as the task of finding a function H that satisfies

$$H(r) = H_0 + aH_1(r) + bH_2(r) + cH_3(r) + dH_4(r)\,, \tag{3.31}$$

with $H_0 \in \mathbb{R}$ and where H_1, H_2, H_3 and H_4 are linearly independent functions such that the resulting linear system of equations remains (uniquely) solvable. For example, another appropriate choice would be $H_1(r) := \sin(r), H_2(r) := \cos(r), H_3(r) := \sin(2r)$ and $H_4(r) := \cos(2r)$.

Besides this natural approach of a smooth ansatz function, one can imagine a variety of further choices for H. This is an essential advantage of the method presented here. In general, H can be chosen in such a way that more complex physical scenarios can be addressed. For instance, one could imagine to construct a velocity profile with much higher values in specific layers compared to others, i.e. an asthenosphere-like scenario. This would imply locally steeper velocity gradients that are in general harder to resolve in a numerical code. It would also provide a strong test on the ability to handle large localised variations in lateral and radial shear stresses. The latter would be of significant value in the testing of a geodynamic mantle model.

Nevertheless, here we focus on the four free parameters and especially fourth-order polynomial ansatz, motivated by our original task of presenting a benchmark for an as-simple-as-possible reference case.

3.4.2 No-slip boundary conditions

From section 3.3.2 we know that in the no-slip case the function H has to satisfy the following four constraints:

$$H(r_0) = 0\,, \quad H(r_1) = 0\,, \quad \dot{H}(r_0) = 0\,, \quad \dot{H}(r_1) = 0\,. \tag{3.32}$$

Following the ansatz in (3.31) this immediately leads to the following system of linear equations:

$$\begin{pmatrix} H_1(r_0) & H_2(r_0) & H_3(r_0) & H_4(r_0) \\ H_1(r_1) & H_2(r_1) & H_3(r_1) & H_4(r_1) \\ \dot{H}_1(r_0) & \dot{H}_2(r_0) & \dot{H}_3(r_0) & \dot{H}_4(r_0) \\ \dot{H}_1(r_1) & \dot{H}_2(r_1) & \dot{H}_3(r_1) & \dot{H}_4(r_1) \end{pmatrix} \begin{pmatrix} a \\ b \\ c \\ d \end{pmatrix} = \begin{pmatrix} -H_0 \\ -H_0 \\ 0 \\ 0 \end{pmatrix}. \tag{3.33}$$

Solving this system for a given H_0 determines the coefficients a, b, c and d and, thus the function H. The latter can then be inserted into (3.29). This leads, straightforwardly, to the spherical harmonic coefficients $T_{l,m}$ of the temperature distribution.

For the fourth-order polynomial ansatz (3.30) we discuss the procedure in a more detailed way. Here the system of linear equations we have to solve is

$$\begin{pmatrix} r_0 & r_0^2 & r_0^3 & r_0^4 \\ r_1 & r_1^2 & r_1^3 & r_1^4 \\ 1 & 2r_0 & 3r_0^2 & 4r_0^3 \\ 1 & 2r_1 & 3r_1^2 & 4r_1^3 \end{pmatrix} \begin{pmatrix} a \\ b \\ c \\ d \end{pmatrix} = \begin{pmatrix} -H_0 \\ -H_0 \\ 0 \\ 0 \end{pmatrix}. \tag{3.34}$$

We choose $H_0 = 1$, $r_0 = 1$ and $r_1 = 2$, which is an almost Earth-like scenario since $r_s/r_c \approx 1.83$, where $r_c := 3,480$ km is the radius of the CMB and $r_s := 6,370$ km is the radius of the Earth's surface. The system of equations then turns into

$$\begin{pmatrix} 1 & 1 & 1 & 1 \\ 2 & 4 & 8 & 16 \\ 1 & 2 & 3 & 4 \\ 1 & 4 & 12 & 32 \end{pmatrix} \begin{pmatrix} a \\ b \\ c \\ d \end{pmatrix} = \begin{pmatrix} -1 \\ -1 \\ 0 \\ 0 \end{pmatrix}, \tag{3.35}$$

with the unique solution $a = -3$, $b = 13/4$, $c = -3/2$ and $d = 1/4$. Thus, the fourth-order polynomial that satisfies the desired boundary conditions is

$$H(r) = \frac{1}{4}\, r^4 - \frac{3}{2}\, r^3 + \frac{13}{4}\, r^2 - 3r + 1\,. \tag{3.36}$$

If we now identify this function with the spherical harmonic coefficients of the toroidal part of the velocity field S_1 in (3.29), we find the respective temperature field by

$$T_1(r) = \frac{\hat{\eta}_0}{\hat{g}_0 \hat{\rho}_0 \alpha} \left(\partial_{r^2}^2 - \frac{l(l+1)}{r^2}\right)^2 H(r)\,. \tag{3.37}$$

Note that the toroidal ansatz function depends neither on degree l nor on order m. Inserting (3.36) into (3.37) yields

$$\begin{aligned}\left(\partial_{r^2}^2 - \frac{l(l+1)}{r^2}\right)^2 H(r) &= \ddddot{H}(r) - \frac{l(l+1)}{r^4}\left(2r^2\ddot{H}(r) - 4r\dot{H}(r) + (6 - l(l+1))H(r)\right) \\ &= \frac{l(l+1)}{r^4}\left(\left(\frac{6}{l(l+1)} + \frac{l(l+1)}{4} - \frac{7}{2}\right) r^4 + \left(9 - \frac{3l(l+1)}{2}\right) r^3\right. \\ &\quad \left. + \left(\frac{13l(l+1)}{4} - \frac{13}{2}\right) r^2 + (6 - 3l(l+1))\, r + l(l+1) - 6\right)\,.\end{aligned} \tag{3.38}$$

Thus, e.g. for the spherical harmonic degree $l = 2$ we find that

$$T_1(r) = -\frac{6\hat{\eta}_0}{\hat{g}_0 \hat{\rho}_0 \alpha r^3}\left(r^3 - 13r + 12\right)\,. \tag{3.39}$$

3.4.3 Free-slip boundary conditions

For the free-slip case we remember that the ansatz function H has to satisfy the following four constraints:

$$H(r_0) = 0\,, \quad H(r_1) = 0\,, \quad \partial_r\left(\frac{1}{r^2}\,\dot{H}\right)(r_0) = 0\,, \quad \partial_r\left(\frac{1}{r^2}\,\dot{H}\right)(r_1) = 0\,. \tag{3.40}$$

Applying (3.31) immediately leads to the following system of linear equations:

$$\begin{pmatrix} H_1(r_0) & H_2(r_0) & H_3(r_0) & H_4(r_0) \\ H_1(r_1) & H_2(r_1) & H_3(r_1) & H_4(r_1) \\ \partial_r\left(\frac{1}{r^2}\,\dot{H}_1\right)(r_0) & \partial_r\left(\frac{1}{r^2}\,\dot{H}_2\right)(r_0) & \partial_r\left(\frac{1}{r^2}\,\dot{H}_3\right)(r_0) & \partial_r\left(\frac{1}{r^2}\,\dot{H}_4\right)(r_0) \\ \partial_r\left(\frac{1}{r^2}\,\dot{H}_1\right)(r_1) & \partial_r\left(\frac{1}{r^2}\,\dot{H}_2\right)(r_1) & \partial_r\left(\frac{1}{r^2}\,\dot{H}_3\right)(r_1) & \partial_r\left(\frac{1}{r^2}\,\dot{H}_4\right)(r_1) \end{pmatrix} \begin{pmatrix} a \\ b \\ c \\ d \end{pmatrix} = \begin{pmatrix} -H_0 \\ -H_0 \\ 0 \\ 0 \end{pmatrix}\,. \tag{3.41}$$

In analogy to the no-slip case we take a more detailed look at the polynomial case (3.30), which leads to

$$\begin{pmatrix} r_0 & r_0^2 & r_0^3 & r_0^4 \\ r_1 & r_1^2 & r_1^3 & r_1^4 \\ -2/r_0^3 & -2/r_0^2 & 0 & 4 \\ -2/r_1^3 & -2/r_1^2 & 0 & 4 \end{pmatrix} \begin{pmatrix} a \\ b \\ c \\ d \end{pmatrix} = \begin{pmatrix} -H_0 \\ -H_0 \\ 0 \\ 0 \end{pmatrix}\,. \tag{3.42}$$

For the choice $H_0 = 1$, $r_0 = 1$, $r_1 = 2$, this system turns into

$$\begin{pmatrix} 1 & 1 & 1 & 1 \\ 2 & 4 & 8 & 16 \\ -2 & -2 & 0 & 4 \\ -1/4 & -1/2 & 0 & 4 \end{pmatrix} \begin{pmatrix} a \\ b \\ c \\ d \end{pmatrix} = \begin{pmatrix} -1 \\ -1 \\ 0 \\ 0 \end{pmatrix}\,, \tag{3.43}$$

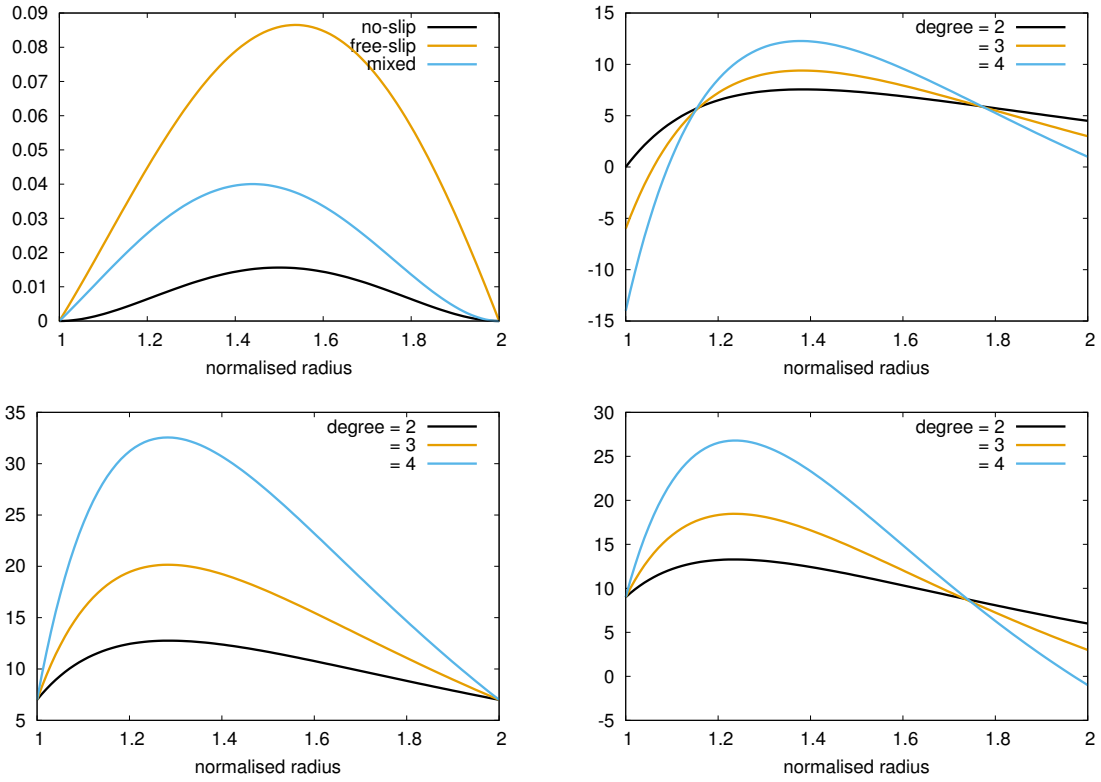

Figure 3.2: This figure shows the polynomial H for the different kinds of boundary conditions (upper left), as well as the resulting forcing terms f from (3.50) for different harmonic degrees l and no-slip (upper right), free-slip (lower left) and mixed (lower right) boundary conditions.

with the unique solution $a = -7/2$, $b = 49/12$, $c = -15/8$ and $d = 7/24$. Thus, the fourth-order polynomial that satisfies the desired boundary conditions is

$$H(r) = \frac{7}{24}\, r^4 - \frac{15}{8}\, r^3 + \frac{49}{12}\, r^2 - \frac{7}{2}\, r + 1\,. \tag{3.44}$$

Inserting this polynomial into (3.29) then yields the desired temperature distribution as already described in detail in the previous section.

3.4.4 Mixed boundary conditions

In this section, we combine the results from both previous sections, defining an Earth-like scenario that contains a no-slip condition on the outer shell - surface - and a free-slip condition on the inner shell - CMB - of the volume boundary. Combining the various properties of both types of boundary conditions we find as necessary constraints for H:

$$H(r_0) = 0\,, \quad H(r_1) = 0\,, \quad \partial_r \left(\frac{1}{r^2}\, \dot{H} \right) (r_0) = 0\,, \quad \dot{H}(r_1) = 0\,. \tag{3.45}$$

Table 3.1: In this table, we present the coefficients of the radial forcing function, i.e. the temperature field, depending on the harmonic degree l, for the specific polynomial ansatz function H that was chosen in this work.

coefficient	no-slip	free-slip	mixed
c_0	$\frac{1}{4}(12-\mu_l^2)(2-\mu_l^2)$	$\frac{7}{24}(12-\mu_l^2)(2-\mu_l^2)$	$\frac{3}{8}(12-\mu_l^2)(2-\mu_l^2)$
c_1	$\frac{3}{2}\mu_l^2(6-\mu_l^2)$	$\frac{15}{8}\mu_l^2(6-\mu_l^2)$	$\frac{17}{8}\mu_l^2(6-\mu_l^2)$
c_2	$\frac{13}{4}\mu_l^2(\mu_l^2-2)$	$\frac{49}{12}\mu_l^2(\mu_l^2-2)$	$\frac{17}{4}\mu_l^2(\mu_l^2-2)$
c_3	$3\mu_l^2(2-\mu_l^2)$	$\frac{7}{2}\mu_l^2(2-\mu_l^2)$	$\frac{7}{2}\mu_l^2(2-\mu_l^2)$
c_4	$\mu_l^2(\mu_l^2-6)$	$\mu_l^2(\mu_l^2-6)$	$\mu_l^2(\mu_l^2-6)$

Again, applying (3.31) leads to the following system of linear equations:

$$\begin{pmatrix} H_1(r_0) & H_2(r_0) & H_3(r_0) & H_4(r_0) \\ H_1(r_1) & H_2(r_1) & H_3(r_1) & H_4(r_1) \\ \partial_r\left(\frac{1}{r^2}\dot{H}_1\right)(r_0) & \partial_r\left(\frac{1}{r^2}\dot{H}_2\right)(r_0) & \partial_r\left(\frac{1}{r^2}\dot{H}_3\right)(r_0) & \partial_r\left(\frac{1}{r^2}\dot{H}_4\right)(r_0) \\ \dot{H}_1(r_1) & \dot{H}_2(r_1) & \dot{H}_3(r_1) & \dot{H}_4(r_1) \end{pmatrix} \begin{pmatrix} a \\ b \\ c \\ d \end{pmatrix} = \begin{pmatrix} -H_0 \\ -H_0 \\ 0 \\ 0 \end{pmatrix}. \tag{3.46}$$

Inserting (3.30) here leads to

$$\begin{pmatrix} r_0 & r_0^2 & r_0^3 & r_0^4 \\ r_1 & r_1^2 & r_1^3 & r_1^4 \\ -2/r_0^3 & -2/r_0^2 & 0 & 4 \\ 1 & 2r_1 & 3r_1^2 & 4r_1^3 \end{pmatrix} \begin{pmatrix} a \\ b \\ c \\ d \end{pmatrix} = \begin{pmatrix} -H_0 \\ -H_0 \\ 0 \\ 0 \end{pmatrix}. \tag{3.47}$$

For the choice $H_0 = 1$, $r_0 = 1$, $r_1 = 2$, this system turns into

$$\begin{pmatrix} 1 & 1 & 1 & 1 \\ 2 & 4 & 8 & 16 \\ -2 & -2 & 0 & 4 \\ 1 & 4 & 12 & 32 \end{pmatrix} \begin{pmatrix} a \\ b \\ c \\ d \end{pmatrix} = \begin{pmatrix} -1 \\ -1 \\ 0 \\ 0 \end{pmatrix}, \tag{3.48}$$

with the unique solution $a = -7/2$, $b = 17/4$, $c = -17/8$ and $d = 3/8$. Thus, the fourth-order polynomial that satisfies the desired boundary conditions is

$$H(r) = \frac{3}{8}\,r^4 - \frac{17}{8}\,r^3 + \frac{17}{4}\,r^2 - \frac{7}{2}\,r + 1\,. \tag{3.49}$$

In analogy to the two previous sections, inserting this polynomial into (3.29) then yields the desired temperature distribution. In general, applying the differential operator in (3.29) to a fourth-order polynomial - here H - results in a rational function $f(r)$. Its form can be expressed as

$$f(r,l) = \sum_{k=0}^{4} \frac{c_k(l)}{r^k}\,, \tag{3.50}$$

with coefficients $c_k(l) \in \mathbb{R}$, $k = 0, ..., 4$, that vary with degree l. Table 3.1 lists these coefficients resulting from our three different selections of boundary condition pairs, while Figure 3.2 gives a graphical representation of the function for some selected harmonic degrees in case of all three settings.

Table 3.2: Details of the meshes used in our experiments: *mt* represents the number of subdivisions along the edges of the initial triangles of the icosahedron, *#refs* the number of refinement steps performed, *#tets* the number of tetrahedrons in the fine mesh, *#dofs* the number of degrees of freedom in the Stokes problem, *#resolution* the approximate resolution on the outer surface when scaled to the Earth's radius.

mt	#refs	#tets	#dofs	resolution
32	4	1,966,080	$1.3 \cdot 10^6$	240 km
64	5	15,728,640	$10.4 \cdot 10^6$	120 km
128	6	125,829,120	$83.6 \cdot 10^6$	60 km

3.5 Numerical experiments

We demonstrate the applicability of our suggested accuracy benchmark by testing it within the prototype of a new mantle convection framework. The latter is based on Hierarchical Hybrid Grids (HHG), a carefully designed and implemented software package for high performance finite element simulations with multigrid solvers. HHG employs an unstructured mesh for geometry resolution which is then refined in a regular fashion. The resulting mesh hierarchy is well suited to implement matrix-free geometric multigrid methods. Multigrid techniques form an essential building block in any large-scale Stokes solver, most commonly as pre-conditioner within a Krylov solver, or alternatively as inner solver in a Schur complement approach or in the form of a monolithic solver that treats the full Stokes system all-at-once. For details on HHG and the mantle convection prototype implementation see e.g. Bergen and Hülsemann (2004); Bergen et al. (2005, 2006, 2007); Gmeiner et al. (2015); Bauer et al. (2016, 2019).

For our tests we implemented the no-slip version of the benchmark that was presented in the previous chapter, i.e. we generate a synthetic velocity field v by means of the polynomial ansatz function H from (3.36). Selecting a degree and order pair (l, m) the temperature field that is generated by v can be derived using (3.50) and is used as forcing term for the Stokes equation in HHG.

The Stokes problem is solved on a thick spherical shell with inner radius 1 and outer radius 2. This domain is discretised using an icosahedral meshing approach, similar to the one described in Baumgardner (1985); Baumgardner and Frederickson (1985), to generate a coarse input mesh for HHG. The resulting mesh is composed of 480 tetrahedra. The latter are then uniformly refined several times following the rules of Bey (1995). The resulting new vertices are then projected onto radial layers to form the actual computational mesh (see Weismüller, 2016; Bauer et al., 2019). Table 3.2 gives further details on the meshes used in our experiments.

On the mesh the Stokes problem is discretised with P_1 elements, i.e. first-order Lagrangian ansatz functions. As this approach is not inf-sup stable, we stabilise it by treating pressure on a mesh that is one times less often refined than the one for velocity, a strategy commonly referred to as P_1-iso-P_2 approach.

We make two comments concerning the discretisation approach. The original HHG framework and, thus, also the prototype convection code employed in our tests was basically limited to P_1 elements. A new framework, based on the original HHG ideas, is currently being developed which supports data structures allowing to implement more sophisticated element types. Details on the new framework, denoted HyTeG, can be found in Kohl et al. (2019). Also, the tested configurations are very moderate for HHG, which has been shown to be able to efficiently solve the core equations of mantle convection with up to 10^{13} dofs (Gmeiner et al., 2016), and been successfully used to simulate geodynamical models involving variable viscosity and dynamic topography with up to 10^{11} dofs (Bauer et al., 2019).

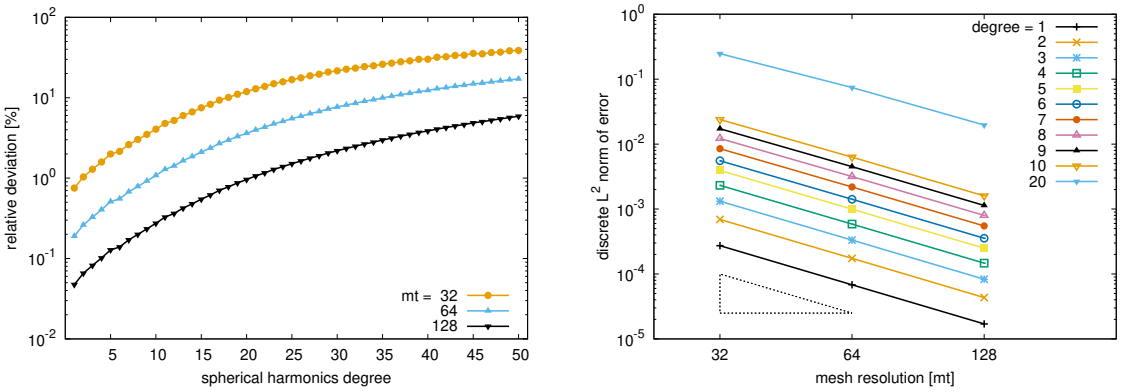

Figure 3.3: Relative deviation and discrete L^2 norm of the error for different harmonic degrees and mesh resolutions.

However, for our purposes such extreme resolutions are not necessary.

The linear system of equations resulting from the discretisation process is solved using a classical Schur complement approach with conjugate gradients (CG) as outer iteration and multigrid (MG) as inner iteration, both implemented in HHG in a matrix-free fashion, see Bauer et al. (2016) for details. We stop the iteration once the discrete L^2 norm of the error has not changed for four consecutive steps. Due to the moderate problem sizes tested the simulations could be run on the Tectonic High-Performance Simulator (TETHYS-2G), a machine dedicated to geophysical capacity simulations, (Oeser et al., 2006). The solution for v that is calculated with HHG can then be compared against the synthetic field.

Figure 3.3 presents the results of our experiments. Here we always fixed the order m to be zero and only varied the harmonic degree and the mesh resolution. The left part of the figure shows the development of the relative deviation for varying harmonic degree. This quantity represents the ratio of the discrete L^2 norm of the error, between the analytic velocity and its reconstructed discrete approximation, and the L^2 norm of the analytic velocity itself. The results are as were to be expected. The relative deviation increases with harmonic degree, as high-frequency structures are of course harder to resolve, while it reduces with increased resolution. For mt=128 the observed relative deviation is always smaller than 6% for all l up to degree 50 and smaller than 1% for $l \leqslant 20$.

In the right part of Figure 3.3 the discrete L^2 norm of the absolute error is shown for selected degrees. As one can see we obtain second-order convergence in this quantity, just as one would expect from Finite Element theory for piecewise-linear ansatz functions.

It is quite obvious that during an ongoing project and development of a new numerical code, benchmark tests like the one presented in this work, are crucial to verify the suitability of the selected numerical algorithms and the correctness of their implementation.

3.6 Discussion

Modern supercomputers provide immense computational power. This trend is bound to continue with exa-scale machines looming on the horizon. For geodynamicists this means that it is possible to construct models of dynamic processes in the Earth that are more and more sophisticated. On the one hand, in forward models, higher spatial resolutions - on the km-scale for the whole Earth's mantle - may be implemented and simulations be conducted over longer times scales using more complex

physics. On the other hand, in inverse models, determinations of the unknown initial temperature distribution of the Earth's mantle at some point in the past may become feasible (e.g., Colli et al., 2018). Here repeated executions of forward and adjoint runs are necessary to achieve an iterative approach to the optimal initial condition, resulting in higher computational costs. In order to exploit these trends to their full potential, efficient methods for the testing and verification of individual code components for numerical accuracy are important. To this end, mantle convection benchmarks have relied on the computation with different codes of a few well-defined problem(s).

In this work, we presented a detailed derivation of a semi-analytic solution to the 3-D Stokes equation in a spherical shell using methods of spectral analysis. Whereas a coupled system of second-order partial differential equations evolves from the original continuity and momentum equation, we find essential simplifications. Our approach ends up with a single ordinary differential equation that relates the velocity field directly to the flow inducing driving forces. The simplification arises from various assumptions we make on the flow properties. Due to imposed incompressibility, the intrinsic three free parameters of the velocity field are reduced to two, a poloidal and a toroidal component. Furthermore, a constant viscosity inside the whole domain enforces the toroidal part to vanish, and one single free parameter remains.

The derived direct relation between velocity and driving forces is only valid under the described assumptions on the flow properties. If we additionally allow for a radially varying viscosity and/or density profile, we end up with a more complex linear system of differential equations (Richards and Hager, 1984) that needs to be solved by a propagator matrix approach. A further level of complexity can be introduced by making this radial viscosity profile even temperature-dependent. A spectral representation of the resulting coupled system of momentum and energy equation can be found in Kameyama et al. (2013), where a linear stability analysis on the onset of thermal convection of a fluid in a spherical shell is described.

The derived relation of our work can be exploited to determine the forcing term from a prescribed velocity field. In other words, for a given velocity field it is possible to compute the corresponding right-hand side. This feature lends itself to the design of a benchmark set-up for numerical Stokes solvers, where a velocity field is sought for a given right-hand side. Our benchmark is self-contained and can be performed without relying on the numerical solutions from other codes. Implementation of the benchmark is straightforward as it relies on building blocks, such as the Stokes solver and tools to evaluate the associated Legendre functions for spherical harmonics, that are readily available in 3-D spherical mantle convection codes. We demonstrate the applicability of the benchmark by verifying the convergence behaviour of the Stokes solver in the prototype of a new mantle convection modelling framework for high performance computing based on Hierarchical Hybrid Grids.

Chapter 4

The Earth's gravitational field

4.1 Mathematical formulation

Recent satellite missions like CHAMP, GRACE and GOCE have been measuring the Earth's gravitational field in a highly accurate way. Due to the (almost) global coverage of the satellite's orbit, a nearly uniform dataset is provided and may be analysed and interpreted by a variety of scientists. Since the Earth's gravitational field is a direct response of the processes, i.e. redistribution of masses, within the Earth's interior, gravity is one of the most important datasets that geoscientists are provided with. Newton's law states that the gravitational force between two bodies with masses m_x at the position $x \in \mathbb{R}^3$ and m_y at $y \in \mathbb{R}^3$ is proportional to their respective masses and inversely proportional to the distance between them. At x we find:

$$F_{\text{grav}}(x) = -G\frac{m_x m_y}{|x-y|^3}\,(x-y)\,, \tag{4.1}$$

where $G = 6.67 \cdot 10^{-11}\ \mathrm{m}^3/(\mathrm{kg}\cdot\mathrm{s}^2)$ is the gravitational constant. With $F_{\text{grav}}(x) = m_x g(x)$ with $g(x)$ the gravitational acceleration at x, we find a representation of g, independent of m_x:

$$g(x) = -\frac{Gm_y}{|x-y|^3}\,(x-y)\,. \tag{4.2}$$

This is the gravitational acceleration that can be observed at the point x. The presented scenario, involving two point masses can be extended to $N \in \mathbb{N}$ point masses m_i, $i = 1, ..., N$, that are located at $y_i \in \mathbb{R}^3$, $i = 1, ..., N$. In the limit $N \to \infty$, we can interpret the masses as a density distribution in the considered volume V:

$$g(x) = -G\sum_{i=1}^{N}\frac{m_i}{|x-y_i|^3}\,(x-y_i) \xrightarrow{N\to\infty} -G\int_V \frac{\rho(y)}{|x-y|^3}\,(x-y)\,\mathrm{d}V(y)\,. \tag{4.3}$$

Furthermore, it can be shown that the gravitational field is a potential, i.e. there exists a scalar field U such that $g(x) = -\nabla U(x)$. It can easily be verified that

$$U(x) = -\frac{Gm_y}{|x-y|}\,, \tag{4.4}$$

for the single point mass scenario. In analogy, for a density distribution we find that

$$U(x) = -G\int_V \frac{\rho(y)}{|x-y|}\,\mathrm{d}V(y)\,. \tag{4.5}$$

Remembering (1.171), we notice that we can express the inverse distance in terms of a spherical harmonic expansion. Defining $x := R\xi$ and $y := r\eta$ with $\xi, \eta \in \Omega$ and $r, R \in \mathbb{R}^+$, $R > r$, we immediately find that

$$\begin{aligned} U(x) &= -G \int_V \frac{1}{R} \sum_{l=0}^{\infty} \left(\frac{r}{R}\right)^l \frac{4\pi}{2l+1} \sum_{m=-l}^{l} Y_{l,m}(\xi)\, Y_{l,m}(\eta)\, \rho(y)\, \mathrm{d}V(y) \\ &= -\sum_{l=0}^{\infty} \sum_{m=-l}^{l} Y_{l,m}(\xi)\, \frac{4\pi G}{2l+1} \frac{1}{R^{l+1}} \int_V r^l\, Y_{l,m}(\eta)\, \rho(y)\, \mathrm{d}V(y)\,. \end{aligned} \tag{4.6}$$

Note that here we assumed x to be located in the exterior of the mass distribution. From this representation we see that the spherical harmonic coefficients of U can thus be expressed by

$$\boxed{U_{l,m}(R) = -\frac{4\pi G}{2l+1} \frac{1}{R^{l+1}} \int_V r^l\, Y_{l,m}(\eta)\, \rho(y)\, \mathrm{d}V(y)\,.} \tag{4.7}$$

In case that the observation point x is located below the mass distribution, i.e. $R < rR$ in the terms from above, the roles of r and R in the expansion of the inverse distance interchange and we end up with:

$$\boxed{U_{l,m}(R) = -\frac{4\pi G}{2l+1} R^l \int_V \frac{1}{r^{l+1}}\, Y_{l,m}(\eta)\, \rho(y)\, \mathrm{d}V(y)\,.} \tag{4.8}$$

Even though it is not possible to explicitly calculate the integral on the right-hand side, yet - the volume V is still arbitrary at this point - nevertheless, we can already identify the harmonic coefficients $\rho_{l,m}(r)$ of the underlying density field, hidden in the surface part of the volume integral. Thus, one of the most important observations that we can make from this representation, is the direct **coupling** between the potential and density harmonic coefficients of same degree and order. Later, when we explicitly discuss spherical geometries, this coupling becomes even more evident (see e.g. (4.23)).

The essential coupling factor $(r/R)^l$ (or $(R/r)^l$, respectively) indicates that the gravitational signal of a density structure fades out exponentially with growing distance to the observer. This effect even amplifies exponentially with increasing harmonic degree. As a consequence, for high harmonic degrees, the potential coefficients can be identified almost directly with the respective density coefficients of the masses that are *closest* to the observer. Applied to the Earth, this means that small scale density structures that are located in the deep mantle, are just invisible for a gravitational observer at the surface. Thus, we can already deduce from here, that in order to explain the higher harmonic degrees of the Earth's gravitational field, we will probably have to look at processes that are located close to the Earth's surface. Signals from the deep mantle only survive the whole way up to the observer if they are generated by large scale structures, represented by the very low harmonic degrees. In the upcoming sections, we will find out that these immediate deductions that we just took from the representation (4.7) indeed turn out to be true.

Furthermore, in (4.7) we see that the dependence on the location of the observer only enters the equation through the factor of R^{l+1} in the denominator. Now, choosing the respective radial position as R_1 (in the exterior of the volume), we can rephrase (4.7) as

$$U_{l,m}(R_1) = \frac{1}{R_1^{l+1}}\, C\,, \tag{4.9}$$

where C is some fixed value that is dependent on the mass distribution. From this representation we immediately find that for a different radial location R_2 outside the volume, the harmonic coefficients

at the two different radii are related to each other by

$$U_{l,m}(R_2) = \left(\frac{R_1}{R_2}\right)^{l+1} U_{l,m}(R_1)\,. \tag{4.10}$$

For $R_2 > R_1$ this transformation is called **upward continuation**, where for $R_2 < R_1$ it is called **downward continuation**. Without diving much into details here, from the previous formula it can already be deduced that the process of upward continuation is stable, where the downward continuation is unstable since in that case, the fraction R_1/R_2 is greater than 1 and grows exponentially with degree l. Thus, in the process of downward continuation, errors and noise in the higher degree harmonics are getting amplified. The concept of stability in this context can directly be linked to the ill- and well-posedness criteria of Hadamard (1902) for inverse problems. Now choosing R from above as the lower reference radius, we can express the potential at any $x \in \mathbb{R}^3$ with $|x| = r > R$, $x = r\xi$, $\xi \in \Omega$, in terms of the coefficients at radius R by

$$U(x) = \sum_{l=0}^{\infty} \sum_{m=-l}^{l} \left(\frac{R}{r}\right)^{l+1} U_{l,m}(R)\, Y_{l,m}(\xi)\,. \tag{4.11}$$

In particular, we can use this expression to determine the radial derivative of the potential in terms of the harmonic coefficients. Here we find that

$$\partial_r U(x) = -\sum_{l=0}^{\infty} \sum_{m=-l}^{l} \frac{l+1}{r} \left(\frac{R}{r}\right)^{l+1} U_{l,m}(R)\, Y_{l,m}(\xi)\,. \tag{4.12}$$

In the following, we will have a closer look at some particular harmonic coefficients of the gravitational potential, especially in terms of their physical meaning. Returning to (4.7) and using the explicit representation of the spherical harmonics (1.219), we find that

$$\begin{aligned} U_{0,0}(R) &= -\frac{4\pi G}{R} \int_V Y_{0,0}(\eta)\, \rho(y)\, \mathrm{d}V(y) \\ &= -\frac{\sqrt{4\pi} G}{R} \int_V \rho(y)\, \mathrm{d}V(y) \\ &= -\sqrt{4\pi}\, \frac{GM}{R}\,, \end{aligned} \tag{4.13}$$

with the total mass M of the volume. $(GM)/R$ equals the gravitational potential of a homogeneous sphere with mass M and radius R. Thus, all coefficients of degree greater than zero describe the deviation of the potential from the one of a solid sphere. Here we also recognise the reason why in the geodetic community, the spherical harmonic normalisation is not set to 1 but to $\sqrt{4\pi}$. This geodetic normalisation yields that the $U_{0,0}$ coefficient exactly equals the *reference potential* $(GM)/R$. Furthermore, in geodesy it is also common to extract this factor from the harmonic coefficients in order to achieve $U_{0,0} = 1$.

When we examine the harmonic coefficients of degree 1 in detail, we find by using again (1.219) that

$$\begin{aligned} U_{1,0}(R) &= -\sqrt{\frac{4\pi}{3}} \frac{G}{R^2} \int_V r\, t\, \rho(y)\, \mathrm{d}V(y)\,, \\ U_{1,1}(R) &= -\sqrt{\frac{4\pi}{3}} \frac{G}{R^2} \int_V r \sqrt{1-t^2}\, \cos\varphi\, \rho(y)\, \mathrm{d}V(y)\,, \\ U_{1,-1}(R) &= -\sqrt{\frac{4\pi}{3}} \frac{G}{R^2} \int_V r \sqrt{1-t^2}\, \sin\varphi\, \rho(y)\, \mathrm{d}V(y)\,. \end{aligned} \tag{4.14}$$

Having a closer look at the integrals, we see that here we find all vector components from the transformation of spherical polar into Cartesian coordinates (see (1.24)), i.e. the integrals can be rewritten as

$$U_{1,0} : \int_V x_3\,\rho(y)\,\mathrm{d}V(y)\,, \quad U_{1,1} : \int_V x_1\,\rho(y)\,\mathrm{d}V(y)\,, \quad U_{1,-1} : \int_V x_2\,\rho(y)\,\mathrm{d}V(y)\,. \tag{4.15}$$

From mechanics it is known that these integrals represent the coordinates of the center of mass. Thus, if we follow the convention that the origin of our coordinate system falls into the center of mass (**geocentric coordinate system**) - which we do and which is used in the actual measurements of gravitational data that we present in the following chapter - then all these integrals vanish and all harmonic coefficients of degree 1 turn out to be zero.

Furthermore, in Section 4.8 we will show that the degree 2 coefficients can directly be translated into components of the inertia tensor of the considered volume. Since per definition the x_3 axis falls into the rotation axis, i.e. the largest principle axis of inertia, the inertia tensor is diagonal with respect to the x_3 component, i.e. all off-diagonal elements that include x_3 vanish. From the **McCullagh formula** (4.85) and (4.86) that we will derive in Section 4.8 we see that these non-diagonal elements correspond to the harmonics of order 1, i.e. the $U_{2,1}$ and $U_{2,-1}$ coefficient of the gravitational potential. Thus, we also expect these two coefficients to vanish. Actually, in the satellite derived data that we will present in the next section, both of these coefficients are not exactly zero due to slight differences between the Earth's rotational axis and largest principle axis of inertia but negligibly small compared to the other coefficients (three orders of magnitude smaller). These five non-present coefficients in the harmonic expansion of the gravitational potential are called **forbidden** or **inadmissible harmonics** (Heiskanen and Moritz, 1967).

Now, we continue by examining special cases of (4.7) and (4.8) that will be useful in the following proceeding. If we assume the volume V to be a spherical shell that is bounded by the radii $r_0 < r_1$ we find for $R > r$ that

$$U_{l,m}(R) = -\frac{4\pi G}{2l+1}\frac{1}{R^{l+1}}\int_{r_0}^{r_1} r^{l+2}\int_\Omega Y_{l,m}(\eta)\,\rho(r\eta)\,\mathrm{d}\omega(\eta)\,\mathrm{d}r\,. \tag{4.16}$$

In case of a constant density $\hat{\rho}_0$, we can put $\hat{\rho}_0$ outside the integral and the previous relation simplifies to

$$U_{l,m}(R) = -\frac{4\pi G\hat{\rho}_0}{(2l+1)(l+3)}\frac{r_1^{l+3}-r_0^{l+3}}{R^{l+1}}\int_\Omega Y_{l,m}(\eta)\,\mathrm{d}\omega(\eta)\,. \tag{4.17}$$

This representation will explicitly be used in Section 4.7 where the gravity signals of spherical cubes with constant density need to be calculated. There, the integration on the right-hand side will then not be executed over the whole unit sphere Ω but only over a part of it, which will make the explicit evaluation quite complex. If we indeed consider a complete spherical shell with constant density, the integral simplifies remarkably. In this case we can rephrase (4.17) and find

$$\begin{aligned} U_{l,m}(R) &= -\frac{(4\pi)^{\frac{3}{2}}G\hat{\rho}_0}{(2l+1)(l+3)}\frac{r_1^{l+3}-r_0^{l+3}}{R^{l+1}}\int_\Omega Y_{l,m}(\eta)\,\frac{1}{\sqrt{4\pi}}\,\mathrm{d}\omega(\eta) \\ &= -\frac{(4\pi)^{\frac{3}{2}}G\hat{\rho}_0}{(2l+1)(l+3)}\frac{r_1^{l+3}-r_0^{l+3}}{R^{l+1}}\int_\Omega Y_{l,m}(\eta)\,Y_{0,0}(\eta)\,\mathrm{d}\omega(\eta)\,. \end{aligned} \tag{4.18}$$

Now, due to the orthonormality of the spherical harmonics, the degree zero coefficient is the only one that is not vanishing and can be determined as:

$$U_{0,0}(R) = -\sqrt{4\pi}\,\frac{G}{R}\left(\frac{4}{3}\pi\left(r_1^3-r_0^3\right)\hat{\rho}_0\right)\,. \tag{4.19}$$

This result perfectly coincides with our previous interpretation of the zero harmonic (4.13) since here, on the right-hand side, we find the total mass of the spherical shell.

If we again switch the roles of r and R and define the observation point to be located below the mass distribution, i.e. in this example in the interior of the spherical shell, (4.16) turns into

$$U_{l,m}(R) = -\frac{4\pi G}{2l+1} R^l \int_{r_0}^{r_1} \frac{1}{r^{l-1}} \int_{\Omega} Y_{l,m}(\eta)\, \rho(r\eta)\, \mathrm{d}\omega(\eta)\, \mathrm{d}r\,, \tag{4.20}$$

and instead of (4.17) we find

$$U_{l,m}(R) = \frac{4\pi G \hat{\rho}_0}{(2l+1)(l-2)} \left(\frac{1}{r_1^{l-2}} - \frac{1}{r_0^{l-2}} \right) R^l \int_{\Omega} Y_{l,m}(\eta)\, \mathrm{d}\omega(\eta)\,. \tag{4.21}$$

Also here, we can exploit the orthonormality of the spherical harmonics to find for the only non-vanishing coefficient $U_{0,0}$ that

$$U_{0,0}(R) = -\sqrt{4\pi}\, (2\pi G \hat{\rho}_0) \left(r_1^2 - r_0^2 \right)\,. \tag{4.22}$$

Here, it is very interesting to see that there is no more dependence on R on the right-hand side of the equation. This means that the gravitational potential is constant everywhere inside the spherical shell and as a consequence there is no gravitational acceleration. The interior of a spherical shell with a homogeneous density distribution is gravity-free space.

As we already have discussed before, we can identify the surface integral on the right-hand side of (4.16) and (4.20) with the spherical harmonic coefficients of the density distribution. In this way, we can reformulate (4.16) as

$$U_{l,m}(R) = -\frac{4\pi G}{2l+1} \frac{1}{R^{l+1}} \int_{r_0}^{r_1} r^{l+2} \rho_{l,m}(r)\, \mathrm{d}r\,, \tag{4.23}$$

and for $R < r$ we find:

$$U_{l,m}(R) = -\frac{4\pi G}{2l+1} R^l \int_{r_0}^{r_1} \frac{1}{r^{l-1}}\, \rho_{l,m}(r)\, \mathrm{d}r\,. \tag{4.24}$$

Finally, we discuss the scenario that we have already come across in Section 2.3 when we investigated an explicit solution method for the Stokes system in mantle dynamics, i.e. the propagator matrix approach. Here we divided our domain of interest, the spherical shell, into n equidistant layers of thickness $\Delta r := (r_1 - r_0)/n$ with layer boundaries b_j, $j = 1, ..., n+1$. Each of these sub-shells has a constant density, or more precisely, constant respective harmonic coefficients $\rho_{l,m}(b_j)$. Under these conditions, the integral in (4.23) turns into a finite sum and the coefficients of the exterior solution can be written as:

$$U_{l,m}(R) = -\frac{4\pi G}{2l+1} \frac{1}{R^{l+1}} \sum_{j=1}^{n} \rho_{l,m}(b_j) \int_{b_j}^{b_{j+1}} r^{l+2}\, \mathrm{d}r\,. \tag{4.25}$$

Here, one could easily solve the integrals on the right-hand side exactly, like we also did before in various other representations. But at this point it is common and regularly found in literature to additionally approximate the radial integrals by the product of layer thickness and the value of the

integrand at one of the boundaries. This simplification is perfectly valid if the radial grid is sufficiently fine. Under this assumption, (4.25) becomes

$$U_{l,m}(R) = -\frac{4\pi G}{2l+1} \sum_{j=1}^{n} b_j \left(\frac{b_j}{R}\right)^{l+1} \rho_{l,m}(b_j)\, \Delta r\,. \tag{4.26}$$

In analogy, for the interior solution we find

$$U_{l,m}(R) = -\frac{4\pi G}{2l+1} \sum_{j=1}^{n} b_j \left(\frac{R}{b_j}\right)^{l} \rho_{l,m}(b_j)\, \Delta r\,. \tag{4.27}$$

These are the most commonly used representations of the harmonic coefficients of the gravitational potential for a given layered density distribution inside the Earth's mantle.

At last we again make a detour to the distributional space. As we have learned before in this work, within the concept of *fundamental solutions* (or Green's functions), it is crucial to convert the underlying equations into a distributional formulation and represent the driving quantities - here the density field - in terms of a delta distribution. Thus, if we set - see e.g. Section 2.3.2 for a detailed explanation - $\rho_{l,m}(r) = \delta(r - b_j)$ for a fixed layer b_j, $j \in \{1, ..., n\}$, we immediately find from (4.23) and (4.24) that for $R > b_j$ we have

$$U_{l,m}(R) = -\frac{4\pi G}{2l+1}\, b_j \left(\frac{b_j}{R}\right)^{l+1}, \tag{4.28}$$

and in the case of $R < b_j$ we find

$$U_{l,m}(R) = -\frac{4\pi G}{2l+1}\, b_j \left(\frac{R}{b_j}\right)^{l}. \tag{4.29}$$

These are exactly the relations that we already used in Section 2.4 in the context of defining appropriate boundary conditions for the linear system of differential equations that evolved from the Stokes equation (see (2.142) and (2.143)).

Moreover, in the previous chapters, we have learned that for all governing equations, like e.g. the Stokes or the continuity equation, it was very helpful to have a representation in terms of differential operators instead of an integral formulation. The advantage here lies in the possible conversion of the respective operators into spherical coordinates and the exploitation of the eigenfunction property of the spherical harmonics. In Chapter 1 we already gave a brief insight into the strategy on how to find an equivalent formulation of the gravitational potential, i.e. the gravitational Poisson equation (1.108):

$$\Delta U(x) = 4\pi G \rho(x)\,. \tag{4.30}$$

For the complete proof, one needs a descent basis of distributional theory, which is beyond the scope of this work. Here, the reader is referred to e.g. Wermer (1974). Nevertheless, one special case of this equation, i.e. the statement that the gravitational potential is harmonic outside a mass distribution, is not difficult to prove. We define $V \subset \mathbb{R}^3$ to be closed and choose an $x \notin V$ as the observation point. Starting from the representation (4.3) of the gravitational acceleration, we apply the divergence to both sides of the equation to find:

$$\nabla_x \cdot g(x) = -G\, \nabla_x \cdot \int\limits_V \frac{\rho(y)}{|x-y|^3}\,(x-y)\,\mathrm{d}V(y) = -G \int\limits_V \rho(y)\, \nabla_x \cdot \left(\frac{x-y}{|x-y|^3}\right) \mathrm{d}V(y)\,. \tag{4.31}$$

Since $x \notin V$ and V is closed, the integrand contains no singularity and thus, interchanging differentiation and integration is valid without further concerns. If V was not closed, x could theoretically be

an accumulation point of V and thus, again produce a singularity in the integrand. Now, a straightforward calculation shows that

$$\begin{aligned}\nabla_x \cdot \left(\frac{x-y}{|x-y|^3}\right) &= \frac{1}{|x-y|^3}\,\nabla_x \cdot (x-y) + (x-y)\cdot\nabla_x \left(\sum_{i=1}^{3}(x_i-y_i)^2\right)^{-\frac{3}{2}} \\ &= \frac{3}{|x-y|^3} + (x-y)\cdot\left(\sum_{i=1}^{3}\epsilon^i\left(-\frac{3\,(x_i-y_i)}{|x-y|^5}\right)\right) \\ &= \frac{3}{|x-y|^3} - \frac{3}{|x-y|^5}\sum_{i=1}^{3}(x_i-y_i)^2 = 0\,.\end{aligned} \tag{4.32}$$

With this information, (4.31) immediately turns into

$$\nabla_x \cdot g(x) = 0\,. \tag{4.33}$$

Including the relation of g to the gravitational potential U, $g = -\nabla U$, we end up with the Laplace equation

$$\Delta U(x) = 0\,, \tag{4.34}$$

for all $x \notin V$.

4.2 Measurement and representation

Next to the previously introduced gravitational potential U itself, there are a couple of (equivalent) alternative ways to represent the Earth's gravitational field. A very popular method is the usage of the so-called **geoid**, a representation that is based on the comparison of the actual potential U to a reference figure and its corresponding (reference) potential - which we denote by U_0 in the following. Here, we investigate how much the actual potential level U on the (virtual) surface of the reference figure deviates from the reference potential U_0. We then define the geoid height N for any point on this reference surface as the elevation (in [m]) that we have to move radially up or down to feel the potential U_0. Thus, under the assumption of a reference figure with a surface that is homeomorphic to the unit sphere - like the most common choice of e.g. a spherical or ellipsoidal object - we can define the geoid as a function on the unit sphere $N : \Omega \to \mathbb{R}$.

In theory, since it always depends on the context and the objects under consideration, the reference potential U_0 also may vary along its surface, i.e. also be a function on the unit sphere. But in practice, it is most common to choose a reference object with a surface that has the same potential U_0 everywhere. In this case, also the geoid is - per definition - an equipotential surface. While per se, it is just a mathematical construct, this certain property makes it also very useful in a practical context. Since the potential is equal everywhere along the surface, the gradient of the potential, i.e. the vector of gravitational acceleration g, is orthogonal to the geoid at each point on its surface. This makes the geoid very interesting e.g. in the context of plumb lines (see also Heiskanen and Moritz, 1967). Furthermore, since there are no gravitational forces tangential to the geoid surface, a fluid would take exactly the form of the geoid to be in equilibrium - without taking external forces into account. Therefore, considering the real Earth, the ocean surfaces can be regarded as being a good approximation to the Earth's geoid.

Since per definition - as being a disturbed quantity (compare to the 'tilde' quantities of the previous chapters) - in most cases the geoid height N is much smaller than the radius (or radii) of the reference surface, the application of Taylor's series provides a suitable way to determine N explicitly. More precisely, for the potential at a point $x_N \in \mathbb{R}^3$ with $|x_N| = R + N$, where $N \ll R$ and $x_N = (R+N)\xi$, $\xi \in \Omega$, we find to first order that

$$U(x_N) = U(x) + \partial_r U(x) N(\xi)\,, \tag{4.35}$$

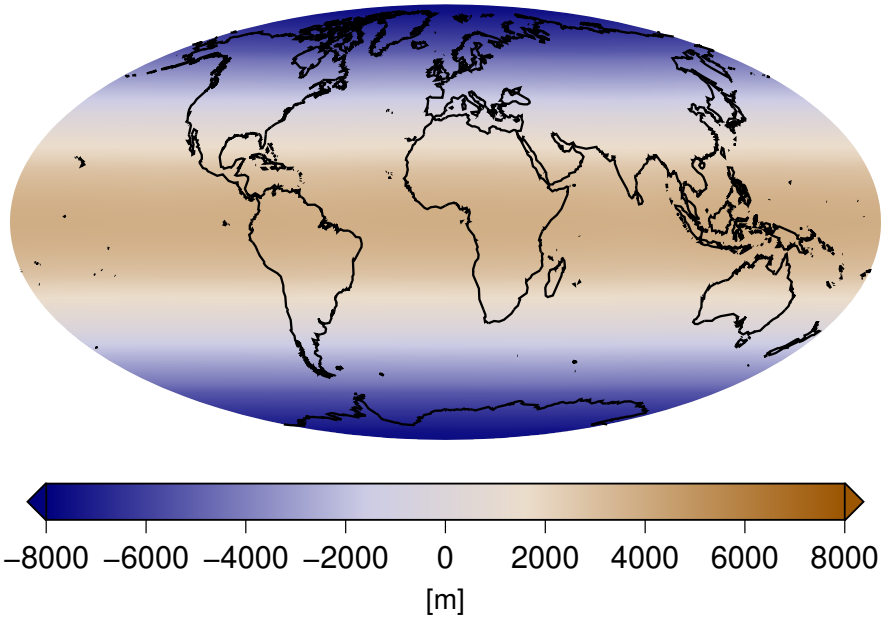

Figure 4.1: Geoid derived from the GRACE data set EIGEN-5C using the reference potential of a non-rotating reference frame. The predominant effect is the equatorial bulge and the polar flattening due to the centrifugal force.

where $x \in \mathbb{R}^3$ with $|x| = R$ and $x = R\xi$ with the same $\xi \in \Omega$ as above is a point on the reference surface. Since $g(x) = -\nabla U(x)$ and assuming that the tangential components of g are significantly smaller than the radial parts, we can approximate $\partial_r U(x) \approx |g(x)|$. Inserting this into (4.35) then yields

$$N(\xi) = \frac{U(x_N) - U(x)}{|g(x)|} = \frac{U_0(\xi) - U(x)}{|g(x)|} = -\frac{\tilde{U}(x)}{|g(x)|}\,, \tag{4.36}$$

where $\tilde{U}(x)$ - in analogy to the previous chapter - denotes the disturbed potential with respect to $U_0(\xi)$. The above transformation between geoid and gravitational potential is called **Brun's formula**. Note that in this work we use the convention that the gravitational potential is negative and tends to zero towards infinity. Thus, a negative disturbed potential equals a positive density anomaly, such that the previous relation indeed identifies a geoid high with *mass surplus* and a geoid low with *mass deficit*.

While in theory, the reference potential may be chosen arbitrarily, one plausible strategy is to choose it in such a way that the zero harmonics of reference and actual field are identical. In this way one can ensure that the total mass of both volumes of consideration are exactly the same. A non-vanishing difference between the degree zero terms would only result in an overall positive or negative shift in the amplitude of the geoid but not affect its lateral shape. Furthermore, since when using a geocentric coordinate approach there are no degree 1 terms in the gravitational potential - as we showed in the previous section - the first non-zero coefficients in the harmonic representation of the geoid are then the degree 2 terms.

Note that so far, the above statements only consider a scenario where there are no rotational effects. This is perfectly fine for all analytic models that we have derived in the course of this work. In this case, we can identify U_0 and $\tilde{U}$ one-to-one with the already introduced quantities. The geoid reference object then simply states as a solid sphere with radius R (or r_1 as in Chapter 2) and constant

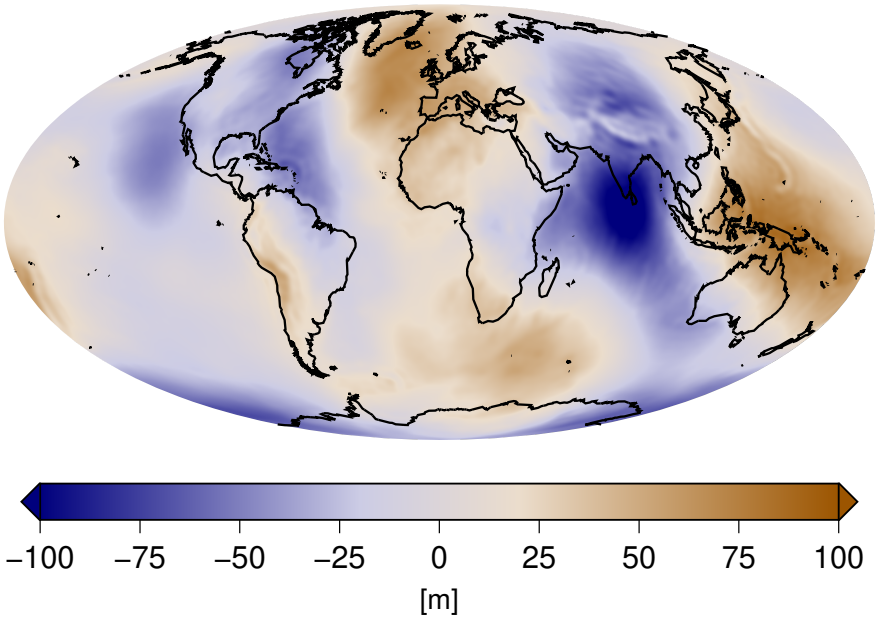

Figure 4.2: Geoid derived from the GRACE data set EIGEN-5C using the potential of the WGS 84 ellipsoid as the reference potential.

potential U_0. In very simple models (like e.g. the benchmark scenarios of Chapter 3), we can even consider to approximate $|g(x)|$ by a reference acceleration g_0.

But when we do a step towards observational quantities, e.g. gravitational signals or models that are derived from satellite based measurements, we are suddenly situated in a rotating reference frame. Here, the centrifugal force plays a non-negligible role and contributes to the total observed acceleration, creating an equatorial bulge and a polar flattening, which makes the Earth resemble more an ellipsoid than a sphere, both, in physical and in gravitational terms. In order to respect these additional physics in our notation, we substitute - for both observed and reference field - the purely gravitational potential U by the **geopotential** Φ that contains contributions from both gravitational and centrifugal effects. We then have

$$N_{\text{rot}}(\xi) = -\frac{\Phi(x) - \Phi_0(\xi)}{|\gamma(x)|}\,, \tag{4.37}$$

where $\Phi_0(\xi)$ is the respective reference geopotential and $\gamma(x) := -\nabla\Phi(x)$ the acceleration in terms of the geopotential. In contrast to the non-rotating case, due to the centrifugal content, the reference potential Φ_0 now can no longer be identified with the potential of a homogeneous sphere but with the one of a homogeneous ellipsoid. In order to illustrate the difference between the rotating and the non-rotating reference frame and to get an idea how much the centrifugal force influences the measurements, in Figure 4.1 we plot geoid data (up to degree $l = 100$) - derived from the satellite mission GRACE - using the non-rotating reference potential U_0 instead of the geopotential Φ_0 in the previous equation. We see that in this 'raw' data, the bulge is by far the predominant observation and in terms of the geoid, we notice an overall range in the amplitudes between ± 8 km. Here we used the EIGEN-5C data (see Foerste et al., 2008, in addition, a detailed description and data can be retrieved from *http://op.gfz-potsdam.de/grace/results/grav/g007_eigen-05c.html*), a hybrid gravity model up to harmonic degree and order 360 that is derived by combined satellite measurement from GRACE and various terrestrial data sets.

Since we just learned that the centrifugal part is not negligible and contributes a large signal to the overall data, the remaining task is now how to exactly choose the reference geopotential Φ_0 in order to take this effect into account. Here, the geodetic and geophysics community follow completely different approaches and goals. In geodesy, the goal is first, to find a reference ellipsoid that fits the observed data in the best possible way. And here, 'best' means that the goal is to minimise the (norm of) the respective geoid that corresponds to the chosen ellipsoid. Second, since there is a variety of institutes, research labs and scientists that process and work with the observed data, the goal is also to define a reference ellipsoid that is accepted in the whole community such that all publications may refer to the same reference field. In this way one would accomplish a high order of consistency throughout all published gravitational models. These two considerations have led to the **World Geodetic System (WGS)**, a universal standard with the latest revision WGS 84, that declares the reference to be the ellipsoid with semi-major axis $a = 6,378,137\,\mathrm{m}$ and semi-minor axis $b = 6,356,752.314245\,\mathrm{m}$, which results in an inverse flattening of $1/f = 298.257223563$. In particular, WGS 84 is the reference system that is used by the **Global Positioning System (GPS)**.

When looking at the shape of the geoid in Figure 4.1 a natural feeling arises that also here, a representation in spherical harmonics may be appropriate. Due to the rotational emergence, the ellipsoid is symmetric with respect to the equator and has no longitudinal dependence. Remembering the three different kinds of spherical harmonics of a fixed degree (compare to Figure 1.6), we see that only the zonal harmonics of even degree (odd degrees are not symmetric with respect to the equator) are able to contribute to this shape. Thus, we deduce that the only difference between U_0 and Φ_0 can be found in the even zonal harmonics. In reality, we even find that only the (2,0) and the (4,0) harmonic contains a significant contribution to the total signal. Using the parameters above, it is possible to determine these coefficients for the WGS 84 ellipsoid that can then be used as a reference value for all geoid calculations. Here, we find for the first two even zonal harmonics (Lemoine et al., 1997) that

$$\Phi_{2,0}^{\mathrm{WGS}} = \frac{1}{\sqrt{10\pi}} \frac{M_E\, G}{R_E}\, 0.10826 \cdot 10^{-2}\,, \quad \Phi_{4,0}^{\mathrm{WGS}} = -\frac{1}{\sqrt{18\pi}} \frac{M_E\, G}{R_E}\, 0.23709 \cdot 10^{-5}\,, \tag{4.38}$$

where M_E is the total mass and R_E the mean radius of the Earth. Using this reference system in (4.37) we find the **geodetic** geoid, derived from the gravity model EIGEN-5C, shown in Figure 4.2 with the famous pronounced geoid low over India. All effects due to the rotational bulge now *seem* to be erased and the geoid mainly reflects processes of the Earth's interior.

We deliberately chose the word *seem* in the last sentence since we know that the WGS reference geoid was designed just to provide a best fitting model but has no direct physical meaning. Thus, the geophysics community follows a completely different approach for the definition of the reference potential Φ_0. Geophysicists are interested in processes of the Earth's interior and in particular want to use the gravity data as a constraint for modelling these effects. Thus, the main goal here is to remove as much information as possible from the set of measured gravity data that does not correspond to processes of the solid Earth. More precisely, geophysicists are not interested in an ellipsoid that provides the best fit to the gravity data but want the resulting geoid to contain as little noise or error sources as possible with respect to processes inside the Earth. Thus, the idea here is to explicitly simulate or in other words, to create a model for the effects of the centrifugal force and use the respective 'purely physical' ellipsoid as a reference. Since this ellipsoid can in physical terms be described as being in a **hydrostatic equilibrium**, it is also called **hydrostatic ellipsoid**. In consequence, the geoid corresponding to the hydrostatic ellipsoid is regularly referred to in literature as **non-hydrostatic geoid**, since here, all hydrostatic effects are removed. As a personal side remark: people are regularly confused by this name since one could easily also imagine the contrary term 'hydrostatic geoid' for the same object. Here, the idea would be to especially emphasise the correspondence to the hydrostatic ellipsoid that serves as the basis object. So, you better make sure to explain in detail what you mean when using these expressions naively in public.

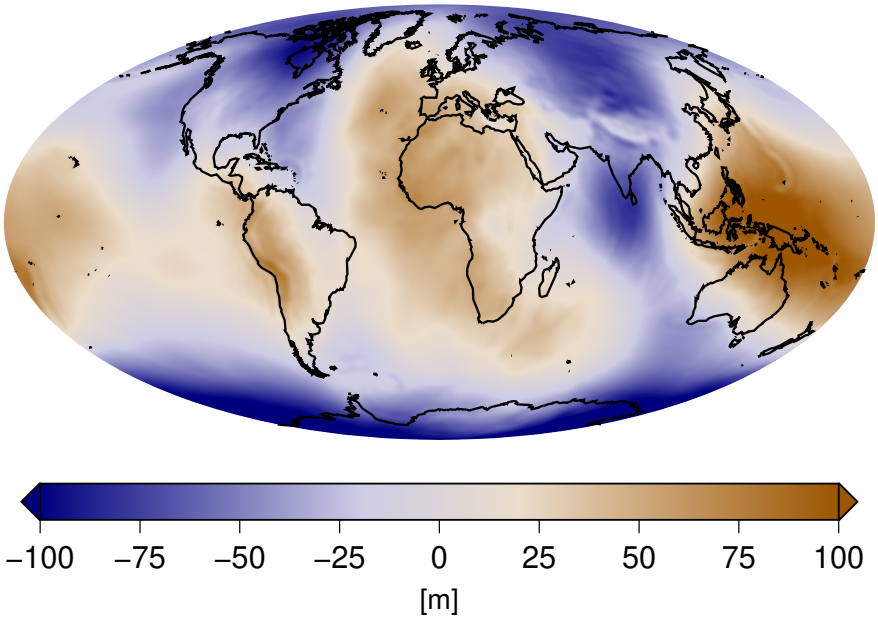

Figure 4.3: (Non-hydrostatic) geoid derived from the GRACE data set EIGEN-5C using the hydrostatic reference ellipsoid derived by Chambat et al. (2010).

A standard reference that developed the underlying equations and provided values for the respective $(2,0)$ and $(4,0)$ harmonics has been for a long time Nakiboglu (1982). In 2010, Chambat et al. (2010) provided an updated version of the work by Nakiboglu (1982), where some original errors were corrected and more recent values for estimates of the total mass and inertia of the Earth were used. The final values determined by Chambat et al. (2010) then state as

$$\Phi_{2,0}^{\mathrm{HYD}} = \frac{1}{\sqrt{10\pi}} \frac{M_E\, G}{R_E}\, 0.10712 \cdot 10^{-2}\,, \quad \Phi_{4,0}^{\mathrm{HYD}} = -\frac{1}{\sqrt{18\pi}} \frac{M_E\, G}{R_E}\, 0.296 \cdot 10^{-5}\,. \tag{4.39}$$

We see that - naturally - the coefficients of WGS and hydrostatic ellipsoid are similar but nevertheless, these differences turn out to be quite essential. This becomes more evident when we explicitly compare the data derived geoid corresponding to both reference frames. Already from the coefficients we can deduce that the WGS ellipsoid is more 'pronounced' than the hydrostatic one. This means that in the WGS system the gravitational effects arising from interior process are underestimated in the equatorial region and overestimated in polar regions. Exactly this shift can be observed when looking at the non-hydrostatic geoid, shown in Figure 4.3, where the Indian geoid low is elevated compared to the WGS geoid and the most pronounced low is now located in the area of the Ross Sea (Antarctica). Furthermore, we also see that the overall amplitudes are higher in the non-hydrostatic geoid than in the WGS version. This is a totally expected behaviour since the WGS system is especially constructed in the way that it minimises the residual geoid amplitude. Thus, the geoid with respect to *any* other reference frame will have larger amplitudes compared to WGS. Due to these essential differences, it is obligatory to use the non-hydrostatic reference frame in studies that try to refer gravity signals to geophysical processes. Thus, also in this work, from now on, we will only refer to the non-hydrostatic geoid as our reference model.

Besides the geoid, there is also a second common representation of the (disturbed) potential, which is the **gravity anomaly** Δg. It is defined as the difference of the absolute value of the gravitational acceleration on the geoid and of the one on the reference surface. Note that in contrast to our previous

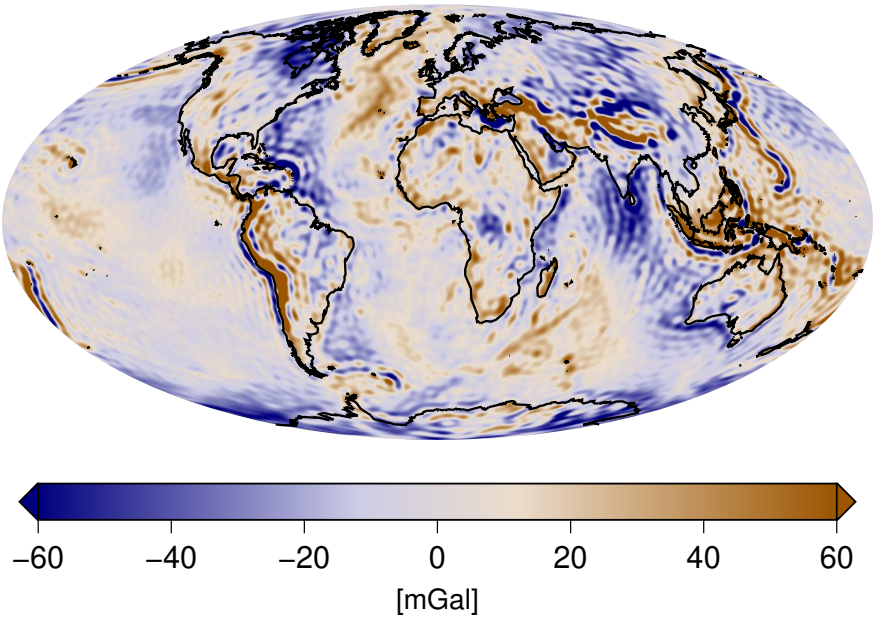

Figure 4.4: (Non-hydrostatic) gravity anomalies derived from EIGEN-5C.

convention for lower case letters, Δg is not a vector but a scalar quantity (and Δ does neither denote the Laplacian nor a (formal) difference), but we decided here to stick to the established notation in geodetic literature. We can safely do this without totally confusing the reader since this quantity will only appear explicitly in this section. Where we could think about the radial derivative $\partial_r \tilde{U}$ of the disturbing potential as being a good approximation for Δg at a first glance, we also have to take into account that the normal vector on the geoid differs from the one on the reference potential. Thus, the vectors of gravitational acceleration do not point into the same direction on both surfaces. From these considerations an additional correction terms arises (see e.g., Heiskanen and Moritz, 1967, for a detailed derivation) and we find for a point $x \in \mathbb{R}^3$ on the reference surface with $|x| = R$ and $x = R\xi$, $\xi \in \Omega$, that

$$\Delta g(\xi) = \partial_r \tilde{U}(x) + \frac{2}{R}\tilde{U}(x)\,. \tag{4.40}$$

Note that in analogy to the geoid, also the gravity anomaly can be regarded as a function on the unit sphere Ω. Also here, the information about the reference object is implicitly included in the disturbed potential $\tilde{U}$.

At this point - a little bit triggered by the radial derivative in the previous equation - we want to focus again on the spherical harmonic perspective and especially investigate how the harmonic coefficients of the different representations of the potential, that we have discussed in this section so far, are related to each other. Using (4.12) for the case $r = R$, we can restate (4.40) in terms of the spherical harmonic coefficients of the disturbed potential as

$$\begin{aligned}\Delta g(\xi) &= -\sum_{l=2}^{\infty}\sum_{m=-l}^{l}\frac{l+1}{R}\,\tilde{U}_{l,m}(R)\,Y_{l,m}(\xi) + \frac{2}{R}\sum_{l=2}^{\infty}\sum_{m=-l}^{l}\tilde{U}_{l,m}(R)\,Y_{l,m}(\xi)\\ &= -\frac{1}{R}\sum_{l=2}^{\infty}\sum_{m=-l}^{l}(l-1)\,\tilde{U}_{l,m}(R)\,Y_{l,m}(\xi)\,.\end{aligned} \tag{4.41}$$

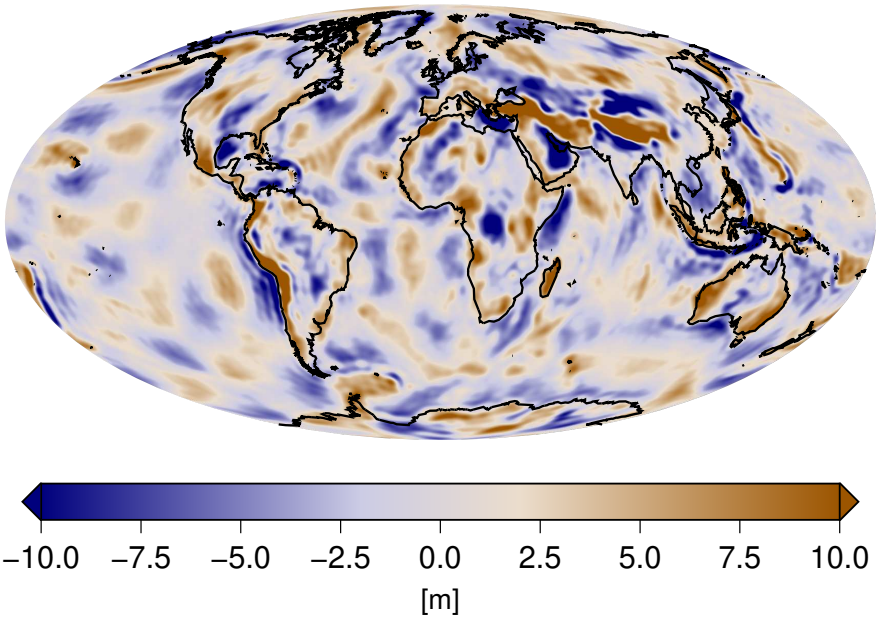

Figure 4.5: Filtered non-hydrostatic geoid (harmonic degrees $l = 12 - 100$) derived from EIGEN-5C.

Note that the summation starts at degree 2 since the degree 0 and degree 1 terms in the disturbed potential vanish in our case, as already demonstrated above. Since due to Brun's formula (4.36), there is a straightforward relation between the geoid and the disturbed potential, the spherical harmonic representation of the geoid immediately states as:

$$N(\xi) = -\frac{1}{|g(x)|} \sum_{l=2}^{\infty} \sum_{m=-l}^{l} \tilde{U}_{l,m}(R)\, Y_{l,m}(\xi)\,. \tag{4.42}$$

Summarised, we find that the harmonic coefficients of the three different representations of the disturbed potential, i.e. the potential $\tilde{U}$ itself, the geoid N and the gravity anomaly Δg, are related to each other by:

$$\begin{aligned} N_{l,m} &= -\frac{1}{|g(x)|}\, \tilde{U}_{l,m}(R)\,, \\ \Delta g_{l,m} &= -\frac{1}{R}\,(l-1)\,\tilde{U}_{l,m}(R) = \frac{|g(x)|}{R}\,(l-1)\,N_{l,m}\,. \end{aligned} \tag{4.43}$$

In particular, here we see that even in the case that N had contributions from degree 1 harmonics, they would vanish in the gravity anomalies due to the factor of $(l-1)$. In general, the unit for the gravity anomalies is $\mathrm{m/s^2}$ but due to usual small magnitude that can be observed in gravity data, one introduces the unit **Gal**, defined by $1\,\mathrm{Gal} := 0.01\,\mathrm{m/s^2}$ and $\mathrm{mGal} = 10^{-5}\,\mathrm{m/s^2}$. Since the Earth's reference gravity acceleration at the surface is approximately $10\,\mathrm{m/s^2}$, 1 mGal is the equivalent of approximately one millionth part of the surface gravity.

Furthermore, the degree dependent factor of $(l-1)$ leads to an emphasis of the higher degrees in the representation of the gravity anomalies compared to the geoid. In Figure 4.4 we present the data of Figure 4.3, i.e. gravity data derived from EIGEN-5C using the hydrostatic ellipsoid, in terms of gravity anomalies. We immediately notice the effect of the factor $(l-1)$ that yields that much more small scale structures (higher degrees) can be seen that were 'hidden' in the representation of the

geoid, even it is the exact same data set. We can interpret the gravity as a kind of high-pass filter of the geoid, where only higher frequencies are pronounced. In order to underline this interpretation, in Figure 4.5 we again show the geoid of Figure 4.3 but without the lower harmonic degrees $2 - 11$. We see that this filtered version of the geoid corresponds to the gravity anomalies quite well.

4.3 The rigid Earth

In this section, we take a first step into the process of trying to explain the origin of the observed gravitational signals that we presented in the previous section and trying to assign them to different origins within the Earth's interior. The question of what is the closest *look* we can get inside the Earth, leads us to the research field of **seismic tomography**. Here, in principle, one uses the concept of ray theory and tries to solve the inverse problem of deducing material properties in the Earth's interior from travel times and/or complete waveforms of seismic waves (see e.g., Fichtner, 2011, for a detailed review), detected at a broad range of seismometers distributed around the Earth.

Mineralogical methods allow to convert the found seismic properties - assuming a certain material composition, temperature and pressure (depth) - into one another and even into other material properties like e.g. density. In practice, this means that using an appropriate assumption about the radial temperature and pressure stratification inside the Earth's mantle, e.g. based on a convection model or even just PREM, it is possible to convert the seismological quantities that arise from seismic tomography into a mineralogically consistent density model for the Earth's mantle. In the following course of our work, we make use of the global seismic tomography s-wave model by Grand et al. (1997). The s-wave speed anomalies of this model are converted into respective density anomalies by applying the published mineralogical model by Piazzoni et al. (2007). Furthermore, for all our following investigations, we will cut the seismic model at a depth of 150 km and do not incorporate density structures above this barrier into our models. This is due to the fact that in these shallow depth levels, the seismic models are strongly dominated by crustal effects that do not play a significant role in global mantle flow and thus, would lead to artefacts. In Figure 4.6 we show the resulting density distribution for various depth slices. From now on, this model will serve as our 'standard' density model for the Earth's mantle at the present time.

Note that the previous two paragraphs mirror the actual situation in an extremely(!) simplified way. Both seismic tomography and mineralogy form scientific research fields on their own, provided with own theories, experiments, data, (un)certainties, error models, ... We are aware that this density model that from here, we take 'for granted' contains an accumulation of all errors and ambiguities on the way from the seismometer to the mineralogical conversion scheme.

Due to the low Reynolds number flow behaviour of the Earth's mantle (mainly due to the high viscosity), we know that with a given density structure, a force balance is reached instantaneously and the current flow field can be determined by the Stokes equation. Now, we apply the methods that we learned about solving the Stokes equation in Chapter 2 and use the derived global density field - represented as deviations from a radial mean - as an input to the driving vector on the right-hand side of the equation. There is a controversy about how to choose this radial mean that on the one hand, serves as the basis for the density deviations in the driving vector and on the other hand enters the Stokes matrices on the left-hand side of the equation. The first possibility is to simply calculate radial means based on the absolute density values that are provided by the mineralogical model. The essential drawback of this method is that this radial density structure is derived in a purely mineralogical context and thus, need not to coincide with a density profile that is consistent with real mantle convection in the Earth. Second, simulations that are based on real Earth parameters, should include a density profile that suits the gravitational acceleration $g = 9.81\,\mathrm{m/s^2}$ that is measured at the Earth's surface. A profile derived from mineralogy has no such intrinsic constraint. To overcome this inconsistency it is a valid approach to only extract density deviation percentages from the min-

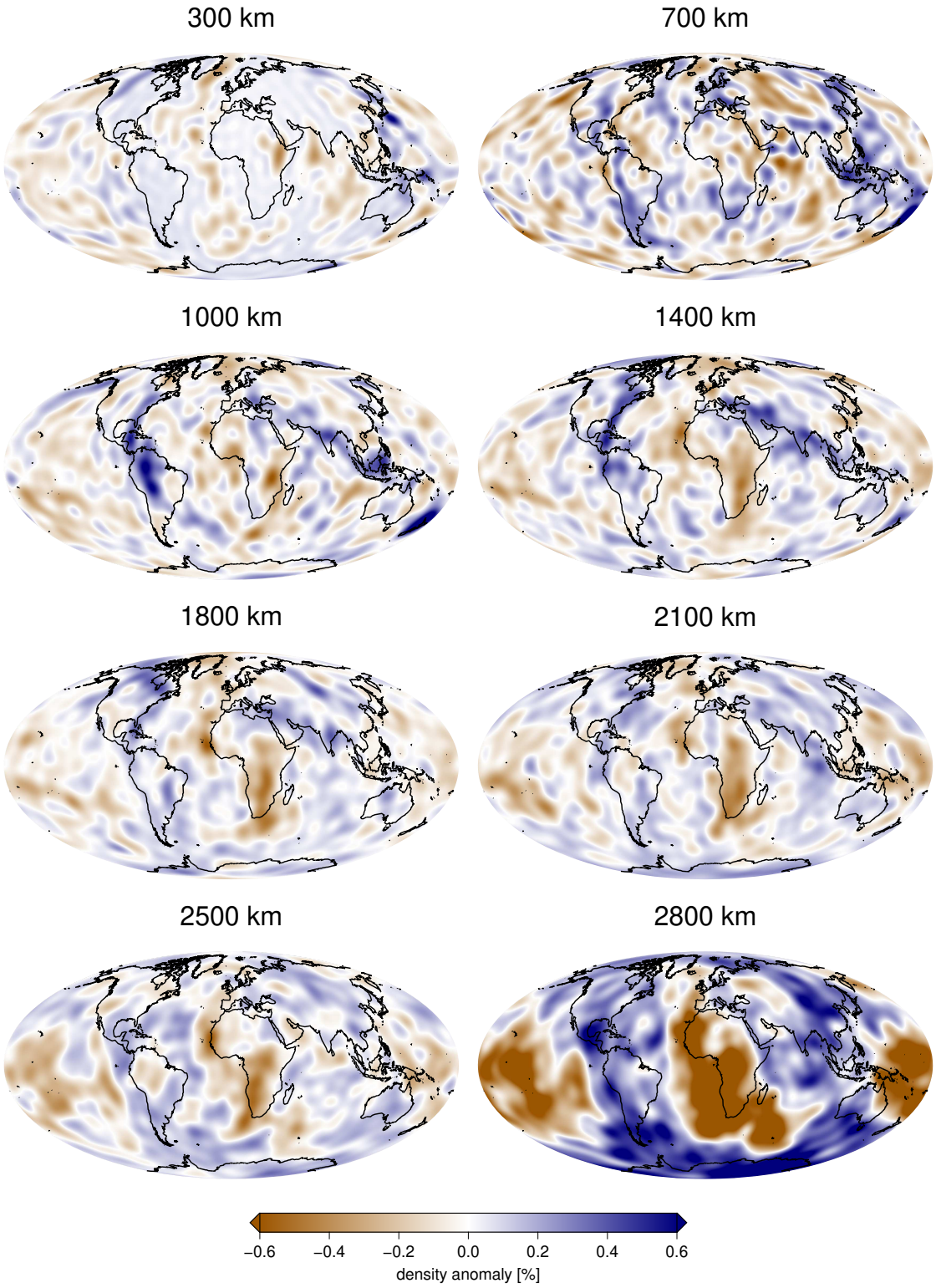

Figure 4.6: Density anomalies derived from the s-wave seismic tomography model of Grand et al. (1997). The s-wave velocities were converted into density values by using the mineralogical model of Piazzoni et al. (2007).

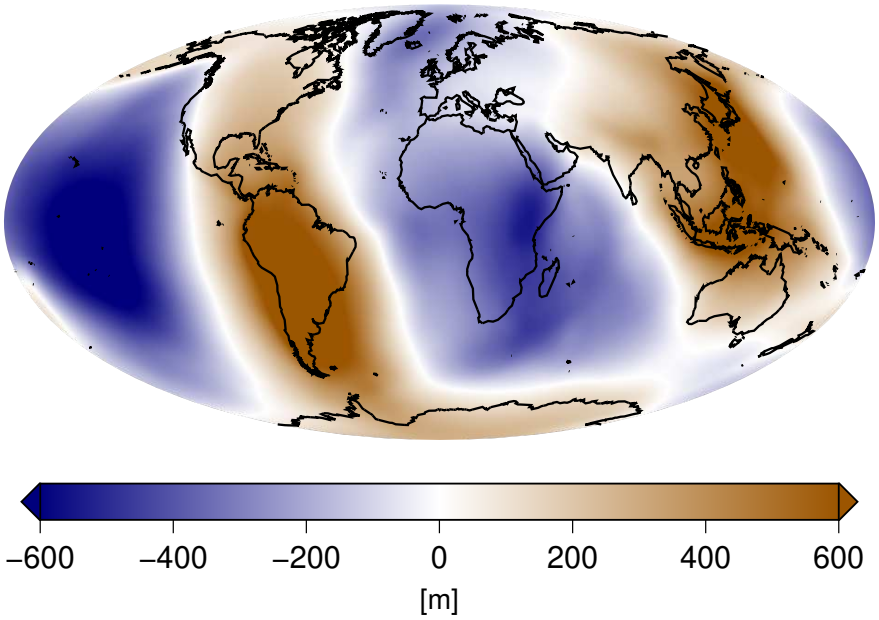

Figure 4.7: Geoid of a global density field derived from seismic tomography. We notice an overall dominance of degree 2 and a correlation of slab regions with geoid highs and regions with ascending mantle plumes with geoid lows. The overall amplitude exceeds the satellite based data by a factor of $4-5$.

eralogical model, and combine them with an externally derived radial profile. Here, an appropriate choice is a density profile from a prior mantle circulation model or as an alternative, the radial density profile provided by PREM, in order to have a best fit to real data. In our calculations, we decided to choose a density profile from a prior mantle circulation model that contains similar intrinsic physical parameters in order to (subjectively) achieve the highest degree of consistency.

Assuming a certain radial viscosity profile, we can now solve the Stokes equation by the propagator approach as presented in Chapter 2 and determine the global velocity and stress field inside the Earth's mantle. We choose a free-slip boundary condition at the CMB and a no-slip boundary condition at the Earth's surface. With this choice we want to take account for the tectonic plates that are not explicitly incorporated in our analytic model - which is even impossible without creating inconsistencies (see paragraph before (2.66) for a technical explanation). Furthermore, with the given density structure, we can also determine the respective gravitational potential. Actually, this is of our primary interest, since we are able to compare this model data to the actual data we presented in the previous section, i.e. the satellite based measurements of the gravitational field.

Figure 4.7 shows the gravitational field, in terms of the geoid, up to spherical harmonic degree $l = 31$, that is derived from the density model based on the seismic tomography by Grand et al. (1997). We notice that the overall structure is dominated by degree 2 and regions that we can identify with cold, dense slabs within the mantle are associated with geoid highs, where regions, where we find hot, upwelling material within the Earth's mantle, e.g. the East Pacific rise or the African plume, especially Afar, are associated with geoid lows. This is basically just what we expect from Newton's gravitational law.

The most remarkable feature of this synthetic geoid is the excessive amplitude level compared to

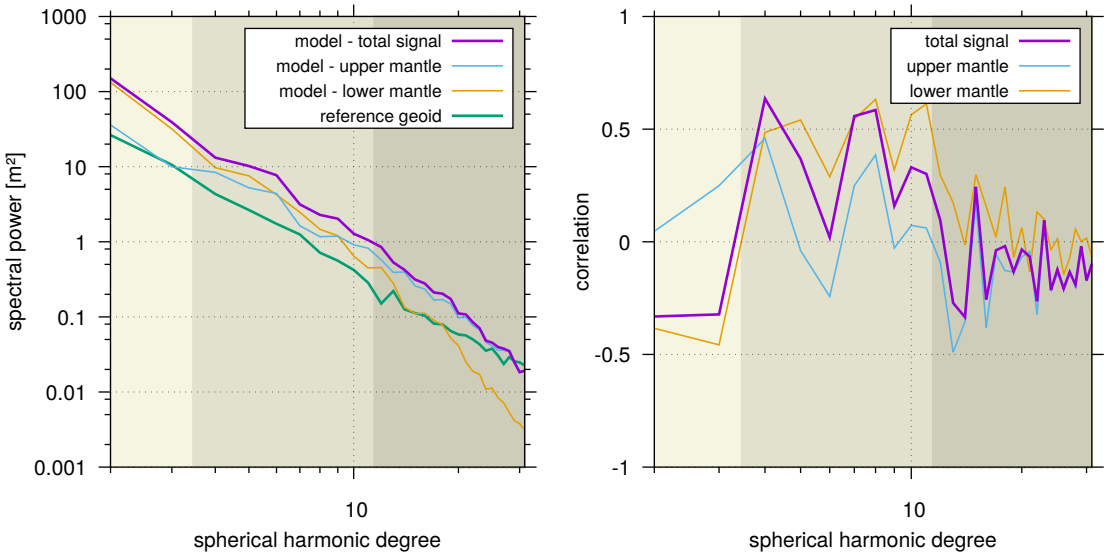

Figure 4.8: Left: spectral power of the harmonic degrees of the model geoid derived from a density model based on seismic tomography, compared to the spectral powers of the reference geoid. Right: degree dependent correlation of model and reference geoid. In both graphs, also the contribution of upper (up to 500 km depth) and lower mantle (from 500 depth) to the total signal is shown. The different background colours are chosen to illustrate the frequency bands with a dominating upper or lower mantle signal (or both).

the satellite derived geoid. The amplitudes of this model exceed the data easily by a factor of $4-5$. Moreover, also the overall geoid pattern shows almost no similarities to the observed gravitational field. This observation can also be formulated in mathematical terms. Since we are already situated in the frequency domain, a suitable mathematical measure for the similarity of two scalar fields A and B, is the correlation κ between their harmonic coefficients. The correlation is defined as the coefficient covariance divided by the product of the respective variances, i.e. more precisely, we find:

$$\kappa(A,B) := \frac{\sum\limits_{l,m} A_{l,m}\, B_{l,m}}{\sqrt{\left(\sum\limits_{l,m} A_{l,m}^2\right)\left(\sum\limits_{l,m} B_{l,m}^2\right)}}\,. \tag{4.44}$$

Due to the Cauchy-Schwarz(-Bunjakowski) inequality (1.4), the absolute value of κ is always less or equal than 1. Where a correlation of 1 corresponds to a perfect fit of both fields, a correlation of 0 indicates no similarity at all. A correlation of -1 also declares a perfect correspondence, but with both fields having opposite signs. The correlation is only capable of measuring similarities in *shape* and is not sensitive to *amplitudes*. Where in the definition above, we consider all harmonic degrees and orders, it is also possible to define the correlation $\kappa_l(A,B)$ for a single harmonic degree. Here, we keep the degree l fixed and only consider the summation over all orders, corresponding to this fixed degree.

For the model geoid of Figure 4.7, we find a correlation to the (non-hydrostatic) reference geoid of $\kappa = -0.019$, thus, from a purely mathematical perspective, there is no similarity between model and dataset at all. However, in Figure 4.8 we compare both model and dataset in an even more detailed way, especially in terms of harmonic degrees and second, we subdivided the Earth's mantle into an upper and lower part, with the imaginary break at 500 km depth. In the left figure, we plot the power spectrum s_l, a measure of the *strength* of each harmonic degree in terms of the amplitude.

More precisely, for a scalar field A and harmonic degree l, we have

$$s_l(A) := \sqrt{\frac{1}{2l+1} \sum_{m=-l}^{l} A_{l,m}^2}\,. \tag{4.45}$$

Additionally to the total model signal, we also show the power spectrum graphs for the contribution of upper and lower mantle density anomalies. Besides the overall large amplitude of the model geoid, we notice that in the very low degrees, i.e. $l = 2$ and $l = 3$ the signal almost solely consists of lower mantle origin, where in the higher frequency band, starting from degree 12, the total signal is almost identical to the upper mantle contribution. In the medium degrees $l = 4$ to $l = 11$, we have a 'mixed zone', where both upper and lower mantle density anomalies equally contribute to the total signal. We illustrated this division into three harmonic sectors by choosing different background colours in the plots. Where this property of the power spectrum is not totally surprising since we already learned in the first section of this chapter that small scale structures far away from the observer exponentially fade out due to the factor of $(r/R)^l$ in the harmonic coefficients. Thus, we already expected that the deep mantle has basically no influence on the higher harmonic degree. But the intriguing result here is that we see this partition into the three different harmonic sectors also on the right plot, where we present the correlation of the different harmonic degrees. From here we get the insight that the overall bad correlation of -0.019 mainly is due to non-matching lower degrees $l = 2$ and $l = 3$, where we even find an anti-correlation of around -0.4. In the middle sector, the correlation is ok, even good for some degrees and only from degree $l = 12$ on, the correlation rapidly decreases again and similar to the power spectrum, we see that from here, the correlation is influenced only by upper mantle structure (the purple curve equals the blue curve).

Summarised, from the previous result we have to conclude that it seems that so far, we have missed essential parts of the physics. First, from our recent investigations, we may conclude that there is an additional mechanism that primarily influences the lowest harmonic degrees 2 and 3 of the geoid and further, there must be a second mechanism that just enters the system around a harmonic degree of 12 and higher. Moreover, from the degree dependent correlations we learned that the answer to the lower degree mechanism must lie in the deeper mantle where for the higher harmonic degree, the answer should be hidden in shallower structures. We will find the answer to the first question in the next section.

4.4 Dynamic topography

Remembering the kernels that we developed in Chapter 2 for the Stokes flow, we notice that independent of the choice of the boundary conditions, in contrast to the radial velocity, poloidal velocity and poloidal stress, we are always facing a non-zero radial stress at both domain boundaries (see Figure 2.2 - Figure 2.9). Where these values are intrinsic (and correct) solutions of the stress field inside the spherical shell, this solution does not know about the physical conditions outside the domain. In reality, the flow would always try to behave in a way that the stresses are continuous across the domain boundaries. Especially at the surface, where we have air (or water) above the boundary, it becomes evident that with a non-zero radial stress at the boundary there was a unrealistic discontinuity, since the stress drops to zero just above the surface (the same scenario applies at the inner domain boundary, with the difference that there, the stress does not drop to zero). But in contrast to the mathematical formulation, in reality, the boundaries are not fixed in space (and time) and the flow deflects the boundaries exactly in a way that these discontinuities do not occur.

Thinking about gravitational aspects, as a consequence, these deflections also naturally change the total gravitational signal since e.g. a positive deflection at the surface means that air/water is replaced by mantle material. At the CMB, a positive deflection would induce denser core material to replace mantle material and the other way around. Since these deflections are flow induced and thus, change

dynamically over time, they are called **dynamic topography**. In this 'updated' scenario, a dense, cold downwelling that intrinsically leads to a geoid high, also induces a *negative* boundary deflection at the surface and at the CMB, which both yield a negative contribution to the total gravitational signal. For a hot, light upwelling, the scenario exactly states the other way around. The intrinsic negative geoid signal is balanced by the positive distribution of both topography signals at the surface and at the CMB. Even if these considerations have only been of qualitative nature yet, they already indicate a probable amplitude reduction of the total gravitational signal. Based on the results of the previous section, this is exactly what we hoped for. Furthermore, the sign of the total gravitational signal is not determined a-priori any more but will now depend on the ratio between the gravitational signal from the dynamic topography and from the density anomaly itself. It will turn out that this ratio is strongly dependent first, on the flow parameters, especially the viscosity structure and second, on the location of the density anomaly within the mantle.

In order to quantify this flow induced dynamic topography, we need to determine the change in radial stress that would be caused by a positive or negative deflection and then determine the point of equilibrium where there is no discontinuity across the (newly defined) boundary any more. Having a look at the representation of the stress tensor (see e.g. (2.43)), we immediately see that by far, the main contribution to the radial stress is the hydrostatic pressure, where the pressure and stress deviations caused by the flow only have a minor contribution to the total stress signal. Thus, applying the hydrostatic principle, an additional topography of h_r at a radius r causes a pressure (and thus, negative stress) difference of

$$P_h(r) = -\sigma_{rr}^{(h)}(r) = (\rho_2 - \rho_1) g_0(r)\, h_r \,, \tag{4.46}$$

compared to the *undisturbed* state, at the bottom of the topography. Here, ρ_1 and ρ_2 are the respective densities of the adjacent layers, where layer 2 is located below layer 1 and we neglect any changes in g due to the additional (or reduced) height and lateral density variation. Equating this hydrostatic stress $\sigma_{rr}^{(h)}(r)$ with the boundary value of the radial stress, derived from the Stokes system, we can deduce the surface deflection that is needed to create this stress level at the mathematically fixed boundary:

$$\begin{aligned} & \sigma_{rr}(r) = \sigma_{rr}^{(h)}(r) \\ \Rightarrow \quad & \sigma_{rr}(r) = -(\rho_2 - \rho_1) g_0(r)\, h_r \\ \Rightarrow \quad & h_r = -\frac{\sigma_{rr}(r)}{(\rho_2 - \rho_1) g_0(r)} \,. \end{aligned} \tag{4.47}$$

In literature, the previous relations are commonly also derived in an equivalent way, arguing with a Taylor expansion of the radial stress around the fixed boundary (see e.g., Panasyuk et al., 1996). We have to be aware that in this form, these equations are only valid above the respective density anomaly, i.e. at the upper domain boundary. At the lower boundary, we are facing a sign change due to an inverted perspective and a sign jump in the radial stress that occurs at the location of the density anomaly (see kernels). This sign chance can also be illustrated by imagining a density anomaly inside the Earth's core, i.e. below the lower domain boundary, that drives an equivalent velocity field around the CMB but with the exact opposite radial stress distribution. To take this scenario into account, we can rephrase the previous relation as

$$h_r = -\frac{\sigma_{rr}(r)}{(\rho_{\text{in}} - \rho_{\text{out}}) g_0(r)} \,, \tag{4.48}$$

where 'in' and 'out' are meant in terms of the flow domain, i.e. the Earth's mantle. The choice of the used reference densities for the inner and outer regions is of significant importance since these values influence the amplitude of the dynamic topography and in the following, also the resulting gravitational potential or geoid. For the density jump at the CMB, we choose $\rho_{\text{C}} \approx 9.900\,\text{kg/m}^3$ that is provided by PREM (Dziewonski and Anderson, 1981) for the core density near the boundary. The

values for the Earth's mantle mainly depend on the choice if we want to incorporate incompressibility or not. For an incompressible model, where the radial density ρ_0 does not vary with depth, we may choose the already introduced $\hat{\rho}_0 = 4.500\,\mathrm{kg/m^3}$ as a consistent mean value. These values yield a density jump of $\rho_{\mathrm{MS}} = 4.500(3.480)\,\mathrm{kg/m^3}$ between mantle and surface (air or (in brackets) water, with an assumed density of $\rho_{\mathrm{w}} = 1.020\,\mathrm{kg/m^3}$) and $\rho_{\mathrm{CM}} = 5.400\,\mathrm{kg/m^3}$ between core and mantle.

In a compressible model, the density increases approximately by a factor of 2 from the upper mantle to the CMB. PREM and also radial mean values generated by a numerical mantle circulation model here suggest approximate values of $\rho_{\mathrm{UM}} = 3.380\,\mathrm{kg/m^3}$ for the upper mantle and $\rho_{\mathrm{LM}} = 5.560\,\mathrm{kg/m^3}$ for the lower mantle. Thus, using these values we find a density jump of $\rho_{\mathrm{MS}} = 3.380(2.360)\,\mathrm{kg/m^3}$ at the upper and $\rho_{\mathrm{CM}} = 4.340\,\mathrm{kg/m^3}$ at the lower domain boundary (also compare to the scenarios investigated by Panasyuk et al., 1996). Summarised, the flow induced dynamic topography at the Earth's surface then states as

$$h_S = -\frac{\sigma_{rr}(r_1)}{g_0(r_1)\,\rho_{\mathrm{MS}}}\,, \tag{4.49}$$

and in analogy, at the CMB, we find

$$h_C = \frac{\sigma_{rr}(r_0)}{g_0(r_0)\,\rho_{\mathrm{CM}}}\,. \tag{4.50}$$

But these relations are only true to first order. When investigating the stress levels at the boundaries, we also have to take account of an additional effect that we already mentioned when we evaluated the different contributions to the buoyancy force in Chapter 2. Due to self-gravitational effects, the deviatoric gravitational potential U_1, directly and indirectly generated by the density anomalies inside the mantle, changes the **gravitational pressure** that is exerted by the material outside the flow domain onto the domain boundaries. In other words, a negative deviatoric potential attracts the material of the Earth's core by a small amount which yields a force onto the CMB from below, counteracting the stress that is induced by the flow itself. In principle, the same applies at the Earth's surface but here, the self-gravitation is amplifying the deformation in case of a negative deviatoric potential. Nevertheless, here, we have a much minor (or even no) effect due to the small density of water/air. Introducing these self-gravitational terms into the previous relations (recalling that U_1 is negative for a positive density anomaly), we find the following final expressions for the dynamic topography at the Earth's surface and the CMB - now in terms of the spherical harmonic coefficients and also in terms of the scaled quantities in order to be able to embed these equations into the Stokes system in the following:

$$\boxed{\begin{aligned} h_S &= -\frac{\sigma_1(r_1) - U_1(r_1)\rho_S}{g_0(r_1)\,\rho_{\mathrm{MS}}} = -\frac{\hat{\eta}_0\left(\bar{\sigma}_1(r_1) - \bar{U}_1(r_1)\rho_S/\hat{\rho}_0\right)}{r_1\,g_0(r_1)\,\rho_{\mathrm{MS}}}\,, \\ h_C &= \frac{\sigma_1(r_0) - U_1(r_0)\rho_C}{g_0(r_0)\,\rho_{\mathrm{CM}}} = \frac{\hat{\eta}_0\left(\bar{\sigma}_1(r_0) - \bar{U}_1(r_0)\rho_C/\hat{\rho}_0\right)}{r_0\,g_0(r_0)\,\rho_{\mathrm{CM}}}\,, \end{aligned}} \tag{4.51}$$

where now, h_S and h_C also depend on the harmonic degree l. Where the effect of self-gravity on the gravitational potential remains indisputable, in literature, the term *dynamic topography* is treated ambiguously. Authors differ in including the self-gravitational effect into the total topographic height or not. But commonly, in the geophysical community, most authors only refer to the flow induced parts $h_S^{(f)}$ and $h_C^{(f)}$ as *dynamic topography*, i.e. here we have (independent of the gravitational effect that we will derive in the following):

$$h_S^{(f)} = -\frac{\sigma_1(r_1)}{g_0(r_1)\,\rho_{\mathrm{MS}}}\,, \quad h_C^{(f)} = \frac{\sigma_1(r_0)}{g_0(r_0)\,\rho_{\mathrm{CM}}}\,. \tag{4.52}$$

Now that we derived a closed representation of the amplitude of the dynamic topography at both domain boundaries, we are also able to quantitatively determine the influence of the deflected boundaries on the gravitational potential. Now, the disturbed gravitational potential does not depend only

on the density anomalies inside the Earth's mantle any more but is also coupled indirectly to the flow properties.

We now return to the Stokes system (2.165) that we derived in Chapter 2. Where in (2.145) we only took the gravitational effect from the density anomaly into account, now, we also have to include the disturbed potential caused by the dynamic topography at the surface and at the CMB into both boundary conditions. In order to calculate the gravitational potential of these additional 'blocks' with height h_S (h_C) and constant density ρ_{MS} (ρ_{CM}), we can apply (4.26) and (4.27) - under the assumption of just one single layer. For the total gravity signal at the CMB we then find the following expression:

$$U_1(r_0) = -\frac{4\pi G}{2l+1}\left(b_j\left(\frac{r_0}{b_j}\right)^l + r_1\left(\frac{r_0}{r_1}\right)^l h_S\,\rho_{\mathrm{MS}} + r_0\left(\frac{r_0}{r_0}\right)^l h_C\,\rho_{\mathrm{CM}}\right). \tag{4.53}$$

Inserting (4.51) yields

$$U_1(r_0) = -\frac{4\pi G}{2l+1}\left(b_j\left(\frac{r_0}{b_j}\right)^l - r_1\left(\frac{r_0}{r_1}\right)^l \frac{\sigma_1(r_1) - U_1(r_1)\rho_S}{g_0(r_1)} + r_0\frac{\sigma_1(r_0) - U_1(r_0)\rho_C}{g_0(r_0)}\right). \tag{4.54}$$

In analogy, for the surface it holds that

$$U_1(r_1) = -\frac{4\pi G}{2l+1}\left(b_j\left(\frac{b_j}{r_1}\right)^{l+1} + r_1\left(\frac{r_1}{r_1}\right)^{l+1} h_S\,\rho_{\mathrm{MS}} + r_0\left(\frac{r_0}{r_1}\right)^{l+1} h_C\,\rho_{\mathrm{CM}}\right). \tag{4.55}$$

Also here, applying (4.51) yields

$$U_1(r_1) = -\frac{4\pi G}{2l+1}\left(b_j\left(\frac{b_j}{r_1}\right)^{l+1} - r_1\frac{\sigma_1(r_1) - U_1(r_1)\rho_S}{g_0(r_1)} + r_0\left(\frac{r_0}{r_1}\right)^{l+1}\frac{\sigma_1(r_0) - U_1(r_0)\rho_C}{g_0(r_0)}\right). \tag{4.56}$$

In analogy, for the scaled quantities (be aware of the different scaling of r_0 and r_1 quantities), we find

$$\begin{aligned}
\bar{U}_1(r_0) &= -\frac{4\pi G}{2l+1}\left(\frac{\hat{\rho}_0}{\hat{\eta}_0}r_0^2\left(\frac{r_0}{b_j}\right)^{l-1} - r_1\left(\frac{r_0}{r_1}\right)^{l+1}\frac{\bar{\sigma}_1(r_1)\hat{\rho}_0 - \bar{U}_1(r_1)\rho_S}{g_0(r_1)} + r_0\frac{\bar{\sigma}_1(r_0)\hat{\rho}_0 - \bar{U}_1(r_0)\rho_C}{g_0(r_0)}\right),\\
\bar{U}_1(r_1) &= -\frac{4\pi G}{2l+1}\left(\frac{\hat{\rho}_0}{\hat{\eta}_0}b_j^2\left(\frac{b_j}{r_1}\right)^l - r_1\frac{\bar{\sigma}_1(r_1)\hat{\rho}_0 - \bar{U}_1(r_1)\rho_S}{g_0(r_1)} + r_0\left(\frac{r_0}{r_1}\right)^l\frac{\bar{\sigma}_1(r_0)\hat{\rho}_0 - \bar{U}_1(r_0)\rho_C}{g_0(r_0)}\right).
\end{aligned} \tag{4.57}$$

Also using the previously defined abbreviations $\gamma^{(l)}$, $\psi^{(l-1)}$ (see (2.150)), i.e.

$$\gamma^{(l)} = \frac{4\pi G}{2l+1}\,b_j^2\left(\frac{b_j}{r_1}\right)^l, \quad \psi^{(l-1)} = \frac{4\pi G}{2l+1}\,r_0^2\left(\frac{r_0}{b_j}\right)^{l-1}, \tag{4.58}$$

and introducing

$$\alpha^{(l)} := \frac{4\pi G}{2l+1}\frac{r_0}{g_0(r_0)}, \quad \beta^{(l)} := \frac{4\pi G}{2l+1}\frac{r_1}{g_0(r_1)}, \quad q := \frac{r_0}{r_1}, \tag{4.59}$$

these relations turn into

$$\begin{aligned}
&\alpha^{(l)}\hat{\rho}_0\bar{\sigma}_1(r_0) + \left(1 - \alpha^{(l)}\rho_C\right)\bar{U}_1(r_0) - \beta^{(l)}q^{l+1}\left(\hat{\rho}_0\bar{\sigma}_1(r_1) - \rho_S\bar{U}_1(r_1)\right) = -\psi^{(l-1)}\frac{\hat{\rho}_0}{\hat{\eta}_0},\\
&\alpha^{(l)}q^l\left(\hat{\rho}_0\bar{\sigma}_1(r_0) - \rho_C\bar{U}_1(r_0)\right) - \beta^{(l)}\bar{\sigma}_1(r_1)\hat{\rho}_0 + \left(1 + \beta^{(l)}\rho_S\right)\bar{U}_1(r_1) = -\gamma^{(l)}\frac{\hat{\rho}_0}{\hat{\eta}_0}.
\end{aligned} \tag{4.60}$$

With a slight rearrangement of the previous relations, we can illustrate the different contributions to the gravitational potential at both boundaries even better. In particular, we see how effects at the opposite boundary only contribute with the distance factor q^l and q^{l+1}, respectively:

$$\begin{aligned}
\bar{U}_1(r_0) &= -\underbrace{\psi^{(l-1)}\frac{\hat{\rho}_0}{\hat{\eta}_0}}_{\substack{\text{density}\\ \text{anomaly}}} - \underbrace{\alpha^{(l)}\hat{\rho}_0\bar{\sigma}_1(r_0)}_{\substack{\text{dyn. topo}\\ \text{CMB}}} + \underbrace{\beta^{(l)}\hat{\rho}_0\bar{\sigma}_1(r_1)q^{l+1}}_{\substack{\text{dyn. topo}\\ \text{surface}}} + \underbrace{\alpha^{(l)}\rho_C\bar{U}_1(r_0)}_{\substack{\text{self-gravity}\\ \text{core}}} - \underbrace{\beta^{(l)}\rho_S\bar{U}_1(r_1)q^{l+1}}_{\substack{\text{self-gravity}\\ \text{air/water}}}, \\
\bar{U}_1(r_1) &= -\underbrace{\gamma^{(l)}\frac{\hat{\rho}_0}{\hat{\eta}_0}}_{\substack{\text{density}\\ \text{anomaly}}} - \underbrace{\alpha^{(l)}\hat{\rho}_0\bar{\sigma}_1(r_0)q^l}_{\substack{\text{dyn. topo}\\ \text{CMB}}} + \underbrace{\beta^{(l)}\hat{\rho}_0\bar{\sigma}_1(r_1)}_{\substack{\text{dyn. topo}\\ \text{surface}}} + \underbrace{\alpha^{(l)}\rho_C\bar{U}_1(r_0)q^l}_{\substack{\text{self-gravity}\\ \text{core}}} - \underbrace{\beta^{(l)}\rho_S\bar{U}_1(r_1)}_{\substack{\text{self-gravity}\\ \text{air/water}}}.
\end{aligned} \tag{4.61}$$

Compared to our previous Stokes system, the two boundary values for the gravitational potential cannot be determined a-priori any more. They now serve as two additional unknowns in the system of linear equations. But together with the two relations (4.61) there is still enough information such that the total system remains solvable. We go back to the end of Chapter 2 where we find the final form of the (merged) propagator equation (2.164). Here, we now have to incorporate $\bar{U}_1(r_0)$ and $\bar{U}_1(r_0)$ into the fifth row of the vectors of unknowns. The equation then takes the form:

$$\begin{pmatrix} 0 \\ -\bar{v}_2(r_1)f_S - v_S/\mu_l(1-f_S) \\ -\bar{\sigma}_1(r_1) \\ -\bar{\sigma}_2(r_1)(1-f_S) \\ -\bar{U}_1(r_1) \\ -\bar{W}_1(r_1) \end{pmatrix} = P^{(0)} \begin{pmatrix} 0 \\ -\bar{v}_2(r_0)f_C - v_C\mu_l(1-f_C) \\ -\bar{\sigma}_1(r_0) \\ -\bar{\sigma}_2(r_0)(1-f_C) \\ -\bar{U}_1(r_0) \\ -\bar{W}_1(r_0) \end{pmatrix} - P^{(j)} \begin{pmatrix} 0 \\ 0 \\ g_0 b_j/\hat{\eta}_0 \\ 0 \\ 4\pi G\hat{\rho}_0 b_j^2/\hat{\eta}_0 \\ 0 \end{pmatrix}. \tag{4.62}$$

In analogy to Chapter 2, if we rearrange this equation in terms of the now eight unknown variables, we find in combination with (4.61) an 8×8 system of linear equations $Cx = b$ - an extended version of (2.165) - with

$$C = \begin{pmatrix}
-P^{(0)}_{1,3} & -P^{(0)}_{1,2(2-f_C)} & -P^{(0)}_{1,5} & -P^{(0)}_{1,6} & 0 & 0 & 0 & 0 \\
-P^{(0)}_{2,3} & -P^{(0)}_{2,2(2-f_C)} & -P^{(0)}_{2,5} & -P^{(0)}_{2,6} & 0 & f_S & 0 & 0 \\
-P^{(0)}_{3,3} & -P^{(0)}_{3,2(2-f_C)} & -P^{(0)}_{3,5} & -P^{(0)}_{3,6} & 1 & 0 & 0 & 0 \\
-P^{(0)}_{4,3} & -P^{(0)}_{4,2(2-f_C)} & -P^{(0)}_{4,5} & -P^{(0)}_{4,6} & 0 & 1-f_S & 0 & 0 \\
-P^{(0)}_{5,3} & -P^{(0)}_{5,2(2-f_C)} & -P^{(0)}_{5,5} & -P^{(0)}_{5,6} & 0 & 0 & 1 & 0 \\
-P^{(0)}_{6,3} & -P^{(0)}_{6,2(2-f_C)} & -P^{(0)}_{6,5} & -P^{(0)}_{6,6} & 0 & 0 & 0 & 1 \\
\alpha^{(l)}\hat{\rho}_0 & 0 & 1-\alpha^{(l)}\rho_C & 0 & -\beta^{(l)}\hat{\rho}_0 q^{l+1} & 0 & \beta^{(l)}\rho_S q^{l+1} & 0 \\
\alpha^{(l)}\hat{\rho}_0 q^l & 0 & -\alpha^{(l)}\rho_C q^l & 0 & -\beta^{(l)}\hat{\rho}_0 & 0 & 1+\beta^{(l)}\rho_S & 0
\end{pmatrix},$$

$$x = \begin{pmatrix}
\bar{\sigma}_1(r_0) \\
\bar{v}_2(r_0)f_C + \bar{\sigma}_2(r_0)(1-f_C) \\
\bar{U}_1(r_0) \\
\bar{W}_1(r_0) \\
\bar{\sigma}_1(r_1) \\
\bar{v}_2(r_1)f_S + \bar{\sigma}_2(r_1)(1-f_S) \\
\bar{U}_1(r_1) \\
\bar{W}_1(r_1)
\end{pmatrix}, \tag{4.63}$$

$$b = \begin{pmatrix} P^{(0)}_{1,2} v_C/\mu_l(1-f_C) + (P^{(j)}_{1,\cdot} \cdot \bar{\alpha}_0)/b_j & \\ P^{(0)}_{2,2} v_C/\mu_l(1-f_C) + (P^{(j)}_{2,\cdot} \cdot \bar{\alpha}_0)/b_j & -v_S/\mu_l(1-f_S) \\ P^{(0)}_{3,2} v_C/\mu_l(1-f_C) + (P^{(j)}_{3,\cdot} \cdot \bar{\alpha}_0)/b_j & \\ P^{(0)}_{4,2} v_C/\mu_l(1-f_C) + (P^{(j)}_{4,\cdot} \cdot \bar{\alpha}_0)/b_j & \\ P^{(0)}_{5,2} v_C/\mu_l(1-f_C) + (P^{(j)}_{5,\cdot} \cdot \bar{\alpha}_0)/b_j & \\ P^{(0)}_{6,2} v_C/\mu_l(1-f_C) + (P^{(j)}_{6,\cdot} \cdot \bar{\alpha}_0)/b_j & \\ -\psi^{(l-1)}\hat{\rho}_0/\hat{\eta}_0 & \\ -\gamma^{(l)}\hat{\rho}_0/\hat{\eta}_0 & \end{pmatrix}.$$

For the sake of completeness, here we also state the equivalent backward propagator system $C^{(B)}x = b^{(B)}$ with

$$C^{(B)} = \begin{pmatrix} 0 & 0 & 0 & 0 & -B^{(1)}_{1,3} & -B^{(1)}_{1,2(2-f_S)} & -B^{(1)}_{1,5} & -B^{(1)}_{1,6} \\ 0 & f_C & 0 & 0 & -B^{(1)}_{2,3} & -B^{(1)}_{2,2(2-f_S)} & -B^{(1)}_{2,5} & -B^{(1)}_{2,6} \\ 1 & 0 & 0 & 0 & -B^{(1)}_{3,3} & -B^{(1)}_{3,2(2-f_S)} & -B^{(1)}_{3,5} & -B^{(1)}_{3,6} \\ 0 & 1-f_C & 0 & 0 & -B^{(1)}_{4,3} & -B^{(1)}_{4,2(2-f_S)} & -B^{(1)}_{4,5} & -B^{(1)}_{4,6} \\ 0 & 0 & 1 & 0 & -B^{(1)}_{5,3} & -B^{(1)}_{5,2(2-f_S)} & -B^{(1)}_{5,5} & -B^{(1)}_{5,6} \\ 0 & 0 & 0 & 1 & -B^{(1)}_{6,3} & -B^{(1)}_{6,2(2-f_S)} & -B^{(1)}_{6,5} & -B^{(1)}_{6,6} \\ \alpha^{(l)}\hat{\rho}_0 & 0 & 1-\alpha^{(l)}\rho_C & 0 & -\beta^{(l)}\hat{\rho}_0 q^{l+1} & 0 & \beta^{(l)}\rho_S q^{l+1} & 0 \\ \alpha^{(l)}\hat{\rho}_0 q^l & 0 & -\alpha^{(l)}\rho_C q^l & 0 & -\beta^{(l)}\hat{\rho}_0 & 0 & 1+\beta^{(l)}\rho_S & 0 \end{pmatrix},$$

$$b^{(B)} = \begin{pmatrix} B^{(1)}_{1,2} v_S/\mu_l(1-f_S) - (B^{(j)}_{1,\cdot} \cdot \bar{\alpha}_0)/b_j & \\ B^{(1)}_{2,2} v_S/\mu_l(1-f_S) - (B^{(j)}_{2,\cdot} \cdot \bar{\alpha}_0)/b_j & -v_C/\mu_l(1-f_C) \\ B^{(1)}_{3,2} v_S/\mu_l(1-f_S) - (B^{(j)}_{3,\cdot} \cdot \bar{\alpha}_0)/b_j & \\ B^{(1)}_{4,2} v_S/\mu_l(1-f_S) - (B^{(j)}_{4,\cdot} \cdot \bar{\alpha}_0)/b_j & \\ B^{(1)}_{5,2} v_S/\mu_l(1-f_S) - (B^{(j)}_{5,\cdot} \cdot \bar{\alpha}_0)/b_j & \\ B^{(1)}_{6,2} v_S/\mu_l(1-f_S) - (B^{(j)}_{6,\cdot} \cdot \bar{\alpha}_0)/b_j & \\ -\psi^{(l-1)}\hat{\rho}_0/\hat{\eta}_0 & \\ -\gamma^{(l)}\hat{\rho}_0/\hat{\eta}_0 & \end{pmatrix}. \tag{4.64}$$

Here, we see that only the first six equations that are related to the propagators, differ from the forward propagator system.

Remark 1: The effect of self-gravity

Where in the Stokes system of Chapter 2 we could switch the self-gravitational effect on and off by simply including or neglecting the $\bar{A}_\gamma$-part of the Stokes matrix (see (2.73)), the situation now becomes a little bit more complex when including the gravitational effects of the dynamic topography. Here, we have to pay attention that we also only include the *flow induced* parts of the dynamic topography $h^{(f)}_S$ and $h^{(f)}_C$ (see (4.51)) into the calculation of the gravitational effects. As a consequence, this means that in (4.61), where we gathered all contributions to the gravitational potential, both terms that are related to self-gravitational effects have to be excluded. Under these assumptions, the 8 x 8 system

of linear equations turns into $Cx = b$ with

$$C = \begin{pmatrix} -P^{(0)}_{1,3} & -P^{(0)}_{1,2(2-f_C)} & -P^{(0)}_{1,5} & -P^{(0)}_{1,6} & 0 & 0 & 0 & 0 \\ -P^{(0)}_{2,3} & -P^{(0)}_{2,2(2-f_C)} & -P^{(0)}_{2,5} & -P^{(0)}_{2,6} & 0 & f_S & 0 & 0 \\ -P^{(0)}_{3,3} & -P^{(0)}_{3,2(2-f_C)} & -P^{(0)}_{3,5} & -P^{(0)}_{3,6} & 1 & 0 & 0 & 0 \\ -P^{(0)}_{4,3} & -P^{(0)}_{4,2(2-f_C)} & -P^{(0)}_{4,5} & -P^{(0)}_{4,6} & 0 & 1-f_S & 0 & 0 \\ -P^{(0)}_{5,3} & -P^{(0)}_{5,2(2-f_C)} & -P^{(0)}_{5,5} & -P^{(0)}_{5,6} & 0 & 0 & 1 & 0 \\ -P^{(0)}_{6,3} & -P^{(0)}_{6,2(2-f_C)} & -P^{(0)}_{6,5} & -P^{(0)}_{6,6} & 0 & 0 & 0 & 1 \\ \alpha^{(l)}\hat{\rho}_0 & 0 & 1 & 0 & -\beta^{(l)}\hat{\rho}_0 q^{l+1} & 0 & 0 & 0 \\ \alpha^{(l)}\hat{\rho}_0 q^l & 0 & 0 & 0 & -\beta^{(l)}\hat{\rho}_0 & 0 & 1 & 0 \end{pmatrix}, \tag{4.65}$$

and x and b as above. Additionally, one has to pay attention that here, the propagators inside the matrix C are determined using the Stokes matrix A without the contribution of the self-gravity part $\bar{A}_\gamma$ - as before.

Remark 2: The effect of compressibility

In analogy to the self-gravitational effects, compressibility first enters the system via a distinguished part of the Stokes matrix, $\bar{A}_\beta$ (also see (2.73)), where we find all entries that include the compressibility factor $\chi(r)$. Since in the incompressible scenario, per definition the radial mean densities $\rho_0(r)$ do not vary, i.e. we have $\rho_0(r) = \hat{\rho}_0$ for all r inside the domain, for the compressibility factors it holds that $\chi(r) = 0$ for all r. Thus, by assuming a constant radial mean density for the whole Earth's mantle, the $\bar{A}_\beta$ part of the Stokes matrix vanishes automatically and has not to be excluded manually - in contrast to the self-gravity case. The Stokes matrix remains the only part where compressibility enters the system in a direct way. The two additional constraints (4.61) for the gravitational potential only contain compressible effects in an indirect way - via the stress distribution - and need not to be adapted. Thus, the system of equations $Cx = b$ remains unmodified in the incompressible case.

Nevertheless, one has to pay attention that the choice of compressibility or incompressibility has a direct impact on the absolute value of the dynamic topography at the surface and the CMB due to the changing density contrasts between the interior and the exterior of the domain. As we have learned before, in an incompressible model, we have density jumps of approximately $\rho_{\text{MS}} = 4.500\,\text{kg/m}^3$ and $\rho_{\text{CM}} = 5.400\,\text{kg/m}^3$, where in the compressible case, both values reduce to approximately $\rho_{\text{MS}} = 3.380\,\text{kg/m}^3$ and $\rho_{\text{CM}} = 4.340\,\text{kg/m}^3$. It is important to keep in mind that also these values have to be adjusted accordingly in the respective code segments. Due to (4.51), from these numbers, we expect larger topography amplitudes both at the surface and at the CMB for compressible Earth models.

4.5 Kernel gallery II

In analogy to Section 2.5, also at this point, we want to present examples for the solution of the new extended Stokes system. We proceed in exactly the same way as in the first kernel gallery in Chapter 2 and classify two type of examples. First, fixing the observation point at the Earth's surface and changing the location of the density anomaly (Figures 4.9 - 4.12) and second, changing the observation point and fixing the location of the anomaly at a depth of 1600 km (Figures 4.13 - 4.16). We again investigate the no-slip/no-slip and free-slip/free-slip boundary condition cases and the two viscosity profiles that were presented in Figure 2.1. In this way, one can nicely compare between the respective figures of the two galleries. The main difference to the examples of Chapter 2 is that now, also the gravitational potential is (strongly) influenced by the flow properties.

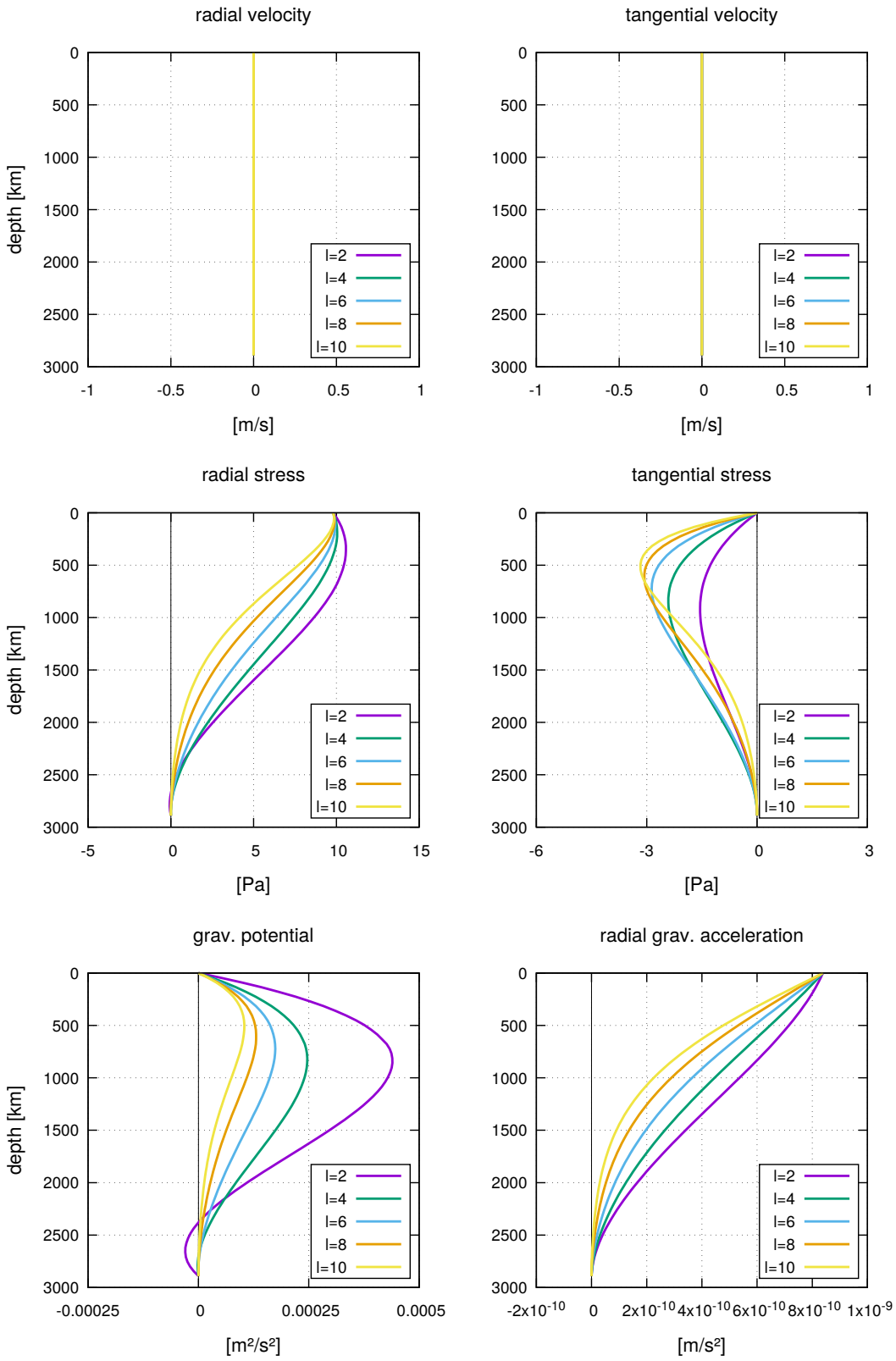

Figure 4.9: Solution of the extended Stokes equation system at the surface for a unit density anomaly of unit radial extension, placed at various depth levels. The flow parameters are no-slip at both boundaries and a uniform viscosity profile.

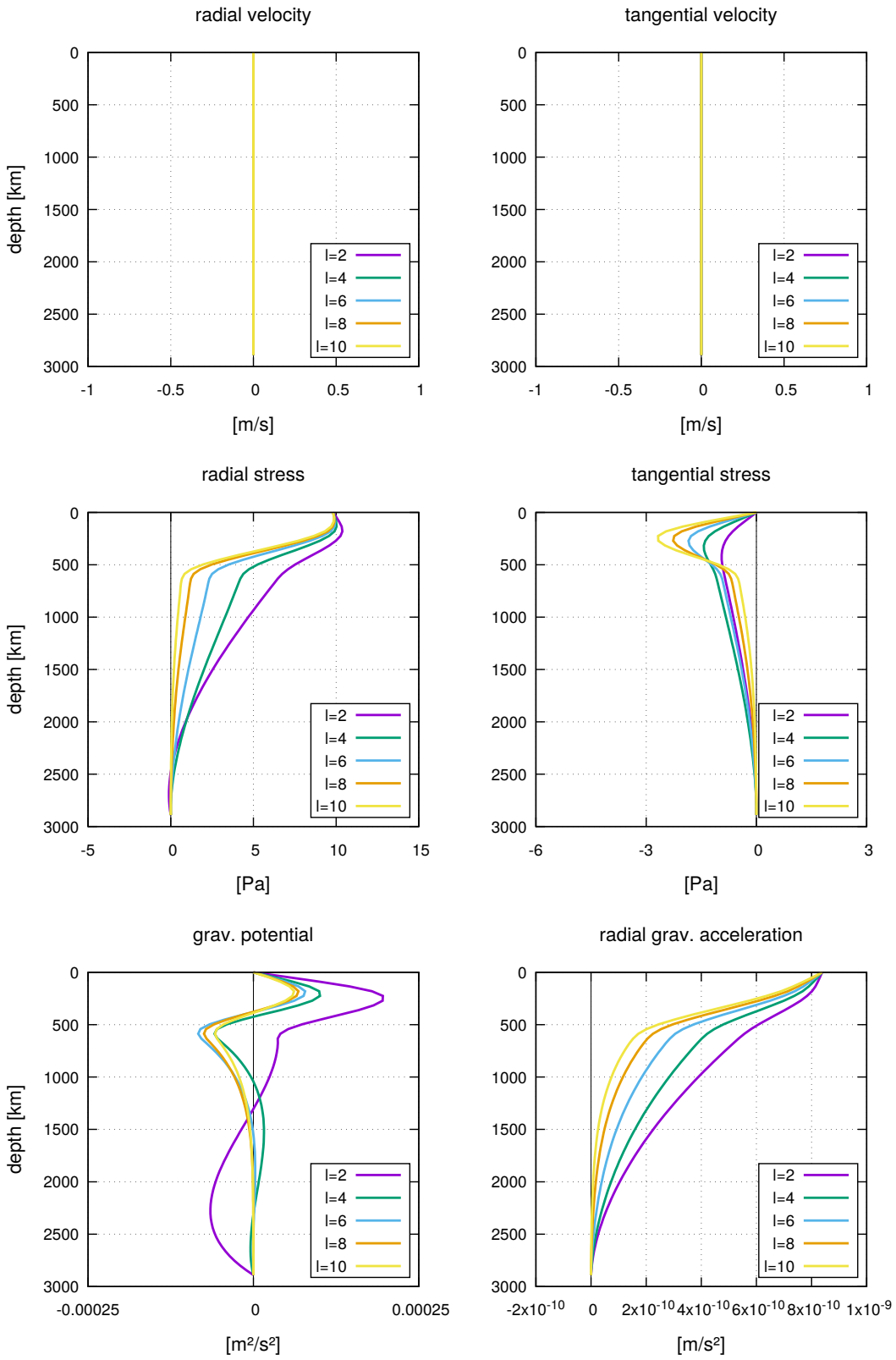

Figure 4.10: Solution of the extended Stokes equation system at the surface for a unit density anomaly of unit radial extension, placed at various depth levels. The flow parameters are no-slip at both boundaries and a viscosity profile with a low viscosity zone in the upper mantle.

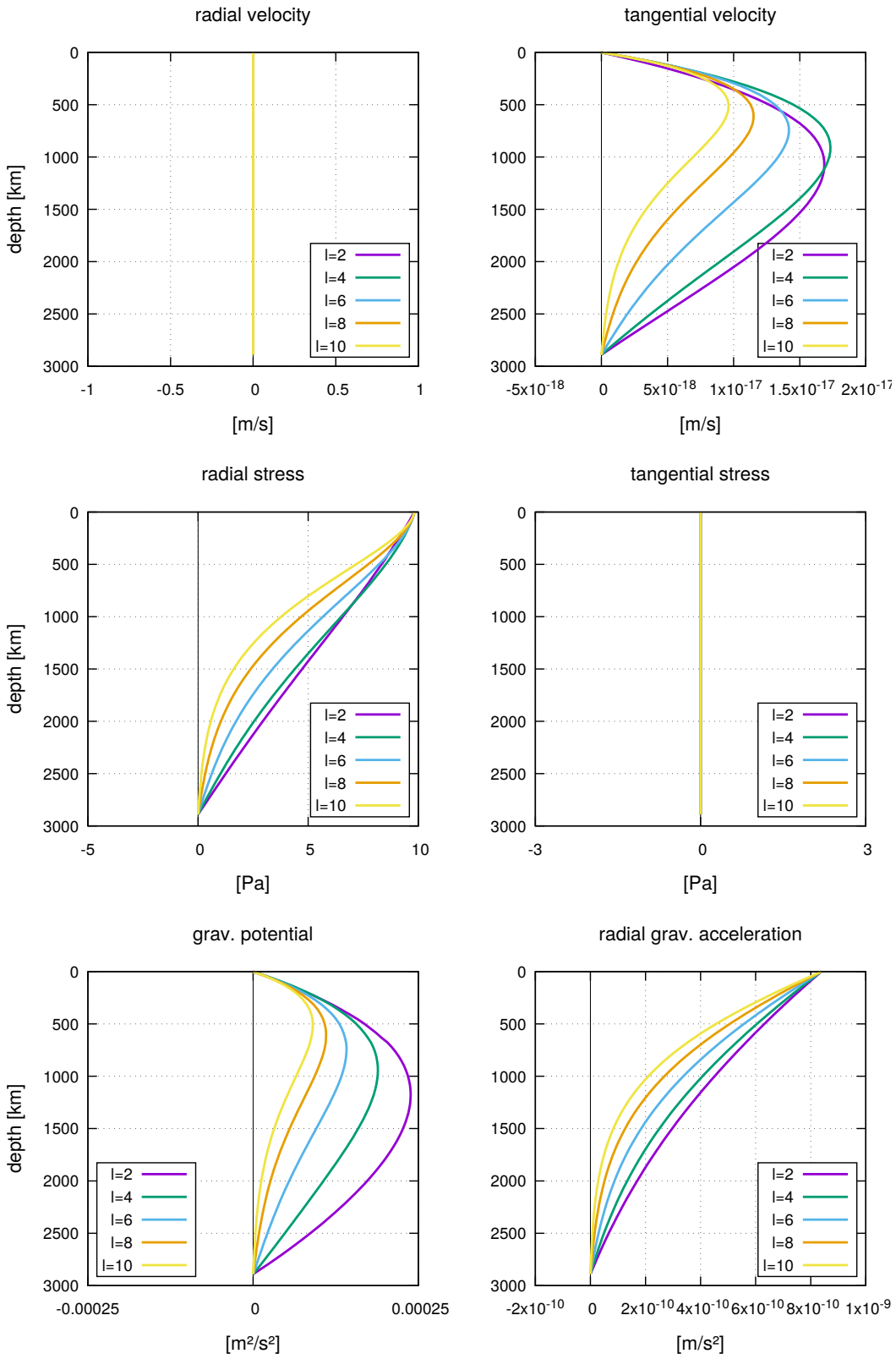

Figure 4.11: Solution of the extended Stokes equation system at the surface for a unit density anomaly of unit radial extension, placed at various depth levels. The flow parameters are free-slip at both boundaries and a uniform viscosity profile.

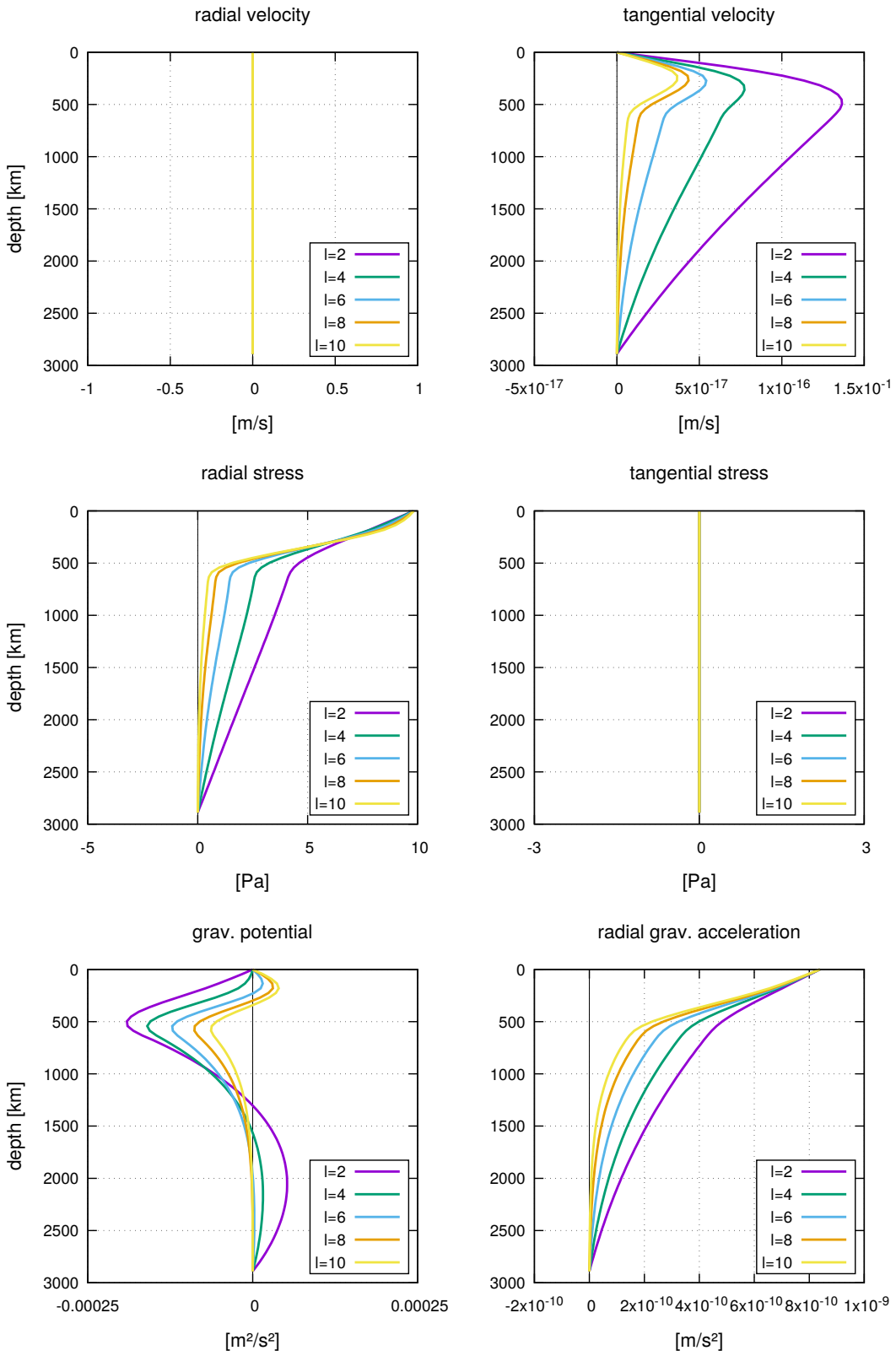

Figure 4.12: Solution of the extended Stokes equation system at the surface for a unit density anomaly of unit radial extension, placed at various depth levels. The flow parameters are free-slip at both boundaries and a viscosity profile with a low viscosity zone in the upper mantle.

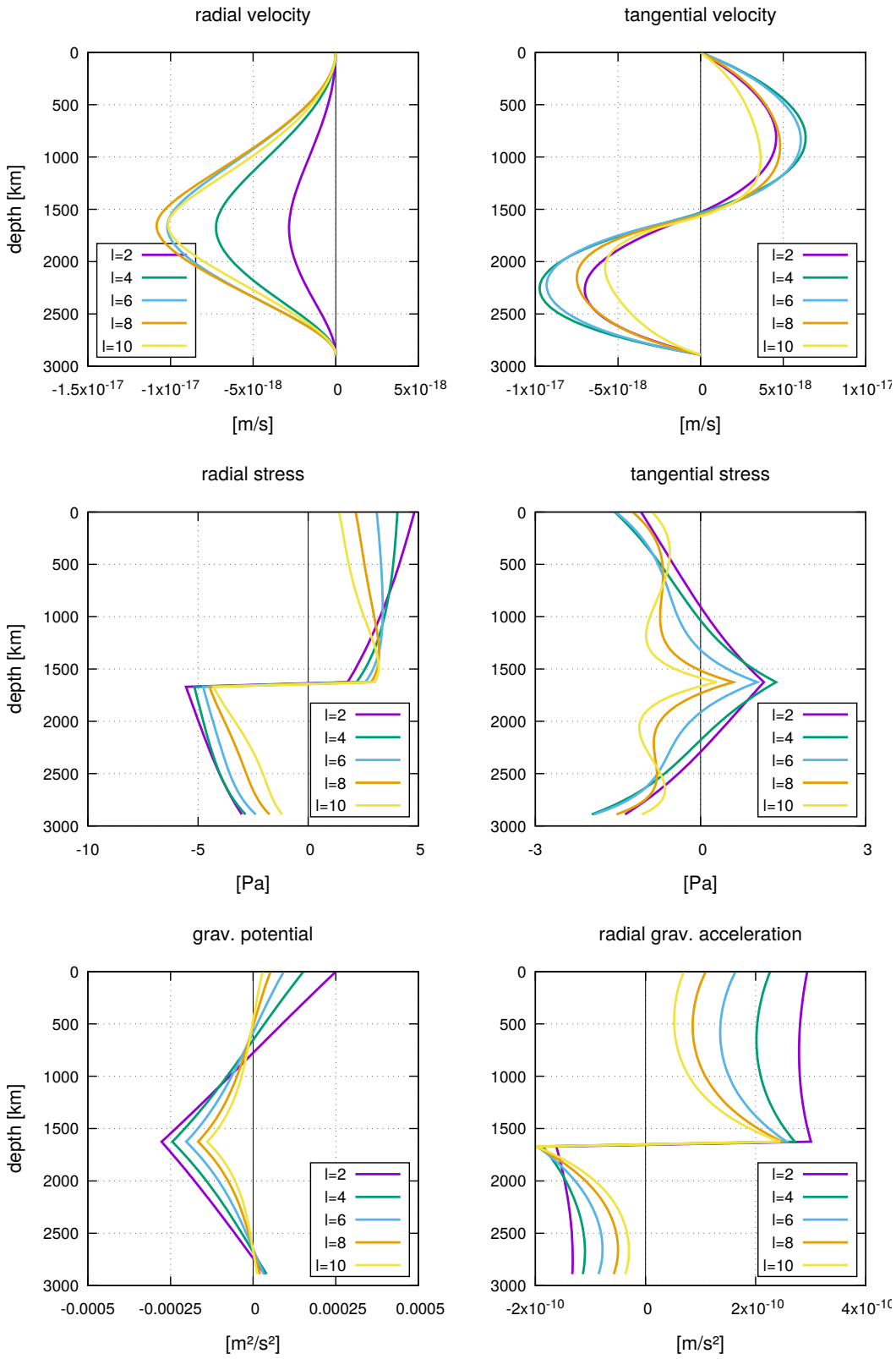

Figure 4.13: Solution of the extended Stokes equation system at various depth levels for a unit density anomaly of unit radial extension, placed at a depth of 1600 km. The flow parameters are no-slip at both boundaries and a uniform viscosity profile.

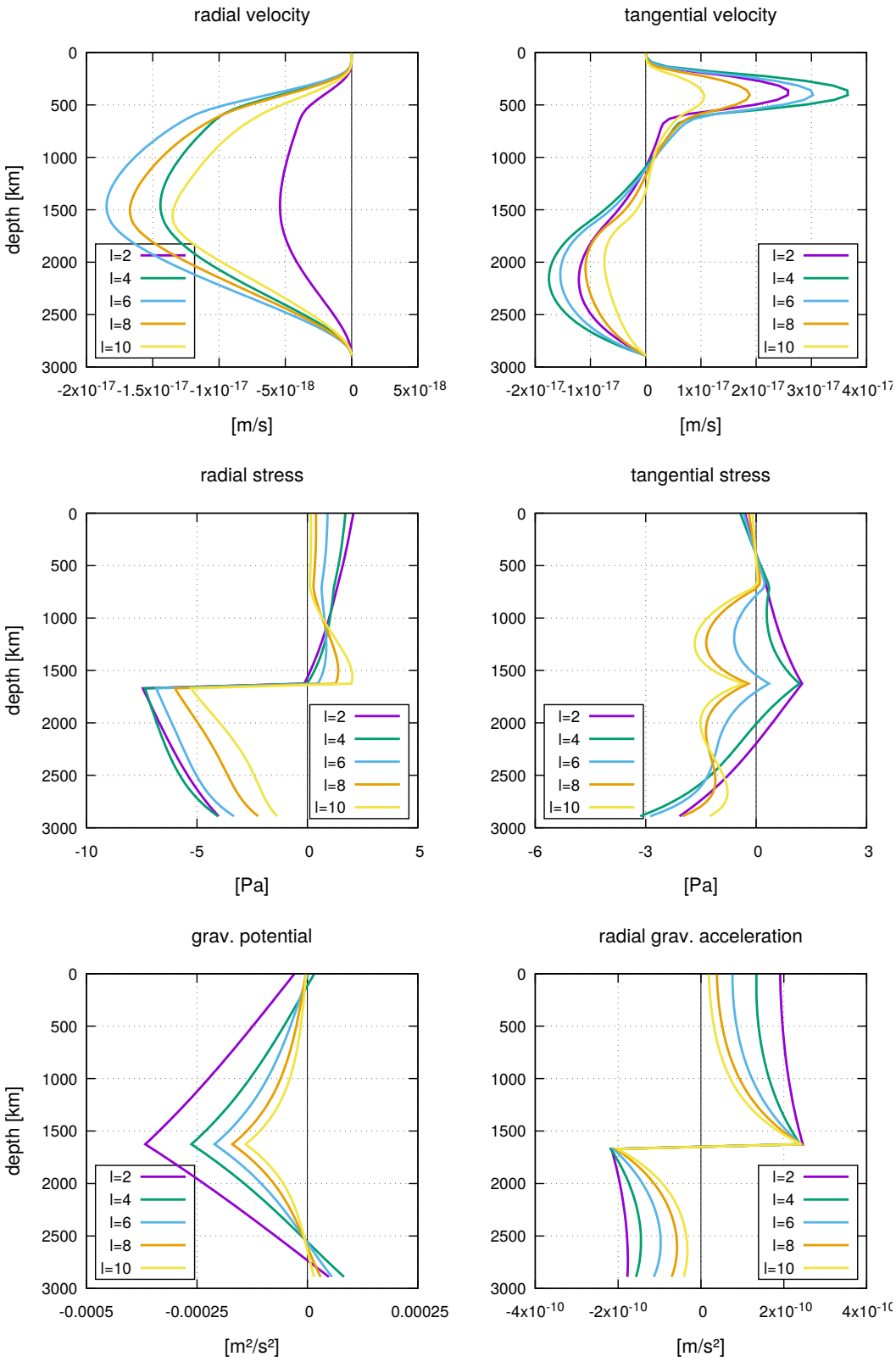

Figure 4.14: Solution of the extended Stokes equation system at various depth levels for a unit density anomaly of unit radial extension, placed at a depth of 1600 km. The flow parameters are no-slip at both boundaries and a viscosity profile with a low viscosity zone in the upper mantle.

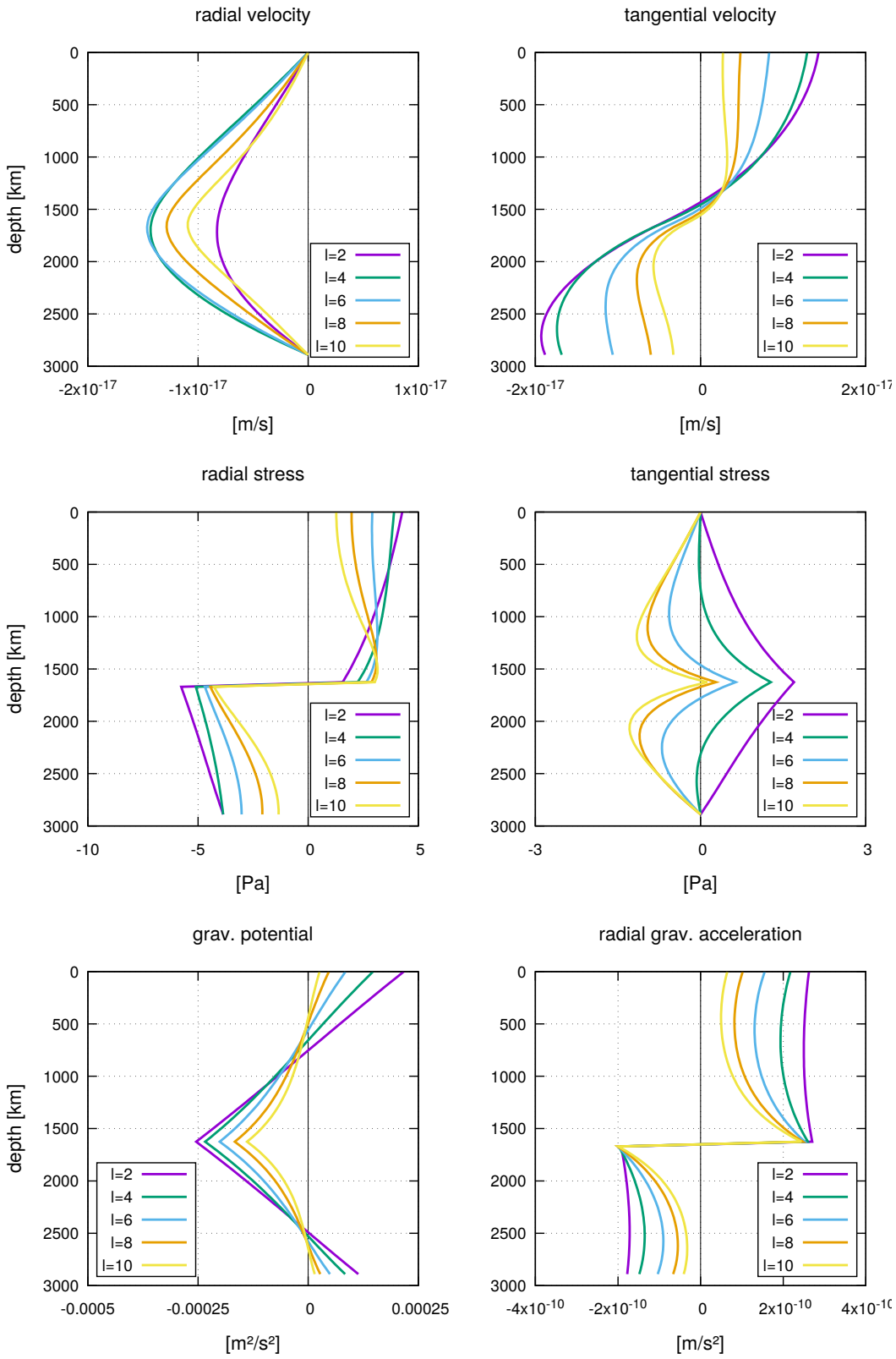

Figure 4.15: Solution of the extended Stokes equation system at various depth levels for a unit density anomaly of unit radial extension, placed at a depth of 1600 km. The flow parameters are free-slip at both boundaries and a uniform viscosity profile.

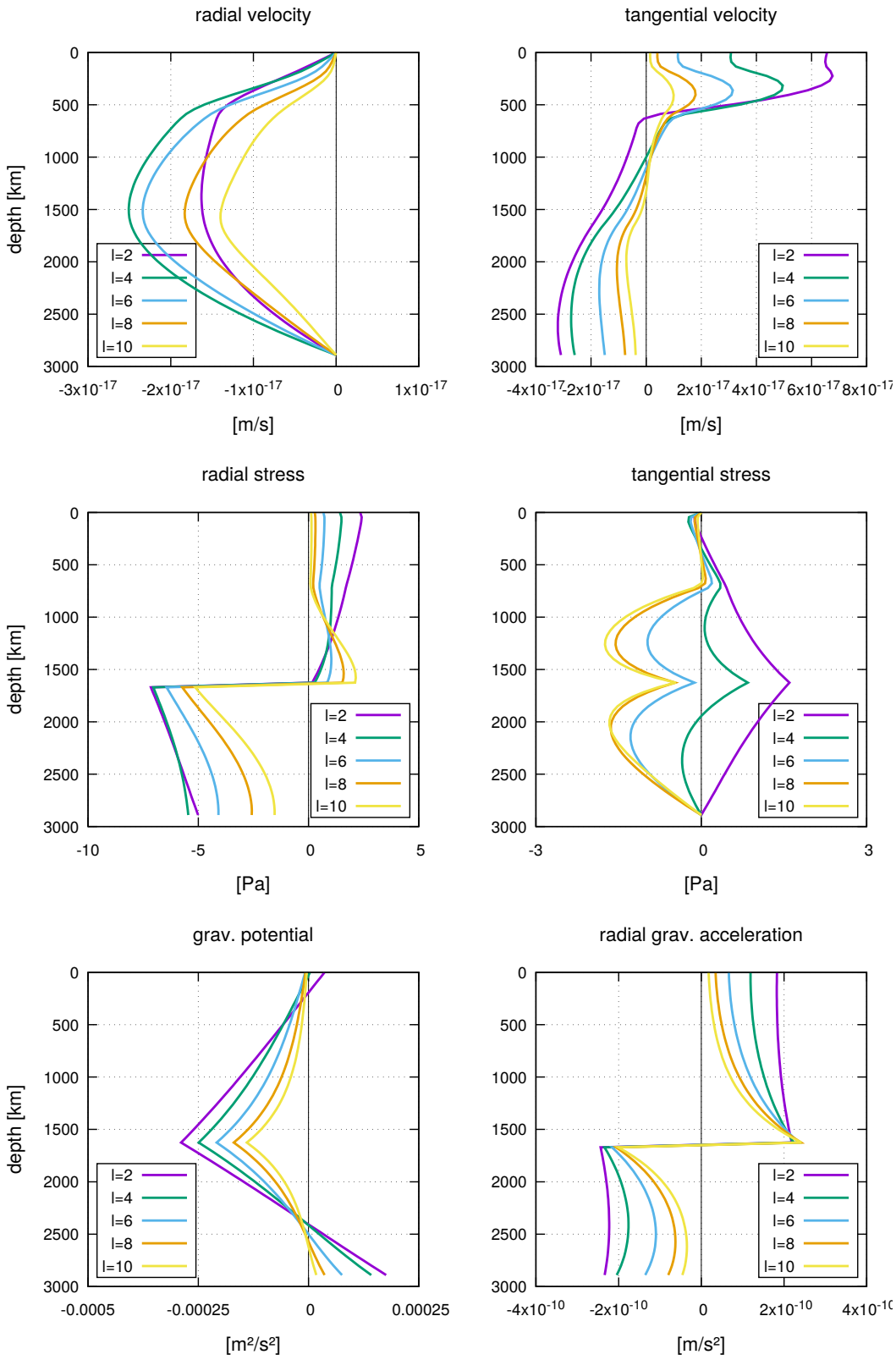

Figure 4.16: Solution of the extended Stokes equation system at various depth levels for a unit density anomaly of unit radial extension, placed at a depth of 1600 km. The flow parameters are free-slip at both boundaries and a viscosity profile with a low viscosity zone in the upper mantle.

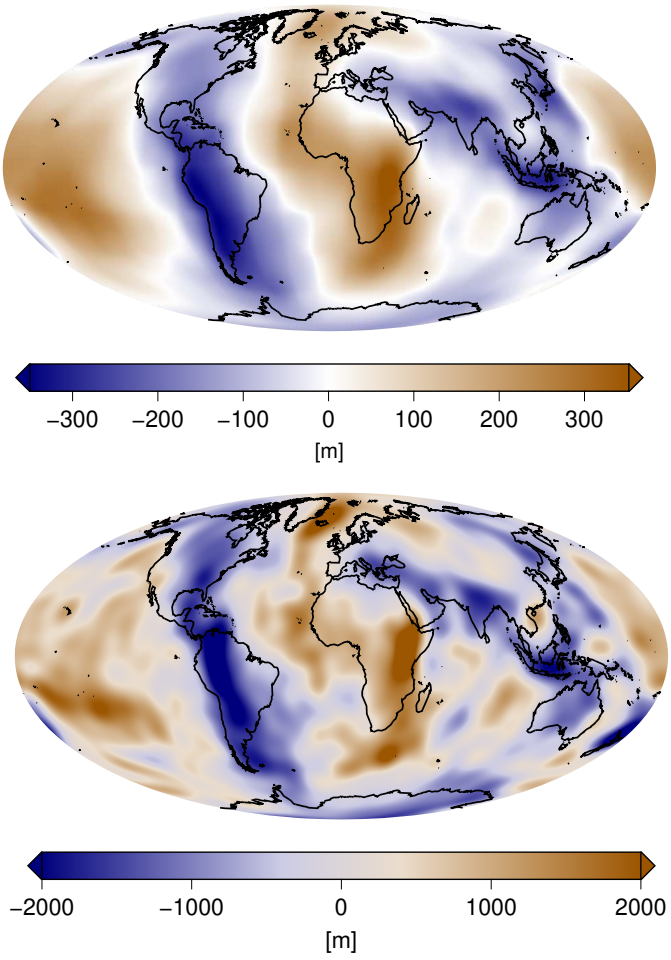

Figure 4.17: Synthetic geoid (top) and flow induced dynamic topography (bottom) of a global density field derived from seismic tomography. The underlying extended Stokes system is solved using a uniform viscosity profile for the whole mantle. We see the overall dominance of the topographic effects in the total gravitational signal. In particular, this geoid serves as the initial guess within the Monte Carlo approach for determining an appropriate radial viscosity profile for the Earth's mantle.

4.6 A Monte Carlo approach

In contrast to the rigid Earth (Section 4.3), we have learned that, including the dynamic topography (Section 4.4), the gravitational signal is in particular (indirectly) also influenced by the underlying mantle flow properties. Especially the assumed viscosity profile has a strong influence on the stress distribution inside the mantle and thus, a direct effect on the amplitude of the flow induced dynamic topography. Since the gravitational effect of the (surface) topography is of similar magnitude (and of opposite sign) as the gravitational effect of the density anomaly itself, the radial viscosity profile also has a strong effect on the total gravitational signal. The remaining question is now how to choose an appropriate viscosity profile that reflects a realistic flow scenario inside the Earth's mantle.

Especially from studies of post glacial rebound (see e.g., Paulson and Richards, 2009), it is possible to infer constraints about the viscosity inside the Earth's mantle. But even without any external knowledge, due to the known gravitational potential at the surface (more precisely, at satellite altitude), the quest for an appropriate viscosity profile can be formulated in terms of an inverse problem,

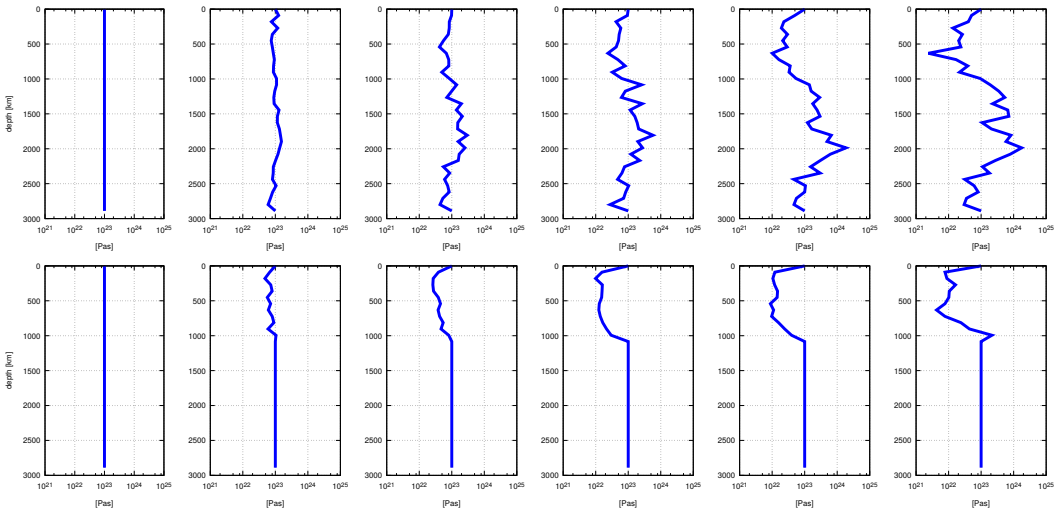

Figure 4.18: From left to right: the evolution of the radial viscosity profile within the Monte Carlo inversion scheme. In the first set of iterations (top) we put no constraints on the profile, where in the second set of iterations (bottom) we kept the viscosity of the lower mantle at a constant level to reduce the number of free parameters. We notice that the inversion scheme in all cases tries to create a viscosity contrast between upper and lower mantle.

using the previously derived Stokes system. Having a look at system and the underlying equations, we can directly infer that the flow velocity scales with the absolute viscosity, but the stresses only depend on velocity *gradients*. This means that the dynamic topography and thus, also the total gravitational potential in general may only serve as a source to constrain radial viscosity *contrasts* and that they are not sensitive to absolute values.

The most straightforward and quite simple way to approach such an inverse problem, is a **Monte Carlo scheme**. Here, the general idea is to select viscosity profiles in a random way and then to look which of them yields a reasonable good fit to the observed data. In our case this means that for each chosen profile, we solve the Stokes system and compare the derived gravitational potential / geoid to the satellite based data in terms of the correlation of the harmonic coefficients and the respective geoid amplitudes.

Under the assumption of no external knowledge, the strategy is to start with a uniform viscosity, i.e. in the Stokes matrix, for all radial layers b_i, $i = 1, ..., N$, we set the viscosity variation factor to $\eta_0^*(b_i) = 1$. It turns out that in this scenario, the synthetic geoid we gain by solving the respective Stokes system, shows a correlation of $\kappa = 0.22$ to our (non-hydrostatic) reference geoid (Figure 4.3). We present this initial state of the Monte Carlo process in Figure 4.17, where we show the model geoid and dynamic topography for a uniform radial viscosity distribution. Since the correlation here is close to zero, we can safely assume that a uniform viscosity is not a good proxy for the real situation inside the Earth's mantle. Moreover, in contrast to our previous model (Figure 4.7) we see an overall amplitude reduction of approximately a factor of two, while the shape of the geoid remained the same but with an inverted sign. This means that in this model, the newly featured dynamic topography has such a large gravitational impact that it even outmatches the pure gravitational signal of the previous model. But comparing our model geoid with the reference geoid in Figure 4.3, we see that actually, we are aiming at regional differences in the question if the dominating effect is the gravitational field of the anomaly itself or the dynamic topography. In the following, we will indeed find that the Monte Carlo scheme delivers a first hint of how this goal may possibly be achieved.

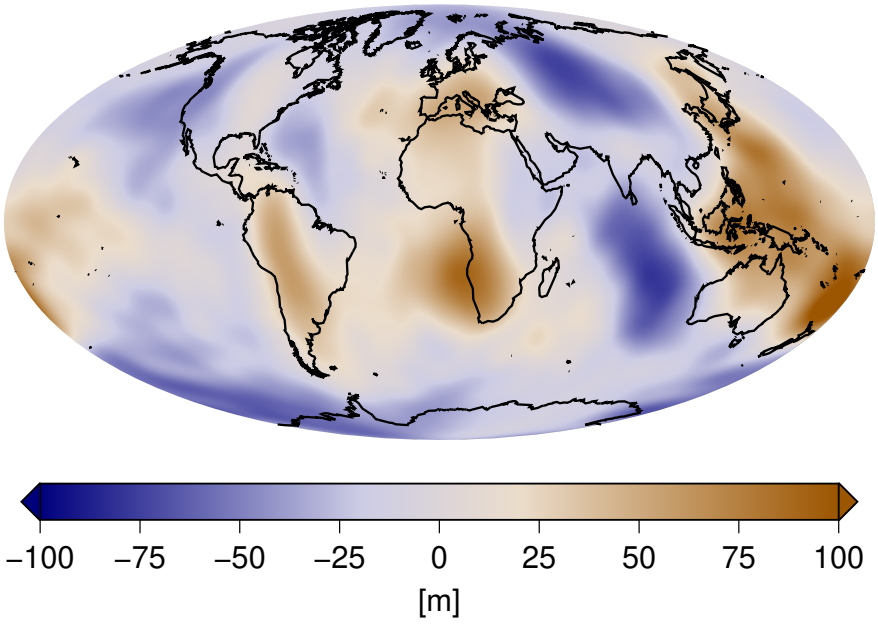

Figure 4.20: Geoid of a global density field derived from seismic tomography, including gravitational signals from dynamic topography. The underlying Stokes system is solved using the viscosity profile of Figure 4.19. Here we find a correlation to the observed data of $\kappa = 0.811$.

Now, starting from the uniform viscosity, in the further iterations, we change the viscosity variation factor of each radial layer by a randomly chosen small amount (at most 5%). If the geoid correlation with the new profile is higher than with the profile of the previous iteration, we keep the new profile and proceed. If not, we take the old profile again and try a completely new random variation on it. In general, with this algorithm, we let the profile develop just in the way that it prefers to. There is only one exception and this is that we put a constraint on the amplitude. The reason for this is quite straightforward. The inversion scheme is designed to optimise the correlation of model and data geoid. However, and as we already learned, the correlation is not capable of reflecting a fit between the *amplitude* of two data sets. Thus, in case that the inversion works, the algorithm will always try to improve the correlation even if this falls together with an unrealistic amplitude. Since the amplitude of our first guess geoid is already multiple factors higher than the reference, we expect the algorithm to scale the amplitude down. This is indeed what happens and in order to prevent the iterative scheme to even approach unrealistic low amplitudes, we force the algorithm to always keep the amplitude above the maximal amplitude of the reference geoid.

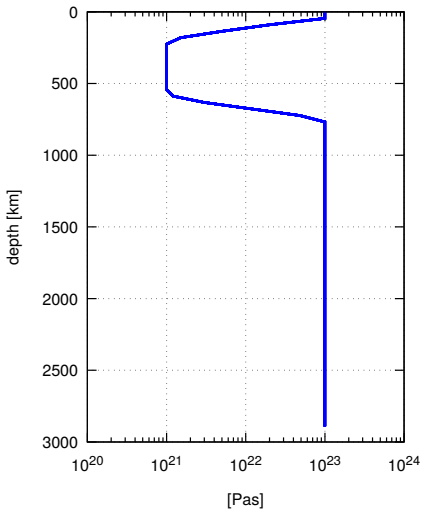

Figure 4.19: The best-fitting viscosity profile derived from the Monte Carlo inversion scheme, after applying *Occam's razor*.

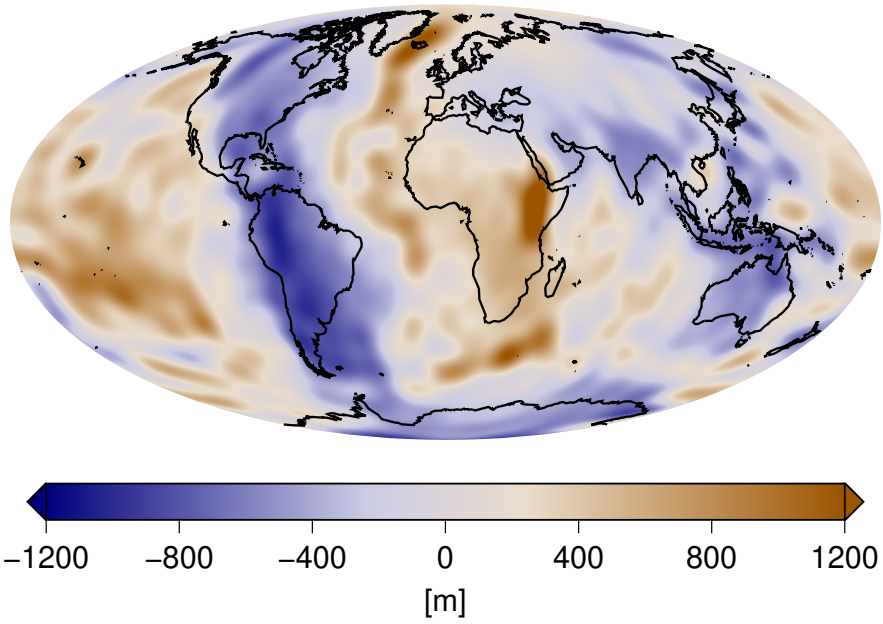

Figure 4.21: Flow induced dynamic topography, driven by a global density field derived from seismic tomography. The underlying Stokes system is solved using the viscosity profile of Figure 4.19.

Now, examining the iterative evolution of the radial viscosity profile, we find the distinct result that the Monte Carlo inversion scheme in all cases tries to enforce a strong viscosity contrast between upper and lower mantle. In a second set of iterations we then tried to reduce the free parameters and keep the viscosity of the lower mantle at a constant level. Also here, the Monte Carlo inversion scheme reduces the viscosity in the upper mantle down to a specific level where the best geoid correlation is achieved. We plot an example of the iterative evolution of the viscosity profile for both sets of the inversion scheme in Figure 4.18. Since we put no further constraints on the profile, we notice a lot of unrealistic and unphysical kinks in the profiles of all stages of the inversion, thus, the results of this (very simplistic) scheme should not be interpreted in every single detail. However, what we certainly learn from this task is that the geodetic data set strongly supports a strong **viscosity contrast between upper and lower mantle**. In literature, this low-viscosity zone is named **asthenosphere** and is indeed a non-debatable feature of the Earth's mantle according to innumerable publications during the past decades.

In this work, we now proceed by applying **Occam's razor** and erase all of the unrealistic kinks and artefacts in the viscosity profile that was produced by the Monte Carlo method. We just use the simplest possible way to implement the desired viscosity contrast, i.e. by assuming a fixed value for the viscosity of the upper and the lower mantle, respectively, including a smooth continuous transition between both values. The resulting radial viscosity profile is shown in Figure 4.19. This certain profile should look familiar to the reader since it is exactly one of the two profiles that we used in both kernel galleries (Section 2.5 and Section 4.5) within the illustrations of the solutions of the Stokes system. And indeed, from our current investigations, this certain choice turns out to be quite a realistic one. From now on, we take this viscosity profile as our standard choice for all further models and simulations.

If we solve the Stokes system using our new standard profile, we find the remarkably good corre-

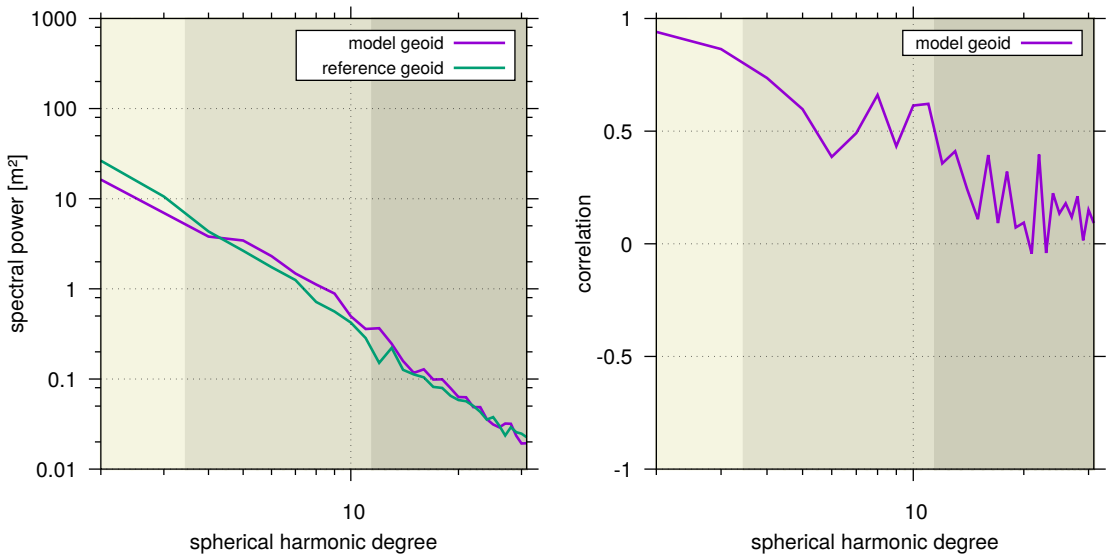

Figure 4.22: Left: Spectral power of the harmonic degrees of the model geoid presented in Figure 4.20 and of the reference geoid. Right: degree dependent correlation of model and reference geoid. In contrast to Figure 4.8 here, the model geoid incorporates effects of dynamic topography. We see a significant improvement of the correlation throughout all harmonic degrees but in particular in the very low frequency band (first harmonic sector).

lation of $\kappa = 0.811$ between model and observed geoid. The iteration scheme indeed did a good effort. We present the model in Figure 4.20 and immediately notice the good fit to the observed data, even in terms of the overall amplitude. In contrast to our previous models, now, there seems to be a regional difference of how certain mass anomalies inside the mantle are treated. We find a geoid high over the African plume - a negative density anomaly, thus here, the gravitational effect of dynamic topography seems to dominate. Contrarily, a geoid high also established over Indonesia, a region where especially young slaps are located, i.e. positive density anomalies. Thus, we can conclude that in this certain region, the gravitational effect from the density structure itself seems to dominate. The secret behind this different regional behaviour lies in the kernel for the gravitational potential that can be seen in Figure 4.12. Here we see that in contrast to the solutions of the Stokes equation in the isoviscous case (and in contrast to the non-extended Stokes system of Chapter 2), the kernel performs a **sign change** within the mantle. This means that the specific depth of a density anomaly decides if this mass will contribute as a positive or a negative signal to the total gravitational field. The reason behind this sign change lies in the kernel of the radial stress - which is proportional to the dynamic topography. Here we see that in the non-isoviscous case, the asthenosphere basically cuts off all stress effects from the deeper mantle. Where e.g. slabs in the mid-mantle have a pronounced topographic effect in the isoviscous case, the asthenosphere in the non-isoviscous case smears this effect out and figuratively prevents all radial stress signals from reaching the surface to create a dynamic topopgraphy. And indeed, comparing the new model to the dynamic topography map shown in Figure 4.17, we notice a drastic amplitude reduction.

As before, we also want to convert this prosaic comparison between different models and data sets into established mathematical means and investigate in Figure 4.22 the power spectrum and correlation in terms of the respective spherical harmonic coefficients. Compared to our previous model, we see an improved fit both on the spectral density side as on the harmonic correlation. Especially the low harmonic degrees now show an almost perfect behaviour. Where this result suggests that we solved the question of the missing physical mechanism in the first harmonic sector, we see that the high

degree harmonics are still not covered appropriately at the current stage.

Before answering this final question, we shortly want to put our focus again on the viscosity profile that we just declared to be our new standard. Here, if we go even one step further and extend our analysis, it can be shown that the found amplitude of the viscosity contrast between asthenosphere and lower mantle can directly be related to the radial strength of this specific layer. Indeed, in studies of post-glacial rebound, Paulson and Richards (2009) showed that their models can rarely be distinguished if they share the same factor of $\eta_0 \cdot D^3$, where η_0 is the factor of the viscosity reduction and D the thickness of the asthenosphere. Thus, e.g. assuming a thickness of 600 km with a viscosity reduction of a factor 100, in case of narrowing the layer to e.g. 300 km we need to increase the viscosity jump by a factor of 8 to 800. And indeed, Schaber et al. (2009) was able to show the same behaviour when investigating the geoid correlation of different models. Though the Monte Carlo approach seemed to be very successful at first glance, in reality, we are facing a trade-off between asthenosphere thickness and viscosity reduction. We see that this is an inherent non-uniqueness of the underlying inverse problem. There are infinitely many viscosity profiles that yield the same gravitational field.

This means that our work and the previously mentioned studies show that static flow and geoid simulations are in general not capable of resolving the asthenospheric properties further than the above presented non-uniqueness. Only additional data sets could in theory serve as further constraints to overcome these ambiguities. Here, one possible approach would be to incorporate a quantity that we have not considered yet in the investigations of this chapter: **time**. We will discuss this new content line in the next and final chapter of this work. There, we will see that including time will give rise to various other major challenges. Technically, this means that we will incorporate the conservation of energy into our governing equations, i.e. adding the energy equation (2.31) to our system. It will immediately become evident that the major challenge here is the determination of appropriate initial conditions for the temperature field. A mathematically elaborate method that finds a way to approach this certain task will be presented in Chapter 5.

Furthermore, since the satellite based gravitational data set is - in geologic time scales - also only a static view at the present time, one could imagine that gravity itself will not play a major role in serving as a constraint for time-dependent mantle flow. But here, two other derived quantities may come to the fore. First, the time evolution of dynamic topography may be related to geological data sets and thus serve as a quantity on its own to constrain the flow parameters. Second, in the final section of this chapter, we build a relation from the gravitational field to the inertia tensor and thus, a time series of modelled gravity data can thus be transferred into varying principle axes of inertia and thus, a change in the rotational axis, which is called **true polar wander** and is a paleomagnetic observable. Thus, by incorporating time, we build a direct link between the research fields of geodynamics, geology and paleomagnetics.

But first, before opening *Pandora's box*, we stay at the present time, keep our focus on the static gravity field and try to find an explanation for the remaining parts of the data set that could not be explained by our previous work so far: the third harmonic sector.

4.7 The crustal field

4.7.1 Topography and isostasy

In the previous sections we have seen that the large scale structures of the Earth's gravity field can be explained in an almost perfect way with the density anomalies in the Earth's mantle - that were derived from seismic tomography - and their induced dynamic topography signals. But nevertheless, Figure 4.22 reveals that apparently, we are still missing out the physical mechanisms that correspond to the *third harmonic sector* of shorter wavelengths.

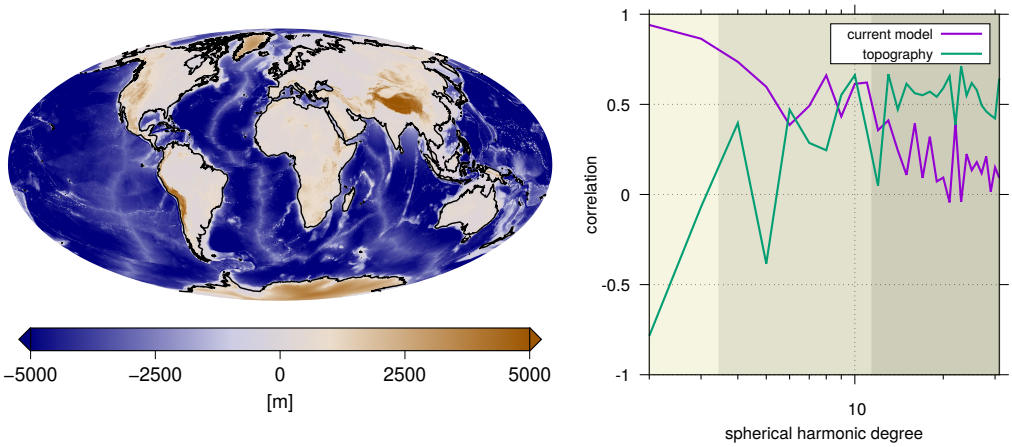

Figure 4.23: Left: the Earth's topography, data set provided by ETOPO (Amante and Eakins, 2009), evaluated on a $12' \times 12'$ grid. Right: degree-dependent correlation of the Earth's topography field (left) and the reference geoid. In addition, we restate the correlation curve of our current geoid model from Figure 4.22.

However, if we have again a closer look at our reference field in terms of the gravity anomalies, which we showed in Figure 4.4, we can definitely recognise some features that remind ourselves of the Earth's topography that we plot in Figure 4.23, like e.g. in a most prominent way, the Himalayas mountain chain. And indeed, thinking in terms of spherical harmonics, the Earth's topography mainly consists of regional and thus, spatially high-frequency features. Furthermore, these crustal mechanisms are not covered by the seismic tomography model at all and thus, have clearly been missing in our previous examinations. Just to clarify, also the previously discussed mechanism of *dynamic* topography is not related at all to these surface processes since, as we have seen, dynamic topography is a pure mantle feature. Facing the similarities between observed gravity anomalies and the Earth's topography, in order to get a primary result if our hypothesis could be true, we try to express these 'similarities' in a mathematical way. In the previous sections we learned that the correlation is a mathematical indicator for similarity. However, in order to be able to correlate the (gridded) topographic data from ETOPO (Amante and Eakins, 2009) with the reference gravitational field, we have to perform a spherical harmonic analysis on the gridded data. Since ETOPO is provided on an equiangular grid, the given data is perfectly suited for the Driscoll-Healy quadrature rule that we presented in Chapter 1 of this work, i.e. using (1.259) we are able to extract the desired frequency information from the data. In Figure 4.23 we show the correlation of the derived harmonic data set to the reference geoid and indeed, we find the astonishing result that even just the topographic heights already show a reasonably good correlation to the gravitational data set. Even without calculating any gravitational signal so far, this indicates that we seem to be on the perfectly right track.

In order to be able to perform a real gravitational analysis of the crustal effects that are related to the observed topography, we need a density model. To this end, we recall the principle of Archimedes that states that a floating body displaces its own weight of the liquid it is floating in. This state is then called **hydrostatic equilibrium** (compare to the stress balance in the context of dynamic topography, see e.g. (4.51)). In the previous chapters and sections we have learned that the Earth behaves as a viscous fluid over long time scales and furthermore, static geoid studies suggested the presence of a less viscous asthenosphere below the uppermost layer of the Earth's interior, the lithosphere. Therefore, it could be appropriate to think about the lithosphere as a body that is floating above a 'liquid' and mobile asthenosphere. In this case, the principle of Archimedes may be applied and it could be proposed that it even holds for topographic features like mountain chains or oceanic trenches. The previously stated equilibrium, which is in this special scenario referred to as **isostatic**

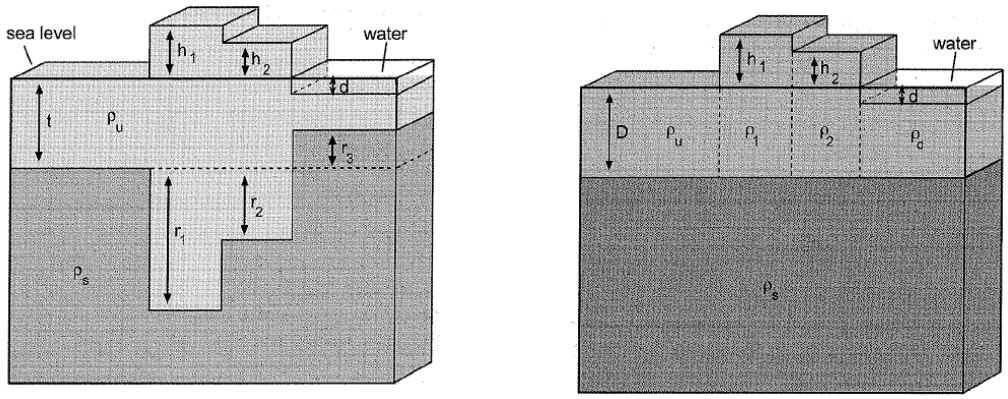

Figure 4.24: The isostatic principle of Airy (left) and Pratt (right). The sketches were taken from Thalhammer et al. (1996)).

equilibrium can naturally be achieved by two different methods. Either we assume regions with a positive topography to be underlain by a lower density structure and the other way around regions with a negative topography, e.g. oceans, to be underlain by a higher density structure than an area at sea-level. This mechanism is called **Pratt isostasy** and is illustrated in the sketch on the right-hand side of Figure 4.24. Using the nomenclature from this figure, in order to fulfil the isostatic principle that each of the vertical columns contains the same total mass, the following relations must be satisfied:

$$D\rho_u = (D+h)\rho_1 = (D-d)\rho_d + d\rho_w\,, \tag{4.66}$$

where ρ_u is a reference density for the crust, ρ_s (which does not appear in the equations) is a reference density for the sub-layer, i.e. the lithosphere, and ρ_w the density of water. h denotes the height about sea level for a positive topography and d the depth of the ocean in case of a negative topography. D is called the **compensation depth**. For each vertical column, this depth marks the barrier between crust and lithosphere. As we can see in Figure 4.24, in case of the Pratt hypothesis, the compensation depth is the same for each vertical column and is a free variable that has to be chosen in advance. Therefore, ρ_s does not show up in the equations since here, the same amount of mass would just be added to each column and this term cancels out. Thus, for given values of D, ρ_u and ρ_w, the column densities ρ_1 and ρ_d are determined by

$$\rho_1 = \frac{D\rho_u}{D+h}\,, \quad \rho_d = \frac{D\rho_u - d\rho_w}{D-d}\,. \tag{4.67}$$

There is a third case we need to consider that is not explicitly shown in the sketch. When we have a closer look at the topography map in Figure 4.23, we see that besides e.g. the Himalayas and Andes, we also find large topographic elevations in Greenland and especially on the continent of Antarctica. But the difference here is that the elevation consists of ice and not of solid rock material. Due to the large density contrast between ice and solid rocks, this has a large impact on the isostatic mechanisms and thus, on the resulting gravitational signal. Indeed, we are able to cope with this situation since the ETOPO files contain information about the exact locations where ice sheets are present. Incorporating this case into the previous equations, i.e. assuming that a block of positive elevation h_1 has the (ice-)density ρ_i, we find:

$$D\rho_u = D\rho_1 + h_1\rho_i \quad \Longrightarrow \quad \rho_1 = \frac{D\rho_u - h_1\rho_i}{D}\,. \tag{4.68}$$

The isostatic **principle of Airy** turns all assumptions of Pratt's hypothesis into the exact opposite. Here, all densities are kept constant but each vertical column now has its own respective compensation

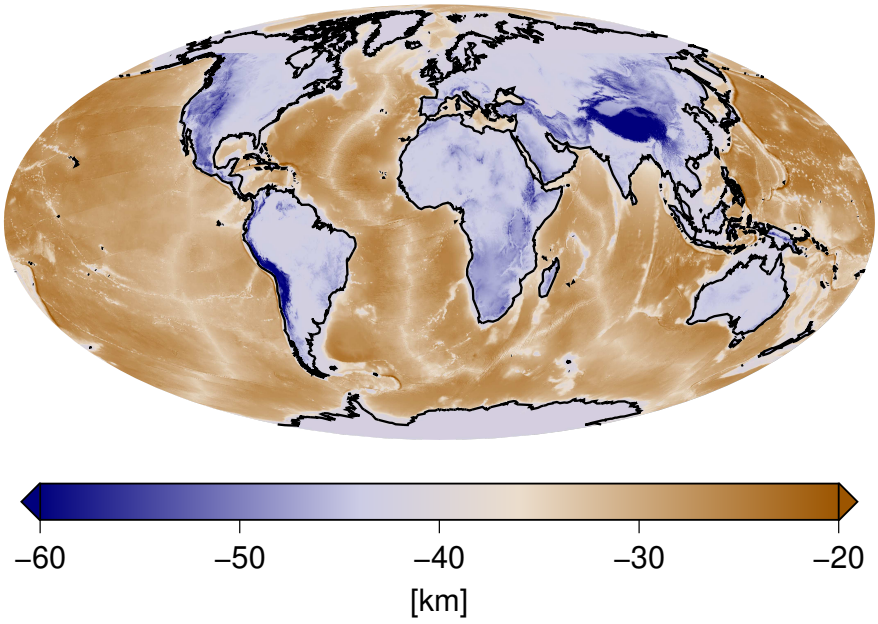

Figure 4.25: Compensation depth of the vertical columns, derived from Airy's isostasy principle. As already indicated in Figure 4.24 we see the deepest *roots* under high mountain chains, where in contrast, oceans in general induce *anti-roots*.

depth. In order to keep the total mass of one single column equal to the reference, an additional density block due to a positive topography needs to be compensated by a respective root that replaces an area of higher density (ρ_s). As we can see in the sketch of Figure 4.24, this yields mountains to have deep *roots* and oceans to cause *anti-roots*, with respect to the reference compensation depth. This reference compensation depth, denoted by t in the sketch, is not a free variable like in Pratt's hypothesis but needs be determined for each of the individual columns separately. From the sketch we see that the reference compensation depth t for sea-level altitudes must always be greater or equal to the sum of the depth of the deepest ocean d and the largest anti-root r_3, using the nomenclature of the sketch. Otherwise, the anti-root would reach into the ocean. This constraint translates into the condition $t \geq d^{\max} + r_3^{\max}$. Furthermore, applying the isostatic principle, we find in the case of Airy's hypothesis that the following relations must hold:

$$\begin{aligned} t\rho_u + r_1\rho_s = (h_1 + t + r_1)\rho_u &= (r_1 + r_3)\rho_s + (t - d - r_3)\rho_u + d\rho_w \\ &= t\rho_u + r_1\rho_s + r_3(\rho_s - \rho_u) - d(\rho_u - \rho_w)\,. \end{aligned} \tag{4.69}$$

Thus, the amplitudes of the respective roots and anti-roots are determined by:

$$r_1 = \frac{h_1\rho_u}{\rho_s - \rho_u}\,, \qquad r_3 = \frac{d(\rho_u - \rho_w)}{\rho_s - \rho_u}\,. \tag{4.70}$$

Also here, incorporating the third case of an assumed ice sheet topography h_1, we find the relation

$$t\rho_u + r_1\rho_s = (t + r_1)\rho_u + h_1\rho_i \quad \Longrightarrow \quad r_1 = \frac{h_1\rho_i}{\rho_s - \rho_u}\,. \tag{4.71}$$

Now, equipped with these relations, we are able to create a crustal model, containing of blocks of constant densities, based on the isostatic principle using the given topographic data set from ETOPO. In the following, we will choose Airy's principle as the hypothesis of our choice, just because

of the simple reason that we have less free parameters than in Pratt's hypothesis. Where at Pratt's, in addition to the reference densities, we would also need to make assumptions about the overall compensation depths - and maybe choose different values for continent and oceans - at Airy's we just need to fix ρ_i, ρ_w, ρ_u and ρ_s. We choose these reference densities to be in accordance to another published crustal model, 3SMAC (Nataf and Ricard, 1996), where we find the values $\rho_i = 1.000\,\mathrm{kg/m^3}$, $\rho_w = 1.020\,\mathrm{kg/m^3}$, $\rho_u = 2.800\,\mathrm{kg/m^3}$ and $\rho_s = 3.400\,\mathrm{kg/m^3}$. Using these values, the respective roots and anti-roots of each vertical column may be calculated using (4.70) and (4.71). In particular, the total compensation depth of each column then states as $D = t + r_1$ for continents and $D = t - r_3$ for oceans, where here, we choose t to be the minimal compensation depth $t = d^{\max} + r_3^{\max}$. The resulting compensation depths of each column are plotted in Figure 4.25, where we indeed see the deep roots under high-elevated mountain chains and large anti-roots at oceanic trenches. The reference compensation depth t for sea-level regions can be determined to be at $t \approx -42$ km.

4.7.2 Mathematical strategy

Now being equipped with a self-consistent isostatic crustal model, the task is to determine the synthetic gravitational potential generated by this certain density structure. Using the previously introduced isostatic hypothesis of Airy, to this end, we divide our domain of interest into $N \in \mathbb{N}$ spherical cubes of constant densities ρ_i, $i = 1, ..., N$, as indicated in Figure 4.26. In the following, we will derive how to calculate the gravitational potential of such a single cube with density ρ_c, measured at a point $x = R\xi$, $|x| = R$, $\xi \in \Omega$. $R - R_E$ has to be larger than the maximum elevation of the crustal structure, i.e. the highest mountain. This can be interpreted as the measurement of a satellite orbiting around the Earth at an altitude of $R - R_E$. We define that in radial direction, the cube extends from r_1 to r_2 and is bounded in tangential direction by the longitudes φ_1 and φ_2 and the polar distances t_1 and t_2. We denote this respective spherical segment as Ω_c. Since the density inside the cube is assumed to be constant, we can immediately apply (4.17) to find for the spherical harmonic coefficients of the generated gravitational potential U^c that

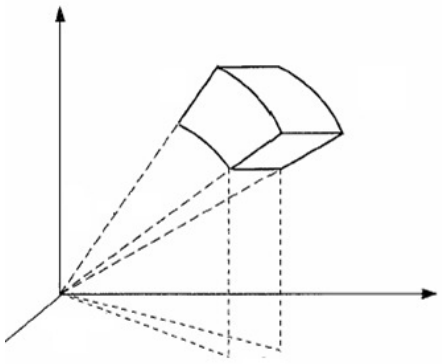

Figure 4.26: The crust is divided into spherical cubes with constant density (sketch taken from Thalhammer et al., 1996).

$$U^c_{l,m}(R) = -\frac{4\pi G\rho_c}{(2l+1)(l+3)} \frac{r_2^{l+3} - r_1^{l+3}}{R^{l+1}} \int\limits_{\Omega_c} Y_{l,m}(\eta)\,\mathrm{d}\omega(\eta)\,. \tag{4.72}$$

Here, in order to be able to calculate the integral on the right-hand side, we use the explicit representation of the spherical harmonics - including the normalised Legendre polynomials - from (1.218) to find

$$\begin{aligned} U^c_{l,m}(R) &= -\frac{4\pi G\rho_c}{(2l+1)(l+3)} \frac{r_2^{l+3} - r_1^{l+3}}{R^{l+1}} \int\limits_{\varphi_1}^{\varphi_2} \int\limits_{t_1}^{t_2} \sqrt{\frac{1}{(1+\delta_{m,0})\pi}}\, \bar{P}_{l,|m|}(t) \begin{cases} \cos(|m|\varphi) \\ \sin(|m|\varphi) \end{cases} \mathrm{d}\varphi\,\mathrm{d}t \begin{cases} m \geq 0\,, \\ m < 0\,. \end{cases} \\ &= -\frac{4\sqrt{\pi}G\rho_c}{(2l+1)(l+3)} \frac{r_2^{l+3} - r_1^{l+3}}{R^{l+1}} \int\limits_{\varphi_1}^{\varphi_2} \sqrt{\frac{1}{(1+\delta_{m,0})}} \begin{cases} \cos(|m|\varphi) \\ \sin(|m|\varphi) \end{cases} \mathrm{d}\varphi \int\limits_{t_1}^{t_2} \bar{P}_{l,|m|}(t)\,\mathrm{d}t \begin{cases} m \geq 0\,, \\ m < 0\,. \end{cases} \end{aligned}$$

$$= \frac{4\sqrt{\pi}G\rho_c}{(2l+1)(l+3)} \frac{r_2^{l+3} - r_1^{l+3}}{R^{l+1}} \begin{cases} \frac{1}{|m|}\left(\sin(|m|\varphi_1) - \sin(|m|\varphi_2)\right) \\ \frac{1}{\sqrt{2}}\left(\varphi_1 - \varphi_2\right) \\ \frac{1}{|m|}\left(\cos(|m|\varphi_2) - \cos(|m|\varphi_1)\right) \end{cases} \int_{t_1}^{t_2} \bar{P}_{l,|m|}(t)\,\mathrm{d}t \begin{cases} m > 0\,, \\ m = 0\,, \\ m < 0\,. \end{cases} \tag{4.73}$$

Due to the linearity of the gravitational potential, the task of determining the total potential U_{tot}, generated by all of the N blocks, reduces to a summation of the harmonic coefficients of each of the cube potentials that we here denote by $U^{(i)}$, $i = 1, ..., N$:

$$U_{\mathrm{tot}}(R) = \sum_{i=1}^{N} U^{(i)}(R) = \sum_{i=1}^{N} \sum_{l,m} U_{l,m}^{(i)}(R)\, Y_{l,m}(\xi) = \sum_{l,m} \left(\sum_{i=1}^{N} U_{l,m}^{(i)}(R) \right) Y_{l,m}(\xi)\,. \tag{4.74}$$

From (4.73) we see that for an explicit calculation of the potentials, the evaluation of *integrals* of the (normalised) associated Legendre polynomials, i.e.

$$\bar{I}_{l,m}(t_1, t_2) := \int_{t_1}^{t_2} \bar{P}_{l,|m|}(t)\,\mathrm{d}t\,, \tag{4.75}$$

for $t_1, t_2 \in [-1, 1]$, is an essential step. In analogy to the well-known recurrence relations for the Legendre polynomials that we derived in Chapter 1, recurrence procedures can also be found for their respective integrals. Here, we implement results from Paul (1978) where the following schemes for the integrals of the normalised Legendre polynomials were derived and carefully checked. Let $l > 1$ and $y_i := \sqrt{1 - t_i^2}$, $i = 1, 2$, then for $m < l$ it can be shown that

$$\begin{aligned} \bar{I}_{l,m}(t_1, t_2) = {} & \frac{1}{l+1} \sqrt{\frac{(2l+1)(2l-1)}{(l-m)(l+m)}} \left(y_1^2\, \bar{P}_{l-1,m}(t_1) - y_2^2\, \bar{P}_{l-1,m}(t_2) \right) \\ & + \frac{l-2}{l+1} \sqrt{\frac{(2l+1)(l+m-1)(l-m-1)}{(2l-3)(l+m)(l-m)}}\, \bar{I}_{l-2,m}(t_1, t_2)\,. \end{aligned} \tag{4.76}$$

For the case $l = m$ we find the following iteration scheme

$$\begin{aligned} \bar{I}_{l,l}(t_1, t_2) = {} & \frac{1}{2l+2} \sqrt{\frac{2l+1}{l(l-1)}} \left(y_2^2\, \bar{P}_{l-1,l-2}(t_2) - y_1^2\, \bar{P}_{l-1,l-2}(t_1) \right) \\ & + \frac{1}{2l+2} \sqrt{\frac{l(2l+1)(2l-1)}{l-1}}\, \bar{I}_{l-2,l-2}(t_1, t_2)\,. \end{aligned} \tag{4.77}$$

Paul (1978) has shown that the previous recurrence relation for $m = l$ is numerically unstable for points that are located in the polar region, i.e. for $|t| \approx 1$. For these special scenarios, a different relation that originates from a Taylor representation of $(1 - t^2)^{-1/2}$ has been derived:

$$\begin{aligned} \bar{I}_{l,l}(t_1, t_2) = {} & \sqrt{\frac{(2l+1)(2l-1)\cdots 3}{2l(2l-2)\cdots 4}} \left(y_1^{l+2} \left(\frac{1}{l+2} + \frac{1}{2} \frac{y_1^2}{(l+4)} + \frac{1 \cdot 3}{2 \cdot 4} \frac{y_1^4}{(l+6)} + ... \right) \right. \\ & \left. - y_2^{l+2} \left(\frac{1}{l+2} + \frac{1}{2} \frac{y_2^2}{(l+4)} + \frac{1 \cdot 3}{2 \cdot 4} \frac{y_2^4}{(l+6)} + ... \right) \right) \\ = {} & \left(y_1^{l+2} \sum_{j=0}^{j_{\max}} \frac{\prod_{k=1}^{j}(2k-1)}{\left(\prod_{k=1}^{j} 2k\right)(l+2(j+1))} y_1^{2j} - y_2^{l+2} \sum_{j=0}^{j_{\max}} \frac{\prod_{k=1}^{j}(2k-1)}{\left(\prod_{k=1}^{j} 2k\right)(l+2(j+1))} y_2^{2j} \right) \\ & \times \sqrt{\frac{\prod_{j=1}^{l}(2(l-j)+3)}{\prod_{j=1}^{l-1}(2(l-j)+2)}}\,, \end{aligned} \tag{4.78}$$

l=60	$(0°, 5°)$		
m	our code	Paul*	error [%]
0	0.548137705785E-02	0.548137850049E-02	-0.263188635108E-04
1	-0.474761583730E-02	-0.474760732301E-02	0.179338467321E-03
2	-0.169633318012E-01	-0.169633306239E-01	0.694052562089E-05
25	-0.364717745907E-17	-0.364719758524E-17	-0.551825700756E-03
30	-0.134465132932E-22	-0.134466017166E-22	-0.657588965580E-03
35	-0.167973992087E-28	-0.167975273604E-28	-0.762920141606E-03
58	-0.152682262798E-62	-0.152684163609E-62	-0.124493027239E-02
59	-0.171767824827E-64	-0.171769999157E-64	-0.126583789914E-02
60	-0.134955038763E-66	-0.134956775310E-66	-0.128674301466E-02
l=60	$(45°, 50°)$		
m	our code	Paul*	error [%]
0	-0.101501811403E-01	-0.101502934228E-01	-0.110619917115E-02
1	0.163371896427E-01	0.163370227936E-01	0.102129451534E-02
2	0.149331880610E-01	0.149333427060E-01	-0.103556825053E-02
25	0.412159553478E-01	0.412161664812E-01	-0.512258634555E-03
30	0.633027336132E-01	0.633025657142E-01	0.265232563446E-03
35	-0.237914912085E-01	-0.237920622310E-01	-0.240005459521E-02
58	-0.428354175582E-06	-0.428357998853E-06	-0.892541041708E-03
59	-0.650247417791E-07	-0.650253457088E-07	-0.928760471408E-03
60	-0.682275133554E-08	-0.682281709959E-08	-0.963884043748E-03
l=100	$(0°, 5°)$		
m	our code	Paul*	error [%]
0	-0.327290673516E-02	-0.327290603108E-02	0.215122339053E-04
1	-0.305798259411E-02	-0.305799103935E-02	-0.276169488267E-03
2	0.535140785031E-03	0.535137868013E-03	0.545096481464E-03
45	-0.290613928686E-30	-0.290616724692E-30	-0.962094124768E-03
50	-0.927121140811E-36	-0.927131041231E-36	-0.106785546944E-02
55	-0.153164505270E-41	-0.153166302422E-41	-0.117333364004E-02
98	-0.712434519253-105	-0.712449302422-105	-0.207497843696E-02
99	-0.621778195895-107	-0.621791227936-107	-0.209588694637E-02
100	-0.380856547661-109	-0.380864609779-109	-0.211679366552E-02
l=100	$(45°, 50°)$		
m	our code	Paul*	error [%]
0	0.120761501689E-01	0.120791752063E-01	-0.250434101141E-01
1	0.194193663745E-01	0.194196687389E-01	-0.155700064481E-02
2	-0.167221122861E-01	-0.167217779233E-01	0.199956483937E-02
45	-0.128075968186E-01	-0.128076596002E-01	-0.490188180191E-03
50	-0.186984771543E-02	-0.186983132913E-02	0.876351936596E-03
55	-0.408698562889E-02	-0.408706067914E-02	-0.183628901416E-02
98	-0.115089495372E-10	-0.115091070674E-10	-0.136874393810E-02
99	-0.135912052963E-11	-0.135914144133E-11	-0.153859610527E-02
100	-0.111947034646E-12	-0.111926685751E-12	0.181805571783E-01

Table 4.1: A comparison of the values of the Legendre integrals determined by our code to the values given by Paul (1978).

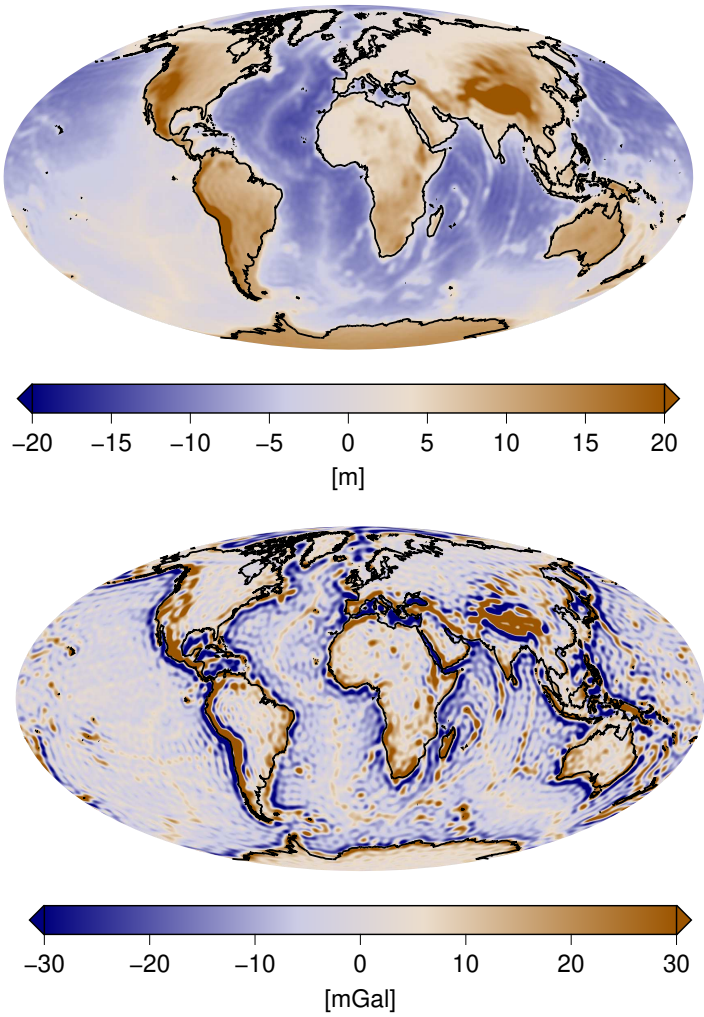

Figure 4.27: Geoid (top) and respective gravity anomalies (bottom) derived from our isostatic crustal model, based on the isostatic principle of Airy.

with a large enough $j_{\max}$ such that a suitable convergence is achieved. For the following simulations, we choose $j_{\max} = 100$ and use the Taylor series formula for values of $|t| > 0.87$. Our implementation is tested with the help of Table 1 in Paul (1978), where values for $\bar{I}_{60}^{m}$ and $\bar{I}_{100}^{m}$ for some ϑ_1 $(= \arccos t_1)$ and ϑ_2 $(= \arccos t_2)$ are given. We present our results in Table 4.1. In all cases we do not exceed errors larger than 0.03% which is quite a good value since recurrence formulae are highly sensitive to numerical errors since even small errors are propagated and amplified dramatically due to the repeated application of the scheme.

In the following section we will now apply the previously derived formulae to the isostatic crustal model and investigate if the presented model is indeed capable of explaining the short scale features in the Earth's gravitational field.

4.7.3 Results

Applying the spherical cube calculations of the previous section to our isostatic crustal model, derived from ETOPO and Airy's hypothesis, we find the model geoid that we present in Figure 4.27. Addi-

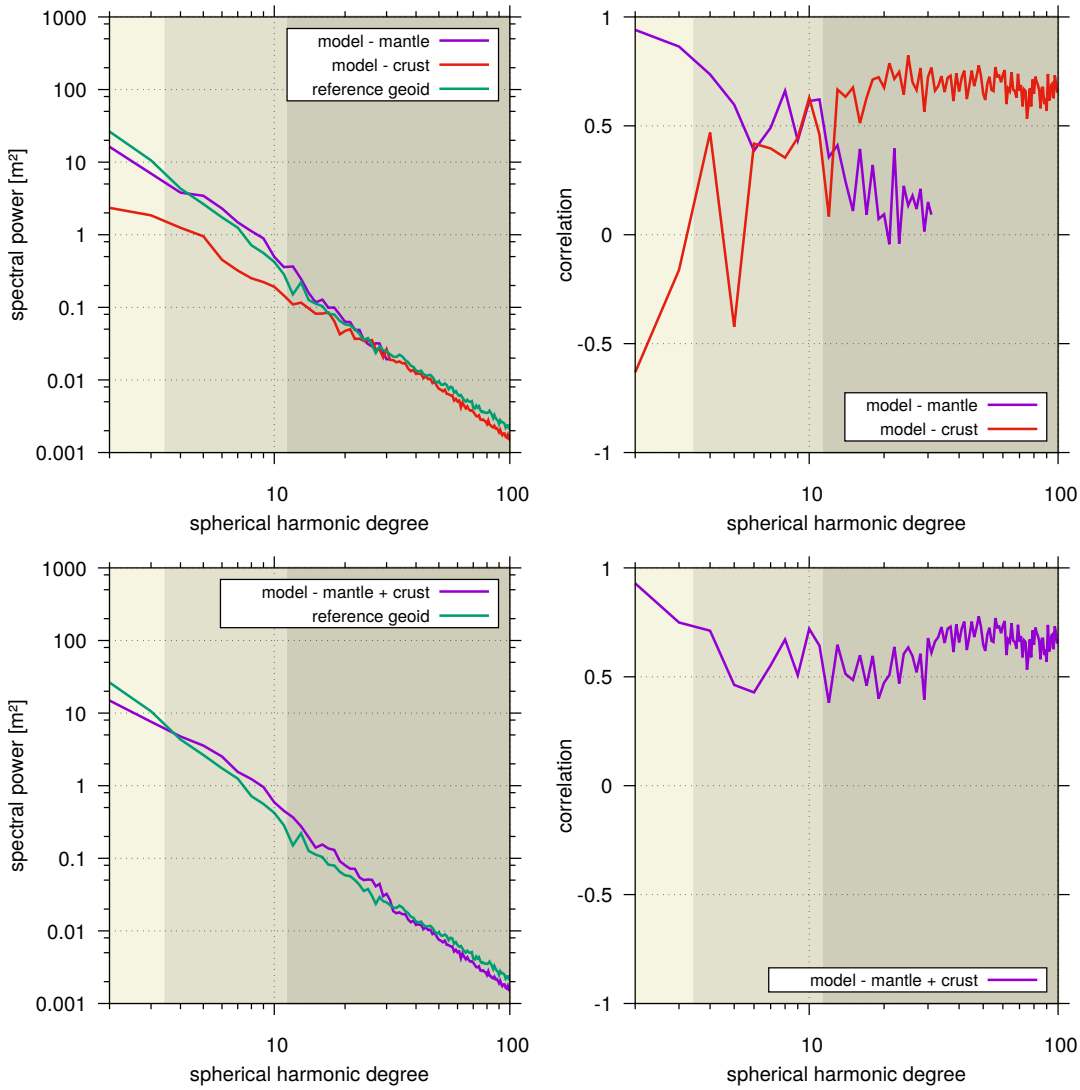

Figure 4.28: Top: spectral power and correlation (to the reference) of the crustal geoid model, derived from Airy's isostatic hypothesis. In addition, we restate the properties of our current mantle geoid model (see Figure 4.22). Bottom: hybrid model of both mantle and crustal features. The resulting correlation shows an almost perfect fit to the observations throughout all harmonic frequency bands.

tionally, we show the respective gravity anomaly map in order to get also a distinct view at the higher harmonic degrees. We see that the geoid mainly reflects the topographic structure, i.e. we find geoid heights generated by elevated mountain chains and geoid lows over oceans. The overall amplitude is much smaller than the observed geoid but this is perfectly what we expected since the main spectral power of the geoid is generated by the lower degree harmonics that we already associated with deeper mantle structures. However, the much more intriguing plot here is the lower one that shows the gravity anomalies. Here, we focus at the high frequency band and indeed find large similarities to the observed gravity anomalies that we presented in Figure 4.4. Finally, we turn these optical similarities again into the common mathematical formalism and show in Figure 4.28 the degree dependent correlation of the derived gravitational field from isostasy to the reference field up to degree $l = 100$. In addition, we restate the correlation curve from our previous geoid model (see Figure 4.22). And indeed, we find that the gravitational field derived from the crustal model shows an astonishing correlation to the observations throughout all harmonic degrees in the third harmonic sector. Furthermore, we also

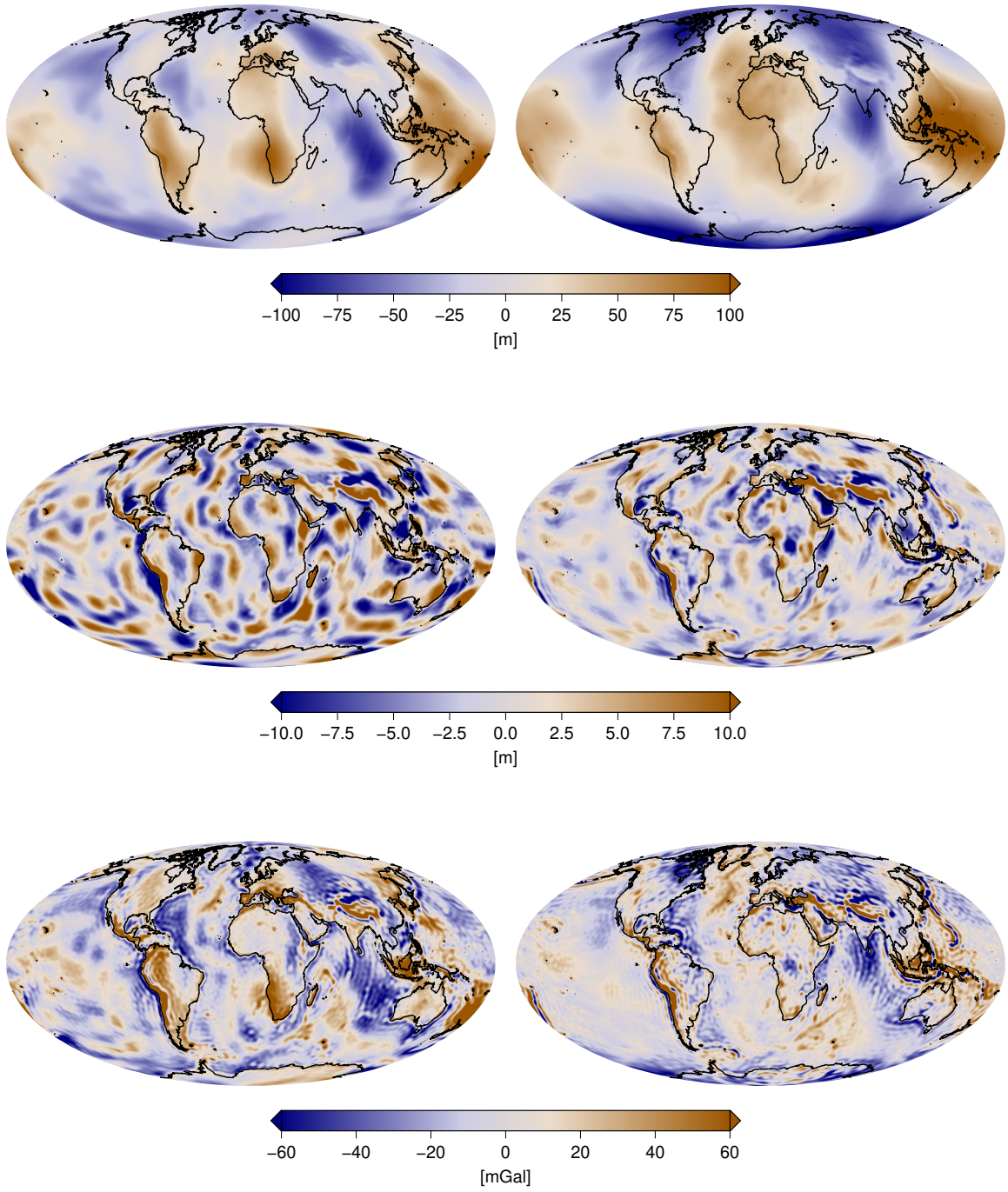

Figure 4.29: The synthetic gravitational field, derived from a hybrid model of crustal and mantle features (left), compared to the observed data set, derived from EIGEN-5C (right). The gravitational field is represented in terms of the geoid (first row), a filtered version of the geoid, where only the harmonic degrees $l = 12 - 100$ are shown (second row) and gravity anomalies (third row).

see that the crustal field has basically little to almost no influence on the harmonics of the first and second sector. This is also illustrated by the much less intense power spectrum of the crustal model in these degrees, compared to the reference field and the model geoid derived from pure mantle structures.

These correlation plots highly suggest to merge both crustal and mantle geoid into one hybrid model. As we have already stated earlier, we even have not considered the uppermost 150 km of the density structure derived from seismic tomography before. Thus, in a final step, we just added the derived crustal to our mantle density structure to gain a final model that is intended to fit both lower and higher harmonic degrees of the observed gravitational field. And indeed, the expected result can be found in the lower part of Figure 4.28, where we see an almost perfect correlation of the hybrid model throughout all harmonic degrees. A plot of the model geoid, generated by this hybrid model can be found in Figure 4.29. The first row shows the total geoid, the second row a filtered version, where only the harmonic degrees of the third frequency sector, i.e. $l = 12 - 100$ are shown. The last row presents the total gravitational field in terms of gravity anomalies. The first column shows the results from our hybrid model, where the second column represents the observed data sets.

We want to finish this chapter with a very brief overview of **true polar wander**, i.e. variations in the Earth's rotational axis over time due to changes in the mass distribution in the Earth's mantle. The mathematical principles behind true polar wander are closely connected to the gravitational potential and thus, worth mentioning in this chapter. Furthermore, since true polar wander directly relates to mass changes in the Earth's mantle, it may even serve as an additional data set that helps to constrain time-dependent mantle circulation models that we will examine in the next and final chapter of this work.

4.8 True polar wander (brief overview)

For a rotating body, a stable axis of rotation can be determined by its inertia tensor, which is a measure of how the mass inside the body is distributed. It turns out that in general, two of the three principle axes of the inertia tensor are stable rotation axes, where the third one always remains unstable. The Earth is a rotating body. Thus, changes of the interior mass distribution due to mantle circulation naturally also leads to a change in the inertia tensor and as a consequence, also to a varying axis of rotation over geological time scales. This time variable change of the Earth's rotation axis due to a change in internal mass distribution is called **true polar wander (TPW)** - in contrast to **apparent polar wander (APW)** which describes the motion of the lithosphere with respect to the magnetic pole. In particular due to paleomagnetic reconstructions (see e.g., Besse and Courtillot, 2002) constraints for true polar wander of the Earth can be determined. These data sets show changes in the rotational axis of approx. $0.3° - 0.5°$ per Myr and a total amplitude of approx. $30°$ over the last 200 Myrs. Thus, due to its natural time-dependency, true polar wander may serve as a valuable data set for constraining time-dependent numerical mantle circulation models. In order to compare model to data, in this case, the task would be to derive synthetic true polar wander paths from the numerical simulations. In this section, we show that indeed, this is possible by explicitly linking the inertia tensor to the gravitational field.

The inertia tensor $I \in \mathbb{R}^{3\times 3}$ is defined in Cartesian coordinates by

$$I_{ij} := \int_V (r^2\,\delta_{ij} - x_i\,x_j)\rho(x)\,\mathrm{d}V(x)\,, \tag{4.79}$$

$i, j = 1, 2, 3$, with $r = |x|$, $x \in \mathbb{R}^3$. Note that I is symmetric. In order to be able to find a connection between this representation and the gravitational potential, as usual, a step into the harmonic perspective will again reveal the essential insights. Here, the obvious first step is to transfer

the formula above from Cartesian in spherical polar coordinates. We find:

$$\begin{aligned}
I_{12} &= -\int_V x_1 x_2\, \rho(x)\, \mathrm{d}V(x) = -\int_V r^2 \big(1-t^2\big)\, \cos\varphi \sin\varphi\, \rho(x)\, \mathrm{d}V(x)\,, \\
I_{23} &= -\int_V x_2 x_3\, \rho(x)\, \mathrm{d}V(x) = -\int_V r^2 t\sqrt{1-t^2}\, \sin\varphi\, \rho(x)\, \mathrm{d}V(x)\,, \\
I_{13} &= -\int_V x_1 x_3\, \rho(x)\, \mathrm{d}V(x) = -\int_V r^2 t\sqrt{1-t^2}\, \cos\varphi\, \rho(x)\, \mathrm{d}V(x)\,, \\
I_{11} &= \int_V (x_2^2 + x_3^2)\, \rho(x)\, \mathrm{d}V(x) = \int_V r^2 \left(t^2 + \big(1-t^2\big)\sin^2\varphi\right)\, \rho(x)\, \mathrm{d}V(x)\,, \\
I_{22} &= \int_V (x_1^2 + x_3^2)\, \rho(x)\, \mathrm{d}V(x) = \int_V r^2 \left(t^2 + \big(1-t^2\big)\cos^2\varphi\right)\, \rho(x)\, \mathrm{d}V(x)\,, \\
I_{33} &= \int_V (x_1^2 + x_2^2)\, \rho(x)\, \mathrm{d}V(x) = \int_V r^2 \big(1-t^2\big)\, \rho(x)\, \mathrm{d}V(x)\,.
\end{aligned} \tag{4.80}$$

In (1.219) we stated the explicit form of the spherical harmonics of degree 2, which we repeat here. In addition, we substitute the $\cos(2\varphi)$ and $\sin(2\varphi)$ terms using the addition theorems

$$\sin(2\varphi) = 2\cos\varphi\sin\varphi\,, \qquad \cos(2\varphi) = \cos^2\varphi - \sin^2\varphi\,. \tag{4.81}$$

We then find:

$$\begin{aligned}
Y_{2,0}(\varphi,t) &= \sqrt{\frac{5}{16\pi}}\,\big(3t^2-1\big)\,, & Y_{2,1}(\varphi,t) &= \sqrt{\frac{15}{4\pi}}\,t\,\sqrt{1-t^2}\,\cos\varphi\,, \\
Y_{2,-1}(\varphi,t) &= \sqrt{\frac{15}{4\pi}}\,t\,\sqrt{1-t^2}\,\sin\varphi\,, & Y_{2,2}(\varphi,t) &= \sqrt{\frac{15}{16\pi}}\,\big(1-t^2\big)\,\big(\cos^2\varphi - \sin^2\varphi\big)\,, \\
Y_{2,-2}(\varphi,t) &= \sqrt{\frac{15}{4\pi}}\,\big(1-t^2\big)\cos\varphi\sin\varphi\,.
\end{aligned} \tag{4.82}$$

Substituting these relations into (4.80) and performing some additional rearrangements in the diagonal components yields the following representation of the inertia tensor in terms of the spherical harmonics:

$$\begin{aligned}
I_{12} &= -\sqrt{\frac{4\pi}{15}}\int_V r^2\, Y_{2,-2}(\varphi,t)\, \rho(x)\, \mathrm{d}V(x)\,, \\
I_{23} &= -\sqrt{\frac{4\pi}{15}}\int_V r^2\, Y_{2,-1}(\varphi,t)\, \rho(x)\, \mathrm{d}V(x)\,, \\
I_{13} &= -\sqrt{\frac{4\pi}{15}}\int_V r^2\, Y_{2,1}(\varphi,t)\, \rho(x)\, \mathrm{d}V(x)\,, \\
I_{11} &= \int_V r^2 \left(t^2 + \frac{1}{2}\big(1-t^2\big)\sin^2\varphi + \frac{1}{2}\big(1-t^2\big)\,\big(1-\cos^2\varphi\big)\right)\, \rho(x)\, \mathrm{d}V(x) \\
&= \int_V r^2 \left(\frac{1}{2}\left(t^2 - \frac{1}{3}\right) + \frac{2}{3} + \frac{1}{2}\big(1-t^2\big)\,\big(\sin^2\varphi - \cos^2\varphi\big)\right)\, \rho(x)\, \mathrm{d}V(x) \\
&= \int_V r^2 \left(\frac{2}{3} + \sqrt{\frac{4\pi}{15}}\left(\sqrt{\frac{1}{3}}\, Y_{2,0}(\varphi,t) - Y_{2,2}(\varphi,t)\right)\right)\, \rho(x)\, \mathrm{d}V(x)\,,
\end{aligned} \tag{4.83}$$

$$
\begin{aligned}
I_{22} &= \int_V r^2 \left(t^2 + \frac{1}{2}\left(1-t^2\right)\cos^2\varphi + \frac{1}{2}\left(1-t^2\right)\,\left(1-\sin^2\varphi\right)\right)\,\rho(x)\,\mathrm{d}V(x) \\
&= \int_V r^2 \left(\frac{1}{2}\left(t^2 - \frac{1}{3}\right) + \frac{2}{3} + \frac{1}{2}\left(1-t^2\right)\left(\cos^2\varphi - \sin^2\varphi\right)\right)\,\rho(x)\,\mathrm{d}V(x) \\
&= \int_V r^2 \left(\frac{2}{3} + \sqrt{\frac{4\pi}{15}}\left(\sqrt{\frac{1}{3}}\,Y_{2,0}(\varphi,t) + Y_{2,2}(\varphi,t)\right)\right)\rho(x)\,\mathrm{d}V(x)\,, \\
I_{33} &= \int_V r^2\left(1-t^2\right)\,\rho(x)\,\mathrm{d}V(x) \\
&= \int_V r^2 \left(\frac{2}{3} - \left(t^2 - \frac{1}{3}\right)\right)\,\rho(x)\,\mathrm{d}V(x) \\
&= \int_V r^2 \left(\frac{2}{3} - \sqrt{\frac{16\pi}{45}}\,Y_{2,0}(\varphi,t)\right)\,\rho(x)\,\mathrm{d}V(x)\,.
\end{aligned}
$$

From here, only a small step is left to find the explicit connection to the harmonic coefficients of the gravitational potential U. To this end, we restate (4.7), where we found that

$$
U_{l,m}(R) = -\frac{4\pi G}{2l+1}\frac{1}{R^{l+1}}\int_V r^l\,Y_{l,m}(\eta)\,\rho(y)\,\mathrm{d}V(y)\,. \tag{4.84}
$$

Finally, by just comparing (4.83) and (4.84) we find that:

$$
\begin{aligned}
I_{12} &= \frac{R^3}{G}\sqrt{\frac{5}{12\pi}}\,U_{2,-2}(R)\,, \\
I_{23} &= \frac{R^3}{G}\sqrt{\frac{5}{12\pi}}\,U_{2,-1}(R)\,, \\
I_{13} &= \frac{R^3}{G}\sqrt{\frac{5}{12\pi}}\,U_{2,1}(R)\,, \\
I_{11} &= -\frac{R^3}{G}\sqrt{\frac{5}{12\pi}}\left(\sqrt{\frac{1}{3}}\,U_{2,0}(R) - U_{2,2}(R)\right) - \int_V \frac{2}{3}\,r^2\,\rho(x)\,\mathrm{d}V(x) \\
I_{22} &= -\frac{R^3}{G}\sqrt{\frac{5}{12\pi}}\left(\sqrt{\frac{1}{3}}\,U_{2,0}(R) + U_{2,2}(R)\right) - \int_V \frac{2}{3}\,r^2\,\rho(x)\,\mathrm{d}V(x) \\
I_{33} &= \frac{R^3}{G}\sqrt{\frac{5}{9\pi}}\,U_{2,0}(R) - \int_V \frac{2}{3}\,r^2\,\rho(x)\,\mathrm{d}V(x)\,.
\end{aligned} \tag{4.85}
$$

Where the non-diagonal terms of the inertia tensor find a direct correspondence to respective potential coefficients, the diagonal terms are combinations. Here, for the inverse transform we find

$$
\begin{aligned}
U_{2,0} &= \frac{G}{R^3}\sqrt{\frac{4\pi}{5}}\left(I_{33} - \frac{1}{2}\left(I_{11}+I_{22}\right)\right)\,, \\
U_{2,2} &= \frac{G}{R^3}\sqrt{\frac{3\pi}{5}}\left(I_{11} - I_{22}\right)\,.
\end{aligned} \tag{4.86}
$$

The relations (4.85) and (4.86) are called **McCullagh's formula**. On the diagonal of I we notice an additional term next to the second degree harmonics of the gravitational potential. Since this term shows up only on the diagonal, it must be related to purely symmetric components of V. Thus, if we transfer the previous relations from the total potential U to the disturbed potential $\tilde{U}$, where

a symmetric reference field is subtracted, these diagonal elements vanish and we find a respective relation between disturbed potential and disturbed inertia tensor with respect to the reference field.

In particular, equipped with the McCullagh formula we can transfer a time series of gravitational potentials into a time series of corresponding inertia tensors, where the time scales can reach e.g. from the lifetime of gravity satellite missions to even geological times. Especially, since the gravitational potential time series is a possible output of a mantle circulation model (e.g. by using the Stokes matrix formalism as presented in this work), in this way it is possible to simulate the variation of the Earth's inertia tensor over a period of $10-100\,\mathrm{Myr}$. Where in a perfect spherical Earth, the rotational axis would adjust almost instantaneously to a change in the principles axes of inertia, in reality, the equatorial bulge due to the centrifugal force provides a large stability mechanism (see e.g., Munk and MacDonald, 1960). Thus, in reality, the rotational axis always follows the largest axis of principle inertia with a certain time delay that mainly depends on the viscoelastic behaviour and adjustment times of the Earth's mantle. The theoretical background for this time-dependent behaviour can be found in the conservation of angular momentum for a rotating system, which states in the case under consideration as the so-called **Liouville equation**. Here we find that

$$\frac{\mathrm{d}}{\mathrm{d}t}\left(I\omega\right)+\omega\wedge\left(I\omega\right)=0\,, \tag{4.87}$$

where $\omega\in\mathbb{R}^3$ is the rotational axis and I the inertia tensor. In practise, here, the inertia tensor is split into three parts. The first part describes the effect of a spherical non-rotating Earth. Here we only find non-vanishing entries on the diagonal of the matrix. A second part contains information about the equatorial bulge through the centrifugal force and its deformation due to a change of the rotational axis. Here, one enters the systematics of **Love numbers** that describe the dynamic response of a system due to a certain stimulus. Thus, this theory is a very close relative to the concept of the kernels, Green's functions and fundamental solutions that we have followed in the course of this work. The third part in the inertia splitting takes account of the change in the interior mass distribution due to mantle convection, where - as already stated before - the McCullagh formula is used to build the connection between disturbed gravity field and inertia tensor.

We used the described formalism to examine mantle circulation models that differ in the assumed value of the CMB temperature (2900 K - 4200 K) in terms of true polar wander paths and amplitudes. This was published in 'Geochemistry, Geophysics, Geosystems' (2009) as 'Schaber K., Bunge H.-P., Schuberth B.S.A., Malservisi R., Horbach A.: Stability of the rotation axis in high-resolution mantle circulation models: Weak polar wander despite strong core heating', doi.org/10.1029/2009GC002541 (see Schaber et al., 2009).

Chapter 5

The adjoint method in geodynamics

This chapter is published in the 'International Journal on Geomathematics' (GEM) (2014) as 'Horbach, A., Bunge, H.-P., Oeser J.: The adjoint method in geodynamics: derivation from a general operator formulation and application to the initial condition problem in a high resolution mantle circulation model', doi.org/10.1007/s13137-014-0061-5 (see Horbach et al., 2014). Where all previous chapters have dealt with the static problem, in the final chapter of this work, we introduce the time-dependency into the governing equations by means of the energy equation (2.31) which is formulated in terms of a differential equation with respect to the temperature field. Thus, we are immediately faced with the problem how appropriate initial conditions for the temperature field may be chosen. Since we cannot expect to have real data for the temperature field for the Earth's state some million years ago, we need to develop new strategies how to overcome this intrinsic problem in mantle dynamics.

The following sections are predominantly taken from the publication, except for passages where adjustments were considered to be appropriate in order to sustain the *flow* of this work. For example in Section 5.3, where the governing equations are introduced, we changed the overall notation in a way that it fits consistently to all former chapters. We also added some additional remarks and references in order to build a connection to the derivations from the previous course of this work.

Moreover, we corrected an error that is contained in the publication, i.e. after (5.60) (which is (59) in the paper), it is written that:

"We discussed earlier that $\widehat{v} \cdot n(x)$ can be arbitrary on the boundary ∂V. Thus we must impose $\gamma(x,t) = 0$ for all $x \in \partial V$ and $t \in I$ on the test function γ to make the surface integral vanish."

This is a wrong statement, since the no-outflow condition forces $\widehat{v}_r = 0$ and the surface integral vanishes without the need of imposing any constraints on γ. Therefore, since γ turns out to play the role of the pressure field in the adjoint momentum equation, we have to set an additional (arbitrary) boundary condition at one of both domain boundaries in order to make this equation remain solvable. In analogy to the forward equations, we then chose $\gamma(x,t) = 0$ for all $x \in S$ and $t \in I$. For the sake of clarity, we want to state that this was just a misprint and all presented calculations were performed using a correct implementation of the boundary conditions.

5.1 Introduction

Mantle convection is a vital part of the Earth system. The continuous deformation produced inside the Earth's mantle by slow, viscous creep has a far greater impact on our planet than might be immediately evident. Reshaping the Earth's surface, mantle convection for instance provides the driving

forces necessary to support large-scale horizontal motion in the form of plate tectonics and the associated earthquake and mountain-building activity.

The time scale of tectonic processes, typically on the order of millions of years, is sufficiently long that the Earth's mantle, although behaving like a solid on seismic time scales and capable of transmitting seismic shear waves, can be treated as a fluid. Mantle convection is thus governed by hydrodynamic field equations expressing the fundamental principles of mass, momentum, and energy conservation (see Jarvis and Mckenzie, 1980, for an extended derivation). Because of the high viscosity of the Earth's mantle (on the order of 10^{21} Pas, see Mitrovica and Forte, 2004, for a review), the momentum conservation law simplifies to the Stokes equation. The inertia terms can be ignored owing to the negligible flow velocities (on the order of cm/year) and accelerations, resulting in an instantaneous balance of frictional and buoyancy forces. Time-dependence enters the mantle convection system through the energy equation, which describes the transport of heat inside the Earth's mantle by advection and conduction.

A rich spectrum of physics is compatible with the governing equations. Powerful computer models are available for simulating the mantle convection process (see Tackley, 2012, for a recent review) and new software is opening a path to exa-scale computing (Burstedde et al., 2013; Gmeiner et al., 2013). However, much uncertainty compromises our knowledge of crucial material parameters (temperature, composition, strength) in the mantle. In principle, it is possible to resolve the uncertainties by testing mantle convection models against constraints gleaned from the geologic record. For instance, paleo-shorelines and the structure of sedimentary basins varied in time, due in part to changes in mantle induced dynamic topography of our planet (see Braun, 2010, for a review of the surface expressions of mantle dynamics). However, geologic events - by definition - happened in the past. Modelling paleo-mantle convection currents, so that they can be linked to the geologic record requires knowledge of the state of the convective system in the past. This state, of course, is not available to us.

Over the past two decades, geophysicists have constructed mantle circulation models (MCMs) to overcome the initial condition problem (Bunge, 1998). The models compensate for lack of initial condition information by postulating *a-priori* a pattern of mantle heterogeneity for an earlier geologic period. A given mantle flow model is integrated forward in time from the assumed initial state to the time of interest, with a model for the history of past plate motion (see e.g., Seton et al., 2012, for a detailed discussion of a particular global plate motion model) serving as the surface boundary condition for velocity in the momentum equation. It would be impossible to obtain meaningful MCMs without past plate motion models: tectonic plates cover 4/5 of the total surface area of the mantle, with the core-mantle boundary (CMB) accounting for the other 1/5. Thus past plate motion models constrain the history of mantle surface velocities by 80 percent, substantially reducing the non-uniqueness inherent in attempts to model mantle flow through time. MCMs have yielded important insight into the relation of mantle heterogeneity and the history of plate motion: they demonstrated that much of the large-scale structure of the Earth's mantle can be attributed to the sinking of dense, old ocean floor to the CMB (e.g., Bunge et al., 2002; McNamara and Zhong, 2005). They also show that the mantle is likely to be of uniform chemical composition at the scale of convection cells (Schuberth et al., 2009a; Davies et al., 2012). Thus past plate motion models provide key constraints also on the mantle thermal structure, as advocated early on by geodynamicists (e.g., Richards and Engebretson, 1992).

The *ad hoc* nature of the initial conditions assumed in MCMs is a limitation and prompted an alternative approach, known as backward advection. Here, an estimate for present day mantle structure, commonly derived from global-scale seismic imaging, serves as the initial condition for a flow calculation. The underlying heat equation is then integrated backward in time, neglecting thermal diffusion. Backward advection exploits the immense convective vigour of the mantle, i.e., for short time periods, on the order of a few million years, thermal advection (which is time-reversible) dominates over diffusion. Running mantle convection models back in time has given us a glimpse of many of the geologic phenomena affected by secular mantle variations. For instance, one has learned that hot spot

movement and significant vertical motion in the interior of continents is associated with the evolving mantle density structure (Steinberger and O'Connell, 1998; Conrad and Gurnis, 2003; Heine et al., 2010; Moucha et al., 2008b). The primary reason for the failure of backward integration as a viable strategy for inferring mantle paleo-structure is simple: it leads to an accumulation of artefacts, especially near thermal boundary layers, where diffusion is, by definition, important; these are not optimal for retrieving the mantle paleo-state (Bunge et al., 2003).

For this reason, optimisation techniques are coming to the fore as a powerful approach to the recovery of past deep Earth structure. Geophysicists seek solutions that minimise the difference between mantle heterogeneity inferred (in some form) from seismic imaging and predictions of dynamic models, subject to optimal initial conditions. This is an inverse problem. Crucial to its solution is that the model derivative be found relative to the unknown initial state. Obtaining the derivative by means of classic finite differencing techniques is impractical due to the large number of parameters (on the order of 10^{12}) in modern dynamic Earth models. The adjoint method, advocated early on in meteorology (Talagrand and Courtier, 1987) and seismology (Tarantola, 1984), is a mathematically elegant and computationally efficient method for obtaining the gradient information needed in the inversion. Increasing computational resources make the adjoint approach attractive across the geosciences - in, for example, oceanography (Menemenlis and Wunsch, 1997), seismology (Tromp et al., 2005; Fichtner et al., 2006a,b), and simulations of tectonics (Iaffaldano et al., 2007) and the geodynamo (Fournier et al., 2010). The adjoint equations for mantle dynamics have been derived using the concept of Lagrangian multipliers (Bunge et al., 2003; Liu and Gurnis, 2008; Ismail-Zadeh et al., 2004) and a detailed discussion of model, data and parameter errors is provided in Bunge et al. (2003).

Here we start with a more general approach. Using a general operator formulation in Hilbert spaces, we derive the adjoint versions of the energy, Stokes and continuity equation. This allows us to connect to recent work in seismology (Fichtner et al., 2006a,b), where the approach was used to derive the adjoint equations for the scalar wave equation in two dimensions. We organise our paper as follows: A first part of the paper consists of a detailed derivation of the adjoint equations in geodynamics. We present a general operator approach to the adjoint method and apply the results to the incompressible mantle flow equations, i.e. conservation of mass, momentum and energy. A second part applies the theory to a high-resolution numerical mantle circulation model. We explore the ability to restore earlier mantle structure and demonstrate the robustness of the method to converge to an optimal initial state.

5.2 Preliminaries

We introduce the adjoint method in a general way using an operator formulation. To this end we recall that one can extend the usual definition of a derivative to general operators. Let X and Y be Banach spaces and $F : X \to Y$ be an operator that maps an element $x \in X$ to an element $y \in Y$. We call F **Fréchet differentiable** at $x_0 \in X$ if and only if there exists a linear and bounded operator $L_{x_0} : X \to Y$ such that:

$$\lim_{h \to 0, h \in X} \frac{\|F(x_0 + h) - F(x_0) - L_{x_0}(h)\|_Y}{\|h\|_X} = 0\,, \tag{5.1}$$

where $\|\cdot\|_X$ and $\|\cdot\|_Y$ are the respective norms in X and Y. If this operator exists for all $x \in X$, then F is Fréchet differentiable and we can define $\mathcal{D}_x F := L_x$ as the Fréchet derivative of F with respect to x. $\mathcal{D}_x F$ is a linear operator that can be applied to any $\delta x \in X$, which is then commonly referred to as the direction of the derivative. Thus, in the following we call $\mathcal{D}_x F(\delta x) \in Y$ the derivative of F with respect to x in the direction δx. The Fréchet derivative $\mathcal{D}.F$ itself can be considered as a mapping $\mathcal{D}.F : X \to \mathcal{L}(X, Y)$, where $\mathcal{L}(X, Y)$ is the set of all linear and bounded operators between X and Y. Here, the term 'direction' is deliberately chosen since there is a direct connection to the well-known directional derivative. More precisely, the Fréchet derivative is a generalisation of the

total differential to Banach spaces.

It can be shown (e.g., Kress, 2014) that the common rules of differentiation (e.g., chain rule, product rule) transfer straightforwardly to Fréchet derivatives. For an operator $H : X \to Z$, with $H(x) := G(F(x))$, $x \in X$ and $F : X \to Y$, $G : Y \to Z$, applying the chain rule yields for the derivative of H with respect to $x \in X$ in the direction $\delta x \in X$:

$$\mathcal{D}_x H(\delta x) = \mathcal{D}_x (G \circ F)(\delta x) = \left(\mathcal{D}_{F(x)} G\right) \left(\mathcal{D}_x F(\delta x)\right) . \tag{5.2}$$

In the course of the upcoming derivations, we will regularly make use of this property.

In the following we have a detailed look at explicit definitions of inner products that we will use in this chapter. As mantle dynamics is a time-dependent process, we denote the relevant time interval with $I := [t_0, t_1]$, where t_1 is the present time and t_0 some point in the past. Our spatial domain of consideration is a spherical shell V, i.e. the Earth's mantle, with boundary $\partial V = S \cup C$, where S denotes the Earth's surface and C the CMB. Thus, we define for two squared-integrable scalar functions (e.g. the temperature and pressure field) $F, G \in \mathrm{L}^2(D)$, $D := V \times I$:

$$\langle F, G \rangle_{\mathrm{L}^2} := \int_D F(z)\, G(z)\, \mathrm{d}z = \int_I \int_V F(x,t)\, G(x,t)\, \mathrm{d}V(x)\, \mathrm{d}t \,, \tag{5.3}$$

and for two squared-integrable vectorial functions (e.g. the velocity field) $f, g \in \mathrm{l}^2(D)$:

$$\langle f, g \rangle_{\mathrm{l}^2} := \int_D f(z) \cdot g(z)\, \mathrm{d}z = \int_I \int_V f(x,t) \cdot g(x,t)\, \mathrm{d}V(x)\, \mathrm{d}t \,. \tag{5.4}$$

Moreover, it can be shown that for Hilbert spaces X, Y and a *linear and bounded* operator $F : X \to Y$ there exists a unique operator $F^* : Y \to X$ with

$$\langle F(x), y \rangle_Y = \langle x, F^*(y) \rangle_X \ , \tag{5.5}$$

for all $x \in X$ and $y \in Y$. This property is a direct consequence of **Riesz' representation theorem**. F^* is then called the **adjoint operator** to F. This property turns out to be a key aspect of the adjoint method, and thus, also giving it its name. As an example, in case of finite-dimensional real spaces and a linear operator A, which then can be identified with a matrix with real entries, we find that $A^* = A^T$ with respect to the Euclidean inner product. Indeed, we will also use this special property in the course of this chapter. While we will not discuss the linearity and boundedness of the respective operators, we will prove the existence of the adjoint operators in the context of mantle convection by determining them explicitly.

5.3 Forward equations and initial condition problem

Also here, all following considerations are built on the fundamental conservation equations. The essential difference to the previous work is the inclusion of the energy equation or in other words, time-dependency. Furthermore - and probably kind of irritating to the reader - in this chapter, we will not consider a harmonic analysis but work with the pure unmodified equations (shock!). We start again with the continuity equation, under the assumption of incompressibility. Then, from (2.10) we may restate

$$\nabla \cdot v = 0 \,. \tag{5.6}$$

Since in the following, we will explicitly include the energy equation and examine its coupling to the momentum equation, it is obligatory to choose a version of the momentum equation that is formulated in terms of temperature. For this reason, we restate (2.37), neglecting the tilde notation for the

disturbed quantities. Furthermore, we also do not consider the second-order effect of self-gravitation. We then arrive at:

$$-\nabla P + \nabla \cdot \left(\eta \left(\nabla v + (\nabla v)^T\right)\right) = -g_0 \alpha \left(T_{\text{av}} - T\right) \hat{\rho}_0 \epsilon^r \,, \tag{5.7}$$

where we explicitly expanded the temperature deviation $\tilde{T} = T_{\text{av}} - T$. In contrast to the previous chapters, here we denote the radial reference temperature by T_{av} (and not by T_0), since T_0 will later be used herein for the initial condition, the temperature at time $t = 0$. In addition to the momentum equation, we restate the explicit representation (2.18) of the stress tensor σ under the assumption of incompressibility:

$$\sigma = -P\mathbb{1}_3 + \eta \left(\nabla v + (\nabla v)^T\right) \,. \tag{5.8}$$

This relation will be necessary in the context of the boundary conditions since in this chapter, we do not have the possibility for an elegant formulation in terms of the harmonic coefficients.

Finally, time-dependency enters the system via the energy equation. Here, we restate (2.31) to find

$$\partial_t T + v \cdot \nabla T - \kappa \Delta T + H = 0 \,. \tag{5.9}$$

The coupled system of continuity, momentum and energy equation can only be solved by defining suitable initial and boundary conditions. Where the determination of the initial temperature is the key topic under consideration in this chapter, at least for the remaining conditions, we can make appropriate assumptions. In analogy to the previous chapters, for the velocity at the surface and the CMB, we may assume a no-slip or free-slip condition. Since we are now considering numerical circulation models and are not restricted to analytical solutions any more, we may also include toroidal velocity components as a boundary condition and use velocity fields that were derived from plate reconstruction models (e.g., Müller et al., 2008; Gurnis et al., 2012) for the tangential part of the velocity field at the surface (Dirichlet condition). More precisely, we set:

$$v_{\text{tan}}(x,t) = v_p(x,t) \,, \quad x \in S,\, t \in I \,. \tag{5.10}$$

In analogy to the models that we calculated in Chapter 4, for the velocity field at the CMB we choose a free-slip boundary condition. The latter reflects the low viscosity of the Earth's outer core - liquid iron - that is in contact with the lower boundary of the mantle. Thus, there exist no shear stresses along that boundary - i.e. $\sigma_{\text{tan}} = 0$ - which turns with (5.8) into:

$$\left(\left(\nabla v(x,t) + (\nabla v(x,t))^T\right) n(x)\right)_{\text{tan}} = 0 \,, \quad x \in C,\, t \in I \,. \tag{5.11}$$

Here, $n(x)$ denotes the outer normal vector at $x \in C$ with respect to the CMB. As we have already learned, this property can be regarded as a Neumann condition for the tangential part of the velocity field (with an additional factor of $1/r$, see Section 3.3.3). For the radial part of the velocity we restate the well-known constraint of a no-outflow condition. Here we set:

$$v_r(x,t) = v(x,t) \cdot n(x) = 0 \,, \quad x \in \partial V,\, t \in I \,. \tag{5.12}$$

The existence of the gradient of the pressure field P in the momentum equation requires a boundary condition at only one of the domain surfaces. We set:

$$P(x,t) = 0 \,, \quad x \in S,\, t \in I \,. \tag{5.13}$$

For the boundary conditions of the temperature field we choose temporally and spatially constant values T_S and T_C (Dirichlet condition) that describe the reference temperatures at the surface and the CMB, i.e. here we have:

$$\begin{aligned} T(x,t) &= T_S \,, \quad x \in S,\, t \in I \,, \\ T(x,t) &= T_C \,, \quad x \in C,\, t \in I \,. \end{aligned} \tag{5.14}$$

The momentum equation is time-independent and does not require an initial condition for velocity and pressure. But now, we come to the crucial part. The energy equation requires an initial condition for temperature, i.e. more precisely we need a T_0 with:

$$T(x, t_0) = T_0(x)\,, \quad x \in V\,. \tag{5.15}$$

As we already remarked before, the paleo state of the Earth's mantle is simply unknown, making it impossible to specify an appropriate initial condition for a mantle circulation model at some time in the past. But in the following, we will explicitly derive how the adjoint method allows us to navigate around this (inherently unsolvable) problem by approaching this difficulty in terms of an optimisation problem.

5.4 A general operator approach to the adjoint method

The goal of the optimisation is straightforward: we start from an unconstrained model trajectory, say a mantle convection model with an arbitrary guess for the initial temperature sometime in the past. Then this trajectory is corrected in such a way that it provides an optimal fit to the available constraints, say the thermal structure of the Earth's mantle today. Mathematically speaking, we minimise an objective (or misfit) function $\chi(p)$ that measures the difference between modelled temperature and a reference thermal field, representative of the Earth's mantle. In general $\chi(p)$ depends on a vector p of various model parameters. But for our problem at hand, p is one-dimensional and consists only of the initial temperature T_0.

Minimisation of χ, e.g. with the help of the conjugate gradient method (Fletcher and Reeves, 1964), requires computing the gradient of χ with respect to the model parameters p. In practice, the forward equations are differential equations. They are solved numerically and often involve discretisations with millions of grid points. This precludes determining the gradient of χ by numerical methods, like e.g. finite differencing. But luckily, the adjoint method is capable of providing a computationally efficient way to obtain this key value.

The misfit function χ may depend not only explicitly on the model parameters p, but also implicitly via a function $u(p)$. As we want to know the change of χ if we change the model parameters p by a small amount δp, we are seeking the Fréchet derivative of χ with respect to p in the direction δp. Applying the chain rule yields:

$$\mathcal{D}_p\chi(u,p)(\delta p) = \partial_u\chi(u,p)\left(\mathcal{D}_p u(\delta p)\right) + \partial_p\chi(u,p)(\delta p)\,. \tag{5.16}$$

Note that the total derivative of χ with respect to p has turned into three derivatives. Now, an important step is that we assume that χ can be expressed in terms of a scalar product, i.e. there exists a function $\widetilde{\chi}$ such that $\chi(u,p) = \langle\widetilde{\chi}(u,p), 1\rangle$. In most applications, this assumption can be satisfied using the L^2 scalar product. Using this representation, we find:

$$\begin{aligned}\mathcal{D}_p\chi(u,p)(\delta p) &= \partial_u\left\langle\widetilde{\chi}(u,p), 1\right\rangle\left(\mathcal{D}_p u(\delta p)\right) + \partial_p\left\langle\widetilde{\chi}(u,p), 1\right\rangle(\delta p)\\ &= \left\langle\partial_u\widetilde{\chi}(u,p)\left(\mathcal{D}_p u(\delta p)\right), 1\right\rangle + \left\langle\partial_p\widetilde{\chi}(u,p)(\delta p), 1\right\rangle\,.\end{aligned} \tag{5.17}$$

Since in practice, the misfit function χ, respectively $\widetilde{\chi}$, is in most cases not very complex, the determination of the partial derivatives $\partial_u\widetilde{\chi}(u,p)$ and $\partial_p\widetilde{\chi}(u,p)$ does commonly not cause insuperable problems. Obtaining $\mathcal{D}_p u$, however, is as hard to calculate as the total derivative of χ itself. In mantle dynamics, $\mathcal{D}_p u$ is a measure of how the initial temperature T_0 influences the temperature T at any point inside the mantle at any later point in time. Thus, it would be very beneficial if there was a way to eliminate this term from the right-hand side of (5.17). Here, our first step is to use the adjoint operators of the derivatives of $\widetilde{\chi}$ to isolate $\mathcal{D}_p u$. In this way, we transform (5.17) into:

$$\mathcal{D}_p\chi(u,p)(\delta p) = \left\langle\mathcal{D}_p u(\delta p), \left(\partial_u\widetilde{\chi}(u,p)\right)^*(1)\right\rangle + \left\langle\delta p, \left(\partial_p\widetilde{\chi}(u,p)\right)^*(1)\right\rangle\,. \tag{5.18}$$

Next we assume that there exists a functional L that depends on u and p with $L(u,p) = 0$. In most cases L is a differential operator - or a combination of differential operators - that describes the underlying physics. In our case, $L(u,p) = 0$ can be thought of as one of the conservation laws we discussed above. For the Fréchet derivative of L we find - in analogy to (5.16) - by applying the chain rule that:

$$0 = \mathcal{D}_p L(u,p)(\delta p) = \partial_u L(u,p)\left(\mathcal{D}_p u(\delta p)\right) + \partial_p L(u,p)(\delta p)\,. \tag{5.19}$$

Note that this equation also contains the derivative $\mathcal{D}_p u$ that we isolated in (5.18). Now, converting (5.19) into a weak formulation allows us to connect both equations. Thus, we multiply both sides with an arbitrary test function Ψ and apply the scalar product. Under the assumption that there also exists an adjoint operator to the partial derivatives of L, (5.19) turns into:

$$\begin{aligned} 0 &= \langle \partial_u L(u,p)\left(\mathcal{D}_p u(\delta p)\right), \Psi\rangle + \langle \partial_p L(u,p)(\delta p), \Psi\rangle \\ &= \left\langle \mathcal{D}_p u(\delta p), \left(\partial_u L(u,p)\right)^*(\Psi)\right\rangle + \left\langle \delta p, \left(\partial_p L(u,p)\right)^*(\Psi)\right\rangle\,. \end{aligned} \tag{5.20}$$

Now, as the last step, adding (5.20) to (5.18) yields:

$$\begin{aligned} \mathcal{D}_p \chi(u,p)(\delta p) = \big\langle \mathcal{D}_p u(\delta p), &\left(\partial_u \widetilde{\chi}(u,p)\right)^*(1) + \left(\partial_u L(u,p)\right)^*(\Psi)\big\rangle \\ &+ \left\langle \delta p, \left(\partial_p \widetilde{\chi}(u,p)\right)^*(1) + \left(\partial_p L(u,p)\right)^*(\Psi)\right\rangle\,. \end{aligned} \tag{5.21}$$

From this representation we now can conclude that the critical term $\mathcal{D}_p u$ on the right-hand side of the equation can be eliminated if it is possible to find a test function Ψ that satisfies:

$$\left(\partial_u L(u,p)\right)^*(\Psi) = -\left(\partial_u \widetilde{\chi}(u,p)\right)^*(1)\,. \tag{5.22}$$

This is the so-called **adjoint equation** to $L(u,p) = 0$. We see that the first task to approach this equation is the determination of the adjoint operator $(\partial_u L)^*$. If then, a test function Ψ can be found such that the previous equation holds, (5.21) reduces to:

$$\mathcal{D}_p \chi(u,p)(\delta p) = \left\langle \delta p, \left(\partial_p \widetilde{\chi}(u,p)\right)^*(1) + \left(\partial_p L(u,p)\right)^*(\Psi)\right\rangle\,. \tag{5.23}$$

Here we notice the presence of $(\partial_p L)^*$ and the test function Ψ from above, which emphasises again that determining adjoint operators to the functional L - respectively to its derivatives - is the crucial aspect of the theory. In order to shed light into the dark, next, we will apply this method explicitly to the governing equations of mantle circulation.

5.5 The adjoint equations in mantle dynamics

5.5.1 The objective function

As we have learned before, the objective - or misfit - function is the key element of our theory. At the end of the day, this is the function that we want to minimise with the help of the adjoint method. Per definition, this function has the requirement to serve as a measure for comparing our geodynamic model to a reference data set. As we discussed earlier, in our specific case, this data set is the temperature distribution inside the Earth's mantle at the present day, inferred from seismological and mineralogical means. A straightforward way to solve this task would be to define the misfit function just as the cumulative difference of model and data temperatures at the present time. Thus - staying in L^2 context - we use the squared difference and set:

$$\chi(T) := \frac{1}{2}\int_V \left(T(T_0,x,t_1) - T_E(x)\right)^2 \,\mathrm{d}V(x)\,, \tag{5.24}$$

where T_E denotes the reference data for the present time t_1, and T is our geodynamic temperature model. In order to emphasise the dependence of the model temperature on the initial state T_0, we

explicitly included T_0 as a parameter of T, together with the location $x \in V$ inside the Earth's mantle and the time $t \in [t_0, t_1]$. Moreover, as required in the previous section, we can express χ in terms of the L^2 scalar product as:

$$\chi(T) = \frac{1}{2} \int_I \int_V \left(T(T_0, x, t) - T_E(x)\right)^2 \delta(t - t_1) \, \mathrm{d}V(x) \, \mathrm{d}t = \langle \widetilde{\chi}(T, \cdot, \cdot), 1 \rangle_{\mathrm{L}^2} \, , \tag{5.25}$$

with

$$\widetilde{\chi}(T, x, t) := \frac{1}{2} \left(T(T_0, x, t) - T_E(x)\right)^2 \delta(t - t_1), \quad x \in V, \, t \in I \, . \tag{5.26}$$

From here on, we follow exactly the steps that we discussed in theory in the course of Section 5.4. We start with (5.18) and calculate the total derivative of the misfit function with respect to T_0, in the direction δT_0. Here, the initial temperature T_0 plays the role of p and the temperature distribution T the role of u in the notation of the previous section. In our case, $\widetilde{\chi}$ does not explicitly depend on T_0, but indirectly via T. Thus, the second term on the right-hand side in (5.18) vanishes and we obtain:

$$\begin{aligned} \mathcal{D}_{T_0} \chi(T)(\delta T_0) &= \left\langle \mathcal{D}_{T_0} T(\delta T_0), \left(\partial_T \widetilde{\chi}\right)^* (1) \right\rangle \\ &= \langle \mathcal{D}_{T_0} T(\delta T_0), \partial_T \widetilde{\chi}(T) \rangle \, , \end{aligned} \tag{5.27}$$

where

$$\partial_T \widetilde{\chi}(T) = \left(T(T_0, x, t) - T_E(x)\right) \delta(t - t_1) \, , \quad x \in V, t \in I \, , \tag{5.28}$$

and we dropped the dependence on x and t in the notation of the function $\widetilde{\chi}$. On the right-hand side of (5.27) we identify $\mathcal{D}_{T_0} T$, the total derivative of the temperature field T with respect to the initial thermal distribution T_0. This term is as hard to calculate as the total derivative of the misfit function itself. Now, recall that in order to eliminate $\mathcal{D}_{T_0} T$ from (5.27) in a next step, we need to use the underlying governing equations and derive their Fréchet derivatives and corresponding weak formulations. Here, we have three coupled forward equations (i.e. three operators L_1, L_2, L_3 in the sense of the previous section). Hence we perform the requested transformations for each of them individually, starting with the energy equation.

5.5.2 The energy equation

As a first step, we take the total derivative of both sides of the forward energy equation (5.9) with respect to T_0 and apply it to the direction δT_0. Using the chain rule we find that:

$$\begin{aligned} &\partial_t (\mathcal{D}_{T_0} T)(\delta T_0) + (\mathcal{D}_{T_0} v)(\delta T_0) \cdot \nabla T + v \cdot \nabla (\mathcal{D}_{T_0} T)(\delta T_0) \\ &- \kappa \Delta (\mathcal{D}_{T_0} T)(\delta T_0) + (\mathcal{D}_{T_0} H)(\delta T_0) = 0 \, . \end{aligned} \tag{5.29}$$

The internal heating H is independent of the initial temperature T_0, thus $\mathcal{D}_{T_0} H(\delta T_0)$ vanishes. Now, we convert the above equation into a weak formulation, multiply each side with an (at this point) arbitrary scalar test function Ψ and apply the inner product $\langle \cdot, \cdot \rangle_{\mathrm{L}^2}$. In order to keep everything as compact as possible, from now on we will drop the differential direction δT_0 in our notation. Furthermore, we denote all Fréchet derivatives with respect to T_0 by a 'hatted' variable, e.g. we rename $\widehat{T} := \mathcal{D}_{T_0} T$. (5.29) then turns into:

$$\boxed{\left\langle \Psi, \partial_t \widehat{T} \right\rangle_{\mathrm{L}^2} + \langle \Psi, \widehat{v} \cdot \nabla T \rangle_{\mathrm{L}^2} + \left\langle \Psi, v \cdot \nabla \widehat{T} \right\rangle_{\mathrm{L}^2} - \left\langle \Psi, \kappa \Delta \widehat{T} \right\rangle_{\mathrm{L}^2} = 0 \, .} \tag{5.30}$$

This equation serves as our basis in this subsection. Now, the crucial point is to isolate $\widehat{T}$ in the respective terms. At first glance, this sounds like a very challenging task but it turns out that in this

work, we have already come across a variety of transformation rules that we can apply in the following (see in particular Chapter 1). Furthermore, as the test function Ψ is arbitrary, another strategy is it to choose Ψ in such a way that its properties are useful for the required transformations. The determination of these properties will play an essential role in the course of all upcoming derivations.

We start with the first term on the left-hand side of (5.30), where we apply partial integration with respect to time, and arrive at:

$$\begin{aligned}\left\langle \Psi, \partial_t \widehat{T} \right\rangle_{\mathrm{L}^2} &= \int_I \int_V \Psi \left(\partial_t \widehat{T} \right) \,\mathrm{d}V(x)\,\mathrm{d}t \\ &= \int_V \left(\Psi \widehat{T} \right) \Big|_{t=t_0}^{t_1} \,\mathrm{d}V(x) - \int_I \int_V (\partial_t \Psi)\, \widehat{T} \,\mathrm{d}V(x)\,\mathrm{d}t \\ &= \int_V \left(\Psi(x,t_1)\, \widehat{T}(x,t_1) - \Psi(x,t_0)\, \widehat{T}(x,t_0) \right) \mathrm{d}V(x) - \left\langle \partial_t \Psi, \widehat{T} \right\rangle_{\mathrm{L}^2} .\end{aligned} \tag{5.31}$$

As a side remark, in our notation, from now on we will also drop the dependence on (x,t) of any function, where it is not explicitly necessary. We see that the second term on the right-hand side of the equation already has the desired form, i.e. we isolated $\widehat{T}$ inside the inner product. The first term still looks a little bit more complicated but here, we see that in order to make the first part of the integral vanish, we could just impose $\Psi(x,t_1) = 0$ for all $x \in V$ on the test function Ψ. Thus, we already found one property that we could put as a constraint on the test function that would be very helpful for reaching our goals. Furthermore, since $\widehat{T}(x,t_0) = (\mathcal{D}_{T_0} T_0)(\delta T_0) = \delta T_0$, also the second part of the integral can be simplified and (5.31) turns into:

$$\left\langle \Psi, \partial_t \widehat{T} \right\rangle_{\mathrm{L}^2} = - \left\langle \widehat{T}, \partial_t \Psi \right\rangle_{\mathrm{L}^2} - \int_V \Psi(x,t_0)\, \delta T_0(x) \,\mathrm{d}V(x) . \tag{5.32}$$

The next term in (5.30) that involves $\widehat{T}$ contains no time but spatial derivatives. We apply the identity $F(\nabla G \cdot u) = \nabla \cdot (FGu) - FG(\nabla \cdot u) - G(\nabla F \cdot u)$, that is valid for any scalar fields F, G and a vector field u, and find:

$$\begin{aligned}\left\langle \Psi, v \cdot \nabla \widehat{T} \right\rangle_{\mathrm{L}^2} = \int_I \int_V \nabla \cdot \left(\Psi \widehat{T} v \right) \,\mathrm{d}V(x)\,\mathrm{d}t - \int_I \int_V \Psi \widehat{T} \left(\nabla \cdot v \right) \,\mathrm{d}V(x)\,\mathrm{d}t \\ - \int_I \int_V \widehat{T} \left(\nabla \Psi \cdot v \right) \,\mathrm{d}V(x)\,\mathrm{d}t .\end{aligned} \tag{5.33}$$

Conservation of mass (5.6) allows us to drop the second term in this equation. Furthermore, with the help of the divergence theorem, we can convert the volume integral in the first term into a surface integral. We then find:

$$\left\langle \Psi, v \cdot \nabla \widehat{T} \right\rangle_{\mathrm{L}^2} = \int_I \int_{\partial V} \Psi \widehat{T} \left(v(x,t) \cdot n(x) \right) \,\mathrm{d}\omega(x)\,\mathrm{d}t - \left\langle \widehat{T}, v \cdot \nabla \Psi \right\rangle_{\mathrm{L}^2} , \tag{5.34}$$

where $n(x)$ is the unit outer normal at $x \in \partial V$. Here, we recognise the no-outflow condition inside the surface integral. Thus, this term also vanishes, and we find without any further constraints on the test function Ψ that:

$$\left\langle \Psi, v \cdot \nabla \widehat{T} \right\rangle_{\mathrm{L}^2} = - \left\langle \widehat{T}, v \cdot \nabla \Psi \right\rangle_{\mathrm{L}^2} . \tag{5.35}$$

In the third term that involves $\widehat{T}$ in equation (5.30) we find the Laplace operator. Applying Green's second identity (1.145) yields:

$$\begin{aligned}\left\langle \Psi, \kappa\Delta\widehat{T} \right\rangle_{\mathrm{L}^2} = \kappa \int_I \int_{\partial V} \Psi \left(\nabla\widehat{T} \cdot n \right) \,\mathrm{d}\omega(x)\,\mathrm{d}t - \kappa \int_I \int_{\partial V} \widehat{T}\,(\nabla\Psi \cdot n)\,\mathrm{d}\omega(x)\,\mathrm{d}t \\ + \kappa \int_I \int_V \widehat{T}\,(\Delta\Psi)\,\mathrm{d}V(x)\,\mathrm{d}t\,.\end{aligned} \tag{5.36}$$

We assumed T to be constant at the boundaries, i.e. $T(x,t) = T_{S/C}$ on ∂V. This implies $\widehat{T}(x,t) = 0$ on ∂V, and the second term vanishes. The normal derivative of $\widehat{T}$, i.e. $(\nabla\widehat{T} \cdot n)$ in the first integral, in contrast, can be arbitrary. But in order to eliminate this term, we could force Ψ to vanish at the boundaries, i.e. $\Psi(x,t) = 0$ for all $x \in \partial V$ and $t \in I$. Under these constraints, we find that:

$$\left\langle \Psi, \kappa\Delta\widehat{T} \right\rangle_{\mathrm{L}^2} = \kappa \int_I \int_V \widehat{T}\,(\Delta\Psi)\,\mathrm{d}V(x)\,\mathrm{d}t = \left\langle \widehat{T}, \kappa\Delta\Psi \right\rangle_{\mathrm{L}^2}\,. \tag{5.37}$$

Note that this equation shows that - under the assumed constraints and boundary conditions - the Laplace operator is **self-adjoint**. Now that we discussed all terms in (5.30) that contains the Fréchet derivative of T, we can collect our results and rewrite (5.30) as follows:

$$\boxed{-\int_V \Psi(x,t_0)\,\delta T_0(x)\,\mathrm{d}V(x) + \langle \Psi, \widehat{v}\cdot\nabla T\rangle_{\mathrm{L}^2} - \left\langle \widehat{T}, \partial_t\Psi + v\cdot\nabla\Psi + \kappa\Delta\Psi \right\rangle_{\mathrm{L}^2} = 0\,.} \tag{5.38}$$

We were able to perform these transformations under the constraints that

$$\boxed{\begin{aligned}\Psi(x,t_1) &= 0\,, \quad x \in V,\\ \Psi(x,t) &= 0\,, \quad x \in V,\, t \in I\,.\end{aligned}} \tag{5.39}$$

Now, adding the left-hand side of (5.38) to (5.27), we can reformulate the derivative of the misfit function as:

$$\begin{aligned}\mathcal{D}_{T_0}\chi(T)(\delta T_0) = \left\langle \widehat{T}, \partial_T\widetilde{\chi}(T) - \partial_t\Psi - v\cdot\nabla\Psi - \kappa\Delta\Psi \right\rangle_{\mathrm{L}^2} + \langle \widehat{v}, \Psi\nabla T\rangle_{\mathrm{l}^2} \\ - \int_V \Psi(x,t_0)\,\delta T_0(x)\,\mathrm{d}V(x)\,,\end{aligned} \tag{5.40}$$

where we also isolated the derivative $\widehat{v}$ of the velocity field, by expressing the L^2 in terms of the l^2 scalar product. At this point, we notice that imposing the additional constraint

$$\partial_t\Psi + v\cdot\nabla\Psi + \kappa\Delta\Psi = \partial_T\widetilde{\chi}(T)\,, \tag{5.41}$$

on the test function Ψ would cancel $\widehat{T}$ in the above equation, which was our primary goal. Unfortunately, we notice an additional Fréchet derivative $\widehat{v} = \mathcal{D}_{T_0}v$ in the second term, a measure of how the initial temperature field - through the buoyancy force - influences the velocity field at any point in time and space. Obviously, the calculation of $\mathcal{D}_{T_0}v$ is no less expensive than the determination of $\mathcal{D}_{T_0}T$ itself. In the next section, we will see that the momentum equation will provide us with some help to address this problem.

However, the high viscosity of the Earth's mantle ($\approx 10^{21}$ Pas) yields a spatially non-localised velocity field that is much smoother than the respective temperature field. Thus, $\mathcal{D}_{T_0}v$ can be considered as

small compared to $\mathcal{D}_{T_0}T$ in the context of mantle circulation and one may choose to drop the term in the previous equation (see e.g., Liu and Gurnis, 2008). With this simplification, (5.40) reduces to

$$\mathcal{D}_{T_0}\chi(T)(\delta T_0) = -\int_V \Psi(x,t_0)\,\delta T_0(x)\,\mathrm{d}V(x)\,, \tag{5.42}$$

if the additional constraint (5.41) holds for Ψ and all $x \in V$ and $t \in I$. We note that this simplification will not be valid for low viscosity fluids, where the velocity field is spatially more localised. In adjoint geodynamo simulations for the Earth's core (see e.g., Fournier et al., 2010; Li et al., 2011) the $\mathcal{D}_{T_0}v$ term is significant, and a system of adjoint equations comparable to those we will derive in the following sections must be solved.

5.5.3 The momentum equation

In analogy to the previous section, as the first step, we take the total derivative of both sides of the momentum equation (5.7) with respect to T_0 and apply it to the direction δT_0. We then find:

$$\begin{aligned}&\nabla\cdot\left(\eta\left(\nabla\left(\mathcal{D}_{T_0}v\right)(\delta T_0)+\left(\nabla\left(\mathcal{D}_{T_0}v\right)(\delta T_0)\right)^T\right)\right)-\nabla(\mathcal{D}_{T_0}P)(\delta T_0)\\&+g_0\alpha\left((\mathcal{D}_{T_0}T_{\mathrm{av}})(\delta T_0)-(\mathcal{D}_{T_0}T)(\delta T_0)\right)\hat{\rho}_0\epsilon^r=0\,.\end{aligned} \tag{5.43}$$

The radial average temperature T_{av} is independent of T_0, such that the derivative $\mathcal{D}_{T_0}T_{\mathrm{av}}$ vanishes. Again for clarity of notation, we drop from here on the direction δT_0 in our notation, and use the hat notation for the Fréchet derivatives. Now, as the second step, we convert this equation into a weak formulation, i.e. we multiply each hand side with an (at this point) arbitrary *vectorial* test function φ and apply the inner product $\langle\cdot,\cdot\rangle_{\mathrm{l}^2}$, to find:

$$\boxed{\left\langle\varphi,\nabla\cdot\left[\eta\left(\nabla\widehat{v}+(\nabla\widehat{v})^T\right)\right]\right\rangle_{\mathrm{l}^2}-\left\langle\varphi,\nabla\widehat{P}\right\rangle_{\mathrm{l}^2}-\left\langle\varphi,g_0\alpha\hat{\rho}_0\widehat{T}\epsilon^r\right\rangle_{\mathrm{l}^2}=0\,.} \tag{5.44}$$

As before, the task is now to isolate the total derivative $\widehat{v}$ in the respective terms, examining each of the scalar products separately. Using the identity

$$\nabla\cdot(F(\nabla u)v)-\nabla\cdot(F(\nabla v)u)=v\cdot(\nabla\cdot(F\nabla u))-u\cdot(\nabla\cdot(F\nabla v))\,, \tag{5.45}$$

that is valid for any vector fields u, v and a scalar field F, we can convert the first term in (5.44) into:

$$\begin{aligned}\left\langle\varphi,\nabla\cdot\left[\eta\left(\nabla\widehat{v}+(\nabla\widehat{v})^T\right)\right]\right\rangle_{\mathrm{l}^2}=&\int_I\int_V\nabla\cdot\left[\eta\left(\nabla\widehat{v}+(\nabla\widehat{v})^T\right)\varphi\right]\,\mathrm{d}V(x)\,\mathrm{d}t\\&-\int_I\int_V\nabla\cdot\left[\eta\left(\nabla\varphi+(\nabla\varphi)^T\right)\widehat{v}\right]\,\mathrm{d}V(x)\,\mathrm{d}t\\&+\int_I\int_V\widehat{v}\cdot\left(\nabla\cdot\eta\left(\nabla\varphi+(\nabla\varphi)^T\right)\right)\,\mathrm{d}V(x)\,\mathrm{d}t\,.\end{aligned} \tag{5.46}$$

First, we have a look at the first two integrals on the right-hand side of the previous equation. Applying the divergence theorem yields:

$$\begin{aligned}&\int_I\int_V\nabla\cdot\left[\eta\left(\nabla\widehat{v}+(\nabla\widehat{v})^T\right)\varphi\right]\,\mathrm{d}V(x)\,\mathrm{d}t-\int_I\int_V\nabla\cdot\left[\eta\left(\nabla\varphi+(\nabla\varphi)^T\right)\widehat{v}\right]\,\mathrm{d}V(x)\,\mathrm{d}t\\&=\int_I\int_{\partial V}\eta\left(\left(\nabla\widehat{v}+(\nabla\widehat{v})^T\right)\varphi\right)\cdot n(x)-\eta\left(\left(\nabla\varphi+(\nabla\varphi)^T\right)\widehat{v}\right)\cdot n(x)\,\mathrm{d}\omega(x)\,\mathrm{d}t\,,\end{aligned} \tag{5.47}$$

where $n(x)$ is the outer normal at $x \in \partial V$. At this point, we can elegantly exploit the formerly mentioned property that the adjoint of a real matrix is equal to its transposed. We reformulate the respective dot products with the normal vector n in terms of an inner product and then find that the right-hand side of (5.47) is equal to

$$\begin{aligned}&\int_I \int_{\partial V} \eta \left\langle \varphi, \left(\nabla \widehat{v} + (\nabla \widehat{v})^T\right)^* n(x) \right\rangle - \eta \left\langle \widehat{v}, \left(\nabla \varphi + (\nabla \varphi)^T\right)^* n(x) \right\rangle \,\mathrm{d}\omega(x)\,\mathrm{d}t \\ &= \int_I \int_{\partial V} \eta\, \varphi \cdot \left(\left((\nabla \widehat{v})^T + \nabla \widehat{v}\right) n(x)\right) - \eta\, \widehat{v} \cdot \left(\left((\nabla \varphi)^T + \nabla \varphi\right) n(x)\right) \,\mathrm{d}\omega(x)\,\mathrm{d}t\,.\end{aligned} \tag{5.48}$$

Now, we have a closer look at the remaining integrals and think about the boundary conditions that we imposed on v in our forward equations. In the first part of the integral, we recognise the free-slip condition (5.11) for the CMB that implies that $(\nabla \widehat{v} + (\nabla \widehat{v})^T)\, n(x)$ has no tangential component for all $x \in C$ and $t \in I$. Thus, we only have to consider the radial components here. In addition, also the integral over the Earth's surface S remains. In the second part of the integral, we immediately notice that the radial components at both boundaries vanish, due to the no-outflow condition. Furthermore, since we impose plate velocities at the surface (see (5.10)), the tangential part of the surface velocity does not depend on T_0 and thus, its derivative also vanishes. Thus, the remains of (5.48) state as:

$$\begin{aligned}&\int_I \int_S \eta\, \varphi \cdot \left(\left(\nabla \widehat{v} + (\nabla \widehat{v})^T\right) n(x)\right) \,\mathrm{d}\omega(x)\,\mathrm{d}t + \int_I \int_C \eta\, \varphi_r \left(\left(\nabla \widehat{v} + (\nabla \widehat{v})^T\right) n(x)\right)_r \,\mathrm{d}\omega(x)\,\mathrm{d}t \\ &- \int_I \int_C \eta\, \widehat{v} \cdot \left(\left(\nabla \varphi + (\nabla \varphi)^T\right) n(x)\right) \,\mathrm{d}\omega(x)\,\mathrm{d}t\,.\end{aligned} \tag{5.49}$$

If we have a careful look at this term, we see that we can make all parts vanish, if we impose on the up-to-now arbitrary test function φ the same boundary conditions that are satisfied by v. More precisely, in our case, for φ it must hold that

$$\boxed{\begin{aligned} \varphi_{\tan}(x,t) &= 0\,, \quad x \in S,\, t \in I\,, && \text{(no-slip)} \\ ((\nabla \varphi + (\nabla \varphi)^T)\, n(x))_{\tan} &= 0\,, \quad x \in C,\, t \in I\,, && \text{(free-slip)} \\ \varphi_r(x,t) &= 0\,, \quad x \in \partial V,\, t \in I\,. && \text{(no-outflow)} \end{aligned}} \tag{5.50}$$

It can easily be verified that also for all other possible choices of no-slip/free-slip combinations as boundary conditions for the velocity field v, they transfer into equal boundary conditions for φ. Under these constraints (5.46) then drastically simplifies to:

$$\left\langle \varphi, \nabla \cdot \left[\eta \left(\nabla \widehat{v} + (\nabla \widehat{v})^T\right)\right] \right\rangle_{\mathrm{l}^2} = \left\langle \widehat{v}, \nabla \cdot \left[\eta \left(\nabla \varphi + (\nabla \varphi)^T\right)\right] \right\rangle_{\mathrm{l}^2}\,. \tag{5.51}$$

Now we have isolated the total derivative $\widehat{v}$ in the first part of equation (5.44). But the second term in (5.44) contains the total derivative $\widehat{P} = \mathcal{D}_{T_0} P$ of the pressure field P with respect to the initial temperature T_0. As before, determining the latter would be as costly as the calculation of $\mathcal{D}_{T_0} T$ and $\mathcal{D}_{T_0} v$ itself. Nevertheless, we also try to isolate $\widehat{P}$ within the inner product. We apply the identity $\nabla \cdot (Fu) = F\, \nabla \cdot u + u \cdot \nabla F$, which holds for any scalar field F and vector field u, and again the divergence theorem to find:

$$\begin{aligned}\left\langle \varphi, \nabla \widehat{P} \right\rangle_{\mathrm{l}^2} &= \int_I \int_V \nabla \cdot \left(\widehat{P} \varphi\right) \,\mathrm{d}V(x)\,\mathrm{d}t - \int_I \int_V \widehat{P}\, (\nabla \cdot \varphi) \,\mathrm{d}V(x)\,\mathrm{d}t \\ &= \int_I \int_{\partial V} \left(\widehat{P} \varphi\right) \cdot n(x)\,\mathrm{d}\omega(x)\,\mathrm{d}t - \left\langle \widehat{P}, \nabla \cdot \varphi \right\rangle_{\mathrm{L}^2}\,.\end{aligned} \tag{5.52}$$

$\widehat{P}$ can become arbitrary at the boundaries but remembering that we just have imposed the no-outflow condition on φ, i.e. $\varphi_r(x,t) = \varphi(x,t) \cdot n(x) = 0$ for all $x \in \partial V$ and $t \in I$, the surface integral vanishes and we obtain:

$$\left\langle \varphi, \nabla \widehat{P} \right\rangle_{\mathrm{l}^2} = - \left\langle \widehat{P}, \nabla \cdot \varphi \right\rangle_{\mathrm{L}^2} . \tag{5.53}$$

What still remains is the third term on the left-hand side of (5.44). Here, we find the total derivative of the temperature field T, which we encountered in the energy equation before. Expressing the l^2 scalar product in terms of the L^2 scalar product allows us to combine the results from the energy and the momentum equation later on:

$$\left\langle \varphi, g_0 \alpha \hat{\rho}_0 \widehat{T} \epsilon^r \right\rangle_{\mathrm{l}^2} = \left\langle \widehat{T}, g_0 \alpha \hat{\rho}_0 \epsilon^r \cdot \varphi \right\rangle_{\mathrm{L}^2} = \left\langle \widehat{T}, g_0 \alpha \hat{\rho}_0 \varphi_r \right\rangle_{\mathrm{L}^2} . \tag{5.54}$$

At the end, we again collect the results of this section and rewrite equation (5.44) as follows:

$$\boxed{\left\langle \widehat{v}, \nabla \cdot \left[\eta \left((\nabla \varphi) + (\nabla \varphi)^T \right) \right] \right\rangle_{\mathrm{l}^2} + \left\langle \widehat{P}, \nabla \cdot \varphi \right\rangle_{\mathrm{L}^2} - \left\langle \widehat{T}, g_0 \alpha \hat{\rho}_0 \varphi_r \right\rangle_{\mathrm{L}^2} = 0 .} \tag{5.55}$$

Note that as before, this representation is only valid under the constraints (5.50). Now, adding the left-hand side of (5.55) to (5.40) leads us to the following updated expression for the total derivative of the objective function χ:

$$\begin{aligned} \mathcal{D}_{T_0} \chi(T)(\delta T_0) = \; & \left\langle \widehat{T}, \partial_T \widetilde{\chi}(T) - \partial_t \Psi - v \cdot \nabla \Psi - \kappa \Delta \Psi - g_0 \alpha \hat{\rho}_0 \varphi_r \right\rangle_{\mathrm{L}^2} \\ & + \left\langle \widehat{v}, \Psi \, \nabla T + \nabla \cdot \left[\eta \left(\nabla \varphi + (\nabla \varphi)^T \right) \right] \right\rangle_{\mathrm{l}^2} + \left\langle \widehat{P}, \nabla \cdot \varphi \right\rangle_{\mathrm{L}^2} \\ & - \int_V \Psi(x, t_0) \, \delta T_0(x) \, \mathrm{d}V(x) . \end{aligned} \tag{5.56}$$

Here, we now see that the inner product term corresponding to $\widehat{v}$ would vanish if φ satisfied

$$\Psi \, \nabla T + \nabla \cdot \left[\eta \left(\nabla \varphi + (\nabla \varphi)^T \right) \right] = 0 . \tag{5.57}$$

Likewise, $\widehat{P}$, the total derivative of the pressure field, would vanish if φ was divergence-free. This condition immediately reminds of the continuity equation for the velocity field v in the forward equations. Having this in mind, we notice that the derived adjoint equations are generally quite similar to the forward equations. Here, φ takes the role of the velocity field and indeed, in literature one commonly refers to φ as the **adjoint velocity field**. In the forward momentum equation, one satisfies $\nabla \cdot v = 0$ by adjusting the pressure field P such that the resulting velocity field v becomes divergence-free. Mathematically speaking, the gradient of pressure serves as a Lagrangian multiplier (e.g., Braess, 2001). Unluckily, we do not see such a possibility in the current equations, yet. But there is still one step to go.

5.5.4 The continuity equation

As in the two previous sections, we take the total derivative of both sides of the underlying equation with respect to T_0 and apply it to the direction δT_0. For incompressible flow, the continuity equation simplifies to a divergence-free criterion, and we find:

$$\boxed{\nabla \cdot (\mathcal{D}_{T_0} v)(\delta T_0) = 0 .} \tag{5.58}$$

Multiplication with another (scalar) test function γ and applying the inner product $\langle\cdot,\cdot\rangle_{\mathrm{L}^2}$ yields:

$$\langle\gamma, \nabla\cdot\widehat{v}\rangle_{\mathrm{L}^2} = 0\,. \tag{5.59}$$

We apply the identity $\nabla\cdot(Fu) = F\,\nabla\cdot u + u\cdot\nabla F$ that is valid for any scalar field F and any vector field u, and - as usual - the divergence theorem, to obtain:

$$\langle\gamma, \nabla\cdot\widehat{v}\rangle_{\mathrm{L}^2} = \int_I\int_{\partial V}(\gamma\widehat{v})\cdot n(x)\;\mathrm{d}\omega(x)\;\mathrm{d}t - \langle\widehat{v}, \nabla\gamma\rangle_{\mathrm{l}^2}\;. \tag{5.60}$$

In the surface integral, we recognise again the no-outflow condition, i.e. $\widehat{v}_r = 0$, such that this integral vanishes. Thus, without the need of putting any constraints on the test function γ, we can rewrite (5.59) as:

$$\boxed{-\langle\widehat{v}, \nabla\gamma\rangle_{\mathrm{l}^2} = 0\,.} \tag{5.61}$$

Next to the effect that we were again successful in isolating $\widehat{v}$, the previous equation has a very interesting additional implication. Since γ is arbitrary and we did not need to put any constraints on it to reach this representation, we can deduce from here that in general, the inner product of $\widehat{v}$ and *any gradient field* vanishes. As we have seen before, this is an immediate consequence of the no-outflow condition and the divergence theorem. Thus, this very remarkable property also holds true for the forward velocity field v.

Back to the adjoint equations, we are now able to add the left-hand side of this equation to (5.56). Then, we gain the final expression for the total derivative of the misfit function χ:

$$\begin{aligned}\mathcal{D}_{T_0}\chi(T)(\delta T_0) = &\left\langle\widehat{T}, \partial_T\widetilde{\chi}(T) - \partial_t\Psi - v\cdot\nabla\Psi - \kappa\Delta\Psi - g_0\alpha\hat{\rho}_0\varphi_r\right\rangle_{\mathrm{L}^2}\\ &+\left\langle\widehat{v}, \Psi\,\nabla T + \nabla\cdot\left[\eta\left(\nabla\varphi + (\nabla\varphi)^T\right)\right] - \nabla\gamma\right\rangle_{\mathrm{l}^2}\\ &+\left\langle\widehat{P}, \nabla\cdot\varphi\right\rangle_{\mathrm{L}^2}\\ &-\int_V\Psi(x,t_0)\,\delta T_0(x)\,\mathrm{d}V(x)\,.\end{aligned} \tag{5.62}$$

5.5.5 Summary

We introduced scalar (Ψ, γ) and vectorial (φ) test functions to find the total derivative of the objective function $\mathcal{D}_{T_0}\chi(T)(\delta T_0)$, determined by equation (5.62). From this representation, we see that the three total derivatives $\widehat{v}$, $\widehat{T}$ and $\widehat{P}$ vanish if we impose the following constraints on the test functions:

$$\nabla\cdot\varphi = 0\,, \tag{5.63a}$$

$$\Psi\,\nabla T + \nabla\cdot\left[\eta\left(\nabla\varphi + (\nabla\varphi)^T\right)\right] - \nabla\gamma = 0\,, \tag{5.63b}$$

$$\partial_t\Psi + v\cdot\nabla\Psi + \kappa\Delta\Psi + g_0\alpha\hat{\rho}_0\varphi_r = \partial_T\widetilde{\chi}(T)\,, \tag{5.63c}$$

with $\partial_T\widetilde{\chi}(T) = (T(T_0,x,t) - T_E(x))\,\delta(t-t_1)$, $x\in V$, $t\in I$. One calls these equations the **adjoint equations** in mantle dynamics. They must hold for all $x\in V$ and $t\in I$. Their similarity to the forward energy, momentum and continuity equation allows one to refer to Ψ as the **adjoint temperature**, to φ as the **adjoint velocity** and to γ as the **adjoint pressure**. And indeed, this similarity is not only visually attractive but has also direct implications on practical solution methods. Due to this property, a solution strategy - i.e. a numerical code - that is formulated for the forward problem, can - with little adaptation - immediately be used to solve the *adjoint* equations.

Since the latter are differential equations, they require initial and boundary conditions for their solution. To this end, we collect the following previously derived constraints reminiscent to the boundary conditions of the forward equations:

$$\begin{aligned} \Psi(x,t) &= 0\,, \quad && x \in \partial V,\, t \in I\,, \\ \varphi_{\tan}(x,t) &= 0\,, && x \in S,\, t \in I\,, \\ ((\nabla\varphi + (\nabla\varphi)^T)\, n(x))_{\tan} &= 0\,, && x \in C,\, t \in I\,, \\ \varphi_r(x,t) &= 0\,, && x \in \partial V,\, t \in I\,. \end{aligned} \tag{5.64}$$

We notice that the adjoint transformations have not forced us to put any constraints on the test function γ so far. But since this quantity takes the role of the pressure in the adjoint momentum equation (5.63b), due to the presence of the gradient, in analogy to the forward equation, we have to set an (arbitrary) boundary condition at one of both boundaries such that the equation remains solvable. In the forward equation we set $P(x,t) = 0$ for all $x \in S$ and $t \in I$, thus, here, we follow the same approach for the adjoint pressure and set

$$\gamma(x,t) = 0\,, \quad x \in S,\, t \in I\,. \tag{5.65}$$

Furthermore, the initial condition for temperature is replaced by a **terminal condition** for the adjoint temperature field Ψ:

$$\Psi(x,t_1) = 0\,, \quad x \in V\,. \tag{5.66}$$

The adjoint equations do not only relate the adjoint variables Ψ, γ and φ. They are additionally coupled to the forward temperature T and velocity field v. In practice this requires solutions of the forward problem, before one solves the adjoint equations. From (5.62) we see that if solutions to the adjoint equations are found, the total derivative of the objective function with respect to T_0 in the direction δT_0 reduces to:

$$\mathcal{D}_{T_0}\chi(T)(\delta T_0) = -\int_V \Psi(x,t_0)\,\delta T_0(x)\,\mathrm{d}V(x)\,. \tag{5.67}$$

This expression now only depends on the differentiation direction δT_0 and the adjoint temperature Ψ at time t_0. At this point, the only remaining question is how to choose an appropriate differentiation direction for our purpose. Since we - and the optimisation scheme - are interested in how the misfit function reacts to a change in the initial temperature T_0 at one specific point $y \in V$ inside our domain, the only reasonable[1] differentiation direction states as

$$\delta T_0(x) = \delta_y(x) = \delta(y - x)\,, \quad x \in V\,, \tag{5.68}$$

for any fixed $y \in V$. This leads to the final representation of the derivative of the misfit function for any fixed $y \in V$:

$$\mathcal{D}_{T_0}\chi(T)(\delta_y) = -\Psi(y,t_0)\,. \tag{5.69}$$

At the end of this section, we want to summarise our gained insights in form of an algorithmic procedure that describes in detail how to optimise the initial condition for the temperature in a numerical mantle circulation model:

(a) Solve the forward equations (5.6), (5.7), (5.9), using T_0^i, $i \in \mathbb{N}$ as the initial condition for the temperature field. Appropriate choices for the *first guess* initial condition T_0^0 will be discussed in Section 5.6. Store temperature $T(x,t)$ and velocity $v(x,t)$ for all $t \in I$ and $x \in V$ (i.e. at all grid points for all time steps when using a numerical scheme).

[1] "Let a physicist choose a function for an integrand
and he'll pick a delta function every time."
(old Chinese saying)

(b) Compute the difference of the temperature field at the end of the forward simulation, $T(T_0^i, \cdot, t_1)$, and the reference field T_E.

(c) Solve the adjoint equations (5.63a), (5.63b), (5.63c) backwards in time. Use the result from (b) as the driving source for the adjoint energy equation (see (5.63c)). The stored values for T and u from (a) have to be used during the backward simulation.

(d) The adjoint temperature at the *end* of the backward simulation, $\Psi(\cdot, t_0)$, determines the negative gradient of the misfit function with respect to the initial condition (see (5.69)).

(e) Update the initial condition T_0^i using the result of (d), e.g. by applying the conjugate gradient method (see Section 5.6), and start again from step (a), using the updated initial condition T_0^{i+1}.

Besides choosing an a-priori fixed $N \in \mathbb{N}$ for the total number of iterations, one may think about an exit criterion in step (b) when the difference between model and reference falls below a certain (a-priori chosen) border.

5.6 Computational example

5.6.1 Modelling assumptions for global mantle flow

We apply the theory outlined above to the initial condition problem in global mantle flow. The example demonstrates the technical aspects of the adjoint method in geodynamics and proceeds in three steps. First, we take a representation of present day mantle structure, derived from a published tomographic model of the Earth's mantle. This allows us to define the objective function χ, see (5.24). Second, we compute the gradient of the objective function for the unknown paleo mantle structure corresponding to a time period 40 million years (Myrs) before present. The time span is chosen for computational reasons, as longer integrations periods exceed our computational resources. Third, we model an initial condition field that is optimal relative to our definition of the present day mantle structure and the assumed geodynamic Earth model.

Our geodynamic forward model is identical to the published Mantle Circulation Model M2 of Schuberth et al. (2009a). M2 compares well with a number of tomographic shear velocity models in terms of spectral characteristics (essentially a statement on flow length scales) and the amplitude of seismic velocity anomalies. This is crucial for computing a meaningful objective function. The mantle flow equations are solved with the help of the parallel finite element code TERRA (Bunge et al., 1996, 1997), implemented on a cluster dedicated to large-scale geophysical modelling (Oeser et al., 2006). M2 employs a computational mesh with more than 80 million finite elements throughout the mantle. This is equivalent to horizontal grid points located every 30 km on the surface, decreasing to half the value at the CMB, with a uniform radial grid spacing of 25 km. The high resolution relative to earlier MCMs (e.g., Bunge et al., 2002) is crucial to represent the convective vigour of the Earth's mantle with a Rayleigh number (based on internal heating) of $\mathrm{Ra} \approx 10^8$. It is also one of the reasons that the heterogeneity strength of M2 provides a good match to tomographic studies (Schuberth et al., 2009b).

Apart from high numerical resolution, we restrict M2 to a minimum number of modelling assumptions: (1) a large-scale flow structure related to the history of plate motions (Müller et al., 2008; Gurnis et al., 2012), (2) a simple radial three-layer viscosity profile consistent with observations of post-glacial rebound and the geoid (e.g., Hager and Richards, 1989; Paulson et al., 2007), (3) an isochemical whole mantle flow in the pyrolite composition, and (4) a significant core heat flux of 12 TW (35 percent of the outflow at the top of the mantle) owing to a thermal boundary condition that sets the CMB temperature to 4200 K (see Boehler, 2000, for a review). The latter agrees with considerations of elastic parameters and the melting curve of iron under core conditions. Combined with seismic constraints, this places estimates of the inner-core boundary temperature at $5400 - 5700$ K (Steinle-Neumann et al., 2001). Assumed values for the three-layer viscosity profile are 10^{23}, 10^{21}

and 10^{23}Pas in the lithosphere, the upper and the lower mantle, respectively, separated at depths of 100 and 650 km. M2 incorporates the dynamical effects of compressibility that are associated with the non-negligible density increase of about a factor of 2 from the Earth's surface to the CMB (e.g., Dziewonski and Anderson, 1981). As is customary, we apply the anelastic fluid formulation (Jarvis and Mckenzie, 1980; Glatzmaier, 1988), which ignores the time derivative of density in the continuity equation and assumes that convective flow velocities are small compared to the local sound speed. In the Earth's mantle, where acoustic waves propagate many orders of magnitude faster than oceanic plate velocities, the assumption is valid. Detailed modelling parameters and a quantitative comparison of M2 with a range of tomographic mantle studies are given in Schuberth et al. (2009b, 2012).

We derive our estimate for present day mantle structure from the global shear-wave tomographic model of Grand et al. (1997). Elastic mantle heterogeneity of the S-wave study is converted into thermal variations using a thermodynamically self-consistent model of mantle mineralogy (Piazzoni et al., 2007) in the pyrolite composition. The mineralogic model computes equilibrium phase assemblages for the CFMAS (CaO FeO MgO Al_2 O_3 SiO_2) compositional system by Gibbs free energy minimisation. Note that the CFMAS system is consistent with our assumption of isochemical flow. The initial condition for mantle flow sometime in the past is necessarily unknown. Thus, for the sake of simplicity, we opt for using the present day mantle structure as our *first guess* of the unknown mantle structure 40 Myrs ago.

5.6.2 Gradient of the misfit function and optimised initial condition field

Starting from the terminal condition (5.66) for the adjoint temperature, one must solve the adjoint energy equation backwards in time. To this end, we recall the sign change in the adjoint diffusion term $\kappa\Delta\Psi$, compared to the forward energy equation, which makes the adjoint temperature equation numerically stable to backward integration. Minimisation of the objective function χ then proceeds iteratively, through repeated solutions of the system of forward and adjoint equations. We apply the conjugate gradient method (Fletcher and Reeves, 1964), starting with our *first guess* T_0^0 for the initial temperature as noted before, and update the initial condition field $N \in \mathbb{N}$ times. Then, for all $i = 1, ..., N$, we find that

$$T_0^i(x) = T_0^{i-1}(x) + \gamma\, \mathcal{D}_{T_0}\chi(T)(\delta(x - \cdot))\,, \tag{5.70}$$

where $\gamma \in \mathbb{R}$ is a step size, determined by the conjugate gradient scheme. Inserting (5.69) then yields:

$$T_0^i(x) = T_0^{i-1}(x) - \gamma\, \Psi(x, t_0)\,. \tag{5.71}$$

The efficiency of the iterative procedure in minimising χ is evident from Figure 5.1. Here we compare the heterogeneity prediction of our flow model at the present day (middle column) to the mantle structure (right column) imaged by the S-wave study of Grand et al. (1997). Already after 7 conjugate gradient iterations (8 forward and 7 adjoint iterations), there is a good match for both fields particularly in the lower mantle. Agreement is also good in the hot thermal boundary layer near the CMB. This is an interesting result since in this region, thermal conduction per definition dominates over advection. Since diffusion is a non-invertible process, one might expect poorer convergence here than in other regions of the mantle. The success of the inversion scheme even in this region underlines the strength of the adjoint method. In the mid mantle, cold regions associated with subducting slabs are sharper and more pronounced in the flow model compared to the tomographic image. The difference reflects the high numerical resolution of the computational model, combined with the fact that seismic tomography invariably delivers a filtered image of true mantle heterogeneity. Near the surface, anomalous regions in the tomography associated with deep continental roots (Jordan, 1978) are not fitted by the MCM. This is expected, since our geodynamic model does not account for the complex thermo-chemical nature of the continental lithosphere (e.g., Artemieva, 2009). Minimising the objective function χ requires changes to the assumed *first guess* initial condition. In Figure 5.2 we illustrate these changes by showing the adjoint temperature Ψ at time t_0 at different depth levels after adjoint iteration 1, 2 and 7, respectively. Since Ψ represents the gradient of the misfit function (see (5.69))

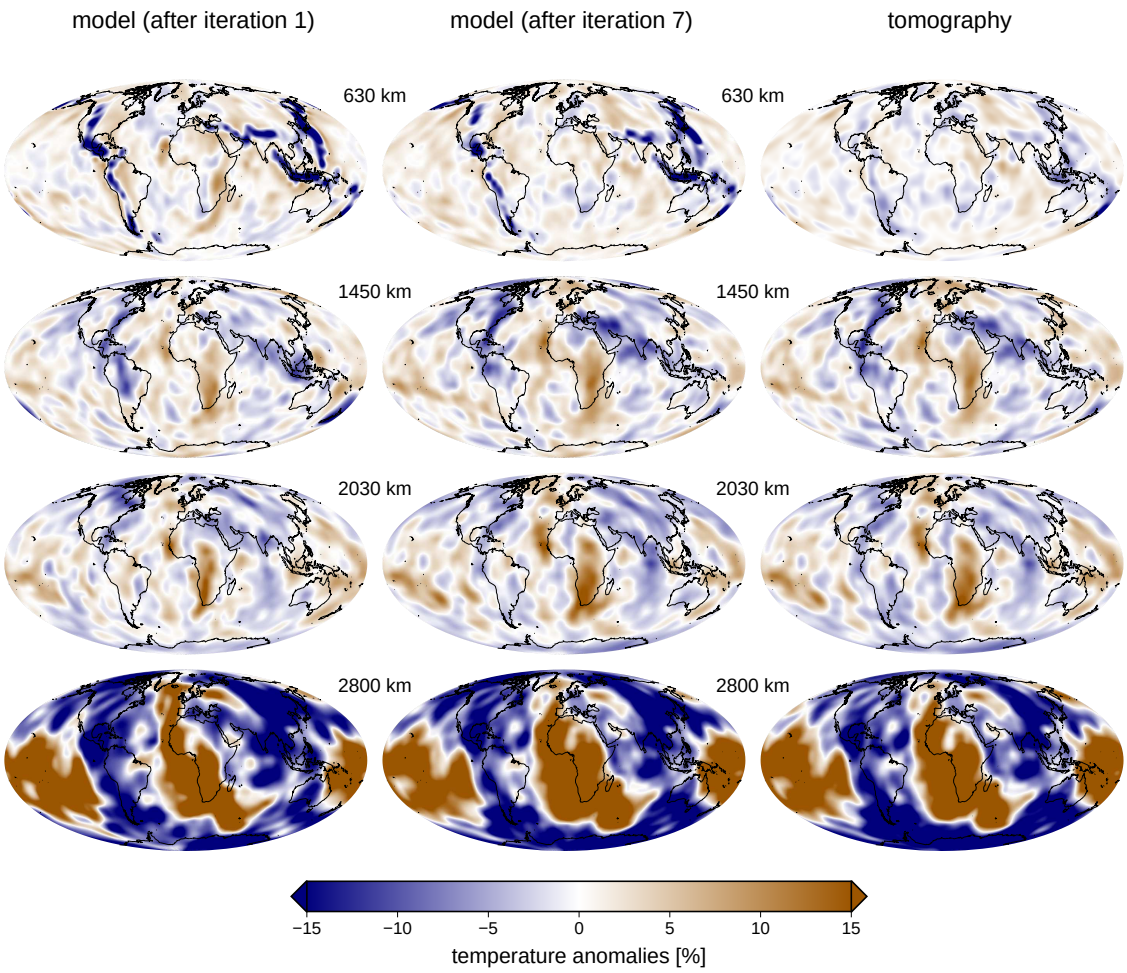

Figure 5.1: Present day lateral temperature variation in the Earth's mantle (red = hot, blue = cold) at four depth levels $(630, 1450, 2030, 2800$ km) predicted after 40 Myrs of model run from an adjoint mantle circulation model (left, middle), which was started for the sake of simplicity from a *first guess* initial condition (see text) corresponding a representation of present day mantle heterogeneity as mapped by the seismic shear wave study of Grand et al. (1997) (right column). Adjoint model shown after 1 (left) and 7 (middle) conjugate gradient iterations. The optimisation improves the fit of the geodynamic model relative to present day mantle structure, i.e. the seismic study, in each iteration by minimising the objective function χ, see equation (5.24). A good match between seismic (right) and geodynamic model after 7 (middle) conjugate gradient iterations confirms the efficiency of the adjoint method in minimising the objective function. Note the excellent agreement between geodynamic and seismic heterogeneity in the mid mantle, and also near the CMB, even though thermal conduction dominates over advection in the lowest mantle region. In the upper mantle, slabs are sharper and more pronounced in the geodynamic model, as expected, owing to the high numerical resolution of the computational model.

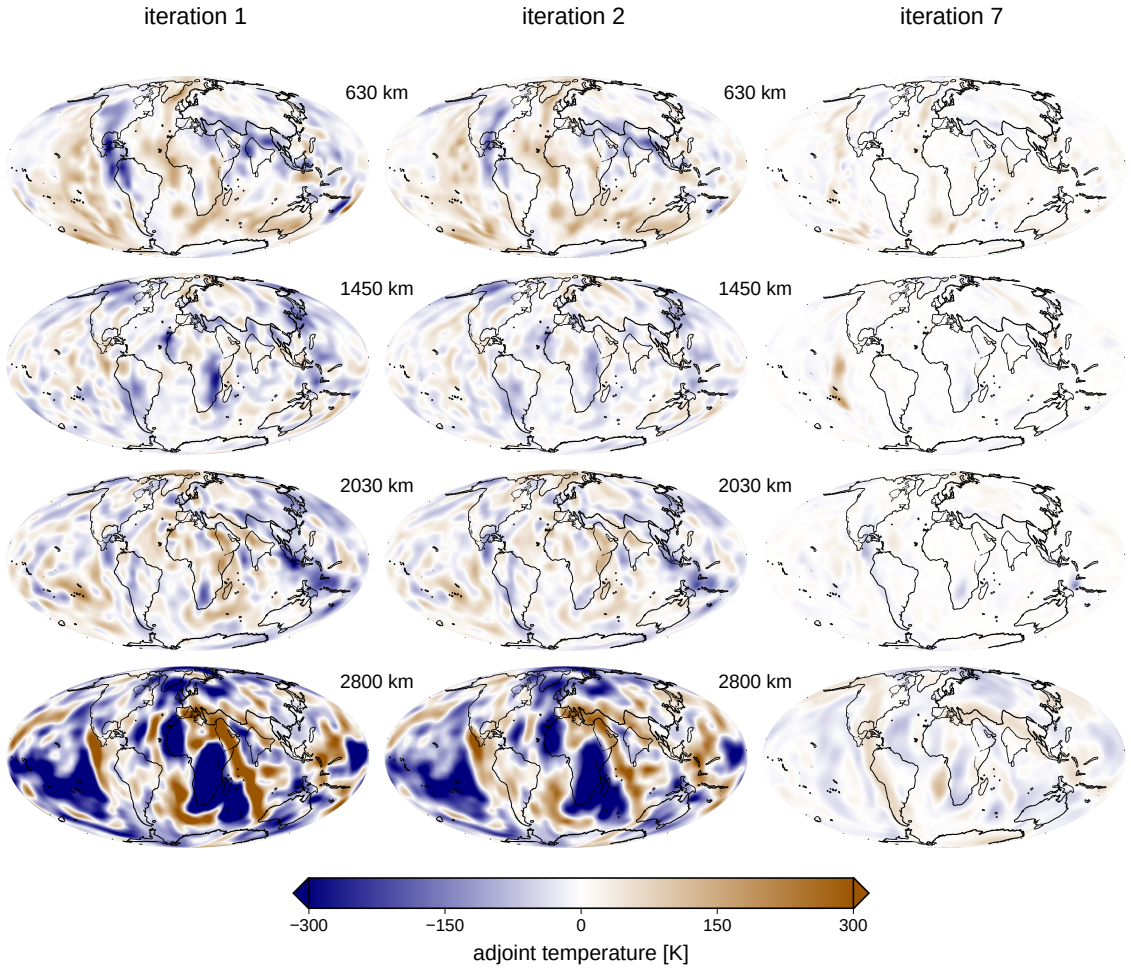

Figure 5.2: Adjoint temperature Ψ at time t_0, i.e. gradient of objective function χ (see equation (5.24)), at four depth levels $(630, 1450, 2030, 2800$ km) after adjoint iteration 1 (left), 2 (middle) and 7 (right), indicating where the *first guess* initial condition (see text) of unknown mantle structure 40 Myrs ago must be adjusted by the conjugate gradient scheme in order to minimise the objective function. There are large amplitudes of Ψ in the first iterations (left, middle) as expected, especially near the CMB, where diffusion dominates advection. Importantly, at iteration 7 (right), the amplitude is reduced in all depth levels, indicating an optimal initial condition (relative to the particular representation of present day mantle structure, i.e. the seismic study of Grand et al. (1997), and the assumed parameters of the geodynamic model) has been found.

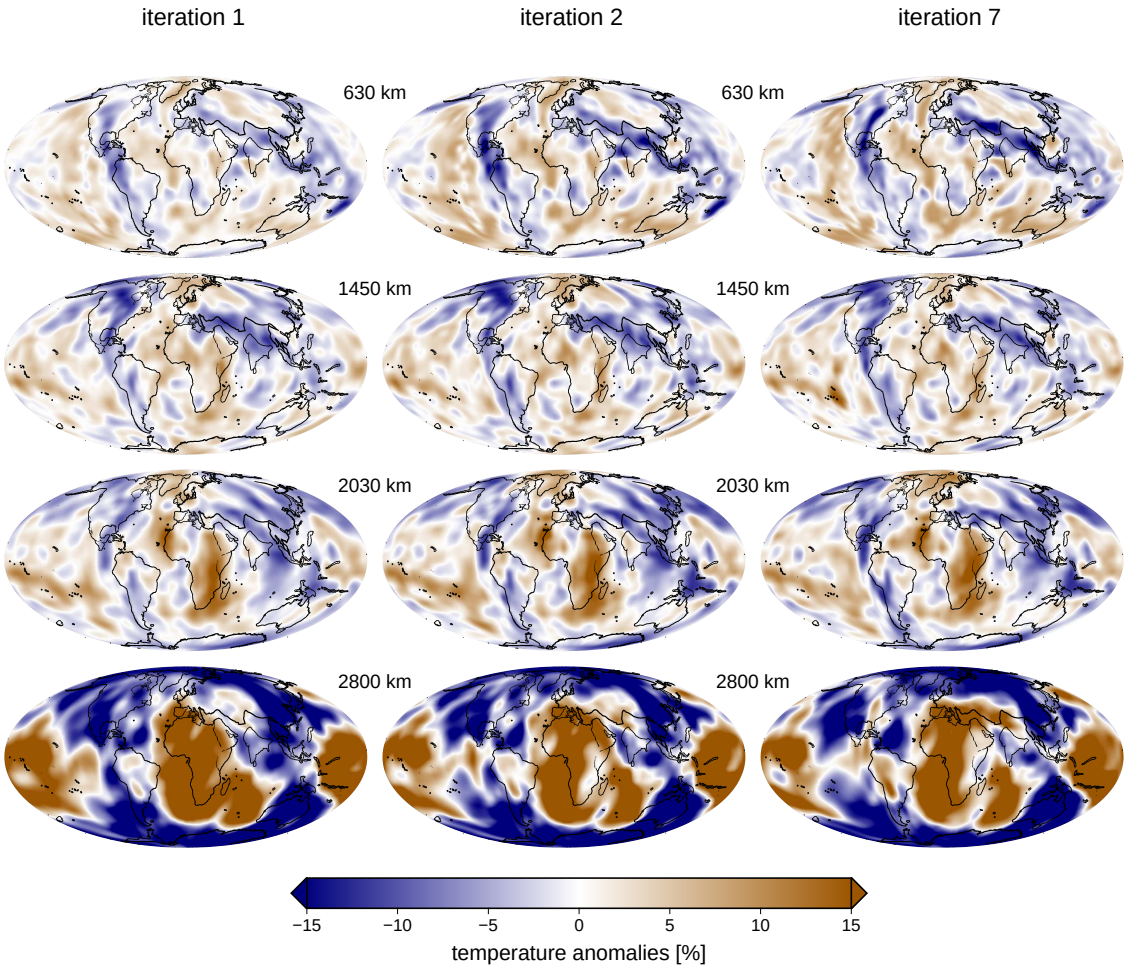

Figure 5.3: Lateral temperature variations (red = hot, blue = cold) in the Earth's mantle 40 Myrs ago predicted from the adjoint mantle circulation model after 1 (left), 2 (middle), and 7 (right) conjugate gradient iterations at four depth levels $(630, 1450, 2030, 2800$ km). Iteration 7 (right) corresponds to the *best guess* initial condition, where we must qualify that the predicted heterogeneity is optimal relative to the particular representation of present day mantle structure, i.e. the seismic study of Grand et al. (1997) (see Figure 5.1, right), and the assumed parameters of the geodynamic model (see text). Compared to the seismic study we note that the optimisation scheme requires lateral adjustment in mantle heterogeneity near the CMB, where horizontal flow dominates over vertical motion. In the upper and mid mantle cold downwellings and hot upwellings are adjusted primarily in their vertical location.

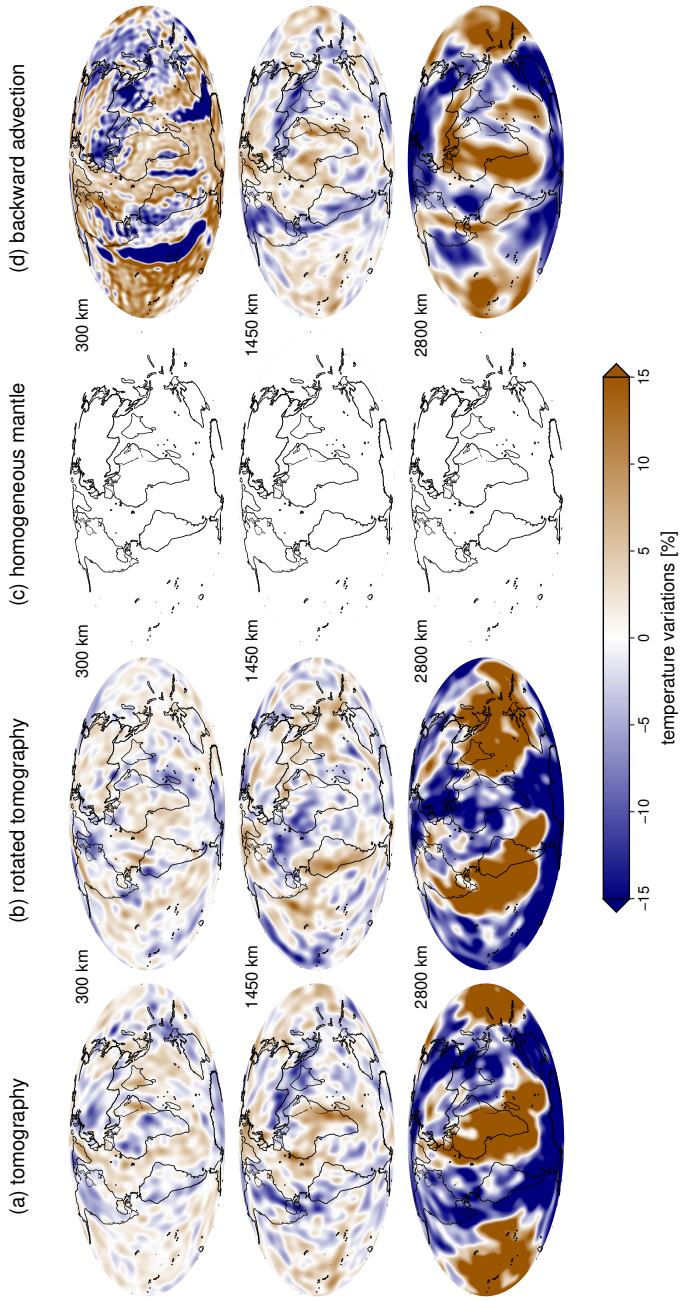

Figure 5.4: Four *first guess* starting models T_0^0 for the unknown initial temperature distribution (red = hot, blue = cold) of the Earth's mantle 40 Myrs ago, shown at three depth levels (330, 1450, 2800 km). (a) Lateral temperature variations at present day derived from a particular tomographic representation of the Earth's mantle, i.e. the seismic shear wave study of Grand et al. (1997), see text. This field may be regarded as a reasonable approximation of the unknown initial condition, as the restoration period of 40 Myrs is small relative to a mantle transit time (Bunge, 1998). (b) Rotated tomography field derived from a 90 degrees westward rotation of the initial condition field (a), where prominent cold and hot mantle regions associated with thermal up and downwellings are interchanged relative to (a). (c) Laterally homogeneous temperature distribution derived by averaging lateral heterogeneity at each radial level in the initial condition field (a). (d) Temperature distribution derived from 40 Myrs backward advection of the initial condition field (a). Note that artificial cold downwellings beneath the global mid ocean ridge system, for instance at the East Pacific Rise, are associated with backward advection, which degrades the convergence measure in Figure 5.5.

Figure 5.2 shows, where the initial condition must be adjusted to achieve a reduction of the overall misfit. Looking at results after the first adjoint iteration, we notice that large changes to the *first guess* initial condition are needed predominately in the thermal boundary layer region near the CMB. In other mantle regions, much smaller changes are necessary. Importantly, after adjoint iteration 7, the overall amplitude of Ψ in all depth levels is reduced. This indicates that a nearly optimal initial condition has been found by the adjoint procedure, and that there is little need for further change.

The iterative adjustments yield an optimised initial condition field, which we show in Figure 5.3. We present the prediction of the geodynamic model for mantle heterogeneity at 40 Myrs ago, for adjoint iteration 1, 2 and 7, respectively. It is not surprising that the most pronounced changes relative to the *first guess* initial condition occur in the vicinity of the CMB. The large changes in this region reflect the large amplitude of the adjoint temperature Ψ at time t_0 in the CMB region, as observed before in Figure 5.2. The net effect, after 7 iterations of the adjoint procedure, is a significant change in the lateral CMB heterogeneity structure compared to the *first guess* initial condition (see Figure 5.1). This is consistent with expectations for large scale mantle dynamics, as horizontal flow dominates over vertical motion in the CMB region (Bunge et al., 1997). Notable changes in other mantle regions are associated with the prominent, cold downwellings under the Americas and the Indo-Asian regions. In the updated initial condition field, these downwellings are placed higher up in the mantle by the adjoint procedure, corresponding to a location at an earlier time. The change reflects the dominance of vertical over horizontal transport in the mid mantle, and is thus expected.

5.6.3 Convergence measures and sensitivity to first guess initial conditions

It is important to verify how the choice of the *first guess* for the unknown initial condition affects the convergence of the optimisation problem. Full waveform inversion in seismology (Fichtner, 2011) shows that a good starting model for seismic heterogeneity is crucial in the successful misfit minimisation between synthetic and observed seismogram, owing to the large number of local minima in the inverse problem. A spectral approach improves the convergence, with long wavelength structure fitted in the early iterations before one models finer scale seismic heterogeneity. The initial condition problem in geodynamics differs from seismology in that the momentum balance of mantle flow is represented by a Stokes system, in contrast to the hyperbolic wave equation. In this case, significant control is exerted by the boundary conditions. Thus the known motion of the lithospheric plates influences the accompanying large-scale flow in the Earth's mantle, an insight exploited early on in the global mantle flow models of Hager and O'Connell (1978, 1979). We test the robustness of our results to changes in the *first guess* initial condition and show four different initial temperature T_0^0 fields in Figure 5.4. Present day mantle structure as a proxy for unknown mantle heterogeneity 40 Myrs ago is illustrated in Figure 5.4 (a). We used this starting field in the previous section, as noted before. An alternative choice, shown in Figure 5.4 (b), also takes the *first guess* initial condition from Figure 5.4 (a). But we rotate the starting field T_0^0 by 90 degrees, yielding a pattern of mantle heterogeneity, where cold and warm regions are interchanged.

Our third choice, intended to reflect more fully our lack of initial condition information, utilises a 1-D temperature profile (Figure 5.4 (c)) with no lateral heterogeneity. We obtain this starting field by averaging lateral heterogeneity at each radial level from the initial condition field shown in Figure 5.4 (a). The starting fields in Figs. 5.4 (b,c) are designed to challenge the convergence of the adjoint procedure: their buoyancy structure is either identical to zero or opposing the large scale flow implied by the present day mantle structure.

Our fourth approach, Figure 5.4 (d), to produce a *first guess* initial condition employs backward advection (e.g., Steinberger and O'Connell, 1997; Moucha et al., 2008a). Starting from the representation of present day mantle heterogeneity (Figure 5.4 (a)), we run our MCM backward in time for 40 Myrs, solving the energy equation (5.9) backwards in time and reversing the sign of the diffusion term for the sake of numerical stability.

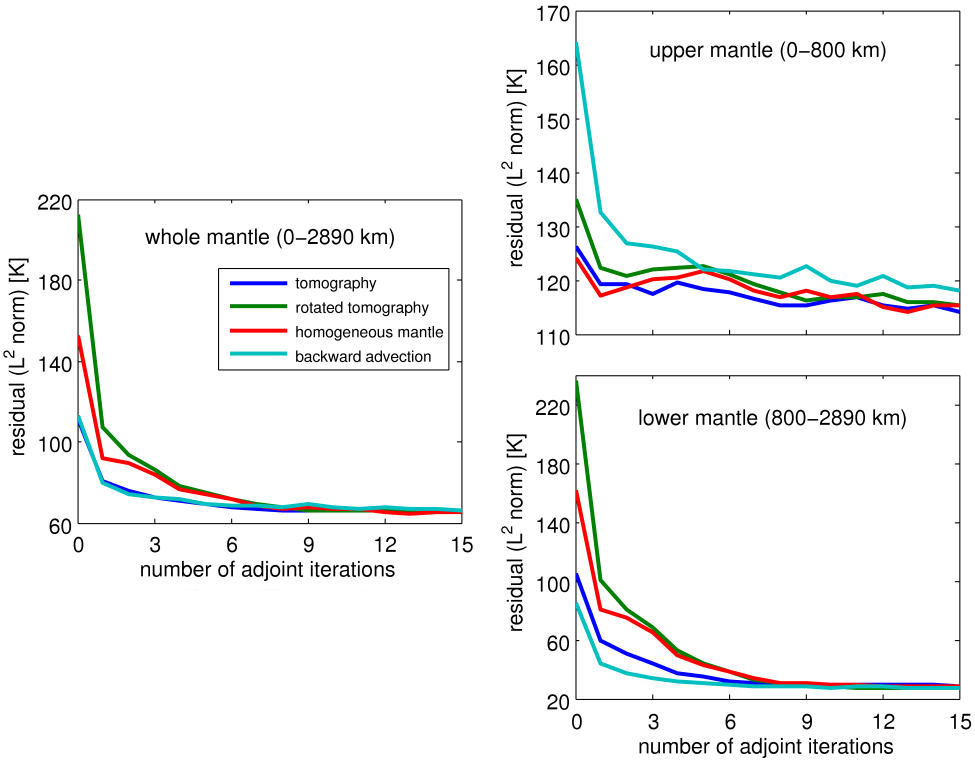

Figure 5.5: Temperature residual (L^2 norm) between geodynamic model at present day and tomography as function of adjoint iteration for the four *first guess* starting models T_0^0 of the unknown initial temperature shown in Figure 5.4. The residual over the whole mantle (top) is also shown divided into its contributions from the upper ($0-800$ km) and the lower ($800-2890$ km) mantle (mid, bottom panel). Convergence is reached after a few iterations, regardless of the choice for T_0^0. While there is an excellent overall fit in the lower mantle, convergence in the upper mantle is weaker, owing to crustal features not resolved by the geodynamic model. In the upper mantle, the geodynamic model that was initialised from backward advection yields poorest convergence, due to artefacts near thermal boundary layers (see Figure 5.4). In the lower mantle, the rotated tomography model starts with the poorest fit. But after a few iterations, all models yield similar convergence.

Figure 5.5 shows how the efficiency of minimising χ depends on our starting models. The temperature residual in the L^2 norm between the MCM at present time and the tomographic mantle image as a function of the adjoint iteration serves as a quantitative measure of the misfit. To facilitate a physical interpretation of the misfit, we divide the residual into contributions from the upper ($0-800$ km) and the lower ($800-2890$ km) mantle each, in addition to the mantle as a whole. In general, the first five iterations are the most significant for correcting the initial condition. We also notice that the overall magnitude of the residual is smaller in the lower than the upper mantle, owing the effects of crustal structure and subducting slabs. But importantly, we see that the choice of the initial starting model has little effect on the overall convergence behaviour.

After one adjoint and forward iteration, as expected, the rotated tomography starting field yields the worst fit to the present day mantle structure. But after a few iterations there is the same convergence as if we had started with a more reasonable proxy for the unknown initial condition, e.g., the tomography field or the backward advection model. In the upper mantle, the model that started from backward advection shows the poorest convergence, reflecting artefacts near thermal boundary

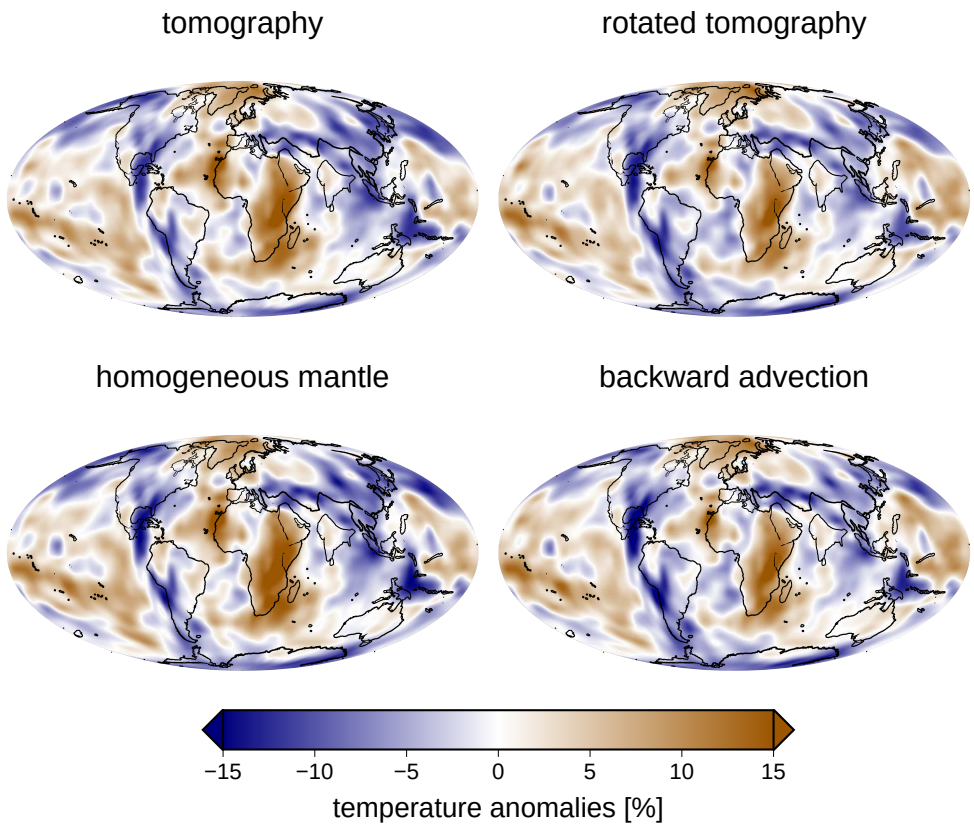

Figure 5.6: *Best guess* initial condition temperature distribution at 2000 km depth (red = hot, blue = cold) in the Earth's mantle 40 Myrs ago predicted by the adjoint method after 7 iterations for the four starting models shown in Figure 5.4. Note that all models, regardless of their *first guess* initialisation, show the same temperature heterogeneity, demonstrating uniqueness in the inverse problem. The uniqueness property may be explained by the prescribed surface velocity field which serves as a regularisation of the inverse problem (see text).

layers that arise from backward advection, as mentioned before. In the lower mantle, the rotated tomography model starts with a poor fit to the present day mantle structure. But after a few iterations, all models show a similar convergence behaviour. This is confirmed by looking at Figure 5.6, which gathers depth slices at 2000 km of the optimal initial condition at 40 Myrs ago for each of the four models. Here even at smaller scale structures, the models look quite similar.

5.7 Discussion

We presented a general operator formulation of the adjoint theory in Hilbert spaces. We applied the theory to the three coupled conservation equations for mantle flow in geodynamics and demonstrated the ability of the method to restore an earlier mantle structure in a high resolution global mantle circulation model.

Reformulating the initial condition problem in geodynamics as a general optimisation problem yields the task of determining the derivative of a physical observable, i.e. the objective function (5.24), relative to the initial condition. Where standard means to obtain the derivative by finite differencing become impractical, owing to the large parameter space of modern geodynamic mantle models, the

adjoint method allows us to determine the derivative in a way that is computationally efficient and mathematically elegant.

The adjoint and forward equations are similar. Their similarity originates from self-adjoint or near self-adjoint differential operators in the equations. Thus in addition to computational efficiency, there is a practical consideration: any existing numerical code that solves the forward problem may be used to solve the adjoint equations with little adaptation. Our derivation of the adjoint equations shows that boundary conditions in the forward equations translate one-to-one into corresponding boundary conditions in the adjoint equations. As well, the initial condition of the forward problem is replaced by a terminal condition in the adjoint equations, making it necessary to solve the adjoint equations backward in time.

Thermal residuals at the final stage of the model run act as the source term of the adjoint energy equation (5.63c). The residuals are transported backward in time by the adjoint advective term along a trajectory governed by the forward velocity field. The coupling of forward and adjoint variables is a crucial part of the adjoint theory. It is here that physical constraints from the forward system enter as information into the restoration problem. The adjoint energy equation also contains an adjoint diffusive term, which corrects thermal diffusion effects back in time. This contrasts to the approach of backward advection (see e.g., Steinberger and O'Connell, 1998), where one neglects thermal diffusion at the expense of artefacts near thermal boundary layers (Bunge et al., 2003). Finally there is an adjoint buoyancy term in the adjoint energy equation. This term couples the adjoint energy and momentum equation through the adjoint velocity field φ which is computed from the adjoint momentum equation (5.63b). The adjoint buoyancy term corrects for errors in the forward velocity field that arise from errors in the assumed initial condition. Constraints on the adjoint velocity field (in our derivation a condition on incompressibility) enter through the adjoint continuity equation (5.63a).

Ignoring the adjoint buoyancy (and hence the adjoint momentum and continuity equation) in the restoration problem (e.g., Liu and Gurnis, 2008) is equivalent to the assumption that initial condition errors have no influence on the forward velocity field (see (5.40). While strictly speaking, this would be incorrect, we note that the viscosity of the Earth's mantle is high, so that errors in the forward velocity field are smooth relative to those in the initial condition field. The inherent smoothness of the Stokes system dampens the influence from erroneous initial conditions on the forward velocity field. This interpretation agrees with the self-adjoint nature of the momentum equation in mantle flow and links to simplified implementations of the adjoint equations in mantle flow. We note that the mantle flow problem in this regard differs from adjoint systems of the geodynamo (e.g., Fournier et al., 2010; Li et al., 2011).

The adjoint problem in geodynamics has a one-to-one analogy in seismology. Here dissipation is the equivalent physical phenomenon to diffusion. If we ignore dissipation, in analogy to backward advection, the wave equation may be inverted by integrating the wavefield back in time. Alternatively, one may account for dissipation. The adjoint method in seismology (full waveform inversion) then introduces constraints of the physical system in a way that is similar to the adjoint system in geodynamics, by coupling forward and backward wavefield (Tromp et al., 2005; Fichtner et al., 2006a).

A computational bottleneck is associated with the coupling of forward and adjoint system, because the full temperature and velocity field must be stored at each time step of the forward run. Our choice of 40 Myrs for the restoration period is dictated by computational considerations, mainly the storage capacity of our local cluster system TETHYS (Oeser et al., 2006). Our geodynamic models involve a computational mesh with more than 80 million finite elements. The models run on 512 cores of our computer system and need a disk space of $\approx$ 20 GB per node ($\approx$ 10 TB total). The iterative nature of the optimisation scheme, moreover, requires repeated solutions of the forward and adjoint equations to achieve convergence. Each forward-backward iteration needs a runtime of $\approx$ 1 week. Thus $\approx$ 2 months of runtime were necessary to complete the 7 conjugate gradient iterations presented here for

each of the four starting models.

The existence of a strong global minimum for the initial condition problem is the most important finding in our study. Hadamard (1902) classified well-posed inverse problems by existence, uniqueness and stability of the solution. It is reasonable to expect that the initial condition problem in mantle convection is ill-posed: the governing equations are non-linear and there is a loss of information due to thermal diffusion processes. In other words, uniqueness and stability are in question. In seismology the existence of a variety of local minima for the objective function is known, and spectral methods help to regularise full waveform tomography (Fichtner, 2011). Relevant to mantle convection, however, is the uniqueness theorem by Serrin (1959). It states that two incompressible Stoke systems are equivalent, if they share identical initial and boundary conditions. Knowledge of the history of plate motion amounts to satisfying one of the two conditions of the uniqueness theorem. Past plate motion models therefore provide constraints not only on the mantle thermal structure through the history of subduction. They also regularise the accompanying large-scale mantle flow, an insight that informs the pioneering work of Hager and O'Connell (1978, 1979). Figure 5.6 illustrates the strength of the regularisation. The four different starting models we used as our *first guess* for the unknown initial condition lead to the same optimal initial condition field after a small number of adjoint iterations. Our results agree with the finding of Vynnytska and Bunge (2015) who demonstrate that the restoration problem of mantle flow becomes ill-posed, if one assumes a (free-slip) surface boundary condition that does not include knowledge on the history of the surface velocity field.

The source term of the adjoint energy equation equals the partial derivative of the misfit function (see (5.63c)). So the choice of the latter affects the optimal initial condition determined by the adjoint procedure. While we restrict ourselves in this paper for the sake of convenience to a simple L^2 difference between model and reference field, one could consider more sophisticated measures of the objective function. For instance, one could account for variations in the spatial resolution of tomographic models as well as the inherently different resolution between heterogeneity computed by mantle circulation models and seismic tomographic representations of mantle structure. Here we recall that comparing two data sets with locally different resolutions suggests a spectral or wavelet based approach (e.g., Freeden et al., 1998; Freeden, 2001; Freeden et al., 2003), yielding a locally adaptive definition of the objective function.

We must qualify our results by drawing attention to an important limitation of this study. While our adjoint simulations reveal the existence of a strong global minimum in the initial condition problem of mantle convection, we obtained the minimum relative to a particular representation of mantle heterogeneity, i.e. the seismic study of Grand et al. (1997), and relative to the particular modelling parameters in our mantle circulation study (Schuberth et al., 2009a). A minimum number of modelling assumptions was made in the geodynamic model for the sake of simplicity: we assumed isochemical flow with mantle heterogeneity dominated by thermal effects, and we considered a simple three-layer mantle viscosity profile consistent with post-glacial rebound and geoid studies (e.g., Hager and Richards, 1989; Paulson et al., 2007). Our justification for the former is straightforward. Mounting evidence from mineralogy (e.g., Zhang et al., 2013) and geodynamics (e.g., Schuberth et al., 2009b; Forte et al., 2010; Davies et al., 2012) suggests that whole mantle flow of pyrolitic composition provides a good match to seismic observations. But it is clear that more studies on complex thermo-chemical mantle flow scenarios (Tackley, 2012) will help to complement these findings. Our choice for the latter is more uncertain, as we lack a robust description of the mantle deformation behaviour in the exotic regime of low strain rates, high temperature, and high pressure that characterises the deep Earth. Spasojevic et al. (2009) used uplift data of the Western United States to optimise the viscosity profile in an adjoint model of mantle flow. Their result required the specification of a high viscosity layer (stress guide) embedded in the upper mantle beneath the continent, which makes them difficult to interpret. But it is clear that future applications of the adjoint method in geodynamics must be directed at improving our understanding of the rheologic properties of the Earth's mantle.

Outlook

First, at this point, we hope that with this work we may provide a valuable service to all students, senior scientists and whoever crosses the path with analytical solution methods to the Stokes equation and the infamous propagator matrix technique. It took more than a decade to overcome all traps and pitfalls that are hidden in the course of the derivation of these solution methods and we sincerely hope to ease the way of future scientists at least in this regard.

But besides the detailed derivation of the Stokes matrix and propagator approach, at the end of this work we even opened Pandora's box and tried to address the intrinsically unsolvable initial condition problem in mantle dynamics. Applied to a high-resolution numerical mantle circulation code, we successfully showed the convergence of the iterative adjoint method to an 'optimal' solution for the initial temperature condition in the energy equation. Furthermore, we showed that even in case of an initial guess that was artificially constructed in the most possible inconsistent way, the iteration scheme still converges to the 'right' solution. As shown by Vynnytska and Bunge (2015) this is most probable due to the velocity boundary condition at the surface that we chose to be set to velocities derived from plate reconstruction models. It seems to be that the influence of this boundary condition is so large that in any case, even literally, everything is pushed into the right direction. In general, these and our results give hope to future adjoint simulations but at the same time, also rise the question, which model parameters the adjoint method is even sensitive to. In this work, we were in particular interested in the radial viscosity profile and demonstrated in Chapter 4 that with pure static flow models, there will always be a trade-off and infinitely many solutions remain. We raised the hope that with time-dependent models we will be able to distinguish between feasible profiles but at the current development stage, this is not even clear. In our opinion, now that we demonstrated that the adjoint method works in principle - and not only in artificially constructed test scenarios, but even with real data - the main task in the course of the upcoming years could (or even should?) be the focus on analysing the sensitivity of the adjoint method to the various free parameters, e.g. the viscosity profile, the used plate reconstruction model or for instance, the used tomography for the reference field at the final state. A first and already very profound work addressing this certain topic has just been published by Colli et al. (2020). However, in our opinion this is only a first step in a long process of examining and revealing the true capability of the adjoint method in geodynamics.

In the last chapter we derived the adjoint equations of mantle dynamics using a general operator approach. Where in principle, we gained a coupled system of adjoint equations that is very similar to the forward system, we found - only by experiment - that it seems to be that in the adjoint runs, the influence of the momentum equation is so little that it completely decouples and even may be entirely neglected. This has the apparent advantage that we saved most of the required computational time since the momentum equation is - due to its elliptic nature - by far the most time-consuming part of the solver. Nevertheless, from a mathematical and even physical point of view it still remains unclear why exactly this is the case. This is an apparent contrast to the forward equations that has not been understood very well up to this point. This topic may be gathered under the umbrella of the general future task of examining the capability and also the intrinsic properties of the adjoint method in a more detailed and structured way.

Probably the most powerful feature of the adjoint method is that in principle, it opens the door and builds a connection to various other disciplines in the geosciences. Not that the adjoint method only determines an 'optimal' initial state of the Earth's mantle at some time in the past, it creates a whole *trajectory*, a complete and consistent time evolution of the temperature field inside the Earth and - that is the essential point - also of all derived quantities like e.g. the Earth's gravitational field, dynamic topography or True Polar Wander paths. Today, it seems that there is a high probability that among these observables, in particular the time evolution of dynamic topography will play an essential role in further adjoint simulations. Numerous geological data sets seem to be capable of providing estimates of uplift or subsidence rates, at least at certain times in the past and for selected regions. Thus, one of the key research points in the future will be the incorporation of these newly available data into the modelling process and to exploit them for constraining and - hopefully - reducing the model parameter space. It may also well be that there are additional useful data sets available from geoscientific research fields, where at the present time, no one could even imagine a possible connection to geodynamics.

Bibliography

Abramowitz M., Stegun I.A., 1965. Handbook of Mathematical Functions with Formulas, Graphs and Mathematical Tables. US Department of Commerce, National Bureau of Standards, Applied Mathematics series 55.

Achilles R., Bonfiglioli A., 2012. The early proofs of the theorem of Campbell, Baker, Hausdorff, and Dynkin. Arch. Hist. Exact Sci., 66 (3), 295–358.

Amante C., Eakins B.W., 2009. ETOPO1 1 Arc-Minute Global Relief Model: Procedures, Data Sources and Analysis. NOAA Tech. Memo. NESDIS NGDC-24. Natl. Geophys. Data Center, NOAA.

Artemieva I.M., 2009. The continental lithosphere: Reconciling thermal, seismic, and petrologic data. Lithos, 109 (1-2), 23–46.

Backus G., 1986. Poloidal and toroidal fields in geomagnetic field modeling. Rev. Geophys., 24 (1), 75.

Bauer S., Huber M., Ghelichkhan S., Mohr M., Rüde U., Wohlmuth B., 2019. Large-scale simulation of mantle convection based on a new matrix-free approach. J. Comput. Sci., 31, 60–76.

Bauer S., 2018. New Approaches for Efficient on-the-fly FE Operator Assembly in a High-performance Mantle Convection Framework. PhD Thesis, LMU Munich.

Bauer S., Bunge H.-P., Drzisga D., Gmeiner B., Huber M., John L., Mohr M., Rüde U., Stengel H., Waluga C., Weismüller J., Wellein G., Wittmann M., Wohlmuth B., 2016. Hybrid Parallel Multigrid Methods for Geodynamical Simulations. In H.J. Bungartz, P. Neumann, E. Wolfgang (editors), Softw. Exascale Comput. – SPPEXA 2013-2015, volume 113 of Lecture Notes in Computational Science and Engineering, pp. 211–235. Springer.

Baumgardner J.R., 1985. Three-dimensional treatment of convective flow in the earth's mantle. J. Stat. Phys., 39 (5-6), 501–511.

Baumgardner J.R., Frederickson P.O., 1985. Icosahedral Discretization of the Two-Sphere. SIAM J. Numer. Anal., 22 (6), 1107–1115.

Bergen B., Gradl T., Hülsemann F., Rüde U., 2006. A Massively Parallel Multigrid Method for Finite Elements. Comput. Sci. Eng., 8 (6), 56–62.

Bergen B., Hülsemann F., 2004. Hierarchical hybrid grids: data structures and core algorithms for multigrid. Numer. Linear Algebr. Appl., 11 (23), 279–291.

Bergen B., Hulsemann F., Rude U., 2005. Is 1.7 x 10^10 Unknowns the Largest Finite Element System that Can Be Solved Today? In ACM/IEEE SC 2005 Conf., pp. 5–5. IEEE.

Bergen B., Wellein G., Hülsemann F., Rüde U., 2007. Hierarchical hybrid grids: achieving TERAFLOP performance on large scale finite element simulations. Int. J. Parallel, Emergent Distrib. Syst., 22 (4), 311–329.

Besse J., Courtillot V., 2002. Apparent and true polar wander and the geometry of the geomagnetic field over the last 200 Myr. J. Geophys. Res. Solid Earth, 107 (B11), EPM 6–1–EPM 6–31.

Bey J., 1995. Tetrahedral grid refinement. Computing, 55 (4), 355–378.

Birch F., 1947. Finite Elastic Strain of Cubic Crystals. Phys. Rev., 71 (11), 809–824.

Blankenbach B., Busse F., Christensen U., Cserepes L., Gunkel D., Hansen U., Harder H., Jarvis G., Koch M., Marquart G., Moore D., Olson P., Schmeling H., Schnaubelt T., 1989. A benchmark comparison for mantle convection codes. Geophys. J. Int., 98 (1), 23–38.

Boehler R., 2000. High-Pressure experiments and the phase diagram of Lower Mantle and Core materials. (1998), 221–245.

Boussinesq J., 1903. Théorie analytique de la chaleur: mise en harmonie avec la thermodynamique et avec la théorie mécanique de la lumière, volume 2. Gauthier-Villars.

Braess D., 2001. Finite elements: Theory, fast solvers, and applications in solid mechanics. Cambridge University Press.

Braun J., 2010. The many surface expressions of mantle dynamics. Nat. Geosci., 3 (12), 825–833.

Bunge H.-P., 1997. Numerical models of mantle convection. PhD Thesis, University of California, Berkeley.

Bunge H.-P., 1998. Time Scales and Heterogeneous Structure in Geodynamic Earth Models. Science (80-.)., 280 (5360), 91–95.

Bunge H.-P., Hagelberg C.R., Travis B.J., 2003. Mantle circulation models with variational data assimilation: inferring past mantle flow and structure from plate motion histories and seismic tomography. Geophys. J. Int., 152 (2), 280–301.

Bunge H.-P., Kennett B.L.N., 2008. Geophysical Geocontinua. Cambridge University Press.

Bunge H.-P., Richards M.A., Baumgardner J.R., 2002. Mantle–circulation models with sequential data assimilation: inferring present–day mantle structure from plate–motion histories. Philos. Trans. R. Soc. London. Ser. A Math. Phys. Eng. Sci., 360 (1800), 2545–2567.

Bunge H.-P., Richards M.A., Baumgardner J.R., 1996. The effect of depth-dependent viscosity on the planform of mantle convection. Nature, 379 (6564), 436–438.

Bunge H.-P., Richards M.A., Baumgardner J.R., 1997. A sensitivity study of three-dimensional spherical mantle convection at 10 8 Rayleigh number: Effects of depth-dependent viscosity, heating mode, and an endothermic phase change. J. Geophys. Res. Solid Earth, 102 (B6), 11991–12007.

Burstedde C., Stadler G., Alisic L., Wilcox L.C., Tan E., Gurnis M., Ghattas O., 2013. Large-scale adaptive mantle convection simulation. Geophys. J. Int., 192 (3), 889–906.

Chambat F., Ricard Y., Valette B., 2010. Flattening of the Earth: Further from hydrostaticity than previously estimated. Geophys. J. Int., 183 (2), 727–732.

Clenshaw C.W., 1955. A note on the summation of Chebyshev series. Math. Comput., 9 (51), 118–120.

Colli L., Bunge H.P., Oeser J., 2020. Impact of model inconsistencies on reconstructions of past mantle flow obtained using the adjoint method. Geophys. J. Int., 221 (1), 617–639.

Colli L., Ghelichkhan S., Bunge H.-P., 2016. On the ratio of dynamic topography and gravity anomalies in a dynamic Earth. Geophys. Res. Lett., 43 (6), 2510–2516.

Colli L., Ghelichkhan S., Bunge H.-P., Oeser J., 2018. Retrodictions of Mid Paleogene mantle flow and dynamic topography in the Atlantic region from compressible high resolution adjoint mantle convection models: Sensitivity to deep mantle viscosity and tomographic input model. Gondwana Res., 53, 252–272.

Condon E.U., Shortley G.H., 1935. The Theory of Atomic Spectra. Cambridge University Press, Cambridge.

Conrad C.P., Gurnis M., 2003. Seismic tomography, surface uplift, and the breakup of Gondwanaland: Integrating mantle convection backwards in time. Geochemistry, Geophys. Geosystems, 4 (3).

Coonen J.T., 1980. An Implementation Guide to a Proposed Standard for Floating-Point Arithmetic. Computer (Long. Beach. Calif)., 13 (1), 68–79.

Davies D.R., Goes S., Davies J., Schuberth B.S.A., Bunge H.-P., Ritsema J., 2012. Reconciling dynamic and seismic models of Earth's lower mantle: The dominant role of thermal heterogeneity. Earth Planet. Sci. Lett., 353-354 (0), 253–269.

Driscoll J.R., Healy D.M., 1994. Computing Fourier Transforms and Convolutions on the 2-Sphere. Adv. Appl. Math., 15 (2), 202–250.

Dziewonski A.M., Anderson D.L., 1981. Preliminary reference Earth model. Phys. Earth Planet. Inter., 25 (4), 297–356.

Fichtner A., Bunge H.-P., Igel H., 2006a. The adjoint method in seismology - I. Theory. Phys. Earth Planet. Inter., 157 (1-2), 86–104.

Fichtner A., Bunge H.-P., Igel H., 2006b. The adjoint method in seismology - II. Applications: traveltimes and sensitivity functionals. Phys. Earth Planet. Inter., 157 (1-2), 105–123.

Fichtner A., 2011. Full Seismic Waveform Modelling and Inversion. Advances in Geophysical and Environmental Mechanics and Mathematics. Springer Berlin Heidelberg, Berlin, Heidelberg.

Fletcher R., Reeves C.M., 1964. Function minimization by conjugate gradients. Comput. J., 7 (2), 149–154.

Foerste C., Flechtner F., Stubenvoll R., Rothacher M., Kusche J., Neumayer H.K., Biancale R., Lemoine J., Barthelmes F., Bruinsma S., Koenig R., Dahle C., 2008. A new global combined high-resolution GRACE-based gravity field model of the GFZ-GRGS cooperation. In AGU Fall Meet. Abstr., volume 2008, pp. G13A–0626.

Forte A.M., Peltier W.R., 1987. Plate tectonics and aspherical Earth structure: the importance of poloidal- toroidal coupling. J. Geophys. Res., 92 (B5), 3645–3679.

Forte A.M., Quéré S., Moucha R., Simmons N.A., Grand S.P., Mitrovica J.X., Rowley D.B., 2010. Joint seismic-geodynamic-mineral physical modelling of African geodynamics: A reconciliation of deep-mantle convection with surface geophysical constraints. Earth Planet. Sci. Lett., 295 (3-4), 329–341.

Fournier A., Hulot G., Jault D., Kuang W., Tangborn A., Gillet N., Canet E., Aubert J., Lhuillier F., 2010. An introduction to data assimilation and predictability in geomagnetism. Space Sci. Rev., 155 (1-4), 247–291.

Freeden W., 2001. A General Construction Principle of Wavelets. Min. Sky, pp. 53–70.

Freeden W., Gervens T., Schreiner M., 1998. Constructive Approximation on the Sphere (With Applications to Geomathematics). Oxford Science Publication, Clarendon Press.

Freeden W., Maier T., Zimmermann S., 2003. A survey on wavelet methods for (geo) applications. Rev. Matemática Complut., 16 (1).

Freeden W., Michel V., 2004. Multiscale Potential Theory. Birkhäuser Boston, Boston, MA.

Gantmacher F.R., 1960. The theory of matrices. 1 (1960). Chelsea Publishing Company, New York.

Gauss C.F., 1814. Methodus nova integralium valores per approximationem inveniendi. Königliche Gesellschaft der Wissenschaften, Göttingen.

Gauss C.F., 1839. Allgemeine Theorie des Erdmagnetismus, Resultate aus den Beobachtungen des Magnetischen Vereins im Jahre 1838. Sci. Mem. Sel. from Trans. Foreign Acad. Learn. Soc. from Foreign Journals, pp. 184–251.

Gerya T.V., Yuen D.A., 2003. Characteristics-based marker-in-cell method with conservative finite-differences schemes for modeling geological flows with strongly variable transport properties. Phys. Earth Planet. Inter., 140 (4), 293–318.

Ghelichkhan S., Bunge H.-P., 2018. The adjoint equations for thermochemical compressible mantle convection: derivation and verification by twin experiments. Proc. R. Soc. A Math. Phys. Eng. Sci., 474 (2220), 20180329.

Ghelichkhan S., Bunge H.-P., 2016. The compressible adjoint equations in geodynamics: derivation and numerical assessment. GEM - Int. J. Geomathematics, 7 (1), 1–30.

Glatzmaier G.A., 1988. Numerical simulations of mantle convection: Time-dependent, three-dimensional, compressible, spherical shell. Geophys. Astrophys. Fluid Dyn., 43 (2), 223–264.

Gmeiner B., Gradl T., Gaspar F., Rüde U., 2013. Optimization of the multigrid-convergence rate on semi-structured meshes by local Fourier analysis. Comput. Math. with Appl., 65 (4), 694–711.

Gmeiner B., Huber M., John L., Rüde U., Wohlmuth B., 2016. A quantitative performance study for Stokes solvers at the extreme scale. J. Comput. Sci., 17 (3), 509–521.

Gmeiner B., Rüde U., Stengel H., Waluga C., Wohlmuth B., 2015. Towards Textbook Efficiency for Parallel Multigrid. Numer. Math. Theory, Methods Appl., 8 (1), 22–46.

Grand S.P., van der Hilst R., Widiyantoro S., 1997. High resolution global tomography : a snapshot of convection in the Earth. Geol. Soc. Am. TODAY, 7 (4), 1–7.

Gronwall T.H., 1914. On the Degree of Convergence of Laplace's Series. Trans. Am. Math. Soc., 15 (1), 1.

Gurnis M., Turner M., Zahirovic S., DiCaprio L., Spasojevic S., Müller R.D., Boyden J., Seton M., Manea V.C., Bower D.J., 2012. Plate tectonic reconstructions with continuously closing plates. Comput. Geosci., 38 (1), 35–42.

Hadamard J., 1902. Sur les problèmes aux dérivées partielles et leur signification physique. Princet. Univ. Bull., 13 (49-52), 28.

Hager B.H., 1984. Subducted slabs and the geoid: Constraints on mantle rheology and flow. J. Geophys. Res. Solid Earth, 89 (B7), 6003–6015.

Hager B.H., O'Connell R.J., 1978. Subduction zone dip angles and flow driven by plate motion. Tectonophysics, 50 (2-3), 111–133.

Hager B.H., O'Connell R.J., 1979. Kinematic models of large-scale flow in the Earth's mantle. J. Geophys. Res., 84 (B3), 1031.

Hager B.H., O'Connell R.J., 1981. A simple global model of plate dynamics and mantle convection. J. Geophys. Res. Solid Earth, 86 (B6), 4843–4867.

Hager B.H., Richards M.A., 1989. Long-Wavelength Variations in Earth's Geoid: Physical Models and Dynamical Implications. Philos. Trans. R. Soc. A Math. Phys. Eng. Sci., 328 (1599), 309–327.

Healy D., Rockmore D., Kostelec P., Moore S., 2003. FFTs for the 2-Sphere-Improvements and Variations. J. Fourier Anal. Appl., 9 (4), 341–385.

Heine C., Müller R.D., Steinberger B., DiCaprio L., 2010. Integrating deep Earth dynamics in paleogeographic reconstructions of Australia. Tectonophysics, 483 (1-2), 135–150.

Heiskanen W.A., Moritz H., 1967. Physical geodesy. Freeman and Company, San Francisco.

Heuser H., 1981. Lehrbuch der Analysis, Teil 2. Vieweg + Teubner, Wiesbaden.

Heuser H., 1986. Funktionalanalysis. Teubner, Stuttgart.

Hobson E.W., 1955. The Theory of Spherical and Ellipsoidal Harmonics. Chelsea Pub Co., New York.

Holmes S.A., Featherstone W.E., 2002. A unified approach to the Clenshaw summation and the recursive computation of very high degree and order normalised associated Legendre functions. J. Geod., 76 (5), 279–299.

Horbach A., 2008. Analysis of the Cosmic Microwave Background Observed by WMAP. Diploma Thesis, TU Kaiserslautern.

Horbach A., Bunge H.-P., Oeser J., 2014. The adjoint method in geodynamics: derivation from a general operator formulation and application to the initial condition problem in a high resolution mantle circulation model. GEM - Int. J. Geomathematics, 5 (2), 163–194.

Horbach A., Mohr M., Bunge H.-P., 2020. A semi-analytic accuracy benchmark for Stokes flow in 3-D spherical mantle convection codes. GEM - Int. J. Geomathematics, 11 (1), 1.

Iaffaldano G., Bunge H.-P., Bücker M., 2007. Mountain belt growth inferred from histories of past plate convergence: A new tectonic inverse problem. Earth Planet. Sci. Lett., 260 (3-4), 516–523.

Ismail-Zadeh A., Schubert G., Tsepelev I., Korotkii A., 2004. Inverse problem of thermal convection: Numerical approach and application to mantle plume restoration. Phys. Earth Planet. Inter., 145 (1-4), 99–114.

Ivory J., 1824. On the figure requisite to maintain the equilibrium of a homogeneous fluid mass that revolves upon an axis. Philos. Trans. R. Soc. London, 114, 85–150.

Jackson D., 1912. On the Degree of Convergence of the Development of a Continuous Function According to Legendre's Polynomials. Trans. Am. Math. Soc., 13 (3), 305.

Jacobi C.G.J., 1826. Ueber Gauß neue Methode, die Werthe der Integrale näherungsweise zu finden. J. für die reine und Angew. Math. (Crelles Journal), (1), 301–308.

Jacobi C.G.J., 1827. Ueber eine besondere Gattung algebraischer Functionen, die aus der Entwicklung der Function (1-2xz+z^2)^1/2 entstehen. J. für die reine und Angew. Math. (Crelles Journal), (2), 223–226.

Jarvis G.T., Mckenzie D.P., 1980. Convection in a compressible fluid with infinite Prandtl number. J. Fluid Mech., 96 (3), 515–583.

Jordan T.H., 1978. Composition and development of the continental tectosphere. Nature, 274 (5671), 544–548.

Kameyama M., Ichikawa H., Miyauchi A., 2013. A linear stability analysis on the onset of thermal convection of a fluid with strongly temperature-dependent viscosity in a spherical shell. Theor. Comput. Fluid Dyn., 27 (1-2), 21–40.

van Keken P.E., King S.D., Schmeling H., Christensen U.R., Neumeister D., Doin M.-P., 1997. A comparison of methods for the modeling of thermochemical convection. J. Geophys. Res., 102 (B10), 22477–22495.

Kohl N., Thönnes D., Drzisga D., Bartuschat D., Rüde U., 2019. The HyTeG finite-element software framework for scalable multigrid solvers. Int. J. Parallel, Emergent Distrib. Syst., 34 (5), 477–496.

Kress R., 2014. Linear Integral Equations, volume 82 of Applied Mathematical Sciences. Springer New York, New York, NY.

Landau L., Lifshitz E., 1959. Course of theorical physics, V.6 Fluid Mechanics. Pergamon Press.

Legendre A.-M., 1785. Recherches sur l'attraction des spheroides homogenes. L'Académie R. Des Sci., 10, 411–435.

Lemoine F.G., Smith D.E., Kunz L., Smith R., Pavlis E.C., Pavlis N.K., Klosko S.M., Chinn D.S., Torrence M.H., Williamson R.G., Cox C.M., Rachlin K.E., Wang Y.M., Kenyon S.C., Salman R., Trimmer R., Rapp R.H., Nerem R.S., 1997. The Development of the NASA GSFC and NIMA Geopotential Model EGM96. January 2016, pp. 461–469.

Li K., Jackson A., Livermore P.W., 2011. Variational data assimilation for the initial-value dynamo problem. Phys. Rev. E - Stat. Nonlinear, Soft Matter Phys., 84 (5), 1–16.

Liu L., Gurnis M., 2008. Constraining Dynamic Properties of Mantle 2 3.1 Need for Assimilation of Time-Dependent Data in Real Problems. 113 (April), 1–17.

Love A.E.H., 1911. Some Problems of Geodynamics. Dover, New York.

Luther A., 2007. Vector Field Approximation on Regular Surfaces in Terms of Outer Harmonic Representations. PhD Thesis, TU Kaiserslautern.

Mayer C., 2003. Wavelet Modelling of Ionospheric Currents and Induced Magnetic Fields From Satellite Data. PhD Thesis, TU Kaiserslautern.

Mayer C., 2007. Lecture Notes in Geomathematics. TU Kaiserslautern.

McEwen J.D., Wiaux Y., 2011. A Novel Sampling Theorem on the Sphere. IEEE Trans. Signal Process., 59 (12), 5876–5887.

McNamara A.K., Zhong S., 2005. Thermochemical structures beneath Africa and the Pacific Ocean. Nature, 437 (7062), 1136–1139.

Menemenlis D., Wunsch C., 1997. Linearization of an oceanic general circulation model for data assimilation and climate studies. J. Atmos. Ocean. Technol., 14 (6), 1420–1443.

Michel V., 2013. Lectures on Constructive Approximation. Birkhäuser Boston, Boston.

Mitrovica J.X., Forte A.M., 2004. A new inference of mantle viscosity based upon joint inversion of convection and glacial isostatic adjustment data. Earth Planet. Sci. Lett., 225 (1-2), 177–189.

Moucha R., Forte A.M., Mitrovica J.X., Rowley D.B., Quéré S., Simmons N.A., Grand S.P., 2008a. Dynamic topography and long-term sea-level variations: There is no such thing as a stable continental platform. Earth Planet. Sci. Lett., 271 (1-4), 101–108.

Moucha R., Forte A.M., Rowley D.B., Mitrovica J.X., Simmons N.A., Grand S.P., 2008b. Mantle convection and the recent evolution of the Colorado Plateau and the Rio Grande Rift valley. Geology, 36 (6), 439.

Müller R.D., Sdrolias M., Gaina C., Roest W.R., 2008. Age, spreading rates, and spreading asymmetry of the world's ocean crust. Geochemistry, Geophys. Geosystems, 9 (4), 1–19.

Munk W.H., MacDonald G.J.F., 1960. The Rotation of the Earth. A geophysical discussion. Cambridge University Press, New York.

Murnaghan F.D., 1944. The Compressibility of Media under Extreme Pressures. Proc. Natl. Acad. Sci., 30 (9), 244–247.

Nakiboglu S.M., 1982. Hydrostatic theory of the Earth and its mechanical implications. Phys. Earth Planet. Inter., 28 (4), 302–311.

Nataf H.C., Ricard Y., 1996. 3SMAC: An a priori tomographic model of the upper mantle based on geophysical modeling. Phys. Earth Planet. Inter., 95 (1-2), 101–122.

Neumann F.E., 1838. Über eine neue Eigenschaft der Laplaceschen Yˆ(n) und ihre Anwendung zur analytischen Darstellung derjenigen Phanomene, welche Functionen der geographischen Lange und Breite sind. Astron. Nachrichten, 15 (21), 313–324.

Oeser J., Bunge H.-P., Mohr M., 2006. Cluster Design in the Earth Sciences: TETHYS. In M. Gerndt, D. Kranzlmüller (editors), High Perform. Comput. Commun. - Second Int. Conf. HPCC 2006, Munich, Ger., volume 4208 of Lecture Notes in Computer Science, pp. 31–40. Springer, Berlin.

Panasyuk S.V., Hager B.H., Forte A.M., 1996. Understanding the effects of mantle compressibility on geoid kernels. Geophys. J. Int., 124 (1), 121–133.

Parsons B., Daly S., 1983. The relationship between surface topography, gravity anomalies, and temperature structure of convection. J. Geophys. Res., 88 (B2), 1129.

Paul M.K., 1978. Recurrence relations for integrals of Associated Legendre functions. Bull. Géodésique, 52 (3), 177–190.

Paulson A., Richards M.A., 2009. On the resolution of radial viscosity structure in modelling long-wavelength postglacial rebound data. Geophys. J. Int., 179 (3), 1516–1526.

Paulson A., Zhong S., Wahr J., 2007. Inference of mantle viscosity from GRACE and relative sea level data. Geophys. J. Int., 171 (2), 497–508.

Pekeris C.L., 1935. Thermal convection in the interior of the Earth. Geophys. J. Int., 3, 343–367.

Piazzoni A.S., Steinle-Neumann G., Bunge H.-P., Dolejš D., 2007. A mineralogical model for density and elasticity of the Earth's mantle. Geochemistry, Geophys. Geosystems, 8 (11), n/a–n/a.

Popov I.Y., Lobanov I.S., Popov S.I., Popov A.I., Gerya T.V., 2014. Practical analytical solutions for benchmarking of 2-D and 3-D geodynamic Stokes problems with variable viscosity. Solid Earth, 5 (1), 461–476.

Ricard Y., Fleitout L., Froidevaux C., 1984. Geoid heights and lithospheric stresses for a dynamic Earth. Ann. Geophys., 2 (3), 267–286.

Richards M.A., Engebretson D.C., 1992. Large-scale mantle convection and the history of subduction. Nature, 355 (6359), 437–440.

Richards M.A., Hager B.H., 1984. Geoid anomalies in a dynamic Earth. J. Geophys. Res., 89 (7), 5987–6002.

Richards M.A., Yang W.-S., Baumgardner J.R., Bunge H.-P., 2001. Role of a low-viscosity zone in stabilizing plate tectonics: Implications for comparative terrestrial planetology. Geochemistry, Geophys. Geosystems, 2 (8).

Rodrigues O., 1816. Memoires sur l'attraction des sphéroides. Corresp. sur l'École Impériale Polytech., 3 (3), 361–385.

Rudi J., Ghattas O., Malossi A.C.I., Isaac T., Stadler G., Gurnis M., Staar P.W.J., Ineichen Y., Bekas C., Curioni A., 2015. An extreme-scale implicit solver for complex PDEs. In Proc. Int. Conf. High Perform. Comput. Networking, Storage Anal., SC '15, pp. 1–12. ACM Press, New York, USA.

Schaber K., Bunge H.-P., Schuberth B.S.A., Malservisi R., Horbach A., 2009. Stability of the rotation axis in high-resolution mantle circulation models: Weak polar wander despite strong core heating. Geochemistry, Geophys. Geosystems, 10 (11).

Schuberth B.S.A., Bunge H.-P., Steinle-Neumann G., Moder C., Oeser J., 2009a. Thermal versus elastic heterogeneity in high-resolution mantle circulation models with pyrolite composition: High plume excess temperatures in the lowermost mantle. Geochemistry, Geophys. Geosystems, 10 (1).

Schuberth B.S.A., Bunge H.-P., Ritsema J., 2009b. Tomographic filtering of high-resolution mantle circulation models: Can seismic heterogeneity be explained by temperature alone? Geochemistry, Geophys. Geosystems, 10 (5).

Schuberth B.S.A., Zaroli C., Nolet G., 2012. Synthetic seismograms for a synthetic Earth: long-period P- and S-wave traveltime variations can be explained by temperature alone. Geophys. J. Int., 188 (3), 1393–1412.

Serrin J., 1959. Mathematical Principles of Classical Fluid Mechanics. Handb. der Phys., VIII, 125–263.

Seton M., Müller R., Zahirovic S., Gaina C., Torsvik T.H., Shephard G., Talsma A., Gurnis M., Turner M., Maus S., Chandler M., 2012. Global continental and ocean basin reconstructions since 200Ma. Earth-Science Rev., 113 (3-4), 212–270.

Sneeuw N., 1994. Global spherical harmonic analysis by least-squares and numerical quadrature methods in historical perspective. Geophys. J. Int., 118 (3), 707–716.

Spasojevic S., Liu L., Gurnis M., 2009. Adjoint models of mantle convection with seismic, plate motion, and stratigraphic constraints: North America since the Late Cretaceous. Geochemistry, Geophys. Geosystems, 10 (5).

Steinberger B., O'Connell R.J., 1997. Changes of the Earth's rotation axis owing to advection of mantle density heterogeneities.

Steinberger B., O'Connell R.J., 1998. Advection of plumes in mantle flow: implications for hotspot motion, mantle viscosity and plume distribution. Geophys. J. Int., 132 (2), 412–434.

Steinle-Neumann G., Stixrude L., Cohen R.E., Gülseren O., 2001. Elasticity of iron at the temperature of the Earth's inner core. Nature, 413 (6851), 57–60.

Tackley P.J., 2012. Dynamics and evolution of the deep mantle resulting from thermal, chemical, phase and melting effects. Earth-Science Rev., 110 (1-4), 1–25.

Takeuchi H., Hasegawa Y., 1965. Viscosity Distribution within the Earth. Geophys. J. Int., 9 (5), 503–508.

Talagrand O., Courtier P., 1987. Variational assimilation of meteorological observations with the adjoint vorticity equation. I: Theory. Q. J. R. Meteorol. Soc., 113 (478), 1311–1328.

Tarantola A., 1984. Linearized inversion of seismic reflection data. Geophys. Prospect., 32 (6), 998–1015.

Thalhammer M., Ricard Y., Le Stunff Y., Rummel R., Ilk K., 1996. Application of Spaceborne Gravimetry to Research on the Interior of the Earth.

Tromp J., Tape C., Liu Q., 2005. Seismic tomography, adjoint methods, time reversal and banana-doughnut kernels. Geophys. J. Int., 160 (1), 195–216.

Vynnytska L., Bunge H.-P., 2015. Restoring past mantle convection structure through fluid dynamic inverse theory: regularisation through surface velocity boundary conditions. GEM - Int. J. Geomathematics, 6 (1), 83–100.

Weismüller J., 2016. Development and application of high performance software for mantle convection modeling. PhD Thesis, Ludwig-Maximilians-Universität München, Fakultät für Geowissenschaften.

Weismüller J., Gmeiner B., Ghelichkhan S., Huber M., John L., Wohlmuth B., Rüde U., Bunge H.-P., 2015. Fast asthenosphere motion in high-resolution global mantle flow models. Geophys. Res. Lett., 42 (18), 7429–7435.

Wermer J., 1974. Potential Theory. Advances in Geophysical and Environmental Mechanics and Mathematics. Springer Berlin Heidelberg, Berlin, Heidelberg.

Zhang Z., Stixrude L., Brodholt J., 2013. Elastic properties of MgSiO3-perovskite under lower mantle conditions and the composition of the deep Earth. Earth Planet. Sci. Lett., 379, 1–12.

Zhong S., Liu X., 2016. The long-wavelength mantle structure and dynamics and implications for large-scale tectonics and volcanism in the Phanerozoic. Gondwana Res., 29 (1), 83–104.

Zhong S., McNamara A., Tan E., Moresi L., Gurnis M., 2008. A benchmark study on mantle convection in a 3-D spherical shell using CitcomS. Geochemistry, Geophys. Geosystems, 9 (10).

Acknowledgements

There is no question about where my first and most cordial thanks go to. I thank you, Peter, for your unconditional support throughout these numerous years. When I started my PhD I had no idea about geophysics at all. Some people might argue that this is still the case - which probably is partially true - but at least I have gained a lot of experience over these years and most of my current knowledge is based on our various extensive discussions. Especially in times of the rising adjoints, we spent an uncountable number of hours in your office discussing the results. That is the essence of science, right? At least it felt like that.
I am sure to have disappointed you when I decided to leave the scientific world behind me right in the middle of my PhD. But you always accepted this decision in a very professional manner and even continued to support me during the following couple of years when I was away from the institute and trapped in a world where life just felt so mundane. Even in those times, your support has not reduced even though there were periods where I probably was not the most reliable person on Earth - to express it in a positive way ... The amount of my gratitude towards your unconditional support can not be measured any more in a traditional (and/or mathematical) way. Thank you for everything, for being my mentor and especially now, for giving me the opportunity to this 'comeback'!

And when talking about comeback, I have to explain that approximately two years ago, the idea of quitting my job in industry without having a backup and trying to develop again into a scientific direction evolved in the back of my head like a virus. During this time I had a lot of fruitful and deep conversations with a friend of mine, Tobi, who supported me a lot and deeply encouraged me to proceed in the way I intended to at this time. I want to thank you a lot for this. I am not sure if I were in the current situation without your words.

The basis of my mathematical education was mainly formed by one person. Now almost 17 years ago (half of my life), in 2003 I took my first maths class at the Technical University of Kaiserslautern. 'Analysis I', lectured by Volker Michel. Where 'Lineare Algebra' always left some strange, uncomfortable feeling in my stomach, the lecture by Volker already got me in the first moment. During my studies, our paths have crossed a couple of times, I even became your last Diploma student in Kaiserslautern and up until now, your excellence in teaching and mentoring and your commitment to mathematical details is something I am admiring and permanently aiming at. From you I learned to be persistent and to question everything until it is entirely understood. Now I know that this is a real gift ... and a curse ... but there is no alternative.

Since the gravitational field has played an important role in my thesis, already from the first weeks of my PhD there was a close connection to the Institute of Astronomical and Physical Geodesy at the TUM. Thank you, Reiner Rummel and Roland Pail for always welcoming me in a very cordial way. It is very helpful to discuss scientific topics with very experienced scientists from a different institute. There is little more intriguing than leaving your personal 'bubble' from time to time. Needless to say that it has also always been a personal pleasure and honour! Furthermore, for two years, I had the opportunity to co-lecture the "Introduction to Earth System Science" with Reiner Rummel. This turned out to be one of the most significant and challenging experiences in my early scientific career. When a mathematician has to talk about geophysics ...

When talking about mathematicians ... it is always good to have a 'partner in crime'. So, thank you, Marcus, for keeping the mathematics flag up high at the institute! Always when I had the impression that nobody understands me, I knew where I could go ... and in particular I am very thankful that we have shared a lot of teaching experiences over the years. I really learned a lot from you and besides, it was always fun discussing about exercises, exams, grades and stuff ... :)

When it comes to IT, I have no clue what I am doing at all. So thanks a lot, Jens, for always coping with my total ignorance, honestly. I always tried to destroy as little as possible ... and thank you for regularly extending my account even if I was not at the institute any more and only checked my geophysics mailbox once a year or even less ...

Now after a total of almost 12 years after the start of my PhD and 6 net years at the institute, a lot of people have crossed my path. So probably, I will forget to mention a couple of names here, please don't be mad at me. When writing this section, I was thinking about my various office mates I had during these years ... and I am still not sure if I can recall everybody. But ok, let's give it a try, in chronological order: Andreas Fichtner, Christoph Moder, Moritz Bernauer, Thomas Chust, Roberta Esposito, Lorenzo Colli, Eva Eibl, Jens Weismüller, Sophie Roud, Tobias Megies, Sandra Ostner and - last but not least - Max Moorkamp :)

Ok, now, besides the usual 'I also thank everybody else at the institute, especially everyone in the *[insert your division here]* group, I decided to pick up a few nice little stories that are still present in my memory.

Well, the first person I met at the institute was Heiner Igel. Probably people don't know but originally, I applied for a PhD position in seismology. I still remember the situation where I showed you how I prepared for my initial talk that I had to give in the process of my application. You basically told me to change everything ... The reason why finally, I didn't end up in seismology but in geodynamics was the at first glance insignificant decision that I did not take the stairs but the elevator at the 4th floor when I was already on my way home on that certain day. This 'small step' changed the line of my entire upcoming life, since here I just accidentally bumped into Peter and he invited me to accompany him to a talk by his diploma student, Katrin Schaber, who referred about geoids ... as you have probably noticed when reading through this work, this topic somehow seemed to have fascinated me. Sometimes life takes strange routes and has a very nice sense of humour, I guess ... each small step you take (even literally) can make a huge difference.
In the end, the person that went into the position that I originally applied for, was a guy called Christian Pelties. We actually have become good friends and I especially thank you for a great time we spent together at AGU in 2009. Brilliant times, especially when suddenly the roof opened ... (sorry, he is the only person that will get this) ... ;)

Why I stayed at the institute and not gave up everything during the first weeks, solely was due to my first office mate, some guy called Andreas Fichtner. In my opinion, he is the most intelligent person on Earth and additionally one of the nicest and most friendly persons I have ever met. At the beginning, I was just unable to cope with the whole situation. As a mathematician I could not find any entrance to the geophysical world and was completely lost, no idea what I was doing here. With time, Andreas' attitude of being very calm and always supportive basically took my initial fear away. You always gave me the feeling of being welcome and you never gave me the impression that you were bothered by the questions I had. And those were a lot and probably most of them stupid ... thank you for being a friend! :)
I will always remember the evening where in 2013, we were at the SIAM conference and wanted to have dinner together at 'Olive Garden'. So, we drove to the address but were absolutely unable to find the spot, it was quite strange and confusing ... until we noticed that we were in the wrong city(!) (am I actually allowed to tell this to people?). We ended up at a very dubious Indian place (and found the real Olive Garden two days later ;)) .....

I cordially apologise to Alan Schiemenz who was present at probably the most embarrassing moment during my PhD. When we were at a conference in Iceland, I was responsible for him being left alone and get lost during one of the social trips we were doing there with the whole conference group. Our bus had an unscheduled stop somewhere in Reykjavik and it was unclear when we can proceed. So, at some point, Alan told me that he leaves the bus to find a restroom somewhere in the near area and in case that we will proceed with our tour during his absence, it would be very nice of me to prevent the bus driver from just driving away ... Well, I am completely unsure what happened inside my brain afterwards but at some point, the bus continued the trip and it took me about 20 minutes to notice that Alan is not in his spot and suddenly a cold shiver ran across my whole body ... Well, we reconvened in the evening and I already apologised a lot but now, you get my apology also in an official written format ... ;)

I thank Simon Stähler for probably the funniest moment during my time as a PhD student when we were driving with the orange bus, on our way back from a conference in Zürich, and both suddenly started singing out loud to a Roxette song that was aired in the radio (I am 99% sure it was 'The Big L.'). When turning my head to the back seats after a while, some professors had kind of a strange facial expression. Still today, I cannot figure out the reasons for that ...

I thank Sia Ghelichkhan first for sharing a common passion for Pink Floyd and second, for having followed my footsteps (and overtaken them) in a very professional and inspiring way. I could not be prouder.

And I thank you, Berta, for your permanent support during the last couple of weeks. You prevented me from going completely crazy in this strange time of parallel thesis writing and Corona confinement. Thank you for everything! :)

THE E...

... oh wait ... I am sorry, I cannot finish without cudos to my family! So, first of all I thank Martin G. for being my best friend and always unconditionally supporting me in literally everything I do! My dad Ottokar and his partner Edith, my mum Gabi and her husband Martin W., all of you for always being there for me when I need you. But my greatest thanks go to my brother Simon and my sister Laura, you both are the best and without you, I would be a much emptier person.

THE END.